frontiers | Research Topics

Pharmacokinetic differences of drugs and their regulatory mechanisms under dual status including normal and diseased organism

Edited by
Zipeng Gong, Ling Ye, Guo Ma, Kaustubh Kulkarni and Yan-Fang Xian

Published in
Frontiers in Pharmacology

ISSN 1664-8714
ISBN 978-2-83251-099-5
DOI 10.3389/978-2-83251-099-5

About Frontiers

Frontiers is more than just an open access publisher of scholarly articles: it is a pioneering approach to the world of academia, radically improving the way scholarly research is managed. The grand vision of Frontiers is a world where all people have an equal opportunity to seek, share and generate knowledge. Frontiers provides immediate and permanent online open access to all its publications, but this alone is not enough to realize our grand goals.

Frontiers journal series

The Frontiers journal series is a multi-tier and interdisciplinary set of open-access, online journals, promising a paradigm shift from the current review, selection and dissemination processes in academic publishing. All Frontiers journals are driven by researchers for researchers; therefore, they constitute a service to the scholarly community. At the same time, the *Frontiers journal series* operates on a revolutionary invention, the tiered publishing system, initially addressing specific communities of scholars, and gradually climbing up to broader public understanding, thus serving the interests of the lay society, too.

Dedication to quality

Each Frontiers article is a landmark of the highest quality, thanks to genuinely collaborative interactions between authors and review editors, who include some of the world's best academicians. Research must be certified by peers before entering a stream of knowledge that may eventually reach the public - and shape society; therefore, Frontiers only applies the most rigorous and unbiased reviews. Frontiers revolutionizes research publishing by freely delivering the most outstanding research, evaluated with no bias from both the academic and social point of view. By applying the most advanced information technologies, Frontiers is catapulting scholarly publishing into a new generation.

What are Frontiers Research Topics?

Frontiers Research Topics are very popular trademarks of the *Frontiers journals series*: they are collections of at least ten articles, all centered on a particular subject. With their unique mix of varied contributions from Original Research to Review Articles, Frontiers Research Topics unify the most influential researchers, the latest key findings and historical advances in a hot research area.

Find out more on how to host your own Frontiers Research Topic or contribute to one as an author by contacting the Frontiers editorial office: frontiersin.org/about/contact

Pharmacokinetic differences of drugs and their regulatory mechanisms under dual status including normal and diseased organism

Topic editors

Zipeng Gong — Guizhou Medical University, China
Ling Ye — Southern Medical University, China
Guo Ma — Fudan University, China
Kaustubh Kulkarni — Blueprint Medicines, United States
Yan-Fang Xian — The Chinese University of Hong Kong, China

Citation

Gong, Z., Ye, L., Ma, G., Kulkarni, K., Xian, Y.-F., eds. (2023). *Pharmacokinetic differences of drugs and their regulatory mechanisms under dual status including normal and diseased organism*. Lausanne: Frontiers Media SA.
doi: 10.3389/978-2-83251-099-5

Table of contents

05 Editorial: Pharmacokinetic differences of drugs and their regulatory mechanisms under dual status including normal and diseased organism
Zipeng Gong, Jie Zhou, Ling Ye, Guo Ma, Yanfang Xian and Kaustubh Kulkarni

08 Compatibility of Fuzi and Ginseng Significantly Increase the Exposure of Aconitines
Ze-Yan Chen, Xu-Ya Wei, Zi-Dong Qiu, Yun Huang, Ting Tan, Yu-Lin Feng, Juan Guo, Guang-Hong Cui, Lu-Qi Huang and Chang-Jiang-Sheng Lai

20 *In Silico* Screening and Validation of PDGFRA Inhibitors Enhancing Radioiodine Sensitivity in Thyroid Cancer
Xuefei Yu, Xuhang Zhu, Lizhuo Zhang, Jiang-Jiang Qin, Chunlai Feng and Qinglin Li

32 Integrating Network Pharmacology and Metabolomics to Elucidate the Mechanism of Action of Huang Qin Decoction for Treament of Diabetic Liver Injury
Xiaomin Xu, Cheng Fang, Yu Wang, Fang Lu and Shumin Liu

45 Antidiabetic Effect of Rehmanniae Radix Based on Regulation of TRPV1 and SCD1
Ye Liu, Ruizheng Zhu, Bei Liu, Wuqing Wang, Ping Yang, Zhonglian Cao, Xiaolei Yang, Wandi Du, Qing Yang, Jingru Liang, Jiarong Hu and Guo Ma

64 Evaluation of Untargeted Metabolomic Strategy for the Discovery of Biomarker of Breast Cancer
Xujun Ruan, Yan Wang, Lirong Zhou, Qiuling Zheng, Haiping Hao and Dandan He

73 JBP485, A Dual Inhibitor of Organic Anion Transporters (OATs) and Renal Dehydropeptidase-I (DHP-I), Protects Against Imipenem-Induced Nephrotoxicity
Chong Wang, Changyuan Wang, Jingjing Wu, Qiang Meng, Huan Jin, Huijun Sun, Taiichi Kaku, Jing Chen, Xiaokui Huo and Kexin Liu

85 Effects of Huangqi Liuyi Decoction in the Treatment of Diabetic Nephropathy and Tissue Distribution Difference of its Six Active Constituents Between Normal and Diabetic Nephropathy Mouse Models
Qun Wang, Ya Shi, Zengguang Wu, Xinli Song, Jinfang Luo, Hong Yang, Xiaolan Chen and Xingde Liu

105 Better Bioactivity, Cerebral Metabolism and Pharmacokinetics of Natural Medicine and Its Advanced Version
Jiaxi Xie, Cailing Zhong, Tingting Wang, Dan He, Luyang Lu, Jie Yang, Ziyi Yuan and Jingqing Zhang

120 Pharmacokinetic Study of Four Major Bioactive Components of Liandan Xiaoyan Formula in Ulcerative Colitis and Control Rats Using UPLC-MS/MS
Kaihui Zhang, Zenghui Lu, Qian Wang, Fangle Liu, Meiqi Wang, Chaozhan Lin and Chenchen Zhu

129 Pharmacokinetics and Main Metabolites of Anwulignan in Mice
Cong Chen, Yanbo Feng, Han Li, Hao Lin, Shu Jing, He Li, Chunmei Wang, Jianguang Chen and Jinghui Sun

142 Midazolam Ameliorates Acute Liver Injury Induced by Carbon Tetrachloride *via* Enhancing Nrf2 Signaling Pathway
Yongyan Zhang, Yadi Zhu, Ying Li, Feng Ji, Guangbo Ge and Hua Xu

154 Comparative Pharmacokinetics of Three Bioactive Diterpenoids of *Rabdosia serra* Extract in Normal and Con A-Induced Liver Injury Rats Using UPLC-MS/MS
Fangle Liu, Yun Zeng, Pengyu Dai, Kaiwen Huang, Kaihui Zhang, Tao Tao, Meiqi Wang, Chenchen Zhu and Chaozhan Lin

164 Evaluation of Herb–Drug Interaction Between Danshen and Rivaroxaban in Rat and Human Liver Microsomes
Xu Wang, Jingjing Fa, Yuanjin Zhang, Shengbo Huang, Jie Liu, Junqing Gao, Lina Xing, Zongjun Liu and Xin Wang

173 Population Pharmacokinetics and Pharmacodynamics of Isoniazid and its Metabolite Acetylisoniazid in Chinese Population
Bing Chen, Hao-Qiang Shi, Meihua Rose Feng, Xi-Han Wang, Xiao-Mei Cao and Wei-Min Cai

186 Metabonomic analysis of abnormal sphingolipid metabolism in rheumatoid arthritis synovial fibroblasts in hypoxia microenvironment and intervention of geniposide
Jiang-Tao Ke, Heng Zhang, Yan-Hong Bu, Pei-Rong Gan, Fang-Yuan Chen, Xin-Tong Dong, Yan Wang and Hong Wu

201 Application of traditional Chinese medicine in film drug delivery system
Qianhang Li, Feng Luo, Pingnan Jiang, Chenxi Feng, Feifei He, Lina Dong, Delin Xu and Junhua Shi

frontiers | Frontiers in Pharmacology

TYPE Editorial
PUBLISHED 12 December 2022
DOI 10.3389/fphar.2022.1063434

OPEN ACCESS

EDITED AND REVIEWED BY
Lin-Lin Chen,
Hubei University of Chinese Medicine, China

*CORRESPONDENCE
Zipeng Gong,
gzp4012607@126.com

SPECIALTY SECTION
This article was submitted to Drug Metabolism and Transport, a section of the journal Frontiers in Pharmacology

RECEIVED 07 October 2022
ACCEPTED 05 December 2022
PUBLISHED 12 December 2022

CITATION
Gong Z, Zhou J, Ye L, Ma G, Xian Y and Kulkarni K (2022), Editorial: Pharmacokinetic differences of drugs and their regulatory mechanisms under dual status including normal and diseased organism.
Front. Pharmacol. 13:1063434.
doi: 10.3389/fphar.2022.1063434

Editorial: Pharmacokinetic differences of drugs and their regulatory mechanisms under dual status including normal and diseased organism

Zipeng Gong[1,2,3]*, Jie Zhou[1], Ling Ye[4], Guo Ma[5], Yanfang Xian[6] and Kaustubh Kulkarni[7]

[1]State Key Laboratory of Functions and Applications of Medicinal Plants, Guizhou Provincial Key Laboratory of Pharmaceutics, School of Pharmacy, Guizhou Medical University, Guiyang, China, [2]Key Laboratory of Basic Pharmacology of Ministry of Education, Zunyi Medical University, Zunyi, China, [3]Guizhou Provincial Engineering Research Center for the Development and Application of Ethnic Medicine and TCM, Guizhou Medical University, Guiyang, China, [4]NMPA Key Laboratory for Research and Evaluation of Drug Metabolism, Guangdong Provincial Key Laboratory of New Drug Screening, School of Pharmaceutical Sciences, Southern Medical University, Guangzhou, China, [5]School of Pharmacy, Fudan University, Shanghai, China, [6]School of Chinese Medicine, Faculty of Medicine, The Chinese University of Hong Kong, Hong Kong Special Administrative Region, Hong Kong, Hong Kong SAR, China, [7]Boundless Bio Inc., San Diego, CA, United States

KEYWORDS

dual status, pharmacokinetic differences, drug metabolizing enzymes, transporters, nuclear receptors, pharmacokinetic-pharmacodynamic model

Editorial on the Research Topic
Pharmacokinetic differences of drugs and their regulatory mechanisms under dual status including normal and diseased organism

Dual status includes healthy state and pathological state. Pharmacokinetics (PKs) is a quantitative study of drug dynamic changes including the process of absorption, distribution, metabolism and excretion (ADME). In the course of innovative drug development, PK study is as important as pharmacodynamic and toxicological research in evaluating new drugs, which also plays a vital role in reducing the risks of new drug development existing in preclinical and clinical study. However, it is irrational that the current preclinical PK data largely come from healthy animals. Firstly, given that drugs are largely taken by patients, they are the ultimate consumers of drugs. Secondly, pathological body could lead to the change of drug metabolizing enzymes, drug transporters and intestinal microflora, which bring about the change of ADME of drugs and have adverse effect of the use of drugs in clinic. Therefore, carrying out the PK studies under pathological conditions would be more significant and closely related to clinic (Gong, et al., 2015).

Generally speaking, compared with the healthy state, the function of some tissues and organs of the body in the pathological conditions might be harmed. For instance, the

expression and activity of drug metabolizing enzymes (DMEs) under diabetic conditions were altered (Chen et al., 2018). When the body was under rheumatoid arthritis conditions, the kind and amount of intestinal microflora were changed (Tajik et al., 2020). Moreover, the gap between adjacent intestinal cells in patients with irritable bowel syndrome was increased (Gong et al.). It is worth mentioning that these changes would alter the PK behavior of the drug. Also, inflammation could regulate the change of DMEs and transporters, and its possible mechanisms might largely involve inflammation-related signaling pathways and nuclear receptors, etc. (Wu et al., 2019), which led to changes in the PK process, efficacy and toxicity of drug. Therefore, the research on regulatory mechanisms causing the PK differences of drugs between healthy state and pathological state should be paid more attentions.

In the main frame of this Research Topic, 16 contributions have been published including but not limited to the following subjects: comparative PKs between healthy state and pathological state, the changes in the expression and activity of DMEs and transporters in pathological state, ADME/toxicity of drug and their regulatory mechanisms, drug-drug interactions mediated by nuclear receptors, DMEs and transporters based on the way of PKs, transcriptomics and metabolomics.

Wang et al. found that the Huangqi Liuyi decoction extract could be effective for improving the renal function when treating diabetic nephropathy. Moreover, the tissue distribution of six active ingredients in Huangqi Liuyi decoction extract could be affected by diabetic nephropathy state.

Zhang et al. compared PK of four main active ingredients of Liandan Xiaoyan Formula(LXF) in healthy and ulcerative colitis rats. They found that main active ingredients of LXF in the ulcerative colitis group had higher exposure than in the healthy group.

Liu et al. investigated the PK differences of three active diterpenoids of *Rabdosia serra* extract in healthy and concanavalin A-induced liver injury rats. They found that the PK process of three active diterpenoids in *Rabdosia serra* extract was influenced by liver injury.

Chen et al. found the compatibility of fuzi and ginseng could improve markedly the *in vivo* exposure of five bioactive ingredients including mesaconitine, benzoylaconitine, benzoylmesaconitine, benzoylhypaconitine, and songorine.

Chen et al. studied the PK behavior and main metabolites of anwulignan in mice. They identified that anwulignan might undergo the enterohepatic circulation. Moreover, seven metabolites were also identified, which mainly involved the demethylation, hydroxylation, dehydroxylation, and demethoxylation.

Liu et al. found *Rehmanniae Radix* (RR) displayed an inspiring antidiabetic effect by reducing the fasting blood glucose and insulin resistance, upregulating the mRNA and protein expressions of transient receptor potential vanilloid 1 (TRPV1), and downregulating mRNA expression of stearoyl-CoA desaturase 1 (SCD1). Therefore, induction of TRPV1 and inhibition of SCD1 by RR was possibly one of its antidiabetic mechanisms.

Ruan et al. evaluated an untargeted metabolomic strategy for discovering the biomarker of breast cancer, which would lay a base for discovering biomarker and investigating the disease mechanism.

Xu et al. elucidated the mechanism of Huang Qin decoction for treating the diabetic liver injury by the combination of metabolomics and network pharmacology.

Ke et al. investigated the mechanism of action of geniposide treating rheumatoid arthritis (RA) by employing metabonomic analysis of abnormal sphingolipid metabolism in RA synovial fibroblasts in hypoxia microenvironment and intervention of geniposide.

Chen et al. established a population pharmacokinetic (PPK) model for isoniazid (INH) and its major metabolite acetylisoniazid (AcINH) in healthy Chinese participants and tuberculosis patients and assessed the role of the NAT2 genotype on the transformation of INH to AcINH.

Wang et al. found JBP485 could save from imipenem nephrotoxicity in rabbits and human kidney 2 cells by increasing imipenem stability and reducing its intracellular accumulation by simultaneously inhibiting the renal organic anion transporters and dehydropeptidase-I.

Zhang et al. demonstrated that midazolam could ameliorate CCl_4-induced acute liver injury and oxidative stress *via* activating the nuclear-factor erythroid 2-related factor 2 (Nrf2) signaling pathway.

Wang et al. evaluated the interaction of danshen and rivaroxaban by using the liver microsomes of rat and human. They found Danshen tablet could inhibit the metabolism of rivaroxaban due to its lipid-soluble ingredients such as dihydrotanshinone I could strongly inhibit the activity of CYP3A and CYP2J.

Xie et al. summarized the solubility, permeability, molecular structure and molecular weight characteristics of various natural medicines that affected cerebral metabolism (NMCs), and reviewed drug delivery systems that enhanced the PK and pharmacodynamic features of NMCs. Moreover, the structure-based *in vivo* metabolic reactions regulated by DMEs and metabolites of NMCs were also reviewed.

Yu et al. identified new platelet-derived growth factor receptor α (PDGFRA) inhibitors from traditional Chinese medicine (TCM) *in silico* and verified their effects of targeting PDGFRA and radioiodine uptake, which could provide a potential drug lead for developing a new radioiodine-refractory thyroid cancer therapy.

Li et al. summarized the research progress of the material composition, pharmaceutical production, clinical application and pharmacology mechanism of various TCM film agents, which might provide a comprehensive reference for further development and utilization of TCM film agents.

Therefore, given that drugs are largely taken by patients, the current topic focused mainly on PK differences of drugs and their regulatory mechanisms under healthy state and pathological state, which could provide reference and ideas for individualized safety and effective drug use, and optimizing the drug evaluation system based on disease states.

Author contributions

All authors listed have made a substantial, direct, and intellectual contribution to the work and approved it for publication.

Funding

This study was funded by the National Natural Science Foundation of China (Nos. 81860734 and 82160789), Guiyang Science and Technology Bureau ((2021) 43-12), the Excellent Young Talents Plan of Guizhou Medical University (No. 2022-104), the project of Key Laboratory of Basic Pharmacology of Ministry of Education, Zunyi Medicial University (KY (2022) 394) and University Student Innovation and Entrepreneurship Project of Guizhou Province (No. S202110660046).

Acknowledgments

We would like to express our gratitude to all the authors for the valuable sharing of their findings and opinions.

Conflicts of interest

KK was employed by the Company Boundless Bio Inc.

The remaining authors declare that the research was conducted in the absence of any commercial or financial relationships that could be construed as a potential conflict of interest.

Publisher's note

References

Chen, F., Li, D. Y., Zhang, B., Sun, J. Y., Sun, F., Ji, X., et al. (2018). Alterations of drug-metabolizing enzymes and transporters under diabetic conditions: What is the potential clinical significance? *Drug Metab. Rev.* 50 (3), 369–397. doi:10.1080/03602532.2018.1497645

Gong, Z. P., Chen, Y., Zhang, R. J., Yang, Q., and Zhu, X. X. (2015). Advances on pharmacokinetics of traditional Chinese medicine under disease states. *China. J. Chin. Mat. Med.* 40 (02), 169–173. doi:10.4268/cjcmm20150202

Gong, Z. P., Yang, Q., Wang, Y. J., Weng, X. G., Li, Y., Dong, Y., et al. (2022). Pharmacokinetic differences of wuji pill components in normal and chronic visceral hypersensitivity irritable bowel syndrome rats attributable to changes in tight junction and transporters. *Front. Pharmacol.* 13, 948678. doi:10.3389/fphar.2022.948678

Tajik, N., Frech, M., Schulz, O., Schälter, F., Lucas, S., Azizov, V., et al. (2020). Targeting zonulin and intestinal epithelial barrier function to prevent onset of arthritis. *Nat. Commun.* 11 (1), 1995. doi:10.1038/s41467-020-15831-7

Wu, K. C., and Lin, C. J. (2019). The regulation of drug-metabolizing enzymes and membrane transporters by inflammation: Evidences in inflammatory diseases and age-related disorders.fiammation: Evidences in infiammatory diseases and age-related disorders. *J. Food Drug Anal.* 27 (1), 48–59. doi:10.1016/j.jfda.2018.11.005

frontiers | Frontiers in Pharmacology

ORIGINAL RESEARCH
published: 26 April 2022
doi: 10.3389/fphar.2022.883898

Compatibility of Fuzi and Ginseng Significantly Increase the Exposure of Aconitines

Ze-Yan Chen[1,2†], Xu-Ya Wei[1,3†], Zi-Dong Qiu[1], Yun Huang[4], Ting Tan[3,5], Yu-Lin Feng[3,5], Juan Guo[1], Guang-Hong Cui[1], Lu-Qi Huang[1,2] and Chang-Jiang-Sheng Lai[1]**

[1]State Key Laboratory Breeding Base of Dao-di Herbs, National Resource Center for Chinese Materia Medica, China Academy of Chinese Medical Sciences, Beijing, China, [2]School of Traditional Chinese Medicine, Guangdong Pharmaceutical University, Guangzhou, China, [3]Jiangxi University of Traditional Chinese Medicine, Nanchang, China, [4]Pharmaceutical College, Hebei Medical University, Shijiazhuang, China, [5]The National Pharmaceutical Engineering Center for Solid Preparation in Chinese Herbal Medicine, Jiangxi University of Traditional Chinese Medicine, Nanchang, China

OPEN ACCESS

Edited by:
Zipeng Gong,
Guizhou Medical University, China

Reviewed by:
Caisheng Wu,
Xiamen University, China
Guo Ma,
Fudan University, China
Jiangeng Huang,
Huazhong University of Science and Technology, China

***Correspondence:**
Lu-Qi Huang
huangluqi01@126.com
Chang-Jiang-Sheng Lai
laichangjiang44@126.com

[†]These authors have contributed equally to this work

Specialty section:
This article was submitted to Drug Metabolism and Transport, a section of the journal Frontiers in Pharmacology

Received: 25 February 2022
Accepted: 05 April 2022
Published: 26 April 2022

Citation:
Chen Z-Y, Wei X-Y, Qiu Z-D, Huang Y, Tan T, Feng Y-L, Guo J, Cui G-H, Huang L-Q and Lai C-J-S (2022) Compatibility of Fuzi and Ginseng Significantly Increase the Exposure of Aconitines. Front. Pharmacol. 13:883898. doi: 10.3389/fphar.2022.883898

The herb-pair ginseng-Fuzi (the root of *Aconitum carmichaelii*) is the material basis of Shenfu prescriptions and is popular in traditional Chinese medicine for the treatment of heart failure, and even shock with severe-stage of COVID-19. A narrow therapeutic window of Fuzi may cause significant regional loss of property and life in clinics. Therefore, systemic elucidation of active components is crucial to improve the safety dose window of Shenfu oral prescriptions. A high performance liquid chromatography-mass spectrometry method was developed for quantification of 10 aconitines in SD rat plasma within 9 min. The limit of detection and the limit of quantification were below 0.032 ng/ml and 0.095 ng/ml, respectively. Furthermore, a systemic comparison with their pharmacokinetic characteristics after oral administration of a safe dosage of 2 g/kg of Fuzi and ginseng-Fuzi decoction for 24 h was conducted. Eight representative diester, monoester, and non-ester aconitines and two new active components (i.e., songorine and indaconitine) were all adopted to elucidating the differences of the pharmacokinetic parameters *in vivo*. The compatibility of Fuzi and ginseng could significantly increase the *in vivo* exposure of active components. The terminal elimination half-life and the area under the concentration-time curve of mesaconitine, benzoylaconitine, benzoylmesaconitine, benzoylhypaconitine, and songorine were all increased significantly. The hypaconitine, benzoylmesaconitine, and songorine were regarded as the main active components *in vivo*, which gave an effective clue for the development of new Shenfu oral prescriptions.

Keywords: Aconitum carmichaelii, ginseng, pharmacokinetics, aconitine, high performance liquid chromatography-mass spectrometry, COVID-19

1 INTRODUCTION

Toxic-efficient dual Chinese medicines have remarkable efficacy and certain toxicity or side effects. If used improperly, it will cause unavoidable toxic side effects, and even endanger patients' lives in serious cases (Wei et al., 2019). Due to the irreplaceability in the potent effects, toxic-efficient dual Chinese medicines are still widely used in clinics. The lateral root of *Aconitum carmichaelii* Debx (named Fuzi) is commonly used for the treatment of rheumatism, heart failure, and renal failure (Wang et al., 2007; Li et al., 2017a; Shuo et al., 2017; Chen et al., 2021). However, it often triggers

aconitine poisoning events due to a narrow therapeutic window (Singhuber et al., 2009; Huang et al., 2018; Qiu et al., 2021a). The main active components in Fuzi are aconitines, including diester alkaloids, i.e., aconitine, mesaconitine and hypaconitine, and monoester alkaloids, i.e., benzoylaconitine, benzoylmesaconitine, and benzoylhypaconitine (Qiu et al., 2021a; Qiu et al., 2021b). However, the diester alkaloids are considered to be the main toxic components for the cardiac and central nervous systems. The toxicity of diester alkaloids is 200–500 times and 2000–4,000 times of monoester alkaloids and non-ester alkaloids, i.e., aconine, mesaconine, and hypaconine, respectively (Liu et al., 2017). The cardiotoxicity target of diester alkaloids is the site 2 of sodium channel. Their cardiotoxicity mechanism is a large influx of Na^+ causes persistent malignant arrhythmias (Chan et al., 1994; Fu et al., 2006; Chen et al., 2013).

Compatibility has been often used to reduce toxicity and increase efficacy (Zhang et al., 2012; Zhang et al., 2013; Liu et al., 2014; Liu et al., 2017; Sun et al., 2018; Qiu et al., 2020a). The pharmacokinetic characterizations of herb-pairs Fuzi-Gancao (Zhang et al., 2013; Zhang H. et al., 2015), Fuzi-ginger (Peng et al., 2013; Zhang W. et al., 2015), Fuzi-Beimu (Yang et al., 2016; Xu et al., 2017), and ginseng-Fuzi (Shenfu) (Li Z. et al., 2015; Yang et al., 2018), and formula [e.g., Wutou Decoction (Dai et al., 2014), Sini Decoction (He et al., 2009; Zhang H. et al., 2015; Zhang W. et al., 2015; Zhou et al., 2019), Dahuang Fuzi Decoction (Liu et al., 2014; Li YX. et al., 2015; Li et al., 2017b), and Shenfu injectable powder (Zhang et al., 2008; Li Z. et al., 2015; Zhang et al., 2016)] have been elucidated (He et al., 2015; Chen et al., 2019; Wei et al., 2019). Currently, the pharmacokinetic studies of aconites were usually reported on Shenfu injection (Zhang et al., 2008; Zhang et al., 2016; Shen et al., 2021). There is no other relevant study with simultaneous quantification of three types of aconitines for oral preparations containing Fuzi-ginseng herb pair (Xu et al., 2020). Shenfu preparations have been commonly used in the treatment of heart failure, and even the shock patient of severe-stage COVID-19. In daily life, the oral drugs are easily accepted by patients and have a promising market prospect in the treatment of chronic heart failure. However, their narrow oral safety dose window makes it difficult to effectively balance cardiac efficacy and cardiotoxicity, resulting in extremely low market share and difficulty in applying new oral drugs. It is urgent to elucidate the *in vivo* active components and compatibility mechanism to develop new oral drugs further.

High performance liquid chromatography coupled with tandem mass spectrometry (HPLC-MS/MS) contains the advantages of high throughput, high sensitivity, and high

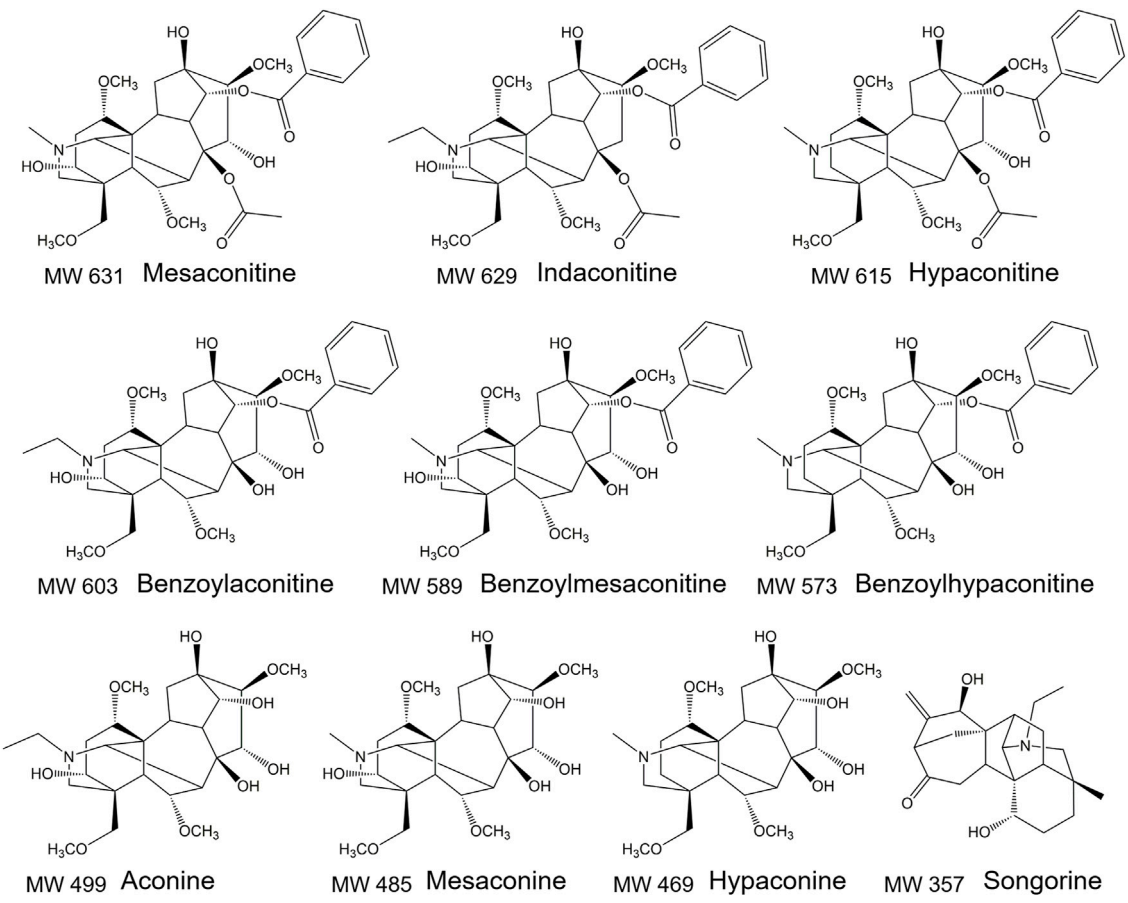

FIGURE 1 | The structure of 10 aconitines.

TABLE 1 | Ion pairs and the detailed parameters in MRM mode.

Components	Retention time (min)	Q1	Q3	Time (ms)	DP (V)	CE (V)
Aconine	0.70	500.1	450.4	25	100	48
Mesaconine	0.70	486.1	436.0	25	100	49
Hypaconine	0.70	470.2	438.4	25	120	44
Songorine	1.13	358.1	340.1	25	129	36
Benzoylmesaconitine	1.17	590.0	540.1	25	120	50
Benzoylaconitine	1.42	604.1	554.2	25	124	50
Berberine	1.54	336.0	320.1	25	115	41
Benzoylhypaconitine	1.58	574.1	542.0	25	120	45
Mesaconitine	2.96	632.4	572.1	25	120	47
Hypaconitine	3.44	616.1	556.2	25	80	44
Indaconitine	3.55	630.2	570.1	25	80	47

resolution for analysis of complex matrix samples (Garran et al., 2019). In this study, an HPLC-MS/MS method for quantification of 10 aconitines components with all three types of structure in rat plasma was developed (**Figure 1**). The method had a lower limit of detection (LOD) and limit of quantification (LOQ) than other methods (Zhang et al., 2014; Xu et al., 2020). The comparative pharmacokinetic study between Fuzi decoction with ginseng-Fuzi decoction was conducted to screen out the *in vivo* active components of Shenfu oral prescriptions. Moreover, the pharmacokinetic parameters of songorine and indaconitine were studied in Shenfu decoction for the first time. The aim is to lay the foundation for the scientific design of the prescription, dosage, and controlled active/toxic combinatorial components of Shenfu oral prescriptions.

2 EXPERIMENTAL

2.1 Materials and Reagents

Processed Aconitum (Heishunpian) was purchased from Sichuan, China. Ginseng was purchased from Tongrentang Chinese Medicine. The specimens were stored in the National Resource Center for Chinese Materia Medica, Chinese Academy of Chinese Medical Sciences. Berberine (internal standard) was purchased from ANPEL Laboratory Technologies (Shanghai) Inc. (Shanghai, China, purity >98%). Eight authentic components including mesaconitine, indaconitine, hypaconitine, benzoylaconitine, benzoylmesaconitine, benzoylhypaconitine, aconine, and songorine were supplied by Beijing Rongcheng Xinde Technology Development Co., Ltd. (Beijing, China, HPLC purity >98%). Another two authentic components including mesaconine and mesaconine were acquired from Chengdu Must Biotechnology Co., Ltd. (Chengdu, Sichuan, China). The purity of each component was >98%, as determined by HPLC analysis. Pure water was prepared from Mill-Q water purification system (Billerica, MA, United States). Methanol and acetonitrile (HPLC grade) were purchased from ThermoFisher Scientific (San Jose, CA, United States). Ammonium chloride (AR) was purchased from Aladdin Industrial Corporation (Shanghai, China).

2.2 Animals

Male Sprague-Dawley (SD) rats (n = 12) weighted 180–220 g were supplied by Laboratory Animal Science and Technology Center, Jiangxi University of Traditional Chinese Medicine (Nanchang, Jiangxi, China). Animals were housed under standard conditions for a week of adjustable feeding. All animal experiments were carried out according to the Guidelines for the Care and Use of Laboratory Animals and were approved by the Animal Ethics Committee of Jiangxi University of Traditional Chinese Medicine.

2.3 Preparation of Standard Solutions

A series of mixed working solutions at gradient concentrations were prepared by dissolving appropriate amounts of 10 aconitines with methanol and gradient dilution. The frozen plasma samples were thawed naturally at room temperature, 10 μL of mixed working solutions and 90 μL plasma were mixed and vortexed for 1 min with sufficient mixing. The 10 μL of internal standard solution (berberine, 500 ng/ml) and 300 μL of methanol were added. All samples were vortexed at 2,500 rpm for 3 min and centrifuged at 10,000 rpm for 10 min at 4°C. The supernatant was collected and was then dried under nitrogen at 40°C. The 100 μL of methanol was added to redissolve the residue. After vortexing for 1 min, the resolution was centrifuged at 14,000 rpm for 10 min at 4°C, and the supernatant was collected and stored at −20°C until analysis.

2.4 Sample Preparation

The 12.5 g of processed Fuzi powder were weighed and soaked for 30 min in water (1:10, *w*/*v*), then was decocted for 30 min. The filtrate through 8 layers of gauze was collected. The residues were re-decocted by 8 times of water for 30 min. The two filtrates were combined and concentrated by rotary evaporator at 40°C to 0.175 g/ml (in terms of Fuzi) of Fuzi extract was prepared, containing mesaconitine 0.03 μg/ml, indaconitine 0.12 μg/ml, hypaconitine 1.04 μg/ml, benzoylaconitine 10.16 μg/ml, benzoylmesaconitine 36.40 μg/ml, benzoylhypaconitine 14.28 μg/ml, aconine 2.04 μg/ml, mesaconine 6.02 μg/ml, hypaconine 2.74 μg/ml, songorine 9.04 μg/mL. As for Shenfu extract, the mass ratio

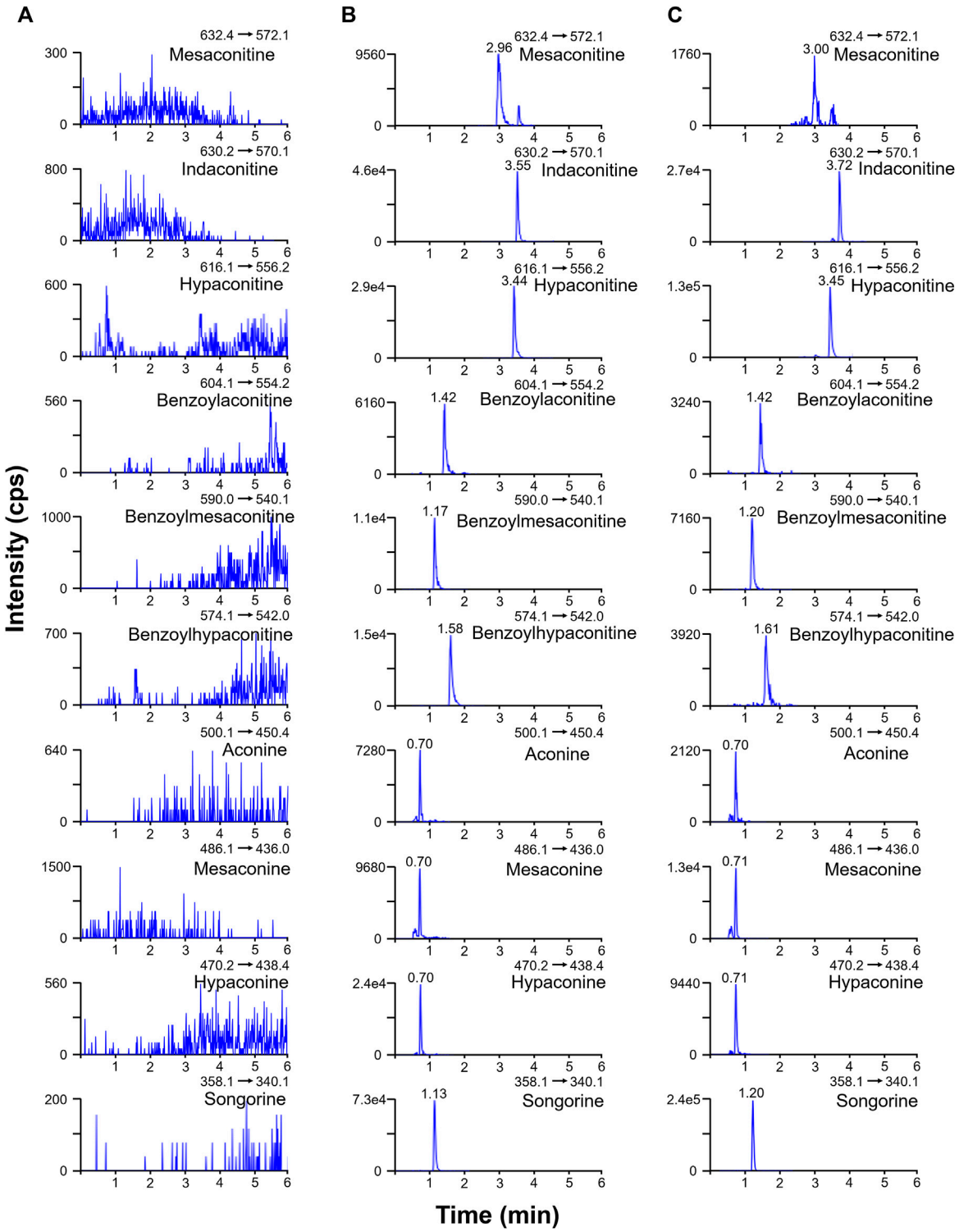

FIGURE 2 | Multiple reaction monitoring chromatograms of blank plasma **(A)**, spiked standard solution in blank plasma **(B)**, and the rat plasma sample at 45 min after oral administration of Fuzi **(C)**.

TABLE 2 | Linearity, LOD, and LOQ of target components.

Components	Calibration equation	R^2	Linearity range (ng/ml)	LOD (ng/ml)	LOQ (ng/ml)
Mesaconitine	$Y = 0.012X–3.44e^{-5}$	0.9974	0.0156–31.3	0.0020	0.0059
Indaconitine	$Y = 0.0271X+1.57e^{-4}$	0.9985	0.0625–31.3	0.0159	0.0477
Hypaconitine	$Y = 0.0171X+1.53e^{-3}$	0.9995	0.125–62.5	0.0318	0.0953
Benzoylaconitine	$Y = 0.00591X+0.14e^{-3}$	0.9930	0.0625–31.3	0.0079	0.0238
Benzoylmesaconitine	$Y = 0.00469X+5.87e^{-4}$	0.9962	0.0313–62.5	0.0040	0.0119
Benzoylhypaconitine	$Y = 0.0112X+4.74e^{-4}$	0.9960	0.0156–62.5	0.0020	0.0059
Aconine	$Y = 0.00317X–3.79e^{-5}$	0.9913	0.0625–7.81	0.0159	0.0477
Mesaconine	$Y = 0.00333X+8.12e^{-4}$	0.9964	0.0625–125	0.0079	0.0238
Hypaconine	$Y = 0.00835X+0.01e^{-1}$	0.9956	0.0625–31.3	0.0079	0.0238
Songorine	$Y = 0.0176X+6.58e^{-4}$	0.9956	0.0625–62.5	0.0079	0.0238

TABLE 3 | Precision of target compounds.

Compound	Spiked (ng/ml)	Inter-day precision			Intra-day precision		
		Mean (ng/ml)	RSD (%)	Accuracy (%)	Mean (ng/ml)	RSD (%)	Accuracy (%)
Mesaconitine	0.5	0.47	7.72	94.33	0.46	2.08	91.17
	2	2.17	6.40	108.50	2.00	2.76	99.83
	20	21.17	4.23	105.83	20.00	1.50	100.00
Indaconitine	0.5	0.57	2.32	113.28	0.57	0.34	114.80
	2	1.71	5.14	85.49	1.60	2.86	80.16
	20	16.73	5.54	83.66	15.90	2.86	79.49
Hypaconitine	0.5	0.59	8.11	118.36	0.59	0.79	117.74
	2	1.80	3.92	90.04	1.63	1.86	81.70
	20	19.41	5.75	97.05	18.83	0.61	94.15
Benzoylaconitine	0.5	0.47	7.75	94.09	0.48	4.61	95.84
	2	2.28	1.12	113.96	2.13	1.84	106.56
	20	21.08	8.41	105.38	20.77	1.32	103.84
Benzoylmesaconitine	0.5	0.58	2.26	115.31	0.57	4.18	113.31
	2	1.72	5.51	85.81	1.68	2.56	83.90
	20	20.23	7.15	101.14	18.33	3.98	91.67
Benzoylhypaconitine	0.5	0.45	2.94	90.00	0.42	3.88	84.50
	2	2.16	4.70	108.16	2.03	1.59	101.33
	20	21.89	5.20	109.44	20.95	0.71	104.75
Aconine	0.5	0.57	4.98	113.53	0.59	5.64	117.85
	2	1.86	12.01	92.89	1.62	3.52	81.15
	5	4.86	7.46	97.14	4.77	2.18	95.31
Mesaconine	0.5	0.61	16.76	122.50	0.56	3.36	111.83
	2	2.19	3.20	109.26	2.12	12.80	106.02
	20	21.33	4.92	106.67	21.20	4.72	106.00
Hypaconine	0.5	0.56	8.90	112.97	0.54	1.47	107.06
	2	2.20	9.06	110.02	1.94	2.84	96.85
	20	21.79	4.69	108.96	21.36	0.71	106.82
Songorine	0.5	0.43	4.62	86.50	0.43	0.34	85.33
	2	2.18	3.05	109.17	2.17	3.33	108.67
	20	21.87	2.68	109.33	22.03	1.46	110.17

of Fuzi and ginseng was 1:1. The other preparation steps were the same as those of Fuzi extract, containing 0.10 μg/ml of mesaconitine, 4.85 μg/ml of hypaconitine, 11.70 μg/ml of benzoylaconitine, 28.30 μg/ml of benzoylmesaconitine, 12.10 μg/ml of benzoylhypaconitine, 1.71 μg/ml of aconine, 5.31 μg/ml of mesaconine, 1.68 μg/ml of hypaconine, and 6.25 μg/ml of songorine. The quantification of alkaloids was performed according to our validated HPLC-MS/MS method. All extracts were stored at 4°C.

2.5 Liquid Chromatography With Tandem Mass Spectrometry Conditions

The Shimadzu LC-30AD (Kyoto, Japan) consisted of a binary pump and a sample manager was applied as the LC system. Gradient elution was performed on a Waters ACQUITY UPLC BEH C18 column (1.7 μm, 2.1 mm × 100 mm) protected by a Van Guard BEH C18 column (1.7 μm, 2.1 mm × 5 mm). The column temperature was maintained at 35°C. The experiment was carried out at a flow rate of 0.4 ml/min. The injection

TABLE 4 | Stability of target compounds.

Compound	Spiked ng/mL	Short-term		Long-term		3 times freeze-thaw	
		Mean ± SD (ng/ml)	RSD (%)	Mean ± SD (ng/ml)	RSD (%)	Mean ± SD (ng/ml)	RSD (%)
Mesaconitine	0.5	0.47 ± 0.04	7.63	0.46 ± 0.01	1.90	0.45 ± 0.01	2.11
	2	2.16 ± 0.15	6.98	2.01 ± 0.08	3.89	2.05 ± 0.08	3.70
	20	21.03 ± 1.02	4.86	20.13 ± 0.51	2.55	20.43 ± 0.38	1.85
Indaconitine	0.5	0.57 ± 0.01	0.92	0.57 ± 0.01	2.30	0.56 ± 0.01	1.97
	2	1.70 ± 0.10	5.92	1.61 ± 0.05	3.09	1.63 ± 0.07	4.07
	20	16.77 ± 0.90	5.34	15.86 ± 0.39	2.43	15.96 ± 0.41	2.58
Hypaconitine	0.5	0.59 ± 0.05	8.07	0.59 ± 0.01	1.41	0.58 ± 0.03	5.54
	2	1.78 ± 0.10	5.70	1.65 ± 0.06	3.64	1.72 ± 0.11	6.68
	20	19.44 ± 1.09	5.63	18.80 ± 0.13	0.70	18.75 ± 0.04	0.23
Benzoylaconitine	0.5	0.48 ± 0.02	4.95	0.47 ± 0.03	7.45	0.46 ± 0.02	4.41
	2	2.25 ± 0.08	3.42	2.16 ± 0.8	3.81	2.21 ± 0.11	4.94
	20	21.30 ± 1.67	7.85	20.55 ± 0.27	1.34	20.33 ± 0.53	2.60
Benzoylmesaconitine	0.5	0.58 ± 0.01	2.54	0.57 ± 0.02	4.15	0.58 ± 0.01	2.26
	2	1.73 ± 0.09	5.22	1.67 ± 0.04	2.25	1.65 ± 0.02	1.44
	20	19.92 ± 1.58	7.94	18.64 ± 1.25	6.72	18.99 ± 1.03	5.42
Benzoylhypaconitine	0.5	0.45 ± 0.01	3.22	0.42 ± 0.02	4.50	0.43 ± 0.02	4.73
	2	2.14 ± 0.13	6.02	2.05 ± 0.05	2.25	2.09 ± 0.03	1.54
	20	21.67 ± 1.29	5.97	21.16 ± 0.32	1.52	21.21 ± 0.27	1.26
Aconine	0.5	0.55 ± 0.04	6.75	0.55 ± 0.03	5.19	0.53 ± 0.02	3.54
	2	1.70 ± 0.11	6.65	1.73 ± 0.28	16.39	1.73 ± 0.24	13.63
	5	4.82 ± 0.36	7.49	4.72 ± 0.09	1.95	4.51 ± 0.18	4.02
Mesaconine	0.5	0.57 ± 0.07	13.05	0.59 ± 0.04	6.25	0.58 ± 0.10	18.00
	2	2.24 ± 0.11	4.83	2.15 ± 0.12	5.79	2.22 ± 0.04	1.88
	20	21.63 ± 1.16	5.36	20.90 ± 0.61	2.91	20.93 ± 0.55	2.63
Hypaconine	0.5	0.55 ± 0.05	8.89	0.55 ± 0.03	5.29	0.54 ± 0.04	7.17
	2	2.07 ± 0.12	5.66	2.07 ± 0.15	7.23	2.10 ± 0.26	12.32
	20	21.64 ± 1.05	4.85	21.52 ± 0.30	1.41	21.26 ± 0.53	2.50
Songorine	0.5	0.42 ± 0.01	2.45	0.44 ± 0.02	3.50	0.43 ± 0.02	4.69
	2	2.19 ± 0.07	3.20	2.17 ± 0.07	3.07	2.18 ± 0.08	3.57
	20	21.97 ± 0.67	3.03	21.93 ± 0.15	0.70	21.73 ± 0.47	2.17

volume was 2 μL. The mobile phase was acetonitrile (solvent B)—water (solvent A) containing 0.5 mM ammonium chloride. Gradient elution was performed as follow: 0–2 min 35% B, 2–4 min 35–85% B, 4–6 min 85–90% B, 6–7 min 90–100% B, 7–9 min 100% B, 9–9.5 min 100–35% B, and 9.5–12.5 min 35% B. QTRAP 4500 mass spectrometer (Applied Bio-systems, AB Sciex, United States) coupled with ESI source was employed in the MS/MS analysis. Mass spectrum parameters were set as follows: Curtain Gas = 35 psi, Collision Gas = Medium, IonSpray Voltage = 4500 V, Temperature = 550°C, and Gas1 = Gas2 = 55 psi. MRM mode was adopted to detect the target components and internal standard (50 ng/ml). The DP and CE were automatically optimized to enhance the intensity of ion pairs of all the target components. All samples were analyzed by LC-MS in positive ion mode.

2.6 Method Validation

2.6.1 Specificity

The specificity was investigated by comparing the chromatograms of blank rat plasma, corresponding spiked plasma, and rat plasma sample at 45 min after oral administration of Fuzi, to exclude the interference of endogenous substances and metabolites.

2.6.2 Linearity, Limit of Detection, and Limit of Quantification

For the calibration curve, the gradient dilution was used to obtain a series of solutions with gradient concentrations (0.001–125 ng/ml) for LC-MS analysis. The regression equation and correlation coefficient (R^2) were calculated using the concentration of the component as the horizontal coordinate (X, ng/mL) and the ratio of the integrated peak area of the component to the internal standard as the vertical coordinate (Y). The concentration was used as the LOD and the LOQ at the signal-to-noise ratio (S/N) equal to 3 and 10, respectively.

2.6.3 Precision and Stability

The QC samples of high, medium, and low concentrations were injected six times consecutively and replicated for three consecutive days, and the intra-day precision and precision were calculated and expressed as relative standard deviation (RSD). The stability assay of the high, medium, and low concentrations of mixed standards in plasma samples was conducted. All prepared samples were stored for 12 h at room temperature to evaluate their room temperature stability. As for freeze-thaw stability, the plasma samples were stored for 12 h at room temperature and then 12 h at −20°C, and repeated three times. The plasma samples of the long-term stability analysis

TABLE 5 | Recovery and matrix effect of PK method.

Compound	Spiked ng/mL	Recovery		Matrix effect	
		Mean (%)	RSD (%)	Mean (%)	RSD (%)
Mesaconitine	0.5	105.22	2.96	90.38	3.81
	2	104.61	4.49	87.66	4.92
	20	109.87	2.19	90.09	7.72
Indaconitine	0.5	101.55	4.56	97.81	8.15
	2	105.44	6.74	95.51	5.93
	20	110.96	3.15	97.29	7.00
Hypaconitine	0.5	109.50	3.08	106.81	3.93
	2	107.67	4.24	108.32	7.45
	20	109.67	2.17	86.04	7.05
Benzoylaconitine	0.5	111.88	9.46	95.65	3.69
	2	109.76	7.71	110.54	9.95
	20	106.18	2.43	97.94	8.38
Benzoylmesaconitine	0.5	103.44	4.52	83.35	2.12
	2	102.78	4.95	88.45	3.03
	20	108.75	4.82	109.16	5.42
Benzoylhypaconitine	0.5	107.03	2.10	90.72	0.84
	2	104.04	2.96	105.93	7.47
	20	105.69	2.93	94.86	5.77
Aconine	0.5	104.41	7.08	87.82	6.21
	2	106.76	4.91	105.70	13.84
	5	100.69	5.53	116.04	10.92
Mesaconine	0.5	101.67	10.84	110.47	14.64
	2	105.51	14.35	108.25	7.43
	20	109.49	7.67	108.84	9.95
Hypaconine	0.5	98.20	9.88	97.60	11.17
	2	100.90	8.22	83.20	7.74
	20	100.82	11.04	116.22	9.86
Songorine	0.5	83.24	12.37	87.25	4.35
	2	85.17	2.16	102.45	7.06
	20	95.18	1.75	93.01	7.81

should be stored for 15 days at −20°C. All samples were injected under the same conditions for LC-MS analysis and their mean concentration, standard deviation (SD), and RSD were calculated.

2.6.4 Recovery and Matrix Effect

The pre-extraction samples were prepared according to the preparation of standard solutions. The blank plasma was prepared with the same method, and then 10 μL of 500 ng/ml internal standard solution and 90 μL of mixed standard solution were added to redissolve the residue. These samples were recorded as post-extraction samples. All samples were analyzed by the same LC-MS conditions and the extraction recoveries were calculated according to **formula 1**.

$$\text{Extraction recovery } \% = \frac{A_{pre-extraction\ sample} / A_{internal\ standard}}{A_{post-extraction\ sample} / A_{internal\ standard}} \quad (1)$$

The mixed working solutions were prepared in methanol with high, medium, and low concentrations respectively and analyzed by the same LC-MS conditions. The matrix effect was calculated according to **formula 2**.

$$\text{Matrix effect } \% = \frac{A_{post-extraction\ sample} / A_{internal\ standard}}{A_{mixed\ solution} / A_{internal\ standard}} \quad (2)$$

2.7 Pharmacokinetics

Male SD rats were randomly divided into two groups of six rats each for Fuzi and Shenfu groups. The animals were acclimatized and fed for 7 days. Before the experiment, the animals fasted for 12 h without water. The animals were administered by the same dosage (equal to 2 g/kg of Fuzi). The blood was collected into heparinized tubes before (0 h), 0.25, 0.5, 0.75, 1, 1.5, 2.5, 4, 6, 8, 12, and 24 h after administration, and centrifuged at 4,000 rpm for 10 min at 4°C. 100 μL of supernatant was obtained and stored at −80°C before analysis. The corresponding peak area integration values were recorded. The concentration was calculated using the corresponding calibration equation.

2.8 Statistical Analysis

The drug concentration-time curve was plotted using time as the horizontal coordinate and the mean value of the blood concentration corresponding to each time point as the vertical coordinate. The relevant pharmacokinetic parameters, including terminal elimination half-life ($T_{1/2}$), area under the concentration-time curve ($AUC_{0\text{-}t}$), mean residence time ($MRT_{0\text{-}t}$), time to achieve maximum concentration (T_{max}), and maximum plasma concentration (C_{max}), were calculated using non-compartment analysis with DAS software and expressed as mean ± standard deviation. The relative bioavailability was calculated by **formula 3**. The comparison of the main

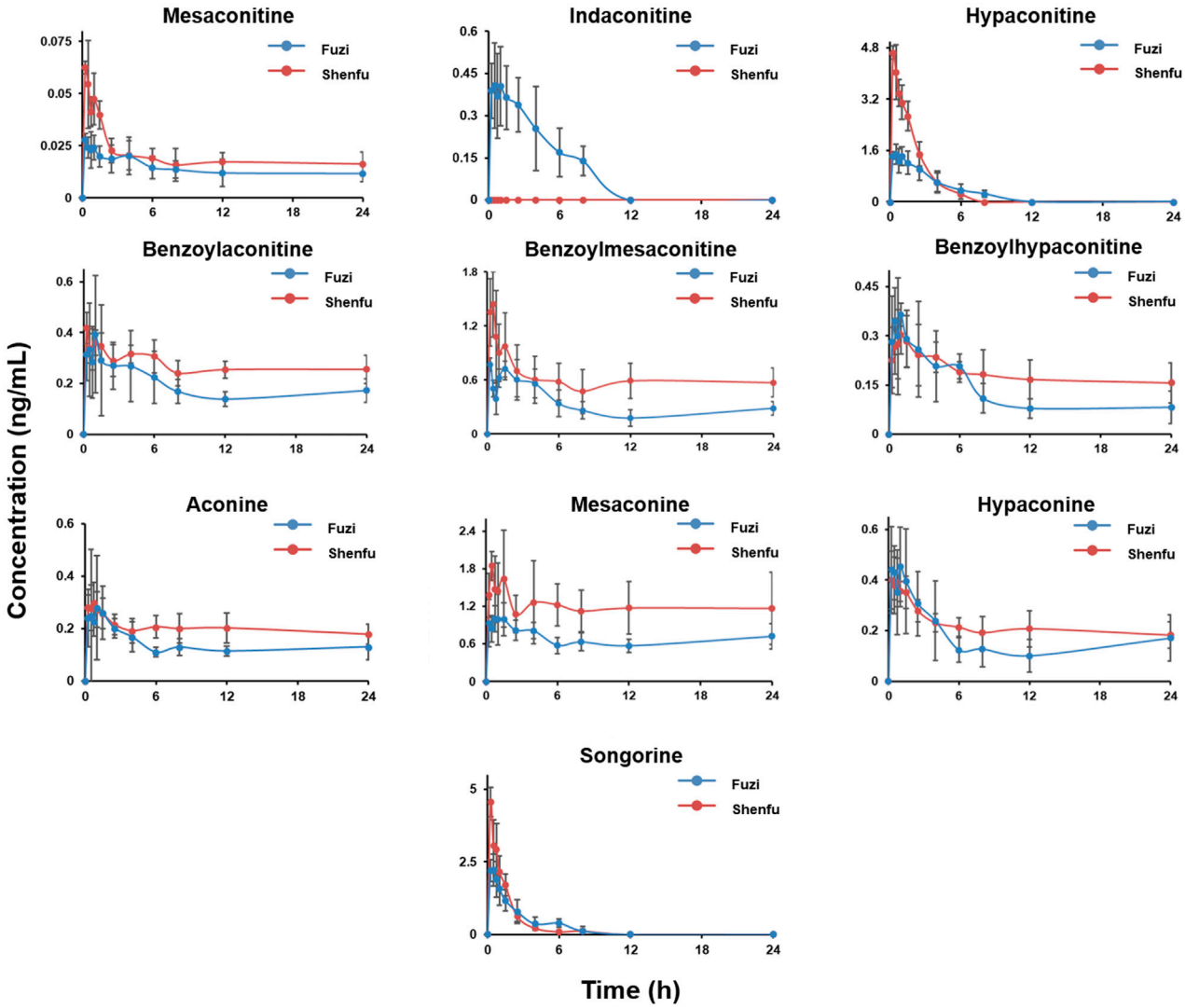

FIGURE 3 | The concentration-time profile of aconitines after oral administration of Fuzi and Shenfu. The dosage of Fuzi is all 2 g/kg in two groups.

pharmacokinetic parameters between the Fuzi group and the Shenfu group was performed by independent samples t-test with SPSS software.

$$Relative\ bioavailabilit\,y\,(\,F_{rel},\,\%) = \frac{AUC_{0-t,\,Shenfu}}{AUC_{0-t,\,Fuzi}} \qquad (3)$$

3 RESULT AND DISCUSSION

3.1 Optimization of High Performance Liquid Chromatography Coupled With Tandem Mass Spectrometry Conditions

The ion spray voltage (3.5–5.0 kV) and source temperature (350–550°C) were optimized in the positive ion mode to determine the mass spectrometry conditions in terms of the response intensity and noise intensity of the components. The final mass spectrometry conditions were determined as follows: positive ion mode Curtain Gas = 35 psi, Collision Gas = Medium, Ion Spray Voltage = 4500 V, Temperature = 550°C, Gas1 = Gas2 = 55 psi. The ESI-MS was injected at a flow rate of 7 μL/min and the optimized mass spectrometry conditions were used for the analysis. The collision energy (CE) and declustering potential (DP) were automatically optimized by the instrument. The final ion pairs and related parameters were determined as **Table 1**. The 0.5 mM ammonium chloride in the study had no significant inhibitory effect on aconitines with LOD below 0.03 ng/ml. Column temperatures were optimized at 30, 35, 40, and 45°C, and small differences were found. To avoid degradation of aconitines, which are easily decomposed by heat, during the analysis and resulting in reduced accuracy, 35°C was chosen as the analytical column temperature in this experiment and the

TABLE 6 | Comparison with the pharmacokinetic parameters of aconitines in Fuzi before and after compatibility of ginseng (mean ± SD, n = 6).

Components	Fuzi					Shenfu					Relative bioavailability/ (F_{rel}, %)
	$T_{1/2}$/h	AUC_{0-t}/(ng/mL·min)	MRT_{0-t}/(ng/mL·min)	T_{max}/h	C_{max}/(ng/ml)	$T_{1/2}$/h	AUC_{0-t}/(ng/mL·min)	MRT_{0-t}/(ng/mL·min)	T_{max}/h	C_{max}/(ng/ml)	
Mesaconitine	21.74 ± 3.85	0.33 ± 0.07	10.73 ± 1.29	0.50 ± 0.09	0.02 ± 0.00	89.71 ± 9.32***	0.46 ± 0.07**	10.58 ± 1.80	0.50 ± 0.07	0.05 ± 0.00	144.00 ± 35.83
Indaconitine	2.36 ± 0.35	2.29 ± 0.62	3.88 ± 0.58	0.50 ± 0.10	0.41 ± 0.15	-	-	-	-	-	-
Hypaconitine	2.07 ± 0.53	6.16 ± 0.64	3.29 ± 0.50	0.50 ± 0.10	1.48 ± 0.34	2.65 ± 0.50	8.93 ± 1.10***	1.94 ± 0.26**	0.50 ± 0.06	4.04 ± 0.16***	146.12 ± 22.30
Benzoylaconitine	9.28 ± 0.18	4.47 ± 0.54	10.79 ± 2.16	1.00 ± 0.07	0.39 ± 0.22	80.39 ± 16.01	6.43 ± 0.90**	11.59 ± 1.39	1.00 ± 0.12	0.37 ± 0.05	144.94 ± 23.37
Benzoylmesaconitine	6.48 ± 1.03	7.56 ± 0.91	10.02 ± 0.80	1.50 ± 0.21	0.83 ± 0.07	524.59 ± 99.67***	14.55 ± 3.64**	11.38 ± 1.71	0.50 ± 0.06***	1.44 ± 0.36**	195.96 ± 53.55
Benzoylhypaconitine	4.65 ± 0.65	3.11 ± 0.53	8.79 ± 1.41	1.00 ± 0.11	0.36 ± 0.03	32.55 ± 5.35***	4.42 ± 0.51**	10.91 ± 1.31*	1.00 ± 0.15	0.30 ± 0.05*	147.07 ± 37.80
Aconine	-	3.30 ± 0.43	11.05 ± 2.80	1.00 ± 0.04	0.28 ± 0.12	89.78 ± 14.78	4.78 ± 1.04*	11.49 ± 1.42	0.75 ± 0.08***	0.30 ± 0.07	147.42 ± 43.85
Mesaconine	124.13 ± 18.62	16.31 ± 2.61	11.74 ± 2.00	0.75 ± 0.09	1.00 ± 0.16	304.61 ± 57.87***	28.64 ± 3.44***	11.81 ± 1.65	0.50 ± 0.10**	1.85 ± 0.22***	177.17 ± 17.37
Hypaconine	18.31 ± 2.01	3.98 ± 1.35	10.61 ± 3.60	1.00 ± 0.12	0.45 ± 0.17	75.83 ± 13.64	5.15 ± 0.77	10.98 ± 2.74	0.75 ± 0.07**	0.39 ± 0.11	141.60 ± 47.45
Songorine	2.17 ± 0.31	5.56 ± 0.67	2.77 ± 0.66	0.50 ± 0.07	2.22 ± 0.53	2.56 ± 0.53	5.69 ± 0.71	2.00 ± 0.38*	0.50 ± 0.02	3.07 ± 0.33**	103.05 ± 20.96

*$p < 0.05$; **$p < 0.01$; ***$p < 0.001$.

sample tray temperature was set at 4°C. Ultimately, the 10 aconitines were all determined within 9 min (**Figure 2**).

3.2 Results of Method Validation

Representative chromatograms of blank rat plasma, corresponding spiked plasma, and plasma samples from rats 45 min after oral administration are shown in **Figure 2**, indicating good specificity and no interference from endogenous substances and metabolites in the experiment. In blank plasma, all 10 aconitines were not detected. The calibration curve of the target components exhibited good linearity in the range of 0.0156–125 ng/ml, with $R^2 > 0.99$ (**Table 2**). The LOD and LOQ of the target components were of 0.002–0.032 ng/ml and 0.006–0.095 ng/ml, respectively. For most components, the inter-day and intra-day precision with RSD were between 80 and 120% (**Table 3**) and were stable in short-term, long-term, and freeze-thaw experiments with RSD less than 10% (**Table 4**). The extraction recoveries and matrix effects for most components were in the range of 85–115% (**Table 5**), indicating that the pretreatment method met the requirements and the matrix had no significant effect on the target components. Generally, the quantification results were deemed accurate and reliable. Since its many measurement points of aconitine, a major diester alkaloid in raw Fuzi, were significantly below the lower limit of the linear calibration range of 0.125 ng/ml, it would be difficult to determine its concentration in real plasma samples. Therefore, the subsequent comparative pharmacokinetic study of aconitine was not carried out in this study.

3.3 Comparative Pharmacokinetic Study

As can be seen from **Figure 3**, in terms of the overall trend, a distinct peak shape is visible in both the Fuzi and Shenfu groups. In the plasma concentration-time curve of the diester alkaloids and monoester alkaloids, double peaks were evident (e.g., benzoylaconitine). This has been similar in other studies (Liu et al., 2014; Li et al., 2016; Zhang et al., 2020). This biabsorption phenomenon may come from multiple-sites absorption and enterohepatic circulation (Zhang et al., 2020). In Fuzi and Shenfu decoctions, the monoester alkaloids benzoylaconitine, benzoylmesaconitine, and benzoylhypaconitine were the main class of components. However, the monoester alkaloids, non-ester alkaloids, and hypaconitine were the main components *in vivo*. This compatibility had a significant decrease of *in vivo* exposure of an active diester alkaloid indaconitine (Yu et al., 2021). This may be because some components of ginseng prevent the dissolution of indaconitine in Shenfu decoction. The short T_{max} and $T_{1/2}$ of the aconitines (**Table 6**) exhibited the distinct characteristics of fast absorption and rapid elimination after oral administration of the extract of Fuzi (Song et al., 2015; Xu et al., 2017) and Shenfu. In contrast, the long $T_{1/2}$ of some components (e.g., benzoylmesaconitine in the Shenfu group) may be since half of the C_{max} had not yet been reached at the end of the 24 h experiment. It is noteworthy that in this study, the minor diester alkaloid yunaconitine was not detected in Fuzi and Shenfu decoctions and the rat plasma.

The minimum toxic doses of mesaconitine and hypaconitine in humans have been reported as 0.0035 and 0.0162 mg/kg, respectively (Qiu et al., 2020b), which can be converted to 21.88 and 101.25 μg/kg in rats (Huang et al., 2004). The doses of the two diester alkaloids in this experiment were 0.34 μg/kg for mesaconitine and 11.86 μg/kg for hypaconitine in Fuzi decoction, and 1.80 μg/kg for mesaconitine and 87.03 μg/kg for hypaconitine in Shenfu decoction. After the application of our developed toxicity prediction method (Qiu et al., 2020a; Qiu et al., 2020b), it was found that the *in vivo* holistic weighted toxicity (HWT) value was less than 1, indicating all alkaloids were below the minimum toxic doses. Therefore, the three diester alkaloids showed no toxicity but only medicinal effects under the present conditions. As **Table 6** shown, *in vivo* exposure of Fuzi and Shenfu groups, the hypaconitine and benzoylmesaconitine are representatively active components of the diester alkaloid and monoester alkaloid, respectively. As for compatibility, the mechanism of drug interactions is complicated. This study attempts to clarify these interactions between aconitines and ginsenosides. Comparing the drug concentration-time curves of Fuzi group and Shenfu group (**Figure 3**), it was found that in some alkaloids with higher absorption (e.g., hypaconitine and songorine), the Shenfu group decreased to plateau more quickly than the Fuzi group. However, their $AUC_{0\text{-t}}$ values of Shenfu groups (5.69 for songorine, 8.93 for hypaconitine) were higher than those of Fuzi group (5.56 for songorine, 6.16 for hypaconitine), indicating the hypaconitine and songorine in the Shenfu group was significantly faster than those of Fuzi group in the elimination phase. The main reason might be that the ginsenoside Rg_1 could promote absorption of aconitines (Xu et al., 2020) and up-regulate *in vivo* expression of CYP450 for accelerating the metabolism of hypaconitine and songorine (Li et al., 2019). The exposure concentrations of other aconitines were higher in Shenfu group, especially for the diester alkaloid (i.e., mesaconitine), monoester alkaloids (i.e., benzoylaconitine, benzoylmesaconitine, and benzoylhypaconitine) (He et al., 2015; Xie et al., 2021), and non-ester alkaloids (i.e., aconine and mesaconine). Their $T_{1/2}$ and $AUC_{0\text{-t}}$ would be significantly increased in Shenfu group (**Table 6**), which may be caused by the inhibitory of the P-glycoprotein (P-gp)-mediated aconitines efflux by *in vivo* metabolites of ginsenosides (Chen et al., 2009; Tang et al., 2012; Li et al., 2014). These phenomena were consistent with Xu's study (Xu et al., 2020). Among all exposed components, songorine, a non-ester alkaloid with good anti-arrhythmic effects (Dzhakhangirov et al., 1997; Khan et al., 2018) and cardioprotection efficacy (Li et al., 2021), showed a larger C_{max} within 1 h, which could effectively eliminate the potential cardiotoxicity of the diester alkaloids (e.g., mesaconitine and hypaconitine). In short, the compatibility of Fuzi and ginseng could significantly increase the *in vivo* exposure of the active ingredients.

4 CONCLUSION

An HPLC-MS-based method was developed for the quantification of 10 aconitines in rat plasma within 9 min, with the LOD of 0.002–0.032 ng/ml and LOQ of 0.006–0.095 ng/ml. A comparative pharmacokinetic study was conducted in SD rats orally administered with the Fuzi and Shenfu decoction. Under safe dosage, it was found that for most alkaloids, including diester type alkaloids (mesaconitine and hypaconitine) and monoester alkaloids (benzoylaconitine, benzoylmesaconitine, and benzoylhypaconitine), were exposed more in Shenfu group ($AUC_{0\text{-t}}$ were 0.46–14.55 ng/mlmin) than in Fuzi group ($AUC_{0\text{-t}}$ were 0.33–7.56 ng/mlmin). Except for the hypaconitine, other components were metabolized more slowly in Shenfu group than in Fuzi group. Therefore, the compatibility of Fuzi and ginseng could significantly increase the bioavailability (103.05–195.96%) and efficiency of active components *in vivo*. songorine containing a potential anti-cardiotoxicity ability showed a larger C_{max}. Ultimately, the hypaconitine, benzoylmesaconitine, and songorine could be considered as the main active components in Shenfu oral prescriptions. This study aims to achieve clinical "efficacy enhancement" and lay the foundation for the scientific design of new Shenfu oral prescriptions.

DATA AVAILABILITY STATEMENT

The original contributions presented in the study are included in the article/Supplementary Material, further inquiries can be directed to the corresponding authors.

ETHICS STATEMENT

The animal study was reviewed and approved by the experimental animal ethics committee of Jiangxi University of traditional Chinese Medicine.

AUTHOR CONTRIBUTIONS

C-J-SL and L-QH designed and supported the research. Z-YC, X-YW, Z-DQ, TT and Y-LF conducted the research. X-YW, Z-YC, YH, JG, G-HC and C-J-SL analyzed the data and wrote the manuscript. C-J-SL and L-QH had primary responsibility for the final content.

FUNDING

This work was supported by the National Natural Science Foundation of China (No. 82074012), the CACMS Innovation Fund (No. CI2021A05051), and the Fundamental Research Funds for the Central Public Welfare Research Institutes (No. ZZ13-YQ-090-C1).

REFERENCES

Chan, T. Y., Tomlinson, B., Tse, L. K., Chan, J. C., Chan, W. W., and Critchley, J. A. (1994). *Aconitine* Poisoning Due to Chinese Herbal Medicines: A Review. *Vet. Hum. Toxicol.* 36 (5), 452–455.

Chen, L., Yang, J., Davey, A. K., Chen, Y. X., Wang, J. P., and Liu, X. Q. (2009). Effects of Diammonium Glycyrrhizinate on the Pharmacokinetics of Aconitine in Rats and the Potential Mechanism. *Xenobiotica* 39 (12), 955–963. doi:10.3109/00498250903271997

Chen, L. L., Lai, C. J., Mao, L. Y., Yin, B. W., Tian, M., Jin, B. L., et al. (2021). Chemical Constituents in Different Parts of Seven Species of *Aconitum* Based on UHPLC-Q-TOF/MS. *J. Pharm. Biomed. Anal.* 193, 113713. doi:10.1016/j.jpba.2020.113713

Chen, R. C., Sun, G. B., Zhang, Q., Ye, Z. G., and Sun, X. B. (2013). Advances in Studies on Toxicity of Aconite. *Zhongguo Zhong Yao Za Zhi* 38 (8), 1126–1129.

Chen, Y., Liang, X. G., Liu, H. N., Xiong, Y. L., Sun, R. J., Yan, X. J., et al. (2019). Different Compatibility Ratio and Clinical Application of Shenfutang. *Chin. J. Exp. Tradit. Med. Form.* 25 (3), 220–225. doi:10.13422/j.cnki.syfjx.20190331

Dai, P. M., Wang, Y., Ye, L., Zeng, S., Zheng, Z. J., Li, Q., et al. (2014). Pharmacokinetic Comparisons of Benzoylmesaconine in Rats Using Ultra-performance Liquid Chromatography-Tandem Mass Spectrometry after Administration of Pure Benzoylmesaconine and Wutou Decoction. *Molecules* 19 (10), 16757–16769. doi:10.3390/molecules191016757

Dzhakhangirov, F. N., Sultankhodzhaev, M. N., Tashkhodzhaev, B., and Salimov, B. T. (1997). Diterpenoid Alkaloids as a New Class of Antiarrhythmic Agents. Structure-Activity Relationship. *Chem. Nat. Compd.* 33 (2), 190–202. doi:10.1007/bf02291540

Fu, M., Wu, M., Qiao, Y., Wang, Z., and Wang, Z. (2006). Toxicological Mechanisms of *Aconitum* Alkaloids. *Pharmazie* 61 (9), 735–741.

Garran, T. A., Ji, R., Chen, J. L., Xie, D., Guo, L., Huang, L. Q., et al. (2019). Elucidation of Metabolite Isomers of Leonurus Japonicus and Leonurus Cardiaca Using Discriminating Metabolite Isomerism Strategy Based on Ultra-high Performance Liquid Chromatography Tandem Quadrupole Time-Of-Flight Mass Spectrometry. *J. Chromatogr. A.* 1598, 141–153. doi:10.1016/j.chroma.2019.03.059

He, J. L., Zhao, J. W., Ma, Z. C., Wang, Y. G., Liang, Q. D., Tan, H. L., et al. (20152015). Serum Pharmacochemistry Analysis Using UPLC-Q-TOF/MS after Oral Administration to Rats of Shenfu Decoction. *Evid. Based Complement. Alternat Med.* 2015, 973930. doi:10.1155/2015/973930

He, L. P., Di, B., Du, Y. X., Yan, F., Su, M. X., Liu, H. Q., et al. (2009). Development and Validation of a High-Performance Liquid Chromatography-Tandem Mass Spectrometry Method for the Rapid Simultaneous Quantification of Aconitine, Mesaconitine, and Hypaconitine in Rat Plasma after Oral Administration of Sini Decoction. *J. Anal. Toxicol.* 33, 588–594. doi:10.1093/jat/33.9.588

Huang, G., Yang, L., Zhou, W., Tang, X., Wang, Y., Ma, Z., et al. (2018). Study on Cardiotoxicity and Mechanism of "Fuzi" Extracts Based on Metabonomics. *Int. J. Mol. Sci.* 19 (11), 3506. doi:10.3390/ijms19113506

Huang, J. H., Huang, X. H., Chen, Z. Y., Zheng, Q. S., and Sun, R. Y. (2004). Dose Conversion Among Different Animals and Healthy Volunteers in Pharmacological Study. *Chin. J. Clin. Pharmacol. Ther.* 9, 1069–1072.

Khan, H., Nabavi, S. M., Sureda, A., Mehterov, N., Gulei, D., Berindan-Neagoe, I., et al. (2018). Therapeutic Potential of Songorine, a Diterpenoid Alkaloid of the Genus *Aconitum*. *Eur. J. Med. Chem.* 153 (10), 29–33. doi:10.1016/j.ejmech.2017.10.065

Li, H., Zhang, G., Ma, M., Su, P., Yang, Y., Chen, T., et al. (2019). Study on Regulation of CYP450 Enzyme System to Reduce Liver Toxicity through the Compatibility of Radix Aconiti Lateralis Praeparata with *Panax Ginseng* C. A. Mey and *Glycyrrhiza Uralensis* Fisch. *Chin. J. New Drug* 28 (24), 2948–2953.

Li, N., Wang, D., Ge, G., Wang, X., Liu, Y., and Yang, L. (2014). Ginsenoside Metabolites Inhibit P-Glycoprotein *In Vitro* and *In Situ* Using Three Absorption Models. *Planta Med.* 80 (04), 290–296. doi:10.1055/s-0033-1360334

Li, Y., Feng, Y. F., Liu, X. T., Li, Y. C., Zhu, H. M., Sun, M. R., et al. (2021). Songorine Promotes Cardiac Mitochondrial Biogenesis via Nrf2 Induction during Sepsis. *Redox Biol.* 38, 101771. doi:10.1016/j.redox.2020.101771

Li, Y., Li, Y. X., Dang, J., Luo, L., Yuan, A., Zhao, M. J., et al. (2017a). Simultaneous Determination and Comparative Pharmacokinetics of Fuzi Water-Soluble Alkaloids between Normal and Acute Heart Failure Rats by Ultra Performance Liquid Chromatography Method. *J. Chromatogr. Sci.* 55 (7), 719–728. doi:10.1093/chromsci/bmx026

Li, Y., Li, Y. X., Zhao, M. J., Yuan, A., Gong, X. H., Zhao, M. J., et al. (2017b). The Effects of Rheum Palmatum L. On the Pharmacokinetic of Major Diterpene Alkaloids of Aconitum Carmichaelii Debx. in Rats. *Eur. J. Drug Metab. Pharmacokinet.* 42 (3), 441–451. doi:10.1007/s13318-016-0356-z

Li, Y. X., Gong, X. H., Li, Y., Zhang, R. Q., Yuan, A., Zhao, M. J., et al. (2015b). The Influence of Aconitum Carmichaelii Debx. On the Pharmacokinetic Characteristics of Main Components in Rheum Palmatum L. *Phytother. Res.* 29 (8), 1259–1264. doi:10.1002/ptr.5369

Li, Y., Zhao, M. J., Yuan, A., Gong, X. H., Peng, C., and Li, Y. X. (2016). Effect of Dosage on Pharmacokinetic Characteristics of Total Alkaloids from Aconiti Lateralis Radix Praeparata in Rats. *Chin. J. Exp. Tradit. Med. Form.* 22 (22), 82–85. doi:10.13422/j.cnki.syfjx.2016220082

Li, Z., Zhang, R., Wang, X., Hu, X., Chen, Y., and Liu, Q. (2015a). Simultaneous Determination of Seven Ginsenosides in Rat Plasma by High-Performance Liquid Chromatography Coupled to Time-Of-Flight Mass Spectrometry: Application to Pharmacokinetics of Shenfu Injection. *Biomed. Chromatogr.* 29 (2), 167–175. doi:10.1002/bmc.3272

Liu, S., Li, F., Li, Y., Li, W., Xu, J., and Du, H. (2017). A Review of Traditional and Current Methods Used to Potentially Reduce Toxicity of Aconitum Roots in Traditional Chinese Medicine. *J. Ethnopharmacol.* 207, 237–250. doi:10.1016/j.jep.2017.06.038

Liu, X., Li, H., Song, X., Qin, K., Guo, H., Wu, L., et al. (2014). Comparative Pharmacokinetics Studies of Benzoylhypaconine, Benzoylmesaconine, Benzoylaconine and Hypaconitine in Rats by LC-MS Method after Administration of Radix Aconiti Lateralis Praeparata Extract and Dahuang Fuzi Decoction. *Biomed. Chromatogr.* 28 (7), 966–973. doi:10.1002/bmc.3102

Peng, W. W., Li, W., Li, J. S., Cui, X. B., Zhang, Y. X., Yang, G. M., et al. (2013). The Effects of Rhizoma Zingiberis on Pharmacokinetics of Six Aconitum Alkaloids in Herb Couple of Radix Aconiti Lateralis-Rhizoma Zingiberis. *J. Ethnopharmacol.* 148 (2), 579–586. doi:10.1016/j.jep.2013.04.056

Qiu, Z. D., Chen, J. L., Zeng, W., Ma, Y., Chen, T., Tang, J. F., et al. (2020a). Real-time Toxicity Prediction of *Aconitum* Stewing System Using Extractive Electrospray Ionization Mass Spectrometry. *Acta Pharm. Sin. B* 10 (5), 903–912. doi:10.1016/j.apsb.2019.08.012

Qiu, Z. D., Wei, X. Y., Sun, R. Q., Chen, J. L., Tan, T., Xu, J. Q., et al. (2020b). Limitation Standard of Toxic Aconitines in *Aconitum* Proprietary Chinese Medicines Using On-Line Extraction Electrospray Ionization Mass Spectrometry. *Acta Pharm. Sin. B* 10 (8), 1511–1520. doi:10.1016/j.apsb.2019.12.009

Qiu, Z. D., Wei, X. Y., Wang, Y. N., Chen, J. L., Tan, T., Zhang, X. P., et al. (2021b). Quality Tracing Evaluation Strategies of Compatible Materials in *Aconitum* Proprietary Chinese Medicines. *J. Pharm. Biomed. Anal.* 192, 113654. doi:10.1016/j.jpba.2020.113654

Qiu, Z. D., Zhang, X., Wei, X. Y., Chingin, K., Xu, J. Q., Gao, W., et al. (2021a). Online Discovery of the Molecular Mechanism for Directionally Detoxification of Fuzi Using Real-Time Extractive Electrospray Ionization Mass Spectrometry. *J. Ethnopharmacol.* 277, 114216. doi:10.1016/j.jep.2021.114216

Shen, B. Q., Qu, C., Mi, L., Wang, H. Y., and Yang, H. (2021). Simultaneous Quantification of Twenty-Eight Components of Shenfu Injection in Rat Plasma by UHPLC-QQQ MS and its Application to a Pharmacokinetic Study. *J. Pharm. Biomed. Anal.* 203, 114211. doi:10.1016/j.jpba.2021.114211

Shuo, X. U., Liang, X., Qiong, L. I., and Jin, P. (2017). Advances on Chinese Herbal Medicine *Aconiti Lateralis Radix Praeparata*. *Northwest. Pharm. J.* 32 (2), 248–254.

Singhuber, J., Zhu, M., Prinz, S., and Kopp, B. (2009). Aconitum in Traditional Chinese Medicine: a Valuable Drug or an Unpredictable Risk? *J. Ethnopharmacol.* 126 (1), 18–30. doi:10.1016/j.jep.2009.07.031

Song, S., Tang, Q., Huo, H., Li, H., Xing, X., and Luo, J. (2015). Simultaneous Quantification and Pharmacokinetics of Alkaloids in Herba Ephedrae-Radix *Aconiti Lateralis* Extracts. *J. Anal. Toxicol.* 39 (1), 58–68. doi:10.1093/jat/bku113

Sun, W., Yan, B., Wang, R., Liu, F., Hu, Z., Zhou, L., et al. (2018). *In Vivo* acute Toxicity of Detoxified Fuzi (Lateral Root of *Aconitum Carmichaeli*) after a Traditional Detoxification Process. *EXCLI J.* 17, 889–899. doi:10.17179/excli2018-1607

Tang, L., Gong, Y., Lv, C., Ye, L., Liu, L., and Liu, Z. (2012). Pharmacokinetics of Aconitine as the Targeted Marker of Fuzi (*Aconitum Carmichaeli*) Following Single and Multiple Oral Administrations of Fuzi Extracts in Rat by UPLC/MS/MS. *J. Ethnopharmacol.* 141 (2), 736–741. doi:10.1016/j.jep.2011.08.070

Wang, Z., Wang, Z., Wen, J., and He, Y. (2007). Simultaneous Determination of Three Aconitum Alkaloids in Urine by LC-MS-MS. *J. Pharm. Biomed. Anal.* 45 (1), 145–148. doi:10.1016/j.jpba.2007.04.016

Wei, X. Y., Qiu, Z. D., Chen, J. L., Sun, R. Q., Huang, L. Q., and Lai, C. J. (2019). Research Advancement in Mechanisms of Processing and Compatibility for Detoxication of Aconitums. *Zhongguo Zhong Yao Za Zhi* 44 (17), 3695–3704. doi:10.19540/j.cnki.cjcmm.20190629.301

Xie, G., Ma, Z., Mei, Y., Zhang, X., Tan, H., and Gao, Y. (2021). Evaluation of Pharmacokinetics of *Aconiti Lateralis* Radix of Shenfu Prescription in Rats with Heart Failure. *Chin. J. Pharm.* 18 (07), 632–636. doi:10.19803/j.1672-8629.2021.07.08

Xu, Y., Li, Y., Zhang, P., Yang, B., Wu, H., Guo, X., et al. (2017). Sensitive UHPLC-MS/MS Quantitation and Pharmacokinetic Comparisons of Multiple Alkaloids from Fuzi- Beimu and Single Herb Aqueous Extracts Following Oral Delivery in Rats. *J. Chromatogr. B Analyt Technol. Biomed. Life Sci.* 1058, 24–31. doi:10.1016/j.jchromb.2017.05.016

Xu, Y., Yang, L., Liang, K., An, R., Wang, X., and Zhang, H. (2020). Pharmacokinetic Effects of Ginsenoside Rg1 on Aconitine, Benzoylaconine and Aconine by UHPLC-MS/MS. *Biomed. Chromatogr.* 34 (4), e4793. doi:10.1002/bmc.4793

Yang, B., Xu, Y., Wu, Y., Wu, H., Wang, Y., Yuan, L., et al. (2016). Simultaneous Determination of Ten Aconitum Alkaloids in Rat Tissues by UHPLC-MS/MS and its Application to a Tissue Distribution Study on the Compatibility of Heishunpian and Fritillariae Thunbergii Bulbus. *J. Chromatogr. B Analyt Technol. Biomed. Life Sci.* 1033, 242–249. doi:10.1016/j.jchromb.2016.08.033

Yang, L., Wang, Y., Huang, G., Li, J., Zhang, Z., Ma, Z., et al. (20182018). Simultaneous Evaluation of the Influence of *Panax Ginseng* on the Pharmacokinetics of Three Diester Alkaloids after Oral Administration of Aconiti Lateralis Radix in Rats Using UHPLC/QQQ-MS/MS. *Evid. Based Complement. Alternat Med.* 2018, 6527549. doi:10.1155/2018/6527549

Yu, X., Liu, H., Xu, X., Hu, Y., Wang, X., and Wen, C. (2021). Pharmacokinetics of Yunaconitine and Indaconitine in Mouse Blood by UPLC-MS/MS. *J. Chromatogr. B* 1179, 122840. doi:10.1016/j.jchromb.2021.122840

Zhang, F., Tang, M. H., Chen, L. J., Li, R., Wang, X. H., Duan, J. G., et al. (2008). Simultaneous Quantitation of Aconitine, Mesaconitine, Hypaconitine, Benzoylaconine, Benzoylmesaconine and Benzoylhypaconine in Human Plasma by Liquid Chromatography-Tandem Mass Spectrometry and Pharmacokinetics Evaluation of "SHEN-FU" Injectable Powder. *J. Chromatogr. B Analyt Technol. Biomed. Life Sci.* 873 (2), 173–179. doi:10.1016/j.jchromb.2008.08.008

Zhang, H., Liu, M., Zhang, W., Chen, J., Zhu, Z., Cao, H., et al. (2015a). Comparative Pharmacokinetics of Three Monoester-Diterpenoid Alkaloids after Oral Administration of *Acontium Carmichaeli* Extract and its Compatibility with Other Herbal Medicines in Sini Decoction to Rats. *Biomed. Chromatogr.* 29 (7), 1076–1083. doi:10.1002/bmc.3394

Zhang, J., Gao, W., Hu, X., Liu, Z., and Liu, C. (2012). The Influence of Compatibility of Traditional Chinese Medicine on the Pharmacokinetic of Main Components in Fructus Aurantii. *J. Ethnopharmacol.* 144 (2), 277–283. doi:10.1016/j.jep.2012.09.009

Zhang, J. M., Liao, W., He, Y. X., He, Y., Yan, D., and Fu, C. M. (2013). Study on Intestinal Absorption and Pharmacokinetic Characterization of Diester Diterpenoid Alkaloids in Precipitation Derived from Fuzi-Gancao Herb-Pair Decoction for its Potential Interaction Mechanism Investigation. *J. Ethnopharmacol.* 147 (1), 128–135. doi:10.1016/j.jep.2013.02.019

Zhang, Q., Ma, Y. M., Wang, Z. T., and Wang, C. H. (2014). Pharmacokinetics Difference of Multiple Active Constituents from Decoction and Maceration of Fuzi Xiexin Tang after Oral Administration in Rat by UPLC-MS/MS. *J. Pharm. Biomed. Anal.* 92, 35–46. doi:10.1016/j.jpba.2013.12.038

Zhang, W., Zhang, H., Sun, S., Sun, F. F., Chen, J., Zhao, L., et al. (2015b). Comparative Pharmacokinetics of Hypaconitine after Oral Administration of Pure Hypaconitine, Aconitum Carmichaelii Extract and Sini Decoction to Rats. *Molecules* 20 (1), 1560–1570. doi:10.3390/molecules20011560

Zhang, Y., Tian, D., Huang, Y., Li, L., Mao, J., Tian, J., et al. (2016). Pharmacokinetic Evaluation of Shenfu Injection in Beagle Dogs after Intravenous Drip Administration. *Acta Pharm. Sin. B* 6 (6), 584–592. doi:10.1016/j.apsb.2016.05.006

Zhang, Y., Zong, X., Wu, J. L., Liu, Y., Liu, Z., Zhou, H., et al. (2020). Pharmacokinetics and Tissue Distribution of Eighteen Major Alkaloids of *Aconitum Carmichaelii* in Rats by UHPLC-QQQ-MS. *J. Pharm. Biomed. Anal.* 185, 113226. doi:10.1016/j.jpba.2020.113226

Zhou, Q., Meng, P., Wang, H., Dong, X., and Tan, G. (2019). Pharmacokinetics of Monoester-Diterpenoid Alkaloids in Myocardial Infarction and normal Rats after Oral Administration of Sini Decoction by Microdialysis Combined with Liquid Chromatography-Tandem Mass Spectrometry. *Biomed. Chromatogr.* 33 (1), e4406. doi:10.1002/bmc.4406

Conflict of Interest: The authors declare that the research was conducted in the absence of any commercial or financial relationships that could be construed as a potential conflict of interest.

Publisher's Note: All claims expressed in this article are solely those of the authors and do not necessarily represent those of their affiliated organizations, or those of the publisher, the editors and the reviewers. Any product that may be evaluated in this article, or claim that may be made by its manufacturer, is not guaranteed or endorsed by the publisher.

frontiers | Frontiers in Pharmacology

ORIGINAL RESEARCH
published: 12 May 2022
doi: 10.3389/fphar.2022.883581

In Silico Screening and Validation of PDGFRA Inhibitors Enhancing Radioiodine Sensitivity in Thyroid Cancer

Xuefei Yu[1†], *Xuhang Zhu*[4†], *Lizhuo Zhang*[5], *Jiang-Jiang Qin*[3*], *Chunlai Feng*[1*] and *Qinglin Li*[2*]

[1]School of pharmacy, Jiangsu University, Zhenjiang, China, [2]The Cancer Hospital of the University of Chinese Academy of Sciences (Zhejiang Cancer Hospital), Institute of Basic Medicine and Cancer (IBMC), Chinese Academy of Sciences, Key Laboratory of Head & Neck Cancer Translational Research of Zhejiang Province, Hangzhou, China, [3]Institute of Basic Medicine and Cancer (IBMC), Chinese Academy of Sciences, Hangzhou, China, [4]Thyroid surgery, The Cancer Hospital of the University of Chinese Academy of Sciences (Zhejiang Cancer Hospital), Institute of Basic Medicine and Cancer (IBMC), Chinese Academy of Sciences, Hangzhou, China, [5]Department of Head and Neck Surgery, Center of Otolaryngology-Head and Neck Surgery, Zhejiang Provincial People's Hospital (People's Hospital of Hangzhou Medical College), Hangzhou, China

Aberrant activation of platelet-derived growth factor receptor α (PDGFRA) has been implicated in tumorigenesis and radioiodine resistance of thyroid cancer, indicating its therapeutic potential. In the present study, we confirmed the association between PDGFRA and radioiodine resistance in thyroid cancer using bioinformatics analysis and constructed a prediction model of PDGFRA inhibitors using machine learning and molecular docking approaches. We then performed a virtual screening of a traditional Chinese medicine (TCM) derived compound library and successfully identified 4',5,7-trimethoxyflavone as a potential PDGFRA inhibitor. Further characterization revealed a significant inhibitory effect of 4',5,7-trimethoxyflavone on PDGFRA-MAPK pathway activation, and that it could upregulate expression of sodium iodide symporter (NIS) as well as improve radioiodine uptake capacity of radioiodine-refractory thyroid cancer (RAIR-TC), suggesting it a potential drug lead for the development of new RAIR-TC therapy.

Keywords: PDGFRA inhibitors, virtual screening, radioiodine-refractory thyroid cancer, traditional Chinese medicine, machine learning

OPEN ACCESS

Edited by:
Zipeng Gong,
Guizhou Medical University, China

Reviewed by:
Junqing Huang,
Jinan University, China
Qiyang Shou,
Zhejiang Chinese Medical University, China
Yuan Ping,
Zhejiang University, China

***Correspondence:**
Qinglin Li
qinglin200886@126.com
Chunlai Feng
feng@ujs.edu.cn
Jiang-Jiang Qin
jqin@ucas.ac.cn

[†]*These authors have contributed equally to this work and share first authorship*

Specialty section:
This article was submitted to Drug Metabolism and Transport, a section of the journal Frontiers in Pharmacology

Received: *25 February 2022*
Accepted: *07 April 2022*
Published: *12 May 2022*

Citation:
Yu X, Zhu X, Zhang L, Qin J-J, Feng C and Li Q (2022) In Silico Screening and Validation of PDGFRA Inhibitors Enhancing Radioiodine Sensitivity in Thyroid Cancer. Front. Pharmacol. 13:883581. doi: 10.3389/fphar.2022.883581

1 INTRODUCTION

Thyroid cancer is one of the most common endocrine system malignancies, especially in women. The latest global malignancies statistics from the International Agency for Research on Cancer (GLOBOCAN 2020) revealed thyroid cancer the 9th most common malignant tumor in the world and the 5th most common among women. With an estimated 586,000 new cases and 44,000 deaths in 2020, the incidence of thyroid cancer has been on the rise (Bray et al., 2018; Miller et al., 2020; Sung et al., 2021). Differentiated thyroid cancer (DTC) is the most common thyroid cancer. As it retains the function of thyroid follicular cells to a certain extent, most DTC patients are treated in standard surgical and radioactive iodine (RAI) treatments with good prognosis, especially when DTC is limited to the thyroid or only involves the cervical lymph nodes (Ferlay et al., 2019). However, the risk of local recurrence and distant metastasis could be as high as 20 and 10%, which has been the main cause of death in thyroid cancer patients (Anderson et al., 2013; Liu et al., 2019).

The radioiodine uptake characteristics of patients with metastatic lesions are positively correlated with their treatment prognosis (van Tol et al., 2003). As statistics showed, the 10-year survival rate of patients with aberrant radioiodine uptake has been much lower than that of patients with radioiodine uptake (Durante et al., 2006). Therefore, improving the radioiodine uptake of RAIR-TC has been considered one of the most effective treatments.

PDGFRA is a cell surface receptor tyrosine kinase. PDGFRA can bind to its corresponding ligand PDGF and then activate downstream signaling pathways to regulate cell proliferation, migration and angiogenesis (Heldin and Westermark, 1999; Heldin and Lennartsson, 2013; Roskoski, 2018). The overexpression of PDGFRA is closely associated with radioiodine resistance (Lopez-Campistrous et al., 2016) and distant metastasis (Lin et al., 2021) in human thyroid cancer. Lopez-campistou et al. have (Lopez-Campistrous et al., 2016) found that overexpression and/or aberrant activation of PDGFRA decreased the expression levels of TG and NIS by disrupting the transcriptional activity and nuclear localization of TTF1 in both cell and animal models. When PDGFRA was inhibited, the uptake of radioiodine was restored, and the migration, invasion potential and tumor burden were also reduced. Currently, sorafenib (Brose et al., 2014), which can target PDGFRA, has been approved for marketing by National Medical Products Administration, while Lenvatinib (Schlumberger et al., 2015; Porcelli et al., 2021) and Pazopanib (Chow et al., 2017) have entered the stage of clinical research. However, these medications are multi-targeted tyrosine kinase inhibitors, and further development of selective PDGFRA inhibitors is in urgent need.

Over the years, TCM has achieved certain clinical success in the treatment of thyroid cancer. According to the different symptoms of thyroid cancer before and after the operation, the corresponding TCM treatment can significantly improve the patients' quality of life (Chang and Li, 2018; Han et al., 2021). At the same time, TCM can also improve the uptake rate of radioiodine in thyroid cancer cells. Mechanism studies have revealed an important role of TCM in regulating NIS expression and improving radioiodine uptake (Yu et al., 2013; Hardin et al., 2016). In this study, we aimed to identify new PDGFRA inhibitors from TCM *in silico* and verify their effects of targeting PDGFRA and radioiodine uptake.

2 MATERIALS AND METHODS

2.1 Correlation Between RDGFRA and Radioiodine Uptake of Thyroid Cancer

2.1.1 Expression Analysis of PDGFRA in Oncomine Database

To investigate the expression difference of *PDGFRA* in RAIR-TC and radioiodine-sensitive thyroid cancer, the expression of *PDGFRA* in different thyroid cancer was collected by inputting two keywords *PDGFRA* and thyroid cancer in the Oncomine database (https://www.oncomine.org/). Since DTC was not subdivided into radioiodine-sensitive and radioiodine-refractory type in the public database, DTC was regarded as radioiodine-sensitive type. GraphPad Prism version 8 (GraphPad Software, California, United States) was used for mapping.

TABLE 1 | Compounds for model construction.

Category	Label		
	Positive	Negative	Total number
Training set	345	455	800
Test set	78	122	200
Screening set	—	—	2994

2.1.2 Protein-Protein Interaction (PPI) Networks Analysis

Protein-protein interaction (PPI) networks functional enrichment analysis was executed using the searching tool for recurring instances of neighbouring genes (STRING) 11.0 (https://string-db.org/), which is used to explore interactions among proteins. The protein names or sequences of PDGFRA were input, and the sample type of "homo sapiens" was selected. The results of PPI networks were downloaded.

2.1.3 Overall Survival Analysis of *PDGFRA*

To investigate relationship between *PDGFRA* and prognosis of thyroid cancer, the overall survival analysis of *PDGFRA* was conducted. The original data for survival analysis were obtained from the cBioPortal database (https://www.cbioportal.org/). The expression value of *PDGFRA* in the top 25% was considered as high expression, and the rest was intermediate or low expression. Then, the overall survival-time plot of *PDGFRA* was assessed by Kaplan-Meier plot and Log-Rank analysis.

2.1.4 Correlation Analysis Between *PDGFRA* and Thyroid-specific Genes

To further investigate the correlation between *PDGFRA* and radioiodine uptake capacity of thyroid cancer, correlation analysis between *PDGFRA* and thyroid-specific genes (*NIS*, *PAX8*, *TTF1*) were performed using R commands. The expression data of *PDGFRA*, *NIS*, *PAX8*, and *TTF1* were obtained from cBioPortal database. Pearson correlation coefficient was used to evaluate the correlation between thyroid-specific genes and *PDGFRA*.

2.2 Screening of Novel Inhibitors of PDGFRA

The virtual screening workflow adopted in this study is shown in **Figure 1.**

2.2.1 Construction of the Data Sets

All the 504 PDGFRA inhibitors were collected from the Binding Database (http://www.bindingdb.org/bind/index.jsp). Among them, 423 compounds with IC_{50} ≤10 μM were considered active and the rest were considered inactive. Another inactive dataset of 496 molecules was collected from the CHEMBL database (https://www.ebi.ac.uk/chembl/), which was randomly selected as an assumed non-inhibitor dataset. Subsequently, a set

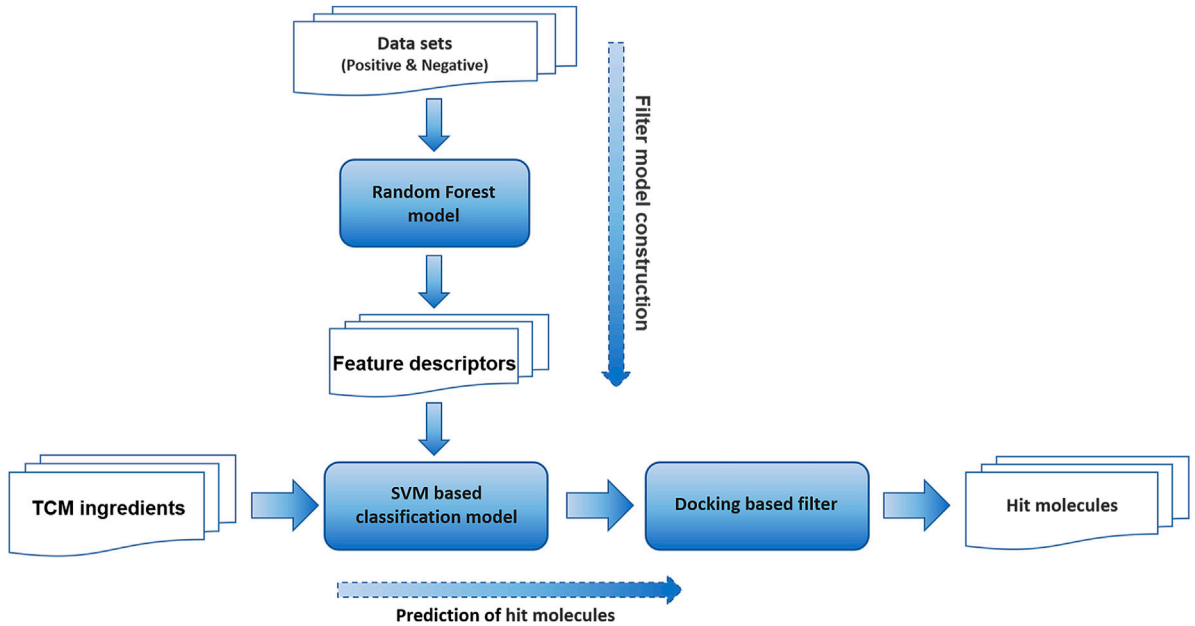

FIGURE 1 | The virtual screening workflow adopted in this study.

of 423 compounds as active molecules were taken, and the remaining 81 inactive molecules along with 496 randomly selected molecules constituted the inactive dataset. Both active dataset and inactive dataset were randomly divided into training and test set in a 4:1 ratio. Thus, we have 800 compounds in the training set, out of which 345 were active ones, the remaining 455 were inactive. Likewise, we have a total of 200 compounds in the test set, out of which 78 were active and the remaining 122 were inactive (**Table 1**).

A total of 2994 Chinese herbal ingredients from 116 Chinese herbal medicines used in thyroid cancer treatment and patient physical quality regulation were collected from Traditional Chinese Medicine Systems Pharmacology Database and Analysis Platform (TCMSP, https://old.tcmsp-e.com/tcmsp.php) and Traditional Chinese Medicine Integrated Database (TCMID, http://www.megabionet.org/tcmid/) as a screening set (**Table 1**).

2.2.2 Random Forest Model-Based Feature Screening

To obtain the feature descriptors of compounds, Random Forest model was constructed. First, a total of 354 descriptors for the compounds were calculated using the Molecular Operating Environment 2020 (MOE, Chemical Computing Group ULC, Montreal, Canada) after energy minimization (Vilar et al., 2008). Then, the training set was used to train the Random Forest model, and the parameters "n_estimator", "max_depth", "min_sample_split", and "min_sample_leaf" were optimized to determine the best parameters of the Random Forest model. Finally, The Random Forest model was constructed by using the best parameters, and the model performance was investigated by the test set. Descriptors with the feature importance scores greater than 0.0037 calculated by the model were selected as feature descriptors.

2.2.3 Support Vector Machine (SVM) Based Prediction Model

Based on the feature descriptors screened by Random Forest model, SVM based prediction model was constructed with radial basis function (RBF) kernel function. Two hyperparameters (c, γ) were optimized by grid search and 7-fold cross-validation (7-CV). After generating the SVM based prediction model using 7-CV of the training set, the generated model was further validated using the test set. The statistical parameters Accuracy (ACC), Precise (P), and Recall (R) were calculated to test the validity of generated model.

2.2.4 Molecular Docking

All the molecular docking studies were carried out by MOE. The crystal structure of PDGFRA (PDB ID: 5K5X) was selected for the docking studies and retrieved from the RCSB Protein Data Bank (PDB, https://www.rcsb.org/; Bahmani et al., 2021). The 3D structure of screened compounds was retrieved from the PubChem database (https://pubchem.ncbi.nlm.nih.gov/). After the protein and compounds were pretreated separately, the binding sites on the receptor and compounds were studied by blind docking. Finally, for all compounds, the lowest energy conformation was used for further analysis.

2.3 *In vitro* Biological Activity Evaluation of Screened PDGFRA Inhibitors

2.3.1 Cell Culture

Cell lines Nthy-ori-3-1, BCPAP, TPC1, 8505C, and IHH4 were obtained from Zhejiang Provincial People's Hospital (Hangzhou, China). Nthy-ori-3-1, BCPAP, TPC1, and

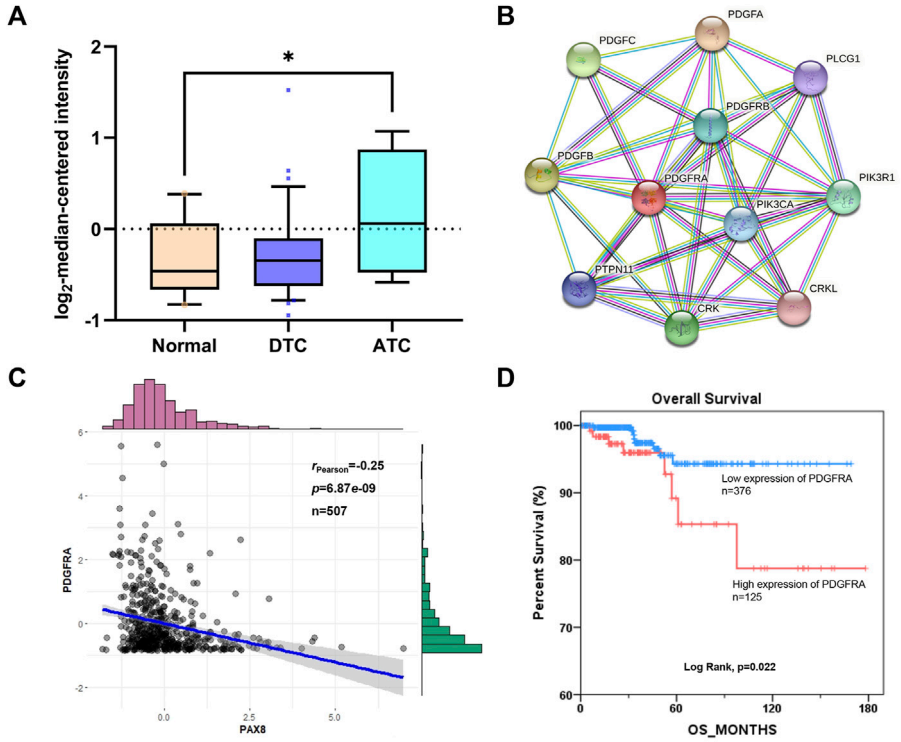

FIGURE 2 | The correlation between RDGFRA and radioiodine uptake of thyroid cancer. **(A)** The expression of *PDGFRA* in different types of thyroid cancer from Oncomine database. *, p <0.05, compared with normal group. **(B)** The biological correlation between PDGFRA and related regulatory genes was analyzed based on STRING database. **(C)** Correlation between *PDGFRA* and *PAX8* based on cBioPortal database. **(D)** Kaplan-Meier plot of overall survival-time of *PDGFRA* mRNA expression based on cBioPortal database. DTC: Differentiated Thyroid Cancer; ATC: Anaplastic Thyroid Cancer.

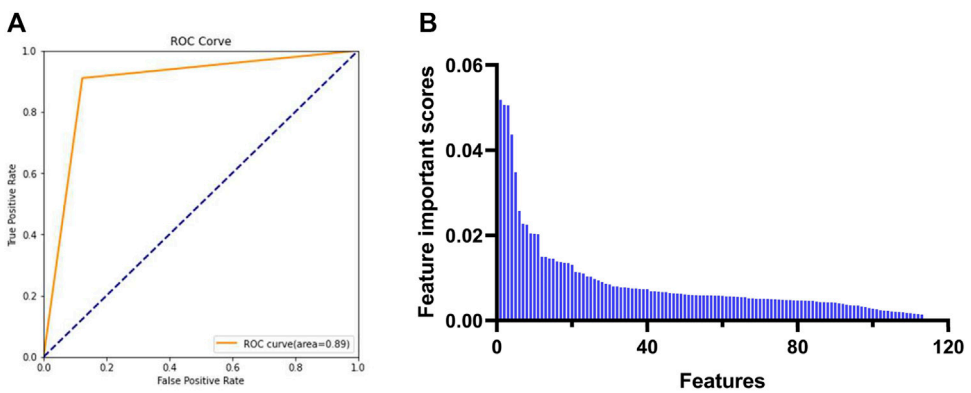

FIGURE 3 | Selection of feature descriptors based on Random Forest model. **(A)** AUC of Random Forest model under the best parameters. **(B)** Feature importance scores calculated by the Random Forest model. AUC: area under receiver operating characteristic curve.

IHH4 cell lines were maintained in RPMI 1640 supplemented with 10% FBS plus 1% penicillin-streptomycin solution, while 8505C cells were maintained in DMEM supplemented with 10% FBS plus 1% penicillin-streptomycin solution. All the cell lines were cultured at 37°C in a humidified 5% CO_2 incubator.

2.3.2 Cell Viability Assay

Cells were incubated in 96-well plates at a density of 5×10^3 cells/well for 24 h. The cells were treated with the indicated concentrations of compounds for 72 h and then incubated with Cell Counting Kit-8 (CCK-8) reagent (Biosharp, Anhui, China) at 37°C for 2 h. The absorbance was measured at 450 nm on the Spark® multimode

TABLE 2 | Optimal parameters and overall Performance of Random Forest Prediction Model.

v	n_estimator	max_depth	min_sample_split	min_sample_leaf	ACC (%)	P	R (%)
7	177	17	2	1	89	83%	91

v: Number of folds for cross-validation; ACC: accuracy; P: precision; R: recall.

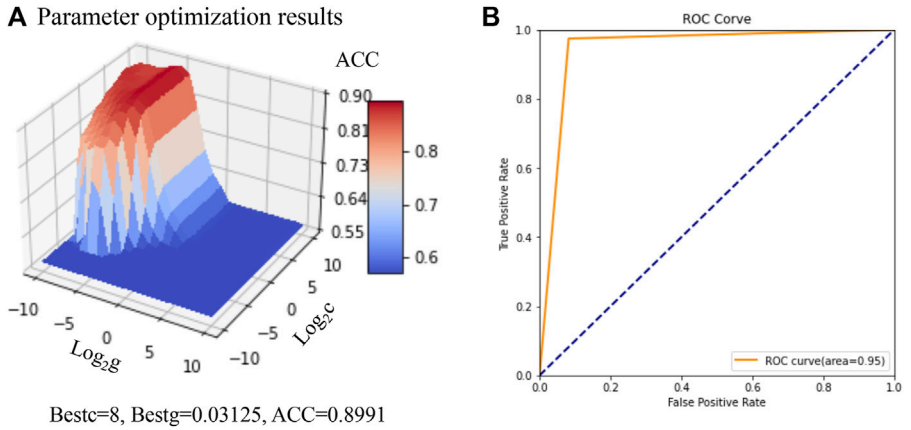

FIGURE 4 | Construction and optimization of SVM based prediction model. **(A)** Parameter optimization results based on Grid search and cross validation. **(B)** AUC of SVM based prediction model under the best parameters. AUC: area under receiver operating characteristic curve.

microplate reader (Tecan, Männedorf, Switzerland). All compounds were purchased from Shanghai Red Peony Biotechnology Co., LTD. (Shanghai, China).

2.3.3 Western Blot Analyses

The treated IHH4 cells were lysed with a cell lysate containing RIPA buffer [50 mM Tris (pH 7.4), 150 mM NaCl, 1% Triton X-100, 1% sodium deoxycholate, 0.1% Sodium dodecyl sulfate (SDS), sodium orthovanadate, sodium fluoride, Ethylene Diamine Tetraacetic Acid (EDTA), leupeptin et al.], supplemented with 1 mM phenylmethylsulphonyl fluoride (PMSF) and 10% phosphatase inhibitors on ice for 15 min. The protein extract was obtained after centrifugation at 4°C at 13,000 rpm for 15 min. The protein concentration was evaluated using Pierce BCA protein assay reagent (Biosharp, Anhui, China). Running samples were prepared by adding a sample diluent and 5× SDS-polyacrylamide gel electrophoresis (SDS-PAGE) loading buffer, and the protein denaturation is performed at 100°C for 10 min. The protein extract samples were separated by SDS-PAGE and transferred to 0.45 μm polyvinylidene difluoride (PVDF) membrane. Then, membranes were blocked with 5% skimmed milk powder in 1× Tris-Buffered Saline and Tween 20 (TBST) for 1 h, followed by incubation with primary antibodies at 4°C overnight. After being cleaned 3 times with TBST, the protein bands were incubated with anti-mouse or anti-rabbit IgG horseradish peroxidase (HRP) linked secondary antibody (Cell Signaling Technology, Danvers, United States) for 2 h. After being washed 3 times with TBST, the protein bands were finally visualized with SuperSignal West Pico chemiluminescence substrate (Biosharp, Anhui, China). The antibodies used for the western blot were as follows: monoclonal antibodies against phospho-PDGFRA (Tyr754, Cat. No. 2992), Na^+/K^+ ATPase (Cat. No. 3010), and GAPDH (Cat. No. 5174) were purchased from Cell Signaling Technology (Danvers, United States). The PDGFRA (Cat. No. ab134123) and NIS (Cat. No. ab242007) monoclonal antibody was purchased from Abcam (Cambridge, United States). The p38 MAPK (Cat. No. sc-7972) and phospho-p38 MAPK (Tyr 182, Cat. No. sc-7973) monoclonal antibodies were purchased from Santa Cruz Biotechnology (Dallas, United States). All antibodies were diluted at 1:1000 in the study.

2.3.4 Cellular Thermal Shift Assay (CETSA)

CETSA is used to detect the binding of compounds to PDGFRA (Martinez Molina et al., 2013). Cells were incubated in 15 cm cell culture plates at a density of 3×10^7 cells/well for 24 h. The cells were treated with the indicated concentrations (0, 80 μM) of compounds for 1.5 h and then cells were digested with trypsin and collected by centrifugation. After washing with PBS, the cells were re-suspended with 1 ml PBS containing 1% PMSF. The cell suspension was placed in a series of PCR tubes (control vs. treated) and then subjected to thermal shock for 3.5 min in an appropriate thermal cycle (37–67°C), followed by incubation at room temperature for 3min. The suspensions were then subjected to two freeze-thaw cycles in liquid nitrogen, and vortex treatment was carried out after each thawing. The suspensions were centrifuged at 4°C for 20 min at 2,000 rpm and the supernatants were transferred to new PCR tubes. Running samples were prepared by adding SDS-PAGE loading buffer and then heated to denature at 100°C for 10 min. Finally, the proteins were analyzed by western blot.

TABLE 4 | Optimal parameters and overall Performance of SVM based prediction model.

v	c	Gamma	Kernel	ACC (%)	P (%)	R (%)
7	8	0.03135	rbf	94	88	97

v: Number of folds for cross-validation; ACC: accuracy; P: precision; R: recall.

TABLE 5 | Screening results of active TCM ingredients based on SVM based prediction model.

CID	Name	TCM name	CID	Name	TCM name
11066	Oxyberberine	Coptidis Rhizoma	5281636	Gentisin	Dipsaci Radix
68077	Tangeretin	Citrus Reticulata、Citri Reticulatae Pericarpium Viride, Aurantii Fructus Immaturus	5281704	Afrormosin	licorice、Spatholobus Suberectus Dunn
79730	4',5,7-Trimethoxyflavone	Aurantii Fructus Immaturus	5317756	Glycycoumarin	licorice
124050	Isoglycyrol	Licorice	5319013	Licoricone	licorice
150032	Menisporphine	Phellodendri Chinrnsis Cortex	5319422	3'-Methoxydaidzein	Polygonati Rhizoma
160921	Nevadensin	Asparagi Radix	5319744	3'-O-Methylorobol	Ecliptae Herba
161271	Salvigenin	Scutellariae Barbatae Herba、Scutellariae Radix	5320083	Glycyrol	licorice、Amygdalus Communis Vas
161748	Myricanone	Chuanxiong Rhizoma	5320290	Onjixanthone I	Forsythiae Fructus
185034	Sainfuran	Radix Bupleuri	5352005	Retusin	Agastacherugosus (Fisch.etMey)O.Ktze
442694	Batatasin I	Rhizoma Dioscoreae	11983285	Confusarin	Dendrobium nobile Lindl
480787	Glycyrin	licorice	13965473	Odoratin	licorice、Spatholobus Suberectus Dunn
480817	Gancaonin V	licorice	13970974	4,6-Dimethoxy-7-(3-methylbut-2-enoxy)furo [2,3-b]quinoline	Dendrobium nobile Lindl
629964	4',5,7,8-Tetramethoxyflavone	Aurantii Fructus Immaturus	14187587	Isoglycycoumarin	licorice
688717	3-Hydroxy-2',4',7-trimethoxyflavone	Lonicerae Japonicae Flos	14353376	5-Hydroxy-7,8,4'-trimethoxyflavone	Scutellariae Barbatae Herba
5281601	Apigenin dimethylether	Scutellariae Barbatae Herba、Lonicerae Japonicae Flos、Epimrdii Herba	44257530	Phaseol	licorice、Amygdalus Communis Vas

2.3.5 Radioiodine Uptake

Radioiodine uptake experiments at the cellular level were performed as reported by Weiss (Weiss et al., 1984) with appropriate adjustments. 1×10^6 cells were cultured in 6-well plates and treated with compounds for 24 h after adherence. Then, the cells were washed with phosphate-buffered saline (PBS) 3 times. One group of experimental cells was cultured with serum-free medium at 37 °C for 2 h, digested by trypsin, and counted by hemocytometer. The other group of parallel cells was added 1 ml serum-free medium containing 1 μCi $Na^{131}I$ and cultured at 37°C for 2 h. The cells were washed by precooled PBS 3 times, digested by trypsin, and the cell suspension was collected by releasing free tubes. Counts per minute (CPM) of radioactivity was measured using GC-1500 γ radiation immunity arithmometer (ZONKIA, Anhui, China) and the effect of compounds on radioiodine uptake was evaluated using CPM/10^5 cells as the unit of cellular radioiodine uptake.

2.4 Statistical Analysis

All statistical analysis were done using GraphPad Prism version 8. Survival Analysis were performed using Statistical Product and Service Solutions 20 (SPSS, IBM, United States) software. Significance of the difference was calculated by independent-Sample t-test. A p-value <0.05 was considered statistically significant. All data in the figures are presented as means ± SD.

3 RESULTS

3.1 Correlation Between PDGFRA and Radioiodine Uptake of Thyroid Cancer

To confirm the correlation between RDGFRA and radioiodine uptake of thyroid cancer, the expression of *PDGFRA*, protein-protein interaction network, correlation with thyroid-specific genes, and survival differences were analyzed. As shown in **Figure 2A**, anaplastic thyroid carcinoma (ATC) is a type of RAIR-TC due to poor radioiodine uptake. The expression of *PDGFRA* in ATC is significantly higher than that in normal thyroid cells, which confirmed that the expression of *PDGFRA* in RAIR-TC is higher than that in normal thyroid or radioiodine-sensitive thyroid cancer. PPI networks (**Figure 2B**) showed a strong interaction between PDGFRA and PI3K (Score >0.9). PI3K pathway has been confirmed to affect radioiodine uptake of thyroid cells (Kogai et al., 2008; Liu et al., 2012), which is another evidence that PDGFRA is related to the uptake of radioiodine. Correlation analysis between *PDGFRA* and

TABLE 3 | The 93 molecular descriptors filtered by the Random Forest model.

Descriptor class	Descriptors	Number
Physical properties	apol, h_logD, rsynth	3
Subdivided surface areas	SlogP_VSA0,SlogP_VSA1, SlogP_VSA2,SlogP_VSA3,SlogP_ VSA4,SlogP_VSA5,SlogP_VSA9,SMR_ VSA1,SMR_VSA2,SMR_VSA3,SMR_ VSA4,SMR_VSA7	12
Atom counts and bond counts	a_aro,a_ICM,a_nN,a_nS,b_1rotN,b_ 1rotR,b_max1len,chiral,opr_brigid	9
Partial charge descriptors	PEOE_RPC+,PEOE_RPC-,PEOE_VSA+0,PEOE_VSA+1,PEOE_VSA+2,PEOE_VSA+3, PEOE_VSA-0,PEOE_VSA- 1,PEOE_VSA-3,PEOE_VSA-4,PEOE_VSA-5,PEOE_VSA-6, PEOE_VSA_FHYD, PEOE_VSA_FNEG,Q_RPC+,Q_RPC-	16
Pharmacophore feature descriptors	a_don, vsa_acc, vsa_don, vsa_other	4
Adjacency and distance matrix descriptors	BalabanJ,BCUT_PEOE_0,BCUT_SLOGP_1,GCUT_PEOE_1,GCUT_SLOGP_0,GCUT_SLOGP_1	6
Potential energy descriptors	E,E_ang,E_ele,E_oop,E_sol,E_tor	6
MOPAC descriptors	MNDO_dipole	1
Surface area descriptors	dens,glob,npr1,pmi1,pmiX,pmiY,pmiZ,std_ dim2,std_dim3,vsurf_A,vsurf_CP,vsurf_CW2,vsurf_ EDmin1,vsurf_EWmin1,vsurf_HB1,vsurf_ HL1,vsurf_IW1,vsurf_IW7,vsurf_IW8	19
Conformation dependent Charge Descriptors	ASA+,ASA-,ASA_P,CASA-,dipole,dipoleX,dipoleY,dipoleZ,FASA+,FASA-	10
Hueckel theory descriptors	h_ema,h_logD,h_pavgQ,h_pKa,h_pKb,h_pstates,h_pstrain	7

thyroid-specific genes showed that although the expression of *PDGFRA* was not correlated with *NIS* and *TTF1*, it was negatively correlated with *PAX8* (**Figure 2C**, **Supplementary Figure S1**). Kaplan-Meier plot of overall survival-time of *PDGFRA* mRNA expression showed that high expression of *PDGFRA* affected the prognosis of patients (**Figure 2D**). In summary, PDGFRA plays an important role in the uptake or transport of radioiodine in thyroid cancer and is a reliable target for reversing RAIR-TC radioiodine resistance.

3.2 Selection of Feature Descriptors Based on Random Forest Model

To obtain the feature descriptors, the molecular descriptors of a preconstructed dataset consisting of 423 known PDGFRA inhibitors (positive) and 577 non-inhibitors (negative) were calculated by MOE software, as shown in **Supplementary Tables S1, S2**. In order to increase the accuracy of the subsequent model and reduce the amount of computation, the initial 354 descriptors were preprocessed. Descriptors with null or missing values, a repeat rate of more than 80% and a standard deviation of less than or equal to 0.05, and highly correlated with others (correlation coefficients >80%) were all removed. Finally, 117 molecular descriptors were chosen for building the Random Forest model. The Grid Search result showed that when the values of parameters n_estimator, max_depth, min_sample_split, and min_sample_leaf were 177, 17, 2, and 1, respectively, the model demonstrated the best accuracy (89%) and AUC (area under receiver operating characteristic curve, 0.89) (**Table 2** and **Figure 3A**). Finally, 93 feature descriptors were selected based on the feature importance scores calculated by the Random Forest model, which were shown in **Table 3** and **Figure 3B**.

3.3 Construction, Evaluation of SVM Based Prediction Model, and Prediction of PDGFRA Potential Inhibitors

Based on 93 feature descriptors selected by the Random Forest model constructed above, the initial SVM based prediction model was constructed. The parameters of the SVM based prediction model were optimized based on the grid search algorithm and 7-fold cross validation, and the ACC, P, R and AUC of the model was taken as the evaluation index. When the value of parameters c was 8 and the value of parameters γ was 0.03135, the model demonstrated the best accuracy (90%) for the training set (**Figure 4A**). When the optimized model was used for the prediction of the test set, the prediction accuracy was 94%, while the AUC was 0.95 (**Table 4** and **Figure 4B**). 97% of the positive samples were properly predicted for the 78 PDGFRA inhibitors, while for the 122 non-inhibitors, 92% of the negative samples were properly predicted. Collectively, these results confirmed that the constructed SVM classification model had a greatly good capability to distinguish the PDGFRA inhibitors and non-inhibitors.

The optimal SVM based prediction model was then used to screen potential PDGFRA inhibitors. 30 of 2994 compounds

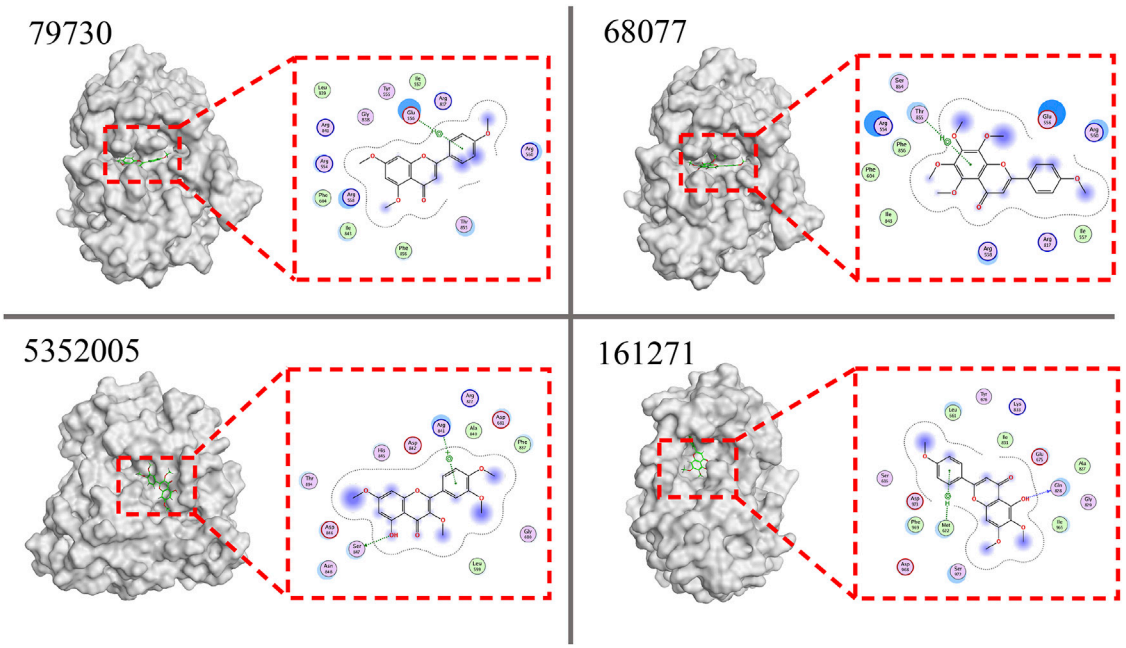

FIGURE 5 | Docking results of the top 4 compounds with PDGFRA. 79730, 68077, 5352005, and 161271 are PubChem CID of 4',5,7-Trimethoxyflavone, Tangeretin, Retusin, and Salvigenin, respectively. PDGFRA protein is shown as a white surface model, while the ligand is shown as a green stick model. The hydrogen bond is shown as the dotted lines. In the 2D interaction diagram, the ligand is shown as a chemical formula, the residues are shown in purple circles marked with their names, and the hydrogen bond is shown as the green dotted lines.

passed through this filter were predicted as potential PDGFRA inhibitors, which were shown in **Table 5**.

3.4 Molecular Docking Study

To evaluate the interactions of 30 candidate compounds screened based on the SVM based prediction model with PDGFRA, molecular docking study was carried out by MOE software. The active site of PDGFRA mainly consists of three parts, including ATP binding site, activation loop, and the amino acids available active site (Bahmani et al., 2021). Compounds that bind to the active sites of PDGFRA may be more effective in inhibiting PDGFRA. The docking results of compounds and PDGFRA were shown in **Table 6**. Nineteen compounds were hydrogen-bonded to the reported PDGFRA active region. Among the nineteen compounds, the top 10 compounds available for purchase were selected for subsequent experimental verification according to the principle of the lowest scores (**Figure 5**, **Supplementary Figure S2**).

3.5 *In vitro* Activity Evaluation of Screened PDGFRA Inhibitors

To confirm that the previously screened inhibitors can inhibit PDGFRA and improve the radioiodine uptake capacity of thyroid cancer, biological validation of the selected inhibitors was carried out. In this study, normal thyroid epithelial cell line Nthy-ori-3-1, DTC cell lines BCPAP, TPC1, and IHH4, and ATC cell line 8505C were used as cell models. The effects of ten potential PDGFRA inhibitors on the viability of these cell lines were fully explored through the CCK8 experiment (**Figure 6A**, **Supplementary Figure S3**). the PDGFRA expression levels in IHH4 and 8505C cell lines were much higher than that of normal thyroid cells and other DTC cells (**Figure 6B**). Therefore, the compounds that exert its anticancer activity in a PDGFRA-dependent manner have better effect on IHH4 and 8505C cell lines than the others. Then Oxyberberine, 4',5,7-trimethoxyflavone, and Glycyrol were selected according to this screening principle. Radioiodine uptake experiments showed that among the three compounds, 4',5,7-trimethoxyflavone had the best enhancement on the uptake of radioiodine by IHH4 cells (**Figure 6C**, **Supplementary Figure S4**). Later, this study mainly explored the mechanism of 4',5,7-trimethoxy-flavone enhancing radioiodine uptake capacity of thyroid cancer. Western blot assay showed that 4',5,7-trimethoxyflavone inhibited the phosphorylation activation of PDGFRA and p38 MAPK in a concentration- and time-dependent manner (**Figures 6D,E**). The CETSA was further performed to detect the binding of 4',5,7-trimethoxyflavone to PDGFRA. The results showed that 4',5,7-trimethoxyflavone increased the thermal stability of PDGFRA, indicating that the compound could bind to PDGFRA (**Figure 6F**). This result was consistent with the prediction of molecular docking. Only when NIS is accurately located on the membrane, it can play its role in radioiodine uptake. We further showed that 4',5,7-trimethoxyflavone could increase NIS expression in cell membrane and cytoplasm at the same time (**Figure 6G**).

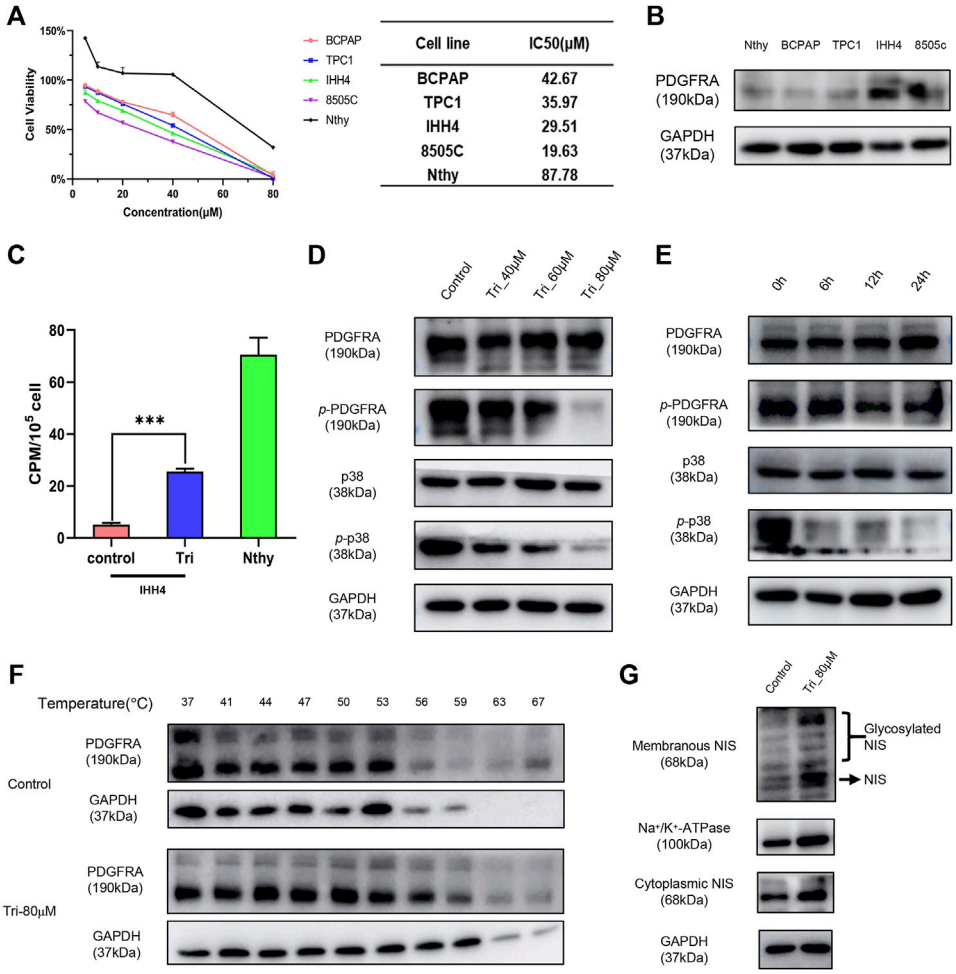

FIGURE 6 | Biological validation of the virtually screened PDGFRA inhibitors. **(A)** The effect of 4',5,7-trimethoxyflavone on the viability of thyroid carcinoma cells and normal thyroid cells. **(B)** The expression of PDGFRA in thyroid carcinoma cells and normal thyroid cells. **(C)** The effect of 4',5,7-trimethoxyflavone on radioiodine uptake capacity of IHH4 cell line. **(D,E)** The effect of 4',5,7-trimethoxyflavone on protein expression of p-PDGFRA and p-p38. **(F)** The binding of 4',5,7-trimethoxyflavone to PDGFRA was examined by the CETSA test. **(G)** The effect of 4',5,7-trimethoxyflavone on expression and cellular location of NIS. ***, p <0.001, compared with control group. Nthy: Nthy-ori-3-1 cell line; Tri: 4',5,7-trimethoxyflavone; p-PDGFRA: phospho-PDGFRA (Tyr754); p-p38: phospho-p38 MAPK (Tyr 182).

TABLE 6 | Docking results of potential inhibitors with PDGFRA.

CID	S	NHBa	Binding site	CID	S	NHB[a]	Binding site
11066	−6.03787	1	GLU556	5281636	−5.09768	2	ILE965/SER783
68077	−6.36916	1	THR855	5281704	−5.76621	1	ARG560
79730	−6.50424	1	GLU556	5317756	−6.18588	0	—
124050	−5.93374	0	—	5319013	−6.12188	0	—
150032	−5.51394	0	—	5319422	−5.3683	2	GLU556/ARG554
160921	−5.67415	0	—	5319744	−5.35448	0	—
161271	−6.12935	2	GLN828/MET622	5320083	−5.89688	1	ARG554
161748	−6.14682	1	LYS833	5320290	−5.55545	0	—
185034	−5.70737	0	—	5352005	−6.20545	2	SER847/ARG841
442694	−5.52984	1	ARG560	11983285	−5.63999	1	ARG817
480787	−5.8909	2	GLU556/ARG817	13965473	−5.63319	0	—
480817	−5.84344	1	ASP968	13970974	−5.84314	2	ARG554/THR855
629964	−6.08919	2	TYR679/GLY680	14187587	−6.21415	0	—
688717	−6.19365	1	ARG597	14353376	−5.47657	2	GLU675/ILE965
5281601	−5.77296	1	ARG560	44257530	−5.74329	0	—

[a]*NHB: number of hydrogen bonds.*

4 DISCUSSION AND CONCLUSION

Thyroid cancer is one of the most common endocrine tumors with an increasing incidence worldwide, among which RAIR-TC has a low survival rate due to its low radioiodine uptake rate. PDGFRA was found to reduce the expression of TG and NIS by disrupting the transcriptional activity and nuclear localization of TTF1, thus affecting the uptake of radioiodine (Lopez-Campistrous et al., 2016). Through the analysis of public database, this study also found that PDGFRA was closely connected with the genes and pathways related to radioiodine absorption in thyroid cancer (**Figures 2B,C**). In addition, PDGFRA also has an impact on the prognosis of thyroid cancer (**Figure 2D**), which is consistent with reported research (Lin et al., 2021). Currently, Sorafenib is the only PDGFRA inhibitor clinically used for the treatment of RAIR-TC in China, but Sorafenib can't enhance the overall survival of patients (Brose et al., 2014). Therefore, further development of novel inhibitors of PDGFRA is still needed.

To build a PDGFRA inhibitors screening model with high accuracy, we combined the random forest model, SVM based prediction model, and molecular docking model. The Random forests model is commonly used for the predictive performance of multiple important drug transporters, targets, and drug properties, and is currently used to measure the importance of feature descriptors (Svetnik et al., 2003; Xu and Li, 2018). The Random Forest model, which takes the classification accuracy as the criterion function, has the advantages of high accuracy and good robustness. Screening the most important feature descriptors with Random Forest model first can greatly increase the accuracy of subsequent screening of PDGFRA inhibitors. SVM solves the classification problem by mapping data to a higher-dimensional space using nonlinear kernel functions to find the optimal separation hyperplane. Although the SVM has difficulties in multi-classification and large-scale training samples, it has good robustness and strong generalization ability for the classification of small sample data. The SVM based prediction model has been widely used in the field of chemical informatics to discover and design new drugs with excellent biological activities (Yabuuchi et al., 2011). Based on the SVM based prediction model and Random Forest model, this study constructed a screening model for PDGFRA inhibitors with 94% accuracy, and the prediction accuracy for positive compounds even reached 97%, confirming the reliability of the subsequent screening of 30 potential PDGFRA inhibitors. To further improve the accuracy of drug screening and reduce experimental costs, a molecular docking model was constructed to investigate the binding of candidate drugs to the active region of PDGFRA. Molecular Docking is mainly based on the principles of geometric matching and energy matching, using computer algorithms to predict the best binding mode for the receptor-ligand complex (Kitchen et al., 2004). Based on the docking results, 19 candidate compounds were further screened to bind PDGFRA active region.

According to the optimal 10 candidate compounds obtained by molecular docking results, the CCK8 experiments were performed to determine their inhibitory effects on different thyroid cancer cells. Since the expression level of PDGFRA in IHH4 and 8505C cell line was higher than that in other DTC cell lines, PDGFRA inhibitors should have better inhibitory effects on IHH4 and 8505C cell viability than other DTC cell lines (TPC1, BCPAP) and normal thyroid cells (Nthy-ori-3–1). Therefore, Oxyberberine, 4',5,7-trimethoxyflavone, and Glycyrol that have better anticancer activity on IHH4 and 8505C were selected for further experimental verification (**Figure 6A**, **Supplementary Figure S3**). Radioiodine uptake experiments showed that among the three compounds, 4',5,7-trimethoxyflavone had the best enhancement on the uptake of radioiodine by IHH4 cells (**Supplementary Figure S4**). Though the enhancement on the radioiodine uptake of 4',5, 7-trimethoxyflavone in IHH4 cells was still not up to the uptake of radioiodine by normal thyroid cells (Nthy-ori-3–1), but it had a better effect on improving the uptake of radioiodine in RAIR-TC. Unfortunately, this study didn't compare whether the combination of 4',5,7-Trimethoxyflavon and radioactive iodine improved the therapeutic effect of radioactive iodine, and relevant studies will be carried out in the future.

In thyroid cancer, the MAPK signaling pathway is closely related to radioiodine uptake capacity, and its abnormal activation will lead to the loss of the expression of genes required for thyroid hormone biosynthesis, including NIS, TPO, and TG, thus reducing the radioiodine uptake capacity of thyroid cancer (Nagarajah et al., 2016). MAPK pathway is also regulated by PDGFRA (Rosenkranz et al., 2000; Hayashi et al., 2015). Therefore, we hypothesized that 4',5,7-trimethoxyflavone promoted NIS expression or membrane localization by inhibiting PDGFRA-MAPK pathway, thus improving radioiodine uptake in thyroid cancer. This hypothesis was confirmed by western blot assays *in vitro*, 4',5,7-trimethoxyflavone inhibited PDGFRA phosphorylation and the activation of the downstream MAPK signaling pathway, mainly the p38 MAPK pathway, and thus restored NIS expression in both membrane and cytoplasm (**Figures 6D,E,G**). Moreover, 4',5,7-trimethoxyflavone has been confirmed as an inhibitor of PDGFRA through CETSA and western blot assays (**Figure 6F**).

4',5,7-trimethoxyflavone has been observed to show several bioactivities, such as anti-allergy (Kobayashi et al., 2015), anti-Alzheimer (Youn et al., 2016), anti-cancer (Zheng et al., 2010), anti-inflammatory (During and Larondelle, 2013), and vasorelaxation effect (Tep-areena and Sawasdee, 2010), as well as enhancing the uptake of radioiodine in RAIR-TC as current study indicated. Metabolism of 4',5,7-trimethoxyflavone mainly contains demthylation and phase II conjugation (Mekjaruskul et al., 2012), and pharmacokinetics of 4',5,7-trimethoxyflavone showed dose- and time-dependence (Elhennawy and Lin, 2018). The difference in 4',5,7-trimethoxyflavone dose influenced the plasma concentration-time curve of single intravenous administration, the mean residence time, the dose normalized maximum plasma concentration (C_{max}) and area under the plasma concentration-time curve of single oral administration. Oral administration of 4',5,7-trimethoxyflavone for 1 week could accelerate elimination and reduce plasma exposure. Despite the pharmacokinetic defects of 4',5,7-trimethoxyflavone, it is still a promising drug lead with wide application.

In conclusion, with the successful construction of PDGFRA inhibitor screening model using machine learning and molecular docking approaches, we identified novel active ingredients from TCM that could improve the iodine sensitivity of RAIR-DTC. Among the selected TCM ingredients, 4',5,7-trimethoxyflavone showed the best *in vitro* activity, which significantly upregulated the expression of NIS by targeting PDGFRA and inhibited PDGFRA activation, and therefore could enhance the radioiodine uptake capacity of thyroid cancer cells. This study provides support for the development of better RAIR-DTC therapy and potentially promotes the application of TCM in thyroid cancer treatment.

DATA AVAILABILITY STATEMENT

The original contributions presented in the study are included in the article/**Supplementary Material**, further inquiries can be directed to the corresponding authors.

AUTHOR CONTRIBUTIONS

CF, QL, and J-JQ designed and supervised the study. XY constructed SVM classification model and predicted the PDGFRA potential inhibitors. XY, XZ, and LZ confirmed the activity of screened PDGFRA inhibitors. XY, XZ, and LZ analyzed the data. QL and XY wrote the manuscript. CF and J-JQ edited the manuscript. All the authors participated in the interpretation of the results and approved the final version of the manuscript.

FUNDING

This work was supported by Natural Science Foundation of China (82074286, 82173346); Zhejiang Medical and Health Science and Technology Project (2020PY002); Department of Science and Technology of Zhejiang Province (LGF21H160007); Natural Science Foundation of Jiangsu Province (BK20191428) and the Science and Technology Innovation Fund of Zhenjiang-International Cooperation Projects (GJ2021012).

SUPPLEMENTARY MATERIAL

The Supplementary Material for this article can be found online at: https://www.frontiersin.org/articles/10.3389/fphar.2022.883581/full#supplementary-material

REFERENCES

Anderson, R. T., Linnehan, J. E., Tongbram, V., Keating, K., and Wirth, L. J. (2013). Clinical, Safety, and Economic Evidence in Radioactive Iodine-Refractory Differentiated Thyroid Cancer: a Systematic Literature Review. *Thyroid* 23 (4), 392–407. doi:10.1089/thy.2012.0520

Bahmani, A., Tanzadehpanah, H., Hosseinpour Moghadam, N., and Saidijam, M. (2021). Introducing a Pyrazolopyrimidine as a Multi-Tyrosine Kinase Inhibitor, Using Multi-QSAR and Docking Methods. *Mol. Divers* 25 (2), 949–965. doi:10.1007/s11030-020-10080-8

Bray, F., Ferlay, J., Soerjomataram, I., Siegel, R. L., Torre, L. A., and Jemal, A. (2018). Global Cancer Statistics 2018: GLOBOCAN Estimates of Incidence and Mortality Worldwide for 36 Cancers in 185 Countries. *CA Cancer J. Clin.* 68 (6), 394–442. doi:10.3322/caac.21492

Brose, M. S., Nutting, C. M., Jarzab, B., Elisei, R., Siena, S., Bastholt, L., et al. (2014). Sorafenib in Radioactive Iodine-Refractory, Locally Advanced or Metastatic Differentiated Thyroid Cancer: a Randomised, Double-Blind, Phase 3 Trial. *Lancet* 384 (9940), 319–328. doi:10.1016/S0140-6736(14)60421-9

Chang, Q., and Li, Y. (2018). Effect of Huangqi Fuzheng Decoction on Immune Function and Quality of Life of Patients with Thyroid Cancer after Operation. *Chin. Arch. Tradit. Chin. Med.* 36 (3), 691–693. doi:10.13193/j.issn.1673-7717.2018.03.043

Chow, L. Q., Santana-Davila, R., Pantel, A., Roth, M., Anderson, L. N., Failor, A., et al. (2017). A Phase I Study of Pazopanib in Combination with Escalating Doses of 131I in Patients with Well-Differentiated Thyroid Carcinoma Borderline Refractory to Radioiodine. *PLoS One* 12 (6), e0178325. doi:10.1371/journal.pone.0178325

Durante, C., Haddy, N., Baudin, E., Leboulleux, S., Hartl, D., Travagli, J. P., et al. (2006). Long-term Outcome of 444 Patients with Distant Metastases from Papillary and Follicular Thyroid Carcinoma: Benefits and Limits of Radioiodine Therapy. *J. Clin. Endocrinol. Metab.* 91 (8), 2892–2899. doi:10.1210/jc.2005-2838

During, A., and Larondelle, Y. (2013). The O-Methylation of Chrysin Markedly Improves its Intestinal Anti-inflammatory Properties: Structure-Activity Relationships of Flavones. *Biochem. Pharmacol.* 86 (12), 1739–1746. doi:10.1016/j.bcp.2013.10.003

Elhennawy, M. G., and Lin, H. S. (2018). Dose- and Time-dependent Pharmacokinetics of Apigenin Trimethyl Ether. *Eur. J. Pharm. Sci.* 118, 96–102. doi:10.1016/j.ejps.2018.03.022

Ferlay, J., Colombet, M., Soerjomataram, I., Mathers, C., Parkin, D. M., Piñeros, M., et al. (2019). Estimating the Global Cancer Incidence and Mortality in 2018: GLOBOCAN Sources and Methods. *Int. J. Cancer* 144 (8), 1941–1953. doi:10.1002/ijc.31937

Han, Q., Xu, N., Chen, B., Wu, W., and Sheng, L. (2021). Safety and Efficacy of Prunella Vulgaris Preparation in Adjuvant Treatment of Thyroid Nodules: A Meta-Analysis. *Med. Baltim.* 100 (41), e27490. doi:10.1097/MD.0000000000027490

Hardin, H., Yu, X. M., Harrison, A. D., Larrain, C., Zhang, R., Chen, J., et al. (2016). Generation of Novel Thyroid Cancer Stem-like Cell Clones: Effects of Resveratrol and Valproic Acid. *Am. J. Pathol.* 186 (6), 1662–1673. doi:10.1016/j.ajpath.2016.02.003

Hayashi, Y., Bardsley, M. R., Toyomasu, Y., Milosavljevic, S., Gajdos, G. B., Choi, K. M., et al. (2015). Platelet-Derived Growth Factor Receptor-α Regulates Proliferation of Gastrointestinal Stromal Tumor Cells with Mutations in KIT by Stabilizing ETV1. *Gastroenterology* 149 (2), 420–e16. doi:10.1053/j.gastro.2015.04.006

Heldin, C. H., and Lennartsson, J. (2013). Structural and Functional Properties of Platelet-Derived Growth Factor and Stem Cell Factor Receptors. *Cold Spring Harb. Perspect. Biol.* 5 (8), a009100. doi:10.1101/cshperspect.a009100

Heldin, C. H., and Westermark, B. (1999). Mechanism of Action and *In Vivo* Role of Platelet-Derived Growth Factor. *Physiol. Rev.* 79 (4), 1283–1316. doi:10.1152/physrev.1999.79.4.1283

Kitchen, D. B., Decornez, H., Furr, J. R., and Bajorath, J. (2004). Docking and Scoring in Virtual Screening for Drug Discovery: Methods and Applications. *Nat. Rev. Drug Discov.* 3 (11), 935–949. doi:10.1038/nrd1549

Kobayashi, S., Kato, T., Azuma, T., Kikuzaki, H., and Abe, K. (2015). Anti-allergenic Activity of Polymethoxyflavones from Kaempferia Parviflora. *J. Funct. Foods* 13, 100–107. doi:10.1016/j.jff.2014.12.029

Kogai, T., Sajid-Crockett, S., Newmarch, L. S., Liu, Y. Y., and Brent, G. A. (2008). Phosphoinositide-3-kinase Inhibition Induces Sodium/iodide Symporter

Expression in Rat Thyroid Cells and Human Papillary Thyroid Cancer Cells. *J. Endocrinol.* 199 (2), 243–252. doi:10.1677/JOE-08-0333

Lin, C.-L., Tsai, M.-L., Chen, Y.-h., Liu, W.-N., Lin, C.-Y., Hsu, K.-W., et al. (2021). Platelet-Derived Growth Factor Receptor-α Subunit Targeting Suppresses Metastasis in Advanced Thyroid Cancer *In Vitro* and *In Vivo*. *Biomol. Ther.* 29 (5), 551–561. doi:10.4062/biomolther.2020.205

Liu, J., Liu, Y., Lin, Y., and Liang, J. (2019). Radioactive Iodine-Refractory Differentiated Thyroid Cancer and Redifferentiation Therapy. *Endocrinol. Metab. Seoul.* 34 (3), 215–225. doi:10.3803/EnM.2019.34.3.215

Liu, Y. Y., Zhang, X., Ringel, M. D., and Jhiang, S. M. (2012). Modulation of Sodium Iodide Symporter Expression and Function by LY294002, Akti-1/2 and Rapamycin in Thyroid Cells. *Endocr. Relat. Cancer* 19 (3), 291–304. doi:10.1530/ERC-11-0288

Lopez-Campistrous, A., Adewuyi, E. E., Benesch, M. G. K., Ko, Y. M., Lai, R., Thiesen, A., et al. (2016). PDGFRα Regulates Follicular Cell Differentiation Driving Treatment Resistance and Disease Recurrence in Papillary Thyroid Cancer. *EBioMedicine* 12, 86–97. doi:10.1016/j.ebiom.2016.09.007

Martinez Molina, D., Jafari, R., Ignatushchenko, M., Seki, T., Larsson, E. A., Dan, C., et al. (2013). Monitoring Drug Target Engagement in Cells and Tissues Using the Cellular Thermal Shift Assay. *Science* 341 (6141), 84–87. doi:10.1126/science.1233606

Mekjaruskul, C., Jay, M., and Sripanidkulchai, B. (2012). Pharmacokinetics, Bioavailability, Tissue Distribution, Excretion, and Metabolite Identification of Methoxyflavones in Kaempferia Parviflora Extract in Rats. *Drug Metab. Dispos.* 40 (12), 2342–2353. doi:10.1124/dmd.112.047142

Miller, K. D., Fidler-Benaoudia, M., Keegan, T. H., Hipp, H. S., Jemal, A., and Siegel, R. L. (2020). Cancer Statistics for Adolescents and Young Adults, 2020. *CA Cancer J. Clin.* 70 (1), 443–459. doi:10.3322/caac.21637

Nagarajah, J., Le, M., Knauf, J. A., Ferrandino, G., Montero-Conde, C., Pillarsetty, N., et al. (2016). Sustained ERK Inhibition Maximizes Responses of BrafV600E Thyroid Cancers to Radioiodine. *J. Clin. Invest.* 126 (11), 4119–4124. doi:10.1172/JCI89067

Porcelli, T., Luongo, C., Sessa, F., Klain, M., Masone, S., Troncone, G., et al. (2021). Long-term Management of Lenvatinib-Treated Thyroid Cancer Patients: a Real-Life Experience at a Single Institution. *Endocrine* 73 (2), 358–366. doi:10.1007/s12020-021-02634-z

Rosenkranz, S., Ikuno, Y., Leong, F. L., Klinghoffer, R. A., Miyake, S., Band, H., et al. (2000). Src Family Kinases Negatively Regulate Platelet-Derived Growth Factor Alpha Receptor-dependent Signaling and Disease Progression. *J. Biol. Chem.* 275 (13), 9620–9627. doi:10.1074/jbc.275.13.9620

Roskoski, R., Jr. (2018). The Role of Small Molecule Platelet-Derived Growth Factor Receptor (PDGFR) Inhibitors in the Treatment of Neoplastic Disorders. *Pharmacol. Res.* 129, 65–83. doi:10.1016/j.phrs.2018.01.021

Schlumberger, M., Tahara, M., Wirth, L. J., Robinson, B., Brose, M. S., Elisei, R., et al. (2015). Lenvatinib versus Placebo in Radioiodine-Refractory Thyroid Cancer. *N. Engl. J. Med.* 372 (7), 621–630. doi:10.1056/NEJMoa1406470

Sung, H., Ferlay, J., Siegel, R. L., Laversanne, M., Soerjomataram, I., Jemal, A., et al. (2021). Global Cancer Statistics 2020: GLOBOCAN Estimates of Incidence and Mortality Worldwide for 36 Cancers in 185 Countries. *CA Cancer J. Clin.* 71 (3), 209–249. doi:10.3322/caac.21660

Svetnik, V., Liaw, A., Tong, C., Culberson, J. C., Sheridan, R. P., and Feuston, B. P. (2003). Random Forest: a Classification and Regression Tool for Compound Classification and QSAR Modeling. *J. Chem. Inf. Comput. Sci.* 43 (6), 1947–1958. doi:10.1021/ci034160g

Tep-areena, P., and Sawasdee, P. (2010). Vasorelaxant Effects of 5,7,4'-Trimethoxyflavone from Kaepmferia Parviflora in the Rat Aorta. *Int. J. Pharmacol.* 6 (4), 419–424. doi:10.3923/ijp.2010.419.424

van Tol, K. M., Jager, P. L., de Vries, E. G., Piers, D. A., Boezen, H. M., Sluiter, W. J., et al. (2003). Outcome in Patients with Differentiated Thyroid Cancer with Negative Diagnostic Whole-Body Scanning and Detectable Stimulated Thyroglobulin. *Eur. J. Endocrinol.* 148 (6), 589–596. doi:10.1530/eje.0.1480589

Vilar, S., Cozza, G., and Moro, S. (2008). Medicinal Chemistry and the Molecular Operating Environment (MOE): Application of QSAR and Molecular Docking to Drug Discovery. *Curr. Top. Med. Chem.* 8 (18), 1555–1572. doi:10.2174/156802608786786624

Weiss, S. J., Philp, N. J., and Grollman, E. F. (1984). Iodide Transport in a Continuous Line of Cultured Cells from Rat Thyroid. *Endocrinology* 114 (4), 1090–1098. doi:10.1210/endo-114-4-1090

Xu, S., and Li, D. (2018). Weighted Feature Selection Algorithm Based on Random Forest. *Statistics Decis.* 34 (18), 25–28. doi:10.13546/j.cnki.tjyjc.2018.18.005

Yabuuchi, H., Niijima, S., Takematsu, H., Ida, T., Hirokawa, T., Hara, T., et al. (2011). Analysis of Multiple Compound-Protein Interactions Reveals Novel Bioactive Molecules. *Mol. Syst. Biol.* 7, 472. doi:10.1038/msb.2011.5

Youn, K., Lee, J., Ho, C.-T., and Jun, M. (2016). Discovery of Polymethoxyflavones from Black Ginger (Kaempferia Parviflora) as Potential β-secretase (BACE1) Inhibitors. *J. Funct. Foods* 20, 567–574. doi:10.1016/j.jff.2015.10.036

Yu, X. M., Jaskula-Sztul, R., Ahmed, K., Harrison, A. D., Kunnimalaiyaan, M., and Chen, H. (2013). Resveratrol Induces Differentiation Markers Expression in Anaplastic Thyroid Carcinoma via Activation of Notch1 Signaling and Suppresses Cell Growth. *Mol. Cancer Ther.* 12 (7), 1276–1287. doi:10.1158/1535-7163.MCT-12-0841

Zheng, X., Zhao, F. F., Liu, Y. M., Yao, X., Zheng, Z. T., Luo, X., et al. (2010). Synthesis and Preliminary Biological Evaluation of Chrysin Derivatives as Potential Anticancer Drugs. *Med. Chem.* 6 (1), 6–8. doi:10.2174/157340610791208763

Conflict of Interest: The authors declare that the research was conducted in the absence of any commercial or financial relationships that could be construed as a potential conflict of interest.

Publisher's Note: All claims expressed in this article are solely those of the authors and do not necessarily represent those of their affiliated organizations, or those of the publisher, the editors and the reviewers. Any product that may be evaluated in this article, or claim that may be made by its manufacturer, is not guaranteed or endorsed by the publisher.

frontiers | Frontiers in Pharmacology

ORIGINAL RESEARCH
published: 25 May 2022
doi: 10.3389/fphar.2022.899043

Integrating Network Pharmacology and Metabolomics to Elucidate the Mechanism of Action of Huang Qin Decoction for Treament of Diabetic Liver Injury

Xiaomin Xu[1†], Cheng Fang[2†], Yu Wang[1], Fang Lu[1] and Shumin Liu[1*]*

[1]Research Institute of Traditional Chinese Medicine, Heilongjiang University of Traditional Chinese Medicine, Harbin, China, [2]Drug Safety Evaluation Center of Heilongjiang University of Chinese Medicine, China

Huang Qin Decoction (HQD), is used for the treatment of diabetic liver injury (DLI) and in this study, its mechanisms were evaluated by metabonomics and system pharmacology. To study the anti-DLI effects of HQD. The 48 male db/db mice were fed adaptively for one week, and a random blood glucose test was performed twice. The db/db mice with a blood glucose level of more than 11.1mol/l were separated into four groups: the model group, the active control group, the high-dose HQD group the low-dose HQD group, the control group consisted of db/m mice. Using the UHPLC/Q-TOF-MS metabolomics approach, 18 metabolites were found to be profoundly altered in the model group, and the levels of these biomarkers were significantly recovered after treatment with HQD. 8 signaling pathways related to HQD, including the Sphingolipid metabolism, Taurine and hypotaurine metabolism, Phenylalanine metabolism, Glutathione metabolism and Glycerophospholipid metabolism, etc. were explored. In addition, the system pharmacology paradigm revealed that HQD contains 141 active ingredients and is related to 265 genes, and 1404 disease genes are related to DLI. The construction of the HQD composition-target-DLI network identified a total of 161 intersection genes. We identified 10 key genes, which is partially compatible with the results of metabolomics. The integrated approach metabolomics and network pharmacology revealed that additional detailed investigation focused on five major targets, including CAT, PTGS2, MAPK3, AKT1, and MAPK8, and their essential metabolites (sphinganine, sphingosine, Glutahione, Oxidized gutahione, Dihydrolipoamide) and pathway (glycerol phospholipid metabolism and tryptophan metabolism). The significant affinity of the primary target for the HQD was confirmed by molecular docking. The results demonstrate that the combination of metabolomics and network pharmacology could be used to reflect the effects of HQD on the biological network and metabolic state of DLI and to evaluate the drug efficacy of HQD and its related mechanisms.

Keywords: metabolomics, network pharmacology, huang qin decoction, diabetic liver injury, metabolite

OPEN ACCESS

Edited by:
Guo Ma,
Fudan University, China

Reviewed by:
Na Lin,
Beijing Key Laboratory of Quality Evaluation of Traditional Chinese Medicine, China
Lixin Duan,
Guangzhou University of Chinese Medicine, China
Erwei Hao,
Guangxi University of Chinese Medicine, China
Decai Tang,
Nanjing University of Chinese Medicine, China

***Correspondence:**
Fang Lu
lufang1004@163.com
Shumin Liu
keji-liu@163.com

†These authors have contributed equally to this work

Specialty section:
This article was submitted to Drug Metabolism and Transport, a section of the journal Frontiers in Pharmacology

Received: *18 March 2022*
Accepted: *18 April 2022*
Published: *25 May 2022*

Citation:
Xu X, Fang C, Wang Y, Lu F and Liu S (2022) Integrating Network Pharmacology and Metabolomics to Elucidate the Mechanism of Action of Huang Qin Decoction for Treament of Diabetic Liver Injury. Front. Pharmacol. 13:899043. doi: 10.3389/fphar.2022.899043

INTRODUCTION

Diabetes is a common metabolic disease characterized by elevated blood sugar levels that may affect nerves, blood vessels, the heart, kidneys, eye, foot, and other organs and tissues, leading to a series of dysfunction and chronic injury. The liver is the main of human metabolism and one of the primary target organs implicated in chronic diseases of diabetes mellitus (Yue et al., 2022). Early liver injury induced by diabetes is sometimes difficult to determine due to the liver's high compensatory function. At the same time, the liver plays a key role in blood glucose management and sugar storage and distribution. As a result, protecting the liver is as important as controlling blood sugar in the management of diabetes (Tanase et al., 2020).

DLI results from multiple factors and mechanisms, such as damage, anti-injury, proliferation repair, and comprehensive regulation. Diabetes-complicated liver damage is characterized by inflammation and oxidative stress induced by blood sugar, fat, protein, water, and electrolyte abnormalities, which leads to impaired liver function and glucose and lipid metabolism (Luo et al., 2018; Zhang et al., 2018). Its pathophysiology is complicated, and there is no particular medication therapy for DLI at the moment (Liu et al., 2013). At present, chemical hypoglycemic medicines are frequently used to treat diabetes by oral administration. These treatments have several problems, including considerable toxic and side effects, various adverse responses, a single target, minor effects, and even liver injury. However, traditional chinese medicine compounds have the characteristics of multi-component, multi-target, multi-pathway comprehensive regulation, and comprehensive intervention, which provides a novel approach for the research and prevention of this disease. As a result, we investigate the protective mechanism of the traditional chinese medicine "HQD" against DLI.

HQD is a traditional prescription for removing heat, alleviating diarrhea, and relieving pain from Zhang Zhongjing's Treatise on Febrile Diseases. It is prepared using the decoction of four traditional Chinese medicines: scutellaria baicalensis (Scutellaria baicalensis Georgi (Lamiaceae) is a popular medicinal plant, Scutellaria baicalensis Georgi), Radix Paeoniae (This product is the dried root of Paeonia lactiflora Pall. Ranunculaceae, Paeonia lactiflora Pall), jujube (This product is the dried and mature fruit of D. Ziziphus jujuba Mill, Ziziphus jujuba Mill), and licorice (This product is the dried root and rhizome of Glycyrrhiza glabra L. legaceae, Glycyrrhiza glabra L). Among them, Scutellaria baicalensis is bitter cold and strong in yin and clears heat in the interior; peony has a slightly bitter and sour taste, relieves pain, restrains yin; bitter and acid complement each other, and has the effect of regulating the middle and preserving yin to stop dysentery. Jujube restores qi and boosts vigor. Data show that HQD has been used in the treatment of gastrointestinal diseases for thousands of years (Enhui C, 2021). Meanwhile, According to modern pharmacological research, HQD contains anti-inflammatory, antibacterial, analgesic, antipyretic, and sedative properties. Scutellaria baicalensis and Radix Paeoniae as the main drugs of decoction, the study has shown participation in the treatment of diabetes and its complications (Cao Min X J et al., 2019; Zheng and Yankun, 2021; Yvette, 2020; Zhang et al., 2021; Fan et al., 2020; Ding et al., 2019; Yan and Jin, 2018; Sun et al., 2019; Gu and Chengjuan, 2020; Radica, 2020; xia et al., 2015), However, whether HQD can treat diabetic liver injury has not been reported, and this experiment elucidate the effect of HQD on diabetic liver injury. Related research has discovered that baicalin, an active ingredient in Scutellaria baicalensis Georgi, has a therapeutic effect on various diabetic complications and can effectively improve rats with diabetes and non-alcoholic fatty liver (Kuo et al., 2019); Paeoniflorin in Radix Paeoniae can inhibit hepatocyte apoptosis by improving oxidative stress and regulating multiple inflammation-related pathways (Wang et al., 2012), Early pharmacodynamic investigations by this study group revealed that HQD may significantly pull back ALT, AST, SOD, and MDA levels, slow down the liver injury, and control blood sugar levels in model mice to achieve preventive and therapeutic disease advantages.

Metabolomics, the qualitative and quantitative analysis of small molecular metabolites in biological samples, as well as the investigation of the relationship between metabolites and research objects, and its application in the discovery of DLI biomarkers are essential for the treatment of a variety of metabolic diseases, including DLI. Biomarkers are important tools for clinical diagnosis. They are regarded as effective methods for integrative research (Wang et al., 2015; Wang et al., 2017). The development of network pharmacology builds on the increasing understanding of protein and molecular interactions and is of great help to understanding the pathogenesis of TCM syndrome and the therapeutic mechanism of TCM (Ning et al., 2018; Guo et al., 2020; Zheng et al., 2021). Therefore, the combination of network pharmacology and metabolomics provides an effective way to scientifically explain the metabolic mechanism of TCM in the treatment of diabetes and its complications.

A metabolomics technique based on ultra-high liquid chromatography-mass spectrometry (UPLC-MS) combined with network pharmacology technology was utilized to demonstrate the therapeutic effect of HQD on DLI to identify potential therapeutic targets. Create a DLI model and use liver metabolomics to test for various metabolites. After that, use network pharmacology to identify possible targets for HQD in the treatment of DLI and to create a complete network of metabolomics and network pharmacology. Finally, molecular docking is used to validate the obtained key targets. This research used a combination of metabolomics and network pharmacology to develop a technique for understanding the potential mechanism of DLI and identifying prospective targets for HQD in DLI management.

EXPERIMENTAL MATERIALS AND METHODS

Experimental Materials

Scutellaria baicalensis Georgi; Radix Paeoniae; Jujube; Licorice (purchased from Hebei Quantai Pharmaceutical Co., Ltd.); Metformin was purchased from Biotopped (CAS NO.: 1115-70-4), Pentobarbital Sodium (SIGMA); Leucine Enkephalin (L9133, Sigma-Aldrich); Methanol (Chromatography grade, Dikma Technology Company); Acetonitrile (Chromatography

grade, Dikma Technology Company); Ultra-high liquid chromatography-time-of-flight tandem mass spectrometer (Wates Company, USA); Cryogenic refrigerated centrifuge (Thermo Scientific Company, USA); KQ-500DB Ultrasonic cleaner (Kunshan Ultrasonic Instrument Co., Ltd.); Nichipet EX micro sampler (10–100 μl, 100–1000 μl, NICHIRYO company, Japan); VX-II multi-tube vortex oscillator (Beijing Tajin Technology Co., Ltd.); Thermo Scientific 995 ultra-low temperature refrigerator (Thermo Scientific Company, USA); Rotary evaporator (SHZ-III YR1813583).

Preparation of HQD: weigh Radix Scutellariae, Radix Paeoniae Alba, Jujube, and Licorice in a 3:2:2:2 ratio, add 10 times the total weight of water in volume, soak for 30 min, decoct for 1 h, and filter. The filtrate is obtained, and the residue is added to 8 times the volume of water and decocted for 1 h again, filtered to obtain the filtrate, and the filtrate obtained from the two times is mixed and concentrated to 1.5 g/ml. Take out part of the concentrate and dilute it with water according to the ratio of 1:2 to get the final concentration of low-dose HQD of 0.5 g/ml.

Scutellaria baicalensis Georgi; Radix Paeoniae; Jujube; Licorice were acquired from the Hebei Quantai Pharmaceutical Co., Ltd. The voucher specimen of the herb was authenticated by Prof. Zhenyue Wang of the Department of Resources and Development of TCM at Heilongjiang University of Chinese Medicine, and it met the standards of the "Pharmacopoeia of the People's Republic of China (2020 edition)". The extract of HQD was obtained from our previous experiments and stored in the theoretical laboratory of TCM properties of Heilongjiang University of Chinese Medicine.

This experimental group has completed the quality standard determination of HQD in the early stage. According to the 2020 Chinese Pharmacopoeia (Committee, 2020), baicalin in Scutellaria should not be less than 8.0%, and paeoniflorin in Radix Paeoniae should not be less than 1.2%. All of these are determined to meet the 2020 Chinese Pharmacopoeia standard. The chromatogram is shown in Fig S.

Experimental Animals

The 48 male db/db mice and 8 db/m mice were purchased from Airmate Technology Co., Ltd (Animal Certificate Number: No.202009670). The mice were fed in a single cage in a clean barrier system, with free to eat and drink, temperature regulated at 20-26°C, humidity-controlled at 40-70%, and alternating animal lighting in the light and dark cycle maintained 12/12 h. The cages and padding were replaced once a week. All animal experiments were conducted following the relevant regulations of Heilongjiang University of Traditional Chinese Medicine's experimental animal ethics committee (DWLL20151108001).

The db/db mice were fed adaptively for 1 week, and a random blood glucose test was performed twice. The db/db mice with a blood glucose level of more than 11.1 mol/L were separated into three groups: the model group (3.75 g/kg), active control group (metformin 250 mg/kg): high-dose HQD group (11.25 g/kg), low-dose HQD group (3.75 g/kg), The control group consisted of db/m mice. After grouping, each group was administered according to the 7.5mg/kg administration volume and administered once daily for 8 weeks.

Sample Processing and Analysis

The mice were anesthetized intraperitoneally with pentobarbital sodium 24 h after the last treatment. Blood samples were taken from the eyeball. After standing (4°C, 60min), the blood samples were centrifuged (3500r/min, 15min, 4°C). After removing the liver tissue, the saline was perfused, sucked dry using filter paper, immediately deposited in liquid nitrogen, frozen, and transported to a - 80°C refrigerator to calculate AST and ATL indices. It is utilized to detect SOD, MDA levels and perform UPLC-TOF-MS analysis. After thawing at room temperature, 9 times the amount of frozen methanol was added for grinding, vortex mixing for 3 min, centrifuged (12000r/min, 15min, 4°C) twice, and the supernatant was kept at -80°C for SOD and MDA level detection and UHPLC/MS analysis.

Detection of Random Blood Glucose

Random blood glucose in the mouse tail vein was measured randomly once every two weeks during the experimental cycle.

Detection of Biochemical Indicators in Biological Tissue Samples

To detect the corresponding indicators, prepare the serum and tissue homogenates and determine the levels of SOD and MDA in liver tissue and the levels of AST and ALT in the serum, according to the kit instructions.

Liver Histopathological Observation

The left liver lobes of each mice were sliced and immediately placed in a formaldehyde-fixed solution. After 48 h, it was usually preserved in paraffin, sectioned, and stained with hematoxylin and eosin (HE). Under a light microscope, the pathological alterations in liver tissue were examined.

UPLC-Q-TOF MS Analysis

UPLC conditions: Chromatographic column; ACQUITY UPLC® BEH C_{18} Chromatographic column (2.1 mm × 50 mm, i.d. 1.7 μm), A is acetonitrile (containing 0.05% formic acid), mobile phase B is water (containing 0.05% formic acid), and the gradient elution program is 0–8 min: 98% -60% B; 8–10 min: 60%-2% B; 10–13 min: 2%-0% B; 13–14 min: 0%-98%B; 14–17min: 98%-98%B; flow rate is 0.40 ml/min, injection volume is 2 μl, column temperature is 40°C, sample chamber temperature: 5°C. Mass spectrometry conditions: Electrospray ion source (ESI) utilizes positive and negative ion modes for detection. The locked mass concentration is 2.0 μg L^{-1}, and the flow rate is 40 μL min^{-1}. Dissolvent gas temperature 350°C, dissolvent gas flow 750.0L/h, ion source temperature 110°C, cone gas flow: 20 L/h, capillary voltage positive ion 1300.0 V, negative ion 1500.0 V; sample cone voltage positive ion 60.0 V, negative ion 70.0 V; use LockSprayTM correction system for online mass correction of leucine enkephalin, data acquisition range m/z 100 ~ 1500 Da, adopt full scan mode.

Multivariate Statistical Analysis of Liver Metabolic Profiles and Identification of Potential Biomarkers

Align the raw data processed by UPLC-Q-TOF-MS, then preprocess the peak matching, noise reduction, and

normalization data. The data from liver tissue were analyzed using the software ProgenesisQI and EZinfo2.0 (MarkerLynx1.4 workstation software), PCA (principal components analysis) was used for unsupervised statistical analysis, and the samples to be tested were grouped and analyzed using supervised partial least squares discriminant analysis (PLS-DA) to obtain the corresponding score map. SIMCA-P software 12.0 should be used for default cross-validation, and 200 random permutations should be utilized to evaluate the data to prevent overfitting of the PLS-DA model. The S-plot and variable importance projection VIP-plot were used to illustrate the dispersion between groups. The specific metabolites were screened using the score map and the deviation change trend across each ion aggregation point group. The substantially different expressed metabolites were discovered using the same standard. Then, as screening criteria, variable importance projection (VIP) > 1 and $p < 0.05$, fold change (FC) > 1.2 were employed to identify specific prospective biomarkers. Through the human metabolome database (HMDB), the Kyoto Encyclopedia of Genes and Genomes (KEGG), MetaboAnalyst (http://www.metaboanalyst.ca/), and other metabolic pathway databases, enrichment analysis and network construction of related metabolic pathways are conducted, and more information on the physiological and pathological status of differential metabolic markers is provided. A large amount of biological information was collected to search for various metabolites and metabolic pathways connected to disease studies.

Network Pharmacological Analysis

The active ingredients in HQD were screened using the TCMSP database under the criteria of 30% oral bioavailability (OB) and 18% drug-like activity (DL), and screened components were supplemented with literature reports. The retrieved components are imported successively into the TCMSP database to predict the target and get the relevant target's protein name. They were imported into the UniProt database for gene name transformation. The corresponding traditional Chinese medicine targets were obtained; the components without relevant targets were screened and removed to obtain the effective HQD components. The Genecards database was utilized to extract "DLI," and the intersection of disease target and drug target was used as the prediction target of drug effect on disease. The UniProt database has been adopted (http://www.uniprot.org/) to regulate the names of genes and proteins.

The target information of the interaction between HQD and DLI obtained above was imported into the STRING database (https://string-db.org/) to determine the connection between potential targets. The protein-protein interaction analysis results from the string database were visually evaluated using the Cytoscape v3.8.2 software, and a protein-protein interaction network was constructed. GO (gene ontology) annotation and KEGG (Kyoto encyclopedia of genes and genomes) pathway enrichment analysis were performed on the obtained HQD anti-DLI target using the ClueGo + CluePedia plug-in Cytoscape v3.8.2. The pathway with $p < 0.05$ was screened. Metscape is used to import the differential metabolites found in metabolomics into Cytoscape to generate a compound reaction enzyme gene network. This structure is designed to illustrate the interactions between metabolites, pathways, enzymes, and genes. The important metabolites and proteins were then identified by connecting the compound reaction enzyme gene network to the core and metabolic pathways.

Molecular Docking

The selected key genes were molecularly docked with the core components of HQD and metformin, respectively. Download the 2D structure of the active components in HQD and the positive drug metformin from the PubChem database, save it in "sdf" format, open it using ChemBio3D, optimize the mechanical structure, and save it in "mol2" format. The target protein's crystal structure is obtained from the RCSB protein database (https://www.rcsb.org/) stored in the pdb format. Convert the ligand and receptor files to pdbqt format using AutoDockTools1.5.6. The structure was improved by eliminating water molecules and replacing them with hydrogen atoms. Autodock Vina was used for the molecular docking investigation.

Statistical Analysis

Statistical analysis was performed using SPSS (26.0) statistical software by applying Chi Square test. p value less than 0.05 was considered as statistically significant.

RESULTS

Random Blood Glucose

Comparison of mice random blood glucose results found that the control group and the model group was particularly significant ($p < 0.01$). The difference between the positive control group and the model group was significant ($p < 0.05$). However, between the high and low dose groups and the model group ($p > 0.05$), indicating that the high and low doses of HQD had no significant effect on the blood glucose of DLI mice, the detailed results are shown in **Figure 1A**.

Observation of the Biochemical Indicators

As seen in **Figures 1B–E**, serum AST and ALT levels in the model group were significantly higher ($p < 0.01$) than in the control group, indicating that the liver function of mice was damaged. Compared to the model group, the high and low dose HQD group and the active control group could recover serum AST and alt levels, Among them, the high-dose HQD group had the most significant effect. Compared to the control group, the level of SOD in the model group's liver homogenate decreased significantly ($p < 0.01$), while the level of MDA increased significantly. In the high and low dose HQD group and the active control group, mice's SOD levels increased while their MDA levels decreased significantly, Among them, the high-dose HQD group had the most significant effect. The results show that HQD reversed blood AST and ALT and SOD and MDA levels in the liver homogenate of DLI mice.

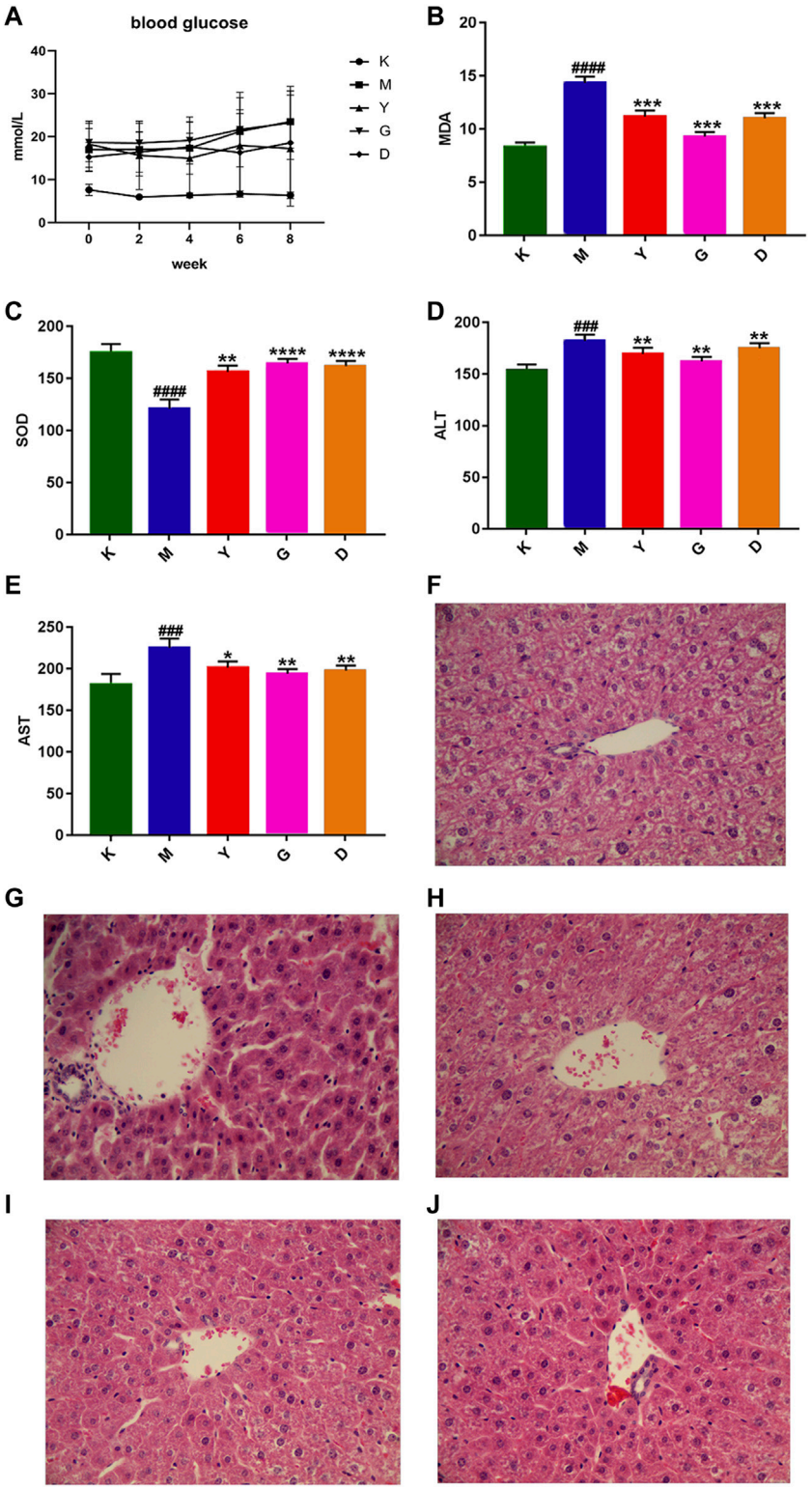

FIGURE 1 | Biochemical indexes were observed together with the histopathological sections. **(A)** Blood glucose changes in mice with DLI (n = 8, ±S); **(B)** Effect of HQD on SOD level in DLI model mice; **(C)** Effect of HQD on MDA level in DLI model mice; **(D)** Effect of HQD on AST level in DLI model mice; **(E)** Effect of HQD on ALT level in DLI model mice; Pathological observation; **(F)** The pathological changes of liver in control group (×20); **(G)** Histopathological changes of liver in model group (×20); **(H)** Histopathological changes of liver in high-dose HQD group (×20); **(I)** Histopathological changes of liver in low-dose HQD group (×20); **(J)** Histopathological changes of liver in active control group (×20). Note: (K: control group; M: model group; Y: Active control group; G: high-dose HQD group; D: low-dose HQD group).

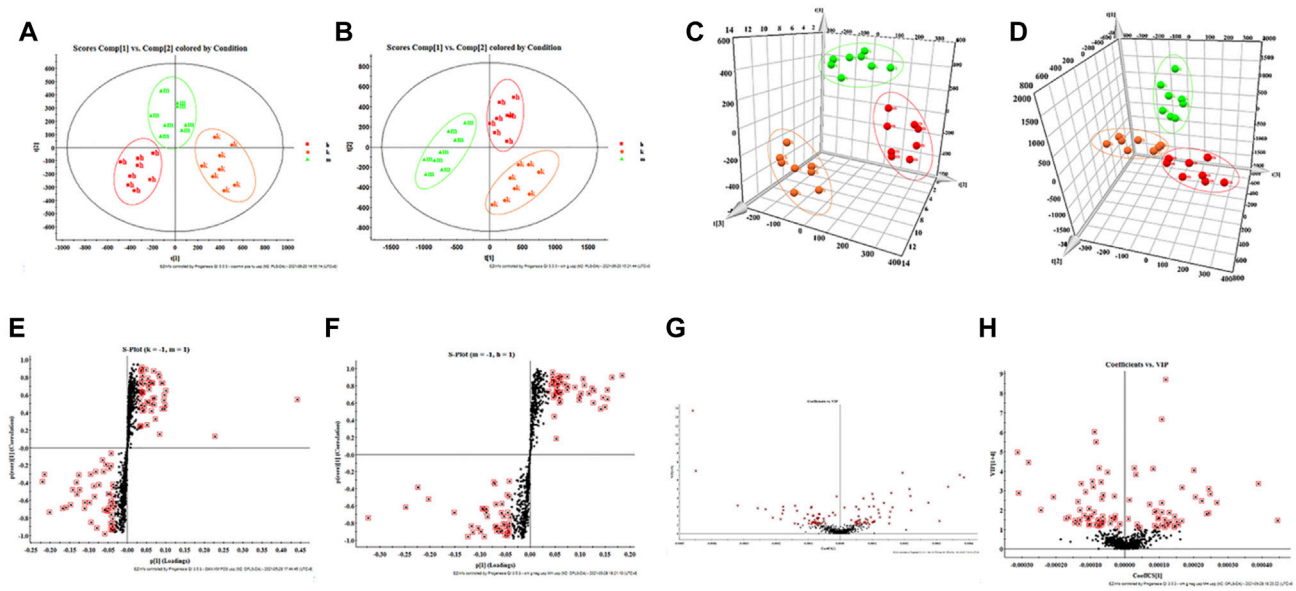

FIGURE 2 | Multivariate statistical analysis of liver metabolism spectrum in DLI mice. **(A)** 2D-PCA score plot in positive ion mode and **(B)** negative ion mode; **(C)** 3D-PCA score plot in positive ion mode and **(D)** negative ion mode; **(E)** S-plot in positive ion mode and **(F)** negative ion mode; **(G)** VIP plot in positive ion mode and **(H)** negative ion mode.

Histopathological Observation

The liver morphology of mice was studied under the microscope using HE staining. The hepatocytes of mice in the control group were tightly clustered and structurally intact, while the hepatocytes in the model group were enlarged and balloon-like in degeneration. The hepatocytes of mice are tightly grouped after the intervention of HQD and metformin, with the full structure and a small number of vacuoles, Among them, the high-dose HQD group had the most significant effect, as shown in **Figures 1F–J**.

Analysis of the Mice Liver Metabolomics Data

Combining the above pharmacodynamic index analysis, the high dose of HQD was selected for metabolomic analysis. By analyzing the data provided by UPLC-TOF-MS, PCA was processed using unsupervised orthogonal partial least squares discriminant analysis to determine the validity of the metabolic profile of mice liver supernatant samples. The results showed that the control group was significantly separated from the model group, indicating the high reliability of the model established in this study; when comparing the control group, the model group, and the HQD group at the same time, it can be found that each group presents its clustering. The HQD group has the trend of callback to the control group, indicating that HQD can improve the deviation of metabolism in **Figure 2A–D**.

According to the s-plot, most metabolite ions concentrate near the edges, with just a few ions deviating from it. These ions deviate from the origin, indicating differences between the two groups; by performing the screening requirements of VIP >1, the VIP plot can be obtained, and prospective biomarkers may be preselected, as illustrated in **Figure 2E–H**.

Endogenous Potential Biomarkers of Liver Metabolism in Mice

The horizontal axis represents different experimental groups. The vertical axis represents biomarkers compared by groups. Each row represents different markers in different samples. Each column represents the expression level of all markers in each sample in the heat map of markers obtained by hierarchical cluster analysis, **Figure 3A**. The color blocks at various places show the relative expression of the position markers. The heat map intuitively depicts the content variations of 18 possible biomarkers between groups. Possible biomarkers in the normal and DLI model groups can be readily separated, as can potential biomarkers in the HQD and model groups. The content level of potential markers in the HQD group is closer to that of the normal control group than that of the model group, as indicated in **Supplementary Table S1** and **Figure 4**.

The biomarkers selected from the HQD group were enriched in mice liver metabolomics using HMDB, KEGG, and other databases. The related metabolic pathways were identified using pathway analysis. Potential pathways should have a critical value greater than 0.10. The data indicate that it operates on eight different pathways, as shown in **Figures 3B,C**. As indicated in **Supplementary Table S2**, the major metabolic pathways with $p < 0.05$ and an effect value >0 include sphingolipid metabolism, taurine, and taurine metabolism, phenylalanine metabolism, glutathione metabolism, tryptophan metabolism, primary bile acid biosynthesis, and steroid hormone biosynthesis. Network pharmacological analysis.

After entering the keyword “Scutellaria baicalensis, Paeonia alba, Jujube, and Licorice” into the TCMSP database, 34 effective

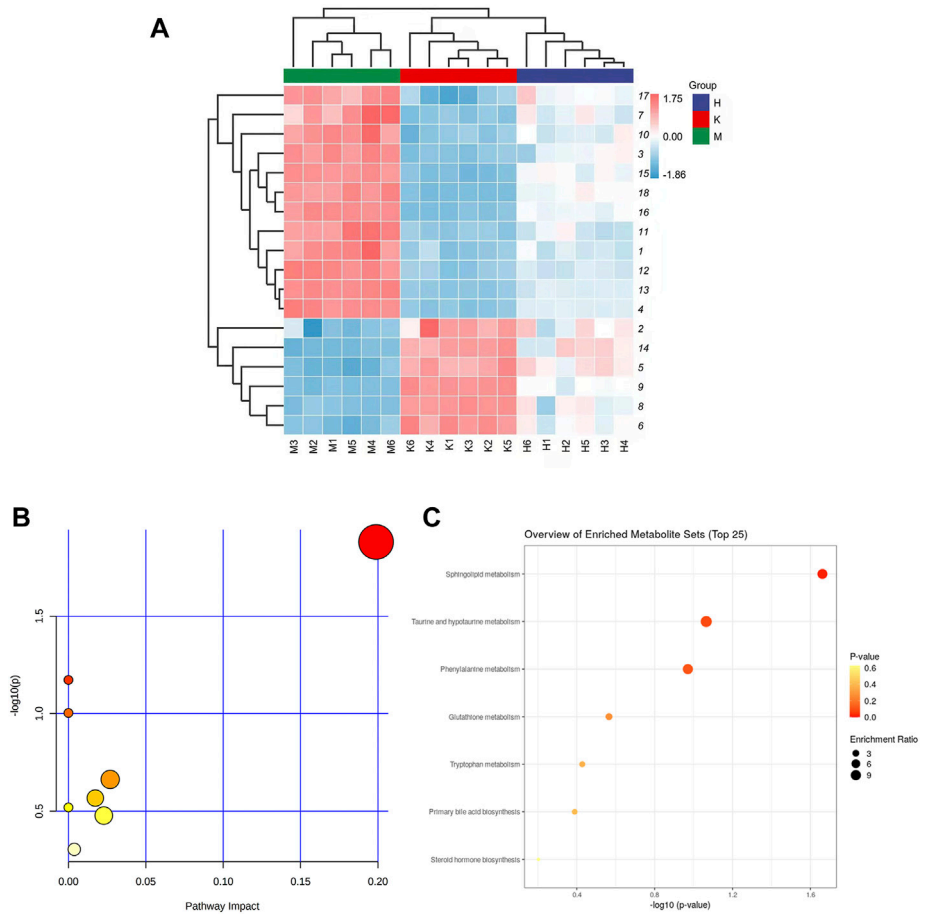

FIGURE 3 | (A) Liver tissue metabolite cluster analysis diagram (The numbers on the right are the serial numbers of metabolites in the **Table 1**; **(B)** Metabolite enrichment analysis bubble diagram; **(C)** Metabolic pathway analysis diagram.

components of Scutellaria baicalensis, eight effective components of Paeonia alba, 20 effective components of Jujube, and 90 effective components of Licorice were screened with OB ≥ 30% and DL ≥ 0.18. As shown in **Supplementary Table S3**, 141 components were obtained after merging and eliminating numerous elements. Obtain the SMILE standard structure of the active ingredients from the PubChem database (https://pubchem.ncbi.nlm.nih.gov/) and import it into the Swiss Target Prediction database (http://swisstargetprediction.ch/) for target prediction and deletion of duplicate targets. A total of 265 active ingredient-related targets have been obtained. Using the keyword "DLI," 1404 potential disease targets were found in the GenBank, Genecards, and OMIM databases. Intersect the medicinal' targets with the disease's targets. We obtained 161 total targets of HQD and DLI after mapping (**Supplementary Table S4**) and drew a Venn diagram, **Figures 5A**. HQD's "component-target-disease-pathway" network diagram is displayed in Cytoscape v3.8.2, **Figures 5B**.

Cytoscape 3.8.2 was used for visual analysis to construct a protein-protein interaction network to identify the essential genes of HQD against DLI, **Figures 5–C**. At the same time, the cytohubba plug-in was used to screen out the core targets, and when combined with the calculation method's score, the top 10 genes (PTGS2, MAPK3, AKT1, MAPK1, PTEN, EGFR, STAT3, CAT, NOS3, IL6) are considered to be the central genes (see **Supplementary Table S5**). ClueGo was used to conduct GO annotation and KEGG pathway enrichment on the potential target genes of HQD against DLI **Figures 5D,E**. According to the GO enrichment analysis results, there is mainly response to an organic substance, cellular response to chemical stimulus, positive regulation of the metabolic process, positive regulation of Metabolic cellular process, and regulation of cell communication. According to KEGG enrichment analysis, pathways in cancer, Hepatitis B, Hepatitis C, PI3K-Akt signaling system, and AGE-RAGE signaling pathway in diabetic complications are all significantly affected.

Integrative Analysis of the Network Pharmacology and Metabolomics

We constructed an interaction network based on metabolomics and network pharmacology to completely understand the mechanism of HQD against DLI. The different metabolites were input into Cytoscape's Metscape plug-in to generate a compound reaction enzyme gene network **Figure 6**. Sphingosine, glutathione,

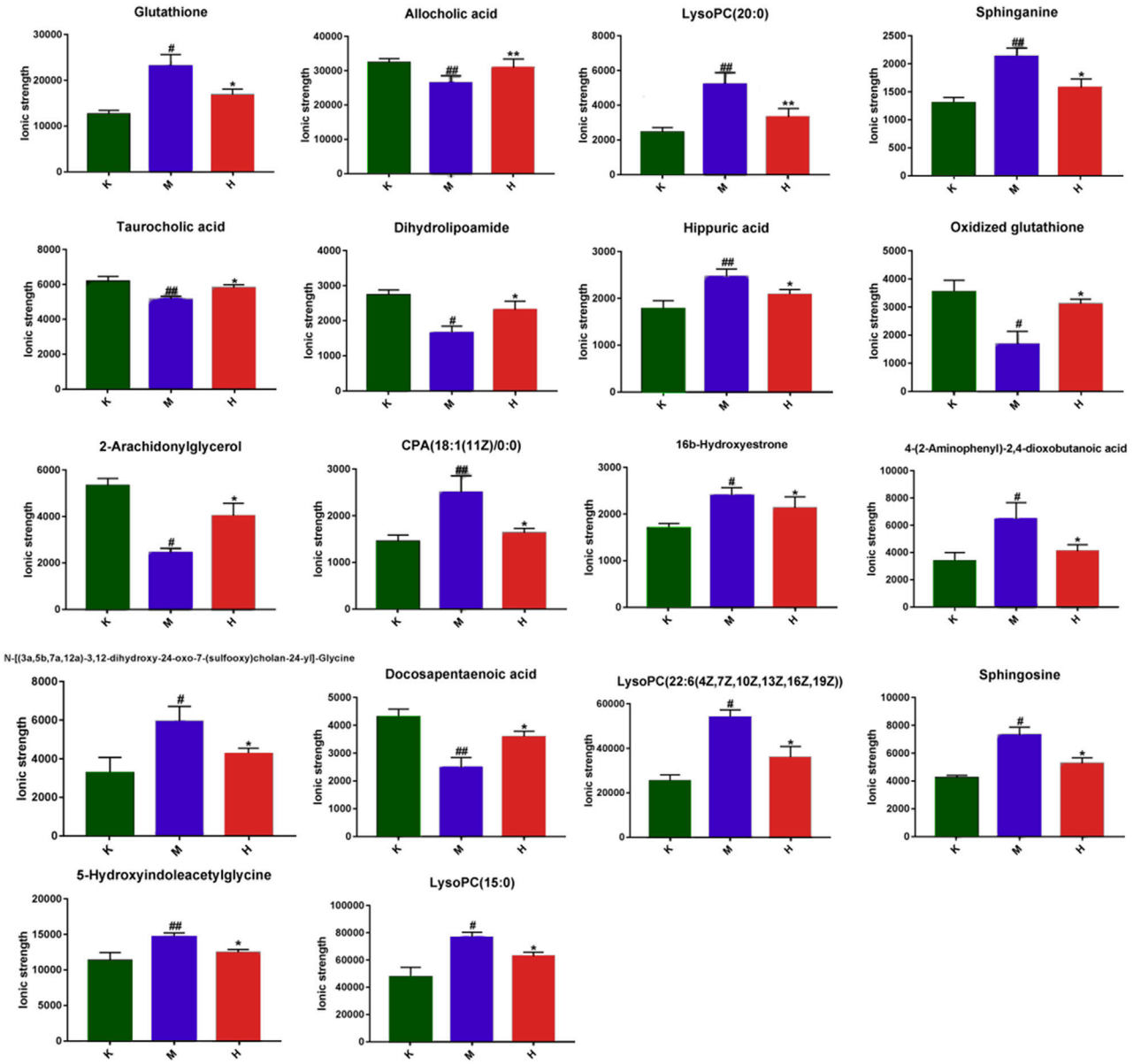

FIGURE 4 | Impact values of potential biomarkers in the liver (Comparison with control group: $^{**}p < 0.01$, $^{*}p < 0.05$; Comparison with model group: $^{\#\#}p < 0.01$, $^{\#}p < 0.05$).

dihydrolipoamide, and oxidized glutathione are the major metabolites found in network pharmacology. Metscape analysis was used to connect potential targets with genes. We identified five important targets: CAT, PTGS2, MAPK3, AKT1, and MAPK8 (**Supplementary Table S6**). Glycerophospholipid metabolism; tryptophan metabolism is the effect pathways. They may have an important role in HQD's therapeutic impact on DLI. Among these genes, PTGS2, MAPK3, and AKT1 are the key genes based on the degree values.

After examining the RCSB protein database, molecular docking may investigate three main targets, further investigating the probability of interaction between the active components of HQD metformin and key targets. The binding energy is used to assess the strength of interactions between small molecules and proteins. If the binding energy is less than 0, it indicates that the ligand molecules may spontaneously bind to the receptor protein. If the binding energy is less than - 5.0 kcal·mol^{-1}, it indicates that they have high binding activity, with the smaller the value indicating better binding activity. According to the molecular docking data, the binding energies of the key active components of HQD to AKT1, MAPK3, and PTGS2 were less than -5.0 kcal·mol^{-1} (**Supplementary Table S7**). The main active components (quercetin, kaempferol, wogonin, beta-sitosterol, naringenin) and target proteins (AKT1, MAPK3, PTGS2) in HQD have strong

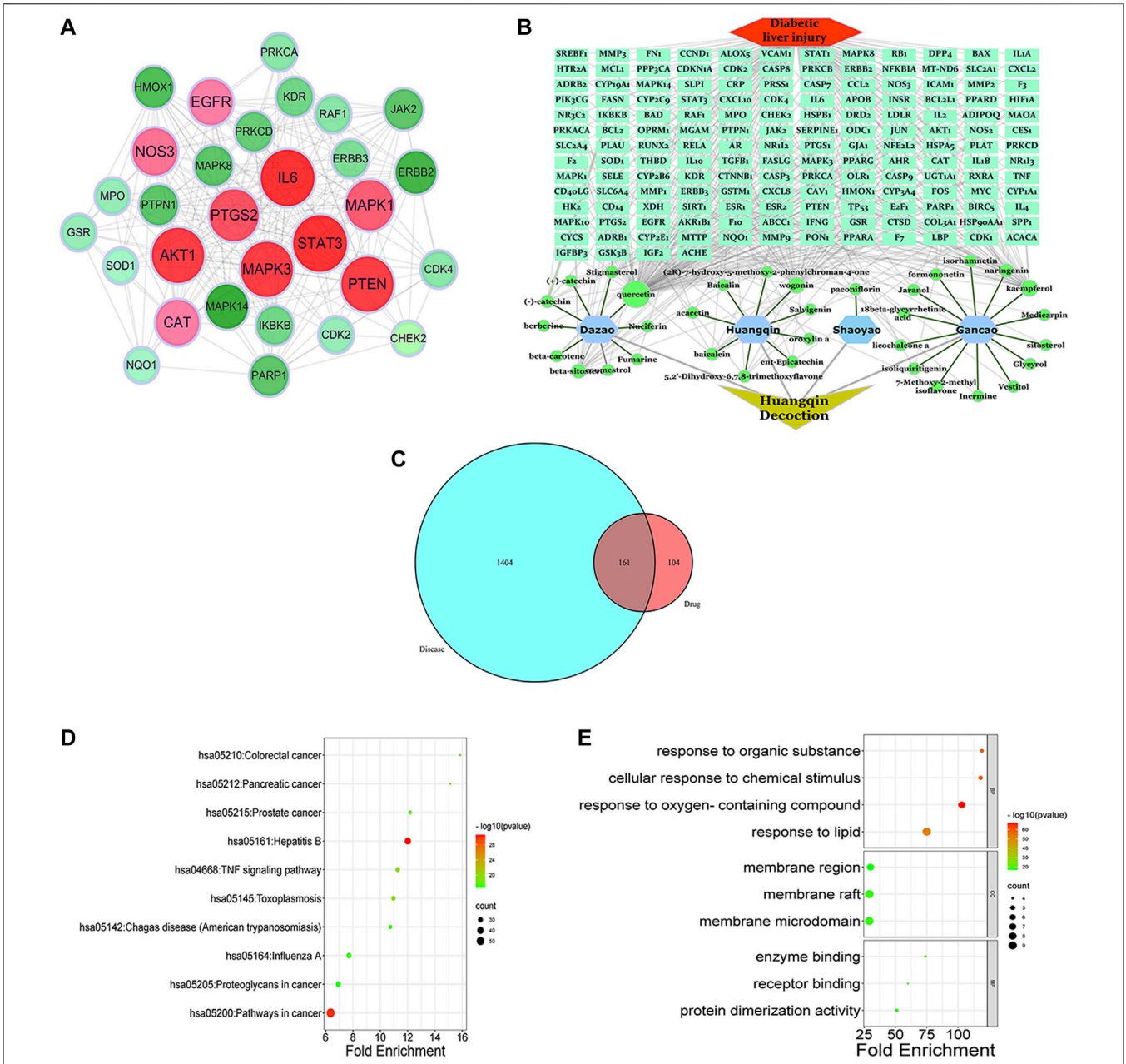

FIGURE 5 | Network pharmacology analysis of HQD for treatment of DLI. **(A)** HQD and DLI intersection target Venn diagram; **(B)** HQD in the treatment of DLI component-target-disease interaction network; **(C)** PPI network diagram of HQD against DLI; **(D)** KEGG pathway enrichment analysis; **(E)** GO enrichment analysis of potential targets.

binding activity, according to the analysis of the results, and the docking structure of the first seven positions is shown in **Figure 7**.

DISCUSSION

Confluence Analysis

Metabolomics technology analyzes low molecular weight endogenous metabolites in biological samples in detail, searches for new diagnostic or prognostic biomarkers of biological diseases, and explains the physiological changes associated with early diseases. On DLI, the metabolites and associated pathways of 18 different types of HQD were identified. On the other hand, Metabolomic investigations are limited to identify probable metabolites and linked pathways without further exploring their direct relationship. Network pharmacology is a systems biology-based methodology. It assesses the pharmacodynamic effects of medications at the molecular level to predict the interaction of natural products and

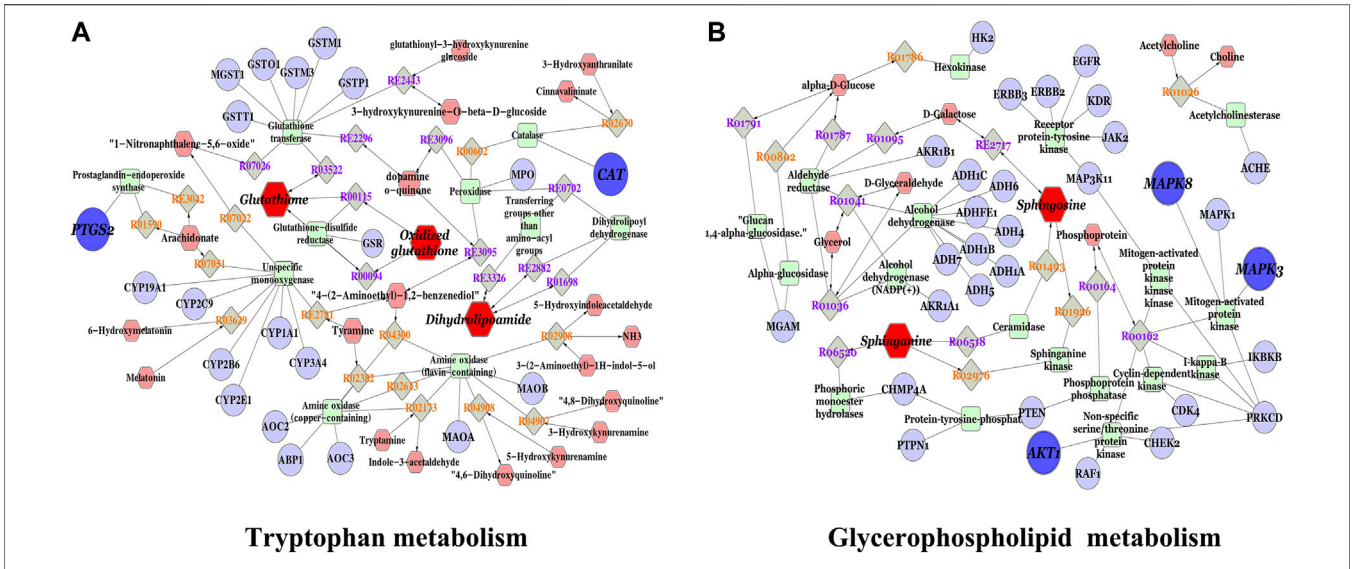

FIGURE 6 | Compound-reaction-enzyme-gene network of key metabolites and targets; **(A)** Tryptophan metabolism; **(B)** Glycerophospholipid metabolism. Red hexagons, gray diamonds, green round rectangles, and purple circles represent active compounds, reactions, proteins, and genes, respectively.

proteins and identify the main mechanisms. Network pharmacology may help confirm the therapeutic management of metabolic networks and identify essential targets and biomarkers. Five important targets (CAT, PTGS2, MAPK3, AKT1, and MAPK8), five critical metabolites (sphinganine, sphingosine, Glutathione, Oxidized gutahione, Dihydrolipoamide), and two linked metabolic pathways (glycerol phospholipid metabolism and tryptophan metabolism) were identified by integrating metabolomics with network pharmacology.

Related pharmacodynamic studies have shown the potential mechanism of HQD in the treatment of DLI. It was shown that HQD might considerably lower blood AST and ALT levels and MDA activity in the liver of model group, increase SOD activity in the liver and alleviate the degree of pathological damage to liver tissue. Endogenous compounds are bound to change in the liver, which is an important organ of human metabolism, and variations in its composition might reflect the entire metabolic profile of the body. The current study used liver metabolomics to investigate the changes in metabolites in the liver of mice and the protective impact of HQD on mice with DLI metabolic disorders from a metabolomics approach.

Lipid Metabolism

Glycerophospholipid metabolism is a form of lipid metabolism, and glycerophospholipids are the most abundant type of phospholipids in the body, being extensively dispersed throughout the biological membranes of numerous organs. The formation and degradation of glycerophospholipid molecules are related to lipid transport throughout the body (Kagan et al., 2016). Phosphatidylcholine, phosphatidylethanolamine, sphingolipids, and lysophosphatidylcholine are the most important lipid metabolites in the metabolism of glycerophospholipids. These lipids are essential components of serum lipoproteins and cell membranes, and they play a role in signal transmission. Through the hydrolysis of phospholipases, the metabolism of glycerophospholipids connects the important signal pathways of bodily fluid metabolism, supports the proper operation of material and energy metabolism, and maintains the balance and steady-state of metabolism. Phospholipase synthesis is another critical connection that influences glycerophospholipid metabolites. If its content is decreased, many phospholipid metabolites will accumulate, resulting in the formation of associated metabolic disorders (Shen et al., 2020). According to studies, DLI may cause glycerophospholipid molecules to be unable to be transported properly throughout the liver, resulting in deposits. Excessive glycerophospholipid deposits, on the other hand, might harm the liver. The glycerophospholipid metabolism in the liver of DLI mice was disrupted in this study, and HQD had a considerable restorative impact on the glycerophospholipid metabolism in DLI mice. In DLI mice, lysophosphatidylcholine and sphingolipid levels were disordered, LysoPC(15:0), LysoPC(20:0), LysoPC(22:6 (4Z,7Z,10Z,13Z,16Z, 19Z)), sphinganine, and sphingosine levels rose, and HQD had a positive impact on this. When combined with network analysis, it is hypothesized that HQD may regulate the levels of LysoPC (15:0), LysoPC(20:0), LysoPC (22:6 (4Z,7Z,10Z,13,16Z, 19Z)) and the levels of sphingolipids sphinganine and sphingosine, thus also regulating the glycerophospholipid metabolism network and achieving disease prevention and treatment. The molecular docking studies demonstrate that the core active components of HQD have a strong binding capacity with AKT and MAPK3, suggesting that HQD may impact AKT1 and MAPK3 Activity, which in turn affects glycerophospholipid metabolism.

Amino Acid Metabolism

As an important component of the human body, amino acids play a critical role in the metabolic pathways of numerous substances. As the basic substance of energy metabolism, the amino acid is a component of protein and an active substance with regulatory effects in a wide range of life activities. The liver is the main

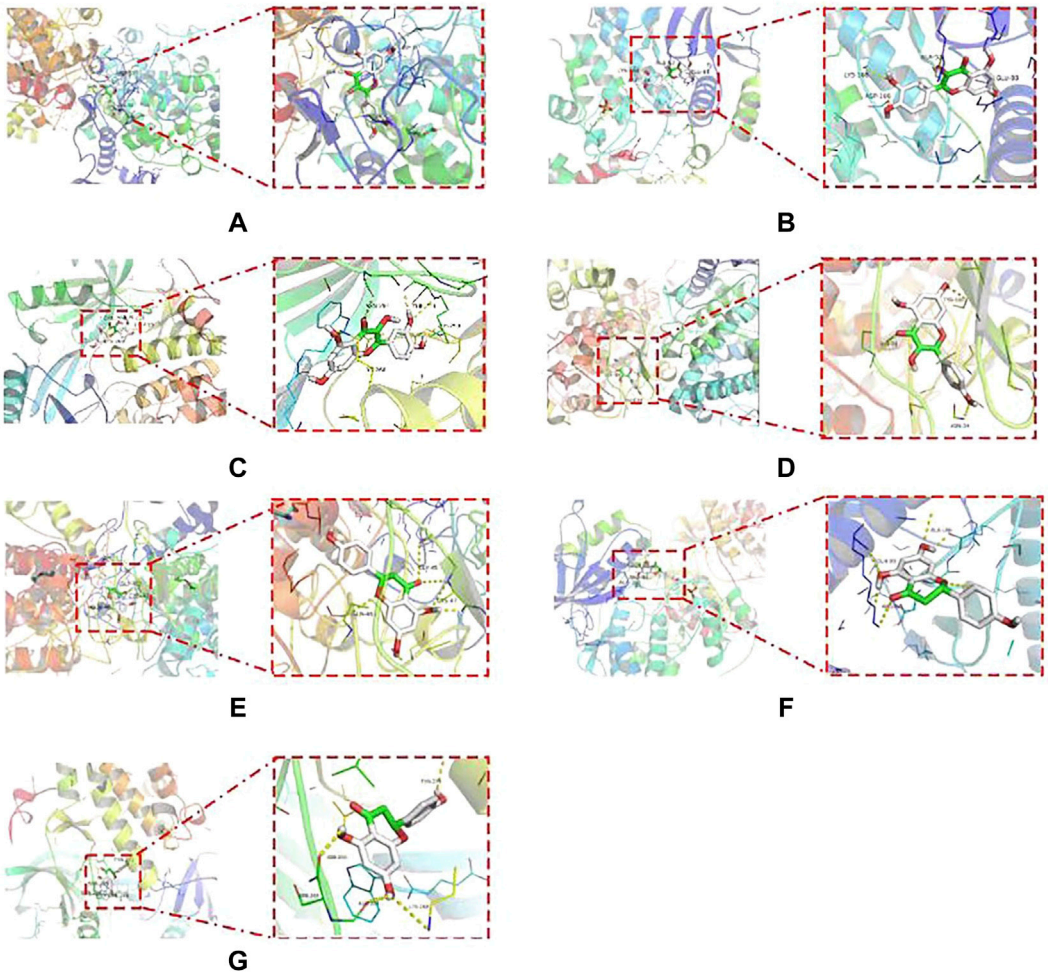

FIGURE 7 | Molecular docking diagram of the first 7 positions of binding energy. **(A)** quercetin and PTGS2; **(B)** Quercetin and MAPK3; **(C)** Quercetin and AKT1; **(D)** Kaempferol and PTGS2; **(E)** Naringenin and PTGS2; **(F)** Naringenin and MAPK3; **(G)** Naringenin and AKT1.

organ of material metabolism. It is essential for amino acid metabolism, protein synthesis, and breakdown. Tryptophan is an important amino acid for the human body. It can synthesize proteins and metabolize them into a range of bioactive molecules (Myint et al., 2013). It is a precursor of the neurotransmitter serotonin, which is employed for protein synthesis or converted into a range of bioactive compounds through the serotonin or kynurenine pathways (KP). The variety of physiological processes controlled by tryptophan reflects the complicated pattern of diseases associated with homeostasis alterations (Comai et al., 2020). Studies have shown that tryptophan metabolism disorder is found in diabetes and psychiatric disorders (Gulaj et al., 2010). During metabolism, tryptophan may be transformed into acetyl coenzyme A and subsequently into acetyl coenzyme A, entering the tricarboxylic acid cycle. It is created during the tricarboxylic acid cycle metabolism α-ketoglutarate, pyruvate, and oxaloacetic acid may be converted into corresponding amino acids by interacting with appropriate ammonia, such as glutamate, aspartic acid, alanine, and so on. Under the control of glutamylcysteine synthase and glutathione synthase, glutamic acid, cysteine, and glycine are condensed into glutathione through peptide bonds (Mutlib et al., 2000; Salyha, 2013; Gong et al., 2020; Xiang et al., 2021). This investigation revealed that, compared to the model group, the HQD treatment group could considerably callback the glutathione and oxidized glutathione concentrations. When combined with network analysis, it is hypothesized that HQD may indirectly restore tryptophan metabolism by controlling glutathione and oxidized glutathione levels, so working as disease prevention and therapy. Further molecular docking research showed that HQD might indirectly alter neurotransmitter production and tryptophan metabolism by changing PTGS2 activity.

CONCLUSION

The combination of network pharmacology and metabolomics analysis in this study can help explain the possible mechanism of HQD in treating DLI and reveal the biological process of HQD in treating DLI through regulating metabolic pathways. A detailed analysis revealed five main targets (CAT, PTGS2, MAPK3, AKT1,

and MAPK8), as well as related metabolites sphinganine, sphingosine, Glutahione, Oxidized gutahione, Dihydrolipoamide and pathways Glycerol phospholipid metabolism and Tryptophan metabolism. Molecular docking was used to confirm these targets. This research provides evidence and theoretical support for future investigation of the mechanism and establishes a framework for clinical application. It is expected to contribute to the development of HQD as a potential complementary medicine for treating DLI. More molecular biological studies are required to confirm the detailed mechanism.

DATA AVAILABILITY STATEMENT

The original contributions presented in the study are included in the article/**Supplementary Material**, further inquiries can be directed to the corresponding authors.

ETHICS STATEMENT

The animal study was reviewed and approved by Heilongjiang University of Chinese Medicine Laboratory Animal Centre.

AUTHOR CONTRIBUTIONS

XX conceived and designed the experiments; CF conducted the experimental work and analysis; YW developed the animal models and drafted the manuscript; FL and SL provided major revisions and comments to the manuscript. All authors reviewed and approved the final manuscript.

FUNDING

This work was supported by grants from Heilongjiang Touyan Innovation Team Program, the Major State Basic Research Development Program (973 Program) of China (project no. 2013CB531804).

SUPPLEMENTARY MATERIAL

The Supplementary Material for this article can be found online at: https://www.frontiersin.org/articles/10.3389/fphar.2022.899043/full#supplementary-material

Supplementary Figure S1 | Determination of baicalin and paeoniflorin by HPLC.

REFERENCES

Cao Min X J, D. Q., Yu, D. A. N., and Zhang, L. I. A. N. G. (2019). Efficacy of Baicalin Soup Combined with Metformin in the Treatment of Type 2 Diabetes and its Effect on the Composition of Intestinal flora and the Level of Insulin Signaling Molecules. *Chin. Arch. Traditional Chin. Med.* 37 (11), 2792–2795.

Comai, S., Bertazzo, A., Brughera, M., and Crotti, S. (2020). Tryptophan in Health and Disease. *Adv. Clin. Chem.* 95, 165–218. doi:10.1016/bs.acc.2019.08.005

Committee, N. P. (2020). *Pharmacopoeia of the People's Republic of China*. Beijing: China Medical Science and Technology Press.

Ding, J. G., Meilin, D. H., Yan, S. H. U. A. I., and Zong, Y. A. N. G. (2019). Overview of the Study on the Combination of Scutellaria Baicalensis - Huang Lian in the Treatment of Type 2 Diabetes Mellitus. *China Pharm.* 30 (17), 2440–2444.

Enhui C, S. Z. (2021). Exploring the Mechanism of Action of Scutellaria Baicalensis Soup in the Treatment of Pig Diarrhea Based on Network Pharmacology. *Prog. Vet. Med.* 42 (11), 111–116.

Fan, Z. Y., Jinghui, Z. Y., and yao, H. U. I. X. I. N. (2020). Effects of Baicalin on Blood Lipids and Liver Function in Rats with Diabetes Mellitus Combined with Non-alcoholic Fatty Liver. *China Mod. Doctor* 58 (09), 29–31.

Gong, Q. Y., Yang, M. J., Yang, L. F., Chen, Z. G., Jiang, M., and Peng, B. (2020). Metabolic Modulation of Redox State Confounds Fish Survival against Vibrio Alginolyticus Infection. *Microb. Biotechnol.* 13, 796–812. doi:10.1111/1751-7915.13553

Gu, W. H., and Chengjuan, W. X. (2020). Experience in the Treatment of Diabetic Erectile Dysfunction with Chuanxiong, Bai Shao and Centipede Powder--A Collection of Three Small Prescriptions by Tong Xiaolin Jilin. *J. Traditional Chin. Med.* 40 (11), 1417–1419.

Gulaj, E., Pawlak, K., Bien, B., and Pawlak, D. (2010). Kynurenine and its Metabolites in Alzheimer's Disease Patients. *Adv. Med. Sci.* 55, 204–211. doi:10.2478/v10039-010-0023-6

Guo, W., Wang, Y., Fan, M., Xie, S., Zhao, H., Wang, J., et al. (2020). Integrating Metabolomics and Network Pharmacology to Explore the Protective Effect of Gross Saponins of Tribulus Terrestris L. Fruit against Ischemic Stroke in Rat. *J. Ethnopharmacol* 263, 113202. doi:10.1016/j.jep.2020.113202

Kagan, V. E., Jiang, J., Huang, Z., Tyurina, Y. Y., Desbourdes, C., Cottet-Rousselle, C., et al. (2016). NDPK-D (NM23-H4)-mediated Externalization of Cardiolipin Enables Elimination of Depolarized Mitochondria by Mitophagy. *Cell Death Differ* 23, 1140–1151. doi:10.1038/cdd.2015.160

Kuo, Y. T., Lin, C. C., Kuo, H. T., Hung, J. H., Liu, C. H., Jassey, A., et al. (2019). Identification of Baicalin from Bofutsushosan and Daisaikoto as a Potent Inducer of Glucose Uptake and Modulator of Insulin Signaling-Associated Pathways. *J. Food Drug Anal.* 27, 240–248. doi:10.1016/j.jfda.2018.07.002

Liu, Q., Ahn, J. H., Kim, S. B., Lee, C., Hwang, B. Y., and Lee, M. K. (2013). Sesquiterpene Lactones from the Roots of Lindera Strychnifolia. *Phytochemistry* 87, 112–118. doi:10.1016/j.phytochem.2012.11.004

Luo, L. M., Qin, L., Zhan, J. H., Pei, G., Zhou, X. J., and Chen, N. H. (2018). Study on Effects of Total Saponins from Lilii Bulbus on Proliferation, Apoptosis, Invasion and Metastasis of Lung Cancer Cells and its Preliminary Mechanism. *Zhongguo Zhong Yao Za Zhi* 43, 4498–4505. doi:10.19540/j.cnki.cjcmm.20180629.001

Mutlib, A. E., Shockcor, J., Espina, R., Graciani, N., Du, A., and Gan, L. S. (2000). Disposition of Glutathione Conjugates in Rats by a Novel Glutamic Acid Pathway: Characterization of Unique Peptide Conjugates by Liquid Chromatography/mass Spectrometry and Liquid Chromatography/NMR. *J. Pharmacol. Exp. Ther.* 294, 735–745.

Myint, A. M., Bondy, B., Baghai, T. C., Eser, D., Nothdurfter, C., Schüle, C., et al. (2013). Tryptophan Metabolism and Immunogenetics in Major Depression: a Role for Interferon-γ Gene. *Brain Behav. Immun.* 31, 128–133. doi:10.1016/j.bbi.2013.04.003

Ning, Z., Wang, C., Liu, Y., Song, Z., Ma, X., Liang, D., et al. (2018). Integrating Strategies of Herbal Metabolomics, Network Pharmacology, and Experiment Validation to Investigate Frankincense Processing Effects. *Front. Pharmacol.* 9, 1482. doi:10.3389/fphar.2018.01482

Radica, l. H. L. M. (2020). Progress on the Mechanism of Action of Total Peony Glycosides in the Treatment of Diabetic Kidney Disease. *Chin. Arch. Traditional Chin. Med.* 38 (03), 126–128.

Salyha, N. O. (2013). Activity of the Glutathione System of Antioxidant Defense in Rats under the Action of L-Glutamic Acid. *Ukr Biokhim Zh (1999)* 85, 40–47. doi:10.15407/ubj85.04.040

Shen, Y., Xie, H. K., Liu, Z. Y., Lu, T., Yu, Z. L., Zhang, L. H., et al. (2020). Characterization of Glycerophospholipid Molecular Species in Muscles from Three Species of Cephalopods by Direct Infusion-Tandem Mass Spectrometry. *Chem. Phys. Lipids* 226, 104848. doi:10.1016/j.chemphyslip.2019.104848

Sun, L. H., Jie, R. J., Hu, X. U. E. J. I. A. N., and Yang, Y. A. N. (2019). Effect of Baicalin on the Expression of Survivin in Rats with Type 2 Diabetic Nephropathy. *Lishizhen Med. Materia Med. Res.* 30 (01), 59–61.

Tanase, D. M., Gosav, E. M., Costea, C. F., Ciocoiu, M., Lacatusu, C. M., Maranduca, M. A., et al. (2020). The Intricate Relationship between Type 2 Diabetes Mellitus (T2DM), Insulin Resistance (IR), and Nonalcoholic Fatty Liver Disease (NAFLD). *J. Diabetes Res.* 2020, 3920196. doi:10.1155/2020/3920196

Wang, M., Chen, L., Liu, D., Chen, H., Tang, D. D., and Zhao, Y. Y. (2017). Metabolomics Highlights Pharmacological Bioactivity and Biochemical Mechanism of Traditional Chinese Medicine. *Chem. Biol. Interact* 273, 133–141. doi:10.1016/j.cbi.2017.06.011

Wang, R., Xiong, A. Z., Teng, Z. Q., Yang, Q. W., Shi, Y. H., and Yang, L. (2012). Radix Paeoniae Rubra and Radix Paeoniae Alba Attenuate CCl4-Induced Acute Liver Injury: an Ultra-performance Liquid Chromatography-Mass Spectrometry (UPLC-MS) Based Metabolomic Approach for the Pharmacodynamic Study of Traditional Chinese Medicines (TCMs). *Int. J. Mol. Sci.* 13, 14634–14647. doi:10.3390/ijms131114634

Wang, Y. Y., Liu, S., Hu, Y., Li, P., and Wan, J.-B. (2015). Current State of the Art of Mass Spectrometry-Based Metabolomics Studies - a Review Focusing on Wide Coverage, High Throughput and Easy Identification. *RSC Adv.* 5 (96), 78728–78737. doi:10.1039/c5ra14058g

xia, X. Q., lingling, Z. Z., and zhu, Q. I. J. I. N. (2015). Modulation of Endoplasmic Reticulum Stress in the Liver of Diabetic Rats by Total Peony Glycosides. *Acta Universitatis Medicinalis Anhui* 50 (10), 1451–1455.

Xiang, Z., Xie, H., Tong, Q., Pan, J., Wan, L., Fang, J., et al. (2021). Revealing Hypoglycemic and Hypolipidemic Mechanism of Xiaokeyinshui Extract Combination on Streptozotocin-Induced Diabetic Mice in High Sucrose/high Fat Diet by Metabolomics and Lipidomics. *Biomed. Pharmacother.* 135, 111219. doi:10.1016/j.biopha.2021.111219

Yan, S. H., and Jin, W. F. (2018). Analysis of the Mechanism of Action of "Pueraria Lobata - Scutellaria Baicalensis" in the Treatment of Diabetes Mellitus Based on Network Pharmacology. *J. Shanxi Univ. Chin. Med.* 41 (05), 173–177.

Yue, S., Shan, B., Peng, C., Tan, C., Wang, Q., and Gong, J. (2022). Theabrownin-targeted Regulation of Intestinal Microorganisms to Improve Glucose and Lipid Metabolism in Goto-Kakizaki Rats. *Food Funct.* 13, 1921–1940. doi:10.1039/d1fo03374c

Yvette, C. Y. Z. J. (2020). Efficacy of Dried Ginger, Scutellaria and Scutellaria Ginseng Soup in the Treatment of Diabetic Gastroparesis with Mixed Cold and Heat. *J. Guangzhou Univ. Traditional Chin. Med.* 37 (06), 1030–1034.

Zhang, C., Changhua, W. Y., Xue, Y. A. N. A. N., ZhoulifenAi, Z. H. I. F. U., and Luo, X. I. A. O. Q. U. A. N. (2021). The Effect of Scutellaria Baicalensis on Ameliorating Liver Tissue Inflammation in Type 2 Diabetic KK-Ay Mice Is Associated with Down-Regulation of TRAF6, IL1α, NF-Kb2, RSK1 and RSK2 Protein Expression. *Lishizhen Med. Materia Med. Res.* 32 (01), 61–33.

Zhang, H. Y., Wang, H. L., Zhong, G. Y., and Zhu, J. X. (2018). Molecular Mechanism and Research Progress on Pharmacology of Traditional Chinese Medicine in Liver Injury. *Pharm. Biol.* 56, 594–611. doi:10.1080/13880209.2018.1517185

Zheng, W. N., and Yankun, Z. D. (2021). Effect of Baicalin on GLP-1 and Glucagon Secretion in Type 2 Diabetic Mice. *Med. J. West China* 33 (10), 1436–1439+1445.

Zheng, Y., Shi, X., Hou, J., Gao, S., Chao, Y., Ding, J., et al. (2021). Integrating Metabolomics and Network Pharmacology to Explore Rhizoma Coptidis Extracts against Sepsis-Associated Acute Kidney Injury. *J. Chromatogr. B Analyt Technol. Biomed. Life Sci.* 1164, 122525. doi:10.1016/j.jchromb.2021.122525

Conflict of Interest: The authors declare that the research was conducted in the absence of any commercial or financial relationships that could be construed as a potential conflict of interest.

Publisher's Note: All claims expressed in this article are solely those of the authors and do not necessarily represent those of their affiliated organizations, or those of the publisher, the editors and the reviewers. Any product that may be evaluated in this article, or claim that may be made by its manufacturer, is not guaranteed or endorsed by the publisher.

frontiers | Frontiers in Pharmacology

ORIGINAL RESEARCH
published: 26 May 2022
doi: 10.3389/fphar.2022.875014

Antidiabetic Effect of *Rehmanniae* Radix Based on Regulation of TRPV1 and SCD1

*Ye Liu[1†], Ruizheng Zhu[2†], Bei Liu[1,3†], Wuqing Wang[2], Ping Yang[1], Zhonglian Cao[1], Xiaolei Yang[1], Wandi Du[1], Qing Yang[1], Jingru Liang[1], Jiarong Hu[1] and Guo Ma[1]**

[1]School of Pharmacy, Fudan University, Shanghai, China, [2]Department of Dermatology, Minhang Hospital, Fudan University, Shanghai, China, [3]Ruijin Hospital, Shanghai Jiao Tong University School of Medicine, Shanghai, China

Purpose: This study aimed to disclose the antidiabetic mechanisms of *Rehmanniae* Radix (RR).

Methods: The antidiabetic effect of RR was studied in Streptozocin (STZ)–induced diabetes mellitus (DM) rats and HepG2 cells with insulin resistance (IR). Antidiabetic targets and signaling pathways of RR were confirmed by the network pharmacology and transcriptome analysis as well as HK2 cells induced by high glucose (HG).

Results: After the DM rats were administrated RR extract (RRE) for 4 weeks, their body weight was 10.70 ± 2.00% higher than those in the model group, and the fasting blood glucose (FBG), AUC of the oral glucose tolerance test, and insulin sensitivity test values were 73.23 ± 3.33%, 12.31 ± 2.29%, and 13.61 ± 5.60% lower in the RRE group, respectively. When compared with the model group, an increase of 45.76 ± 3.03% in the glucose uptake of HepG2 cells with IR was seen in the RRE group. The drug (RR)–components–disease (DM)–targets network with 18 components and 58 targets was established. 331 differentially expressed genes (DEGs) were identified. TRPV1 and SCD1 were important DEGs by the intersectional analysis of network pharmacology and renal transcriptome. The *TRPV1* overexpression significantly inhibited apoptosis and oxidative stress of the HK2 cells induced by HG, while *SCD1* overexpression induced apoptosis and oxidative stress of the HK2 cells induced by low and high glucose. When compared to the HG group, the mRNA and protein expressions of TRPV1 in the presence of RRE (100 μg/ml) increased by 3.94 ± 0.08 and 2.83 ± 0.40 folds, respectively.

Conclusion: In summary, RR displayed an inspiring antidiabetic effect by reducing FBG and IR, upregulating the mRNA and protein expressions of TRPV1, and downregulating mRNA expression of SCD1. Induction of TRPV1 and inhibition of SCD1 by RR was possibly one of its antidiabetic mechanisms.

Keywords: *Rehmanniae* Radix, diabetes mellitus, transient receptor potential vanilloid 1, stearoyl-CoA desaturase 1, network pharmacology, transcriptome

OPEN ACCESS

Edited by:
Ahmed Abdel Moneim, Helwan University, Egypt

Reviewed by:
May Nasser Bin-Jumah, Princess Nourah bint Abdulrahman University, Saudi Arabia
Rami B. Kassab, Helwan University, Egypt

***Correspondence:**
Guo Ma
mg0328@fudan.edu.cn

[†]These authors have contributed equally to this work and share the first authorship

Specialty section:
This article was submitted to Drug Metabolism and Transport, a section of the journal Frontiers in Pharmacology

Received: *13 February 2022*
Accepted: *11 April 2022*
Published: *26 May 2022*

Citation:
Liu Y, Zhu R, Liu B, Wang W, Yang P, Cao Z, Yang X, Du W, Yang Q, Liang J, Hu J and Ma G (2022) Antidiabetic Effect of Rehmanniae Radix Based on Regulation of TRPV1 and SCD1. Front. Pharmacol. 13:875014. doi: 10.3389/fphar.2022.875014

INTRODUCTION

Diabetes mellitus (DM) is a metabolic/endocrine disorder with an increasing incidence and prevalence worldwide. According to the diabetes atlas of the International Diabetes Federation (IDF Diabetes Atlas 10th edition), 537 million adults (20–79 years) suffer from DM. This number is predicted to rise to 643 million by 2030 and 783 million by 2045. A large national survey (Li et al., 2020) indicated that the total number of patients with DM in the Chinese mainland is estimated to be 129.8 million. DM is characterized by hyperglycemia caused directly by insufficient insulin secretion or insulin resistance (IR). Its pathology is irreversible and is often accompanied by many complications. The blood vessels, heart, brain, kidney, nerves, eyes, feet, and other organs are damaged by long-term hyperglycemia, leading to death in severe cases (DiMeglio et al., 2018; Lascar et al., 2018).

Herbs [e.g., *Rehmanniae radix* (Gaert.) Libosch, *Astragalus membranaceus* (Fisch.) Bunge, *Ginkgo biloba* Linn, *Pueraria lobata* (Willd.) Ohwi] have been used to treat DM for thousands of years, those which exhibit favorable antidiabetic effects and low side effects (Yokozawa et al., 1986; Shi et al., 2011; Tong et al., 2012; Wen et al., 2012; Tzeng et al., 2013). As one of the most commonly used antidiabetic herbs, RR has been recorded in Chinese pharmacopoeia and many classical prescriptions such as Liuwei Dihuang decoction, Huanglian Dihuang decoction, and Dangguiliuhuang decoction (Zhang et al., 2008; Cao et al., 2017). *Rehmanniae* Radix (RR) displayed favorable clinical effects in the treatment of metabolic diseases such as DM (Kim et al., 2017). RR and its components, e.g., iridoid glycoside, catalpol, rehmannioside D, oligosaccharide, and polysaccharide, have been proven to ameliorate DM by improving IR, regulating lipid metabolism, protecting islet β cells, and anti-inflammatory and antioxidant (Kitagawa et al., 1971; Zhang et al., 2008; Choi et al., 2013; Zhang et al., 2013; Zhang et al., 2014; Yan et al., 2018).

As everyone knows, herbs possess multicomponent and multi-target characteristics, which makes research on the antidiabetic mechanism of herbs full of challenges. In 2007, Hopkins (2007) proposed the theory of network pharmacology, believing that drugs produce pharmacodynamics and toxic effects based on the interaction of drug–disease–target (Hopkins, 2007, 2008), which coincides with the core idea of the Traditional Chinese medicine (TCM) theory. Network pharmacology provides an opportunity to forecast and explain the mechanism and pharmacodynamic material of antidiabetic herbs. Network pharmacology has been widely used to study the antidiabetic mechanism of multiple herbs and their preparations, e.g., *Coptis chinensis* Franch, *Hedysarum multijugum* Maxim, *Sorghum bicolor* (Linn.) Moench (L.), leaf of *Morus alba* Linn (Xu et al., 2020; Xu et al., 2020c; Guo et al., 2020; Meng et al., 2020; Oh et al., 2020; Pan et al., 2020; Wu and Hu, 2021). At present, there are few studies on RR against DM through network pharmacology.

As a macro approach, transcriptomics has changed the research mode of a single gene and brought omics research into the era of rapid development (Lander et al., 2001; Zhao et al., 2018). The application of transcriptomics in the field of herbs helps in explaining the syndrome differentiation theory of TCM and the action mechanism of herbs at the gene level. The antidiabetic targets and signaling pathways (e.g., PI3K/Akt/FoxO1 and PPARα) of herbs such as *Coptis chinensis* Franch., *Panax ginseng* C. A. Meyer, *Alisma orientale*, and *Potentilla discolor* Bunge have been studied, identified, and validated by transcriptome (Han et al., 2019; Xu et al., 2020b; Yang et al., 2020; Wu et al., 2021).

At present, some targets and signaling pathways of RR and its component catalpol against DM have been revealed, such as AGEs/RAGE/SphK1, Nrf-2, mitogen-activated protein kinases (MAPK), nuclear localization of nuclear factor kappa B (NF-KB), and the AMPKX4/PI3K/AKT signaling pathway (Choi et al., 2013; Lv et al., 2016; Mohamed and Samak, 2017; Yan et al., 2018).

Among the numerous antidiabetic targets, transient receptor potential vanilloid 1 (TRPV1) and stearoyl-CoA desaturase 1 (SCD1) were particularly interesting. TRPV1 was discovered by David Julius in 1997 and was identified as an ion channel that can be activated by heat and capsaicin to cause pain, for which David Julius was awarded the 2021 Nobel Prize. In recent years, numerous studies have demonstrated that TRPV1 plays a vital role in metabolic diseases (Radu et al., 2013). TRPV1 is linked to adipose accumulation and energy expenditure by inhibiting the development of preadipocytes into mature adipocytes and increasing their lipolysis (Zhang et al., 2007). It has been proven that TRPV1 activation may mediate the browning of white adipose tissue (WAT) *via* activating peroxisome proliferators–activated receptors γ (PPARγ), positive regulatory domain containing 16 (PRDM16), and the AMPK signaling pathway (Baskaran et al., 2016), which indicates that TRPV1 is a promising target against DM.

SCD1 is a rate-limiting enzyme that converts saturated fatty acids (SFA) to monounsaturated fatty acids (MUFA). It plays an important role in metabolic abnormalities (Liew et al., 2004; Liu et al., 2013) by affecting insulin sensitivity and lipid metabolism (Popeijus et al., 2008; Sampath and Ntambi, 2011). It is a potential therapeutic target for DM, obesity, hypertension, and dyslipidemia (Enoch et al., 1976).

In this study, the DM rats were constructed to study the antidiabetic efficacy and mechanism of RR. The HepG2 cells with IR were established to study the influence of RR on glucose uptake. The drug (RR)–components–disease (DM)–targets network was established, and the antidiabetic targets and signaling pathways of RR were identified by the combination of network pharmacology and transcriptomics analysis. The role of TRPV1 and SCD1 in the treatment of DM was studied using the HK2 cells with the overexpressions of the two key targets in the low- and high-glucose groups, respectively. Regulation of mRNA and protein expressions of TRPV1 and SCD1 by RRE was assayed by qRT-PCR and western blot. This study will be conducive to disclosing the antidiabetic mechanism of RR from multiple perspectives, especially the regulation of TRPV1 and SCD1.

MATERIALS AND METHODS

Chemicals and Biological Products

Rehmanniae Radix extract (30:1, i.e., 1 g extract/30 g herb) was purchased from Xi'an Xinlu Biotechnology Co., Ltd. (#20200910,

China). Streptozocin (STZ, #S0130), recombinant human insulin (#91077C), and metformin hydrochloride (PHR1084) were obtained from Sigma-Aldrich Inc. (United States). 2-[N-(7-nitrobenz-2-oxa-1,3-diazol-4-yl)amino]-2-deoxyglucose (2-NBDG, #GC10289) was obtained from GlpBio Inc. (United States). Insulin aspart 30 injection (#S20133006) was obtained from Novartis Inc. (Switzerland). cDNA Synthesis SuperMix for qPCR (#11141ES6), qPCR SYBR Green Master Mix (#011199ES08), Annexin V-Alexa Fluor 647/PI Apoptosis Detection Kit (#40304ES60), JC-1 Mitochondrial Membrane Potential Assay Kit (#40706ES60), Mitochondrial ROS Detection Kit (#50102ES02), and CCK-8 assay kit (#40203ES80) were obtained from Yeasen Co., LTD. (China). Lipofectamine 3000 (#L3000075) was obtained from Thermo Scientific (United States). The TRPV1, SCD1, and GAPDH antibodies were obtained from Cell Signaling Technology (United States). The HepG2 and HK2 cells were purchased from ATCC (American Type Culture Collection, United States).

Cell Culture

The human hepatocellular carcinoma cell line (HepG2) was cultured in Dulbecco's modified Eagle's medium (DMEM) with 25.5 mM glucose, 1% penicillin/streptomycin, and 10% fetal bovine serum under 5% CO_2 and 95% air at 37°C. The human renal proximal tubular epithelial cell line (HK2) was cultured in DMEM with 5.5 mM glucose, and all the other conditions remained the same as for HepG2. When the cells grow to about 80% fusion, the passage was carried out in a ratio of 1:2.

Cell Viability

The cells were seeded in 96-well plates at a density of 5×10^4 cells per milliliter. After 24-h culture, the cells were incubated with different stimulation for 48 h. Then, the cell viability was evaluated using the CCK-8 kit (Meilunbio, China) following the manufacturer's instructions. The OD value was detected at 450 nm by a microplate reader. The cell survival rate was calculated according to the following formula:

$$\text{Cell survival rate} = \left[\frac{\text{As} - \text{Ab}}{\text{Ac} - \text{Ab}}\right] \times 100\%,$$

where A_s is the absorbance of the experimental well (given stimulation); A_c is the absorbance of the control wells (no stimulation); and A_b is the absorbance of the blank well (no cells).

Glucose Uptake

The HepG2 cells were cultured in 12-well plates at a density of 5×10^4 cells per milliliter. The optimal concentration (25, 50, 100, 200, and 300 μM) of 2-NBDG (E_x/E_m = 502/530 nm) was explored. The cells were incubated with 2-NBDG solution diluted in glucose-free DMEM for 1 h, with three duplicates at each concentration. After PBS washing, the cells were digested and suspended again and detected within 1 h. Fluorescence was detected by the FITC channel from flow cytometry (FCM), which was characterized by the mean area of FITC, and the results were analyzed by the FlowJo software.

Influence of *Rehmanniae* Radix Extract on HepG2 Cells With Insulin Resistance

The HepG2 cells were cultured in 12-well plates at a density of 5×10^4 cells per milliliter. A high concentration of insulin was used to induce insulin resistance in the HepG2 cells. The HepG2 cells were incubated with a series of insulin solutions (0.5, 5, 10, 20, and 40 μg/ml) for 48 h to determine the optimal insulin concentration so as to reach the lowest glucose uptake. To investigate the influence of RRE on the HepG2 cells with IR, the blank control group [insulin (−), drug (−)], the model group [insulin (+), RRE (−)], the positive control group [insulin (+), 1 mM metformin], and the administration group [insulin (+), 25, 50, 100 μg/ml of RRE] were incubated with the HepG2 cells for 48 h. The assays were performed in triplicates. Then, the glucose uptake detection was performed.

Animals

The rats were reared in the Laboratory Animal Center, School of Pharmacy, Fudan University. The temperature was set at 25 ± 2°C, the humidity was kept at 45–50%. All the animal cages, feed, drinking water, and bedding materials were sterilized by high-pressure steam. All the laboratory operations were conducted in an ultraclean platform. After 2 weeks of adaptive feeding, 15 healthy Sprague Dawley (SD) male rats (200–250 g) were randomized into groups and fasted for 12 h, from which 10 rats were intraperitoneally injected with 1% STZ solution at a dose of 60 mg/kg bodyweight, and an equal volume of saline was intraperitoneally injected into the other five rats. On the 7th day after injection, all the rats were fasted for 12 h, and the fasting blood glucose (FBG) level was tested. When the FBG of the rats was ≥16.7 mmol/L (300 mg/dl), it was considered to meet the standards of DM. The DM rats were randomly divided into the model group (n = 5) and RRE group (n = 5), and the healthy rats (n = 5) were divided into the normal group. The normal group and model group were given an intragastric administration of saline once a day, and the RRE group was given RRE suspension at the dose of 450 mg/kg once a day. The administration lasted for 4 weeks, and the fasting body weight and FBG of all the rats were measured weekly. One week after the last experiment, the kidneys, small intestines, and skeletal muscles of the rats were collected and stored at −80°C. All animal care and experimental protocols complied with the Animal Management Rules of the Ministry of Health of the People's Republic of China and were approved by the Animal Ethics Committee of the School of Pharmacy, Fudan University (Ethics approval No. 2020-04-LY-MG-01, Shanghai, China).

Oral Glucose Tolerance Test and Insulin Sensitivity Test

An oral glucose tolerance test (OGTT) was performed 4 weeks after the administration of RRE. After fasting for 12 h, all the rats were weighed and their FBG was detected. Glucose solution was orally administrated to the rats at the dose of 2 g/kg body weight. Blood glucose was detected at 30, 60, 120, 180, and 240 min after administration. An insulin sensitivity test (IST) was performed a

week after the OGTT. After fasting for 12 h, all the rats were weighed and their FBG were detected. The solution of insulin was injected intraperitoneally into the rats at a dose of 0.8 U/kg body weight. Blood glucose was detected at 30, 60, 120, and 180 min after insulin administration.

Network Pharmacology of *Rehmanniae* Radix

Active Components Screening

All the components of RR were obtained from a systematic pharmacological database of TCM, i.e., TCMSP (https://old.tcmsp-e.com/tcmsp.php). Two ways to filter these components were conducted, one of which was the conditioning of the TCMSP database, which was set at an oral absorption rate (OB) ≥20% and druglikeness (DL) ≥0.1. The second way was the ADME filtering through the SwissADME database (http://www.swissadme.ch/), which included absorption, distribution, metabolism, and excretion. The relevant parameters were calculated by the database when the structural formula of the components was input. The components were included when GI absorption in the pharmacokinetics parameter was high and at least two "yes" appeared in the five parameters of druglikeness (Lipinski, Ghose, Veber, Egan, and Muegge). The components included in the TCMSP and Swiss databases were combined.

Prediction and Intersection of Target

The TCMSP and Swiss databases were used to predict drug-related targets. The protein name of targets obtained from the TCMSP database was converted into the corresponding gene name by the UniProt database (https://www.uniprot.org/). The targets were also predicted using the SwissTargetPrediction database (http://www.swisstargetprediction.ch/) by entering the component structure formula and were screened according to a probability p value >0.4. The drug-related targets were obtained by merging the two databases, of which the repeated targets of the same component were removed. For the disease-related targets, the GeneCards database (http://www.genecards.org/) was searched using "Diabetes" or "diabetic" as the keywords. Venny 2.1.0 tool (https://bioinfogp.cnb.csic.es/tools/venny/index.html)was used to obtain the intersection of the drug-related targets and disease-related targets.

Protein–Protein Interaction Network Construction

Calculation of the intersection targets was performed by the String database platform (https://www.string-db.org/). The conditions were set to *Homo sapiens*, and the minimum required interaction score to ≥0.4. Proteins without interaction were removed. The number of nodes connected by each target was calculated and sorted by R language.

Transcriptome Analysis

The kidney, small intestine, and skeletal muscle tissue samples from the rats (three in each group) were used for the transcriptome analysis by Shanghai Majorbio Bio-pharmTechnology Co., Ltd, using the Illumina HiSeq™ 2500 sequencer. The raw data obtained by the Illumina sequencing platform were analyzed following the process of sequence alignment, transcript assembly, functional annotation and query, and expression analysis. Transcripts per million (TPM) reads were used to characterize gene expression, and the calculation formula is as follows:

$$TPM = \frac{\mathrm{R} \times 10^6}{\left(\frac{R_1}{l_1} + \frac{R_2}{l_2} + \_ + \frac{R_n}{l_n}\right) \times l},$$

where R and L represent the read counts and gene lengths of the genes to be calculated, respectively. R_1–R_n and L_1–L_n represent the read counts and gene lengths of all genes in the sample, respectively.

The DESeq2 software was used to calculate the differential expression of genes according to the TPM value. Differentially expressed genes (DEGs) were identified with the standard of |FC| >1.5 and p value <0.05. The DEGs were intersected and divided into two parts, i.e., upregulation and downregulation, and the 10 DEGs with the lowest p values were selected to verify the gene expression trend by qRT-PCR.

Gene Ontology and Kyoto Encyclopedia of Genes and Genomes Analyses

GO and KEGG enrichment analyses were performed on the DAVID database (https://david.ncifcrf.gov/). The GO terms mainly included molecular functions, cellular components, and biological processes. The KEGG pathway was classified according to the Kyoto Encyclopedia of Genes and Genomes (KEGG) database (https://www.kegg.jp/kegg/pathway.html). When p.adjust was <0.1, the GO terms and KEGG pathways were considered to be significantly enriched.

Quantitative Real-Time Polymerase Chain Reaction

Total RNA of the rat kidney tissues or HK2 cells was isolated using RNAiso Plus (TaKaRa Biotech, China). After reverse-transcription, qRT-PCR was performed by the Applied Biosystems QuantStudio 3 system (Thermo Fisher, American). The reactions were performed following the cycling conditions: 95°C for 10 s, followed by 40 cycles of 95°C for 5 s, 60°C for 30 s, and 72°C for 30 s. The mRNA level of the target genes was normalized and analyzed by the $2^{-\Delta\Delta CT}$ method. The primers were designed from the Prime-BLAST function of the National Center for Biotechnology Information (NCBI) database and synthesized by Shenggong Bioengineering Co., Ltd. (Shanghai, China). The primer sequences are listed in **Supplementary Table S2**.

Cell Transfection

The coding sequences of *TRPV1* and *SCD1* were constructed on pcDNA3.1-3× Flag (+) vector by Hunan Fenghui Biotechnology Co., Ltd. (Fenghui, China). The plasmid extraction was carried out according to the plasmid extraction kit scheme (# DP103-03, Tiangen Biotech, China). The HK2 cells were cultured in 12-well plates at a density of 5×10^4 cells per milliliter for 24 h. Transfection of *TRPV1* and *SCD1* as well as the vector in HK2 cells (1,250 ng plasmids per well) was performed using Lipofectamine® 3000 (#L3000015, Thermo Fisher Scientific,

United States). And every transfection group was divided into low-glucose (5.5 mM) and high-glucose (60 mM) groups with three duplicates. Total RNA was extracted 48 h after transfection, and the gene overexpression was verified by qRT-PCR.

Cell Apoptosis Detection

The HK2 cells transfection was carried out as described above. Apoptosis was evaluated using the Annexin V-Alexa Fluor 647/ Propidium Iodide (PI) Apoptosis Detection Kit 48 h after transfection. The cells were digested by EDTA-free trypsin, washed with PBS, and resuspended with the binding buffer. The cells in each well were incubated with Annexin V-Alexa Fluor 647 (5 μl) and PI (10 μl) at room temperature in the dark for 15 min. The detection was conducted by using the APC and PE channels from FCM within 1 h.

Reactive Oxygen Species Detection

The HK2 cells transfection was carried out as described above. DCFH-DA (10 mM) was diluted with serum-free low-glucose DMEM at a ratio of 1:3000 to obtain the staining solution. 500 μl of the staining solution was added into each well and incubated at 37°C for 30 min. After the probe was transferred, the cells were washed with PBS, digested and resuspended, and detected by FCM within 1 h. The fluorescence intensity of the cells was measured by the FITC channel.

Mitochondrial Superoxide Detection

The HK2 cells transfection was carried out as described above. Mitochondrial superoxide (MitoSOX, 5 mM) was diluted with serum-free low-glucose DMEM at a ratio of 1:1,000 to obtain the staining solution. Probe loading was carried out the same as " ROS detection," but the incubation time was 20 min. The cells were digested and resuspended, and then detected by the PI channel of FCM.

Mitochondrial Membrane Potential Detection

The HK2 cells transfection was carried out as aforementioned. The JC1 staining working solution and buffer solution were configured according to the instruction of the kit. The probe loading and cell collection methods were the same as 1.14. The cells were detected by FCM within 1 h. The fluorescence intensity of the cells was measured by FITC and PE double-channel.

Western Blot

Proteins from the HK2 cells were extracted by using RIPA buffer with 1% of PMSF and protease inhibitor cocktail following the standard protocol, and then protein concentrations were quantified using a bicinchoninic acid (BCA) protein assay kit. Equal amounts of protein extracts were loaded on SDS-PAGE (150 V, 80 min) and electrotransferred to a 0.45-μm PVDF membrane (200 mA, 90 min). The membranes were blocked with 5% nonfat milk for 1 h at room temperature and incubated with primary antibodies overnight at 4°C. On the next day, fluorescence-conjugated secondary antibodies were applied to the membranes for 1 h at room temperature. The membranes were visualized with FluorChem Alpha Imaging (ProteinSimple, United States). Target proteins were normalized to GAPDH and quantified by the ImageJ software.

Effect of *Rehmanniae* Radix Extract on mRNA and Protein Expressions of TRPV1 and SCD1

The HK2 cells were seeded at a density of 5×10^4/ml in 6-well plates. The cells were grouped into low-glucose (LG) and high-glucose (HG) groups; and the HG groups were further divided into groups of RRE administration (25, 100, and 400 μg/ml) and positive control (CAP, capsaicin, 10 μM). Total RNA and protein were extracted after 48 h of the administration, and the mRNA and protein expressions of TRPV1 and SCD1 were detected by qRT-PCR and Western blot, respectively.

Statistical Analysis

The data were analyzed by GraphPad Prism 9.0 software for Windows (GraphPad Software, San Diego, CA). Two-way ANOVA and one-way ANOVA were used. $p < 0.05$ was considered to be significant.

RESULTS

Cytotoxicity of *Rehmanniae* Radix Extract and Glucose

RRE was nontoxic to the HepG2 and HK2 cells within the concentration range of 0–400 μg/ml, and the cell survival rate was above 80% (**Supplementary Figure S1A**). Moreover, the survival rate of the HK2 cells increased with an increase of RRE concentration and decreased with an increase of glucose concentration (5.5–120 mM) (**Supplementary Figure S1B**). The survival rate of the HK2 cells was lower than 80% at 80 mM of glucose (**Supplementary Figure S1C**). Finally, 60 mM was chosen as the concentration for high-glucose stimulation.

Rehmanniae Radix Extract Increases Glucose Uptake of HepG2 Cells With Insulin Resistance

Compared to the blank group, the glucose uptake of the HepG2 cells with IR in the model group was significantly reduced ($p < 0.05$) and that of the positive control group was increased (**Figure 1F**; **Supplementary Figure S2**). Compared to the model group, RRE (25–100 μg/ml) can increase glucose uptake of the cells and inhibit IR of the cells with increasing concentration of RRE, of which the glucose uptake of the cells increases 45.76 ± 3.03% in the RRE (100 μg/ml) group (**Figure 1G**).

Rehmanniae Radix Extract Ameliorates Diabetic Conditions in Streptozocin-Induced Diabetes Mellitus Rats

The DM-related indicators such as body weight, FBG, OGTT, and IST were determined after administrating RRE for 4 weeks (**Figure 1A**). The weekly weight was significantly increased and the weekly FBG was significantly decreased in the rats that of the RRE group than that of the model group during the experimental cycle ($p < 0.05$, **Figures 1B, C**). After the DM

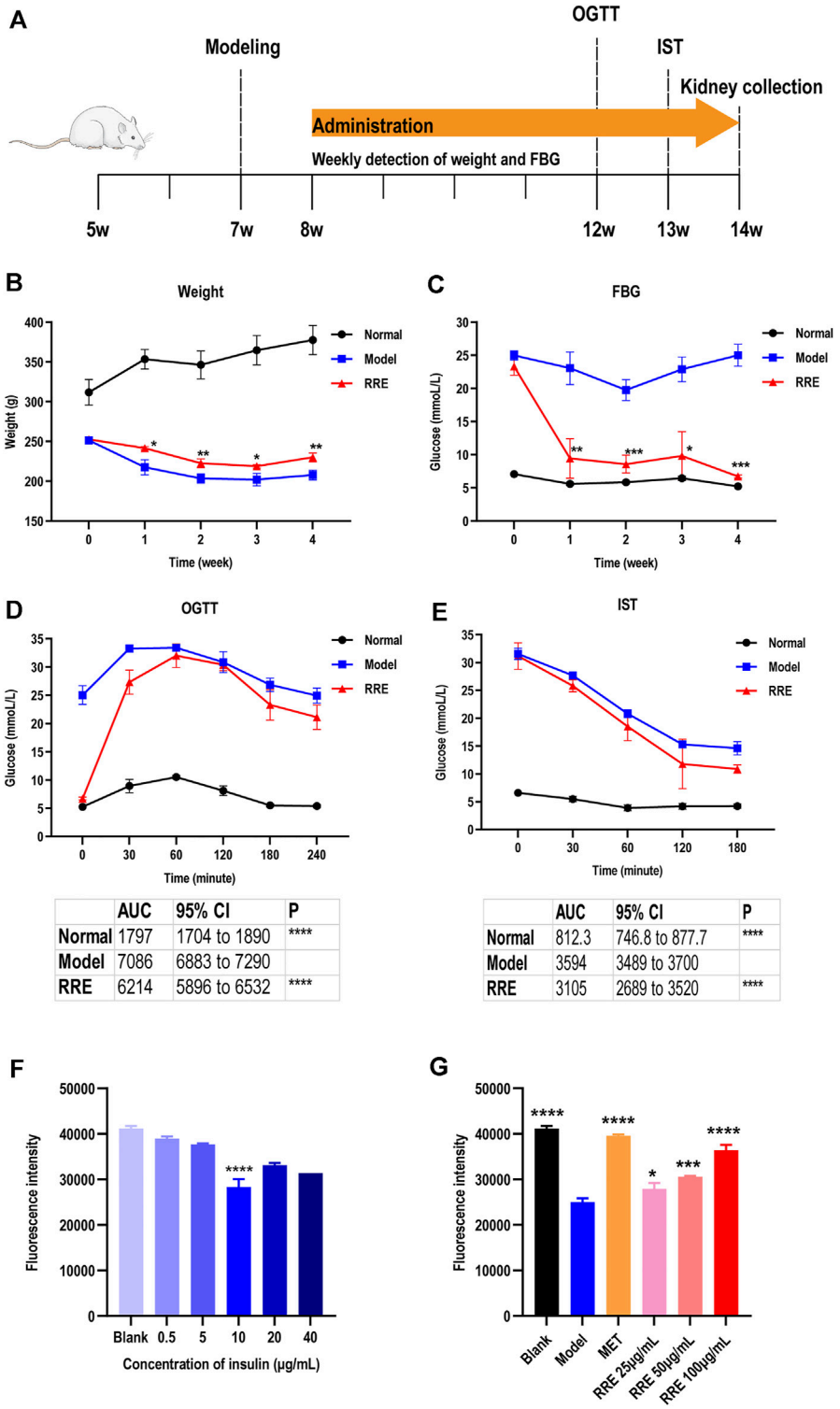

	AUC	95% CI	P
Normal	1797	1704 to 1890	****
Model	7086	6883 to 7290	
RRE	6214	5896 to 6532	****

	AUC	95% CI	P
Normal	812.3	746.8 to 877.7	****
Model	3594	3489 to 3700	
RRE	3105	2689 to 3520	****

FIGURE 1 | Antidiabetic effect of RRE in *in vivo* and *in vitro* studies. **(A)** Schematic timetable for the suggested antidiabetic experiments *in vivo*. The SD rats were induced by STZ at 7 weeks of age. After 4 weeks of RRE administration, the metabolic phenotype of the rats was evaluated by an oral glucose tolerance test (OGTT) at 12 weeks of age, followed by 1 week of recovery time and subsequently an IST. **(B)** Weekly weight of the SD rats in different groups. **(C)** Weekly FBG of the SD rats in different groups. **(D)** Blood glucose of the SD rats at each time point in the OGTT. The table shows the area under the curve (AUC) and its 95% CI. **(E)** Blood glucose at each time point in the insulin sensitivity test. The table shows the area under the curve (AUC) and its 95% CI. **(F)** Influence of different concentrations of insulin on glucose uptake in HepG2 cells. Glucose uptake was characterized by fluorescence intensity of 2-NBDG. ****, comparison with the blank group, $p < 0.0001$. **(G)** Effects of different concentrations of RRE on glucose uptake in the HepG2 cells with insulin resistance (IR). Glucose uptake was characterized by fluorescence intensity of 2-NBDG. MET, Metformin. *, **, ***, ****, comparison with the model group, $p < 0.05$, $p < 0.01$, $p < 0.001$, $p < 0.0001$, respectively.

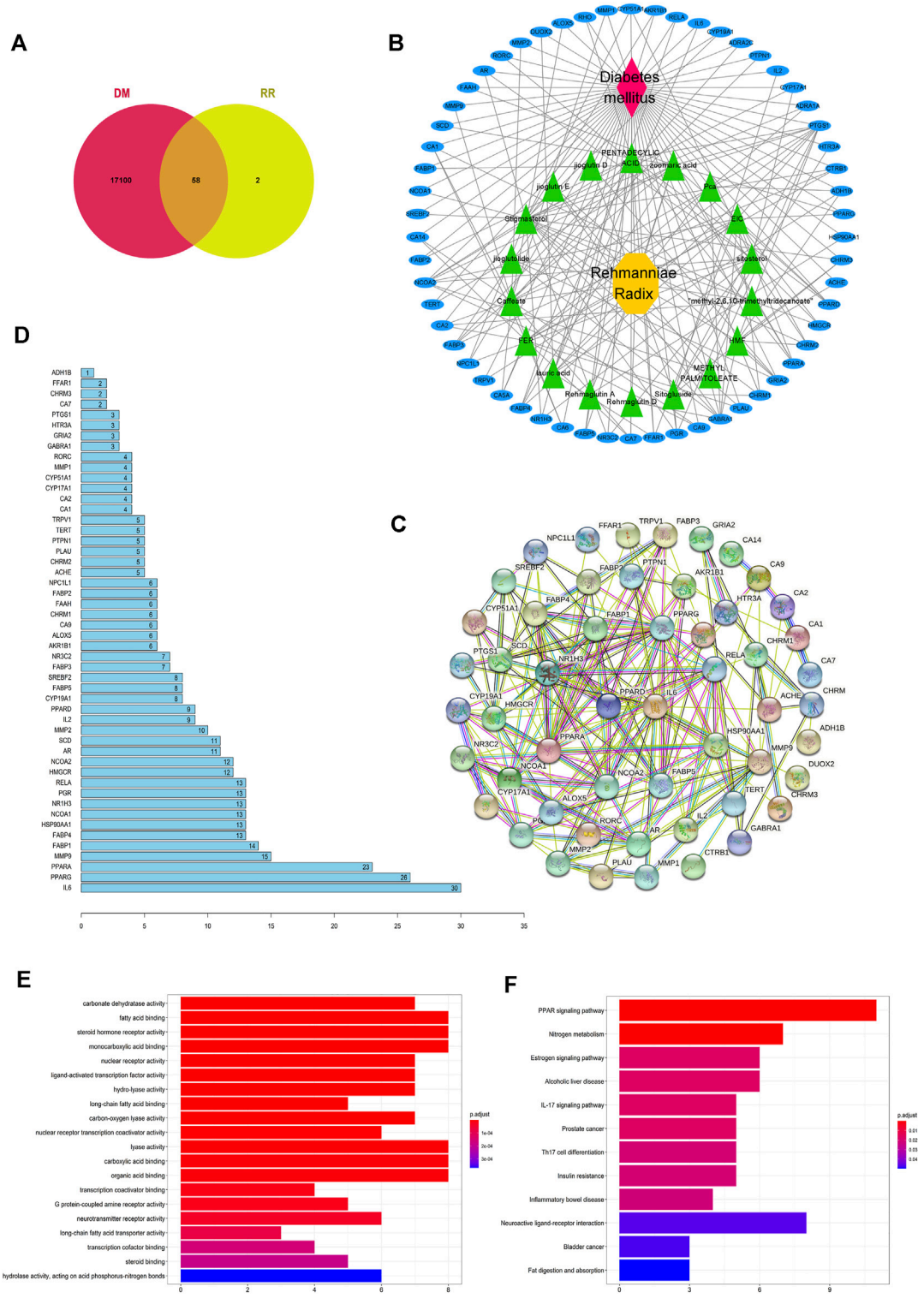

FIGURE 2 | Potential antidiabetic targets of RR were predicted by network pharmacology. **(A)** Venn diagram of the intersection of the targets between RR and DM. **(B)** RR–components–targets–DM network. For the nodes, red represents DM, yellow represents RR, green represents components of RR, and blue represents targets. Edges represent interactions. **(C)** Diagram of the protein–protein interaction (PPI) network. Each node represents a protein, with the protein structure located in the middle of nodes, and edges represent interactions between nodes. **(D)** Histogram of the number of adjoining nodes in the PPI network. The number of adjoining nodes for each gene was calculated and is marked to the right of the histogram. **(E)** Histogram of GO enrichment. The abscissa represents the number of genes enriched in the GO term. The ordinate represents different GO terms, and the color represents the *p* value. Twenty GO terms with the smallest *p* value are listed in the histogram. **(F)** Histogram of KEGG enrichment. The abscissa represents the number of genes enriched in the KEGG pathway. The ordinate represents the different KEGG pathways, and the color represents different *p* value.

rats were administrated RRE for 4 weeks, their weight was 10.70 ± 2.00% higher (**Figure 1B**) and FBG was 73.23 ± 3.33% lower (**Figure 1C**) than those of the model group. For OGTT, the AUC for blood glucose was 12.31 ± 2.29% lower in the rats of the RRE group than in those of the model group (**Figure 1D**). For IST, the AUC for blood glucose was 13.61 ± 5.60% lower in the rats of the RRE group than in those of the model group (**Figure 1E**). All these results indicated that RRE can alleviate DM.

Prediction of Antidiabetic Effect of *Rehmanniae* Radix Extract Based on Network Pharmacology Analysis

Seventy-six components in the RR were screened using the TCMSP database. According to the screening conditions, 17 components were obtained. At the same time, the 76 components were screened using the SwissADME database and 24 of them met the requirements. Thirty-two components were obtained by combining the screened components based on the TCMSP and Swiss databases. One hundred twenty-eight drug targets with 18 components were obtained by combining the TCMSP database and the SwissTargetPrediction database, and 60 targets of these were non-repetitive (**Supplementary Table S1**).

A total of 17,158 diabetes-related targets were screened by the GeneCards database. Fifty-eight targets were obtained by intersecting the 17,158 targets with 60 drug targets of RR (**Figure 2A**). Then, the RR–components–targets–DM network was established, which consisted of 18 components and 58 targets with edges connecting drugs with diseases (**Figure 2B**). From the network, the relationship between the active component and targets was disclosed. The target' PPI network was established to evaluate the significance of different targets, which contained 53 nodes and 208 edges (**Figure 2C**). There were 16 nodes with more than 10 edges, of which IL6 ranked first from sorting the number of edges connected to each node (**Figure 2D**). The family members of the peroxisome proliferators–activated receptors (PPAR), fatty acid binding protein (FABP), matrix metalloproteinase (MMP), and nuclear receptor corepressor (NCOA) occupy the majority. They play important roles in the fight against DM using RR.

Of the GO enrichment analysis of 58 targets, 6 significantly enriched GO terms are DM-related, namely, regulation of the fatty acid binding (GO:0005504), steroid hormone receptor activity (GO:0003707), monocarboxylic acid binding (GO:0033293), lyase activity (GO:0016829), carboxylic acid binding (GO:0031406), and organic acid binding (GO:0043177) (**Figure 2E**). Besides, many GO terms are related to lipid metabolism, which implies these pathways are important for RR against DM.

According to the screening conditions of p.adjust < 0.1 in the KEGG enrichment analysis, 12 pathways were obtained (**Figure 2F**). Among them, the PPAR signaling pathway (hsa03320) ranked first in terms of *p* value and gene count. It indicated that PPAR was one of the important antidiabetic signaling pathways of RR. RR possibly influences the PPAR pathway by affecting its genes (i.e., *PPAR*, *SCD1*, *MMP*, and *FABP*). It is worth mentioning that neuroactive ligand–receptor interaction (hsa:04080) appeared in the enriched KEGG pathways and the gene count (e.g., *TRPV1*) ranked second.

Identification of Antidiabetic Mechanism of *Rehmanniae* Radix Extract by Transcriptomics Analysis

In addition to network pharmacology, we also used the transcriptomics approach to further clarify the potential mechanisms of RRE against DM. The raw data have been deposited in the SRA database of NCBI and the accession number is PRJNA807859.

In the transcriptome analysis of the kidneys, a total of 1,205 DEGs were identified in the control *vs*. model group, 509 of which were upregulated and 696 were downregulated. Compared to the model group, a total of 1,033 DEGs were identified in the RRE group, 474 of which were upregulated and 559 were downregulated.

From the volcano diagram, the fold change of DEGs and their statistical *p* values are intuitively seen (**Figures 3A, B**). In order to clarify the relationship among the DEGs, DM, and RRE, their interactions were analyzed. The results indicated that there were 165 DEGs between the normal *vs*. model group (downregulation) and the model *vs*. RRE group (upregulation) (**Figure 3C**) and that there were 166 DEGs between the normal *vs*. model group (upregulation) and the model *vs*. RRE group (downregulation) (**Figure 3D**), which are an important reference for us to mine DM-related target genes. The DEGs' expression trends by qRT-PCR were mostly consistent with that of the transcriptome analysis (**Figure 4**).

DEGs were enriched by the GO database. The results indicated that 128 GO terms were upregulated (**Figure 5A**) and 314 GO terms were downregulated (**Figure 5B**) in the normal *vs*. model group. Of them, the potential DM-related signal pathways included adipocyte differentiation (e.g., brown fat cell differentiation and positive regulation of fat cell differentiation), lipid synthesis and metabolism (e.g., fatty acid homeostasis, lipid catabolic process, and lipid metabolic process), glycogen synthesis and metabolism (e.g., gluconeogenesis and glycogen biosynthetic process), apoptosis (e.g., apoptotic process and programmed necrotic cell death), oxidative stress (e.g., cellular response to oxidative stress and response to endoplasmic reticulum stress), and inflammation (e.g., chronic inflammatory response and interleukin-1 beta production). In addition, 164 GO terms were upregulated (**Figure 5C**) and 153 GO terms were downregulated (**Figure 4D**) in the model *vs*. RRE group. The DM-related signaling pathways in the model *vs*. RRE group were mostly consistent with those of the normal *vs*. model group.

The results based on the KEGG analysis indicated that 24 KEGG pathways were upregulated (**Figure 5E**), while 66 KEGG pathways were downregulated (**Figure 4F**) in the normal *vs*. model group. Among these KEGG pathways, the metabolic pathways (hso01100) included the largest number of DEGs. In addition, KEGG pathways such as apoptosis, inflammation, glycolipid metabolism, and pancreatic secretion were consistent with that of GO enrichment terms. The AMPK,

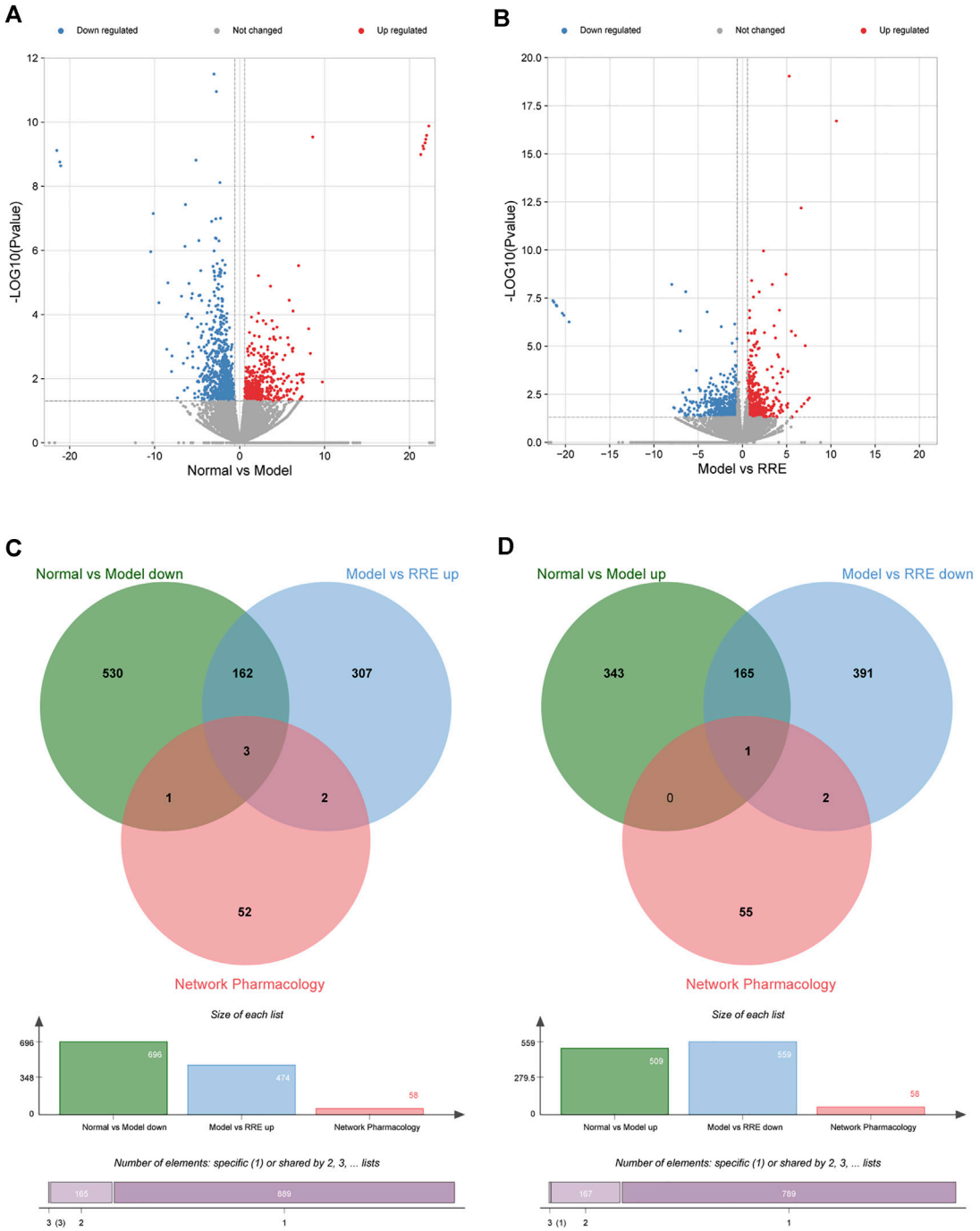

FIGURE 3 | Potential antidiabetic targets of RR were predicted by transcriptome analysis. **(A)** Volcano map shows the number of DEGs in the normal *vs*. model group; **(B)** Volcano map shows the number of DEGs in the model *vs*. RRE group. The abscissa represents the fold change of the gene, and the ordinate represents the *p* value. Each dot in the figure represents a specific gene, the red and blue dots represent significantly upregulated and downregulated genes, respectively, while the gray dots represent nonsignificantly different genes. Screening criteria are |FC| >1.5 and $p < 0.05$. **(C,D)** Venn diagrams: the circles in different colors in the Venn diagram represent a DEGs set and the intersection of the circles represents the number of DEGs shared between each set. **(C)** Intersection of DEGs from the normal *vs*. model group (down) and the model *vs*. RRE group (up) by transcriptomics and network pharmacology analysis. **(D)** Intersection of DEGs from the normal *vs*. model group (up) and the model *vs*. RRE group (down) by transcriptomics and network pharmacology analysis.

cGMP-PKG, RAS, and FoxO signaling pathways as well as IR were also listed in the KEGG pathways. Similarly, 27 KEGG pathways were upregulated (**Figure 5G**), while 29 KEGG pathways were downregulated (**Figure 5H**) in the model *vs*. RRE group. KEGG pathways such as toll-like receptor, PI3K-Akt, cGMP-PKG, calcium signaling pathway, and oxidative

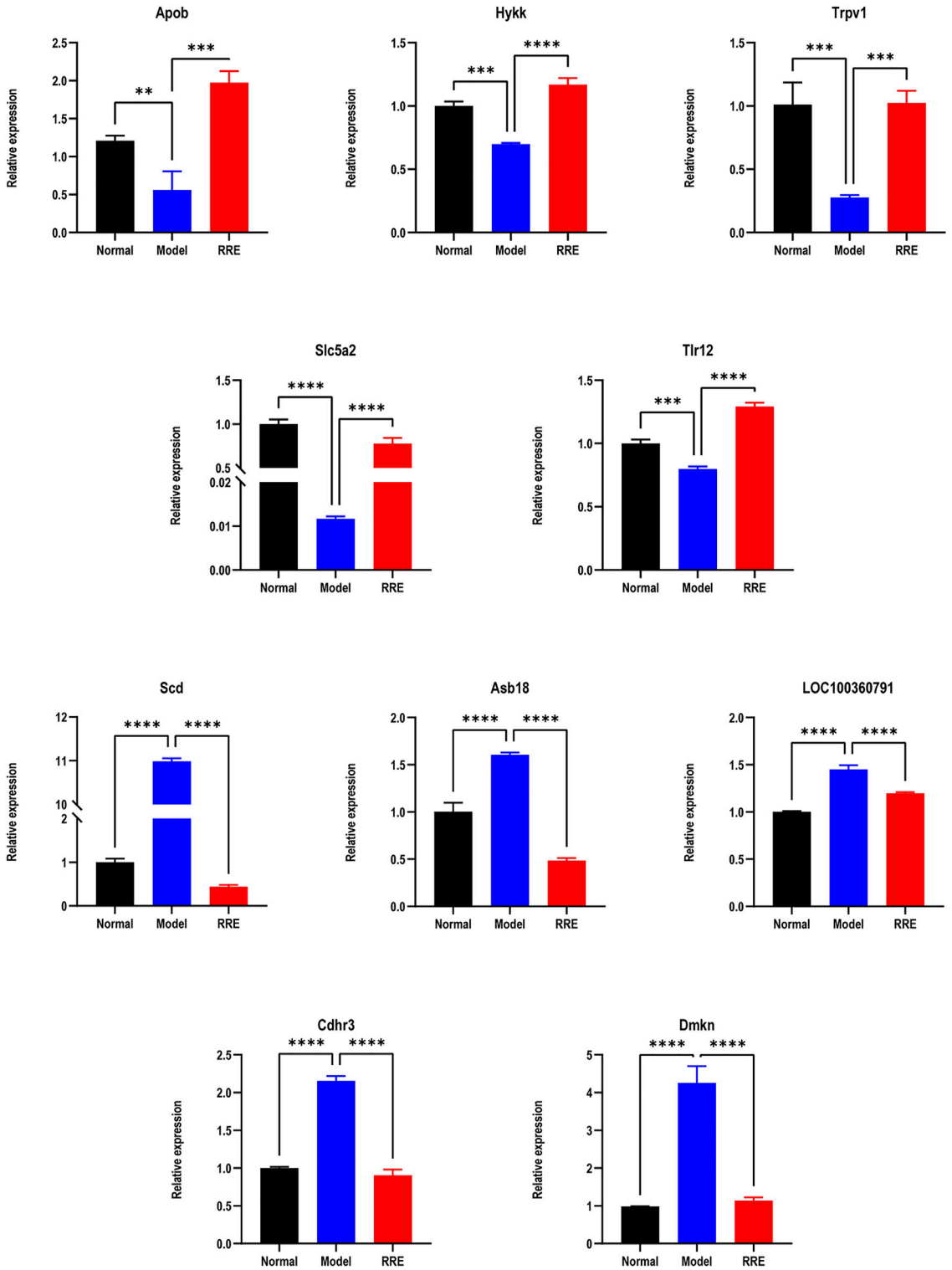

FIGURE 4 | The expression tendency of DEGs by qRT-PCR. Relative expressions of *Apob*, *Hykk*, *Trpv1*, *Slc5a2*, and *Tlr12* in the normal *vs*. model group (down) and the model *vs*. RRE group (up). Relative expression of *SCD1*, *Asb18*, *LOC100360791*, *Cdhr3*, and *Dmkn* in the normal *vs*. model group (up) and the model *vs*. RRE group (down).

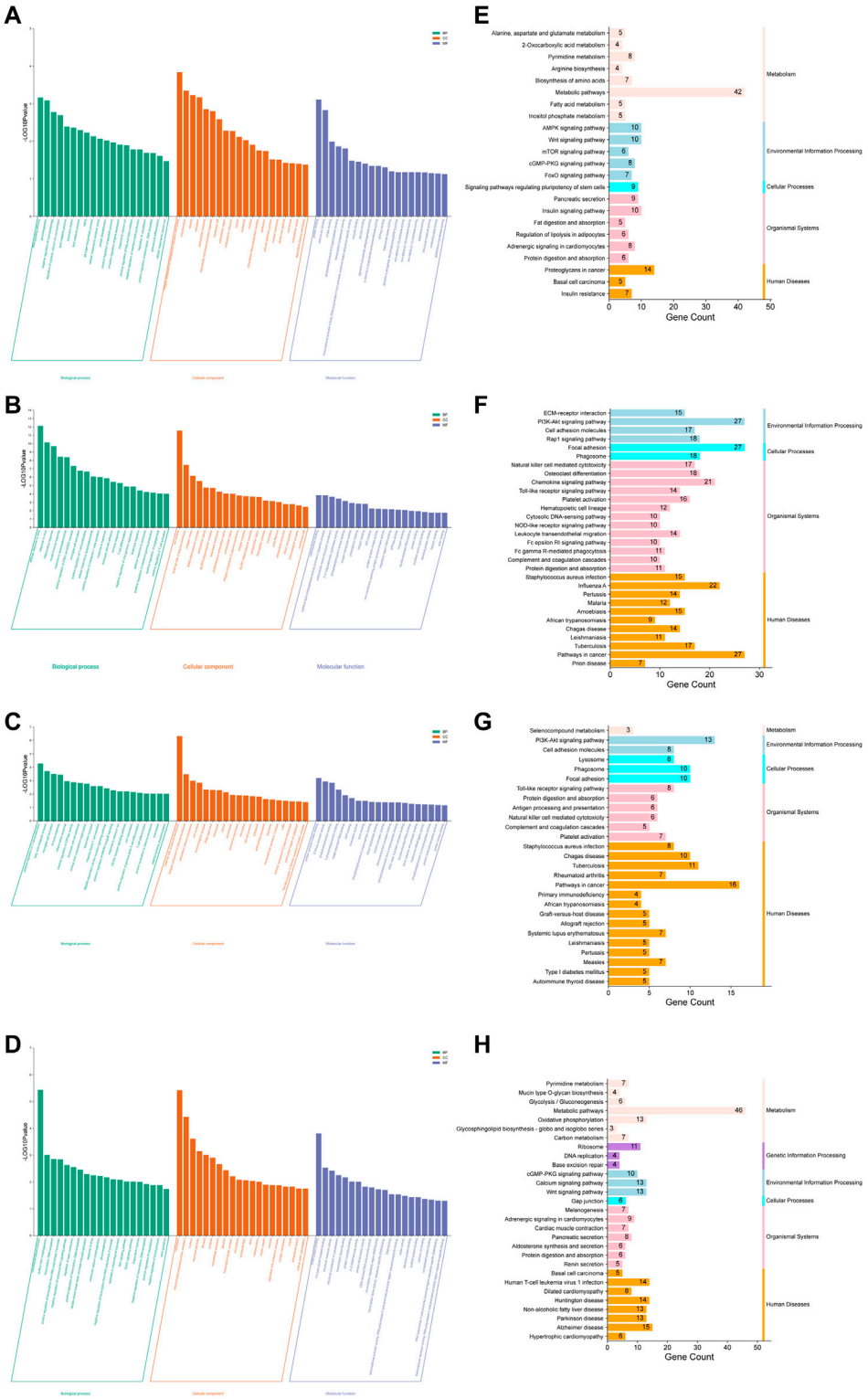

FIGURE 5 | Potential antidiabetic pathways of RR were enriched by the GO and KEGG analyses. **(A–D)** Histogram of GO enrichment analysis: **(A)** the normal *vs*. model group (up); **(B)** the normal *vs*. model group (down); **(C)** the model *vs*. RRE group (up); **(D)** the model *vs*. RRE group (down). The abscissa represents the different GO terms belonging to the three categories, namely, biological process, cellular component, and molecular function. The ordinate represents the logarithmized *p* value (the enrichment result with the 20 minimum *p* values are displayed). **(E–H)** Histogram of KEGG enrichment analysis: **(E)** the normal *vs*. model group (up); **(F)** the normal *vs*. model group (down); **(G)** the model *vs*. RRE group (up); **(H)** the model *vs*. RRE group (down). The abscissa represents a number of genes enriched in this pathway. The left ordinate represents the KEGG pathways, the right ordinate represents the categories of the pathways.

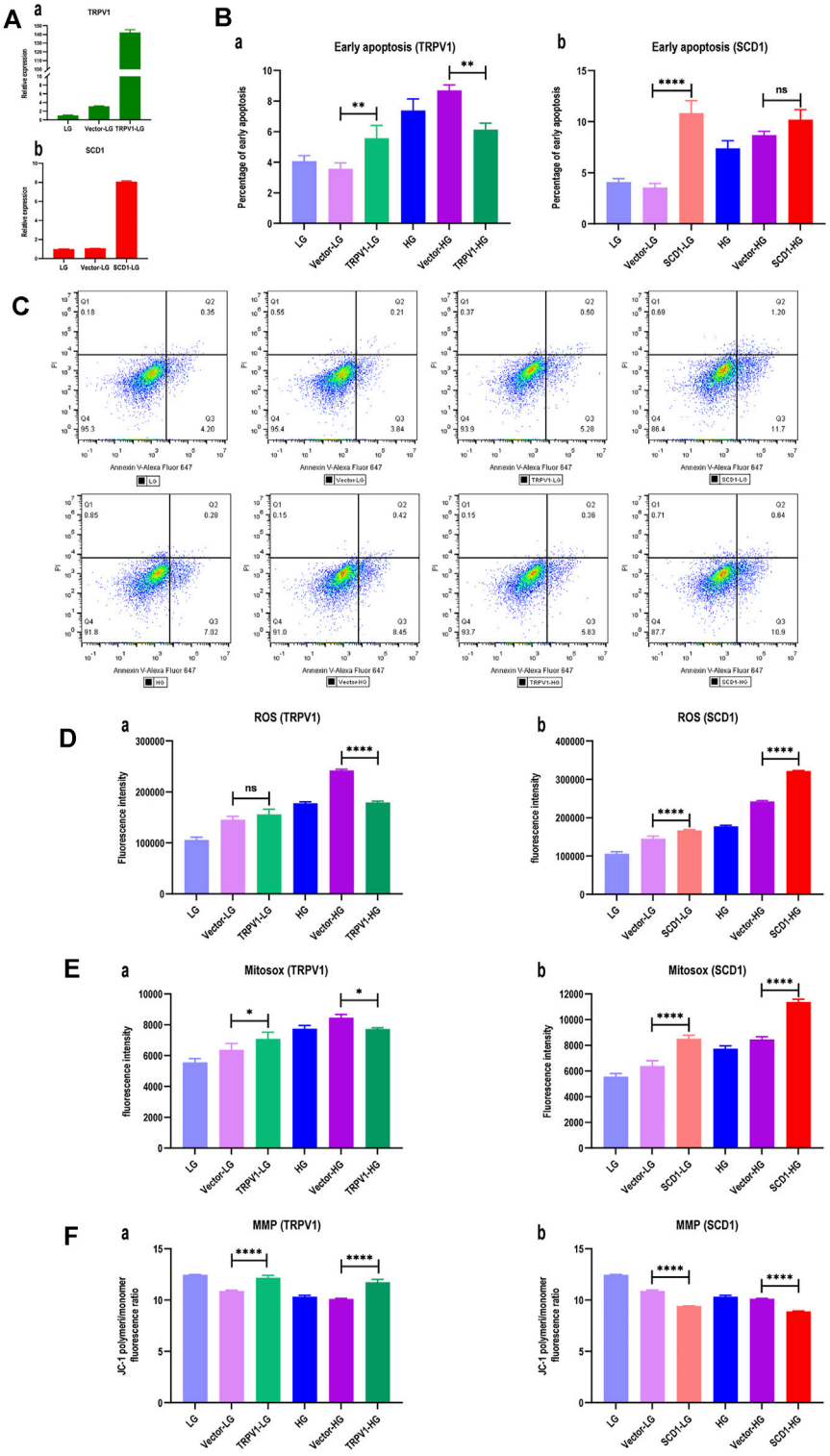

FIGURE 6 | Overexpressions of TRPV1 and SCD1 in HK2 cells: LG, low glucose; Vector-LG, vector plasmid transfected low glucose; TRPV1-LG, TRPV1 plasmid transfected low glucose; SCD1-LG, SCD1 plasmid transfected low glucose; HG, high glucose; Vector-HG, vector plasmid transfected high glucose; TRPV1-HG, TRPV1 plasmid transfected high glucose; SCD1-HG, SCD1 plasmid transfected high glucose. **(A)** Gene expression after transfecting *TRPV1* and *SCD1*: (a) gene expression of *TRPV1*; (b) gene expression of *SCD1*. **(B)** Histogram of percentage of early apoptosis of HK2 cells: (a) percentage of early apoptosis of HK2 cells with overexpression of *TRPV1*; (b) percentage of early apoptosis of HK2 cells with overexpression of *SCD1*. ns, no statistical difference; **, $p < 0.01$; ***, $p < 0.001$. **(C)** Dot plot

(*Continued*)

FIGURE 6 | of flow cytometry for apoptosis detection of HK2 cells, which are gated based on the compensation and positive reference. The ratio of Q3 to live cells represents the percentage of early apoptosis. **(D)** Histogram of intracellular reactive oxygen species (ROS) of HK2 cells: (a) ROS in HK2 cells with overexpression of *TRPV1*; (b) ROS in HK2 cells with overexpression of *SCD1*. ns, no statistical difference; ****, $p < 0.0001$. **(E)** Histogram of mitochondrial superoxide (MitoSOX) of HK2 cells: (a) MitoSOX in HK2 cells with overexpression of *TRPV1*; (b) MitoSOX in HK2 cells with overexpression of *SCD1*. *, $p < 0.05$; ****, $p < 0.0001$. **(F)** Histogram of mitochondrial membrane potential (MMP) of HK2 cells transfected *TRPV1* and *SCD1*, respectively: (a) MMP in HK2 cells with overexpression of *TRPV1*; (b) MMP in HK2 cells with overexpression of *SCD1*. ns, no statistical difference; ****, $p < 0.0001$.

phosphorylation were consistent with that of the GO enrichment terms.

Finally, four collective targets were discovered by the intersection of network pharmacology and transcriptomics analysis, namely, *TRPV1*, *FABP2*, *HSP90AA1*—in the normal *vs*. model group (downregulation) and the model *vs*. RRE group (upregulation) and *SCD1*—in the normal *vs*. model group (upregulation) and the model *vs*. RRE group (downregulation). Among the four targets, *TRPV1* and *SCD1* are the important targets related to DM (Enoch et al., 1976; Radu et al., 2013). *TRPV1* possibly delays the progression of DM and *SCD1* possibly accelerates the progression of DM.

Transcriptome analysis of the small intestine indicated that DEGs and the GO and KEGG pathway enrichment in the normal *vs*. model group and the model *vs*. RRE group showed upregulation and downregulation, respectively (**Supplementary Figures S4, S5**). The transcriptome analysis of the skeletal muscle indicated that DEGs and the GO and KEGG pathway enrichment in the normal *vs*. model group and the model *vs*. RRE group also showed upregulation and downregulation, respectively (**Supplementary Figures S6, S7**). However, the intersection analysis by the transcriptome analysis and network pharmacology indicated that there is only one intersection target in the small intestine and no intersection target in the skeletal muscle (**Supplementary Figures S4, S6**). This suggests that the kidney is the main target organ for the antidiabetic effect of RR.

Overexpressions of TRPV1 and SCD1 Affects Cell Apoptosis and Oxidative Stress

In order to verify the roles of TRPV1 and SCD1 in the treatment of DM, the HK2 cells overexpressed *TRPV1* or *SCD1* were constructed and verified by the qRT-PCR (**Figure 6A**). The detection of cell apoptosis indicated that early apoptosis of HG group was 1.75 times of that of the LG group, indicating that high glucose significantly induced apoptosis of HK2 cells. Compared to the vector-LG group, the apoptosis ratio of the TRPV1-LG group increased. However, the apoptosis ratio of HK2 cells was significantly lower in the TRPV1-HG group than in the vector-HG group ($p < 0.01$) (**Figures 6Ba, C**). The apoptosis ratio of HK2 cells was 3.05 times higher in the SCD1-LG group than in the vector-LG group ($p < 0.0001$). However, compared with the vector-HG group, the apoptosis ratio of HK2 cells in the SCD1-HG group exhibited increased tendencies in the high glucose environment (**Figures 6Bb, C**). Thus, it can be seen that the overexpression of *TRPV1* inhibits early apoptosis induced by high glucose, while the overexpression of *SCD1* can aggravate early apoptosis in the normal environment.

Compared with the vector-HG group, ROS in HK2 cells from the TRPV1-HG group decreased by 25.89% ($p < 0.0001$), which was not seen in the TRPV1-LG *vs*. vector-LG group (**Figure 6Da**). It indicated that the overexpression of *TRPV1* reduces the degree of oxidative stress induced by high glucose. When compared with the vector-LG group, ROS in HK2 cells from the SCD1-LG group was higher ($p < 0.0001$), and when compared with the vector-HG group, ROS in HK2 cells from the SCD1-HG group was greatly increased by 33.01% (**Figure 6Db**). This indicates that the overexpression of *SCD1* enhances cellular oxidative stress both in low-glucose and high-glucose environments.

When compared with the vector-HG group, MitoSOX in HK2 cells from the TRPV1-HG group was decreased ($p < 0.05$), which was not observed in the TRPV1-LG *vs*. vector-LG group (**Figure 6Ea**). This suggests that the overexpression of *TRPV1* reduces the degree of oxidative stress induced by HG. When compared with the vector-LG group, MitoSOX in HK2 cells in the SCD1-LG group was 33.43% higher ($p < 0.0001$) and compared with the vector-HG group, MitoSOX in HK2 cells in the SCD1-HG group was increased by 34.55% (**Figure 6Eb**). This suggests that the overexpression of *SCD1* enhances cellular oxidative stress both in the LG and HG environments.

The mitochondrial membrane potential (MMP) is a more sensitive indicator for oxidative stress. It was found that when compared with the low-glucose group, the MMP of HK2 cells decreased in the high-glucose group. When compared with the vector-LG group, the MMP of HK2 cells in the TRPV1-LG group was significantly elevated ($p < 0.0001$). When compared with the vector-HG group, the MMP of HK2 cells in the TRPV1-HG group increased, indicating that the overexpression of *TRPV1* decreases the influence of high glucose on MMP (**Figure 6Fa**). When compared with the vector-HG group, the MMP of HK2 cells in the SCD1-HG group increased. It is noteworthy that the MMP of HK2 cells increased by three-fourth folds in the SCD1-LG group when compared with the vector-LG group (**Figure 6Fb**). This shows that regardless of the high-glucose environment, *SCD1* is an independent risk factor that affects MMP.

mRNA and Protein Expressions of TRPV1 in the HK2 Cell Were Significantly Increased in the Presence of *Rehmanniae* Radix Extract

The assay of qRT-PCR (**Figure 7**) showed that the mRNA expression of TRPV1 was significantly increased in the presence of RRE (25–400 μg/ml) in the HG group. It had increased by 3.94 ± 0.08 folds when the RRE concentration was 100 μg/ml.

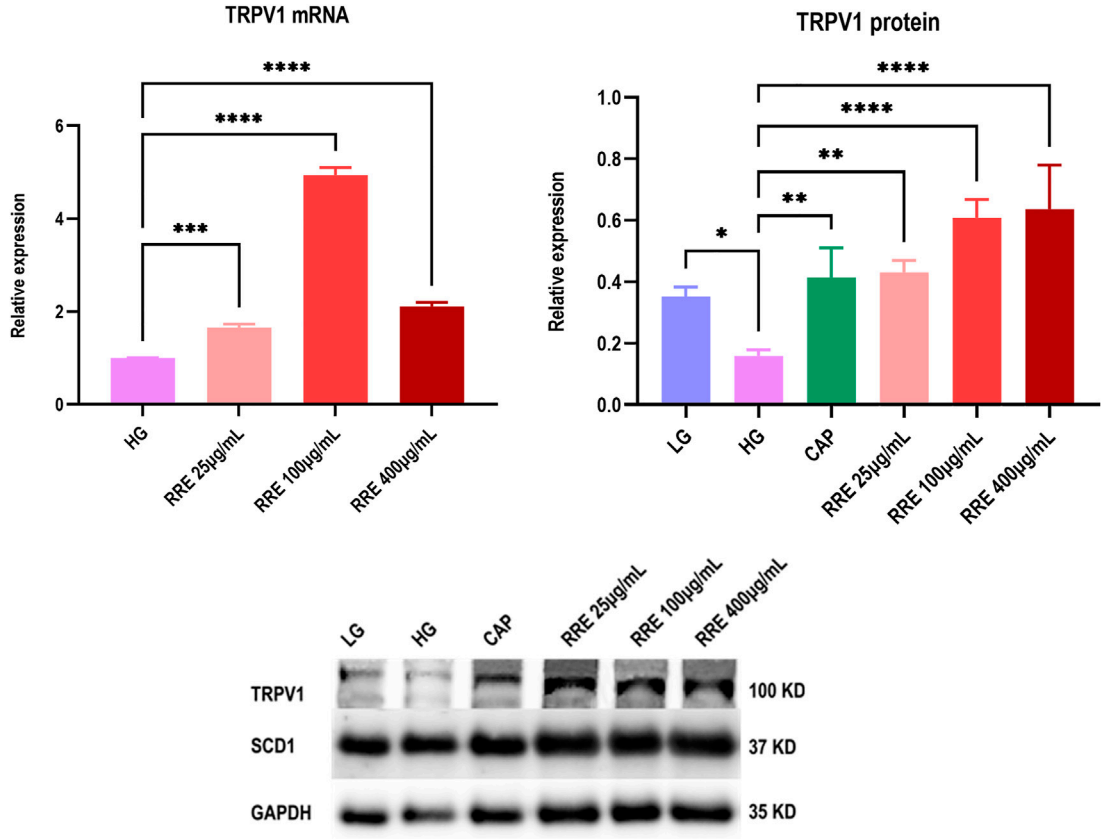

FIGURE 7 | Effect of RRE on mRNA and protein expressions of TRPV1 in HK2 cells: CAP, capsaicin; TRPV1, transient receptor potential vanilloid 1; LG, low glucose; HG, high glucose. Comparison with the HG group, *, $p < 0.05$; **, $p < 0.01$; ***, $p < 0.001$; ****, $p < 0.0001$.

The assay of western blot (**Figure 7**) showed that the TRPV1 protein expression was significantly reduced in the HG group when compared with the LG group. The reducing trend of the protein expression of TRPV1 reversed in the presence of RRE (25–400 μg/ml) in the HG environment and increased by 2.83 ± 0.40 folds when the RRE concentration was 100 μg/ml. This suggests that RRE demonstrates significant antidiabetic effects by upregulating the mRNA and protein expressions of TRPV1 in the diabetic state. It needs to be noted that there was no significant effect on the expressions of both mRNA and protein of SCD1 in the presence of RRE (25–400 μg/ml).

DISCUSSION

In order to systematically and comprehensively disclose the antidiabetic mechanism of herbs (namely, RR), we integrated the methods of network pharmacology and transcriptomics. A total of 18 components of RR and 58 DM-related targets were found by network pharmacology and 331 targets were screened by transcriptomics. Finally, we screened out two important DM-related targets, namely, *TRPV1* and *SCD1*.

As a hot drug target, TRPV1 was discovered in 1997 by David Julius. He won the 2021 Nobel Prize for the research on TRPV1. At present, studies of TRPV1 focus on insulin release, peripheral IR, and renal blood vessels. TRPV1 receptors are mainly distributed in the sensory nerve endings and are also widely expressed in many tissues which are closely related to DM, such as the pancreatic islets, liver, gastrointestinal epithelium, and adipose tissue (Suri and Szallasi, 2008). In recent years, scientists have found TRPV1 plays an important role in metabolic diseases (Radu et al., 2013) and is associated with many signaling pathways such as pancreatic secretion, glucagon signaling, inflammatory mediator regulation of TRP channels, IR, and AMPK (Pabbidi et al., 2008; Sadeh et al., 2013). These signaling pathways are also enriched in our transcriptome analysis.

Activation of TRPV1 leads to a decrease in adipose accumulation and an increase in energy expenditure, which is closely linked to the activation of the PPAR and AMPK signal pathways (Brondani et al., 2012; Baskaran et al., 2016). At present, there are fewer studies on the roles played by TRPV1 in renal glycolipid metabolism. The experimental results of HK2 cells indicate that TRPV1 was upregulated (i.e., activated) by RRE, which possibly affected the PPAR and AMPK pathways and finally affected the treatment of DM.

From the results of the protein–protein interaction, it is clear that the PPAR family had a number of high ranking genes,

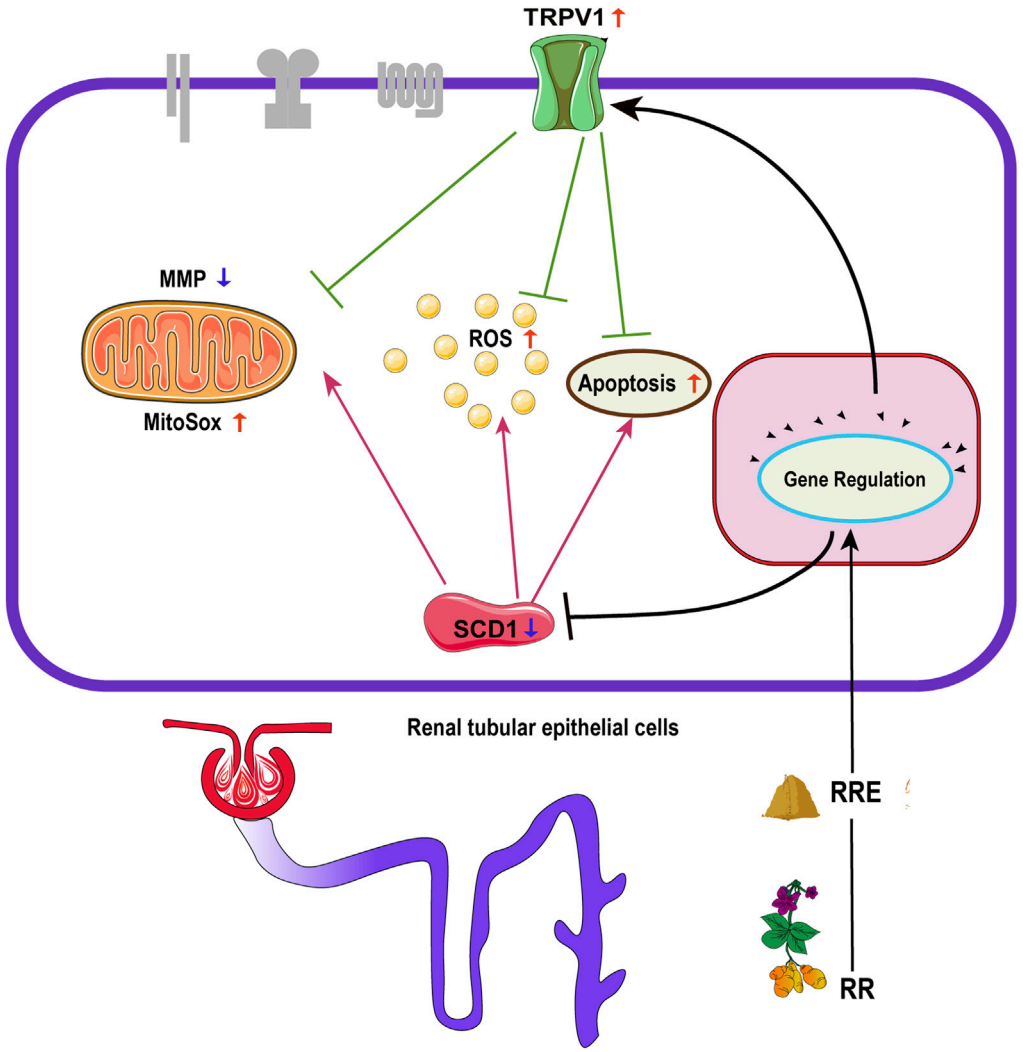

FIGURE 8 | Effect of regulation of TRPV1 and SCD1 by RR on apoptosis, ROS, MitoSOX, and MMP: RR, *Rehmanniae* Radix; RRE, *Rehmanniae* Radix extract; TRPV1, transient receptor potential vanilloid 1; SCD1, stearoyl-CoA desaturase 1; ROS, reactive oxygen species; MitoSOX, mitochondrial superoxide; MMP, mitochondrial membrane potential.

covering *PPARA*/*PPARD*/*PPARG*. In the GO analysis, *PPARs* also appear in fatty acid binding, the steroid hormone receptor activity, the nuclear receptor activity, and the carboxylic acid binding pathways. The PPAR signaling pathway with key targets (e.g., *SCD*, *PPAR*, *FABP*, and *MMP*) is also ranked first in terms of the number of genes based on KEGG analyses (**Supplementary Figure S3**). PPARα plays a key role in the transcriptional regulation of lipoprotein metabolism, affecting the production and catabolism of TG-rich lipoproteins, HDL synthesis, and the *β*-oxidation pathway (Lefebvre et al., 2006). Activation of PPARα can regulate glucose homeostasis, inhibit inflammation and thrombosis, and improve vascular function (Gross et al., 2017; Bougarne et al., 2018). PPARα expresses in glomerular and tubular cells and regulates renal lipid deposition (Braissant et al., 1996). It is reported that selective agonists of PPARα can inhibit renal tubular lipid deposition and reduce oxidative stress (Maki et al., 2017). Hebbachi et al. (2008) found that insulin-sensitive changes in the gene expression of *SCD1* required intact PPARα to mediate.

SCD is one of the key DM-related genes, which is an adipogenic gene and regulated by several upstream genes in the PPAR signaling pathway. Our study found that high *SCD* expressions in the kidneys of STZ-induced diabetic rats, which is consistent with previous studies (Ntambi et al., 2002; Shiwaku et al., 2004; Chow et al., 2013), which were involved in the pathogenic process of DM. After DM rats were treated with RR, the expression levels of *SCD1* decreased in the body, indicating that RR directly or indirectly regulates the expression or function of *SCD1*, thus delaying DM progression.

It should be noted that RRE displayed no significant regulation on the expressions of mRNA and protein of SCD1 on the HK2 cell,

although the rat transcriptome showed a downregulation of SCD1 by RRE. We speculate that the expression of SCD1 is possibly regulated by the metabolites of RRE *in vivo*. It is possible that the HK2 cells lack the enzyme that metabolizes RRE and the metabolites of RRE cannot be produced, which leads to the regulation of SCD1 that could not occur in the *in vitro* experiments.

SCD1 is a rate-limiting enzyme that converts saturated fatty acids (SFA) to monounsaturated fatty acids (MUFA). *SCD1* is selectively expressed in the proximal tubular cells in the kidneys (Zheng et al., 2001). Many studies have shown that SCD1 plays an important role in metabolic abnormalities and regulates insulin sensitivity and controls lipid metabolism (Liew et al., 2004; Popeijus et al., 2008; Sampath and Ntambi, 2011; Liu et al., 2013). This suggests that SCD1 may be a therapeutic target for DM, obesity, hypertension, and dyslipidemia (Enoch et al., 1976). *SCD1* expression is regulated by a variety of hormonal and nutritional factors (Ntambi, 1992; Waters and Ntambi, 1994; Ntambi, 1995; Waters and Ntambi, 1996). It is positively regulated by sterol regulatory element-binding protein 1c (SREBP-1c), carbohydrate response element-binding protein (CHREBP), and liver X receptor (LXR). LXR and SREBP-1c play an important role in regulating insulin-mediated lipid synthesis, while CHREBP mediates glucose-induced lipid synthesis. Thus, the activation of PPARα, LXR, and SREBP-1c, and their regulation of SCD1 are potential pathways in metabolic diseases, but the mechanisms of action in some tissues (e.g., the kidneys) have not yet been elucidated. Our study suggests that the PPAR pathway is indispensable for the pathogenesis and treatment of DM by RRE, which in turn acts to regulate the activity of SCD1 *via* multiple pathways.

TRPV1 and SCD1 play important roles in the treatment of DM. Page et al. (2019) reported that the *SCD1* expression was greatly increased in *TRPV1* knockout mice than in the wild-type mice. It implies that SCD1 activity possibly reduces when *TRPV1* is induced, which is a benefit for the treatment of DM. It is consistent with the findings of our study. A study suggested that TPRV1 regulates the expression of *SCD1* and the endocannabinoid system [e.g., cannabinoid receptor 1 (CB1)]. Meanwhile, activation of CB1 subsequently affects TRPV1 activity and enhances the *SCD1* expression (Hermann et al., 2003; Tóth et al., 2009; Liu et al., 2013). This suggests that there is an interaction between TRPV1 and SCD1 such that we can employ it against DM.

Apoptosis, oxidative stress (e.g., generation of ROS and reduction of MitoSOX and MMP) of cells are important indicators for exploring the mechanisms of the pathogenesis and treatment of DM (Tan et al., 2007; Kim et al., 2011; Habib, 2013; Adelusi et al., 2020). Previous studies have shown that TRPV1 can inhibit endothelial and neuronal apoptosis when activated (Dai et al., 2008). While inhibition of SCD1 can promote oxidative stress and apoptosis of tumor cells (Stambolic and Woodgett, 2006; Hess et al., 2010; Minville-Walz et al., 2010). This suggests that TRPV1 and SCD1 exhibit different effects on apoptosis and oxidative stress in different cells. However, our study found that high glucose increased the proportion of apoptosis and oxidative stress (generation of ROS and MitoSOX, and decrease of MMP) in HK-2 cells. The overexpression of *TRPV1* significantly attenuated apoptosis and oxidative stress induced by high glucose, while the overexpression of *SCD1* enhanced apoptosis and oxidative stress induced by high glucose on HK2 cells (**Figure 8**).

CONCLUSION

In summary, the key antidiabetic targets (e.g., TRPV1 and SCD1) and signaling pathways (PPAR) of RR were disclosed by network pharmacology and transcriptome analysis as well as by *in vitro* cellular experiments. The overexpression of TRPV1 can significantly inhibit cell apoptosis and oxidative stress induced by HG, while the overexpression of SCD1 is a risk factor for the enhancement of cell apoptosis and oxidative stress. RR displayed an inspiring antidiabetic effect by improving weight loss, reducing blood glucose, and improving IR, especially in upregulating the mRNA and protein expressions of TRPV1 and downregulating the mRNA expression of SCD1. TRPV1 and SCD1 are the potential antidiabetic targets of RR. It is of great importance to screen out the inducer of TRPV1 and inhibitors of SCD1 from herbs (e.g., RR) and drugs as potential antidiabetic drugs.

DATA AVAILABILITY STATEMENT

The datasets presented in this study can be found in online repositories. The names of the repository/repositories and accession number(s) can be found below: NCBI SRA; PRJNA807859.

ETHICS STATEMENT

The animal study was reviewed and approved by the Animal Ethics Committee of the School of Pharmacy, Fudan University.

AUTHOR CONTRIBUTIONS

Participated in research design: YL, RZ, and GM; conducted the experiments: YL, RZ, BL, WW, XY, WD, and QY; contributed the new reagents or analytic tools: GM, RZ, PY, and ZC; performed data analysis: YL, GM, JL, and JH; wrote or contributed to the writing of the manuscript: YL and GM.

FUNDING

This work was supported by the National Natural Science Funds of China (Grants 82074109, 81873078, and 81374051); the Science and Research Program of Shanghai Municipal Health

Commission (Grant 201740094); the Science and Research Program of Traditional Chinese Medicine of Shanghai Municipal Health Commission (Grant 2018YP001); and MHHFDU-SPFDU Joint Research Fund (Grants RO-MY201707 and 2021MHJC11).

SUPPLEMENTARY MATERIAL

The Supplementary Material for this article can be found online at: https://www.frontiersin.org/articles/10.3389/fphar.2022.875014/full#supplementary-material

REFERENCES

Adelusi, T. I., Du, L., Hao, M., Zhou, X., Xuan, Q., Apu, C., et al. (2020). Keap1/Nrf2/ARE Signaling Unfolds Therapeutic Targets for Redox Imbalanced-Mediated Diseases and Diabetic Nephropathy. *Biomed. Pharmacother.* 123, 109732. doi:10.1016/j.biopha.2019.109732

Baskaran, P., Krishnan, V., Ren, J., and Thyagarajan, B. (2016). Capsaicin induces browning of white Adipose Tissue and Counters Obesity by Activating TRPV1 Channel-dependent Mechanisms. *Br. J. Pharmacol.* 173 (15), 2369–2389. doi:10.1111/bph.13514

Bougarne, N., Weyers, B., Desmet, S. J., Deckers, J., Ray, D. W., Staels, B., et al. (2018). Molecular Actions of PPARα in Lipid Metabolism and Inflammation. *Endocr. Rev.* 39 (5), 760–802. doi:10.1210/er.2018-00064

Braissant, O., Foufelle, F., Scotto, C., Dauça, M., and Wahli, W. (1996). Differential Expression of Peroxisome Proliferator-Activated Receptors (PPARs): Tissue Distribution of PPAR-Alpha, -beta, and -gamma in the Adult Rat. *Endocrinology* 137 (1), 354–366. doi:10.1210/endo.137.1.8536636

Brondani, L. A., Assmann, T. S., Duarte, G. C., Gross, J. L., Canani, L. H., and Crispim, D. (2012). The Role of the Uncoupling Protein 1 (UCP1) on the Development of Obesity and Type 2 Diabetes Mellitus. *Arq Bras Endocrinol. Metabol* 56 (4), 215–225. doi:10.1590/s0004-27302012000400001

Cao, H., Tuo, L., Tuo, Y., Xia, Z., Fu, R., Liu, Y., et al. (2017). Immune and Metabolic Regulation Mechanism of Dangguiliuhuang Decoction against Insulin Resistance and Hepatic Steatosis. *Front. Pharmacol.* 8, 445. doi:10.3389/fphar.2017.00445

Choi, H. J., Jang, H. J., Chung, T. W., Jeong, S. I., Cha, J., Choi, J. Y., et al. (2013). Catalpol Suppresses Advanced Glycation End-Products-Induced Inflammatory Responses through Inhibition of Reactive Oxygen Species in Human Monocytic THP-1 Cells. *Fitoterapia* 86, 19–28. doi:10.1016/j.fitote.2013.01.014

Chow, L. S., Li, S., Eberly, L. E., Seaquist, E. R., Eckfeldt, J. H., Hoogeveen, R. C., et al. (2013). Estimated Plasma Stearoyl Co-A Desaturase-1 Activity and Risk of Incident Diabetes: the Atherosclerosis Risk in Communities (ARIC) Study. *Metabolism* 62 (1), 100–108. doi:10.1016/j.metabol.2012.06.004

Dai, Z., Xiao, J., Liu, S. Y., Cui, L., Hu, G. Y., and Jiang, D. J. (2008). Rutaecarpine Inhibits Hypoxia/reoxygenation-Induced Apoptosis in Rat Hippocampal Neurons. *Neuropharmacology* 55 (8), 1307–1312. doi:10.1016/j.neuropharm.2008.08.030

DiMeglio, L. A., Evans-Molina, C., and Oram, R. A. (2018). Type 1 Diabetes. *Lancet* 391 (10138), 2449–2462. doi:10.1016/s0140-6736(18)31320-5

Enoch, H. G., Catalá, A., and Strittmatter, P. (1976). Mechanism of Rat Liver Microsomal Stearyl-CoA Desaturase. Studies of the Substrate Specificity, Enzyme-Substrate Interactions, and the Function of Lipid. *J. Biol. Chem.* 251 (16), 5095–5103. doi:10.1016/s0021-9258(17)33223-4

Gross, B., Pawlak, M., Lefebvre, P., and Staels, B. (2017). PPARs in Obesity-Induced T2DM, Dyslipidaemia, and NAFLD. *Nat. Rev. Endocrinol.* 13 (1), 36–49. doi:10.1038/nrendo.2016.135

Guo, M. F., Dai, Y. J., Gao, J. R., and Chen, P. J. (2020). Uncovering the Mechanism of Astragalus Membranaceus in the Treatment of Diabetic Nephropathy Based on Network Pharmacology. *J. Diabetes Res.* 2020, 5947304. doi:10.1155/2020/5947304

Habib, S. L. (2013). Diabetes and Renal Tubular Cell Apoptosis. *World J. Diabetes* 4 (2), 27–30. doi:10.4239/wjd.v4.i2.27

Han, L., Li, T., Du, M., Chang, R., Zhan, B., and Mao, X. (2019). Beneficial Effects of Potentilla Discolor Bunge Water Extract on Inflammatory Cytokines Release and Gut Microbiota in High-Fat Diet and Streptozotocin-Induced Type 2 Diabetic Mice. *Nutrients* 11 (3). doi:10.3390/nu11030670

Hebbachi, A. M., Knight, B. L., Wiggins, D., Patel, D. D., and Gibbons, G. F. (2008). Peroxisome Proliferator-Activated Receptor Alpha Deficiency Abolishes the Response of Lipogenic Gene Expression to Re-feeding: Restoration of the normal Response by Activation of Liver X Receptor Alpha. *J. Biol. Chem.* 283 (8), 4866–4876. doi:10.1074/jbc.M709471200

Hermann, H., De Petrocellis, L., Bisogno, T., Schiano Moriello, A., Lutz, B., and Di Marzo, V. (2003). Dual Effect of Cannabinoid CB1 Receptor Stimulation on a Vanilloid VR1 Receptor-Mediated Response. *Cell Mol Life Sci* 60 (3), 607–616. doi:10.1007/s000180300052

Hess, D., Chisholm, J. W., and Igal, R. A. (2010). Inhibition of stearoylCoA Desaturase Activity Blocks Cell Cycle Progression and Induces Programmed Cell Death in Lung Cancer Cells. *PLoS One* 5 (6), e11394. doi:10.1371/journal.pone.0011394

Hopkins, A. L. (2007). Network Pharmacology. *Nat. Biotechnol.* 25 (10), 1110–1111. doi:10.1038/nbt1007-1110

Hopkins, A. L. (2008). Network Pharmacology: the Next Paradigm in Drug Discovery. *Nat. Chem. Biol.* 4 (11), 682–690. doi:10.1038/nchembio.118

International Diabetes Federation (2021). *IDF Diabetes Atlas*. 10th ed. Available at: https://diabetesatlas.org/atlas/tenth-edition/(Accessed December 24, 2021).

Kim, H. S., Vassilopoulos, A., Wang, R. H., Lahusen, T., Xiao, Z., Xu, X., et al. (2011). SIRT2 Maintains Genome Integrity and Suppresses Tumorigenesis through Regulating APC/C Activity. *Cancer Cell* 20 (4), 487–499. doi:10.1016/j.ccr.2011.09.004

Kim, S. H., Yook, T. H., and Kim, J. U. (2017). Rehmanniae Radix, an Effective Treatment for Patients with Various Inflammatory and Metabolic Diseases: Results from a Review of Korean Publications. *J. Pharmacopuncture* 20 (2), 81–88. doi:10.3831/kpi.2017.20.010

Kitagawa, I., Nishimura, T., Furubayashi, A., and Yosioka, I. (1971). On the Constituents of Rhizome of Rehmannia Glutinosa Libosch. Forma Hueichingensis Hsiao. *Yakugaku Zasshi* 91 (5), 593–596. doi:10.1248/yakushi1947.91.5_593

Lander, E. S., Linton, L. M., Birren, B., Nusbaum, C., Zody, M. C., Baldwin, J., et al. (2001). Initial Sequencing and Analysis of the Human Genome. *Nature* 409 (6822), 860–921. doi:10.1038/35057062

Lascar, N., Brown, J., Pattison, H., Barnett, A. H., Bailey, C. J., and Bellary, S. (2018). Type 2 Diabetes in Adolescents and Young Adults. *Lancet Diabetes Endocrinol.* 6 (1), 69–80. doi:10.1016/s2213-8587(17)30186-9

Lefebvre, P., Chinetti, G., Fruchart, J. C., and Staels, B. (2006). Sorting Out the Roles of PPAR Alpha in Energy Metabolism and Vascular Homeostasis. *J. Clin. Invest.* 116 (3), 571–580. doi:10.1172/jci27989

Li, Y., Teng, D., Shi, X., Qin, G., Qin, Y., Quan, H., et al. (2020). Prevalence of Diabetes Recorded in mainland China Using 2018 Diagnostic Criteria from the American Diabetes Association: National Cross-Sectional Study. *Bmj* 369, m997. doi:10.1136/bmj.m997

Liew, C. F., Groves, C. J., Wiltshire, S., Zeggini, E., Frayling, T. M., Owen, K. R., et al. (2004). Analysis of the Contribution to Type 2 Diabetes Susceptibility of Sequence Variation in the Gene Encoding Stearoyl-CoA Desaturase, a Key Regulator of Lipid and Carbohydrate Metabolism. *Diabetologia* 47 (12), 2168–2175. doi:10.1007/s00125-004-1575-4

Liu, J., Cinar, R., Xiong, K., Godlewski, G., Jourdan, T., Lin, Y., et al. (2013). Monounsaturated Fatty Acids Generated via Stearoyl CoA Desaturase-1 Are Endogenous Inhibitors of Fatty Acid Amide Hydrolase. *Proc. Natl. Acad. Sci. U S A.* 110 (47), 18832–18837. doi:10.1073/pnas.1309469110

Lv, X., Dai, G., Lv, G., Chen, Y., Wu, Y., Shen, H., et al. (2016). Synergistic Interaction of Effective Parts in Rehmanniae Radix and Cornus Officinalis Ameliorates Renal Injury in C57BL/KsJ-Db/db Diabetic Mice: Involvement of Suppression of AGEs/RAGE/SphK1 Signaling Pathway. *J. Ethnopharmacol* 185, 110–119. doi:10.1016/j.jep.2016.03.017

Maki, T., Maeda, Y., Sonoda, N., Makimura, H., Kimura, S., Maeno, S., et al. (2017). Renoprotective Effect of a Novel Selective PPARα Modulator K-877 in Db/db Mice: A Role of Diacylglycerol-Protein Kinase C-NAD(P)H Oxidase Pathway. *Metabolism* 71, 33–45. doi:10.1016/j.metabol.2017.02.013

Meng, X., Ma, J., Kang, A. N., Kang, S. Y., Jung, H. W., and Park, Y. K. (2020). A Novel Approach Based on Metabolomics Coupled with Intestinal Flora Analysis and Network Pharmacology to Explain the Mechanisms of Action of Bekhogainsam Decoction in the Improvement of Symptoms of Streptozotocin-Induced Diabetic Nephropathy in Mice. *Front. Pharmacol.* 11, 633. doi:10.3389/fphar.2020.00633

Minville-Walz, M., Pierre, A. S., Pichon, L., Bellenger, S., Fèvre, C., Bellenger, J., et al. (2010). Inhibition of Stearoyl-CoA Desaturase 1 Expression Induces CHOP-dependent Cell Death in Human Cancer Cells. *PLoS One* 5 (12), e14363. doi:10.1371/journal.pone.0014363

Mohamed, E. M., and Samak, M. A. (2017). Therapeutic Potentials of Mesenchymal Stem Cells on the Renal Cortex of Experimentally Induced Hypertensive Albino Rats: Relevant Role of Nrf2. *Tissue Cell* 49 (2 Pt B), 358–367. doi:10.1016/j.tice.2017.01.003

Ntambi, J. M. (1995). Cellular Differentiation and Dietary Regulation of Gene Expression. *Prostaglandins Leukot. Essent. Fatty Acids* 52 (2-3), 117–120. doi:10.1016/0952-3278(95)90009-8

Ntambi, J. M. (1992). Dietary Regulation of Stearoyl-CoA Desaturase 1 Gene Expression in Mouse Liver. *J. Biol. Chem.* 267 (15), 10925–10930. doi:10.1016/s0021-9258(19)50107-7

Ntambi, J. M., Miyazaki, M., Stoehr, J. P., Lan, H., Kendziorski, C. M., Yandell, B. S., et al. (2002). Loss of Stearoyl-CoA Desaturase-1 Function Protects Mice against Adiposity. *Proc. Natl. Acad. Sci. U S A.* 99 (17), 11482–11486. doi:10.1073/pnas.132384699

Oh, K. K., Adnan, M., and Cho, D. H. (2020). Network Pharmacology of Bioactives from Sorghum Bicolor with Targets Related to Diabetes Mellitus. *PLoS One* 15 (12), e0240873. doi:10.1371/journal.pone.0240873

Pabbidi, R. M., Yu, S. Q., Peng, S., Khardori, R., Pauza, M. E., and Premkumar, L. S. (2008). Influence of TRPV1 on Diabetes-Induced Alterations in thermal Pain Sensitivity. *Mol. Pain* 4, 9. doi:10.1186/1744-8069-4-9

Page, A. J., Hatzinikolas, G., Vincent, A. D., Cavuoto, P., and Wittert, G. A. (2019). The TRPV1 Channel Regulates Glucose Metabolism. *Am. J. Physiol. Endocrinol. Metab.* 317 (4), E667–e676. doi:10.1152/ajpendo.00102.2019

Pan, L., Li, Z., Wang, Y., Zhang, B., Liu, G., and Liu, J. (2020). Network Pharmacology and Metabolomics Study on the Intervention of Traditional Chinese Medicine Huanglian Decoction in Rats with Type 2 Diabetes Mellitus. *J. Ethnopharmacol* 258, 112842. doi:10.1016/j.jep.2020.112842

Popeijus, H. E., Saris, W. H., and Mensink, R. P. (2008). Role of Stearoyl-CoA Desaturases in Obesity and the Metabolic Syndrome. *Int. J. Obes. (Lond)* 32 (7), 1076–1082. doi:10.1038/ijo.2008.55

Radu, B. M., Iancu, A. D., Dumitrescu, D. I., Flonta, M. L., and Radu, M. (2013). TRPV1 Properties in Thoracic Dorsal Root Ganglia Neurons Are Modulated by Intraperitoneal Capsaicin Administration in the Late Phase of Type-1 Autoimmune Diabetes. *Cell Mol Neurobiol* 33 (2), 187–196. doi:10.1007/s10571-012-9883-6

Sadeh, M., Glazer, B., Landau, Z., Wainstein, J., Bezaleli, T., Dabby, R., et al. (2013). Association of the M3151 Variant in the Transient Receptor Potential Vanilloid Receptor-1 (TRPV1) Gene with Type 1 Diabetes in an Ashkenazi Jewish Population. *Isr. Med. Assoc. J.* 15 (9), 477–480.

Sampath, H., and Ntambi, J. M. (2011). The Role of Stearoyl-CoA Desaturase in Obesity, Insulin Resistance, and Inflammation. *Ann. N. Y Acad. Sci.* 1243, 47–53. doi:10.1111/j.1749-6632.2011.06303.x

Shi, X., Lu, X. G., Zhan, L. B., Qi, X., Liang, L. N., Hu, S. Y., et al. (2011). The Effects of the Chinese Medicine ZiBu PiYin Recipe on the hippocampus in a Rat Model of Diabetes-Associated Cognitive Decline: a Proteomic Analysis. *Diabetologia* 54 (7), 1888–1899. doi:10.1007/s00125-011-2147-z

Shiwaku, K., Hashimoto, M., Kitajima, K., Nogi, A., Anuurad, E., Enkhmaa, B., et al. (2004). Triglyceride Levels Are Ethnic-Specifically Associated with an index of Stearoyl-CoA Desaturase Activity and N-3 PUFA Levels in Asians. *J. Lipid Res.* 45 (5), 914–922. doi:10.1194/jlr.M300483-JLR200

Stambolic, V., and Woodgett, J. R. (2006). Functional Distinctions of Protein Kinase B/Akt Isoforms Defined by Their Influence on Cell Migration. *Trends Cel Biol* 16 (9), 461–466. doi:10.1016/j.tcb.2006.07.001

Suri, A., and Szallasi, A. (2008). The Emerging Role of TRPV1 in Diabetes and Obesity. *Trends Pharmacol. Sci.* 29 (1), 29–36. doi:10.1016/j.tips.2007.10.016

Tan, A. L., Forbes, J. M., and Cooper, M. E. (2007). AGE, RAGE, and ROS in Diabetic Nephropathy. *Semin. Nephrol.* 27 (2), 130–143. doi:10.1016/j.semnephrol.2007.01.006

Tong, X. L., Dong, L., Chen, L., and Zhen, Z. (2012). Treatment of Diabetes Using Traditional Chinese Medicine: Past, Present, and Future. *Am. J. Chin. Med.* 40 (5), 877–886. doi:10.1142/s0192415x12500656

Tóth, A., Blumberg, P. M., and Boczán, J. (2009). Anandamide and the Vanilloid Receptor (TRPV1). *Vitam Horm.* 81, 389–419. doi:10.1016/s0083-6729(09)81015-7

Tzeng, T. F., Liou, S. S., and Liu, I. M. (2013). The Selected Traditional Chinese Medicinal Formulas for Treating Diabetic Nephropathy: Perspective of Modern Science. *J. Tradit Complement. Med.* 3 (3), 152–158. doi:10.4103/2225-4110.114893

Waters, K. M., and Ntambi, J. M. (1994). Insulin and Dietary Fructose Induce Stearoyl-CoA Desaturase 1 Gene Expression of Diabetic Mice. *J. Biol. Chem.* 269 (44), 27773–27777. doi:10.1016/s0021-9258(18)47053-6

Waters, K. M., and Ntambi, J. M. (1996). Polyunsaturated Fatty Acids Inhibit Hepatic Stearoyl-CoA Desaturase-1 Gene in Diabetic Mice. *Lipids* 31 Suppl (Suppl. l), S33–S36. doi:10.1007/bf02637047

Wen, X., Zeng, Y., Liu, L., Zhang, H., Xu, W., Li, N., et al. (2012). Zhenqing Recipe Alleviates Diabetic Nephropathy in Experimental Type 2 Diabetic Rats through Suppression of SREBP-1c. *J. Ethnopharmacol* 142 (1), 144–150. doi:10.1016/j.jep.2012.04.028

Wu, F., Shao, Q., Xia, Q., Hu, M., Zhao, Y., Wang, D., et al. (2021). A Bioinformatics and Transcriptomics Based Investigation Reveals an Inhibitory Role of Huanglian-Renshen-Decoction on Hepatic Glucose Production of T2DM Mice via PI3K/Akt/FoxO1 Signaling Pathway. *Phytomedicine* 83, 153487. doi:10.1016/j.phymed.2021.153487

Wu, Q., and Hu, Y. (2021). Systematic Evaluation of the Mechanisms of Mulberry Leaf (Morus alba Linne) Acting on Diabetes Based on Network Pharmacology and Molecular Docking. *Comb. Chem. High Throughput Screen.* 24 (5), 668–682. doi:10.2174/1386207323666200914103719

Xu, M., Li, Z., Yang, L., Zhai, W., Wei, N., Zhang, Q., et al. (2020a). Elucidation of the Mechanisms and Molecular Targets of Sanhuang Xiexin Decoction for Type 2 Diabetes Mellitus Based on Network Pharmacology. *Biomed. Res. Int.* 2020, 5848497. doi:10.1155/2020/5848497

Xu, X., Li, L., Zhang, Y., Lu, X., Lin, W., Wu, S., et al. (2020b). Hypolipidemic Effect of Alisma Orientale (Sam.) Juzep on Gut Microecology and Liver Transcriptome in Diabetic Rats. *PLoS One* 15 (10), e0240616. doi:10.1371/journal.pone.0240616

Xu, X., Niu, L., Liu, Y., Pang, M., Lu, W., Xia, C., et al. (2020c). Study on the Mechanism of Gegen Qinlian Decoction for Treating Type II Diabetes Mellitus by Integrating Network Pharmacology and Pharmacological Evaluation. *J. Ethnopharmacol* 262, 113129. doi:10.1016/j.jep.2020.113129

Yan, J., Wang, C., Jin, Y., Meng, Q., Liu, Q., Liu, Z., et al. (2018). Catalpol Ameliorates Hepatic Insulin Resistance in Type 2 Diabetes through Acting on AMPK/NOX4/PI3K/AKT Pathway. *Pharmacol. Res.* 130, 466–480. doi:10.1016/j.phrs.2017.12.026

Yang, Q., Shu, F., Gong, J., Ding, P., Cheng, R., Li, J., et al. (2020). Sweroside Ameliorates NAFLD in High-Fat Diet Induced Obese Mice through the Regulation of Lipid Metabolism and Inflammatory Response. *J. Ethnopharmacol* 255, 112556. doi:10.1016/j.jep.2020.112556

Yokozawa, T., Suzuki, N., Oura, H., Nonaka, G., and Nishioka, I. (1986). Effect of Extracts Obtained from Rhubarb in Rats with Chronic Renal Failure. *Chem. Pharm. Bull. (Tokyo)* 34 (11), 4718–4723. doi:10.1248/cpb.34.4718

Zhang, L. L., Yan Liu, D., Ma, L. Q., Luo, Z. D., Cao, T. B., Zhong, J., et al. (2007). Activation of Transient Receptor Potential Vanilloid Type-1 Channel Prevents Adipogenesis and Obesity. *Circ. Res.* 100 (7), 1063–1070. doi:10.1161/01.RES.0000262653.84850.8b

Zhang, R., Zhou, J., Li, M., Ma, H., Qiu, J., Luo, X., et al. (2014). Ameliorating Effect and Potential Mechanism of Rehmannia Glutinosa Oligosaccharides on the Impaired Glucose Metabolism in Chronic Stress Rats Fed with High-Fat Diet. *Phytomedicine* 21 (5), 607–614. doi:10.1016/j.phymed.2013.11.008

Zhang, R. X., Li, M. X., and Jia, Z. P. (2008). Rehmannia Glutinosa: Review of Botany, Chemistry, and Pharmacology. *J. Ethnopharmacol* 117 (2), 199–214. doi:10.1016/j.jep.2008.02.018

Zhang, X., Jin, C., Li, Y., Guan, S., Han, F., and Zhang, S. (2013). Catalpol Improves Cholinergic Function and Reduces Inflammatory Cytokines in the Senescent Mice Induced by D-Galactose. *Food Chem. Toxicol.* 58, 50–55. doi:10.1016/j.fct.2013.04.006

Zhao, P., Li, J., Yang, L., Li, Y., Tian, Y., and Li, S. (2018). Integration of Transcriptomics, Proteomics, Metabolomics, and Systems Pharmacology Data to Reveal the Therapeutic Mechanism Underlying Chinese Herbal

Bufei Yishen Formula for the Treatment of Chronic Obstructive Pulmonary Disease. *Mol. Med. Rep.* 17 (4), 5247–5257. doi:10.3892/mmr.2018.8480

Zheng, Y., Prouty, S. M., Harmon, A., Sundberg, J. P., Stenn, K. S., and Parimoo, S. (2001). Scd3--a Novel Gene of the Stearoyl-CoA Desaturase Family with Restricted Expression in Skin. *Genomics* 71 (2), 182–191. doi:10.1006/geno.2000.6429

Conflict of Interest: The authors declare that the research was conducted in the absence of any commercial or financial relationships that could be construed as a potential conflict of interest.

Publisher's Note: All claims expressed in this article are solely those of the authors and do not necessarily represent those of their affiliated organizations, or those of the publisher, the editors, and the reviewers. Any product that may be evaluated in this article, or claim that may be made by its manufacturer, is not guaranteed or endorsed by the publisher.

frontiers | Frontiers in Pharmacology

ORIGINAL RESEARCH
published: 30 May 2022
doi: 10.3389/fphar.2022.894099

Evaluation of Untargeted Metabolomic Strategy for the Discovery of Biomarker of Breast Cancer

Xujun Ruan[1†], Yan Wang[2†], Lirong Zhou[2], Qiuling Zheng[2], Haiping Hao[1]* and Dandan He[3]**

[1]Key Laboratory of Drug Metabolism and Pharmacokinetics, State Key Laboratory of Natural Medicines, China Pharmaceutical University, Nanjing, China, [2]Department of Pharmaceutical Analysis, College of Pharmacy, China Pharmaceutical University, Nanjing, China, [3]Experimental Center of Molecular and Cellular Biology, The Public Laboratory Platform, China Pharmaceutical University, Nanjing, China

OPEN ACCESS

Edited by:
Guo Ma,
Fudan University, China

Reviewed by:
Lei Zhou,
Guangdong Pharmaceutical University, China
Qinglin Li,
University of Chinese Academy of Sciences, China
Yan-Fang Xian,
The Chinese University of Hong Kong, China
Changhui Liu,
Guangzhou University of Chinese Medicine, China

***Correspondence:**
Qiuling Zheng
qiuling_zheng@cpu.edu.cn
Haiping Hao
haipinghao@cpu.edu.cn
Dandan He
cpudandanhe@163.com

[†]These authors have contributed equally to this work

Specialty section:
This article was submitted to Drug Metabolism and Transport, a section of the journal Frontiers in Pharmacology

Received: 11 March 2022
Accepted: 25 April 2022
Published: 30 May 2022

Citation:
Ruan X, Wang Y, Zhou L, Zheng Q, Hao H and He D (2022) Evaluation of Untargeted Metabolomic Strategy for the Discovery of Biomarker of Breast Cancer. Front. Pharmacol. 13:894099. doi: 10.3389/fphar.2022.894099

Discovery of disease biomarker based on untargeted metabolomics is informative for pathological mechanism studies and facilitates disease early diagnosis. Numerous of metabolomic strategies emerge due to different sample properties or experimental purposes, thus, methodological evaluation before sample analysis is essential and necessary. In this study, sample preparation, data processing procedure and metabolite identification strategy were assessed aiming at the discovery of biomarker of breast cancer. First, metabolite extraction by different solvents, as well as the necessity of vacuum-dried and re-dissolution, was investigated. The extraction efficiency was assessed based on the number of eligible components (components with MS/MS data acquired), which was more reasonable for metabolite identification. In addition, a simplified data processing procedure was proposed involving the OPLS-DA, primary screening for eligible components, and secondary screening with constraints including VIP, fold change and *p* value. Such procedure ensured that only differential candidates were subjected to data interpretation, which greatly reduced the data volume for database search and improved analysis efficiency. Furthermore, metabolite identification and annotation confidence were enhanced by comprehensive consideration of mass and MS/MS errors, isotope similarity, fragmentation match, and biological source confirmation. On this basis, the optimized strategy was applied for the analysis of serum samples of breast cancer, according to which the discovery of differential metabolites highly encouraged the independent biomarkers/indicators used for disease diagnosis and chemotherapy evaluation clinically. Therefore, the optimized strategy simplified the process of differential metabolite exploration, which laid a foundation for biomarker discovery and studies of disease mechanism.

Keywords: untargeted metabolomics, strategy evaluation, biomarker discovery, breast cancer, UPLC-MS

INTRODUCTION

Metabolites have been realized to play an important role in the onset of diseases, and are of great significance for disease diagnosis and prevention. Metabolomics is attracting increasing attentions in various areas, such as pathological mechanism studies, pathway analysis, and the exploration of novel biomarkers for diseases, including cancers (Armitage and Southam, 2016; Kumar and Misra,

2019; Liu et al., 2021; Long et al., 2021). According to different research goals, there comes up with untargeted metabolomics and targeted metabolomics (Jasbi et al., 2019; Casari et al., 2021; Baek et al., 2022; Harrieder et al., 2022). Targeted metabolomics concentrates more on the analysis of defined metabolites, which has limited scope but achieves enhanced detection sensitivity and enables the absolute quantification with the application of standards (Roberts et al., 2012; Cai et al., 2015; Zhou and Yin, 2016). Untargeted metabolomics, on the other hand, has superiority in high-throughput detection, which offers a comprehensive and in-depth insight of metabolome profiling (Yuan et al., 2012; Heiles, 2021) and is regarded as the basis for biomarker discovery.

Mass spectrometry (MS) has been regarded as a powerful analytical technique owing to its high detection speed and sensitivity. Its coupling with chromatographic separation, such as gas chromatography and liquid chromatography (LC), has been widely used for metabolomic analysis by providing both molecular weight and structural information (Liu et al., 2013; Alonso et al., 2015; Nash and Dunn, 2019; Hou et al., 2020; Harrieder et al., 2022). Efforts have been done in method development for sample preparation, chromatographic separation and derivatization-based detection to improve the metabolome coverage (Yuan et al., 2018; An et al., 2021; Meng et al., 2021). Besides, computational approaches are also dramatically developed to assist data interpretation and metabolite global annotation (Bonini et al., 2020; Chen et al., 2021; Duehrkop et al., 2021).

Breast cancer has become one of the leading causes threating health in women and its incidence is increasing within recent years. With the development of new therapeutic strategies, the mortality of breast cancer has gradually reduced (DeSantis et al., 2019). Metabolomics has been widely applied for metabolic pathway analysis and biomarker discovery for breast cancer based on the analysis of different biological samples, including cell lines, plasma, serum, tissues, urine and saliva (Tsutsui et al., 2013; Tenori et al., 2015; Zhong et al., 2016; Porto-Figueira et al., 2018), which facilitates the early diagnosis, treatment target exploration and mechanism studies of the disease (Günther, 2015; McCartney et al., 2018; Park et al., 2019; Silva et al., 2019; Long et al., 2021). Methodologies with various sample preparation steps, detection methods, data processing and metabolite annotation procedures were developed, upon which the evaluation is essential before sample analysis due to the difference of sample property or experimental purpose. Herein, sample preparation, data processing procedure, and metabolite identification strategy of untargeted metabolomics were evaluated and subsequently applied for the analysis of serum samples of breast cancer. First, metabolite extraction by different solvents was assessed and evaluation based on the number of components with MS/MS data acquired (defined as eligible components) was regarded to be more reasonable in consideration of metabolite identification. In addition, a simplified data processing procedure was proposed involving orthogonal projections to latent structures discriminant analysis (OPLS-DA) for all detected components, followed up with a primary screening based on the availability of MS/MS data and underwent a secondary screening with criteria of VIP, fold change (FC) and p value. Thus, only differential candidates were subjected to database search, identification and annotation, which greatly reduced the data volume and improved the analysis efficiency. Furthermore, the confidence and accuracy of metabolite identification were enhanced by comprehensively considering mass and MS/MS errors, isotope similarity, fragmentation match and biological source confirmation. On this basis, the evaluated strategy was applied for the analysis of serum samples of breast cancer, upon which the discovery of potential biomarkers would be informative for early diagnosis and chemotherapeutic evaluation of the disease.

MATERIALS AND METHODS

Chemicals and Reagents

Formic acid (FA) was purchased from Sigma-Aldrich (Saint Louis, MO, United States). Ultra-pure H_2O was prepared by a Milli-Q Pure Water System (Bedford, MA, United States). LC-MS grade methanol (MeOH) and acetonitrile (ACN) were purchased from Merck (Darmstadt, Germany).

Clinical Sample Collection and Sample Preparation

Serum samples were collected from Huashan Hospital, Fudan University and stored at −80°C before analysis. The research protocol was approved by the Ethical Committee of Huashan Hospital, Fudan University (KY2021-034), and written informed consents were provided by all participants.

For sample preparation, 400 μl of designed solvent (pre-cooled on ice) was mixed with 100 μl of serum sample and followed up with a 2 min vortex for sufficient extraction and protein precipitation. The obtained mixture was centrifuged at 15,000 g (5 min at 4°C) and directly stored at 4°C (1 h) to ensure the complete protein precipitation. Supernatant (200 μl) was transferred for an additional centrifugation (18,000 g for 5 min at 4°C). Vacuum-dried and re-dissolution by extraction solvent was performed prior to MS analysis if necessary. Quality control (QC) sample was prepared by pooling aliquots of each serum sample investigated in this study, including 58 samples from breast cancer vs. healthy control and 12 samples from breast cancer patients before and after chemotherapy. The prepared QC sample was applied for extraction evaluation and instrumental performance monitoring.

UPLC-MS

Chromatographic separation was performed by a Waters ACQUITY I-Class UPLC system equipped with an ACQUITY UPLC HSS T3 column (2.1 × 100 mm, 1.8 μm, Waters). Parameters were set as follows: column temperature 40°C; flow rate of 0.4 ml/min; injection volume of 4 μl; mobile phase A was H_2O containing 0.1% FA and B was ACN. The gradient elution condition was referenced by previous study (He et al., 2021): 0–1.00 min, 0% B; 1.01–4.00 min, 0–35% B; 4.01–15.50 min, 35–95% B; 15.51–18.00 min, maintaining at 95% B;

18.01–23.00 min, back to 0% B. MS detection and data acquisition were performed by a Q-TOF MS (Waters, Xevo, G2-XS QTof) in both positive and negative ion modes. MS parameters were set as follows: *m/z* range at 50–700 Da; capillary voltage at + 3.0 kV or −2.5 kV for positive or negative ion mode respectively; sampling cone at 40 V; source temperature at 110°C; desolvation temperature at 450°C; cone gas at 50 L/h, desolvation gas at 600 L/h. MassLynx (version 4.1, Waters) was used for data acquisition.

Data Processing

Data processing was performed by Progenesis QI (version 2.0, Waters; denoted as QI), which mainly contained steps of: creation of a new experiment; data import; review alignment; experiment design setup; peak picking; review deconvolution; compounds identification; review compounds; and compound statistics. Notably, adduct ion forms, such as $[M + H]^+$, $[M-H]^-$, $[M + Na]^+$, $[M + K]^+$, $[2M-H]^-$, and $[M + FA-H]^-$, were all included. Different adduct ion forms of a same metabolite were automatically combined to provide an accurate identity. For metabolites having different adduct ion forms, the one with the highest MS intensity was selected to represent the abundance. Databases for metabolite identification and annotation included Human Metabolome Database (HMDB) (http://www.hmdb.ca/), MoNA (http://mona.fiehnlab.ucdavis.edu/), and METLIN (https://metlin. scripps.edu/). Parameters were set as follows: 10 ppm for precursor ion match; 20 ppm for fragment ion match; > 80% for the isotope similarity; ≥ 40 score of identification. The MS/MS spectra for potential biomarkers were manually checked to confirm the assigned identities. Relative quantification of selected metabolites by QI was performed by integration of corresponding extracted ion chromatograms (EICs) and normalized against the total ion chromatogram (TIC). Manually check of EIC was required to ensure the accurate peak picking and correct integration.

Statistical Analysis

Components detected were exported by QI and subjected to EZinfo software (version 3.0, Waters) for OPLS-DA for statistical difference confirmation. Components with variable importance calculated based on S-plots (VIP) > 1, p value <0.05 (student's t-test) and FC > 1.5 were screened. Notably, for the same substance detected under different ion modes, the one with the smallest FC were adapted for further data analysis. Bioinformatics analysis of assigned differential metabolites, including pathway analysis and receiver operating characteristic (ROC) curve, were performed on MetaboAnalyst (version 5.0) (http://www.metaboanalyst.ca/).

RESULTS AND DISCUSSION

Evaluation of Untargeted Metabolomics

Sample preparation. Metabolite extraction and protein precipitation by two commonly used solvents, MeOH and ACN, as well as their mixture (50:50 by volume) were evaluated. The option of 0.1% FA adoption was also explored, as well as vacuum-dried concentration and re-dissolution considering metabolites with low abundance. The analysis of designed solvent-treated QC samples resulted to over 800,000 ions in the positive ion mode, among which ACN-extraction appeared to be the optimal one. In the negative ion mode, at least 500,000 ions were detected upon designed extraction conditions, and MeOH/ACN mixture had a higher efficiency (**Figure 1A**). Nevertheless, it was still hesitant to choose one appropriate solvent while such comparison was rough and inappropriate. Aiming at metabolite identification, evaluation based on eligible components was proposed to be more reasonable. Accordingly, eligible components obtained by designed conditions were in the range of 1,000–1,700 in the positive ion mode, among which MeOH-extraction was optimum with 1,659 components having MS/MS data. Similarly, extraction by designed solvents resulted to eligible components ranging from 700 to 1,200 in the negative ion mode, among which MeOH also emerged by having 1,148 components detected with MS/MS spectra (**Figure 1B**). Interestingly that no significant improvement was observed after concentration, which was probably due to the decomposition of unstable compounds during the tedious vacuum-dried step. Thus, MeOH extraction was applied for subsequent serum sample preparation and the obtained mixture after protein precipitation was directly subjected to MS analysis without further treatment. Moreover, the number of components varied with different extraction solvents further supported the importance of evaluation before sample analysis.

Data processing procedure. Upon UPLC-MS analysis, resulted components (considering MS1 data here) underwent OPLS-DA to ensure the statistical difference between tested groups. For routine procedure (**Figure 2**, in grey dash line), components with MS/MS data were subjected to database search, metabolite identification and differential analysis. Such procedure involved annotation and confirmation for every component, which was informative for revealing the difference in metabolome profiles and metabolomic pathways between tested samples. Aiming at the discovery of biomarker, we proposed a simplified data processing procedure with improved analysis efficiency. As shown in **Figure 2** (in black solid line), OPLS-DA was applied for multivariate analysis. Primary screening was performed to select eligible components, among which differential ones were further isolated by secondary screening with criteria of p value <0.05, VIP >1 and FC > 1.5. Thus, instead of massive identification, only differential candidates were allowed to subsequent database search and identification, which greatly narrowed down the data volume for interpretation.

Metabolite identification strategy. For metabolite identification and annotation, parameters including *m/z* error, fragment error, isotope similarity, and fragmentation match were mainly concerned. Fragmentation match was performed based on databases including METLIN, MoNA and HMDB. The former two contained MS/MS spectra that experimentally collected, while HMDB offered theoretical

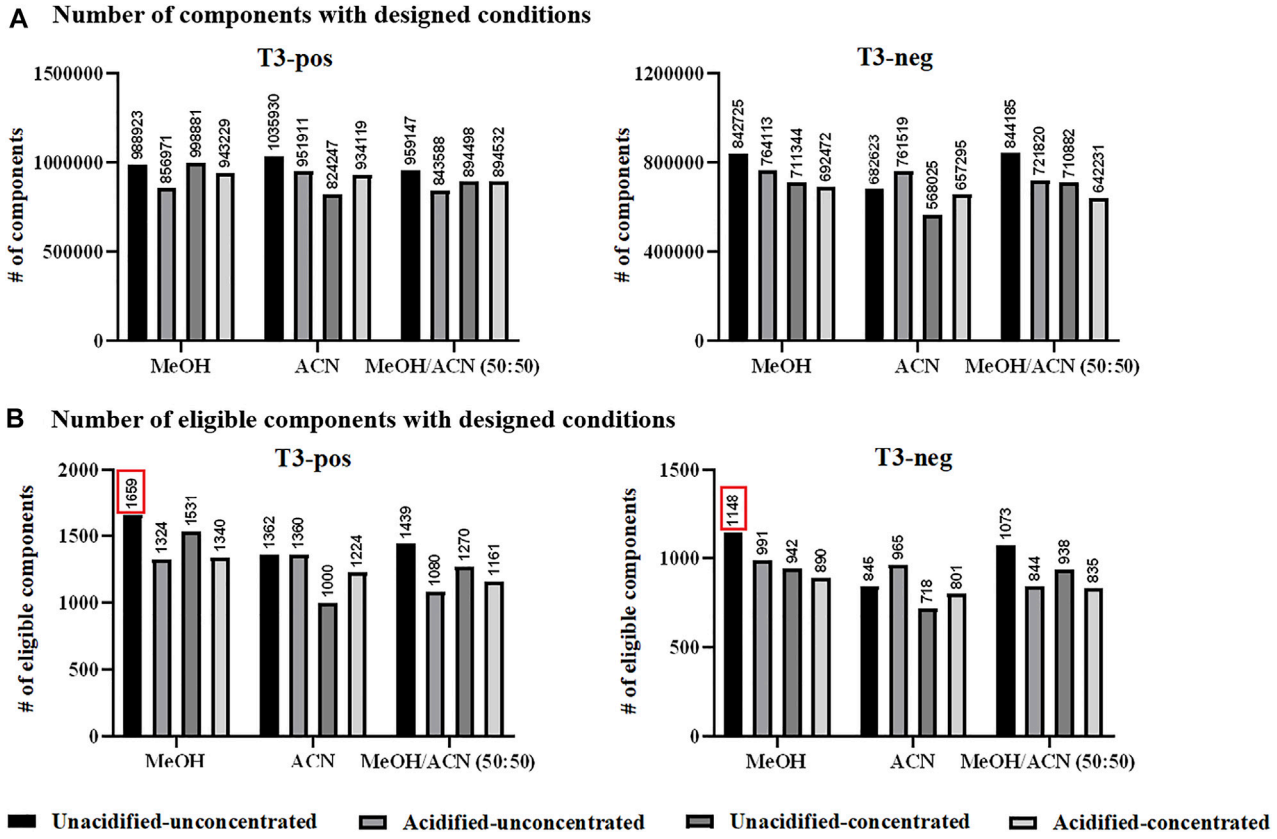

FIGURE 1 | (A) Total number of components (considering MS1 data) detected with designed conditions; and **(B)** total number of eligible components detected with designed conditions. Pos: positive ion mode; neg: negative ion mode.

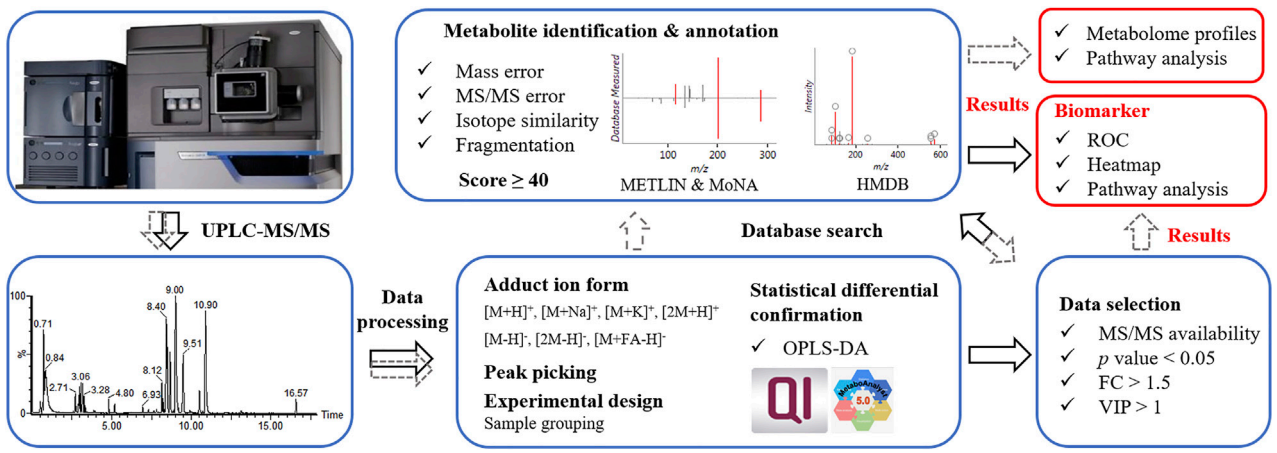

FIGURE 2 | Data processing procedures. Grey dash line referred to a routine data processing procedure; black solid line referred to the proposed simplified procedure.

fragmentation based on molecular structures. Metabolite identification was relied on the Score value from QI, which comprehensively evaluated the match degree of all above mentioned parameters. Based on previous study (Hou et al., 2020), the annotation accuracy and confidence were enhanced by setting a threshold of Score ≥40 for acceptance, which was

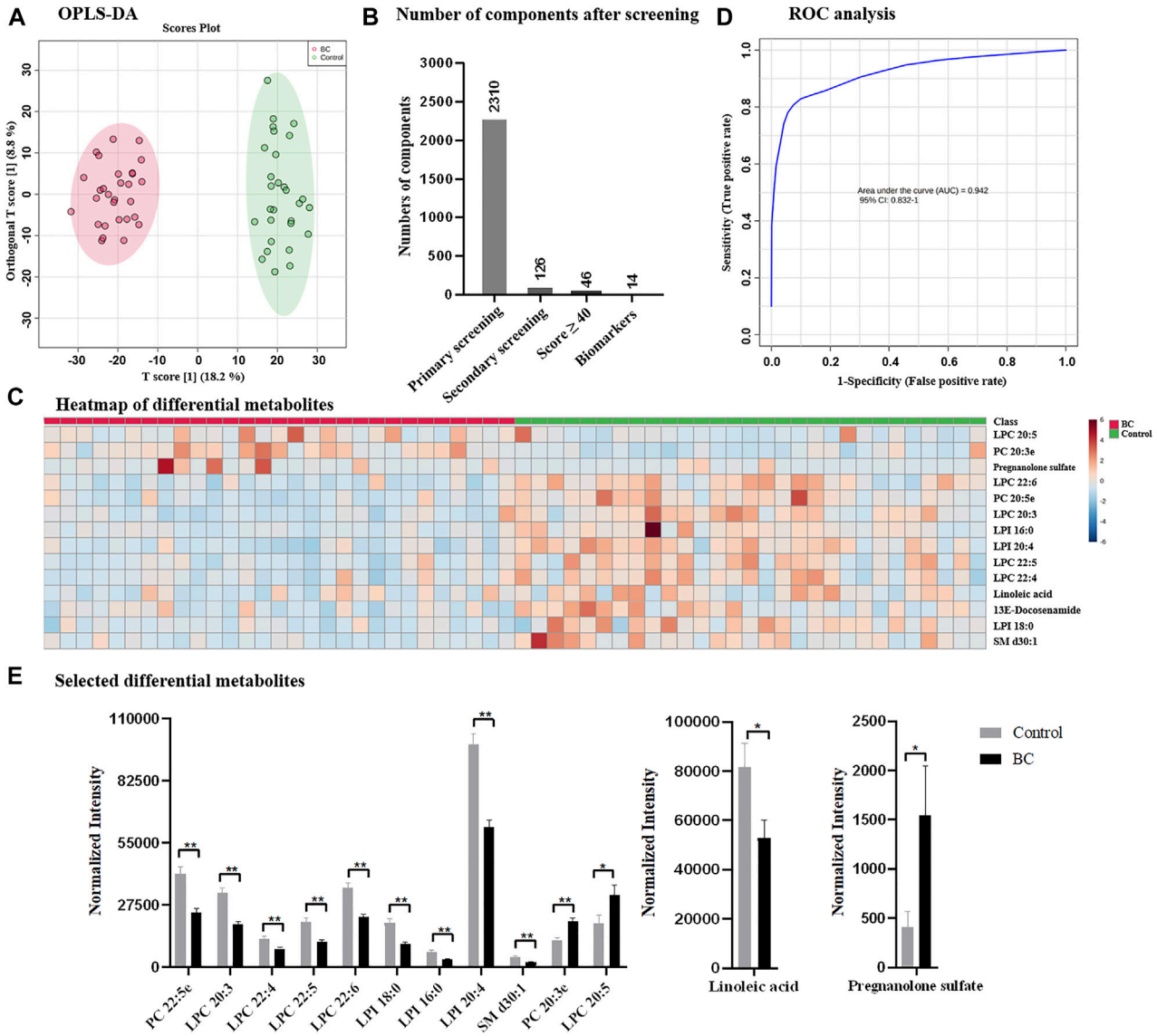

FIGURE 3 | (A) OPLS-DA score plots derived from the serum metabolomics datasets collected from healthy control and breast cancer group; **(B)** number of components after designed screening steps; **(C)** heatmap of differential metabolites; **(D)** ROC analysis; and **(E)** selected differential metabolites between healthy control and breast cancer group. BC: breast cancer.

higher than the one commonly used (≥35). Moreover, biological source information provided complementary information for further confirmation, upon which the structural and biological information was integrated for identification and annotation. Notably that it was possible to exclude a small portion of potential biomarkers based on such data processing procedure and identification strategy, especially for those with MS1 data only or those were not included in the databases we used. However, it was known that the identification of such components was challenge due to limited information provided, which would decrease the annotation confidence and reliability. Thus, such potential biomarkers would not be considered in this study as the identification and annotation with high confidence and accuracy were taken as the primary standard and purpose.

Exploration of Potential Biomarker of Breast Cancer

Following the optimized strategy, 58 serum samples containing 29 from healthy control and 29 from breast cancer patients were investigated. The instrumental stability and reproducibility were assessed by QC sample based on five successive injections prior to sample analysis and interval injections during sample run

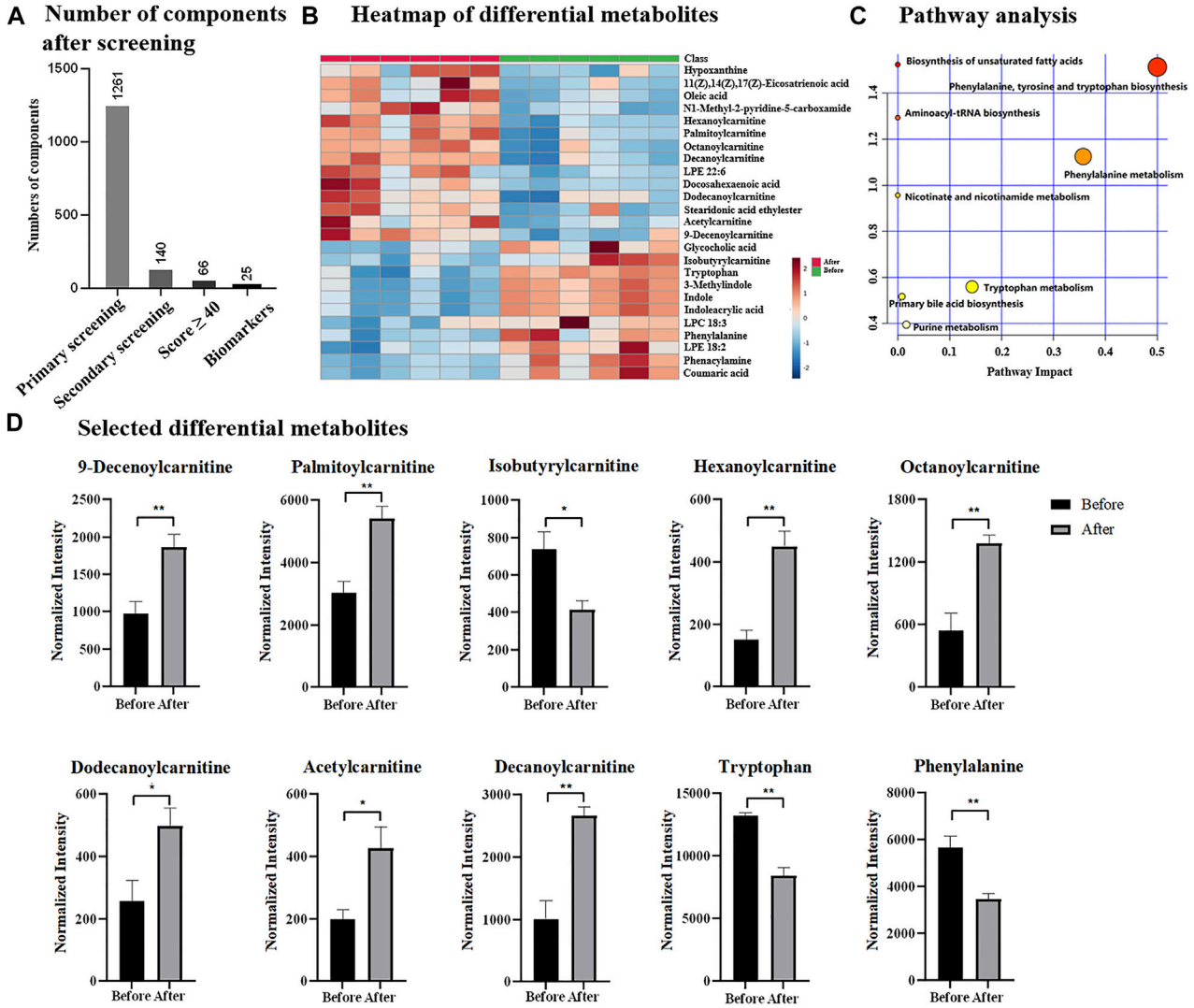

FIGURE 4 | (A) Number of components after designed screening steps; **(B)** heatmap of differential metabolites; **(C)** pathway analysis; **(D)** selected differential metabolites before and after chemotherapy.

(**Supplementary Figure S1A**). Upon UPLC-MS analysis, total 8,399 components (considering MS1 data only) were detected in the positive and negative ion modes. According to OPLS-DA, healthy control and breast cancer group exhibited distinguish metabolome profiles and were completely separated with R^2Y of 96.4% and Q^2 of 83.3% (**Figure 3A**). Following the proposed simplified procedure, primary screening resulted to 2,310 eligible components with qualified MS/MS data and only 126 differential candidates were remained after secondary screening for subsequent database search (**Figure 3B**), which greatly reduced the data volume and saved efforts for data interpretation. The identification by QI further narrowed down the number of metabolites to 46 with Score value ≥40. Upon biological source confirmation, a total of 14 endogenous metabolites were finally emerged (details found in **Supplementary Table S1**; **Supplementary Figure S2**). Heatmap analysis in **Figure 3C** also confirmed that they had quantitatively difference between healthy control and breast cancer group, according to which a considerable number of metabolites were observed down-regulated in breast cancer group. ROC curve analysis was applied to verify the representative of annotated metabolites and AUC of 0.942 in **Figure 3D** confirmed the reliability of identified metabolites, which implied them as potential biomarkers for clinical diagnosis of breast cancer. Differential metabolites mainly belonged to lipids, fatty acid, and fatty amide, some of which were also reported previously (Long et al., 2021) (**Figure 3E**). Lipids accounted for the majority of differential metabolites, including two phosphorylcholines (PCs), five lysophosphatidylcholines (LPCs) and three lysophosphatidylinositol (LPIs), which were also reported to be closely related to the occurrence of breast cancer (Cala et al., 2018;

Song et al., 2020; Long et al., 2021). Besides, linoleic acid, down-regulated in breast cancer group, was reported to be closely related to the regulation of breast cancer involved miRNA expression (Elieh Ali Komi et al., 2021). Pregnanolone sulfate, significantly up-regulated in breast cancer group based on our results, suggested a possible relationship between breast cancer and steroids. (Bicikova et al., 2001). It was worth to mention that the sample size enrolled in this study was limited, which might lead to insufficient discovery and miss other potential biomarkers. A larger sample population or detailed classification in subtypes, disease progression or treatment would be more expected.

Chemotherapy is one of major treatments for breast cancer, thus, the discovery of potential indicators is also essential for monitoring the process or effect of chemotherapy. Herein, total 12 serum samples collected from six breast cancer patients were investigated, including six samples before chemotherapeutic treatment and six samples after chemotherapeutic treatment. Upon UPLC-MS analysis, total 6,130 components (considering MS1 data only) were detected and based OPLS-DA (**Supplementary Figure S3A**), two groups were statistically different by receiving a R^2Y of 99.8% and Q^2 of 77.8%. With the simplified data processing procedure, 1,261 eligible components with qualified MS/MS data were isolated, while 140 of them met the criteria of secondary screening and were remained as differential candidates for database search. Based on QI identification, 66 components received Score value ≥40, and 25 of them were finally emerged as potential biomarkers according to biological source confirmation (**Figure 4A**, details found in **Supplementary Table S2** and **Supplementary Figure S4**). In addition, heatmap analysis illustrated significant quantitative difference among two groups, including 11 metabolites were down-regulated and 14 were up-regulated in chemotherapeutic group (**Figure 4B** and **Supplementary Table S2**). ROC analysis in **Supplementary Figure S3B** confirmed them as representative and potential indicators for monitoring the process or treatment of chemotherapy by achieving AUC of 1.00. Notably that the AUC value of 1.00 was not common, which was probably due to the indeed significant difference of potential metabolites before and after chemotherapeutic treatment. Besides, it was also because of limited sample size, which resulted to overfitting during ROC analysis. The identified potential indicators mainly distributed in biosynthesis of unsaturated fatty acids, aminoacyl-tRNA biosynthesis, nicotinate and nicotinamide metabolism, as well as phenylalanine, tyrosine and tryptophan biosynthesis (**Figure 4C**), some of which had also been reported previously as biomarkers for breast cancer diagnosis (Long et al., 2021). Among differential metabolites included eight carnitine species, suggesting the possible dysregulation of carnitine metabolism and fatty acid β-oxidation process. Phenylalanine and tryptophan were reported previously to be dysregulated and were highly expressed in breast cancer based on tissue or cell investigation (Du et al., 2019; Long et al., 2021). Similarly, indole was also considered as one of biomarkers for breast cancer and discovered to be up-regulated based on plasma analysis (Jasbi et al., 2019). They were observed down-regulated after chemotherapy according to results in **Figure 4D** and **Supplementary Table S2**, suggesting them as potential indicators to track chemotherapeutic treatment and disease recovery. Notably that differential metabolites identified in this study had overlap but not identical with previous studies, which could be attributed to the difference in sample types (tissue, serum or cultured cells). In addition, the differential metabolites identified for chemotherapeutic samples were different from that of breast cancer vs. healthy group, suggesting the possibility that the potential biomarkers for breast cancer diagnosis and chemotherapeutic monitoring were independent. It also implied that for clinical applications, the same potential biomarkers for breast cancer diagnosis were not sufficient for evaluation of chemotherapy, as separated metabolic pathways were probably affected. Thus, the discovery of indicators specified for the evaluation of chemotherapy were highly encouraged and large sample size would be more expected, especially for samples collected from the same subtype, progression of the disease or treatment.

CONCLUSION

In this study, sample preparation, data processing procedure and metabolite identification strategy of untargeted metabolomics were evaluated. Metabolite extraction by different solvents was investigated and reasonable assessment based on the number of eligible components was proposed. A simplified data processing procedure was proposed, involving OPLS-DA for statistical difference confirmation, primary screening based on MS/MS data availability and secondary screening according to criteria including FC, VIP and p value. Such procedure allowed database search for differential components only, which greatly narrowed down the data volume, improved the analysis efficiency and facilitated to reduce false identification results. For identification and annotation, mass error, MS/MS error, isotope similarity and fragmentation match were comprehensively considered and Score ≥40 was set to enhance the identification confidence and accuracy. The evaluated strategy was applied for the analysis of serum samples of breast cancer and the discovery of distinguished metabolites highly encouraged the exploration of independent biomarkers for disease diagnosis and treatment clinically. Therefore, the evaluated strategy was beneficial for the discovery of potential biomarker with the simplified procedure and unambiguous annotation.

DATA AVAILABILITY STATEMENT

The original contributions presented in the study are included in the article/**Supplementary Material**, further inquiries can be directed to the corresponding authors.

ETHICS STATEMENT

The studies involving human participants were reviewed and approved by the Ethical Committee of Huashan Hospital, Fudan

University. The patients/participants provided their written informed consent to participate in this study.

AUTHOR CONTRIBUTIONS

XR: Data curation; Methodology; Software; Validation; Writing—original draft; YW: Data curation; Software; Validation LZ: Data curation; Software QZ: Supervision; Writing—review and editing HH: Supervision, Writing review and editing, Conceptualization DH: Supervision, Writing review and editing, Conceptualization, Visualization.

FUNDING

This work was supported by the National Natural Science Foundation of China (81720108032, 81930109), the National Key Research and Development Programme of China (2021YFA1301300), the Project for Major New Drug Innovation and Development (2018ZX09711001-002-003), and the Project of State Key Laboratory of Natural Medicines at China Pharmaceutical University (SKLNMZZ202020).

ACKNOWLEDGMENTS

We thank Chengyu Chu from Huashan Hospital, Fudan University for clinical sample collection.

SUPPLEMENTARY MATERIAL

The Supplementary Material for this article can be found online at: https://www.frontiersin.org/articles/10.3389/fphar.2022.894099/full#supplementary-material

REFERENCES

Alonso, A., Marsal, S., and Julià, A. (2015). Analytical Methods in Untargeted Metabolomics: State of the Art in 2015. *Front. Bioeng. Biotechnol.* 3, 23. doi:10.3389/fbioe.2015.00023

An, N., Zhu, Q. F., Wang, Y. Z., Xiong, C. F., Hu, Y. N., and Feng, Y. Q. (2021). Integration of Chemical Derivatization and In-Source Fragmentation Mass Spectrometry for High-Coverage Profiling of Submetabolomes. *Anal. Chem.* 93 (32), 11321–11328. doi:10.1021/acs.analchem.1c02673

Armitage, E. G., and Southam, A. D. (2016). Monitoring Cancer Prognosis, Diagnosis and Treatment Efficacy Using Metabolomics and Lipidomics. *Metabolomics* 12 (10), 1–15. doi:10.1007/s11306-016-1093-7

Baek, J., He, C., Afshinnia, F., Michailidis, G., and Pennathur, S. (2022). Lipidomic Approaches to Dissect Dysregulated Lipid Metabolism in Kidney Disease. *Nat. Rev. Nephrol.* 18 (1), 38–55. doi:10.1038/s41581-021-00488-2

Bicíková, M., Számel, I., Hill, M., Tallová, J., and Stárka, L. (2001). Allopregnanolone, Pregnenolone Sulfate, and Epitestosterone in Breast Cyst Fluid. *Steroids* 66 (1), 55–57. doi:10.1016/s0039-128x(00)00140-9

Bonini, P., Kind, T., Tsugawa, H., Barupal, D. K., and Fiehn, O. (2020). Retip: Retention Time Prediction for Compound Annotation in Untargeted Metabolomics. *Anal. Chem.* 92 (11), 7515–7522. doi:10.1021/acs.analchem.9b05765

Cai, Y., Weng, K., Guo, Y., Peng, J., and Zhu, Z.-J. (2015). An Integrated Targeted Metabolomic Platform for High-Throughput Metabolite Profiling and Automated Data Processing. *Metabolomics* 11 (6), 1575–1586. doi:10.1007/s11306-015-0809-4

Cala, M. P., Aldana, J., Medina, J., Sánchez, J., Guio, J., Wist, J., et al. (2018). Multiplatform Plasma Metabolic and Lipid Fingerprinting of Breast Cancer: a Pilot Control-Case Study in Colombian Hispanic Women. *PLoS One* 13 (2), e0190958. doi:10.1371/journal.pone.0190958

Casari, I., Manfredi, M., Metharom, P., and Falasca, M. (2021). Dissecting Lipid Metabolism Alterations in SARS-CoV-2. *Prog. Lipid Res.* 82, 101092. doi:10.1016/j.plipres.2021.101092

Chen, L., Lu, W., Wang, L., Xing, X., Chen, Z., Teng, X., et al. (2021). Metabolite Discovery through Global Annotation of Untargeted Metabolomics Data. *Nat. Methods* 18, 1377–1385. doi:10.1038/s41592-021-01303-3

DeSantis, C. E., Ma, J., Gaudet, M. M., Newman, L. A., Miller, K. D., Goding Sauer, A., et al. (2019). Breast Cancer Statistics, 2019. *CA Cancer J. Clin.* 69 (6), 438–451. doi:10.3322/caac.21583

Du, S., Wang, Y., Alatrash, N., Weatherly, C. A., Roy, D., MacDonnell, F. M., et al. (2019). Altered Profiles and Metabolism of L- and D-Amino Acids in Cultured Human Breast Cancer Cells vs. Non-tumorigenic Human Breast Epithelial Cells. *J. Pharm. Biomed. Anal.* 164, 421–429. doi:10.1016/j.jpba.2018.10.047

Dührkop, K., Nothias, L. F., Fleischauer, M., Reher, R., Ludwig, M., Hoffmann, M. A., et al. (2021). Systematic Classification of Unknown Metabolites Using High-Resolution Fragmentation Mass Spectra. *Nat. Biotechnol.* 39 (4), 462–471. doi:10.1038/s41587-020-0740-8

Elieh Ali Komi, D., Shekari, N., Soofian-Kordkandi, P., Javadian, M., Shanehbandi, D., Baradaran, B., et al. (2021). Docosahexaenoic Acid (DHA) and Linoleic Acid (LA) Modulate the Expression of Breast Cancer Involved miRNAs in MDA-MB-231 Cell Line. *Clin. Nutr. ESPEN* 46, 477–483. doi:10.1016/j.clnesp.2021.09.006

Günther, U. L. (2015). Metabolomics Biomarkers for Breast Cancer. *Pathobiology* 82 (3-4), 153–165. doi:10.1159/000430844

Harrieder, E.-M., Kretschmer, F., Böcker, S., and Witting, M. (2022). Current State-Of-The-Art of Separation Methods Used in LC-MS Based Metabolomics and Lipidomics. *J. Chromatogr. B* 1188, 123069. doi:10.1016/j.jchromb.2021.123069

He, D., Su, Y., Meng, D., Wang, X., Wang, J., and Ye, H. (2021). A Pilot Study Optimizing Metabolomic and Lipidomic Acquisition in Serum for Biomarker Discovery in Nonalcoholic Fatty Liver Disease. *J. Mass Spectrom. Adv. Clin. Lab.* 22, 17–25. doi:10.1016/j.jmsacl.2021.10.001

Heiles, S. (2021). Advanced Tandem Mass Spectrometry in Metabolomics and Lipidomics-Methods and Applications. *Anal. Bioanal. Chem.* 413 (24), 5927–5948. doi:10.1007/s00216-021-03425-1

Hou, Y., He, D., Ye, L., Wang, G., Zheng, Q., and Hao, H. (2020). An Improved Detection and Identification Strategy for Untargeted Metabolomics Based on UPLC-MS. *J. Pharm. Biomed. Anal.* 191, 113531. doi:10.1016/j.jpba.2020.113531

Jasbi, P., Wang, D., Cheng, S. L., Fei, Q., Cui, J. Y., Liu, L., et al. (2019). Breast Cancer Detection Using Targeted Plasma Metabolomics. *J. Chromatogr. B Anal. Technol. Biomed. Life Sci.* 1105, 26–37. doi:10.1016/j.jchromb.2018.11.029

Kumar, A., and Misra, B. B. (2019). Challenges and Opportunities in Cancer Metabolomics. *Proteomics* 19 (21-22), e1900042. doi:10.1002/pmic.201900042

Liu, L., Wang, M., Yang, X., Bi, M., Na, L., Niu, Y., et al. (2013). Fasting Serum Lipid and Dehydroepiandrosterone Sulfate as Important Metabolites for Detecting Isolated Postchallenge Diabetes: Serum Metabolomics via Ultra-high-performance LC-MS. *Clin. Chem.* 59 (9), 1338–1348. doi:10.1373/clinchem.2012.200527

Liu, L., Zhao, J., Zhang, R., Wang, X., Wang, Y., Chen, Y., et al. (2021). Serum Untargeted Metabolomics Delineates the Metabolic Status in Different Subtypes of Non-alcoholic Fatty Liver Disease. *J. Pharm. Biomed. Anal.* 200, 114058. doi:10.1016/j.jpba.2021.114058

Long, N. P., Heo, D., Kim, H. Y., Kim, T. H., Shin, J. G., Lee, A., et al. (2021). Metabolomics-guided Global Pathway Analysis Reveals Better Insights into the Metabolic Alterations of Breast Cancer. *J. Pharm. Biomed. Anal.* 202, 114134. doi:10.1016/j.jpba.2021.114134

McCartney, A., Vignoli, A., Biganzoli, L., Love, R., Tenori, L., Luchinat, C., et al. (2018). Metabolomics in Breast Cancer: A Decade in Review. *Cancer Treat. Rev.* 67, 88–96. doi:10.1016/j.ctrv.2018.04.012

Meng, X., Pang, H., Sun, F., Jin, X., Wang, B., Yao, K., et al. (2021). Simultaneous 3-Nitrophenylhydrazine Derivatization Strategy of Carbonyl, Carboxyl and Phosphoryl Submetabolome for LC-MS/MS-Based Targeted Metabolomics with Improved Sensitivity and Coverage. *Anal. Chem.* 93 (29), 10075–10083. doi:10.1021/acs.analchem.1c00767

Nash, W. J., and Dunn, W. B. (2019). From Mass to Metabolite in Human Untargeted Metabolomics: Recent Advances in Annotation of Metabolites Applying Liquid Chromatography-Mass Spectrometry Data. *TrAC Trends Anal. Chem.* 120, 115324. doi:10.1016/j.trac.2018.11.022

Park, J., Shin, Y., Kim, T. H., Kim, D. H., and Lee, A. (2019). Plasma Metabolites as Possible Biomarkers for Diagnosis of Breast Cancer. *PLoS One* 14, e0225129. doi:10.1371/journal.pone.0225129

Porto-Figueira, P., Pereira, J. A. M., and Câmara, J. S. (2018). Exploring the Potential of Needle Trap Microextraction Combined with Chromatographic and Statistical Data to Discriminate Different Types of Cancer Based on Urinary Volatomic Biosignature. *Anal. Chim. Acta* 1023, 53–63. doi:10.1016/j.aca.2018.04.027

Roberts, L. D., Souza, A. L., Gerszten, R. E., and Clish, C. B. (2012). Targeted Metabolomics. *Curr. Protoc. Mol. Biol.* Chapter 30, Unit 30.2.1–24. doi:10.1002/0471142727.mb3002s98

Silva, C., Perestrelo, R., Silva, P., Tomás, H., and Câmara, J. S. (2019). Breast Cancer Metabolomics: from Analytical Platforms to Multivariate Data Analysis. A Review. *Metabolites* 9 (5), 102. doi:10.3390/metabo9050102

Song, L., Liu, Z., Hu, H. H., Yang, Y., Li, T. Y., Lin, Z. Z., et al. (2020). Proto-oncogene Src Links Lipogenesis via Lipin-1 to Breast Cancer Malignancy. *Nat. Commun.* 11 (1), 5842. doi:10.1038/s41467-020-19694-w

Tenori, L., Oakman, C., Morris, P. G., Gralka, E., Turner, N., Cappadona, S., et al. (2015). Serum Metabolomic Profiles Evaluated after Surgery May Identify Patients with Oestrogen Receptor Negative Early Breast Cancer at Increased Risk of Disease Recurrence. Results from a Retrospective Study. *Mol. Oncol.* 9 (1), 128–139. doi:10.1016/j.molonc.2014.07.012

Tsutsui, H., Mochizuki, T., Inoue, K., Toyama, T., Yoshimoto, N., Endo, Y., et al. (2013). High-Throughput LC-MS/MS Based Simultaneous Determination of Polyamines Including N-Acetylated Forms in Human Saliva and the Diagnostic Approach to Breast Cancer Patients. *Anal. Chem.* 85 (24), 11835–11842. doi:10.1021/ac402526c

Yuan, B. F., Zhu, Q. F., Guo, N., Zheng, S. J., Wang, Y. L., Wang, J., et al. (2018). Comprehensive Profiling of Fecal Metabolome of Mice by Integrated Chemical Isotope Labeling-Mass Spectrometry Analysis. *Anal. Chem.* 90 (5), 3512–3520. doi:10.1021/acs.analchem.7b05355

Yuan, M., Breitkopf, S. B., Yang, X., and Asara, J. M. (2012). A Positive/negative Ion-Switching, Targeted Mass Spectrometry-Based Metabolomics Platform for Bodily Fluids, Cells, and Fresh and Fixed Tissue. *Nat. Protoc.* 7 (5), 872–881. doi:10.1038/nprot.2012.024

Zhong, L., Cheng, F., Lu, X., Duan, Y., and Wang, X. (2016). Untargeted Saliva Metabonomics Study of Breast Cancer Based on Ultra Performance Liquid Chromatography Coupled to Mass Spectrometry with HILIC and RPLC Separations. *Talanta* 158, 351–360. doi:10.1016/j.talanta.2016.04.049

Zhou, J., and Yin, Y. (2016). Strategies for Large-Scale Targeted Metabolomics Quantification by Liquid Chromatography-Mass Spectrometry. *Analyst* 141 (23), 6362–6373. doi:10.1039/c6an01753c

Conflict of Interest: The authors declare that the research was conducted in the absence of any commercial or financial relationships that could be construed as a potential conflict of interest.

Publisher's Note: All claims expressed in this article are solely those of the authors and do not necessarily represent those of their affiliated organizations, or those of the publisher, the editors and the reviewers. Any product that may be evaluated in this article, or claim that may be made by its manufacturer, is not guaranteed or endorsed by the publisher.

frontiers | Frontiers in Pharmacology

ORIGINAL RESEARCH
published: 08 June 2022
doi: 10.3389/fphar.2022.938813

JBP485, A Dual Inhibitor of Organic Anion Transporters (OATs) and Renal Dehydropeptidase-I (DHP-I), Protects Against Imipenem-Induced Nephrotoxicity

Chong Wang[1,2,3], *Changyuan Wang*[2,3], *Jingjing Wu*[2,3], *Qiang Meng*[2,3], *Huan Jin*[2,3], *Huijun Sun*[2,3], *Taiichi Kaku*[4], *Jing Chen*[5], *Xiaokui Huo*[6*†] and *Kexin Liu*[1,2,3*†]

[1]Institute of Integrative Medicine, Dalian Medical University, Dalian, China, [2]Department of Clinical Pharmacology, College of Pharmacy, Dalian Medical University, Dalian, China, [3]Provincial Key Laboratory for Pharmacokinetics and Transport, Liaoning Dalian Medical University, Dalian, China, [4]Japan Bioproducts Industry Co. Ltd, Tokyo, Japan, [5]School of Chemistry and Materials Science, University of Science and Technology of China, Hefei, China, [6]Pharmaceutical Research Center, Second Affiliated Hospital, Dalian Medical University, Dalian, China

OPEN ACCESS

Edited by:
Ling Ye,
Southern Medical University, China

Reviewed by:
Baojian Wu,
Guangzhou University of Chinese Medicine, China
Huidi Jiang,
Zhejiang University, China
Zifei Qin,
First Affiliated Hospital of Zhengzhou University, China

***Correspondence:**
Xiaokui Huo
huoxiaokui@163.com
Kexin Liu
liukexin89@163.com

†ORCID:
Xiaokui Huo
orcid.org/0000-0003-4056-7987
Kexin Liu
orcid.org/0000-0002-0699-8452

Specialty section:
This article was submitted to Drug Metabolism and Transport, a section of the journal Frontiers in Pharmacology

Received: 08 May 2022
Accepted: 23 May 2022
Published: 08 June 2022

Citation:
Wang C, Wang C, Wu J, Meng Q, Jin H, Sun H, Kaku T, Chen J, Huo X and Liu K (2022) JBP485, A Dual Inhibitor of Organic Anion Transporters (OATs) and Renal Dehydropeptidase-I (DHP-I), Protects Against Imipenem-Induced Nephrotoxicity. Front. Pharmacol. 13:938813. doi: 10.3389/fphar.2022.938813

Imipenem (IMP) possesses a broad spectrum of antibacterial activity; however, nephrotoxicity limits its clinical application in patients with renal insufficiency. In our previous studies, a dipeptide, JBP485, a dipeptide with the chemical structure cyclo-trans-4-L-hydroxyprolyl-L-serine, was found to attenuate drug-induced kidney injury. The current study aimed to explore whether JBP485 could relieve IMP-induced kidney injury and clarify the potential molecular pharmacokinetic mechanism. The effects of JBP485 on IMP nephrotoxicity were evaluated in rabbits and human kidney 2 (HK-2) cells. Drug-drug interactions (DDIs) mediated by organic anion transporters (OATs) and dehydropeptidase-I (DHP-I) were explored through pharmacokinetic studies in rats, metabolism assays in the kidney, and uptake studies in OAT-over-expressing cells. The results revealed that JBP485 significantly ameliorated IMP-induced nephrotoxicity in rabbits. Further, incubation of HK-2 cells with JBP485 or cilastatin markedly improved the cell survival rate, inhibited apoptosis and attenuated mitochondrial damage by improving the stability of IMP and reducing its intracellular accumulation. This suggests that DHP-I and OATs might be involved in the protective effect of JBP485. Furthermore, coadministration with JBP485 significantly increased the IMP's plasma concentration as well as the area under the plasma concentration-time curve (AUC), while decreasing IMP renal clearance and cumulative urinary excretion. Moreover, JBP485 reduced IMP uptake in kidney slices and OAT1/3-human embryonic kidney 293 (HEK293) cells. At the same time, the metabolism of IMP by DHP-I was inhibited by JBP485 with an IC_{50} value of 12.15 ± 1.22 μM. Finally, the molecular docking assay revealed a direct interaction between

Abbreviations: AUC, area under the plasma concentration-time curve; BUN, blood urea nitrogen; CRE, creatinine; CLp, plasma clearance; CLR, renal clearance; DHP-I, renal dehydropeptidase-I; DDIs, drug-drug interactions; hOAT, human OAT; HEK293, human embryonic kidney 293; HK-2, human kidney 2; IMP, imipenem; LC-MS/MS, liquid chromatography–tandem mass spectrometry; OATs, renal organic anion transporters; PAH, p-aminophenol acid; t1/2β, half-life.

JBP485 and OAT1/3 or DHP-I. In conclusion, JBP485 protected against IMP nephrotoxicity in rabbits and HK-2 cells by improving IMP stability and reducing its intracellular accumulation via simultaneous inhibition of renal OATs and DHP-I. JBP485 is a promising renoprotective agent and could serve as an effective supplement to reduce IMP-induced adverse renal reactions in the clinical setting.

Keywords: Imipenem, JBP485, OATs, DHP-I, DDI

INTRODUCTION

It has been proved that nephrotoxicity was a common side effect of several antibiotics. It not only limits the use of these drugs but can even cause severe kidney injury. Prevention of nephrotoxicity can increase patients' drug tolerance, allowing higher doses of a drug to be administered for a longer period, thereby increasing the rate of successful treatment (Shayan and Elyasi, 2020). Imipenem (IMP), the first commercially available β-lactam agent of the carbapenem class, possesses broad-spectrum antibacterial activity *in vitro*, enclosing Gram-negative and Gram-positive aerobic and anaerobic species (Benfield and Chrisp, 1992). IMP is rapidly catalysed to toxic and inactive metabolites by the dehydropeptidase-I (DHP-I) enzyme at the luminal side of proximal tubular cells in the kidney; this leads to nephrotoxicity (Huo et al., 2019). Cilastatin is a specific inhibitor of DHP-I with no pharmacological effects; thus, it is usually used as a renoprotective agent in clinic. Therefore, IMP is formulated at a 1–1 mg ratio with cilastatin to prevent rapid hydrolysis of toxic metabolites with accumulation in tubular cells (Hakeam et al., 2019). In addition, our previous study found that both IMP and cilastatin are substrates of human organic anion transporter 1 (OAT1) and OAT3 (Huo et al., 2019; Zhu et al., 2020). Renal OATs have a central role in moving small-molecule endogenous metabolites, drugs and toxins (exogenous and endogenous) between tissues and interfacing body fluids (Nigam, 2018). Numerous evidence indicates that the residual renal secretory capacity, especially via OATs, may be particularly important in the setting of chronic kidney disease. In fact, it is known that the proximal tubule residual function is possible to be central to the remotion of compounds not commonly eliminated by haemodialysis, including many protein-bound small-molecule uremic solutes and toxins (Bush et al., 2020). In our previous studies, cilastatin was found to inhibit IMP transport by hOAT1/3, reduce hOAT1/3-dependent cytotoxicity, and alleviate nephrotoxicity induced by IMP in a concentration-dependent manner (Huo et al., 2019). Therefore, OATs and DHP-I could serve as targets to improve the therapeutic effect of IMP and decrease its toxicity.

JBP485 (cyclo-trans-4-L-hydroxyprolyl-L-serine), a dipeptide, was first isolated from Laennec (a trading name for the hydrolysate of the human placenta) (Cang et al., 2011). It displays notable anti-apoptosis and antioxidant properties (Wu et al., 2008; Yang et al., 2009; Cang et al., 2010; Liu et al., 2011; Wang et al., 2011). Our previous studies demonstrated that JBP485 regulates the expression of OATs and multi-drug resistance-associated protein 2/ABCC2 (MRP2) to attenuate drug-induced kidney injury (Liu et al., 2012; Guo et al., 2013). Moreover, several studies have demonstrated that JBP485 is a substrate of OATs and can inhibit the renal excretion of *p*-aminohippurate (PAH) (Zhang et al., 2010). Considering its OAT inhibitory activity and its antioxidant and anti-apoptosis properties, JBP485 may influence IMP nephrotoxicity when simultaneously administered.

Thus, the purpose of the current study was to explore whether JBP485 can relieve IMP-induced kidney injury and to clarify the mechanism underlying the drug-drug interaction (DDI) between IMP and JBP485. The results revealed that JBP485 ameliorated IMP-induced nephrotoxicity in rabbits and human kidney 2 (HK-2) cells. A liquid chromatography–tandem mass spectrometry (LC-MS/MS) method for determining IMP was established and an *in vivo* pharmacokinetic study, as well as an *in vitro* uptake assay of kidney slices and hOAT1/3-transfected cells, were performed to verify that JBP485 inhibited the renal excretion of IMP. At the same time, the metabolism of IMP by renal DHP-I was also found to be inhibited by JBP485. These findings indicate that OATs and DHP-I are the targets of the DDI between IMP and JBP485 and contribute to the protective effect of JBP485 against IMP-induced nephrotoxicity.

MATERIALS AND METHODS

Materials

IMP was obtained from Dalian Meilun Biology Technology Co., Ltd. (Dalian, China). Cilastatin was purchased from Topscience Co., Ltd. (Shanghai, China). JBP485 was provided by Japan Bioproducts Industry Co., Ltd. (Tokyo, Japan). All other chemicals and reagents utilized in this study were of analytical purity grade and were commercially available.

Animals

Male Wistar rats (weighing 220–250 g) and male New Zealand white rabbits (2.0–3.0 kg) were both obtained from the Experimental Animal Centre of Dalian Medical University (Dalian, China; permit number SCXK 2013-003). All animals were fed a chow diet and allowed free access to water. The animal experiments were executed based on the laboratory animals guidelines of the National Institutes of Health. The animals were fasted for 12 h before experiments, with access to water ad libitum.

Cell Culture

Human embryonic kidney 293 (HEK293) cells and HK-2 cells were grown in Dulbecco's modified Eagle's medium (Invitrogen, Carlsbad, CA) and DMEM/F12 medium (KeyGen, Nanjing, China), respectively, supplemented with 10% (v/v) foetal bovine serum (Invitrogen), 100 U/ml penicillin and 100 mg/ml streptomycin. Cells were cultured at 37°C with a 5% (v/v) CO_2 atmosphere and 95% relative humidity. Cell culture reagents were purchased from Gibco (Grand Island, NY).

Biochemical Assay

The levels of blood urea nitrogen (BUN) and creatinine (CRE) were detected according to the instructions supplied by Nanjing Jiancheng Institute of Biotechnology (Nanjing, China).

Toxicity Study in Rabbits

Rabbits were randomly divided into four groups: (1) control group, (2) IMP (200 mg/kg) group, (3) JBP485 (200 mg/kg) group, (4) IMP (200 mg/kg) + JBP485 (200 mg/kg) group. The doses chosen were set according to our previous study (Huo et al., 2019). Pre-treatment with JBP485 was performed by intraperitoneal administration one day in advance of the toxicity study. Test drugs were diluted in normal saline and were administered intravenously to rabbits via the ear vein at a rate of 5 ml/min. At 0, 24, 48 and 72 h after administration, blood samples (0.5 ml) were collected *via* the ear vein into heparin tubes and the samples were centrifuged at 1,000 × *g* for 10 min to obtain plasma. Plasma samples were stored at −20°C until analysis.

After 72 h, the rabbits were decapitated, and the kidneys should be immediately excised and fixed in neutral 10% buffered formalin. Histopathological examination was conducted through routine haematoxylin-eosin (HE) paraffin embedding. Tissue samples were sectioned and stained with HE.

In Vivo Renal Clearance Experiments

Rats were randomly divided into two groups: 1) IMP alone (45 mg/kg) group, 2) IMP (45 mg/kg) + JBP485 (90 mg/kg) group. Test drugs were diluted in normal saline and were administered intravenously via the left jugular vein. After intravenous administration, blood samples (0.2 ml) were collected through the other side of the jugular vein with heparinized syringes at the time points: 1, 3, 5, 10, 30, 60, 120, 240, 360 and 480 min. After each blood sample collection, 0.2 ml isotonic saline solution was injected. Bladders were cannulated and urine was collected at 2, 4, 6 and 8 h after administration. LC-MS/MS method was used to measure IMP concentrations. Pharmacokinetic parameters, renal clearance (CL_R) and cumulative urinary excretion were calculated.

In Vitro Uptake in Kidney Slices

Rat kidneys were cut into slices with a ZQP-86 tissue slicer (Zhixin Co. Ltd., China), as previously described (Wang et al., 2014). After preincubation for 3 min at 37°C, the kidney slices were transferred to 24-well culture plates having 1 ml fresh oxygenated buffer with IMP (50 μM) and/or JBP485 (50 μM) for further incubation at 37°C under gentle shaking. After incubation for 5, 15 and 30 min, the kidney slices were washed using ice-cold Hanks' balanced salt solution (pH 7.5). Accumulated IMP in the homogenized kidneys was determined by LC-MS/MS.

Uptake By HK-2 Cells and OAT1/3-Transfected HEK293 Cells

HK-2 cells, hOAT1-HEK293 cells, hOAT3-HEK293 cells or mock cells were seeded in 24-well culture plates and cultured for 48 h before the experiment. The cells were washed twice. After adding transport buffer (1 ml) with IMP (50 μM) and/or JBP485 (50 μM), the uptake was initiated. The cells were incubated for 10 min in transport buffer at 37°C. Moreover, the concentration-dependent uptake of IMP and the effects of JBP485 on IMP uptake were examined. The cells were washed and lysed and then transferred into a polythene tube for quantization. Protein was measured according to the bicinchoninic acid procedure (Solarbio, Beijing, China) using bovine serum albumin for the standard.

Metabolism of IMP By HK-2 Cells and Renal DHP-I

The stability of IMP in the medium of HK-2 cells was evaluated according to previously reported methods (Huo et al., 2019). Cells were seeded in 24-well culture plates and cultured for 48 h before each experiment. IMP (50 μM) was added into the medium with or without JBP485 (50 μM) or cilastatin (50 μM). After 0, 1, 2, 4 and 6 h, a 50 μl aliquot of the medium was sampled for determination of IMP by LC-MS/MS.

Renal DHP-I enzyme was obtained from rat renal tissue according to the methodology described in a previous study (Agudelo et al., 2014). Before treatment, DHP-I extract was equilibrated at 37°C for 0.5 h in the culture medium, in the absence or presence of JBP485 (50 μM). The reaction was initiated by the addition of the required concentrations of IMP. The reaction mixture (100 μl) was collected at 0.5, 1, 2 and 3 h to determine the remaining concentration of IMP. Moreover, the concentration-dependent metabolism of IMP (5-200 μM) and the effects of JBP485 (1-100 μM) on IMP (50 μM) metabolism were examined.

Cytotoxicity Assay

The cytotoxicity of IMP on HK-2 cells was evaluated using CCK-8 assays. HK-2 cells were seeded in 96-well plates and cultured overnight. Fresh medium containing 0-5 mM IMP in the absence or presence of 500 μM JBP485 or 500 μM cilastatin was then added, and the cells were incubated for an additional 24 h. A CCK-8 assay (Solarbio, China) was used to determine cell viability.

Cell Apoptosis Analysis

HK-2 cells were seeded in 6-well plates overnight and were cultured for 24 h in the presence of IMP (2 mM) with or without JBP485 (500 μM) or cilastatin (500 μM). HK-2 cells were then stained using an Annexin V-FITC Apoptosis

Detection Kit (Beyotime Institute of Biotechnology, Shanghai, China) and analysed by flow cytometry.

JC-1 Staining

HK-2 cells were seeded in 6-well plates and cultured overnight. Fresh medium containing IMP (2 mM) in the absence or presence of JBP485 (500 μM) or cilastatin (500 μM) was then added, and the cells were incubated for an additional 24 h. Then, the cells were stained with JC-1 (2 μM, Beyotime Institute of Biotechnology, Shanghai, China) and observed by a fluorescence microscope (Leica DM 14000B, Germany).

Molecular Docking Simulation

The molecular docking simulation was conducted to explore the interactions between JBP485 and DHP-I, OAT1 and OAT3. The crystal structure homology models of DHP-I, OAT1 and OAT3 were built by Swiss-model (see "Supporting Information"). The Sybyl/Surflex module (RRID: SCR_000196) was used to simulate molecular docking. The Surflex-Dock program was used to generate the binding conformation of JBP485 to the three proteins using the default parameters. The total score of the binding results represents the affinities. Additionally, PyMOL Molecular Graphics System version 16.1.0.15350 (DeLano Scientific LLC) was used to visualize the docking results.

LC-MS/MS Analysis

The concentrations of analysts in plasma, urine and cell lysate were quantitatively determined using an API 3200 LC-MS/MS system (Applied Biosystems, CA, United States). Chromatographic separation was performed on an Eclipse XDB-C8 column (150 mm × 4.6 mm, 5 μm; Agilent Technology Inc., CA, United States). Acetonitrile and water with 0.1% (v/v) formic acid were used as mobile phase. IMP and its internal standard (bestatin) were detected in positive mode with transitions of m/z 300.1 → 126.1 and m/z 309.1 → 120.3, respectively. PAH and ES were detected in negative mode with transitions of m/z 193.0 →149.0 and m/z 348.9→268, respectively.

Data Analysis

Data are expressed as the mean ± standard deviation (SD). Statistical analysis was performed using SPSS 13.0 software. Student's two-tailed *t*-tests were used when comparing two different groups. One-way ANOVA followed by Dunnett's post hoc tests was used when comparing various groups. In all statistical analyses, $p < 0.05$ were considered statistically significant.

RESULTS

Protective Effect of JBP485 on IMP-Induced Nephrotoxicity in Rabbits

To evaluate the effect of JBP485 on IMP-induced nephrotoxicity in rabbits, IMP was administered to rabbits *via* the ear vein with or without JBP485, and histopathological examinations and renal injury biochemical indicators were used to determine nephrotoxicity. After administration of IMP for 72 h, there was a marked decrease in body weight compared to the control animals. JBP485 alone did not IMP-induced weight loss, although the average body weight was still lower than the control group (**Table 1**). In contrast to body weight, the kidney weight and the kidney weight to body weight ratio were increased in IMP groups compared with the control group. Coadministration with JBP485 reduced the ratio to the normal level. Furthermore, renal morphology was evaluated by gross histological examinations and HE staining. The kidneys exhibited a normal shape and appearance, aside from those in the IMP group, which were significantly swollen and greyish-yellow in appearance (**Figure 1A**). Further, histopathological examinations confirmed the protective effect of JBP485 on IMP-induced nephrotoxicity. In the control group, the kidney slices of rabbits exhibited normal renal tissue morphology after HE staining, while the kidney slices of IMP-treated rabbits exhibited serious renal damage characterized, such as decreased glomerular volume, mesangial cell proliferation, and basement membrane thickening, tubular dilation, renal tubular epithelial cell swelling and necrosis (**Figure 1B**). After coadministration of JBP485, IMP-induced acute structural damage in the rabbit kidneys was significantly reduced (**Figure 1B**). Moreover, IMP increased the levels of plasma CRE (**Figure 1D**) and BUN (**Figure 1C**), and these effects were mitigated by JBP485 treatment. These findings indicate that JBP485 protected against IMP-induced nephrotoxicity.

Protective Effect of JBP485 on IMP-Induced Cytotoxicity in HK-2 Cells

To further clarify the mechanism underlying the protective effect of JBP485 against IMP nephrotoxicity, the cytotoxicity, stability and intracellular accumulation of IMP in HK-2 cells were determined in the presence or absence of JBP485. First, the protein expression levels of OAT1, OAT3 and DHP-I in HK-2 cells were verified by Western blotting. Mouse kidney tissue was used as the positive control. Protein expressions of OAT1, OAT3 and DHP-I were clearly identified in HK-2 cells (**Figure 2A**), indicating that HK-2 cells could be used to evaluate the interactions mediated by these targets. Then, the effect of JBP485 (500 μM) on IMP-induced cytotoxicity was investigated by determining the cell survival rate, apoptosis and mitochondrial membrane potential. IMP exhibited concentration-dependent cytotoxicity in HK-2 cells, with an IC_{50} value of 1.94 ± 0.19 mM; this value was increased to 4.15 ± 0.62 mM in the presence of JBP485 (**Figure 2B**). Meanwhile, cell apoptosis and the mitochondrial membrane potential of HK-2 cells were determined through Annexin V/PI staining and JC-1 staining assays after IMP (2 mM) treatment with or without JBP485 (500 μM). The flow cytometry results indicated that JBP485 attenuated IMP-induced apoptosis in HK-2 cells (**Figure 2C**). Furthermore, IMP induced scattered bright-green fluorescence after JC-1 staining, which was significantly attenuated by co-incubation with JBP485 (**Figure 2D**). In addition, cilastatin treatment

TABLE 1 | Effects of JBP485 on IMP-induced changes in body and kidney weights of rabbits.

Group	Body weight (kg)		Δ Weight (g)	Kidney (g)	Kidney/body (g/kg)
	0 h	72 h			
Control	2.55 ± 0.05	2.59 ± 0.05	40.67 ± 1.76	11.37 ± 0 0.29	4.38 ± 0.03
IMP	2.52 ± 0.13	2.37 ± 0.15	−153.33 ± 21.28*	14.20 ± 0.21*	6.03 ± 0.30*
JBP485	2.65 ± 0.09	2.69 ± 0.09	41.00 ± 1.53#	11.37 ± 0.18#	4.23 ± 0.12#
IMP + JBP485	2.58 ± 0.05	2.61 ± 0.05	22.67 ± 0.88*,#	11.33 ± 0.19#	4.35 ± 0.08#

*Data are expressed as the mean ± SD. *p < 0.05 compared with control; #p < 0.05 compared with IMP group (n = 3).*

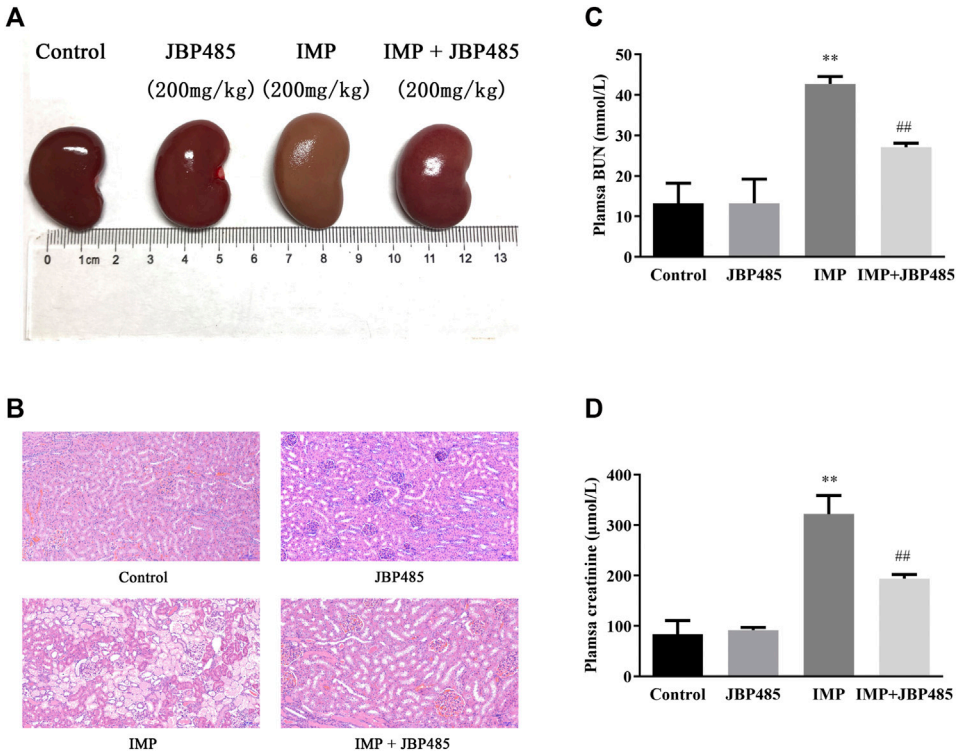

FIGURE 1 | Protective effect of JBP485 on IMP nephrotoxicity in rabbits. Rabbits were injected with IMP (200 mg/kg) through the ear vein in the absence or presence JBP485 (200 mg/kg). The kidneys were collected 72 h after administration of IMP for gross histological observation **(A)** and HE staining **(B)**. Blood samples (0.5 ml) were collected for the determination of BUN **(C)** and CRE **(D)**. Data are expressed as the mean ± SD. $^{**}p < 0.01$ compared with control; $^{\#\#}p < 0.01$ compared with IMP group ($n = 3$).

showed a similar protective effect against IMP-induced cytotoxicity (**Figures 2B–D**). These results suggest that JBP485, as well as cilastatin, protected against IMP-induced cytotoxicity in HK-2 cells. In our previous study (Huo et al., 2019), cilastatin was found to alleviate IMP nephrotoxicity by simultaneously inhibiting renal OATs and DHP-I. Therefore, it was hypothesized that the same mechanism might underlie the effect of JBP485 on IMP nephrotoxicity. Indeed, JBP485 and cilastatin significantly inhibited IMP degradation and improved its stability in the medium of HK-2 cells (**Figure 2E**). Additionally, intracellular accumulation of IMP, as well as OATs substrates PAH and ES, in HK-2 cells was markedly decreased in the presence of JBP485 or cilastatin (**Figure 2F**). These findings clearly indicate that JBP485 protected against IMP cytotoxicity in HK-2 cells by improving IMP stability and reducing its intracellular accumulation. Like cilastatin, JBP485 could be a dual inhibitor of renal OATs and DHP-I, which induces a pharmacokinetic DDI and subsequently impacts IMP nephrotoxicity.

Effect of JBP485 on the Renal Excretion and Plasma Concentration of IMP in Rats

To reveal the potential pharmacokinetic DDIs responsible for the protective effect of JBP485 against IMP-induced nephrotoxicity, IMP plasma concentration and cumulative urinary excretion were investigated when IMP and JBP485 were intravenously co-administered. Concurrent administration of JBP485

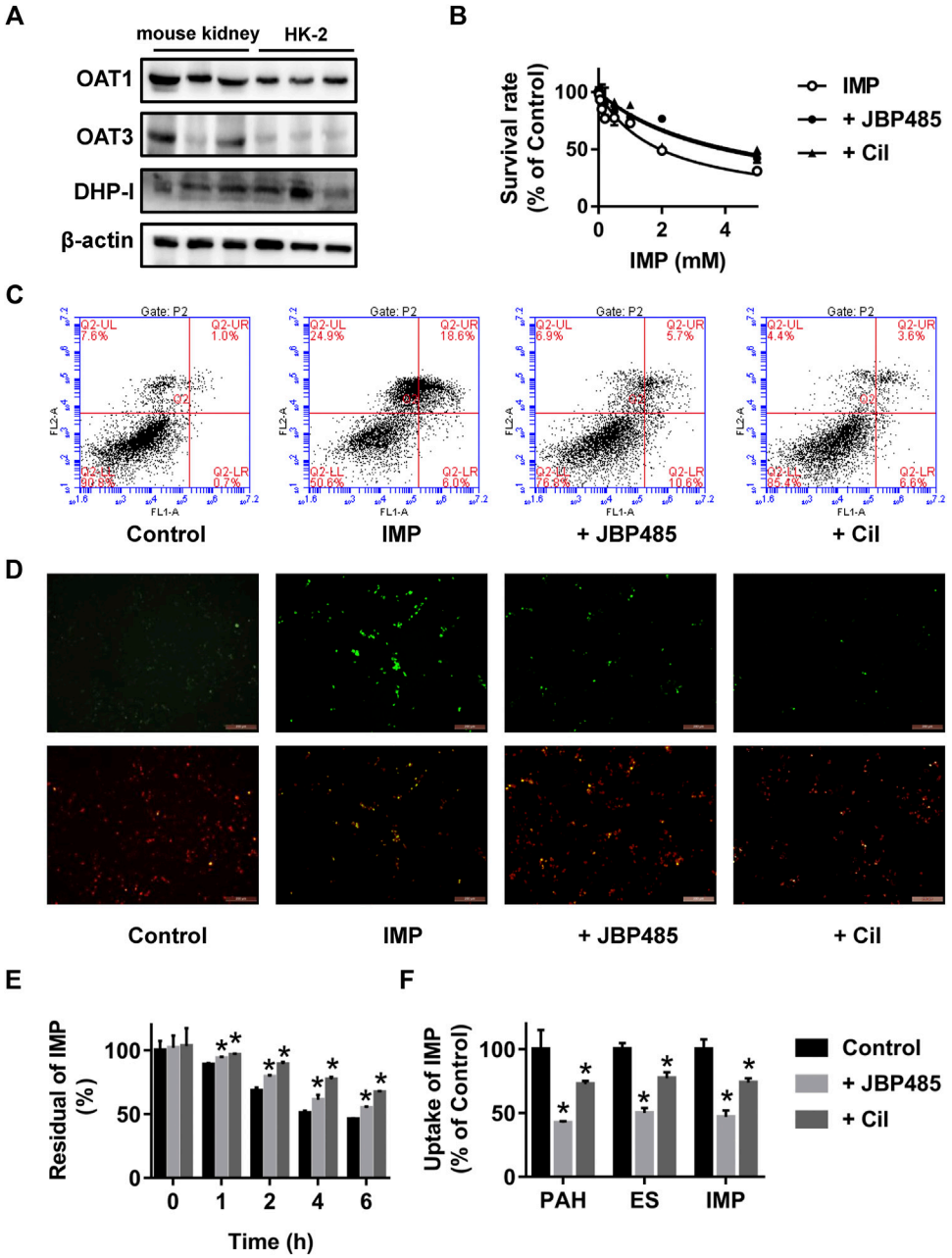

FIGURE 2 | Effect of JBP485 and cilastatin on the cytotoxicity, stability and intracellular accumulation of IMP in HK-2 cells. Protein expression levels of OAT1, OAT3 and DHP-I in HK-2 cells and the mouse kidney by Western blotting **(A)**. HK-2 cells were incubated with IMP (0-5 mM) in the absence or presence of JBP485 (500 μM) or cilastatin (500 μM) for 24 h and cell survival was determined by a CCK-8 assay **(B)**. HK-2 cells were incubated with IMP (2 mM) in the absence or presence of JBP485 (500 μM) or cilastatin (500 μM) for 24 h. Cell apoptosis and the mitochondrial membrane potential were evaluated by Annexin V/PI staining and JC-1 staining assays, respectively **(C,D)**. HK-2 cells were incubated with IMP (50 μM) in the absence or presence of JBP485 (50 μM) or cilastatin (50 μM). The residual concentration of IMP in the medium was determined by LC-MS/MS **(E)**. Intracellular accumulation of IMP in HK-2 cells was determined by LC-MS/MS after incubation with IMP (50 μM) with or without JBP485 (50 μM) or cilastatin (50 μM) for 10 min **(F)**. Data are expressed as the mean ± SD.*$p < 0.05$ compared with control or IMP group ($n = 3$).

significantly increased the plasma concentration of IMP. Furthermore, the area under the plasma concentration-time curve (AUC) and half-life ($t_{1/2\beta}$) of IMP in the coadministration groups were increased (**Table 2**), while the plasma clearance rate (CL_p) of IMP was markedly decreased (**Table 2**; **Figures 3A,B**). JBP485 significantly decreased cumulative urinary excretions over 8 h and the renal clearance rate (CL_R) of IMP compared to the IMP alone group (**Figures 3C,D**). These findings suggest that a pharmacokinetic DDI was induced when IMP and JBP485 were intravenously co-administered and renal excretion of IMP was inhibited by JBP485 in rats.

TABLE 2 | Pharmacokinetic parameters of IMP after intravenous administration of IMP (45 mg/kg) with or without JBP485 (90 mg/kg) in rats.

Parameter	Unit	IMP	IMP + JBP485
C_0	μg/ml	137.7 ± 6.1	279.3 ± 6.3**
$AUC_{0-\infty}$	μg/ml·min	890.8 ± 16.8	2,267.7 ± 309.6*
$t_{1/2\beta}$	h	1.2 ± 0.4	2.3 ± 0.1*
CL_p	ml/min/kg	50.5 ± 1.0	20.1 ± 2.6**
CL_R	ml/min/kg	34.0 ± 0.6	5.0 ± 0.6**

*Data are expressed as the mean ± SD. *p < 0.05 and **p < 0.01 compared with IMP group (n = 3).*

Effect of JBP485 and Cilastatin on IMP Uptake in Kidney Slices and hOAT1-/hOAT3-Transfected HEK293 Cells

To exclude the influence of physiologic conditions, fresh rat kidney slices and hOAT1-/hOAT3-transfected HEK293 cells were used to investigate the target transporters involved in the DDI between IMP and JBP485. First, JBP485 was found to significantly inhibit IMP uptake in a time-dependent manner (**Figure 4A**), suggesting that the DDIs between IMP and JBP485 occurred in the kidney and JBP485 inhibited the renal distribution of IMP. Meanwhile, the effects of JBP485 on the uptake of IMP in hOAT1- and hOAT3-HEK293 cells were verified. The uptake of IMP in hOAT1- and hOAT3-HEK293 cells was inhibited for 10 min following the addition of JBP485 (**Figures 4B,E**). Intracellular levels of IMP in hOAT1- and hOAT3-HEK293 cells were decreased by JBP485 in a concentration-dependent manner, with IC_{50} values of 20.86 ± 1.39 μM (for OAT1) and 46.48 ± 1.27 μM (for OAT3) (**Figures 4D,G**). Moreover, JBP485 inhibited uptake of IMP at varying concentrations in hOAT1- and hOAT3- HEK293 cells (**Figures 4C,F**). Eadie-Hofstee plot analysis showed that JBP485 significantly increased the K_m values of IMP in hOAT1- and hOAT3-HEK293 cells, but did not change V_{max} values (**Table 3**), suggesting competitive inhibition. These results confirm that renal OATs were at least one target of the DDI between JBP485 and IMP.

Effect of JBP485 on IMP Metabolism in Rat Kidney

Previous studies have demonstrated that OATs and DHP-I may be involved in the protective effect of cilastatin on IMP-induced kidney injury and that the metabolites of IMP might have more potent cytotoxicity than IMP (Huo et al., 2019). Current results indicated that JBP485 inhibited IMP renal excretion by OATs. Thus, we further examined whether JBP485 affected the metabolism of IMP. The residual of IMP at different times and concentrations were significantly increased in the presence of JBP485 (**Figures 5A,B**). The IC_{50} value of JBP485 for IMP metabolism by renal DHP-I was calculated to be 12.15 ± 1.22 μM (**Figure 5C**). These findings

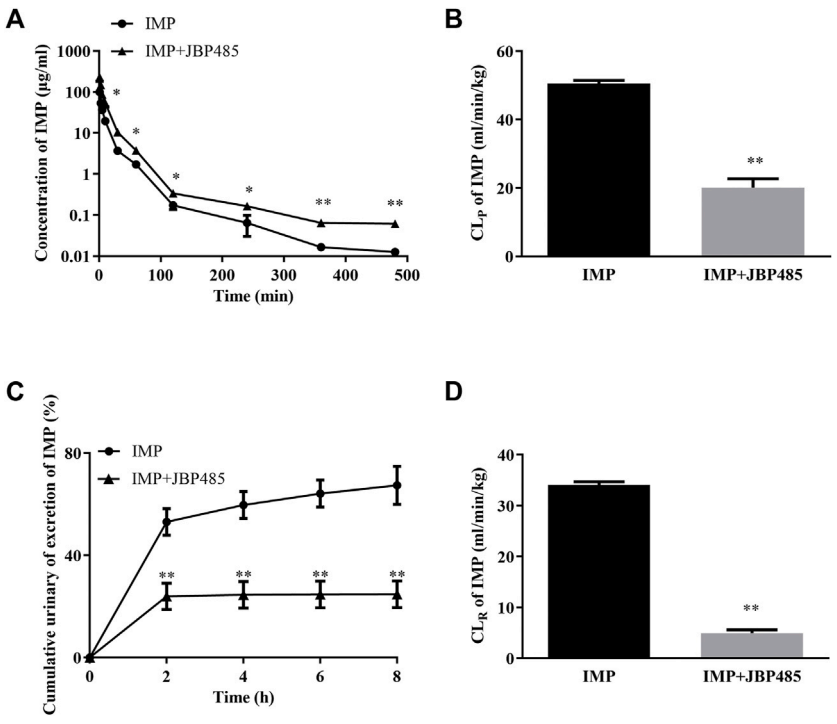

FIGURE 3 | Effect of JBP485 on the pharmacokinetics of IMP in rats. Mean plasma concentration-time curves **(A)**, plasma clearance (CL_P) **(B)**, cumulative urine excretion curves **(C)**, and renal clearances (CL_R) **(D)** of IMP after intravenous administration of IMP and JBP485 in rats. Data are expressed as the mean ± SD. *$p < 0.05$ and **$p < 0.01$ compared with control ($n = 5$).

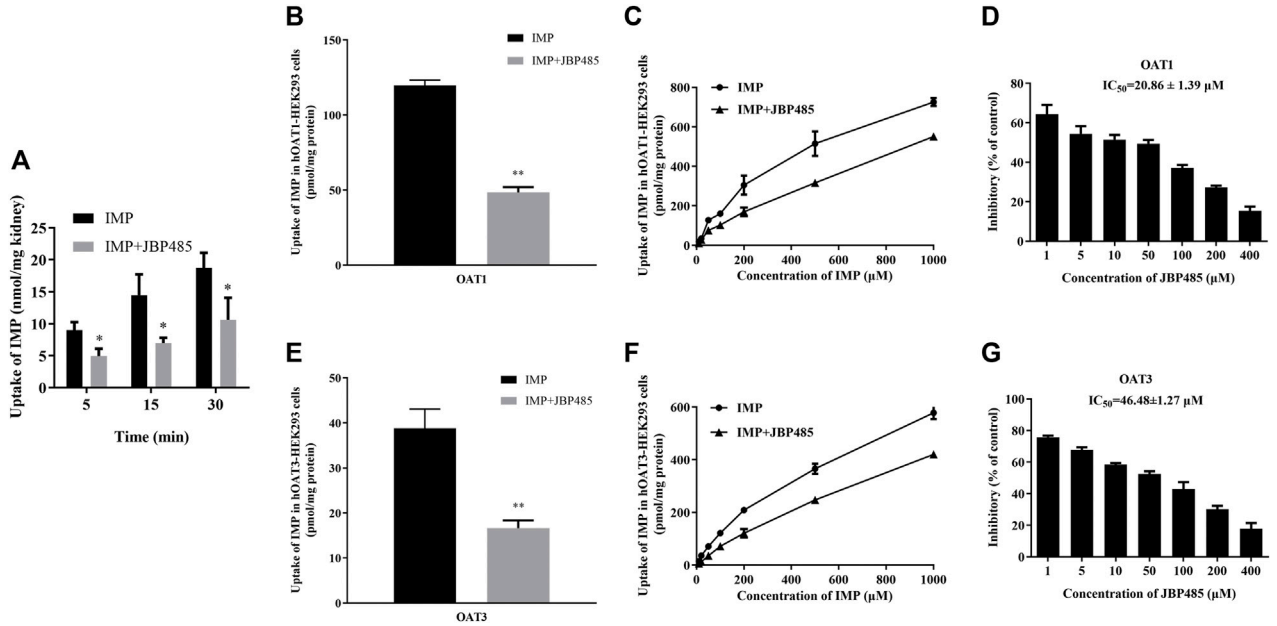

FIGURE 4 | Effect of JBP485 on the uptake of IMP by rat kidney slices and hOAT1/3-HEK293 cells. Inhibition effect of JBP485 (50 μM) on the uptake of IMP (50 μM) in kidney slices **(A)**. Inhibition effect of JBP485 (50 μM) on the uptake of IMP (50 μM) in hOAT1/3-HEK293 cells **(B,E)**. Inhibition effect of JBP485 (50 μM) on the uptake of IMP (10–1,000 μM) in hOAT1/3-HEK293 cells **(C,F)**. Inhibition effect of JBP485 (1–400 μM) on the uptake of IMP (50 μM) in hOAT1/3-HEK293 cells **(D,G)**. Data are expressed as the mean ± SD. $^{*}p < 0.05$ and $^{**}p < 0.01$ compared with control ($n = 3$).

TABLE 3 | K_m and V_{max} values of IMP with or without JBP485 in hOAT1-HEK293 cells and hOAT3-HEK293 cells.

Group	hOAT1-HEK293 cells		hOAT3-HEK293 cells	
	K_m	V_{max}	K_m	V_{max}
IMP	0.564 ± 0.048	0.300 ± 0.027	0.581 ± 0.064	0.450 ± 0.038
IMP + JBP485	0.878 ± 0.024*	0.285 ± 0.021	0.994 ± 0.024*	0.438 ± 0.021

Data are expressed as the mean ± SD. *p *< 0.05 compared with IMP group* (n = *3).*

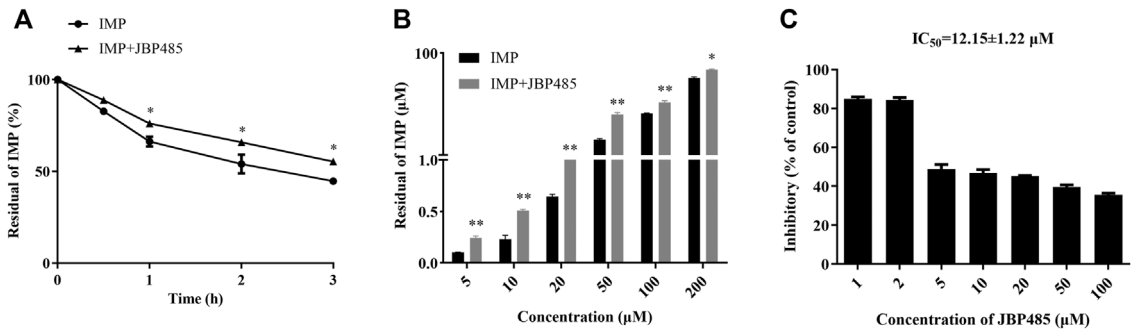

FIGURE 5 | Effects of JBP485 on IMP metabolism in rat kidney. Metabolism of IMP (50 μM) by rat kidney in the presence or absence of JBP485 (50 μM) at 0.5, 1, 2 and 3 h **(A)**. Concentration-dependant metabolism of IMP (5–200 μM) with or without JBP485 (50 μM) **(B)**. Inhibitory effect of JBP485 (1–100 μM) on IMP (50 μM) metabolism in rat kidney **(C)**. Data are expressed as the mean ± SD. $^{*}p < 0.05$ and $^{**}p < 0.01$ compared with control ($n = 3$).

confirm that JBP485 improved the stability of IMP in the rat kidney, which consequently reduced the exposure to toxic metabolites of IMP.

Molecular Docking Simulation

Molecular docking was conducted to explore the molecular interactions between JBP485 and DHP-I, OAT1 and OAT3

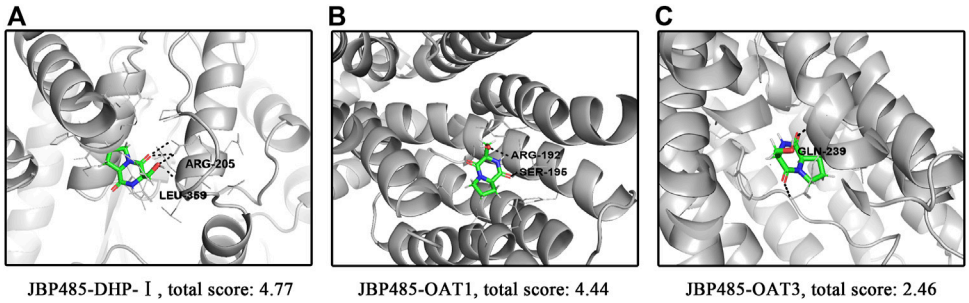

FIGURE 6 | Molecular docking simulation between JBP485 and DHP-I **(A)**, OAT1 **(B)** or OAT3 **(C)**.

(**Figure 6**). The optimal confirmation and total score of JBP485 within these three proteins were compared. As shown in **Figure 6**, JBP485 formed two H-bonds with ARG-205 and LEU-359 of DHP-I, yielding a total score of 4.77, suggesting a good affinity of JBP485 with DHP-1. Further, two H-bonds were formed between JBP485 and OAT1 (ARG-192 and SER-195) with a total score of 4.44. However, only one H-bond was found between JBP485 and OAT3 (with GLN-239), with a total score of 2.46. This suggests that JBP485 exhibited a higher affinity to OAT1 than OAT3.

DISCUSSION

IMP is a carbapenem antibiotic with potent antibacterial activity. However, when IMP is administered alone, it is quickly degraded by DHP-I. DHP-I is a membrane enzyme expressed in the kidneys that hydrolyses a variety of dipeptides. To improve IMP stability, cilastatin, as a potent DHP-I inhibitor, was developed and was found to successfully increase IMP urinary recovery. Our previous studies demonstrated that IMP and cilastatin are substrates of hOAT1 and hOAT3 (Huo et al., 2019; Zhu et al., 2020). Cilastatin was found to inhibit IMP uptake by OATs and reduce renal exposure to IMP, which consequently protected against kidney injury induced by IMP *in vitro* and *in vivo*. Both OATs and DHP-I were found to play vital roles in the renal disposition of IMP and thus, could serve as potential therapeutic targets to prevent IMP nephrotoxicity. JBP485 is a substrate of OATs (Zhang et al., 2010) and exhibits protection against gentamicin or cisplatin-induced renal injury in rats (Liu et al., 2012; Guo et al., 2013). Thus, the present study investigated whether JBP485 could relieve the kidney injury induced by IMP and explored the underlying mechanism.

JBP485 Attenuated IMP Nephrotoxicity *In Vivo* and *In Vitro* Through a Pharmacokinetic DDI

Because rabbits are susceptible to IMP nephrotoxicity (Birnbaum et al., 1985), rabbits were used to evaluate the nephrotoxicity of IMP and the protective effect of JBP485. Nephrotoxicity of IMP was examined after the intravenous administrations of IMP (200 mg/kg) to rabbit (Lim et al., 2008; Huo et al., 2019; Huo et al., 2020; Lyon, 1985). Coadministration of cilastatin (200 mg/kg) prevented the changes induced by Imp in rabbits (Huo et al., 2019). We selected equal dosage of JBP485 (200 mg/kg) to investigate its preventive and therapeutic effect on IMP-induced kidney injury. In JBP485 alone group, BUN, CRE and the shape and appearance of the kidney were similar with control group. This indicated that JBP485 at 200 mg/kg had no toxic effects on rabbit kidneys. Co-administration of IMP with JBP485 significantly improved the renal dysfunction and pathological changes induced by IMP (**Figure 1** and **Table 1**). This suggests that JBP485 protected against IMP-induced renal injury in rabbits. IMP nephrotoxicity has been characterized as mitochondrial damage and renal tubular cell apoptosis (Huo et al., 2019; Cherif et al., 2019). In order to further clarify the protective effect of JBP485 against IMP-induced kidney injury, HK-2 cells were used to avoid the influence of changes in physiological conditions and to predict the effects in humans. HK-2 cells are human-derived proximal tubular epithelial cells and have been commonly used as an *in vitro* model to evaluate drug nephrotoxicity and the potential mechanisms of renal diseases (Qiu et al., 2018; Bejoy et al., 2022). The uremic toxins indoxyl sulphate and p-Cresyl sulphate are taken up into HK-2 cells via OATs and induce cytotoxicity in HK-2 cells, suggesting that OATs are expressed in HK-2 cells and contribute to the cytotoxicity of toxins (Motojima et al., 2003; Miyamoto et al., 2011; Nakano et al., 2021). In the present study, protein expressions of both OAT1/3 and DHP-I were identified in HK-2 cells, which confirms that HK-2 cells are a suitable model for the investigation of DDIs mediated by OAT1/3 and DHP-I. Incubation with JBP485 significantly ameliorated IMP-induced cell apoptosis and mitochondrial dysfunction (**Figures 2B–D**). This confirms the protective effect of JBP485. Meanwhile, JBP485 improved IMP stability and reduced the intracellular accumulation of IMP in HK-2 cells (**Figures 2E,F**). Importantly, these effects of JBP485 were similar to those of cilastatin (**Figures 2B–F**), suggesting that JBP485 is an effective substitute for cilastatin and could serve as a promising agent to reduce the adverse renal effects of IMP in the clinical setting. In our previous studies, IMP metabolites were found to exhibit higher toxicity than the parent drug, and cilastatin ameliorated IMP nephrotoxicity both in rabbits and *in vitro* through inhibition of both OATs and DHP-I (Zhu et al., 2020). In a previous study, we found that the natural product Apigenin protects against IMP nephrotoxicity through OAT inhibition (Mei et al., 2020). Despite its potent inhibitory capacity

against OATs, Apigenin did not improve the stability of IMP (Huo et al., 2020). In the present study, JBP485 attenuated IMP nephrotoxicity, improved its stability, and decreased intracellular exposure, which suggests that JBP485 might serve as a promising dual inhibitor of OATs and DHP-I, and can attenuate IMP nephrotoxicity through a pharmacokinetic DDI.

JBP485 Inhibited Renal OATs and DHP-I

To further investigate the target of the DDI between IMP and JBP485, we focused on OATs which are important transporters in the kidney. Renal transport mediated by OATs facilitates substrate uptake into the kidney, which, conversely leads to higher exposure and then increases the toxic risk (Wang and Sweet, 2013; Nigam, 2015; Huo and Liu, 2018). IMP at 45 mg/kg was used in pharmacokinetic study in rats according to therapeutic doses of IMP commonly used clinically and in previous research (Zhu et al., 2020). The therapeutic dose of IMP or cilastatin commonly used in clinic is 500 mg iv (equal to 7.14 mg/kg), which converting to dose in rats is about 45 mg/kg. The 6.3 fold of human dose equals to the dose of rats, which is a simple method for converting the dosage from human to rats. JBP485 was then administered in a 1:1 and 1:2 ratio with IMP (45 mg/kg). The inhibition of JBP485 (90 mg/kg) on IMP renal elimination was more pronounced than JBP485 (45 mg/kg). In our previous study, JBP485 (100 mg/kg) safely and effectively relived acute renal failure (ARF) induced by cisplatin (Liu et al., 2012). Therefore, we selected the dose of 90 mg/kg to elucidate the effect of JBP485 on renal clearance of IMP in rats. In the present study, urinary secretion of IMP was investigated in rats via bladder intubation, considering the need for rapid sampling to maintain IMP stability. The results revealed that the rats that received the combination of IMP and JBP485 exhibited higher plasma concentrations of IMP, lower cumulative urinary excretion of IMP, and a lower CL_R (**Table 2**; **Figure 3**). These findings indicate that JBP485 inhibited the renal elimination of IMP. Numerous studies have shown that JBP485 can inhibit the renal excretion of OAT substrates, such as bestatin (Zhu et al., 2012), acyclovir (Ye et al., 2012) and entecavir (Xu et al., 2013). Thus, it was hypothesized that OATs might be involved in the DDI between IMP and JBP485. To test this hypothesis, the effects of JBP485 on IMP uptake in kidney slices and hOAT1/3-HEK293 cells were investigated. The uptake of IMP in both kidney slices and transfected cells decreased in the presence of JBP485 (**Figure 4**). Kinetic analysis confirmed that JBP485 significantly increased the K_m values of IMP in hOAT1- and hOAT3-HEK293 cells, but did not change V_{max} values (**Table 3**). This indicates that JBP485, as a substrate of hOAT1 and hOAT3, inhibited the uptake of IMP by hOAT1/3 in a competitive way. Together, these results indicate that hOAT1 and hOAT3 are the target transporters involved in the DDIs between IMP and JBP485 in the kidney.

After IMP enters the kidney, it was rapidly catalysed to inactive and toxic metabolites by DHP-I. This phenomenon not just decreases the activity and effectiveness of IMP, but also can result in kidney injury (Hakeam et al., 2019). In previous research, when cilastatin binds with DHP-I it can interact with apical cholesterol lipid rafts and, therefore, fight off apoptosis and oxidative stress caused by nephrotoxic medications (Shayan and Elyasi, 2020). In addition, cilastatin inhibits DHP-I and successfully prevents the renal damage induced by IMP. Further, cilastatin exerts promising protective effects against a number of other nephrotoxic agents such as vancomycin (Im et al., 2017), diclofenac and cisplatin (Camano et al., 2010; Moreno-Gordaliza et al., 2011; Humanes et al., 2012; Humanes et al., 2017; Moreno-Gordaliza et al., 2018). JBP485 has been confirmed to protect against vancomycin- or cisplatin-induced ARF in rats (Liu et al., 2012; Wen et al., 2018). In the present study, JBP485 was found to inhibit IMP uptake by hOAT1/3, decrease hOAT1/3-dependent cytotoxicity and relieve IMP-induced renal injury. However, to date, there are no studies examining whether JBP485 can inhibit the metabolism of IMP by DHP-I. Thus, a kidney metabolism experiment was performed to investigate the effect of JBP485 on IMP metabolism in the kidneys. The results indicated that JBP485 can inhibit the metabolism of IMP (**Figure 5**). In summary, the protective effect of JBP485 against IMP-induced renal injury was partly due to the inhibition of IMP metabolism by DHP-I.

It has been demonstrated that JBP485 can inhibit OATs transport as well as DHP-I metabolism of IMP. The molecular docking results also confirmed the affinities of JBP485 to DHP-I, OAT1 and OAT3. Previous studies have shown that IMP has minimal affinity for OATs (Suzuki et al., 1989). Thus, we surmised that the transport of OATs was the rate-limiting step in IMP renal elimination. The *in vivo* results demonstrated that when JBP485 was co-administered with IMP, IMP cumulative urinary excretion was significantly reduced. JBP485 had a greater contribution to inhibiting OAT1/3-mediated transport, thus decreasing the renal uptake of IMP. Meanwhile, JBP485 inhibited the metabolism of IMP (part of which is taken up by the kidneys) to toxic metabolites. These two different mechanisms can both attenuate IMP-induced nephrotoxicity.

JBP485 isolated from Laennec can be synthesized by chemical means and is completely free from any pathogens (Nagata et al., 2015). Laennec has been clinically used to treat chronic hepatic injuries for over forty years in Japan (Liu et al., 2000). In systemic administration, JBP485 has already been shown to have no adverse effects in rats and mice (Liu et al., 2000). JBP485 is not toxic for the kidney and in fact protects against renal toxicity as the substrate of OATs. In summary, there were no relevant research about the toxicity and side effects caused by co-administration of JBP485. In present study, JBP485 was well tolerated in rabbits (200 mg/kg) and rats (90 mg/kg). Meanwhile, JBP485 effectively protected the kidney against IMP-induced renal toxicity, suggesting its well established safety and efficacy in animals *in vivo*. On the other hand, the IC_{50} values of JBP485 on DHP-I and OATs were approximate 12 μM and 20-50 μM (**Figure 4** and **Figure 5**). According to FDA guideline, clinical DDI may occur when $[I]/IC_{50}$ is higher than 0.1, suggesting that human plasma concentrations of JBP485 higher than 1-5 μM could induce significant DDI between JBP485 and IMP in human. However, the plasma concentrations of JBP485 in human was not

available. In our previous study, C_{max} of JBP485 in rats after intravenous administration of JBP485 (25 mg/kg) was higher than 650 μM (Zhang et al., 2010), which was high enough to inhibit DHP-I and OATs *in vivo*. Therefore, JBP485 (500 μM) was used to evaluate its protective effect in HK-2 cells. Overall, the dosage or concentration of JBP485 used in present study was safe, effective, and achievable in human. Consequently, the findings have clinical significance.

In conclusion, JBP485 relieved IMP-induced renal injury *in vivo* and *in vitro*. OATs and DHP-I mediated the DDI between IMP and JBP485, which reduced renal exposure to IMP and its toxic metabolites. Thus, JBP485 can serve as a promising agent to reduce the adverse renal effects of IMP in the clinical setting.

DATA AVAILABILITY STATEMENT

The original contributions presented in the study are included in the article/Supplementary Material, further inquiries can be directed to the corresponding authors.

ETHICS STATEMENT

The animal study was reviewed and approved by The ethics committee for animal care of the Health Sector of Dalian Medical University.

AUTHOR CONTRIBUTIONS

XH and KL: conceptualized and conceived the project and edited the manuscript. CW: Performed the experiments, analysed the data and wrote the original manuscript. CW and HJ: Performed part of the experiments. TK and JC: Contributed new reagents or analytic tools. JW, HS, and QM: Involved in data analysis and provided valuable advice. All authors discussed the results and participated in the analysis of the experimental results.

FUNDING

This work was supported by the National Natural Science Foundation of China (81903706).

REFERENCES

Agudelo, M., Rodriguez, C. A., Pelaez, C. A., and Vesga, O. (2014). Even Apparently Insignificant Chemical Deviations Among Bioequivalent Generic Antibiotics Can Lead to Therapeutic Nonequivalence: The Case of Meropenem. *Antimicrob. Agents Chemother.* 58 (2), 1005–1018. doi:10.1128/AAC.00350-13

Bejoy, J., Qian, E. S., and Woodard, L. E. (2022). Tissue Culture Models of AKI: From Tubule Cells to Human Kidney Organoids. *J. Am. Soc. Nephrol.* 33 (3), 487–501. doi:10.1681/ASN.2021050693

Benfield, P., and Chrisp, P. (1992). Imipenem/cilastatin: A Pharmacoeconomic Appraisal of its Use in Intra-abdominal Infections. *Pharmacoeconomics* 1 (6), 443–459. doi:10.2165/00019053-199201060-00005

Birnbaum, J., Kahan, F. M., Kropp, H., and MacDonald, J. S. (1985). Carbapenems, a New Class of Beta-Lactam Antibiotics. Discovery and Development of Imipenem/cilastatin. *Am. J. Med.* 78 (6a), 3–21. doi:10.1016/0002-9343(85)90097-x

Bush, K. T., Singh, P., and Nigam, S. K. (2020). Gut-derived Uremic Toxin Handling *In Vivo* Requires OAT-Mediated Tubular Secretion in Chronic Kidney Disease. *JCI Insight* 5 (7), e133817. doi:10.1172/jci.insight.133817

Camano, S., Lazaro, A., Moreno-Gordaliza, E., Torres, A. M., de Lucas, C., Humanes, B., et al. (2010). Cilastatin Attenuates Cisplatin-Induced Proximal Tubular Cell Damage. *J. Pharmacol. Exp. Ther.* 334 (2), 419–429. doi:10.1124/jpet.110.165779

Cang, J., Zhang, J., Wang, C., Liu, Q., Meng, Q., Wang, D., et al. (2010). Pharmacokinetics and Mechanism of Intestinal Absorption of JBP485 in Rats. *Drug Metab. Pharmacokinet.* 25 (5), 500–507. doi:10.2133/dmpk.dmpk-10-rg-045

Cang, J., Wang, C., Liu, Q., Sun, H., Gao, Y., Kaku, T., et al. (2011). Rapid and Sensitive Determination of JBP485 by High Performance Liquid Chromatography and its Application in Pharmacokinetics in Rat. *J. Liq. Chromatogr. Relat. Technol.* 34 (5), 350–359. doi:10.1080/10826076.2011.551606

Cherif, B., Triki, H., Sahnoun, S., Hamden, K., Sallemi, A., Charfi, S., et al. (2019). Imipenem Toxicity in Male Reproductive Organs as a Result of Inflammatory Microenvironment and Oxidative Stress in Germinal Cells. *Toxicology* 416, 44–53. doi:10.1016/j.tox.2019.02.001

Guo, X., Meng, Q., Liu, Q., Wang, C., Sun, H., Peng, J., et al. (2013). JBP485 Improves Gentamicin-Induced Acute Renal Failure by Regulating the Expression and Function of Oat1 and Oat3 in Rats. *Toxicol. Appl. Pharmacol.* 271 (2), 285–295. doi:10.1016/j.taap.2013.04.029

Hakeam, H. A., AlAnazi, L., Mansour, R., AlFudail, S., and AlMarzouq, F. (2019). Does Nephrotoxicity Develop Less Frequently when Vancomycin is Combined with Imipenem-Cilastatin Than with Meropenem? A Comparative Study. *Infect. Dis. (Lond)* 51 (8), 578–584. doi:10.1080/23744235.2019.1619934

Humanes, B., Lazaro, A., Camano, S., Moreno-Gordaliza, E., Lazaro, J. A., Blanco-Codesido, M., et al. (2012). Cilastatin Protects against Cisplatin-Induced Nephrotoxicity without Compromising its Anticancer Efficiency in Rats. *Kidney Int.* 82 (6), 652–663. doi:10.1038/ki.2012.199

Humanes, B., Camaño, S., Lara, J. M., Sabbisetti, V., González-Nicolás, M. Á., Bonventre, J. V., et al. (2017). Cisplatin-induced Renal Inflammation is Ameliorated by Cilastatin Nephroprotection. *Nephrol. Dial. Transpl.* 32 (10), 1645–1655. doi:10.1093/ndt/gfx005

Huo, X., and Liu, K. (2018). Renal Organic Anion Transporters in Drug-Drug Interactions and Diseases. *Eur. J. Pharm. Sci.* 112, 8–19. doi:10.1016/j.ejps.2017.11.001

Huo, X., Meng, Q., Wang, C., Zhu, Y., Liu, Z., Ma, X., et al. (2019). Cilastatin Protects against Imipenem-Induced Nephrotoxicity via Inhibition of Renal Organic Anion Transporters (OATs). *Acta Pharm. Sin. B* 9 (5), 986–996. doi:10.1016/j.apsb.2019.02.005

Huo, X., Meng, Q., Wang, C., Wu, J., Zhu, Y., Sun, P., et al. (2020). Targeting Renal OATs to Develop Renal Protective Agent from Traditional Chinese Medicines: Protective Effect of Apigenin against Imipenem-Induced Nephrotoxicity. *Phytother. Res.* 34 (11), 2998–3010. doi:10.1002/ptr.6727

Im, D. S., Shin, H. J., Yang, K. J., Jung, S. Y., Song, H. Y., Hwang, H. S., et al. (2017). Cilastatin Attenuates Vancomycin-Induced Nephrotoxicity via P-Glycoprotein. *Toxicol. Lett.* 277, 9–17. doi:10.1016/j.toxlet.2017.05.023

Lim, S. C., Im, Y. B., Bae, C. S., Han, S. I., Kim, S. E., and Han, H. K. (2008). Protective Effect of Morin on the Imipenem-Induced Nephrotoxicity in Rabbits. *Arch. Pharm. Res.* 31 (8), 1060–1065. doi:10.1007/s12272-001-1270-x

Liu, K. X., Kato, Y., Kaku, T. I., Santa, T., Imai, K., Yagi, A., et al. (2000). Hydroxyprolylserine Derivatives JBP923 and JBP485 Exhibit the Antihepatitis Activities after Gastrointestinal Absorption in Rats. *J. Pharmacol. Exp. Ther.* 294 (2), 510–515.

Liu, Z., Wang, C., Liu, Q., Meng, Q., Cang, J., Mei, L., et al. (2011). Uptake, Transport and Regulation of JBP485 by PEPT1 *In Vitro* and *In Vivo*. *Peptides* 32 (4), 747–754. doi:10.1016/j.peptides.2011.01.019

Liu, T., Meng, Q., Wang, C., Liu, Q., Guo, X., Sun, H., et al. (2012). Changes in Expression of Renal Oat1, Oat3 and Mrp2 in Cisplatin-Induced Acute Renal Failure after Treatment of JBP485 in Rats. *Toxicol. Appl. Pharmacol.* 264 (3), 423–430. doi:10.1016/j.taap.2012.08.019

Lyon, J. A. (1985). Imipenem/cilastatin: The First Carbapenem Antibiotic. *Drug Intell. Clin. Pharm.* 19 (12), 895–899.

Mei, D., Chen, B., He, B., Liu, H., Lin, Z., Lin, J., et al. (2020). Erratum: Author Correction to 'Actively Priming Autophagic Cell Death with Novel Transferrin Receptor-Targeted Nanomedicine for Synergistic Chemotherapy against Breast Cancer' [Acta Pharmaceutica Sinica B 2019; 9(5):1061-1077]. *Acta Pharm. Sin. B* 10 (6), 1143–1144. doi:10.1016/j.apsb.2020.03.003

Miyamoto, Y., Watanabe, H., Noguchi, T., Kotani, S., Nakajima, M., Kadowaki, D., et al. (2011). Organic Anion Transporters Play an Important Role in the Uptake of P-Cresyl Sulfate, a Uremic Toxin, in the Kidney. *Nephrol. Dial. Transpl.* 26 (8), 2498–2502. doi:10.1093/ndt/gfq785

Moreno-Gordaliza, E., Giesen, C., Lázaro, A., Esteban-Fernández, D., Humanes, B., Cañas, B., et al. (2011). Elemental Bioimaging in Kidney by LA-ICP-MS as a Tool to Study Nephrotoxicity and Renal Protective Strategies in Cisplatin Therapies. *Anal. Chem.* 83 (20), 7933–7940. doi:10.1021/ac201933x

Moreno-Gordaliza, E., Esteban-Fernández, D., Lázaro, A., Aboulmagd, S., Humanes, B., Tejedor, A., et al. (2018). Lipid Imaging for Visualizing Cilastatin Amelioration of Cisplatin-Induced Nephrotoxicity. *J. Lipid Res.* 59 (9), 1561–1574. doi:10.1194/jlr.M080465

Motojima, M., Hosokawa, A., Yamato, H., Muraki, T., and Yoshioka, T. (2003). Uremic Toxins of Organic Anions Up-Regulate PAI-1 Expression by Induction of NF-kappaB and Free Radical in Proximal Tubular Cells. *Kidney Int.* 63 (5), 1671–1680. doi:10.1046/j.1523-1755.2003.00906.x

Nagata, M., Nakamura, T., Hata, Y., Yamaguchi, S., Kaku, T., and Kinoshita, S. (2015). JBP485 Promotes Corneal Epithelial Wound Healing. *Sci. Rep.* 5, 14776. doi:10.1038/srep14776

Nakano, T., Watanabe, H., Imafuku, T., Tokumaru, K., Fujita, I., Arimura, N., et al. (2021). Indoxyl Sulfate Contributes to mTORC1-Induced Renal Fibrosis via the OAT/NADPH Oxidase/ROS Pathway. *Toxins (Basel)* 13 (12), 909. doi:10.3390/toxins13120909

Nigam, S. K. (2015). What Do Drug Transporters Really Do? *Nat. Rev. Drug Discov.* 14 (1), 29–44. doi:10.1038/nrd4461

Nigam, S. K. (2018). The SLC22 Transporter Family: A Paradigm for the Impact of Drug Transporters on Metabolic Pathways, Signaling, and Disease. *Annu. Rev. Pharmacol. Toxicol.* 58, 663–687. doi:10.1146/annurev-pharmtox-010617-052713

Qiu, X., Zhou, X., Miao, Y., and Li, B. (2018). An *In Vitro* Method for Nephrotoxicity Evaluation Using HK-2 Human Kidney Epithelial Cells Combined with Biomarkers of Nephrotoxicity. *Toxicol. Res. (Camb)* 7 (6), 1205–1213. doi:10.1039/c8tx00095f

Shayan, M., and Elyasi, S. (2020). Cilastatin as a Protective Agent against Drug-Induced Nephrotoxicity: A Literature Review. *Expert Opin. Drug Saf.* 19 (8), 999–1010. doi:10.1080/14740338.2020.1796967

Suzuki, H., Sawada, Y., Sugiyama, Y., Iga, T., Hanano, M., and Spector, R. (1989). Transport of Imipenem, a Novel Carbapenem Antibiotic, in the Rat Central Nervous System. *J. Pharmacol. Exp. Ther.* 250 (3), 979–984.

Wang, L., and Sweet, D. H. (2013). Renal Organic Anion Transporters (SLC22 Family): Expression, Regulation, Roles in Toxicity, and Impact on Injury and Disease. *AAPS J.* 15 (1), 53–69. doi:10.1208/s12248-012-9413-y

Wang, W., Liu, Q., Wang, C., Meng, Q., Kaku, T., and Liu, K. (2011). Effects of JBP485 on the Expression and Function of PEPT1 in Indomethacin-Induced Intestinal Injury in Rats and Damage in Caco-2 Cells. *Peptides* 32 (5), 946–955. doi:10.1016/j.peptides.2011.01.031

Wang, C., Wang, C., Liu, Q., Meng, Q., Cang, J., Sun, H., et al. (2014). Aspirin and Probenecid Inhibit Organic Anion Transporter 3-mediated Renal Uptake of Cilostazol and Probenecid Induces Metabolism of Cilostazol in the Rat. *Drug Metab. Dispos.* 42 (6), 996–1007. doi:10.1124/dmd.113.055194

Wen, S., Wang, C., Huo, X., Meng, Q., Liu, Z., Yang, S., et al. (2018). JBP485 Attenuates Vancomycin-Induced Nephrotoxicity by Regulating the Expressions of Organic Anion Transporter (Oat) 1, Oat3, Organic Cation Transporter 2 (Oct2), Multidrug Resistance-Associated Protein 2 (Mrp2) and P-Glycoprotein (P-Gp) in Rats. *Toxicol. Lett.* 295, 195–204. doi:10.1016/j.toxlet.2018.06.1220

Wu, J., Wang, C., Liu, Q., Yang, T., Zhang, Q., Peng, J., et al. (2008). Protective Effect of JBP485 on Concanavalin A-Induced Hepatocyte Toxicity in Primary Cultured Rat Hepatocytes. *Eur. J. Pharmacol.* 589 (1-3), 299–305. doi:10.1016/j.ejphar.2008.04.066

Xu, Q., Wang, C., Meng, Q., Liu, Q., Sun, H., Peng, J., et al. (2013). OAT1 and OAT3: Targets of Drug-Drug Interaction between Entecavir and JBP485. *Eur. J. Pharm. Sci.* 48 (4-5), 650–657. doi:10.1016/j.ejps.2012.12.024

Yang, T., Wu, J., Wang, C., Liu, Q., Ma, X., Peng, J., et al. (2009). Protective Effect of JBP485 on Concanavalin A-Induced Liver Injury in Mice. *J. Pharm. Pharmacol.* 61 (6), 767–774. doi:10.1211/jpp.61.06.0009

Ye, J., Liu, Q., Wang, C., Meng, Q., Peng, J., Sun, H., et al. (2012). Inhibitory Effect of JBP485 on Renal Excretion of Acyclovir by the Inhibition of OAT1 and OAT3. *Eur. J. Pharm. Sci.* 47 (2), 341–346. doi:10.1016/j.ejps.2012.06.004

Zhang, J., Wang, C., Liu, Q., Meng, Q., Cang, J., Sun, H., et al. (2010). Pharmacokinetic Interaction between JBP485 and Cephalexin in Rats. *Drug Metab. Dispos.* 38 (6), 930–938. doi:10.1124/dmd.110.032060

Zhu, Y., Meng, Q., Wang, C., Liu, Q., Sun, H., Kaku, T., et al. (2012). Organic Anion Transporters Involved in the Excretion of Bestatin in the Kidney. *Peptides* 33 (2), 265–271. doi:10.1016/j.peptides.2012.01.007

Zhu, Y., Huo, X., Wang, C., Meng, Q., Liu, Z., Sun, H., et al. (2020). Organic Anion Transporters also Mediate the Drug-Drug Interaction between Imipenem and Cilastatin. *Asian J. Pharm. Sci.* 15 (2), 252–263. doi:10.1016/j.ajps.2018.11.006

Conflict of Interest: Author TK is employed by Japan Bioproducts Industry Co. Ltd.

The remaining authors declare that the research was conducted in the absence of any commercial or financial relationships that could be construed as a potential conflict of interest.

Publisher's Note: All claims expressed in this article are solely those of the authors and do not necessarily represent those of their affiliated organizations, or those of the publisher, the editors and the reviewers. Any product that may be evaluated in this article, or claim that may be made by its manufacturer, is not guaranteed or endorsed by the publisher.

frontiers | Frontiers in Pharmacology

ORIGINAL RESEARCH
published: 21 June 2022
doi: 10.3389/fphar.2022.934720

Effects of Huangqi Liuyi Decoction in the Treatment of Diabetic Nephropathy and Tissue Distribution Difference of its Six Active Constituents Between Normal and Diabetic Nephropathy Mouse Models

Qun Wang, Ya Shi, Zengguang Wu, Xinli Song, Jinfang Luo, Hong Yang, Xiaolan Chen and Xingde Liu*

Guizhou University of Traditional Chinese Medicine, Huaxi University Town, Guiyang, China

The purpose of this study was to investigate the effects of Huangqi Liuyi decoction extract (HQD) on diabetic nephropathy (DN), and the tissue distribution difference of six main active ingredients of HQD between normal and DN mouse models. DN mice were administered HQD for 12 weeks to investigate its efficacy in the treatment of DN. Liquid chromatography-tandem mass-spectrometry (HPLC-MS/MS) was used to analyze the tissue distribution of the six active ingredients of HQD in normal and DN mice, including astragaloside IV, calycosin-7-O-β-D-glucoside, calycosin glucuronide, ononin, formononetin, and glycyrrhizic acid. DN mice treated with HQD showed significantly decreased fasting blood glucose (FBG), 24-h urinary protein (24 h U-Alb), blood urea nitrogen (BUN), serum creatinine (Scr), and triglyceride levels (TG) ($p < 0.05$). Moreover, there were no significant differences in pharmacodynamics between HQD and Huangqi Liuyi decoction. Treated mice also had decreased expression of collagen I, α–smooth muscle actin (α-SMA), and vimentin; and upregulated expression of E-cadherin in their kidneys. Compared to normal mice, distributions of the six ingredients in the liver, heart, spleen, lungs, kidneys, stomach, small intestine, brain, and muscle of DN mice were different. The results indicated that the HQD could be used for the treatment of DN and to improve renal function. The pathological state of diabetic nephropathy may affect tissue distribution of HQD active ingredients in mice.

Keywords: huangqi liuyi decoction, pharmacodynamics, HPLC- MS/MS, tissue distribution, active ingredients, nephropathy mouse models

OPEN ACCESS

Edited by:
Ling Ye,
Southern Medical University, China

Reviewed by:
Jiangeng Huang,
Huazhong University of Science and Technology, China
Guo Ma,
Fudan University, China

****Correspondence:***
Qun Wang
gywq198856@163.com

Specialty section:
This article was submitted to Drug Metabolism and Transport, a section of the journal Frontiers in Pharmacology

Received: *03 May 2022*
Accepted: *27 May 2022*
Published: *21 June 2022*

Citation:
Wang Q, Shi Y, Wu Z, Song X, Luo J, Yang H, Chen X and Liu X (2022) Effects of Huangqi Liuyi Decoction in the Treatment of Diabetic Nephropathy and Tissue Distribution Difference of its Six Active Constituents Between Normal and Diabetic Nephropathy Mouse Models. Front. Pharmacol. 13:934720. doi: 10.3389/fphar.2022.934720

1 INTRODUCTION

Diabetic nephropathy (DN) is an irreversible condition characterized by a continuous decline in the glomerular filtration rate, proteinuria, microalbuminuria, and increased blood pressure (Xiao et al., 2008; Nowak et al., 2018; Kopel et al., 2019). Most individuals with DN progress to end-stage kidney disease (Noor et al., 2020). Prevention or early treatment of DN lowers

treatment costs and improves the survival rate and quality of life of patients (Correa-Rotter and Gonzalez-Michaca, 2005). Traditional Chinese medicines (TCMs) have been applied in the clinical treatment of various diseases (Peng et al., 2020). TCMs offer unique advantages in the prevention of diabetic complications because of their limited side effects and/or reduced toxicity (Shi et al., 2011; Sun et al., 2016). Huangqi Liuyi decoction has been used in China since the Song dynasty. It is composed of *Radix Astragali* and *Radix Glycyrrhizae*. *Astragali* inhibits the formation of kidney interstitial fibrosis and retards the development of diabetic nephropathy. *Glycyrrhizae* decreases fasting blood-glucose and kidney oxidative stress (Lu and Wei, 2014; Ma et al., 2019). Huangqi Liuyi decoction significantly decreased fasting blood glucose levels and kidney damage in diabetic rats (Xu et al., 2017; Wen et al., 2018). However, precise and reliable dosing with TCMs remains challenging, which negatively impacts the reproducibility of research and clinical results. Identification of the active constituents of a given compound and ensuring consistency in formulation may overcome the problem with TCM variability (Zhang and Wang, 2005). Relative to DN, our team found that the main active constituents of Huangqi Liuyi decoction were astragalus saponin, astragalus flavone, astragalus polysaccharide, and glycyrrhizic acid (data unpublished). Herein, astragalus saponin, astragalus flavone, astragalus polysaccharide, and glycyrrhizic acid were recombined into mixed extract (HQD), and its effect on DN was determined.

In recent years, ample research has shown that the absorption, tissue distribution, and metabolism of drugs can be affected by the disease state. The pharmacokinetic characteristics in pathological conditions are different from those in the normal condition in a manner directly related to the efficacy and adverse reactions of drugs (Shang et al., 2017; Yang and Liu, 2019; Zhang et al., 2020). Thus, it is necessary to compare the tissue-distribution characteristics of drugs under both normal and pathological conditions. In the present study, a liquid chromatography–tandem mass-spectrometry (HPLC-MS/MS) method was established to investigate differences in the distribution of HQD in tissues and organs under normal and pathological conditions. This study provides additional insights into the safe usage of HQD, and TCMs in general, in healthy mice and those with diabetic nephropathy.

2 MATERIALS AND METHODS

2.1 Materials

The reference standards of astragaloside IV (purity >99.0%), calycosin-7-O-β-D-glucoside (purity >98.0%), calycosin glucuronide (purity >98.0%), formononetin (purity >98.0%), ononin (purity >98.0%), and glycyrrhetinic acid (purity >99.0%) were set. Internal standards (IS) were puerarin and digoxin, both with a purity >98.0%, which were obtained from the National Institute for the Control of Pharmaceutical and Biological Products (Beijing, China).

Rosiglitazone (H20052465) was obtained from Shengjitang Pharmaceutical Co., Ltd. (Guizhou, China). Valsartan (H20090319) was obtained from Yijian Pharmaceutical Co., Ltd. (Shangdong, China). Detection kits for 24-h urinary protein (U-Alb) (20180416), serum creatinine (Scr) (20180108), blood urea nitrogen (BUN) (20171215), total cholesterol (TC) (20181005), and triglycerides (TGs) (20171203) were obtained from Nanjing Jiancheng Biological Engineering Research Institute (Nanjing, China). Anti–α–smooth muscle actin (SMA) (BM0002), anti–E cadherin (PB0583), anti–collagen I (BA0325), and anti-vimentin (PB9359) antibodies were obtained from Boster Biological Technology Co., Ltd. (Wuhan, China). A 3,3′-diaminobenzidine immunohistochemistry color-development kit (ZIL-9018) and universal kit (PV-6000) were obtained from Zhongshan Jinqiao Biotechnology Co., Ltd. (Beijing, China).

A mixture of four active constituents (HQD) from Huangqi Liuyi decoction was self-made. In the early stage, the research group determined the preparation process of astragalus saponins, astragalus flavones, astragalus polysaccharides, and glycyrrhizic acid extract. Astragalus saponins and astragalus flavones extract were prepared by macroporus resin column, astragalus polysaccharides extract was prepared by water extraction and alcohol precipitation, and glycyrrhizic acid extract was prepared by acid precipitation. The extract content of each component extracted from three batches of *Astragalus* and *Glycyrrhiza* is shown in **Table 1**.

According to the ratio of Huagqi Liuyi decoction (*Astragalus*: *Glycyrrhiza*, 6:1), we used 18 kg of *Astragalus* and 3 kg of Glycyrrhiza, through processing, to obtain 121.59 g of astragalus saponins (73.92%, including 2.65% of astragaloside IV), 40.72 g of astragalus flavone (68.93%, including 1.71% of

TABLE 1 | The content of each component (x±SD, n = 3).

Extract	Component	Content (%)
Astragalus saponins extract	Astragalus saponins	72.97 ± 1.06
	Astragaloside IV	2.72 ± 0.10
Astragalus flavones extract	Astragalus flavones	70.58 ± 2.16
	Calycosin-7-O-β-D-glucoside	1.67 ± 0.08
	Calycosin-glucuronide	1.45 ± 0.10
	Ononin	0.91 ± 0.09
	Formononetin	0.32 ± 0.02
Astragalus polysaccharides extract		67.12 ± 2.60
Glycyrrhizic acid extract		81.02 ± 1.04

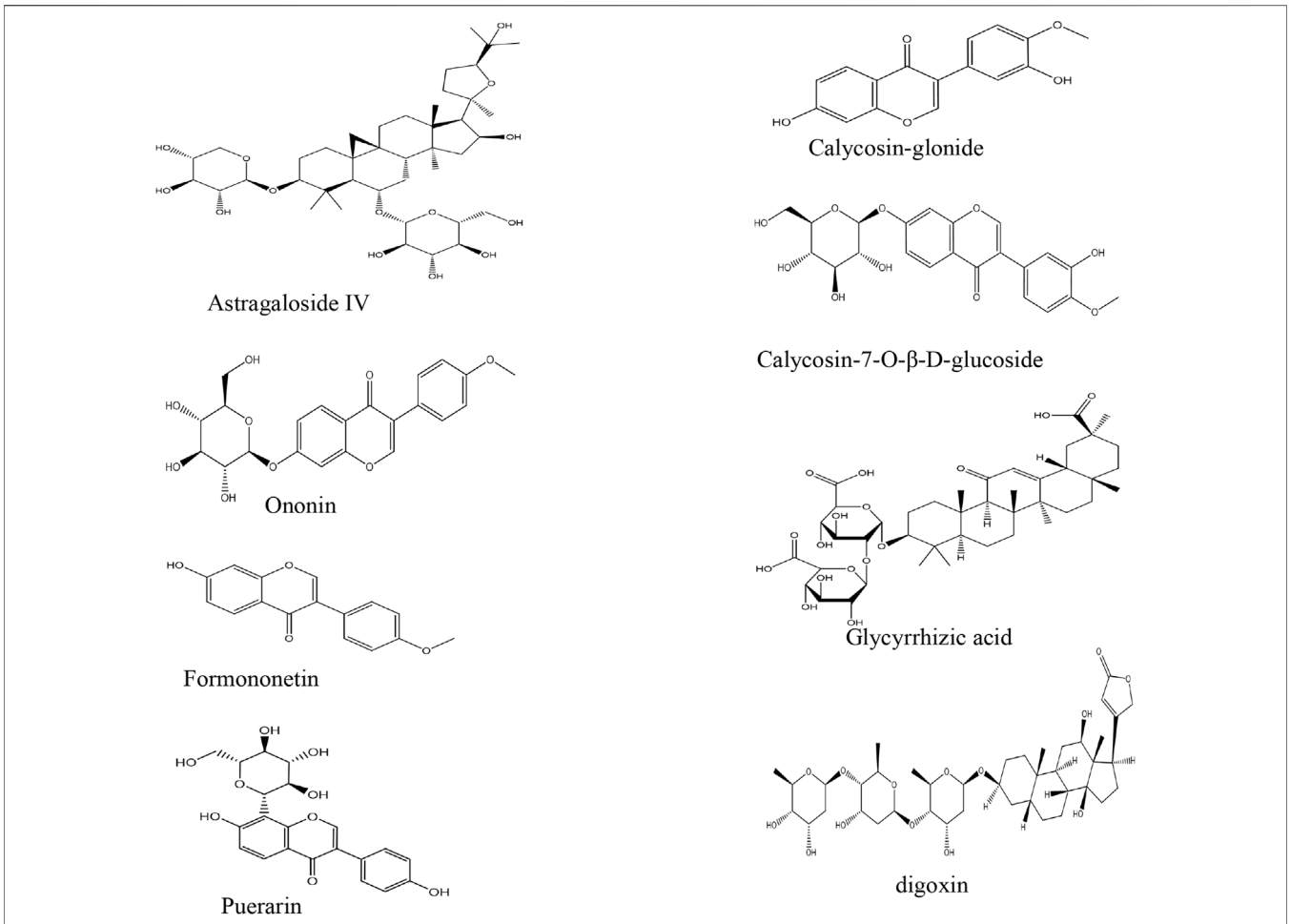

FIGURE 1 | The chemical structure of six analytes.

calycosin-7-O-β-D-glucoside, 1.53% of calycosin-glucuronide, 0.93% of ononin, and 0.31% of formononetin), 262.52 g of astragalus polysaccharides (68.67%), and 31.72 g of glycyrrhetinic acid (81.09%). By mixing astragalus saponins, astragalus flavones, astragalus polysaccharides dry extract, and glycyrrhizin extract together, the HQD samples needed for this experiment were obtained.

2.2 Animals

Db/db mice can develop nephropathy at 12 weeks of age (Gerald, 2013; Ponchiardi et al., 2013). Ten-week-old db/db male mice and db/m mice were obtained from the Model Animal Research Center of Nanjing University [qualified no. SCXK (Su) 2018–0012] and raised for 2 weeks in a specific-pathogen free laboratory (SPF) at the Experimental Animal Center of Guizhou University of Traditional Chinese Medicine. All mice were housed in polypropylene cages and maintained under standard conditions (25 ± 20°C; relative humidity, 60% ± 5%). Animal studies complied with the European Community guidelines (EEC Directive of 1986; 86/609/EEC) and were approved by the Animal Ethical Committee of Guizhou University of Traditional Chinese Medicine (NO1902137).

2.3 Effect of Huangqi Liuyi Decoction on Diabetic Nephropathy

2.3.1 Determination of Biochemical Indexes

Male db/db mice aged 12 weeks were randomly divided into 6 groups of 6 mice each. Twelve-week-old db/m mice served as a control group. The clinical crude drug dosage of Huangqi Liuyi decoction was *Astragalus* 60 g/d and *Glycyrrhiza* 10 g/d, with a total dose of 70 g/d (Xv et al., 2017). *Astragalus* and *Glycyrrhiza* were decocted 3 times, the extract was concentrated and dried, and the dosage of db/db mice was converted according to the above clinical dosage of the drug. The dosage of Huangqi Liuyi decoction was 10.62 g/kg. Mice treated with rosiglitazone (0.61 mg/kg) and valsartan (12.13 mg/kg) served as a positive control group. The doses of HQD in high-, medium-, and low-dose groups were 0.96 g/kg, 0.48 g/kg, and 0.24 g/kg, respectively, which were 4 times, 2 times, and 1 times the clinical dosage. Each group was treated daily for 12 weeks. The control group was given the same volume of distilled water. All mice were fasted for 12 h before the experiment, the FBG level was measured. In addition, 24-h urine was collected, and the 24-h U-Alb level

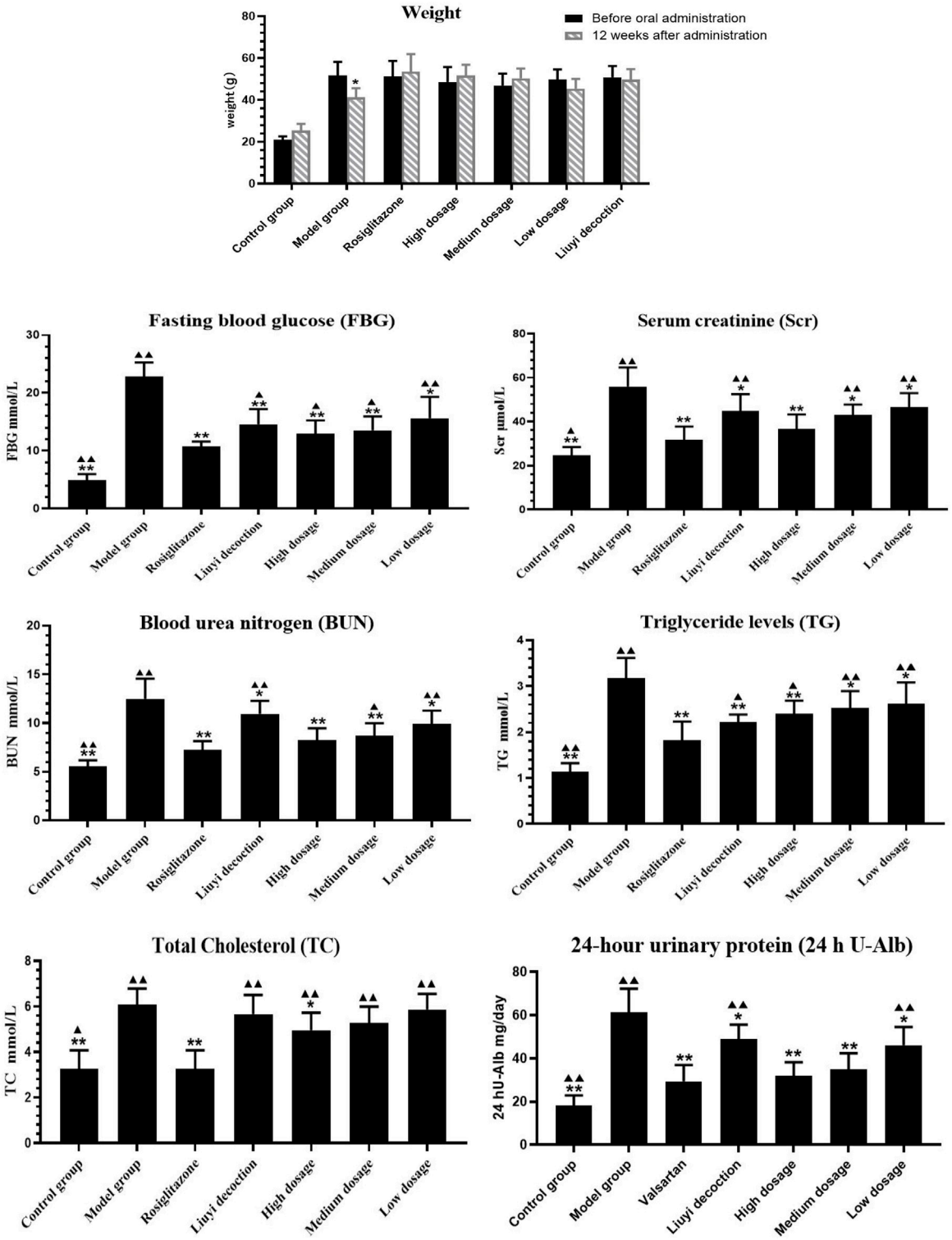

FIGURE 2 | Results of biochemical indexes in each group ($\bar{x}$±SD, $n = 6$). ps: vs. Model group, $^{*}P<0.05$, $^{**}P<0.01$; VS positive control group, $^{▲}P<0.05$, $^{▲▲}P<0.01$.

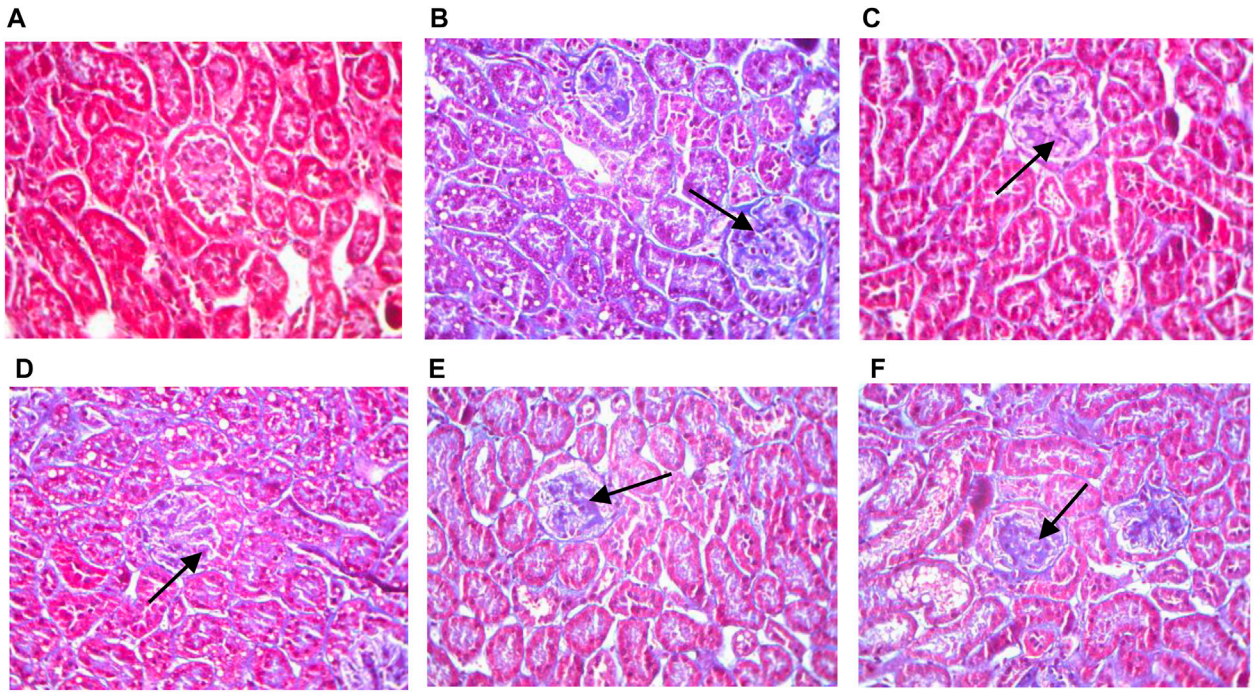

FIGURE 3 | Kidneys pathological sectioning of various groups (Masson ×400). Control group **(A)**; model group **(B)**; high dosage **(C)**; medium dosage **(D)**; low dosage **(E)**; Huangqi Liuyi decoction **(F)**.

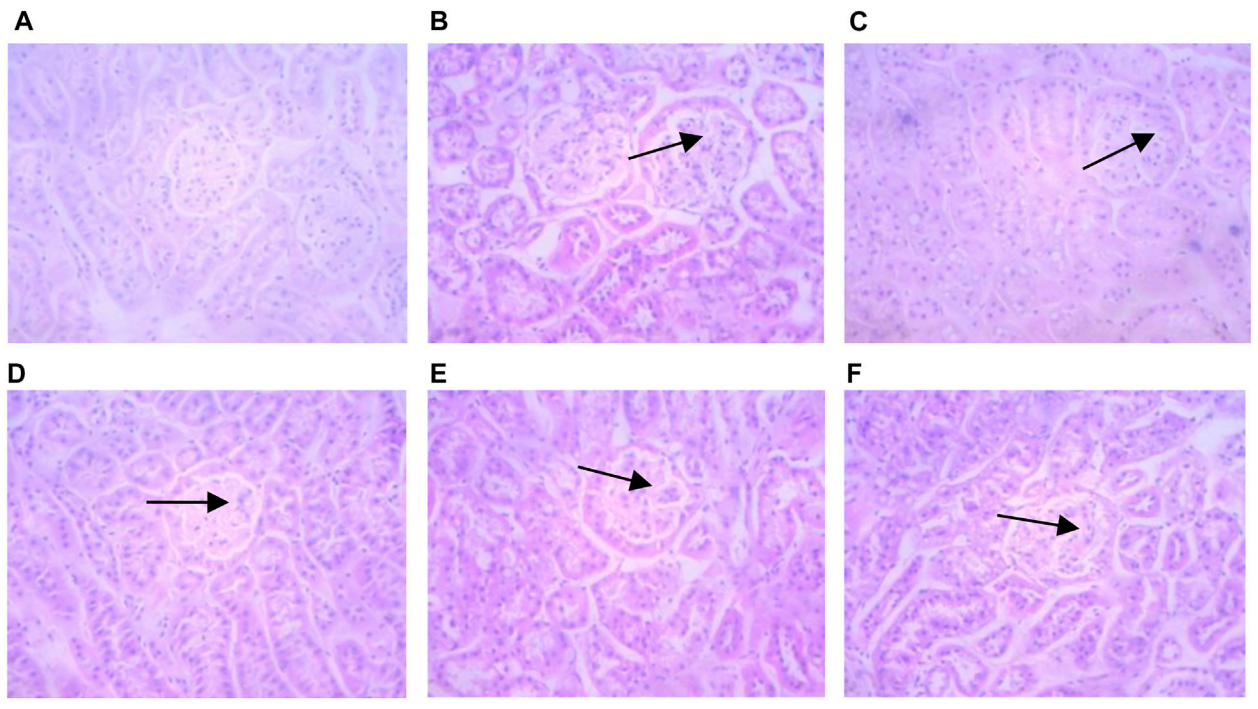

FIGURE 4 | Kidneys pathological sectioning of various groups (HE ×400). Control group **(A)**; model group **(B)**; high dosage **(C)**; medium dosage **(D)**; low dosage **(E)**; Huangqi Liuyi decoction **(F)**.

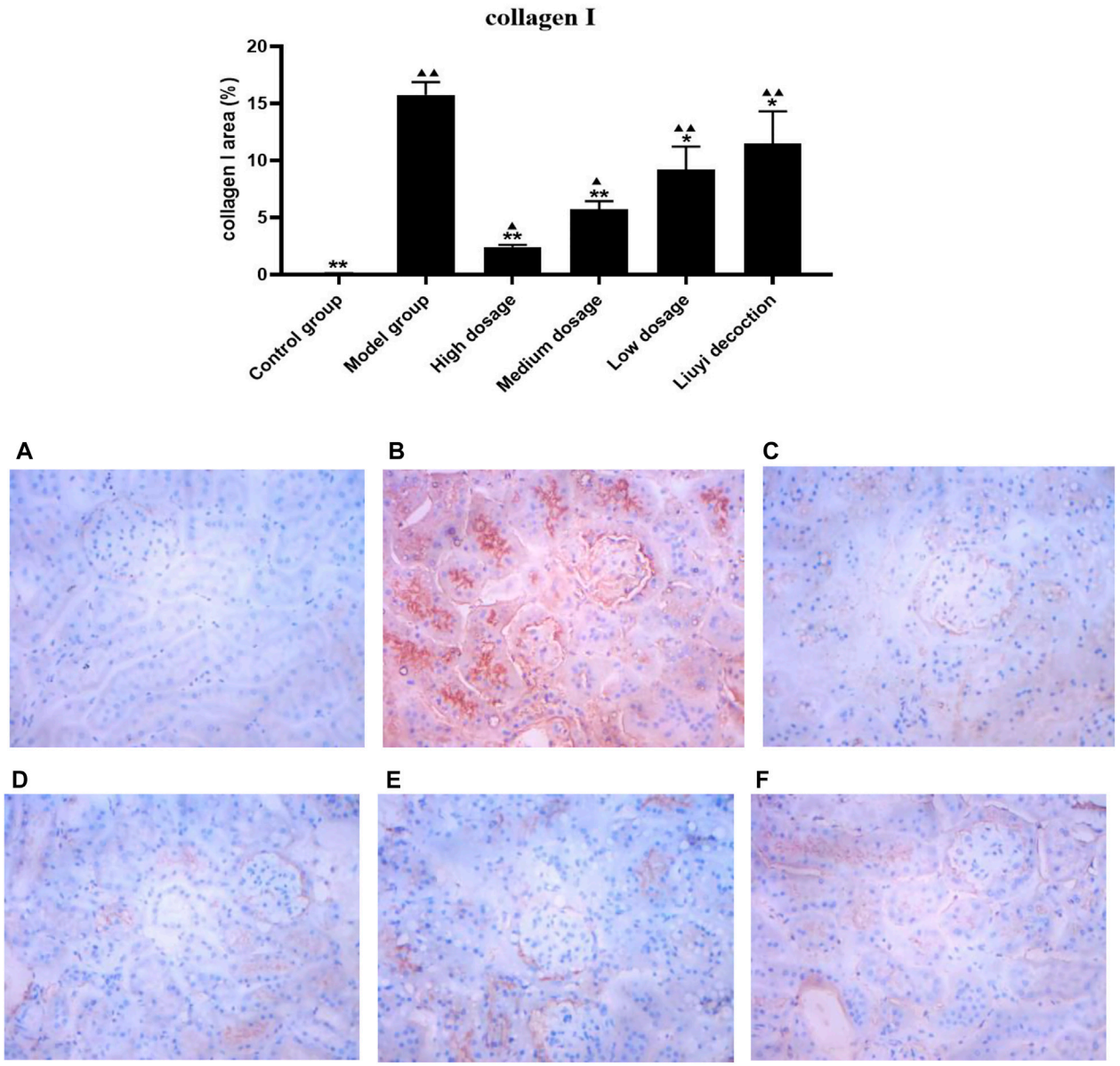

FIGURE 5 | Effect of HQD on the expressions of collagen I in kidney (×400). Control group **(A)**; model group **(B)**; high dosage **(C)**; medium dosage **(D)**; low dosage **(E)**; Huangqi Liuyi decoction **(F)**. ps: vs. Model group, $^{*}P<0.05$, $^{**}P<0.01$; vs. control group, $^{\blacktriangle}P<0.05$, $^{\blacktriangle\blacktriangle}P<0.01$ (x±SD, $n=6$).

was determined using a Coomassie brilliant blue quantitative method (Nie et al., 2019). The BUN, Scr, TG, and TC values were determined using a standard biochemical apparatus (Roche, cobacc501, Switzerland). Subsequently, the mice were humanely euthanized and their kidneys harvested.

2.3.2 Histopathology Analysis of Kidney Tissues

Paraffin-embedded kidney specimens were sectioned into slices with a thickness of 3 μm using a microtome. After deparaffinization and rehydration, the slices were stained with hematoxylin and eosin for the assessment of kidney injury and with Masson's trichrome staining for a collagen-deposition assessment. The slices were observed under a light microscope, and images were captured at a magnification of ×400 using the objective lens of an Olympus microscope (Olympus Corporation, Tokyo, Japan). The light microscopy evaluation was conducted by experienced pathologists in a blinded fashion.

2.3.3 Immunohistochemical Assay

Kidney tissue sections (3-μm thickness) were deparaffinized with xylene and rehydrated in a gradient ethanol finishing in phosphate-buffered saline. Endogenous peroxidases were quenched by a few drops of H_2O_2. A citrate buffer solution

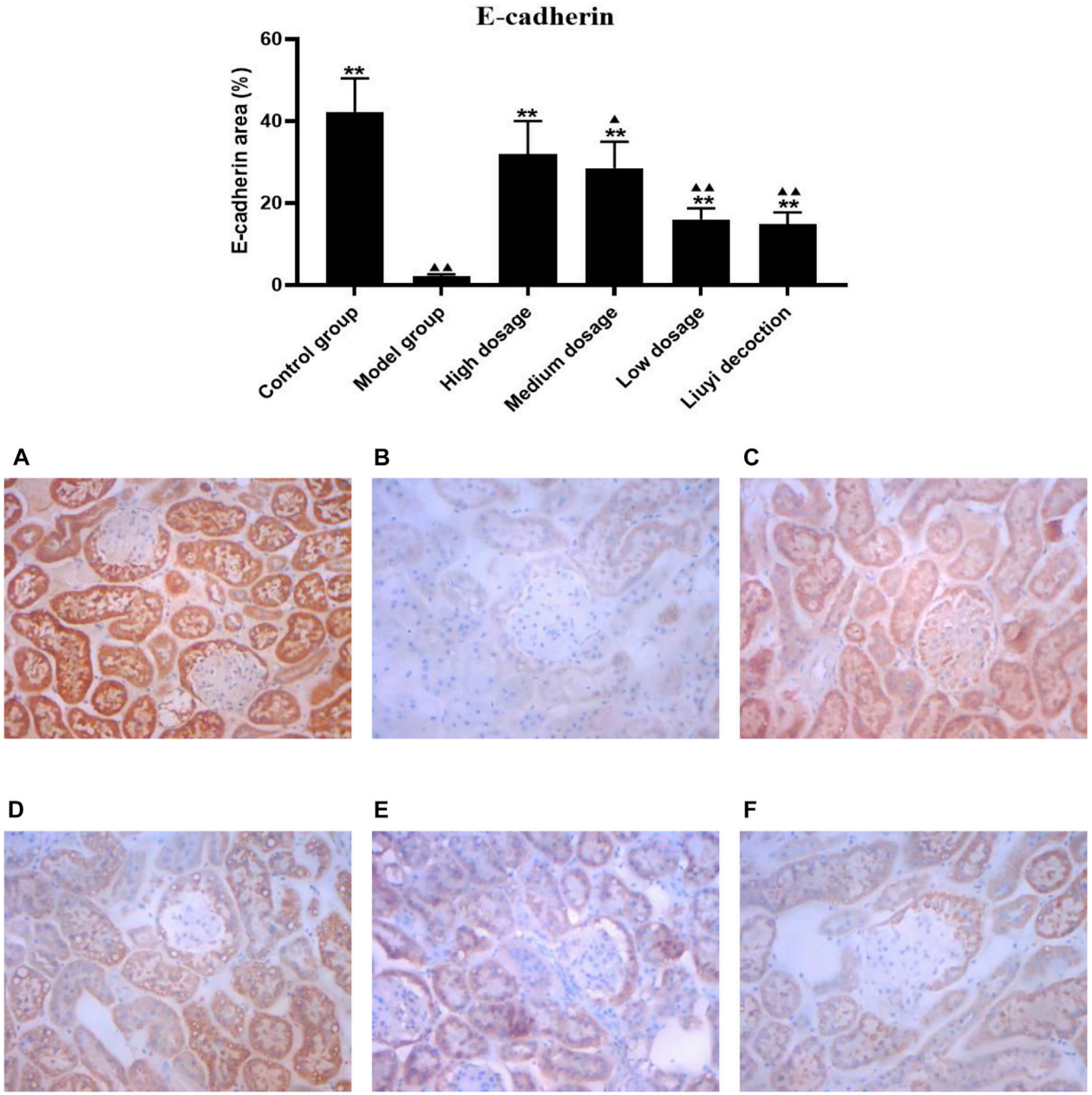

FIGURE 6 | Effect of HQD on the expressions of E-cadherin in kidney (×400). Control group **(A)**; model group **(B)**; high dosage **(C)**; medium dosage **(D)**; low dosage **(E)**; Huangqi Liuyi decoction **(F)**. ps: vs. Model group, $^{*}P<0.05$, $^{**}P<0.01$; vs. control group, $^{▲}P<0.05$, $^{▲▲}P<0.01$ (x±SD, $n=6$).

was used to restore the antigens, and the kidney tissues were then sealed with goat serum. After the sections were incubated with the primary antibody overnight, the secondary antibody was applied. Then, the sections were washed with phosphate-buffered saline, dminobenzidine (DBA) was added for color rendering, and counterstaining was completed with hematoxylin. A positive expression was indicated by a brownish-yellow color. For immunohistochemical staining, the average integrated positive area from 6 randomly chosen regions was calculated by using Image Pro Plus 6.0 image analysis software.

2.3.4 Statistics

All data are presented as mean ± standard deviation values. Statistical analysis between the 2 groups was performed using the Statistical Package for the Social Sciences version 23 software program (IBM Corporation, Armonk, NY, United States). $p \leq 0.01$ and $p \leq 0.05$ between the 2 groups were considered statistically different.

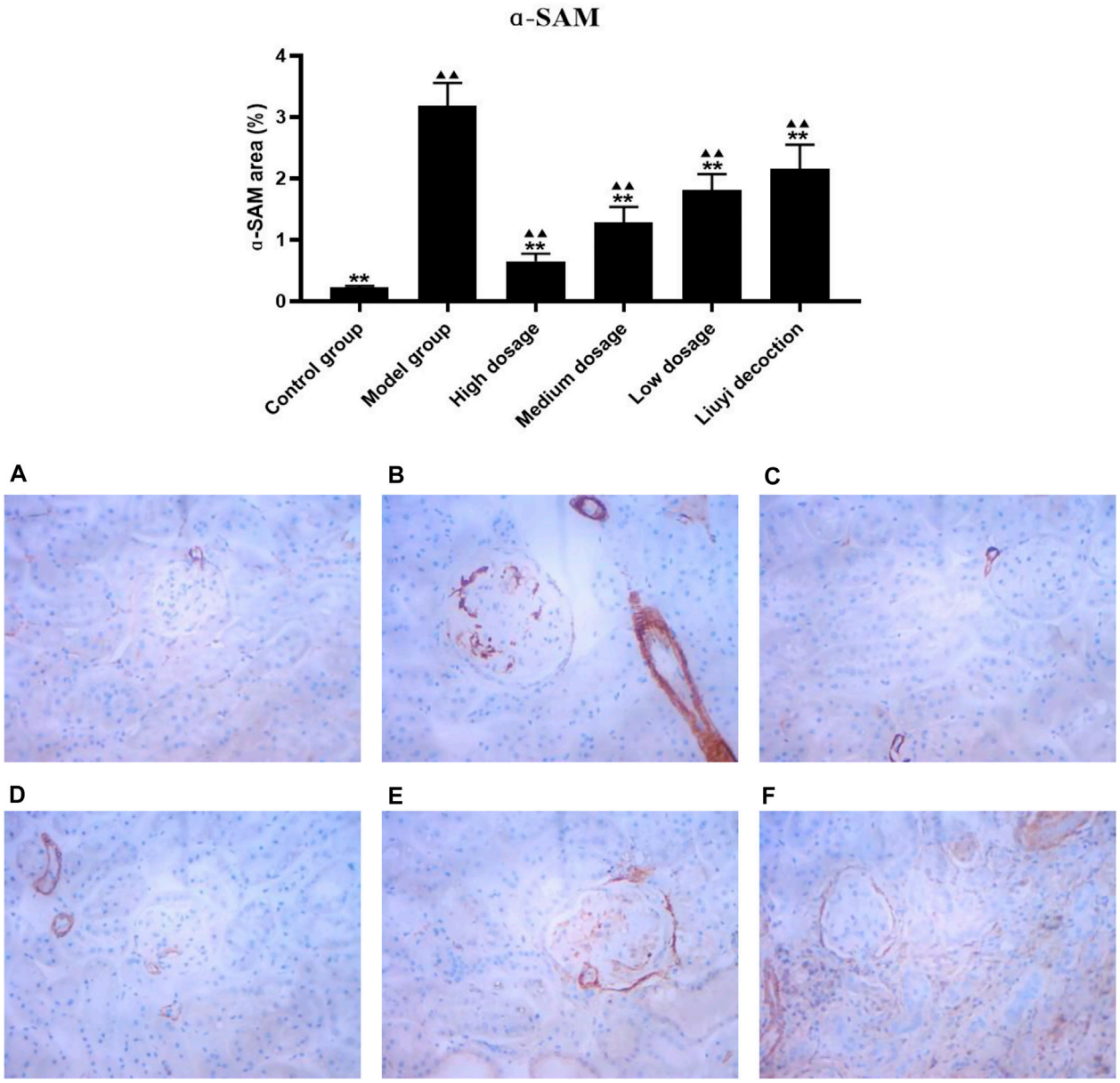

FIGURE 7 | Effect of HQD on the expressions of α-SAM in kidney (×400). Control group **(A)**; model group **(B)**; high dosage **(C)**; medium dosage **(D)**; low dosage **(E)**; Huangqi Liuyi decoction **(F)**. ps: vs. Model group, **P*<0.05, ***P*<0.01; vs. control group, ▲*P*<0.05, ▲▲*P*<0.01 (x±SD, *n*=6).

2.4 Tissue Distribution of Huangqi Liuyi Decoction in Control and Diabetic Nephropathy Mice

2.4.1 Preparation of Standard Samples

Stock solutions were separately prepared by dissolving astragaloside IV (5.34 mg), calycosin-7-O-β-D-glucoside (5.05 mg), calycosin glucuronide (5.19 mg), ononin (5.07 mg), formononetin (5.23 mg), glycyrrhizic acid (5.09 mg), puerarin (IS, 5.08 mg), and digoxin (IS, 5.02 mg) in methanol to yield the following concentrations: astragaloside IV, 0.534 mg/ml; calycosin-7-O-β-D-glucoside, 0.505 mg/ml; calycosin glucuronide, 0.519 mg/ml; ononin, 0.507 mg/ml; formononetin, 0.523 mg/ml; glycyrrhizic acid, 0.509 mg/ml; puerarin, 0.508 mg/ml; and digoxin, 0.502 mg/ml. All solutions were stored at 4°C.

2.4.2 Tissue Sample Preparation

Tissues were accurately weighed and homogenized 4 times with normal saline. Then, 200 μl of tissue homogenate and 20 μl of IS solution (60.9 ng/ml of puerarin and 4.02 μg/ml of digoxin) were added into 400 μl of methanol–acetic acid (40:1, v/v). Samples were vortexed for 2 min and centrifuged at 6,000 r/min for 10 min. The supernatant was transferred and evaporated to dryness with a nitrogen-blowing instrument (Organomation,

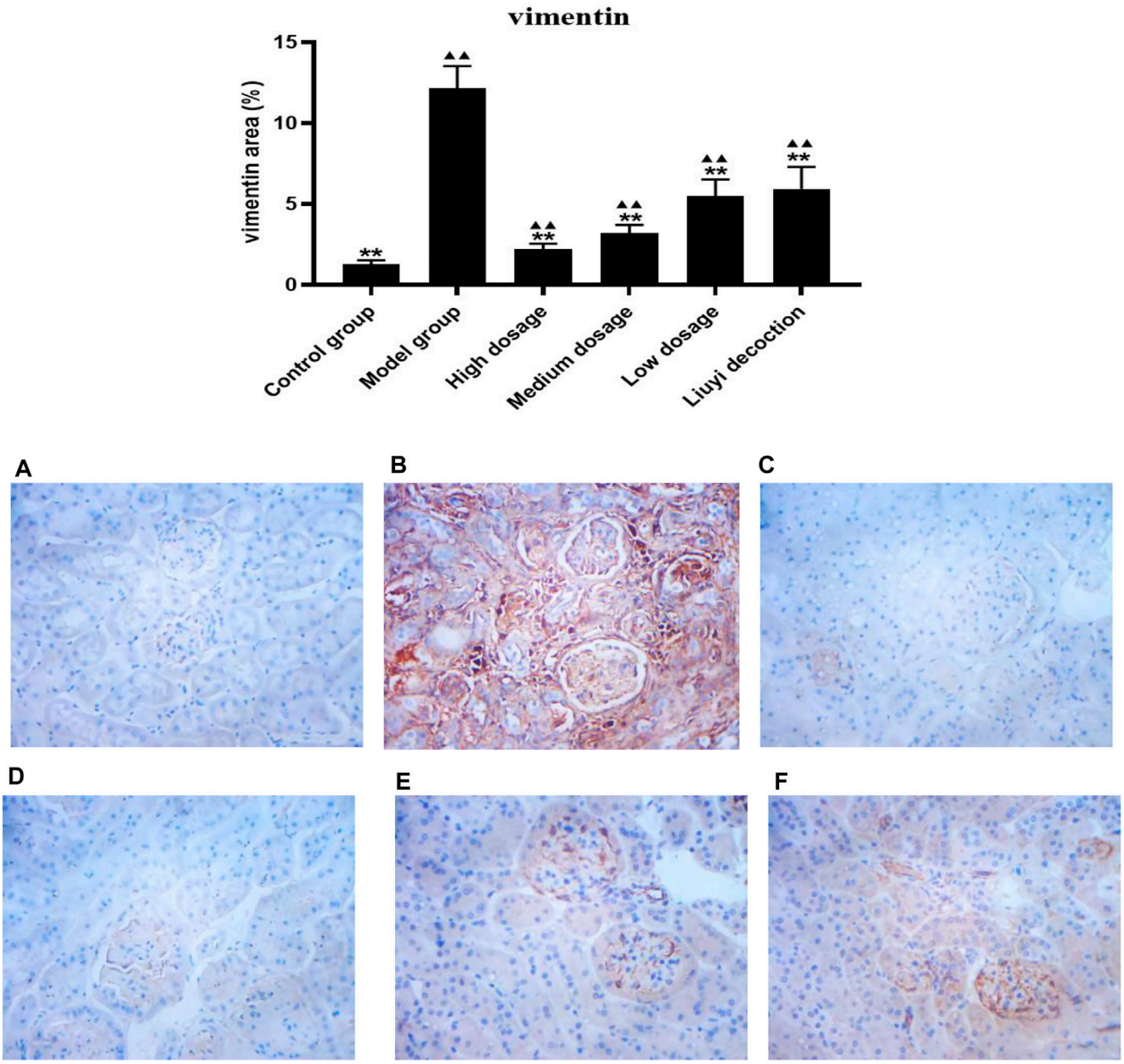

FIGURE 8 | Effect of HQD on the expressions of vimentin in kidney (×400). Control group **(A)**; model group **(B)**; high dosage **(C)**; medium dosage **(D)**; low dosage **(E)**; Huangqi Liuyi decoction **(F)**. ps: vs. Model group, **P*<0.05, ***P*<0.01; vs control group, ▲*P*<0.05, ▲▲*P*<0.01 (x±SD, *n*=6).

Berlin, MA, United States) at 37°C, and the residue was sonicated with 200 μl of 50% methanol and centrifuged for 10 min at 10,000 rpm. One microliter of supernatant was injected into the HPLC-MS/MS system for analysis. Quality control samples were prepared separately in the same way.

2.4.3 Conditions of HPLC-MS/MS

An Acquity HPLC system (Shimadzu Corp., Kyoto, Japan) equipped with a Q-Trap® 5500 triple quadrupole mass spectrometer (AB Sciex, Framingham, MA, United States) was employed for HPLC-MS/MS. The chromatographic conditions of the six constituents of HQD were determined using an Excel2C18-AR system (100 × 2.1 mm, 2 μm; Advanced Chromatography Technologies Ltd., Aberdeen, Scotland) maintained at 30°C. Analysis was completed with a gradient elution of 0.1% formic acid (A) and acetonitrile (B) and a flow rate of 0.4 ml/min. The gradient elution was as follows: 0–0.6 min (90% A), 0.6–2 min (90%→70% A), 2–6 min (70%→35% A), 6–8 min (35%→10% A), 8–9 min (10%→10% A), 9–9.1 min (10%→90% A), and 9.1–12 min (90% A). For MS/MS detection, an electrospray ionization in a multi-reaction monitoring mode was operated with polarity switching between negative and positive ion modes. The mass spectrometer parameters were set as follows: ion spray voltage at 5.5 kV (+) and −4.5 kV (−), source temperature at 600°C, nebulizer pressure at 55 psi, curtain gas at 30 psi, and auxiliary gas

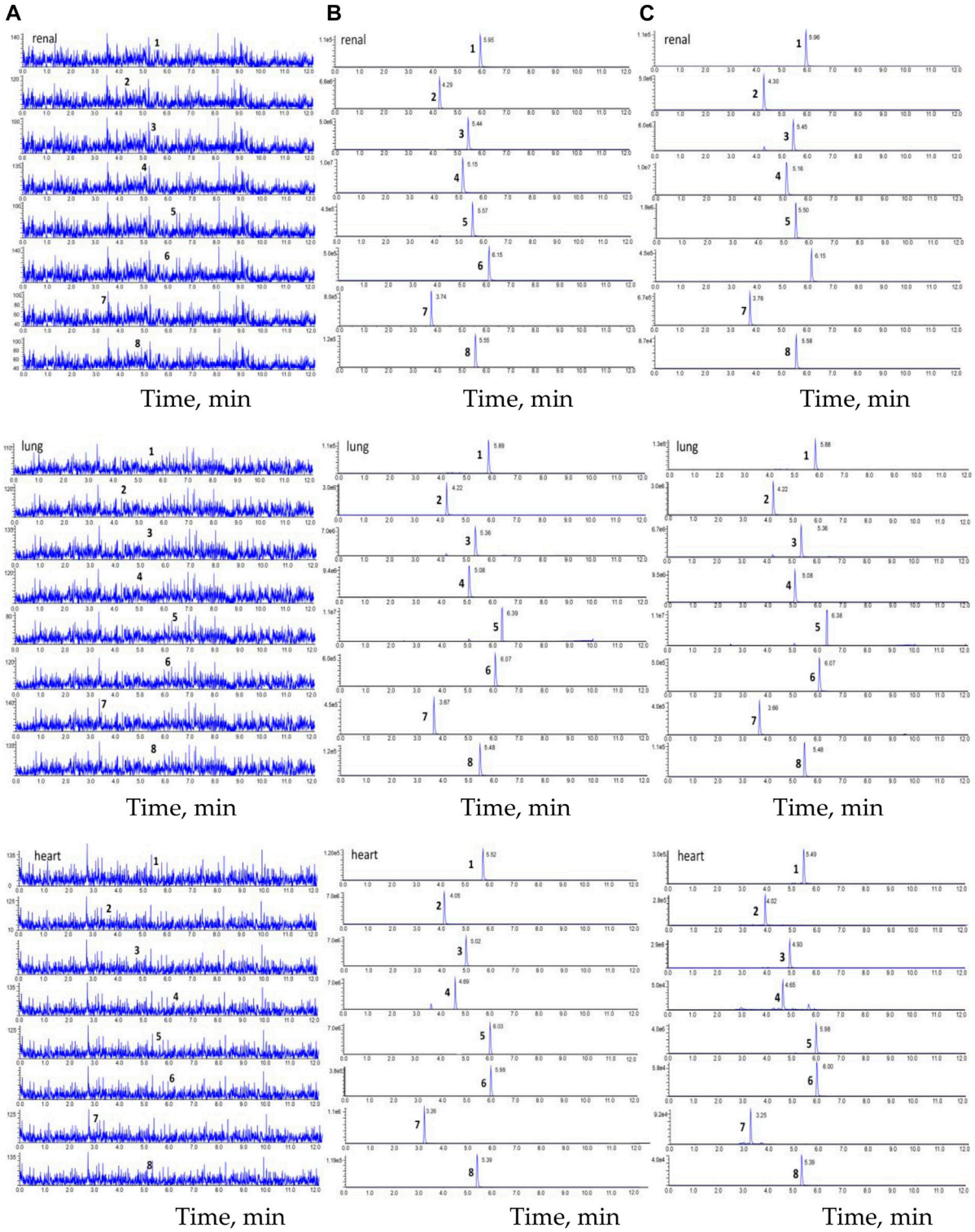

FIGURE 9 | The chromatogram of HPLC-MS/MS. **(A)** blank tissue homogenate sample; **(B)** blank tissue homogenate sample spiked with six compounds and IS; **(C)** The tissue homogenate sample obtained at 30 min after oral HQD. (1. astragaloside IV, 2. calycosin-7-O-β-D-glucoside, 3. calycosin-glucuronide, 4. ononin, 5. formononetin, 6. glycyrrhetinic acid, 7. puerarin, and 8. digoxin).

TABLE 2 | Calibration curve and LOQ of six ingredients in tissue homogenate samples.

Biological sample	Analyte	Calibration curve	r	Linear range	LLOQ ng/g	LOD ng/g
Kidney	Astragaloside IV	y = 0.4594x ± 1.0711	0.9990	5.34–1335	5.34	0.1
	Calycosin-7-O-β-D-glucoside	y = 0.1446x ± 0.1856	0.9992	0.25–50.5	0.25	0.04
	Calycosin-glucuronide	y = 0.1912x ± 0.0975	0.9991	2.60–519	2.60	0.06
	Formononetin	y = 0.0851x ± 0.2989	0.9992	1.05–104.6	1.05	0.02
	Ononin	y = 0.0968x ± 0.1290	0.9991	1.01–101.4	1.01	0.15
	Glycyrrhizic acid	y = 0.0974x ± 0.1794	0.9994	1.02–1018	1.02	0.34
Heart	Astragaloside IV	y = 0.1207x ± 0.2282	0.9991	5.34–1335	5.34	0.1
	Calycosin-7-O-β-D-glucoside	y = 0.0586x ± 0.1121	0.9992	0.25–50.5	0.25	0.04
	Calycosin-glucuronide	y = 0.5242x ± 0.2481	0.9993	2.60–519	2.60	0.06
	Formononetin	y = 0.1101x ± 0.1341	0.9990	1.05–104.6	1.05	0.02
	Ononin	y = 0.0899x ± 0.1431	0.9992	1.01–101.4	1.01	0.15
	Glycyrrhizic acid	y = 0.1445x ± 0.0502	0.9991	1.02–1018	1.02	0.34
	Astragaloside IV	y = 0.6027x ± 0.8407	0.9992	5.34–1335	5.34	0.1
	Calycosin-7-O-β-D-glucoside	y = 0.2430x ± 0.3439	0.9991	0.25–50.5	0.25	0.04
Lung	Calycosin-glucuronide	y = 0.0736x ± 0.0819	0.9991	2.60–519	2.60	0.06
	Formononetin	y = 0.1031x ± 0.3993	0.9990	1.05–104.6	1.05	0.02
	Ononin	y = 0.0855x ± 0.0551	0.9992	1.01–101.4	1.01	0.15
	Glycyrrhizic acid	y = 0.1740x ± 0.1234	0.9993	1.02–1018	1.02	0.34

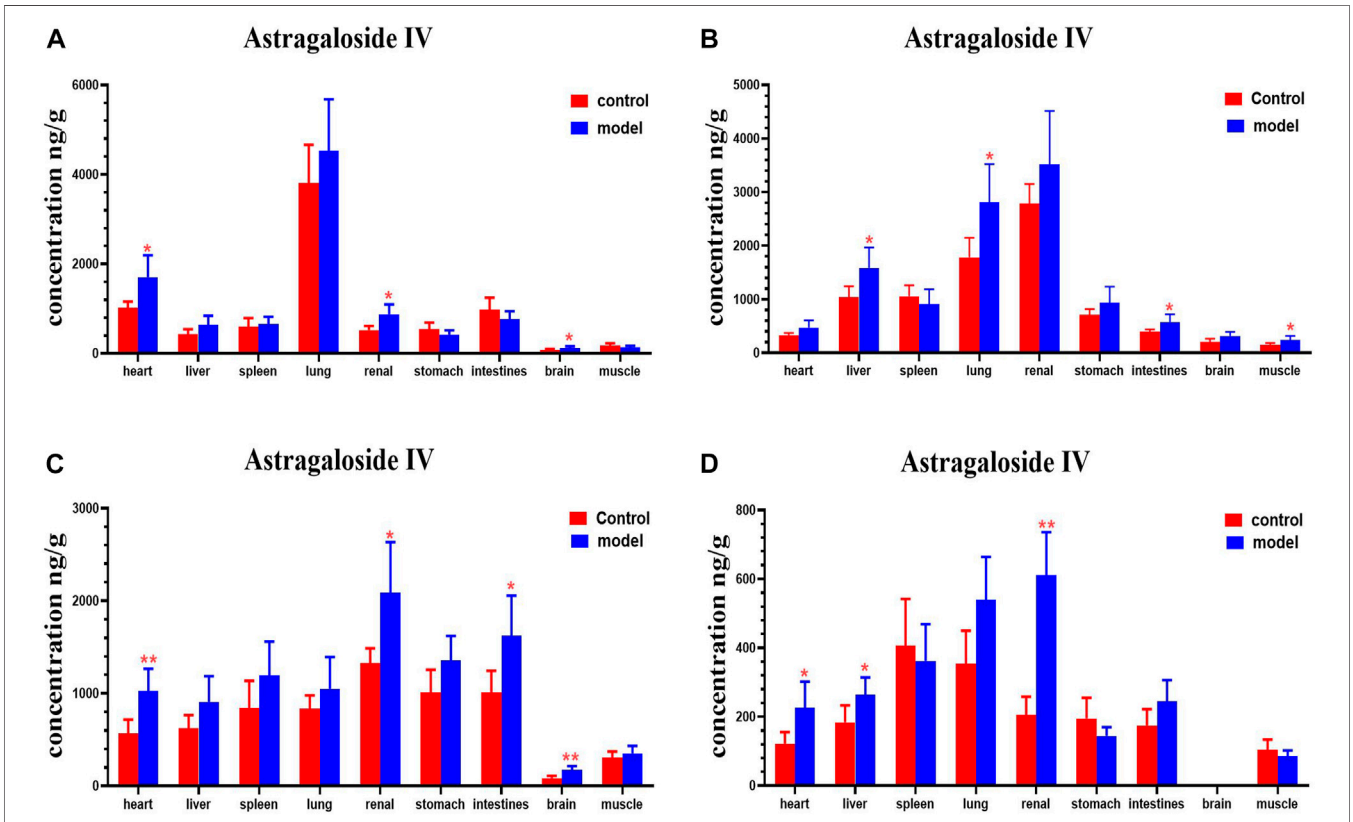

FIGURE 10 | Content of astragaloside IV in different mouse tissue homogenate of the normal and DN models at four different time points after intragastric administration of HQD (x±SD, *n*=8), **(A)** 30 min, **(B)** 2 h, **(C)** 4 h, **(D)** 8 h. Ps: *P < 0.05, **P < 0.01 vs. normal group.

at 55 psi. The multiple reaction monitoring (MRM) analysis was conducted by monitoring the precursor ion to product ion transitions of *m/z* 807.4→627.4 for astragaloside IV, 447.1→285.2 for calycosin-7-O-β-D-glucoside, 285.3→213.2 for calycosin glucuronide, 267.0→252.0 for formononetin, 431.3→269.1 for ononin, 824.4→309.4 for glycyrrhizic acid, 417.1→267.1 for puerarin, and 825.3→649.5 for digoxin. **Figure 1** shows the chemical structure of six analytes.

TABLE 3 | Precision and accuracy of ingredients in tissue homogenate samples ($\bar{x}$ ± SD; n = 6).

Analyte	Biological sample	Concentration of analyte (ng/g)	Mean ± SD (ng/g)	Accuracy (%)	Interday precision RSD (%)	Intraday precision RSD (%)
Astragaloside IV	Heart	26.7	29.01 ± 3.22	108.6 ± 3.83	11.11	6.82
		133.5	142.1 ± 12.68	106.5 ± 9.41	8.92	10.75
		267	264.7 ± 41.44	99.12 ± 15.62	15.66	17.63
	Lung	26.7	25.09 ± 3.27	106.8 ± 13.04	13.04	11.81
		133.5	122.9 ± 14.03	105.2 ± 11.56	11.41	10.50
		267	259.1 ± 19.35	97.10 ± 3.80	7.47	5.77
	Kidney	26.7	27.8 ± 4.45	96.44 ± 16.28	16.00	15.38
		133.5	136.6 ± 6.32	107.7 ± 11.21	4.63	11.97
		267	276.8 ± 22.67	95.61 ± 10.75	8.19	6.90
Calycosin-7-O-β-D-glucoside	Heart	2.53	2.53 ± 0.41	100.05 ± 9.76	16.15	7.53
		12.63	10.92 ± 1.29	86.44 ± 5.42	11.81	12.36
		25.25	24.45 ± 3.97	96.83 ± 15.82	16.23	14.14
	Lung	2.53	2.56 ± 0.18	104.3 ± 8.18	7.04	10.53
		12.63	13.54 ± 1.25	96.60 ± 16.84	9.20	9.66
		25.25	22.93 ± 2.25	97.59 ± 7.69	9.79	7.89
	Kidney	2.53	2.48 ± 0.21	98.50 ± 6.85	8.53	6.95
		12.63	13.82 ± 0.51	106.3 ± 13.87	3.67	14.93
		25.25	22.94 ± 0.32	97.23 ± 5.23	1.38	5.11
Calycosin-glucuronide	Heart	5.19	5.88 ± 0.65	113.3 ± 4.60	11.07	11.87
		51.9	46.24 ± 8.70	87.16 ± 4.78	18.79	11.26
		259.5	262.9 ± 49.63	101.2 ± 9.84	18.87	9.73
	Lung	5.19	4.77 ± 0.65	102.6 ± 7.80	13.60	11.30
		51.9	58.32 ± 4.32	101.7 ± 8.60	7.40	17.58
		259.5	272.1 ± 10.36	99.67 ± 16.15	3.81	16.20
	Kidney	5.19	5.03 ± 0.69	101.3 ± 10.01	13.81	16.78
		51.9	47.84 ± 7.72	104.8 ± 6.42	16.14	5.72
		259.5	259.1 ± 22.77	108.8 ± 10.65	8.79	11.05
Ononin	Heart	5.07	5.79 ± 0.59	114.24 ± 4.48	10.18	11.71
		25.35	27.19 ± 5.07	109.1 ± 7.24	18.62	12.18
		50.7	46.59 ± 6.07	91.90 ± 7.03	13.03	9.70
	Lung	5.07	5.29 ± 0.27	89.60 ± 6.50	5.02	3.91
		25.35	21.27 ± 0.95	116.3 ± 1.28	4.45	1.19
		50.7	45.35 ± 3.69	98.95 ± 7.56	8.13	6.84
	Kidney	5.07	4.35 ± 0.15	88.58 ± 4.94	3.48	7.70
		25.35	22.59 ± 2.5	108.6 ± 5.53	11.09	6.41
		50.7	48.85 ± 1.88	109.2 ± 3.61	3.85	1.60
Formononetin	Heart	5.23	4.84 ± 0.29	92.54 ± 4.85	6.10	9.74
		26.15	24.95 ± 3.45	95.40 ± 13.35	13.83	18.29
		52.3	56.17 ± 8.9	107.4 ± 11.02	15.84	12.63
	Lung	5.23	4.61 ± 0.21	101.9 ± 9.37	4.56	16.32
		26.15	23.38 ± 1.79	105.1 ± 6.40	7.66	15.76
		52.3	54.25 ± 6.31	110.1 ± 4.96	11.64	7.40
	Kidney	5.23	4.52 ± 0.57	112.4 ± 5.94	12.56	11.49
		26.15	22.37 ± 2.99	105.3 ± 11.75	13.36	5.24
		52.3	47.26 ± 5.98	113.7 ± 4.49	12.65	6.48
Glycyrrhizic acid	Heart	50.9	48.39 ± 4.82	95.06 ± 4.49	9.97	9.41
		254.5	285.3 ± 33.65	112.1 ± 5.22	11.79	6.44
		509	525.1 ± 55.03	103.1 ± 10.81	10.48	18.69
	Lung	50.9	55.39 ± 3.4	102.3 ± 8.13	6.13	2.15
		254.5	246.4 ± 22.15	109.3 ± 9.61	8.99	4.49
		509	526.9 ± 86.3	99.56 ± 11.70	16.38	16.25
	Kidney	50.9	53.85 ± 2.94	99.35 ± 7.67	5.46	6.08
		254.5	256.1 ± 10.78	107.4 ± 11.69	4.21	5.76
		509	540.9 ± 38.62	106.2 ± 7.29	7.14	15.89

2.4.4 Method Validation

2.4.4.1 Specificity

The specificity of the method was evaluated by analyzing homogenates of drug-free tissue, homogenates of drug-free tissue containing standard solutions and IS, and homogenates obtained following oral administration of HQD to check whether the determination was interfered with by endogenous substances.

2.4.4.2 Calibration Curves and Linearity

The linearity of the calibration curve was constructed using eight calibration points for tissue homogenate. Briefly, peak

TABLE 4 | The mean recoveries of ingredients in tissue homogenate samples (x ± SD; *n* = 6).

Analyte	Concentration of analyte (ng/ml)	Biological sample	Extraction recovery (%)	RSD%	Matrix effect (%)	RSD%
Astragaloside IV	133.5	Heart	99.59 ± 16.18	16.25	86.82 ± 5.15	5.14
		Lung	112.4 ± 9.66	8.60	97.50 ± 8.32	8.53
		Kidney	84.96 ± 3.76	4.43	106.9 ± 6.48	6.06
Calycosin-7-O-β-D-glucoside	12.63	Heart	95.27 ± 13.23	13.89	108.86 ± 10.8	12.68
		Lung	95.24 ± 7.04	7.39	116.9 ± 2.06	1.76
		Kidney	92.44 ± 5.99	6.48	115.2 ± 2.39	2.08
Calycosin-glucuronide	51.9	Heart	107.3 ± 9.56	8.90	99.45 ± 16.55	16.63
		Lung	89.07 ± 8.11	9.12	108.4 ± 9.14	8.43
		Kidney	90.30 ± 7.14	7.89	99.57 ± 6.12	6.15
Formononetin	26.15	Heart	114.3 ± 3.91	3.42	113.6 ± 5.31	4.67
		Lung	108.0 ± 8.63	7.98	107.0 ± 4.82	4.51
		Kidney	115.7 ± 4.64	4.02	98.60 ± 15.31	15.53
Ononin	25.35	Heart	112.7 ± 5.33	4.73	83.12 ± 2.86	3.44
		Lung	97.71 ± 2.49	2.55	93.04 ± 12.25	13.16
		Kidney	98.44 ± 2.39	2.43	86.87 ± 3.29	3.78
Glycyrrhizic acid	254.5	Heart	83.60 ± 2.25	2.69	102.7 ± 15.92	15.51
		Lung	89.35 ± 2.08	2.33	102.8 ± 5.88	5.73
		Kidney	96.60 ± 3.64	3.77	97.65 ± 4.60	4.71

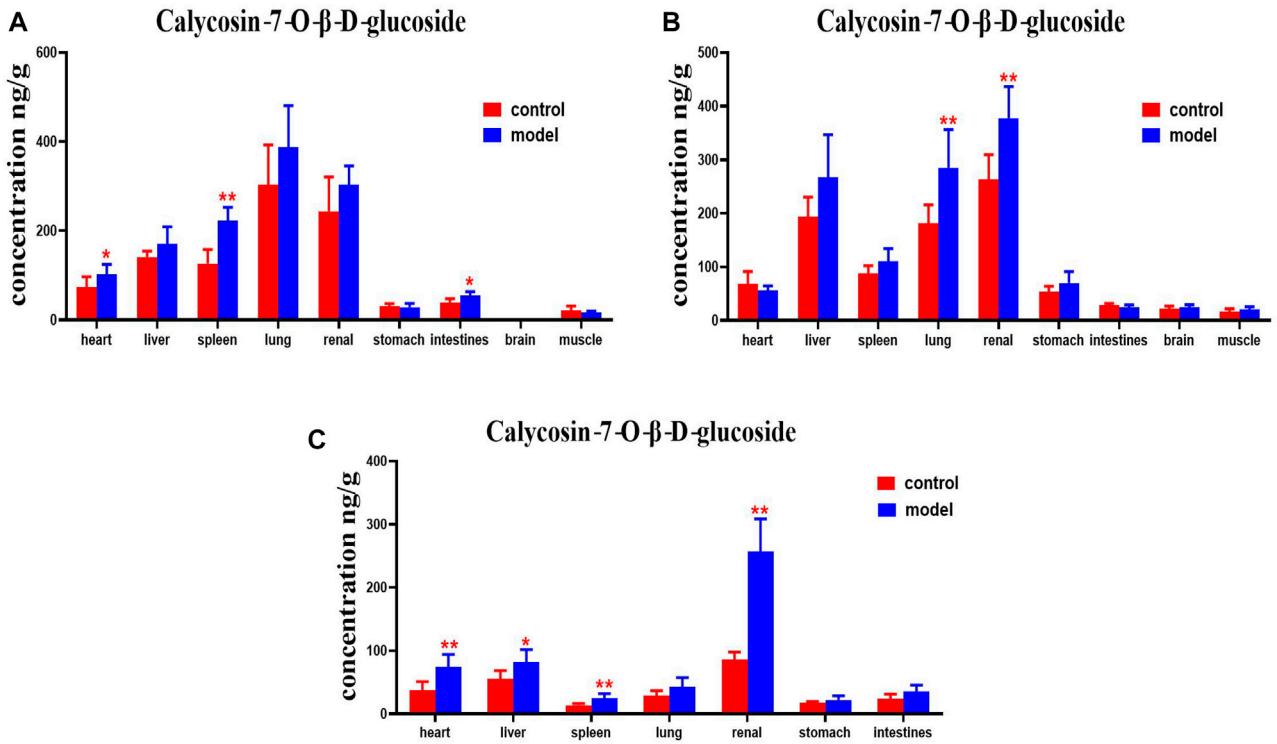

FIGURE 11 | Content of calycosin-7-O-β-D-glucoside in different mouse tissue homogenate of the normal and DN models at four different time points after intragastric administration of HQD (x±SD, *n*=8), **(A)** 30 min, **(B)** 2 h, **(C)** 4 h. Ps: **P* < 0.05, ***P* < 0.01 vs. normal group.

area analyte/IS ratios (Y) were tested against the theoretical concentration of each analyte (X) using $1/X^2$ weighting of the linear regression. The lowest concentration in the calibration curve was defined as the lower limit of quantification.

2.4.4.3 Accuracy and Precision

The quality control samples at three concentration levels of analytes were prepared and operated in parallel according to the above methods of sample preparation. Each concentration was analyzed during six replications. Assay

TABLE 5 | Stability of ingredients in tissue homogenate samples (x ± SD; *n* = 6).

Analyte	Biological sample	Concentration of analyte (ng/g)	Sampler 4 h		–20°C 48 h		Three freeze-thaw	
			Mean ± SD (ng/ml)	RSD%	Mean ± SD (ng/ml)	RSD%	Mean ± SD (ng/ml)	RSD%
Astragaloside IV	Heart	26.7	28.02 ± 2.08	7.44	27.57 ± 2.51	9.12	26.63 ± 3.83	14.39
		133.5	141.6 ± 5.76	4.07	121.0 ± 12.09	9.99	141.8 ± 15.94	11.24
		267	276.3 ± 27.25	9.86	248.4 ± 42.35	17.05	263.3 ± 40.2	15.27
	Lung	26.7	27.06 ± 1.74	6.43	27.7 ± 4.8	17.32	26.76 ± 2.54	9.50
		133.5	136.7 ± 14.6	10.68	134.7 ± 23.05	17.11	136.8 ± 20.39	14.90
		267	258.4 ± 22.45	8.69	257.0 ± 9.82	3.82	280.7 ± 17.52	6.24
	Kidney	26.7	27.35 ± 1.46	5.34	27.83 ± 5.13	18.44	27.17 ± 1.81	6.65
		133.5	150.1 ± 16.42	10.94	139.9 ± 8.52	6.09	137.8 ± 14.78	10.73
		267	283.0 ± 21.23	7.5	260.0 ± 20.38	7.84	253.7 ± 27.29	10.76
Calycosin-7-O-β-D-glucoside	Heart	2.53	2.29 ± 0.45	19.88	2.39 ± 0.22	9.33	2.67 ± 0.44	16.47
		12.63	12.15 ± 0.95	7.8	12.43 ± 0.89	7.16	12.67 ± 0.9	7.07
		25.25	26.25 ± 1.19	4.53	26.54 ± 2.66	10.01	23.84 ± 2.25	9.43
	Lung	2.53	2.6 ± 0.1	3.68	2.71 ± 0.12	4.45	2.52 ± 0.23	9.01
		12.63	13.29 ± 1.09	8.20	12.35 ± 0.6	4.85	12.23 ± 1.26	10.29
		25.25	25.58 ± 1.85	7.24	24.85 ± 1.64	6.58	24.42 ± 2.3	9.41
	Kidney	2.53	2.75 ± 0.24	8.87	2.39 ± 0.23	9.72	2.37 ± 0.37	15.73
		12.63	12.76 ± 1.21	9.52	13.18 ± 0.78	5.89	12.47 ± 0.73	5.88
		25.25	24.7 ± 1.22	4.94	24.32 ± 1.11	4.55	24.15 ± 1.16	4.81
Calycosin-glucuronide	Heart	5.19	4.9 ± 0.71	14.33	4.72 ± 0.67	14.21	4.98 ± 0.38	7.59
		51.9	53.51 ± 3.09	5.78	50.5 ± 3.89	7.70	52.31 ± 3.24	6.19
		259.5	273.1 ± 21.63	7.92	248.1 ± 16.15	6.51	246.4 ± 21.17	8.59
	Lung	5.19	5.14 ± 0.79	15.27	4.86 ± 1.15	23.54	4.77 ± 0.89	18.68
		51.9	53.94 ± 2.69	4.98	51.6 ± 7.51	14.55	50.42 ± 7.7	15.28
		259.5	254.4 ± 22.24	8.74	249.9 ± 22.29	8.92	253.7 ± 40.95	16.14
	Kidney	5.19	4.87 ± 0.88	18.11	5.03 ± 0.59	11.65	4.77 ± 0.46	9.69
		51.9	51.3 ± 1.58	3.08	51.28 ± 5.33	10.40	53.06 ± 5.75	10.84
		259.5	241.6 ± 29.12	12.05	247.6 ± 23.25	9.39	250.3 ± 29.34	11.72
Ononin	Heart	5.07	5.05 ± 0.88	17.48	5.10 ± 0.59	11.54	5.54 ± 0.31	5.58
		25.35	23.75 ± 3.76	15.81	24.05 ± 4.17	17.35	24.17 ± 3.67	15.17
		50.7	49.37 ± 2.58	5.22	50.61 ± 4.73	9.35	49.36 ± 2.62	5.31
	Lung	5.07	5.32 ± 0.49	9.29	5.1 ± 0.19	3.68	5.03 ± 0.42	8.26
		25.35	24.52 ± 0.27	1.12	23.22 ± 4.98	21.45	24.86 ± 1.1	4.44
		50.7	49.15 ± 2.36	4.81	50.88 ± 2.08	4.08	48.89 ± 2.51	5.14
	Kidney	5.07	5.19 ± 0.38	7.23	5.56 ± 0.36	6.48	4.95 ± 0.62	12.54
		25.35	25.98 ± 2.88	11.08	23.37 ± 1.5	6.40	23.25 ± 1.03	4.43
		50.7	49.97 ± 3.04	6.09	51.9 ± 3.07	5.92	49.96 ± 3.16	6.32
Formononetin	Heart	5.23	4.99 ± 0.95	19.03	4.95 ± 0.66	13.31	5.32 ± 0.92	17.31
		26.15	28.08 ± 3.88	13.83	25.2 ± 3.60	14.29	24.6 ± 2.94	11.94
		52.3	47.88 ± 5.64	11.77	48.03 ± 3.61	7.52	49.59 ± 2.52	5.09
	Lung	5.23	5.56 ± 0.73	13.13	5.03 ± 0.88	17.48	4.8 ± 0.82	17.09
		26.15	28.13 ± 5.28	18.79	24.02 ± 4.72	19.67	26.46 ± 4.32	16.34
		52.3	54.71 ± 5.32	9.73	54.9 ± 4.66	8.48	48.82 ± 8.6	17.62
	Kidney	5.23	5.54 ± 0.74	13.32	5.06 ± 1.03	20.35	5.12 ± 0.65	12.63
		26.15	26.81 ± 2.04	7.62	24.24 ± 2.42	10.00	24.55 ± 2.84	11.55
		52.3	54.25 ± 7.07	13.04	48.03 ± 5.16	10.75	49.98 ± 9.62	19.24
Glycyrrhizic acid	Heart	50.9	51.38 ± 0.82	1.60	54.32 ± 6.22	11.45	53.92 ± 4.38	8.13
		254.5	276.9 ± 41.22	14.88	272.1 ± 37.85	13.91	267.5 ± 16.27	6.08
		509	514.5 ± 34.16	6.64	516.6 ± 38.02	7.36	510.5 ± 38.03	7.45
	Lung	50.9	47.41 ± 6.34	13.37	47.21 ± 3.6	7.63	48.9 ± 3.34	6.83
		254.5	232.1 ± 16.92	7.29	236.4 ± 12.72	5.38	257.8 ± 23.04	8.94
		509	502.3 ± 18.54	3.69	504.5 ± 23.51	4.66	501.9 ± 39.3	7.83
	Kidney	50.9	49.16 ± 1.79	3.65	48.28 ± 3.7	7.67	49.34 ± 2.38	4.82
		254.5	243.8 ± 13.46	5.52	234.8 ± 10.26	4.37	239.2 ± 11.75	4.91
		509	504.3 ± 28.95	5.74	507.7 ± 33.35	6.57	499.9 ± 37.44	7.49

precision was calculated using relative standard deviation (RSD, %) and variance, and accuracy is expressed as mean ± standard deviation.

2.4.4.4 Extraction Efficiency and Matrix Effect

The recovery and matrix effect of the analytes were analyzed for medium concentration quality control samples. The extraction

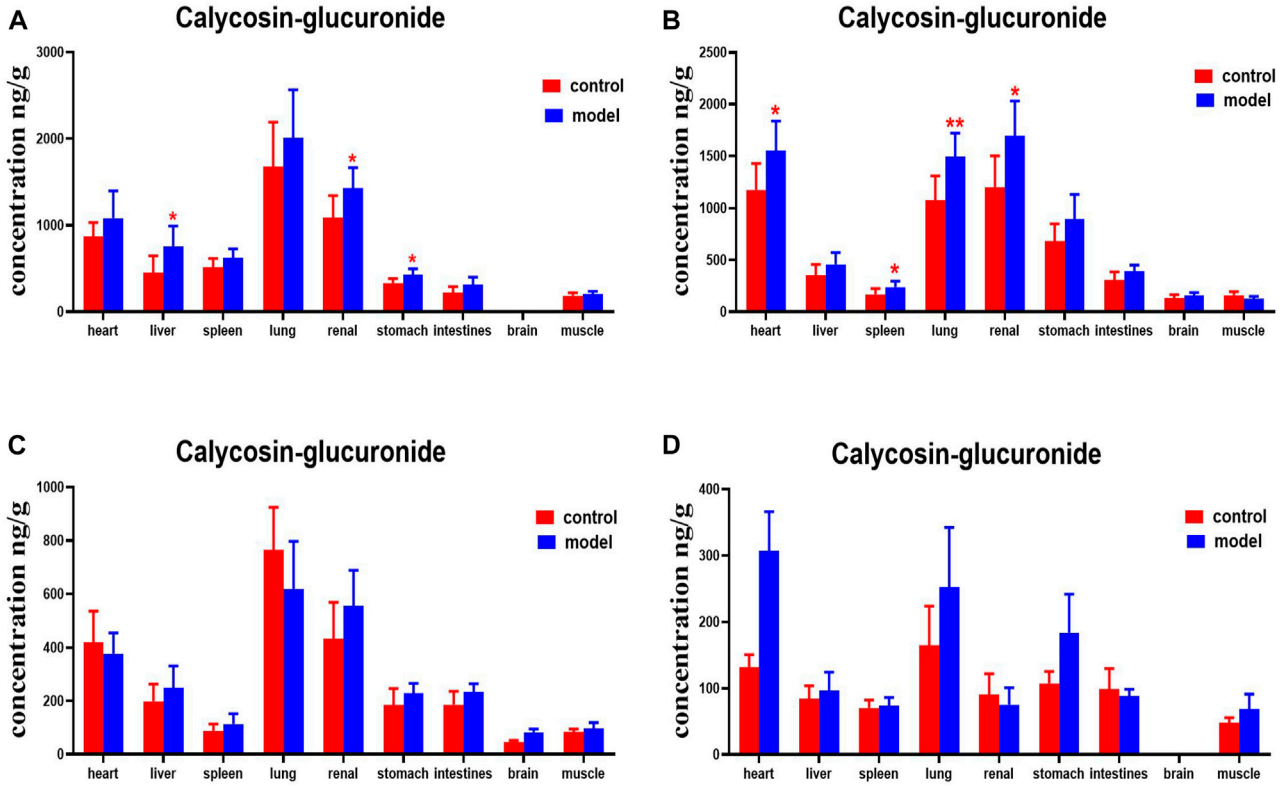

FIGURE 12 | Content of calycosin-glucoside in different mouse tissue homogenate of the normal and DN models at four different time points after intragastric administration of HQD (x±SD, *n*=8), **(A)** 30 min, **(B)** 2 h, **(C)** 4 h, **(D)** 8 h. Ps: *$P < 0.05$, **$P < 0.01$ vs. normal group.

recovery was determined by comparing the response ratio of extracted samples with extracted blank matrix spiked with corresponding concentrations. The matrix effect was evaluated as the peak area ratio of analytes spiked with blank tissue extract at medium concentrations to non-extracted QC standard solutions at equivalent concentrations.

2.4.4.5 Stability

Quality control samples at three concentration levels of tissue samples were prepared to investigate the stability of tissue samples. First, we stored samples at room temperature (approximately 25°C) for 24 h, and then froze (−20°C) them for 48 h and repeated this freezing and thawing cycle three times. The samples were processed based on the above-mentioned sample processing method and then measured by HPLC-MS/MS.

2.4.5 Tissue Distribution

Thirty-two db/db model mice and 32 normal db/m mice were fasted for 12 h. Then, the diabetic and normal mice were randomly divided into 4 groups of 8 mice each. One group of mice served as a unique sampling time point. Mice were given a single dose of HQD (high dosage in efficacy study). Blood was collected by retro-orbital venous puncture at 30 min and 2, 4, and 8 h. Subsequently, the mice were humanely euthanized, and the heart, liver, spleen, lungs, kidneys, stomach, small intestine, brain, and skeletal muscle were collected. Samples were washed with normal saline and stored at −20°C. Before the experiments, the tissues were prepared according to the sample-preparation methods and analyzed by HPLC-MS/MS.

3 RESULTS

3.1 Effect of Huangqi Liuyi Decoction on Diabetic Nephropathy

After 12 weeks, the weight of the model group was significantly decreased, the hair had lost its normal luster and was sparse, and the animals appeared less active. Compared with before administration, the weight of the HQD administration group was not significantly decreased, their fur remained shiny, and the animals were active (**Figure 2**).

Compared to those of the control group, 12-week-old diabetic mice showed increased FBG, BUN, Scr, TG, TC, and 24 h U-Alb levels ($p < 0.05$) (**Figure 2**). Diabetic mice treated with HQD showed lower biochemical parameters compared to untreated ($p < 0.05$). There was no significant difference in parameters between HQD and Huangqi Liuyi decoction treated animals ($p > 0.05$).

Masson's trichrome stained collagen fibers blue, while muscle fibers, cytoplasm, cellulose, and keratin appeared red. Kidney sections from of 12-week-old db/db diabetic mice showed increased collagen fibers in the glomerular basement

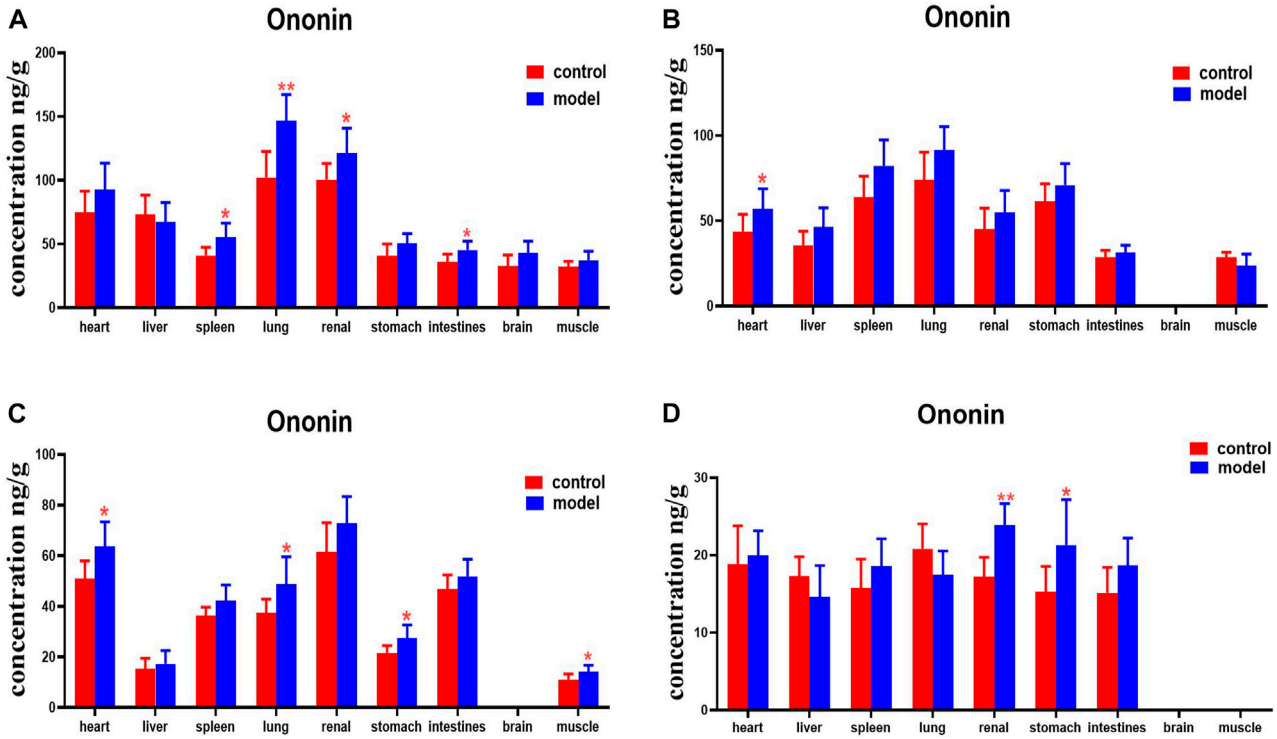

FIGURE 13 | Content of ononin in different mouse tissue homogenate of the normal and DN models at four different time points after intragastric administration of HQD (x±SD, *n*=8), **(A)** 30 min, **(B)** 2 h, **(C)** 4 h, **(D)** 8 h. Ps: *$P < 0.05$, **$P < 0.01$ vs. normal group.

membrane (**Figure 3**). Animals treated with the HQD showed less kidney collagen compared to the model group.

In non-diabetic control mice, the glomerular structure showed no pathologic changes in the glomerular mesangial area (**Figure 4**). Conversely, kidneys from diabetic mice showed mesangial matrix deposition and thickening and nodular sclerosis of the glomerular capillary basement membrane. Diabetic mice treated with HQD showed less kidney damage compared to untreated.

3.2 Protein Expression of Collagen I, E-Cadherin, α-Smooth Muscle Actin, and Vimentin

The semi-quantitative analysis of collagen I, E-cadherin, α-SMA, and vimentin is showed in **Figures 5–8**. Expression of collagen I, α-SMA, and vimentin was significantly increased ($p < 0.01$) and that of E-cadherin was significantly decreased ($p < 0.01$) in kidney sections from diabetic mice compared to kidney samples from non-diabetic mice. In contrast, diabetic animals treated with HDQ or decoction showed less kidney collagen I, α-SMA, and vimentin ($p < 0.05$); and more E-cadherin ($p < 0.01$) versus samples from untreated diabetic mice.

3.3 Tissue Distribution of the Active Constituents of Huangqi Liuyi Decoction in Control and Diabetic Nephropathy Mice

3.3.1 Method Validation of HPLC-MS/MS

3.3.1.1 Specificity

Chromatograms of the blank tissue homogenate (e.g., heart, lung, and renal); blank tissue homogenate spiked with astragaloside IV, calycosin-7-O-β-D-glucoside, calycosin-glucuronide, ononin, formononetin, glycyrrhizic acid, and IS; and tissue homogenate obtained after oral administration of HQD are displayed in **Figure 9**. Good separation was observed among the ingredients, and there was no interference from the endogenous substances in the determination of the six ingredients and IS.

3.3.1.2 Calibration Curves and Linearity

The typical equation of linearity ranges and calibration curves for the six ingredients are shown in **Table 2** (e.g., heart, lungs, and kidneys). The lowest concentration in the calibration curve was defined as the lower limit of quantification. The results show that all correlation coefficients are higher than 0.999, indicating that the concentrations of the six ingredients in mouse tissues correlated well within the linearity ranges.

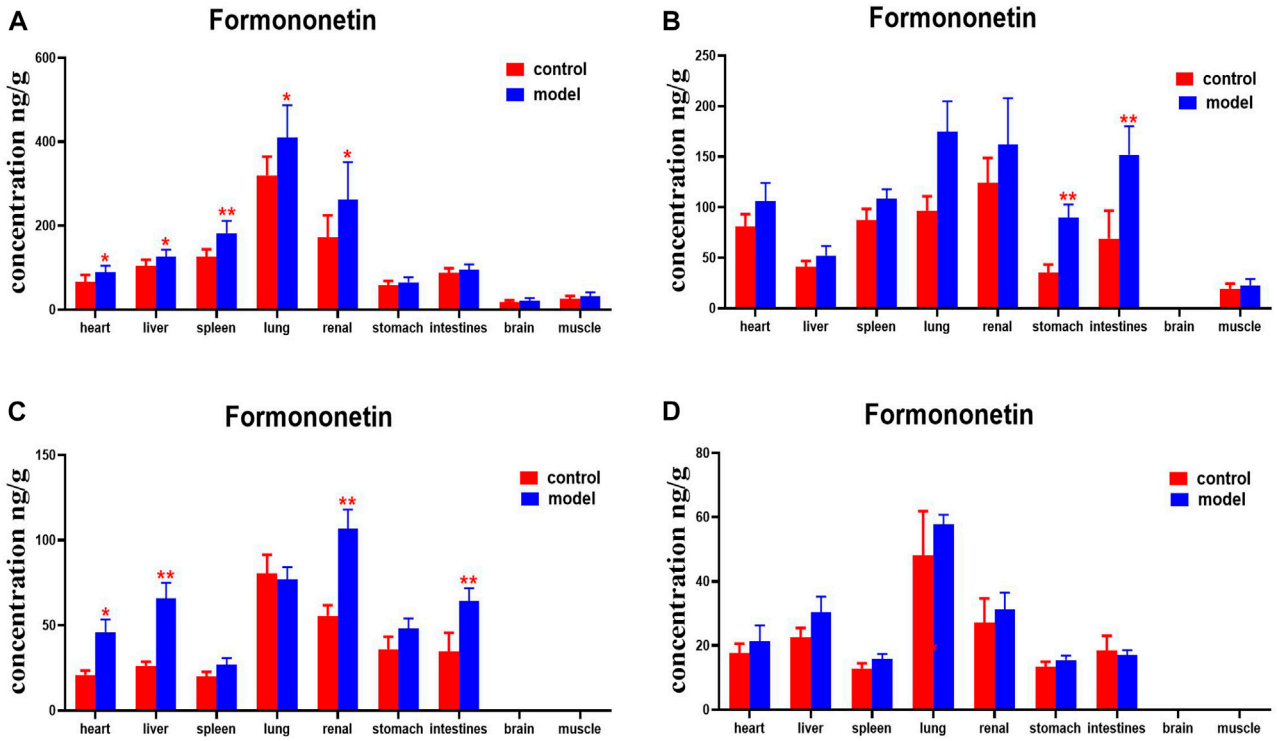

FIGURE 14 | Content of formononetin in different mouse tissue homogenate of the normal and DN models at four different time points after intragastric administration of HQD (x±SD, *n*=8), **(A)** 30 min, **(B)** 2 h, **(C)** 4 h, **(D)** 8 h. Ps: *$P < 0.05$, **$P < 0.01$ vs. normal group.

3.3.1.3 Accuracy and Precision

Intraday and interday precision and accuracy (e.g., heart, lungs, and kidneys) are summarized in **Table 3**. The intraday and interday RSDs were below 20.0%. Thus, the accuracy and precision results met the requirements of biological sample detection.

3.3.1.4 Extraction Efficiency and Matrix Effect

Results of the extraction efficiency and matrix effect analyses are shown in **Table 4** (e.g., heart, lungs, and kidneys). As noted, the recoveries of the six ingredients were precise, consistent, and reproducible at different concentration levels in various tissue samples, and there was no significant matrix interference.

3.3.1.5 Stability

Results of the stability analysis are shown in **Table 5** (e.g., heart, lungs, and kidneys). The stability test results indicated that the mouse tissue samples showed good stability under the three different conditions with a 10% concentration variation compared to the initial values.

3.3.2 Tissue Distribution Study

Following a single oral administration of HQD, the distribution of the six ingredients (astragaloside IV, calycosin-7-O-β-D-glucoside, calycosin glucuronide, ononin, formononetin, and glycyrrhizic acid) between the normal and DN mouse groups were analyzed at different time points (30 min and 2, 4, and 8 h). The six ingredients were detected in all tissue samples from diabetic and non-diabetic mice (**Figures 10**–**(15)**. Astragaloside IV, calycosin-7-O-β-D- glucoside, calycosin glucuronide, ononin, formononetin, and glycyrrhizic acid were found highest in the lungs and kidneys. However, the six active ingredients were minimally found in the brain. As expected, tissue distribution of all ingredients decreased with time.

Compared with the normal group, astragaloside IV levels in the hearts, kidney, and brains of mice with DN were higher at 30 min; levels of astragaloside IV in the livers, lungs, intestines, and muscles of mice with DN were higher at 2 h. Astragaloside IV levels in the hearts, kidneys, intestines and brains of mice with DN were higher at 4 h. Levels of astragaloside IV in the hearts, livers and kidneys of mice with DN were higher at 8 h (**Figure 10**).

Compared with the normal group, DN mice had higher levels of calycosin-7-O-β-D-glucoside in their hearts, spleens and intestines at 30 min. Calycosin-7-O-β-D-glucoside levels in the lungs and kidneys of DN mice were higher at 2 h. Levels of calycosin-7-O-β-D-glucoside in the hearts, livers, spleen, and kidneys of DN mice were higher at 4 h (**Figure 11**).

DN mice had higher levels of calycosin-glucoside in their livers, kidneys, and stomachs than the normal group at 30 min. Levels of calycosin-glucoside in the hearts, spleens, lungs, and kidneys of mice with DN were higher at 2 h (**Figure 12**).

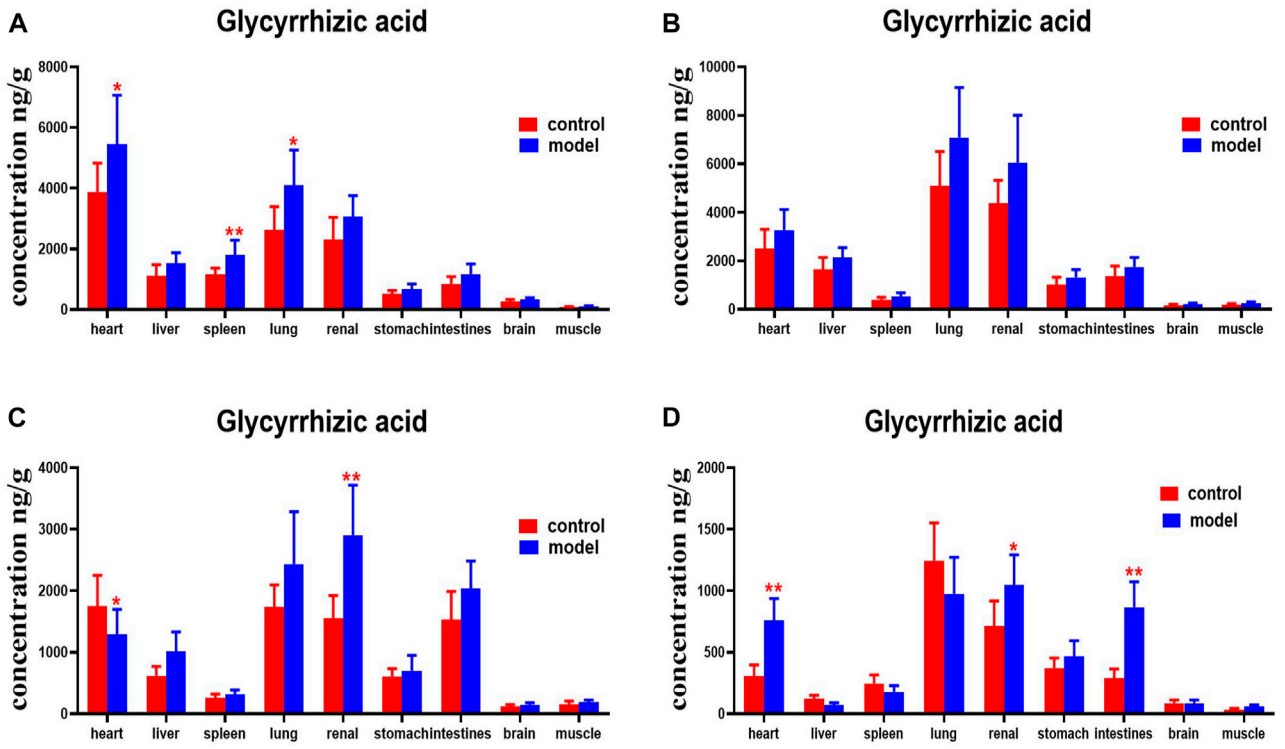

FIGURE 15 | Content of glycyrrhetinic acid in different mouse tissue homogenate of the normal and DN models at four different time points after intragastric administration of HQD (x±SD, *n*=8), **(A)** 30 min, **(B)** 2 h, **(C)** 4 h, **(D)** 8 h. Ps: *$P < 0.05$, **$P < 0.01$ vs normal group.

Ononin levels were higher in the spleens, lungs, kidneys, and intestines of DN mice at 30 min, compared with the normal group. DN mice had higher levels of ononin in their hearts at 2 h. Levels of ononin in their hearts, lungs, stomachs, and muscles were higher at 4 h. Ononin levels in the kidneys and stomachs were higher at 8 h (**Figure 13**).

Compared with the normal group, DN mice had higher levels of formononetin in their hearts, livers, spleens, lungs, and kidneys at 30 min. Formononetin levels were also higher in their stomachs and intestines at 2 h. Levels of formononetin in the hearts, livers, kidneys and intestines of DN mice were higher at 4 h (**Figure 14**).

Compared with the normal group, glycyrrhetinic acid levels were higher in the heart, spleens, and lungs of mice with DN at 30 min. DNs had higher levels of glycyrrhetinic acid in their hearts and kidneys at 4 h. Levels of glycyrrhetinic acid in the hearts, kidneys, and intestines of mice with DN were higher at 8 h (**Figure 15**).

4 DISCUSSION

In this study, we used 12-week-old db/db mice as a diabetic nephropathy mouse model and 12-week-old db/m mice as a normal comparison group. The db/db mouse was a mutant type, with the line of leptin receptor gene defect picked from C57BL/6J mice by the Jackson Laboratory of the United States. The db/db mouse spontaneously develops type 2 diabetes and is similar to clinical type 2 diabetes. db/db mice display obesity, hyperlipidemia, and hyperglycemia after 4 weeks of age. Diabetic nephropathy is found after 8–12 weeks of age (Gerald et al., 2013; Ponchiardi et al., 2013). The experimental results showed that the FBG, Scr, BUN, TC, TG, and 24 h U-Alb of 12-week db/db mice were significantly higher than those of the normal control group ($p < 0.05$). The kidneys of 12-week db/db mice also showed obvious glomerular lesions.

Some researchers have investigated *in vivo* content analysis methods for Huangqi Liuyi decoction (Zeng et al., 2018), but a method for simultaneously quantifying various ingredients in multiple organs has not yet been reported. In this research, HPLC-MS/MS was used to analyze the tissue distribution of the six active ingredients of HQD in normal and DN mice. Furthermore, the methodology, including specificity, linearity, accuracy, precision, extraction efficiency, matrix effect, and stability, was verified. The content of drugs in tissues and organs is usually difficult to measure, in part because there are many factors that interfere with the process. Triple quadrupole mass spectrometry is often used to determine trace components in biological samples, such as blood, urine, and tissue, in pharmacokinetic studies. In its multi-reaction monitoring scanning mode, the precursor ions of the tested component are prescreened in the first quadrupole (Q1), separated in the second quadrupole (Q2), and identified and quantified in the third quadrupole (Q3). In comparison with the traditional triple quadrupole mass spectrometry approach, the QTRAP® LC-MS/MS system (Sciex, Framingham, MA, United States) is equipped with an additional linear ion trap at the third quadrupole (Q3). This new generation of HPLC-MS/MS system, which is equipped with a

unique scanning mode (incorporating multi-reaction ion monitoring, information-dependent acquisition, and enhanced ion scanning), can obtain the most abundant information of the tested components in a single operation, including ion pair retention time, relative peak strength, and mass spectrum. This greatly improves the detection sensitivity. After oral administration of HQD, six ingredients in various tissues of mice were determined by triple quadrupole linear ion trap mass spectrometry. At the same time, the precipitation of protein in mouse tissues by protein precipitants, such as methanol, acetonitrile, and ethyl acetate, was investigated. When methanol was used as a protein precipitant, the sample preparation was time-saving and stable, and the six active ingredients in the measured HQD were least disturbed by endogenous substances. As a consequence, methanol was selected as the precipitation solvent for sample pretreatment. Through methodological investigation, it was found that the established analytical methods of various components in mouse tissue samples met the requirements of biological sample determination.

The phenomenon by which a drug is transported between blood and tissues is called distribution. In oral administration, the drug is first absorbed into blood and then distributed to various tissues and cells throughout the body. The distribution process is usually completed quickly (Chen and Li, 2013). If the main tissue to which the drug is distributed happens to be the drug's site of action, there is a close relationship between drug distribution and efficacy. Drug distribution to a non-active site is often closely related to drug toxicity and accumulation of the drug in the body. Therefore, investigating the *in vivo* distribution characteristics of drugs is useful in forecasting its pharmacological effects as well as the degree of *in vivo* retention and toxic effects (Wei and Zhang, 2004; Hu et al., 2020). In this study, the anti-DN effect of HQD was determined. After oral administration of HQD, six ingredients (astragaloside IV, calycosin-7-O-β-glucoside, calycosin glucuronide, ononin, formononetin, and glycyrrhizic acid) were detected in murine tissues regardless of the presence of diabetes. These six active ingredients were rapidly and widely distributed in multiple organs, albeit mainly in the lungs, kidneys, liver, spleen, and heart, and especially in the kidneys and lungs. Confirmation of the greatest distribution occurring in lung and kidney tissue samples indicates that HQD distribution is targeted at the lungs and kidneys, demonstrating positive significance for the prevention and treatment of nephropathy.

The major audience of drugs are diseased patients. Whether or not the body is in a pathological state has important measures of impact on the pharmacokinetics of the drug. In comparison with the normal condition, the distribution of these six ingredients in the lung, kidney, spleen, and heart increased in mice with DN, and especially in the kidney. The increase in the distribution of kidneys under pathological conditions can effectively guarantee the development of a prescription effect. In short, tissue distribution of the six index ingredients of HQD in the DN model was quite different from that in normal mice, but the reasons for this are still unclear. The concentrations of six active ingredients in the blood can affect their distribution in the tissues. Moreover, the excretion of drugs in the kidneys mainly includes glomerular filtration and renal tubular secretion and reabsorption. Glomerulonephritis and renal tubular lesions in DN mice are obvious compared to those in normal mice (Rick et al., 1987; Kudo et al., 2009; Liu, 2016). Diabetes and renal insufficiency in these mice will lead to a reduction in plasma protein content. As a consequence, the free drug concentration will increase, making more of the drug penetrate into tissues. At the same time, the permeability of blood vessels may change under different pathological conditions, which makes it easier for drugs to penetrate into tissues through capillary vessels, resulting in a change in the drug concentration accordingly. Therefore, the different characteristics of the distribution of six active ingredients may have been caused by the pathological state. However, the underlying mechanism of these differences remains to be further studied. In subsequent studies, we will further explore the mechanism by which the pathological state of diabetic nephropathy changes the tissue distribution of the six active ingredients in HQD.

5 CONCLUSION

HQD could effectively improve diabetes nephropathy. Moreover, a rapid, reliable, and sensitive HPLC/MS-MS method for simultaneous determination of six ingredients in the tissues of DN and normal mice after oral administration of HQD was established and validated. The tissue distribution characteristics of six ingredients in normal and DN model mice after oral administration of HQD were significantly different, but the overall trend was similar. The results might provide a reference for further research on HQD.

DATA AVAILABILITY STATEMENT

The original contributions presented in the study are included in the article/supplementary material, further inquiries can be directed to the corresponding author.

ETHICS STATEMENT

The animal study was reviewed and approved by the Animal Ethical Committee of Guizhou University of Traditional Chinese Medicine.

AUTHOR CONTRIBUTIONS

QW conceived and designed the experiments. QW and YS performed all of the experiments. ZW, XS, JL, HY, XC, and XL contributed to the operation of rats/reagents/materials/analysis tools. QW and YS analyzed the data. QW and YS wrote a draft of the paper.

FUNDING

This research was supported by the First-class Discipline Construction Project in Guizhou Province of China [No.

GNYL (2017) 008], the Project of Guizhou Provincial Department of Education [No. QJHKYZ (2022) 257]. Guizhou characteristic functional foodand TCM preparation development platform KY (2020) 006. the Doctoral Scientific Research Foundation of Guizhou University of Traditional Chinese Medicine [No. (2020) 79].

REFERENCES

Appel, G. (2013). Detecting and Controlling Diabetic Nephropathy: What Do We Know? *Ccjm* 80 (80), 209–217. doi:10.3949/ccjm.80gr.12006

Chen, Z. W., and Li, Z. Y. (2013). *Pharmacology*. Zhengzhou, China: Henan Science and Technology Press.

Correa-Rotter, R., and González-Michaca, L. (2005). Early Detection and Prevention of Diabetic Nephropathy: a Challenge Calling for Mandatory Action for Mexico and the Developing World. *Kidney Int. Suppl.* 68 (98), S69–S75. doi:10.1111/j.1523-1755.2005.09813.x

Dai, X.-X., Su, S.-L., Cai, H.-D., Wei, D.-D., Zheng, T.-Y., Zhu, Z.-H., et al. (2017). Comparative Pharmacokinetics of Acteoside from Total Glycoside Extracted from Leaves ofRehmanniaand Dihuangye Total Glycoside Capsule in Normal and Diabetic Nephropathy Rats. *Biomed. Chromatogr.* 31 (12), e4013. doi:10.1002/bmc.4013

Hu, H., Xiao, H., Bao, H., Li, M., Xue, C., Li, Y., et al. (2020). Tissue Distribution Comparison of Six Active Ingredients from an Eucommiae Cortex Extract between Normal and Spontaneously Hypertensive Rats. *Evid. Based Complement. Altern. Med.* 2020, 2049059–2049116. doi:10.1155/2020/2049059

Kopel, J., Pena-Hernandez, C., and Nugent, K. (2019). Evolving Spectrum of Diabetic Nephropathy. *World J. Diabetes* 10 (5), 269–279. doi:10.4239/wjd.v10.i5.269

Kudo, T., Shimada, T., Toda, T., Igeta, S., Suzuki, W., Ikarashi, N., et al. (2009). Altered Expression of CYP in TSOD Mice: a Model of Type 2 Diabetes and Obesity. *Xenobiotica* 39, 889–902. doi:10.3109/00498250903242592

Liu, J. P. (2016). *Biopharmaceutics and Pharmacokinetics*. Beijing: People's Medical Publishing House.

Lu, X., and Wei, M. G. (2014). Effects of astragalus Polysaccharides on Kidney Interstitial Fibrosis in Rats. *China J. Traditional Chin. Med. Pharm.* 29 (6), 1998–2001. http://www.cnki.net.

Ma, K. K., Ju, Y. H., Chen, Q. Q., Li, W. Z., Li, W. P., et al. (2019). Effect of Astragaloside Ⅳ on Regulation of PI3K/Akt/ FoxO1 Signal in Kidney of Type 2 Diabetic Nephropathy Rats. *Chin. J. Exp. Traditional Med. Formulae* 25 (2), 74–81. doi:10.13422/j.cnki.syfjx.20190227

Nie, H. C., Zheng, X., Ayjulaike, K. D. E., Li, X. R., Adilijinag, Y. M. T., Gao, X. L., et al. (2019). Determination of Whey Protein Content in Different Kinds of Milk by Coomassie Brilliant Blue Method. *J. Food Saf. Qual.* 10 (5), 1138–1142.

Noor, T., Hanif, F., Kiran, Z., Rehman, R., Khan, M. T., Haque, Z., et al. (2020). Relation of Copeptin with Diabetic and Renal Function Markers Among Patients with Diabetes Mellitus Progressing towards Diabetic Nephropathy. *Arch. Med. Res.* 51 (6), 548–555. doi:10.1016/j.arcmed.2020.05.018

Nowak, N., Skupien, J., Smiles, A. M., Yamanouchi, M., Niewczas, M. A., Galecki, A. T., et al. (2018). Markers of Early Progressive Renal Decline in Type 2 Diabetes Suggest Different Implications for Etiological Studies and Prognostic Tests Development. *Kidney Int.* 93 (5), 1198–1206. doi:10.1016/j.kint.2017.11.024

Peng, Y., Ren, D., Song, Y., Hu, Y., Wu, L., Wang, Q., et al. (2020). Effects of a Combined Fucoidan and Traditional Chinese Medicine Formula on Hyperglycaemia and Diabetic Nephropathy in a Type II Diabetes Mellitus Rat Model. *Int. J. Biol. Macromol.* 147, 408–419. doi:10.1016/j.ijbiomac.2019.12.201

Ponchiardi, C., Mauer, M., and Najafian, B. (2013). Temporal Profile of Diabetic Nephropathy Pathologic Changes. *Curr. Diab Rep.* 13 (13), 592–599. doi:10.1007/s11892-013-0395-7

Rick, A. F., Belpaire, F. M., Dello, C., and Bogaert, M. G. (1987). Influence of Enhanced Alpha-1-Acid Glycoprotein Concentration on Protein Binding, Pharmacokinetics and Antiarrhythmic Effect of Lidocaine in the Dog. *J. Pharmacol. Exp. Ther.* 241, 289–293. https://pubmed.ncbi.nlm.nih.gov/.

Shi, X., Lu, X. G., Zhan, L. B., Qi, X., Liang, L. N., Hu, S. Y., et al. (2011). The Effects of the Chinese Medicine ZiBu PiYin Recipe on the hippocampus in a Rat Model of Diabetes-Associated Cognitive Decline: a Proteomic Analysis. *Diabetologia* 54 (7), 1888–1899. doi:10.1007/s00125-011-2147-z

Sun, G. D., Li, C. Y., Cui, W. P., Guo, Q. Y., Dong, C. Q., Zou, H. B., et al. (2016). Review of Herbal Traditional Chinese Medicine for the Treatment of Diabetic Nephropathy. *J. Diabetes Res.* 2016, 5749857. doi:10.1155/2016/5749857

Wei, S. L., and Zhang, Q. (2004). *Biopharmaceutics and Pharmacokinetics*. Beijing, China: Peking University Medical Press.

Wen, L. M., Xu, Y. L., Zhen, L., Zhen, J. Y., and Guo, W. F. (2018). Study on the Effects and Mechanism of astragalus Liuyi Decoction on Type 2 Diabetes Mellitus Rats. *J. Chin. Med. Mater.* 41 (3), 699–702. doi:10.13863/j.issn1001-4454.2018.03.040

Xiao, X., Ma, B., Dong, B., Zhao, P., Tai, N., Chen, L., et al. (2008). Cellular and Humoral Immune Responses in the Early Stages of Diabetic Nephropathy in NOD Mice. *J. Autoimmun.* 32 (2), 85–93. doi:10.1016/j.jaut.2008.12.003

Xu, Y. L., Zheng, Y. J., Li, Z., and Wen, L. M. (2017). Effect of Huangqi Liuyi Tang on Glucose Re-absorption via Kidney Tubular Epithelial Cells in Type 2 Diabetes Model Rats. *Chin. J. Exp. Traditional Med. Formulae* 23 (11), 114–121. doi:10.13422/j.cnki.syfjx.2017110114

Yang, S. L., and Liu, K. X. (2019). Development of Research on Drug Transporters Mediated Interaction between Chinese Medicine and Monomers. *Drug Eval. Res.* 42 (1), 194–203. doi:10.7501/j.issn.1674-6376.2019.01.032

Zeng, J. K., Li, Y. Y., Wang, T. M., Zhong, J., Wu, J. S., Liu, P., et al. (2018). Simultaneous Quantification of Multiple Components in Rat Plasma by UPLC-MS/MS and Pharmacokinetic Study after Oral Administration of Huangqi Decoction. *Biomed. Chromatogr.* 32 (5), e4178. doi:10.1002/bmc.4178

Zhang, B. L., and Wang, Y. Y. (2005). Basic Research on the Key Scientific Issues of Prescriptions-Development of Modern Chinese Medicine by Components. *Chin. J. Nat. Med.* 3 (5), 258–261. http://www.cnki.net.

Zhang, W., Fu, Z. T., Xie, Y., Duan, Z. W., Wang, Y., and Fan, R. H. (2020). High Resolution UPLC-MS/MS Method for Simultaneous Separation and Determination of Six Flavonoids from Semen Cuscutae Extract in Rat Plasma: Application to Comparative Pharmacokinetic Studies in Normal and Kidney-Deficient Rats. *Nat. Prod. Res.* 34 (10), 1446–1451. doi:10.1080/14786419.2018.1511556

Conflict of Interest: The authors declare that the research was conducted in the absence of any commercial or financial relationships that could be construed as a potential conflict of interest.

Publisher's Note: All claims expressed in this article are solely those of the authors and do not necessarily represent those of their affiliated organizations, or those of the publisher, the editors and the reviewers. Any product that may be evaluated in this article, or claim that may be made by its manufacturer, is not guaranteed or endorsed by the publisher.

frontiers | Frontiers in Pharmacology

REVIEW
published: 27 June 2022
doi: 10.3389/fphar.2022.937075

Better Bioactivity, Cerebral Metabolism and Pharmacokinetics of Natural Medicine and Its Advanced Version

Jiaxi Xie[1†], *Cailing Zhong*[1†], *Tingting Wang*[2†], *Dan He*[1†], *Luyang Lu*[3], *Jie Yang*[1], *Ziyi Yuan*[1] *and Jingqing Zhang*[1*]

[1]Chongqing Research Center for Pharmaceutical Engineering, College of Pharmacy, Chongqing Medical University, Chongqing, China, [2]Biochemistry and Molecular Biology Laboratory, Experimental Teaching and Management Center, Chongqing Medical University, Chongqing, China, [3]College of Pharmacy, Southwest Minzu University, Chengdu, China

Currently, many people are afflicted by cerebral diseases that cause dysfunction in the brain and perturb normal daily life of people. Cerebral diseases are greatly affected by cerebral metabolism, including the anabolism and catabolism of neurotransmitters, hormones, neurotrophic molecules and other brain-specific chemicals. Natural medicines (NMs) have the advantages of low cost and low toxicity. NMs are potential treatments for cerebral diseases due to their ability to regulate cerebral metabolism. However, most NMs have low bioavailability due to their low solubility/permeability. The study is to summarize the better bioactivity, cerebral metabolism and pharmacokinetics of NMs and its advanced version. This study sums up research articles on the NMs to treat brain diseases. NMs affect cerebral metabolism and the related mechanisms are revealed. Nanotechnologies are applied to deliver NMs. Appropriate delivery systems (exosomes, nanoparticles, liposomes, lipid polymer hybrid nanoparticles, nanoemulsions, protein conjugation and nanosuspensions, etc.) provide better pharmacological and pharmacokinetic characteristics of NMs. The structure-based metabolic reactions and enzyme-modulated catalytic reactions related to advanced versions of NMs alter the pharmacological activities of NMs.

Keywords: cerebral metabolism, natural medicines, pharmacokinetics, pharmacodynamics, delivery systems

OPEN ACCESS

Edited by:
Zipeng Gong,
Guizhou Medical University, China

Reviewed by:
Yan Xie,
Shanghai University of Traditional Chinese Medicine, China
Yao Fu,
Sichuan University, China
Qingxiang Guan,
Jilin University, China

***Correspondence:**
Jingqing Zhang
13308300303@cqmu.edu.cn

†These authors have contributed equally to this work

Specialty section:
This article was submitted to Drug Metabolism and Transport, a section of the journal Frontiers in Pharmacology

Received: *05 May 2022*
Accepted: *27 May 2022*
Published: *27 June 2022*

Citation:
Xie J, Zhong C, Wang T, He D, Lu L, Yang J, Yuan Z and Zhang J (2022) Better Bioactivity, Cerebral Metabolism and Pharmacokinetics of Natural Medicine and Its Advanced Version. Front. Pharmacol. 13:937075. doi: 10.3389/fphar.2022.937075

INTRODUCTION

Cerebral diseases are usually caused by abnormal cerebral metabolism (anabolism and catabolism) of neurotransmitters, hormones, neurotrophic molecules, and other brain-specific chemicals (Graf et al., 2013). Alzheimer's disease (AD), depression, cerebral injury and brain tumors are four major brain pathologies that induced by aberrant cerebral metabolism. AD is mainly caused by neuroinflammation (Angeloni et al., 2019), loss of neurons, and the accumulation of phosphorylated tau protein and amyloid plaques (Aβ) in the brain (Karch and Goate, 2015). AD has affected over 50 million people worldwide (Najm et al., 2020), leading to the progressive and irreversible loss of memory and other cognitive functions in patients (Nho et al., 2020). Depression results from dysregulated release of neurotransmitters. Depression has been found to occur in 14.8% of males and 14.1% of females worldwide (Kyu et al., 2018). It has become the third leading cause of disability (Corriger and Pickering, 2019). Traumatic brain injury (TBI) remains a common cause of

disability and death worldwide (VanItallie, 2019) and leads to increased neuroinflammation (Karve et al., 2016). TBI is always accompanied by secondary injuries such as spastic cerebral palsy (Enslin et al., 2020), attention deficit hyperactivity disorder (Narad et al., 2018) and cerebral ischemia (Kaur and Sharma, 2018). Glioma, a malignant glial tumor, is the most common tumor in the central nervous system. Glioma has a higher rate of mortality than other tumors (Anjum et al., 2017) and is the second leading cause of death among central nervous system diseases (Bilmin et al., 2019). Targeting uncontrolled tumor proliferation in the brain (Shah and Kochar, 2018) by inhibiting tumor growth or engendering tumor apoptosis would be the most potent gliomas treatment.

Natural medicines (NMs) are known for their high availability, clear efficacy, and low toxicity and economic cost (Yang et al., 2020). Some NMs have been proven to have positive effects by regulating cerebral metabolism to ameliorate brain diseases. However, most NMs that affect cerebral metabolism (NMCs) have low solubility, low permeability and poor pharmacokinetic characteristics. Hence, loading NMCs with advanced drug delivery systems such as exosomes, nanoparticles and liposomes, provides ways to solve this problem.

Here, the relationships between NMCs found through available databases and cerebral metabolism are investigated. The solubility, permeability, molecular structure and molecular weight characteristics of various NMCs are presented. Drug delivery systems that enhance the pharmacokinetic and pharmacodynamic characteristics features of NMCs are reviewed. The structure-based *in-vivo* metabolic reactions modulated by metabolic enzymes and metabolites of NMCs are summarized.

EFFECTS OF NMCS ON CEREBRAL METABOLISM

NMCs have effects on neurotransmitters. Neurotransmitters are chemicals released by axons to transfer information between neurons. Because of the substantial and unique roles neurotransmitters play in brain function, targeting neurotransmitter metabolism is considered a potent approach to treat neurological and psychiatric disorders (Hyman, 2005). Artemisinin, cannabidiol, geniposide and ginsenoside Rb1 are neuroprotective agents (**Supplementary Table S1**) (Liu W. et al., 2015; Watt and Karl, 2017; Zhao J. et al., 2018; Qiang et al., 2018). They treat AD and traumatic cerebral injuries and attenuate secondary injuries by inhibiting nitric oxide (NO) release. NO is a gas neurotransmitter. NO regulates the release of proinflammatory molecules, interacts with reactive oxygen species (ROS), promotes the formation of reactive nitrogen species (RNS), and ultimately causes cellular death (a hallmark of many neurodegenerative diseases and cerebral injuries) (Asiimwe et al., 2016). Evodiamine, icariin, curcumin and ferulic acid mitigate depressive symptoms by raising the levels of serotonin, norepinephrine, monoamine or dopamine (He et al., 2018; Jin et al., 2019; Sasaki et al., 2019; Fusar-Poli et al., 2020; Xie et al., 2020; Zhao et al., 2020; Xu et al., 2021). Baicalin controls symptoms of attention deficit hyperactivity disorder (ADHD) by increasing dopamine levels. Dysfunction of catecholamine and particular dopamine neuronal systems is considered a cause of ADHD (Zhou et al., 2019).

NMCs have effects on hormones. NMCs such as ferulic acid and icariin effectively relieve depressive-like behavior by decreasing the concentrations of corticosterone, adrenocorticotropic hormone (ACTH) and cortisol, which are also called the primary stress hormones. These NMs treat stress-induced depression caused by impaired regulation of the hypothalamic-pituitary-adrenal (HPA) axis (Jin et al., 2019; Zheng et al., 2019).

NMCs have effects on neurotrophic molecules. Neurotrophic molecules (also called neurotrophic factors) are molecules (mostly proteins) derived from neurons that facilitate the survival/differentiation of neurons (Unsicker, 2013). They are composed of neurotrophins, neuroregulatory cytokines, the fibroblast growth factor (FGF) family, the transforming growth factor-β (TGF-β) family, the insulin-like growth factor (IGF) family and other growth factors, such as vascular endothelial growth factor (VEGF). The metabolism of neurotrophic molecules affects the brain metabolism and thus affects neurodegenerative diseases and cerebral injuries.

NMCs have effects on neurotrophins. Neurtrophins are proteins that regulate the survival, growth and programmed cell death of neurons (Unsicker, 2013). Nerve growth factor (NGF) and brain-derived neurotrophic factor (BDNF) are two neurtrophins that play critical physiological roles in peripheral/central nervous system function. NGF and BDNF signaling also regulate neuropathic pain through receptors such as tropomyosin receptor kinase A (TrkA) and B (TrkB) (Khan and Smith, 2015). NMCs such as baicalin, curcumin and ferulic acid augment the levels of BDNF or the receptor TrkB to assuage depressive-like behaviors (Liu et al., 2017; Lu et al., 2019; Sasaki et al., 2019; Fusar-Poli et al., 2020), since depressive patients in the clinic are always found to have reduced BDNF levels in the peripheral system (Liu et al., 2017). Rutin mitigates cerebral ischemia injury by activating estrogen receptor-mediated BDNF-TrkB/NGF-TrkA signaling (Liu et al., 2018), and chlorogenic acid mitigates ischemic injury by increasing the level of NGF in brain tissue (Miao et al., 2017). Oleandrin has a neuroprotective effect in antitumor treatment by enhancing BDNF (Garofalo et al., 2017).

NMCs have effects on neuroregulatory cytokines. Neuroregulatory cytokines such as interleukin-6 (IL-6), ciliary neurotrophic factor (CNTF), leukemia inhibitory factor (LIF), cardiotrophin-1 and cardiotrophin-2 (CT-1 and CT-2), oncostatin-M and neuropoietin are useful in the treatment of neurodegenerative diseases and trauma (Unsicker, 2013). Anti-inflammatory cytokines prohibit the inflammation process, while pro-inflammatory cytokines promote the inflammation cascade (Boshtam et al., 2017). Artemisinin, cannabidiol, oxymatrine and geniposide treat AD by decreasing the expression of IL-6 (Liu et al., 2015b; Watt and Karl, 2017; Qiang et al., 2018; Chen Y. et al., 2019). Overexpression of proinflammatory cytokines provokes neurodegeneration induced by activated microglia, which are thought to clear the Aβ protein. Accordingly,

accumulated Aβ leads to neuroinflammation, neuronal synapse loss and eventually AD (Kaur et al., 2019). The proinflammatory cytokines are released after middle cerebral artery occlusion (MCAO) catalyzed by focal cerebral ischemia/reperfusion (I/R) damages of blood brain barrier, cerebral edema and acute inflammation. Salvianolic acid B relieves cerebral injury by reducing IL-6 expression (Fan et al., 2018) Leonurine, baicalin, geniposide and ferulic acid (Jia et al., 2017; Zhao Y. et al., 2018; Guo et al., 2019; Zheng et al., 2019) reduce IL-6 expression to treat depression (Kim et al., 2016).

NMCs have effects on TGF-β and VEGF. TGF-β is involved in the development, differentiation, angiogenesis, apoptosis and survival of body cells. Anomalous expression or dysregulation of TGF-β leads to neurodegenerative disease, cancers, and so on (Cabello-Verrugio, 2018). TGF-β may act as a pro- or anti-inflammatory cytokine in different contexts. Salvianolic acid B increases TGF-β (acting as an anti-inflammatory factor) to palliate depressive-like behaviors in depressive patients (Zhang et al., 2016), whereas icariin reduces TGF-β (acting as a proinflammatory factor) to treat cerebral ischemia (Jin et al., 2019). VEGF is essential for vascular and nervous system development, and tanshinone IIA activates VEGF to prompt angiogenesis, axon growth, and neuronal survival and to protect nerve cells and resist apoptosis after brain damage (Zhang W. et al., 2017). Leonurine augments VEGF expression, which is conducive to the formation of nuclear factor erythroid 2-related factor 2 (Nrf-2), to treat cerebral ischemic stroke (Xie et al., 2019).

NMCs have effects on other brain-specific chemicals. These chemicals usually participate in regulating neurotransmitters, hormones, and neuroregulatory cytokines to modulate cerebral metabolism. In the treatment of AD, tanshinone IIA, ginsenoside Rd, cannabidiol, oxymatrine, cholic acid, vitamin A, puerarin, icariin, geniposide and curcumin prevent and ameliorate AD by diminishing Aβ deposition and tau protein phosphorylation (Liu et al., 2015a; Karch and Goate, 2015; Zeng J. et al., 2017; Tang and Taghibiglou, 2017; Watt and Karl, 2017; Yan et al., 2017; Yao et al., 2017; Chen Z. et al., 2019; Jin et al., 2019; Majid et al., 2019; He et al., 2020; Fu et al., 2021). Cannabidiol disrupts the Wnt/β-catenin pathway to inhibit tau protein phosphorylation (Watt and Karl, 2017). Ginsenoside Rd, salvianolic acid B and icariin can also treat AD by increasing the expression of α-secretase and soluble amyloid precursor protein alpha (sAPPα), which are negatively related to Aβ formation, or by decreasing the expression of β-secretase, γ-secretase, BACE1, sAPPβ, and amyloid precursor protein (APP), which stimulates Aβ production (Tang et al., 2016; Yan et al., 2017; Jin et al., 2019). Rhynchophylline treats AD by inhibiting erythropoietin-producing hepatocellular A4 (EphA4), which is key in synaptic loss and dysfunction and mediates Aβ (Fu et al., 2021). Capsaicin and salvianolic acid B inhibit AD by inhibiting glycogen synthase kinase 3 beta (GSK-3β), leading to a decrease in inflammatory signaling molecules and preventing tau hyperphosphorylation (Tang et al., 2016; Xu et al., 2017). Neuronal apoptosis plays crucial roles in AD treatment. Tanshinone IIA and ginsenoside Rb1 are AD medicines that upregulate the ratio of Bcl-2 (an antiapoptosis protein) to Bax (a proapoptotic protein) and downregulate caspase-3 (an effector of the main initiator in the apoptotic pathway) (Wang C. et al., 2018; He et al., 2020). Butylphthalide inhibits mitogen-activated protein kinases (MAPKs), which accelerate brain tissue apoptosis, to treat AD (Song et al., 2017). Tanshinone IIA prevents AD by preventing the abnormal expression of glucose regulated protein 78 (GRP78), eukaryotic initiation factor 2-alpha (eIF2α), inositol-requiring enzyme 1α (IRE1α) and activating transcription factor 6 (ATF6) to prevent endoplasmic reticulum (ER) stress, which would induce apoptosis and eventually AD through the CCAAT/enhancer-binding protein homologous protein (CHOP) and c-Jun N-terminal kinase (JNK) pathways, which are also hindered by tanshinone IIA (He et al., 2020). Geniposide activates the GLP-1R/AKT signaling pathway, which exerts neuroprotective effects against AD and depression by preventing apoptosis and inflammatory processes and promoting neurite outgrowth (Liu W. et al., 2015; Zhao J. et al., 2018). Moreover, as mentioned before, the proinflammatory process accelerates AD and the associated deterioration. Artemisinin, tetrandrine, cannabidiol, oxymatrine, and geniposide directly reduce the expression of proinflammatory cytokines such as IL-6, IL-1β, IL-17A, and TNF-α (Liu et al., 2015b; Watt and Karl, 2017; Qiang et al., 2018; Chen Y. et al., 2019; Ren et al., 2021) to control AD. Nuclear factor kappa-light-chain-enhancer of activated B cells (NF-κB), which is suppressed by artemisinin, tetrandrine, cannabidiol, and scutellarein (Watt and Karl, 2017; Qiang et al., 2018; Huang et al., 2019; Ren et al., 2021), and cyclooxygenase, which is impeded by geniposide (Liu et al., 2015b), are always involved in the control of proinflammatory cytokines and inflammatory responses to promote AD. Artemisinin reduces the expression of MyD88, a transducer in the proinflammatory pathway, to alleviate AD (Qiang et al., 2018). Artemisinin and geniposide suppress Toll-like receptor 4 (TLR4) to inhibit the NF-κB and MAPK signaling pathways to ameliorate AD (Liu W. et al., 2015; Qiang et al., 2018). Capsaicin restores the PI3K/AKT signaling pathway to treat T2D-induced AD, since damage to brain insulin signaling might cause AD (Xu et al., 2017). Cannabidiol inhibits S100 calcium-binding protein B (S100B), inducible nitric oxide synthase (iNOS) and glial fibrillary acidic protein (GFAP) to reduce reactive gliosis induced by Aβ (Watt and Karl, 2017).

Leonurine, salvianolic acid B, baicalin, geniposide, and ferulic acid (Zhang et al., 2016; Jia et al., 2017; Zhao Y. et al., 2018; Guo et al., 2019; Zheng et al., 2019) decrease the proinflammatory cytokines IL-1β and TNF-α or increase the antiinflammatory factors IL-10 and TGF-β to assuage depressive-like behavior. Leonurine and curcumin inhibit NF-κB (Jia et al., 2017; Fusar-Poli et al., 2020). Baicalin reduces TLR4 while augmenting the PI3K/AKT/FoxO1 pathway to mitigate depression (Guo et al., 2019). Icariin and curcumin decrease the level of corticotropin-releasing factor (CRF), a protein that leads to the release of cortisol and monoamine oxidase A and B and catalyzes the metabolism of norepinephrine, serotonin, and dopamine (Gu et al., 2017; Jin et al., 2019; Fusar-Poli et al., 2020). Icariin also restores the glucocorticoid receptor (GR) and serotonin 1A receptor levels, facilitating antidepressive behavior by improving HPA axis function (Jin et al., 2019). Baicalin and

ferulic acid increase the levels of synaptic proteins, including postsynaptic density protein 95 and synapsin I, which are inactivated in depressive patients (Liu et al., 2017; Lu et al., 2019).

In addition to leading to AD and depression, the proinflammatory process also contributes to TBI and secondary injuries. Ginsenoside Rb1, salvianolic acid B, and icariin directly decrease the levels of proinflammatory factors, such as IL-1β and TNF-α (Zhao J. et al., 2018; Fan et al., 2018; Jin et al., 2019). Tanshinone IIA suppresses p-NF-κB, p-p38MAPK and iNOS to mitigate SCP (Zhang X. et al., 2017). Ginsenoside Rb1 decreases iNOS, and evodiamine and icariin reduce NF-κB to treat cerebral injury (Zhao et al., 2014; Zhao J. et al., 2018; Jin et al., 2019). Icariin also inhibits the degradation of NF-κB light polypeptide gene enhancer in B-cells inhibitor alpha (IκB-α, an inhibitor of NF-κB), and increases peroxisome proliferator-activated receptor-alpha (PPARα) and peroxisome proliferator-activated receptor-gamma (PPARγ) to upregulate antiinflammatory cytokines and downregulate proinflammatory factors (Morotti et al., 2017; Jin et al., 2019). Leonurine upregulates Nrf-2, which improves oxidative stress in cerebral ischemic stroke and benefits brain tissues by increasing VEGF levels (Xie et al., 2019). Ginsenoside Rb1 inhibits high-mobility group box 1 (HMGB1), a proinflammatory mediator, to disrupt the inflammatory signals (Zhao Y. et al., 2018). Tanshinone IIA activats the PI3K/AKT/mTOR pathway to protect HT-22 cells from oxidative stress injury (Zhu et al., 2017). Ginsenoside Rb1 is neuroprotective against cerebral ischemia by activating the P-AKT/P-mTOR signaling pathway and inhibiting the P-PTEN protein, which is an inhibitor of the PI3K/AKT signaling pathway (Guo et al., 2018). Rutin boosts the levels of estrogen receptor alpha and beta (ERα and ERβ), which modulate the growth, survival and metabolism of cells by regulating downstream targets and activating the BDNF-TrkB and NGF-TrkA signaling pathways, to mitigate cerebral ischemia injury (Liu et al., 2018). Chlorogenic acid increases hypoxia-inducible factor alpha (HIF-1α), which is neuroprotective against cerebral ischemia reperfusion injury by regulating erythropoietin (EPO), VEGF, glucose transporter 1 (GLUT-1) and adrenomedullin (ADM) (Miao et al., 2017). Evodiamine upregulates pAkt and pGSK3β by activating the AKT/GSK signaling pathway to exert anti-inflammatory effects against cerebral ischemia (Zhao et al., 2014). Salvianolic acid B reduced GFAP, ionized calcium-binding adaptor molecule 1, and caspase-3 to suppress astrocyte activation, which diminishes brain cell apoptosis (Fan et al., 2018).

Regarding glioma treatment, Δ9-tetrahydrocannabinol binds to G protein-coupled cannabinoid receptors 1 and 2 (CB1, CB2) to stimulate MAPK and endoplasmic reticulum stress-related pathways to reduce tumor growth (Scott et al., 2014). Salvianolic acid B stimulated intracellular ROS production and eventually caused apoptotic cell death in glioma U87 cells (Wang et al., 2013). Flavokawain B activated the ATF4-DDIT3-TRIB3-AKT-mTOR-RPS6KB1 signaling pathway in human glioblastoma multiforme cells to promote autophagy in glioma cells (Wang J. et al., 2018).

Although some of the mechanisms of effects of NCMs on these diseases remain unclear, and animal experiments are mainly performed for these NCMs, they have shown remarkable impact on the mitigation and prevention of AD, depression, TBI and its following injuries, and glioma.

SOLUBILITY, PERMEABILITY AND STRUCTURAL PROPERTIES OF NMCS

NMC absorption is largely contingent on solubility and permeability. Usually, higher solubility and permeability results in better absorption (Zeng M. et al., 2017; Mo et al., 2018; Yang et al., 2020). The dose number (D_0) and oil-in-water partition coefficient (Log p) numerically represent the solubility and permeability, respectively. The D_0 and Log p of a drug determine its biopharmaceutical classification in the Biopharmaceuticals Classification System (BCS) (Yang et al., 2020).

Most NMCs belong to BCS II, III, or IV, which tend to include drugs with low solubility, permeability, or both (**Supplementary Table 2**) (Charalabidis et al., 2019). NMCs with relatively low solubility, such as some terpenes, alkaloids, acids and esters, vitamins, flavonoids and phenylpropanoids, belong to BCS II, while NMCs with low permeability, such as other alkaloids, flavonoids, glycosides and phenylpropanoids, belong to BCS III. In addition, flavonoids such as puerarin and glycosides such as icariin belong to BCS IV since they have low solubility/low permeability. Obviously, NMCs with limited absorption would lead to further consequences such as poor pharmacokinetic properties and metabolism. Suitable drug delivery systems for NMCs are required to fix this dilemma.

IMPROVED PHARMACOKINETICS AND BIOACTIVITY OF NMC DELIVERY SYSTEMS

The blood-brain barrier (BBB) helps to establish and maintain the microenvironment of the central nervous system (CNS) (Tsou et al., 2017; Liebner et al., 2018). The BBB only allows essential nutrients and certain molecules, such as O_2, CO_2, glucose and ethanol to enter (Tsou et al., 2017; Battaglia et al., 2018; Sharma et al., 2019). In the treatment of CNS diseases, it is a major challenge to make enough drug to across the BBB and achieve an effective concentration in the brain. NMC drug delivery systems (NMC-DDSs) have been developed to facilitate drug transport across the BBB and accumulation in the brain and to improve their efficacy in the CNS (**Tables 1**, **2**) (Auffinger et al., 2013; Battaglia et al., 2018). The main NMC-DDSs include exosomes, nanoparticles, liposomes, lipid polymer hybrid nanoparticles (LPHNPs), nanoemulsions, protein conjugation and nanosuspensions.

Exosomes are cell-derived nanovesicles (Kojima et al., 2018), currently considered to be specific secretory vesicles for intercellular communication (Milane et al., 2015). Exosomes can disrupt the intact BBB by transcytosis (Morad et al., 2019), easily penetrate the BBB and safely delivers therapeutic drugs (Zhu et al., 2019). In addition, exosomes might have

TABLE 1 | Characteristics of NMCs-DDS.

Drug	DDS	Administration route	Advantage	Main excipient	Preparation method	Characterization				References
						Particle size (nm)	Zeta potential (mV)	EE (%)	DL (%)	
Artemisinin	Nanostructured lipid carrier	—	Increase water solubility, site specificity, selective targeting, efficient penetration, glioma cell distribution and internalization, and effective delivery	Transferrin	Solvent evaporation method	145 ± 12.5	24.3 ± 1.5	82.3 ± 7.3	—	Emami et al. (2018)
Tanshinone IIA	Nanoparticle	i.v.	Prolong circulation time, increase plasma concentration, and have better brain delivery efficacy	Cationic albumin	Double emulsion/solvent evaporation method	122 ± 16	−17.8 ± 1.6	85.6 ± 3.2	5.86 ± 0.8	Liu et al. (2013)
	Nanoemulsion	i.v.	Prolong *in vitro* and vivo circulation time, and enhance the bioavailability	Tetramethylpyrazine	Shear stirring method	32.5	−2.78	95.26	—	Chen Y et al. (2019)
	Nanoparticle	i.v.	Better delivery efficacy	Cationic bovine serum albumin	Emulsification and solvent evaporation method	118 ± 14	−19.6 ± 1.4	83.2 ± 2.6	5.69 ± 0.6	Liu et al. (2013)
Capsaicin	Nanoparticle	i.v.	Be able to cross the blood-brain barrier and inhibit the growth of U251 cells	mPEG-PCL	Solvent diffusion method	121.3 ± 2.5	−9.1 ± 2.8	96 ± 5.1	9.4 ± 2.3	Jiang et al. (2015)
Salvianolic acid B	Nanoparticle	Brain injection	Sustain and prolong the *in vitro* release	Poly (ethyl-cyanoacrylate) coated with Tween 80	Emulsion polymerization method	288 ± 1.00	−8.38 ± 3.87	—	—	Grossi et al. (2017)
	Nanoparticle	Brain injection	Sustain and prolong the *in vitro* release	Poly (ethyl-cyanoacrylate)	Emulsion polymerization method	205 ± 2.00	−7.18 ± 2.84	98.70 ± 0.45	53.3 ± 0.24	Grossi et al. (2017)
Rutin	Lipid polymer hybrid nanoparticle	i.v.	Higher rutin bioavailability	Tween 80 coated PEG	Single-step nanoprecipitation technique	272.50 ± 3.39	−5.03 ± 0.18	64.32 ± 1.11	—	Ishak et al. (2017)
	Lipid polymer hybrid nanoparticle	i.v.	Higher rutin bioavailability	TPGS coated PEG	Single-step nanoprecipitation technique	203.00 ± 2.20	−2.52 ± 0.52	74.23 ± 2.14	—	Ishak et al. (2017)
	Lipid polymer hybrid nanoparticle	i.v.	Higher rutin bioavailability	Solutol HS 15 coated PEG	Single-step nanoprecipitation technique	232.4 ± 4.01	−1.76 ± 0.33	68.06 ± 1.50	—	Ishak et al. (2017)
	Nanoparticle	i.v.	Higher bioavailability; enhanced neurobehavioral activity, histopathology and reduced infarction volume effects	Chitosan	Ionic gelation method	92.28 ± 2.96	31.04 ± 1.91	84.98 ± 4.18	39.48 ± 3.16	Ahmad et al. (2016a)
Baicalin	Liposome	i.v.	Prolong the retention time *in vivo*, and increase the drug-concentration in the brain	—	Reverse evaporation method	160–190	−5.7	42 ± 1	—	Li et al. (2018)

(Continued on following page)

TABLE 1 | (*Continued*) Characteristics of NMCs-DDS.

Drug	DDS	Administration route	Advantage	Main excipient	Preparation method	Characterization				References
						Particle size (nm)	Zeta potential (mV)	EE (%)	DL (%)	
	Cationic solid lipid nanoparticle	i.v.	Improve uptake of Baicalin	OX26 antibody	Emulsion evaporation–solidification at low temperature method	47.68 ± 1.65	−0.533 ± 0.115	83.03 ± 0.01	2.90 ± 0.01	Liu et al. (2015b)
Curcumin	Nanosuspension	i.v.	Improve the biodistribution of curcumin in the brain	TPGS	Probe sonicator technique	199 ± 2.5	−15.2 ± 3.3	—	—	Dibaei et al. (2019)
	Nanosuspension	i.v.	Improve the biodistribution of curcumin in the brain	Tween 80	High-pressure homogenizer technique	193 ± 8	−12.9 ± 1.7	—	—	Dibaei et al. (2019)
	Nanoparticle	i.n.	Enhance bioavailability	PNIPAM	Free radical polymerization	92.46 ± 2.8	−16.2 ± 1.42	84.63 ± 4.2	39.31 ± 3.7	Ahmad et al. (2016b)
	Exosome	i.v.	Enhance solubility, bioavailability, and stability and increase drug penetration across the BBB	—	—	117.4 ± 10.5	−4.9	84.8	15.1	Wang H et al. (2019)
	Exosome	i.v.	Improve safety and efficiency	c (RGDyK) peptide	—	145	−26.1	—	—	Tian et al. (2018)
	Exosome	i.v.	Increase drug penetration across the BBB	Superparamagnetic iron oxide	—	122.7 ± 6.5	−24.1 ± 2.2	—	—	Jia et al. (2018)
Rhynchophylline	Nanoparticle	i.v.	Better solubility and bioavailability and prolong circulation time	mPEG-PLGA	Nanoprecipitation method	145.2	—	60	10.3	Xu et al. (2020)

Abbreviations: c(RGDyK) peptide, cyclo(Arg-Gly-Asp-D-Tyr-Lys) peptide; DL, drug loading; EE, encapsulation efficiency; i.n., intranasal injection; i.p., intraperitoneal injection; i.v., intravenous injection; mPEG-PCL, methoxy polyethylene glycol-poly(caprolactone); PNIPAM, ploly-N-isopropylacrylamide; Solutol HS 15, polyethylene glycol-15-hydroxy stearate; TPGS, D-a-Tocopherol polyethylene glycol 1000 succinate; Tween 80, polyethylene glycol sorbitan monooleate.
Note: — refers to not reported.

TABLE 2 | | Pharmacokinetic characteristics of NMC-DDS.

NMCs	Formulation	Administration route	Dosage (mg/kg)	Animal (number)	Pharmacokinetics parameters								References
					AUC_{0-t} (μg·h·ml^{-1})	$AUC_{0-\infty}$ (μg·h·ml^{-1})	C_{max} (μg·ml^{-1})	T_{max} (h)	$t_{1/2}$ (h)	MRT_{0-t} (h)	$MRT_{0-\infty}$ (h)	Cl (L/h·kg)	
Tanshinone IIA	Nanoparticle	i.v.	10	Rats (6)	—	4.83 ± 0.49	—	0.54	8.29 ± 1.37	—	7.96 ± 0.68	0.31 ± 0.06	Liu et al. (2013)
	Nanoemulsion	i.v.	5	Rats (6)	4.55 (0–6 h)	8.03	3.52 ± 0.75	—	5.77	1.96 (0–6 h)	7.35	—	Chen Y et al. (2019)
	Nanoparticle	i.v.	10	Rats (10)	—	4.71 ± 0.58	—	—	8.17 ± 1.28	—	7.89 ± 0.74	0.28 ± 0.05	Liu et al. (2013)
Capsaicin	Nanoparticle	i.v.	—	—	—	—	—	—	—	—	—	—	Jiang et al. (2015)
Salvianolic acid B	Nanoparticle	i.p.	—	—	—	—	—	—	—	—	—	—	Grossi et al. (2017)
	Nanoparticle	i.p.	—	—	—	—	—	—	—	—	—	—	Grossi et al. (2017)
Rutin	Tween 80-lipid polymer hybrid nanoparticle	i.v.	5	Rats (6)	1.14 ± 0.27[a] (0–48 h)	1.59 ± 0.56[a]	0.57 ± 0.13[b]	0.25 ± 0.00	—	—	4.41 ± 1.18	—	Ishak et al. (2017)
	TPGS-lipid polymer hybrid nanoparticle	i.v.	5	Rats (6)	1.11 ± 0.31[a] (0–48 h)	1.80 ± 0.41[a]	0.67 ± 0.34[b]	1.17 ± 0.42	—	—	6.26 ± 4.25	—	Ishak et al. (2017)
	Solutol HS 15-lipid polymer hybrid nanoparticle	i.v.	5	Rats (6)	1.31 ± 0.53[a] (0–48 h)	1.50 ± 0.47[a]	0.66 ± 0.33[b]	1.17 ± 0.44	—	—	3.52 ± 0.78	—	Ishak et al. (2017)
	Nanoparticle	i.n.	10	Rats (6)	0.35 (0–24 h)	—	1.45	2.00	43.68 ± 11.63	—	—	—	Ahmad et al. (2016a)
	Nanoparticle	i.v.	10	Rats (6)	8.50 E-02 (0–24 h)	—	0.39	2.00	39.01 ± 7.41	—	—	—	Ahmad et al. (2016b)
Baicalin	Liposome	i.v.	18	Rats (5)	88.27 (0–8 h)	103.61	52.48 ± 8.18	—	3.17	2.33 (0–6 h)	3.84	2.91 ± 0.25[c]	Li et al. (2018)
	Cationic solid lipid nanoparticle	i.v.	4.42	Rats (3)	—	2.68E-02	2.32E-02	0.94 ± 0.43	—	—	—	—	Liu et al. (2015b)
Curcumin	TPGS-nanosuspension	i.v.	10	Rats (6)	0.89 (0–6 h)	0.96	1.12	0.50	1.45 ± 0.180	0.61 ± 0.050 (0–6 h)	—	0.011 ± 0.001[d]	Dibaei et al. (2019)
	Tween 80-nanosuspension	i.v.	10	Rats (6)	1.79 (0–6 h)	1.87	1.31	0.75	1.94 ± 0.292	0.76 ± 0.194 (0–6 h)	—	0.006 ± 0.001[d]	Dibaei et al. (2019)
	PNIPAM- Nanoparticle	i.n.	0.1	Rats (6)	2.43[e] (0–24 h)	—	2.36 E-03	1.00	7.70	—	—	—	Ahmad et al. (2016a)
	Exosome	i.v.	0.4	Rats (3)	9.03 (0–24 h)	—	0.91	—	9.02	—	—	3.67 E-02	Wang X et al. (2019)
	cRGD-Exosome	i.v.	—	—	—	—	—	—	—	—	—	—	Tian et al. (2018)
	RGE-Exosome-SPION	i.v.	—	—	—	—	—	—	—	—	—	—	Jia et al. (2018)
Rhynchophylline	Tween 80- Nanoparticle	i.v.	1	Rats (6)	—	0.41	0.67	—	1.48	—	—	1.94	Xu et al. (2020)

Abbreviations: cRGD, cyclo(Arg-Gly-Asp-D-Tyr-Lys)-conjugated; i.n., intranasal injection; i.p., intraperitoneal injection; i.v., intravenous injection; PNIPAM, ploly-N-isopropylacrylamide; RGE, neuropilin-1-targeted peptide; Solutol HS 15, polyethylene glycol-15-hydroxy stearate; SPION, superparamagnetic iron oxide nanoparticles; TPGS, D-a-Tocopherol polyethylene glycol 1000 succinate; Tween 80, polyethylene glycol sorbitan monooleate.

Note: — refers to data not reported.

[a] *mg·g^{-1}·h.*

[b] *mg·g^{-1}.*

[c] *ml/(min·kg).*

[d] *(mg/kg)/(ng/ml)/h.*

[e] *(ng·min/ml).*

targeting capabilities after cell source selection and membrane modification (Zhu et al., 2019). Curcumin-primed exosomes secreted by mouse macrophage cells were fabricated to prevent neuronal death and alleviate AD symptoms (Wang H. et al., 2019). Curcumin-primed exosomes led to curcumin acumination 6.5 times higher than that of free curcumin in the brain, 2.5 times higher in the liver and 2.0 times higher in the lung (Wang X et al., 2019). Curcumin and superparamagnetic iron oxide nanoparticles were loaded into exosomes and conjugated with neuropilin-1-targeted peptide by click chemistry to obtain glioma-targeting exosomes with imaging and therapeutic functions (Jia et al., 2018). Compared with free exosomes, target ligand-modified exosomes markedly improved the brain targeting and circulation time of curcumin in the body (Jia et al., 2018). A functional ligand, (cyclo (Arg-Gly-Asp-D-Tyr-Lys) peptide, was conjugated with the bioorthogonal copper-free azide alkyne cyclo-addition (click chemistry) method to form mesenchymal stromal cell-derived exosomes to deliver curcumin to the brain (Tian et al., 2018).

The mechanism by which nanoparticles penetrate the BBB is still not very clear. Currently, the relative theories are listed as follows (Morad et al., 2019; Akel et al., 2021; Alotaibi et al., 2021; Han and Jiang, 2021; Hou et al., 2022): 1) The phagocytosis of nanoparticles by cerebral vascular endothelial cells allows the drug to be released and diffused into the brain; 2) The adsorption of capillary walls prolongs the residence time of drugs in the brain, thereby increases the amount of drugs entering the brain; 3) Nanoparticles open the tight junctions of capillary epithelial cells, and drugs penetrate into the brain from the open gaps; 4) The effect of some modifications of nanoparticles such as polysorbate 80, can efficiently inhibit the efflux pump p-gp glycoprotein. Rutin-encapsulated chitosan nanoparticles were fabricated via an ionic gelation method. After nasal administration, the C_{max}, $t_{1/2}$ and *AUC* in the brain of these nanoparticles were 6-, 1- and 7.3-fold higher than those of free rutin, respectively, the drug targeting efficiency increased by 2.3-fold, and the therapeutic effect increased accordingly (Ahmad et al., 2016b). Poly-N-isopropylacrylamide nanoparticles containing curcumin, demethoxycurcumin and bisdemethoxycurcumin were prepared by free radical polymerization. These nanoparticles increased the C_{max}, $t_{1/2}$ and *AUC* of the three drugs in the brain by approximately 4-, 9- and 5-fold, respectively (Ahmad et al., 2016a). A biodegradable methoxy polyethylene glycol-poly (caprolactone) amphiphilic block copolymer was used to prepare nanoparticle-loaded capsaicin for targeted treatment of glioma. These nanoparticle s had satisfactory slow-release features (Jiang et al., 2015). Rhynchophylline-loaded methoxy poly (ethylene glycol)-poly (DL-lactide-co-glycolic acid) nanoparticles coupled with Tween 80 were used for brain-targeted delivery (Xu et al., 2020).

Liposomes are nontoxic and have good biocompatibility and biodegradability (Pattni et al., 2015). Their phospholipid bilayer structure made them compatible with the lipid layer of the BBB and helped the drug enter the brain (Pattni et al., 2015; Agrawal et al., 2017). In addition, liposomes can be modified with different substances to achieve the ability to cross the BBB. By attaching lipid molecules to neurotransmitters, the resulting neurotransmitter lipidoids can be incorporated into drug-encapsulating liposomes, and give the liposomes ability to penetrate the BBB (Ma et al., 2020). There are various apolipoproteins in plasma that can cross the BBB, and one of the clearance mechanisms of Aβ protein in the brain is through the lipid binding of various apolipoproteins (such as ApoE, ApoA1 and ApoJ). When the receptor-binding region is exposed, it is mediated by the corresponding receptor on the BBB to the periphery. Because the related receptors can be transported in both directions, the peripheral ligands can also be transported to the brain, so that the drug can be transported to the brain to play a role (Zhang et al., 2019). Liposomes improved the lipophilicity of baicalin and further improved its pharmacokinetics in the brain. The C_{max} and *AUC* values of MCAO rats administered with baicalin-loaded liposomes were significantly greater than those of rats administered with baicalin; moreover, the *MRT* increased 2.14-fold, the $t_{1/2}$ increased 2.87-fold, and the renal clearance rate decreased 8.08-fold. The pharmacokinetic parameter improvements led to prolonged retention time and enhanced therapeutic efficacy (Li et al., 2018).

LPHNPs are highly scalable, biodegradable nanocarriers composed of a layer of lipid-coated polymeric cores (polylactic-co-glycolic acid, polyglutamic acid, polylysine, PEG, etc.) (Dehaini et al., 2016; Ishak et al., 2017; Mukherjee et al., 2019). LPHNPs combined with liposomes and nanoparticles have advantages. Rutin delivered by LPHNPs coated with three surfactants, Tween 80, D-α-tocopheryl polyethylene glycol 1000 succinate (TPGS) and Soluted H55 had 160-, 98- and 159-fold higher bioavailability than free rutin, respectively (Ishak et al., 2017).

Nanoemulsions are nanosized droplets with high surface areas (Espinoza et al., 2019), so they have been used to solve drug solubility and stability problems (Bonferoni et al., 2017). The nanoemulsion mainly delivers drugs to the brain by adding excipients that increase BBB permeability or inhibit efflux proteins. The oil-in-water nanoemulsions for codelivery of tanshinone IIA and tetramethylpyrazine had the ability to pass through the BBB and target the brain. The *AUC*s of tanshinone IIA/tetramethylpyrazine or tanshinone IIA nanoemulsions were 6.98- and 5.83-fold higher than those of tanshinone IIA solution, respectively. The MRTs of two formers (117.68 and 123.29 min) were much longer than the latter (56.66 min). The $t_{1/2}$ of the two nanoemulsions were 7.8- and 6.48-fold longer than that of the solution (Chen Z. et al., 2019). The resveratrol nanoemulsion was prepared by adding non-ionic surfactants Pluronic and Cremophor EL as emulsifier. The nanoemulsion was administered through nose to target the brain for AD treatment. The nanoemulsion increased the intracranial concentration of resveratrol by ~87% and the AUC value by ~92% (Kotta et al., 2021).

Proteins such as specific receptors (e.g., transferrin receptor) (Emami et al., 2018; Johnsen et al., 2018) and transporters expressed on the luminal side of brain endothelial cells help drugs cross the BBB through receptor-mediated endocytosis (Zuchero et al., 2016; Johnsen et al., 2018). Transferrin-coupled nanoliposomes were prepared to deliver artemisinin to the brain in a targeted manner (Emami et al., 2018). OX26

monoclonal antibody-conjugated cationic solid lipid nanoparticles were fabricated to improve baicalin distribution within the brain. The *AUC* and C_{max} values of baicalin nanoparticles were 11.08- and 7.88-fold higher than those of baicalin solution, respectively (Liu et al., 2015). Bovine serum albumin-conjugated cationic PEGylated nanoparticles containing tanshinone IIA had a 3.4-, 2.95- and 2.37-fold higher *AUC*, $t_{1/2}$ and MRT than free tanshinone IIA, respectively (Liu et al., 2013).

Tween 80 and TPGS were separately used to coat on the surface of curcumin nanosuspensions by physical adsorption using a high-pressure homogenizer and a probe sonicator. The curcumin delivered by the nanosuspensions had almost 2-fold higher bioavailability than free curcumin (Dibaei et al., 2019).

METABOLIC PATHWAY AND METABOLIC ENZYMES

It is vital to review the reactions and metabolites of NMCs (**Supplementary Table 3**). Most NMs are metabolized through chemical reactions by enzymes, which can cause them to become more active, less active, inactive, innocuous, or even noxious (Mo et al., 2018). Sometimes multiple metabolites are formed simultaneously, further experiments for the metabolism of NCMs are still needed.

In NMC metabolism, phase I reactions are involved in oxidation, reduction, and hydrolysis and are mediated by enzymes such as cytochrome P450 enzymes. Nonpolar functional groups on NMCs are changed into polar molecules (Iyanagi, 2007). Reactions in phase I include the followied chemical reaction (**Eq. 1**):

$$O_2 + NADPH + H^+ + RH \rightarrow NADP^+ + H_2O + ROH \quad (1)$$

Oxidation reactions result in the addition of oxygen or the removal of hydrogen and encompass hydroxylation, dehydrogenation, and demethylation, among which hydroxylation is the most common reaction. Hydroxylation involves the addition of hydroxyl groups to aromatics, alkanes, or cycloalkanes. In the case of tanshinone IIA, two hydroxyl groups are directly added to the parent drug molecule, and the metabolite has been shown to be favorable in treating AD (Liang et al., 2019). Under catalysis by the metabolic enzyme CYP3A4, Δ9-tetrahydrocannabinol is oxidized to 8α (or β)-OH-Δ9-tetrahydrocannabinol, and further oxidized to 8-keto-Δ9-tetrahydrocannabinol (Dinis-Oliveira, 2016). The alkyl side chain of capsaicin is oxidized to a hydroxyl chain (Rollyson et al., 2014). Each phenyl group of evodiamine is oxidized to hydroxyl groups (Wang Y. et al., 2018). The metabolic enzymes CYP3A4 and CYP2E1 are the primary enzymes that hydroxylate butylphthalide (Diao et al., 2013; Diao et al., 2015). Additionally, dehydrogenation of hydroxyl groups to carbonyl groups or alkyl groups to alkenyl groups is found in NMC metabolism. The hydroxyl group on the cyclohexane of cholic acid is dehydrogenated to a carbonyl group by the enzyme CYP3A4 (Funabashi et al., 2020); the hydroxyl side chain of vitamin A is oxidized to a carbonyl group (Libien et al., 2017), and vitamin A was oxidized to all-trans-retinoic acid by retinal dehydrogenases (Clugston and Blaner, 2014). Leonurine is demethylated, which converts the methoxy group to a hydroxyl group (Zhu et al., 2014). Conversely, the addition of hydrogen or the removal of oxygen results in increased reduction reactions. Hydrogenation occurs to salvianolic acid B and ferulic acid when a double carbon is broken due to the addition of hydrogen (Wang et al., 2016; Zhang et al., 2022). Dehydroxylation entails the removal of hydroxyl groups, to further reduce the reduced metabolites of Salvianolic acid B (Zhang et al., 2022). The alkenyl group of ferulic acid is reduced to an alkyl group (Zhao et al., 2015); oxymatrine is reduced by CYP3A4 to matrine (Liu et al., 2015b). In hydrolysis, when reacting with water, compound bonds are broken to produce two compounds: one is bound with hydrogen cleaved from water molecules, and the other is bound with hydroxide. Ginsenoside Rb1 and Rd and puerarin are deglycosylated to lose one or two glucose molecules (Shang et al., 2017; Zhang et al., 2021); baicalin undergoes deglycosylation to form baicalein (Wang et al., 2017). Capsaicin is hydrolyzed to vanillylamine in the liver and skin (Rollyson et al., 2014); rutin undergoes hydrolysis to form metabolites such as quercetin and 3,4-dihydroxytoluene, 3,4-dihydroxyphenylacetic acid and 3,4-dihydroxybenzoic acid (Morales et al., 2018); and chlorogenic acid is hydrolyzed into caffeic acid and quinic acid by esterase (Choi et al., 2018). Geniposide is hydrolyzed to genipin through β-glucuronidase (Zhang W. et al., 2017).

In phase II reactions, NMCs undergo conjugation reactions, including glucuronidation, glycosylation, methylation, sulfonation, sulfation, cysteine conjugation, glucuronide conjugation and glucopyranoside conjugation, through metabolic enzymes such as UDP-glucuronosyltransferases (UGTs), sulfotransferases (SULTs), glutathione S-transferases (GSTs) (Iyanagi, 2007). Tanshinone IIA, geniposide, Δ9-tetrahydrocannabinol and puerarin undergo glucuronidation, which attaches a glucuronide (Dinis-Oliveira, 2016; Zhang X. et al., 2017; Shang et al., 2017; Liang et al., 2019). Salvianolic acid B, rutin, scutellarein, baicalin and puerarin are conjugated with methyl groups via methyltransferase (Shi et al., 2015; Gimenez-Bastida et al., 2017; Shang et al., 2017; Wang et al., 2017; Zhang et al., 2022). Leonurine, geniposide, and puerarin undergo sulfonation by SULTs (Zhu et al., 2014; Zhang W. et al., 2017; Shang et al., 2017); ferulic acid also needs SULTs to undergo sulfation (Wang et al., 2016). Conjugation of glucuronide to evodiamine (Wang C. et al., 2018) or glucopyranoside to baicalin (Wang et al., 2017) also occurs in phase II reactions.

CONCLUSION AND FUTURE PROSPECT

NMCs have appealing benefits as cerebral disease-treating drugs due to their effects on the metabolism of neurotransmitters, hormones, neurotrophic molecules, and other brain-specific chemicals in addition to their low cost, low toxicity, and obvious efficacy. Although the bioavailability/absorption of most NMCs is unsatisfactory, appropriate delivery systems

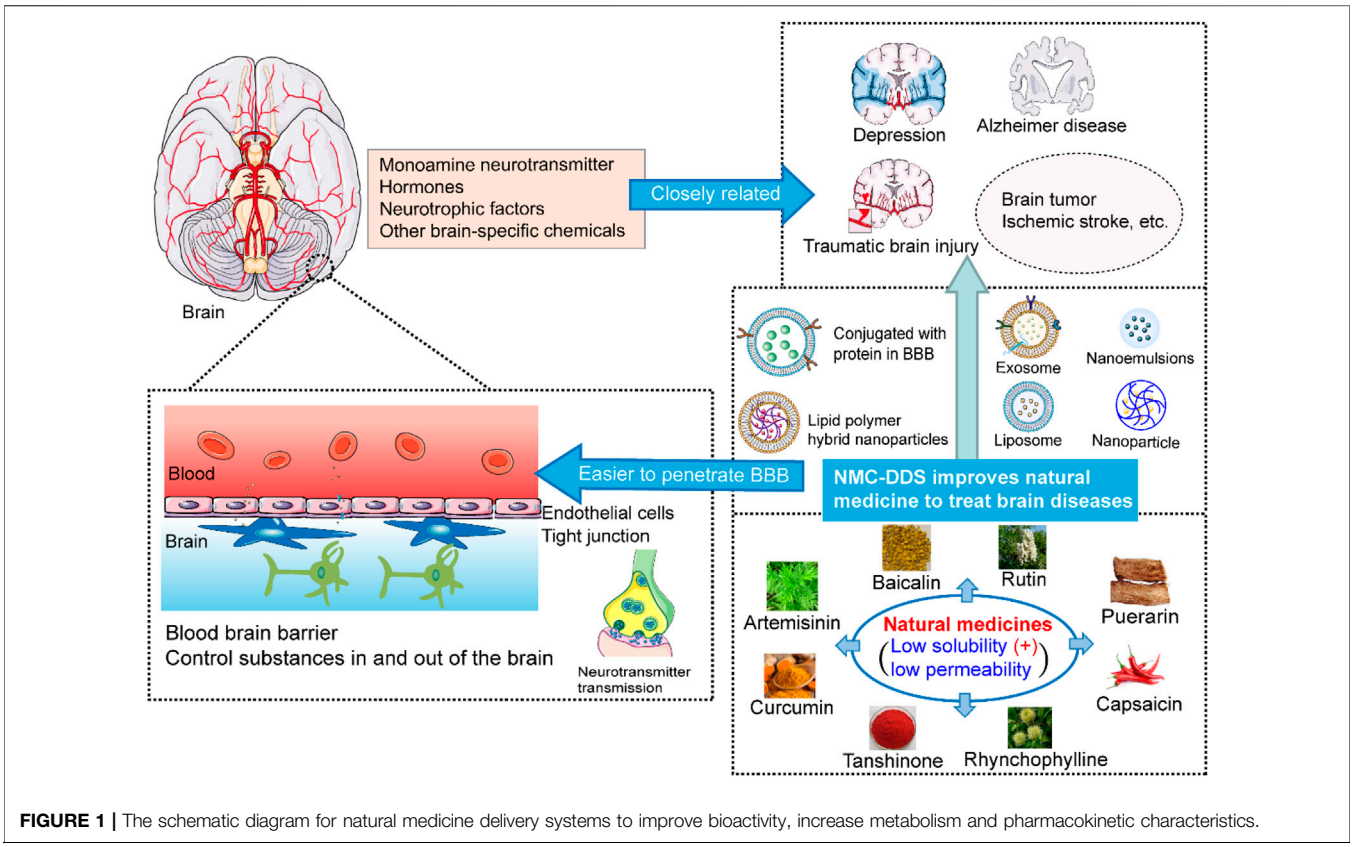

FIGURE 1 | The schematic diagram for natural medicine delivery systems to improve bioactivity, increase metabolism and pharmacokinetic characteristics.

such as novel nanosystems including exosomes, nanoparticles, LPHNPs, nanoemulsions, protein conjugation and nanosuspensions, provide better pharmacological and pharmacokinetic characteristics for NMCs. In addition, the structure-based metabolic reactions of NMCs, which produce more active, less active, inactive, innocuous, or even noxious metabolites, alter the pharmacological activities of NMCs (**Figure 1**). NMCs commonly undergo oxidation, reduction, hydrolysis and conjugation reactions, and metabolic enzymes such as cytochrome P450 enzymes, UGTs, and SULTs are needed in some cases. However, the metabolism and pharmacokinetics data for NMCs are still very limited.

In order to achieve clinical transformation of NMCs and overcome the key challenges ahead, the scientists may focus on the formulation prescription, industrial preparation, stability investigation and toxicity evaluation in the future. Since most of the current pharmacokinetic/pharmacological studies are based on animal experiments, more clinical evidence is needed for further application. NMCs are effective in cerebral-related disorders. They are strong candidates for clinical therapy of cerebral diseases. There have been some progress by now. GV-971 is a sodium oligomannate, which is derived from marine algae. GV-971 was first approved in China for marketing as a drug to mitigate AD. GV-971 (Syed, 2020) inhibits Aβ accumulation and decreases Aβ aggregates toxicity (Wang et al., 2020). Also, in support of the theory of the association between gut dysbiosis and AD, GV-971 ameliorates gut dysbiosis and suppresses neuroinflammation to improve cognition in AD (Wang H et al., 2019). Although debates exist about this drug, it is expected to have good prospects due to the safety and tolerance data obtained from phase III clinical trial evidence (Wang et al., 2020).

AUTHOR CONTRIBUTIONS

JX, CZ, TW, DH, JY and ZY reviewed the literature and drafted the article. LL and JZ conceived, supervised and revised the article. All authors approved the final version.

FUNDING

This work was partially supported by grants from National Natural Science Foundation of China (30973645), Chongqing Association of Science and Technology (2020-11), Chongqing Education Committee (CYS20212).

SUPPLEMENTARY MATERIAL

The Supplementary Material for this article can be found online at: https://www.frontiersin.org/articles/10.3389/fphar.2022.937075/full#supplementary-material

REFERENCES

Agrawal, M., AjazuddinTripathi, D. K., Tripathi, D. K., Saraf, S., Saraf, S., Antimisiaris, S. G., et al. (2017). Recent Advancements in Liposomes Targeting Strategies to Cross Blood-Brain Barrier (Bbb) for the Treatment of Alzheimer's Disease. *J. Control Release* 260, 61–77. doi:10.1016/j.jconrel.2017.05.019

Ahmad, N., Ahmad, I., Umar, S., Iqbal, Z., Samim, M., and Ahmad, F. J. (2016a). Pnipam Nanoparticles for Targeted and Enhanced Nose-To-Brain Delivery of Curcuminoids: Uplc/Esi-Q-Tof-Ms/Ms-Based Pharmacokinetics and Pharmacodynamic Evaluation in Cerebral Ischemia Model. *Drug Deliv.* 23 (7), 2095–2114. doi:10.3109/10717544.2014.941076

Ahmad, N., Ahmad, R., Naqvi, A. A., Alam, M. A., Ashafaq, M., Samim, M., et al. (2016b). Rutin-Encapsulated Chitosan Nanoparticles Targeted to the Brain in the Treatment of Cerebral Ischemia. *Int. J. Biol. Macromol.* 91, 640–655. doi:10.1016/j.ijbiomac.2016.06.001

Akel, H., Csóka, I., Ambrus, R., Bocsik, A., Gróf, I., Mészáros, M., et al. (2021). *In Vitro* Comparative Study of Solid Lipid and Plga Nanoparticles Designed to Facilitate Nose-To-Brain Delivery of Insulin. *Int. J. Mol. Sci.* 22 (24), 13258. doi:10.3390/ijms222413258

Alotaibi, B. S., Buabeid, M., Ibrahim, N. A., Kharaba, Z. J., Ijaz, M., Noreen, S., et al. (2021). Potential of Nanocarrier-Based Drug Delivery Systems for Brain Targeting: A Current Review of Literature. *Int. J. Nanomedicine* 16, 7517–7533. doi:10.2147/IJN.S333657

Angeloni, C., Barbalace, M. C., and Hrelia, S. (2019). Icariin and its Metabolites as Potential Protective Phytochemicals against Alzheimer's Disease. *Front. Pharmacol.* 10, 271. doi:10.3389/fphar.2019.00271

Anjum, K., Shagufta, B. I., Abbas, S. Q., Patel, S., Khan, I., Shah, S. A. A., et al. (2017). Current Status and Future Therapeutic Perspectives of Glioblastoma Multiforme (Gbm) Therapy: A Review. *Biomed. Pharmacother.* 92, 681–689. doi:10.1016/j.biopha.2017.05.125

Asiimwe, N., Yeo, S. G., Kim, M. S., Jung, J., and Jeong, N. Y. (2016). Nitric Oxide: Exploring the Contextual Link with Alzheimer's Disease. *Oxid. Med. Cell Longev.* 2016, 7205747–7205810. doi:10.1155/2016/7205747

Auffinger, B., Morshed, R., Tobias, A., Cheng, Y., Ahmed, A. U., and Lesniak, M. S. (2013). Drug-Loaded Nanoparticle Systems and Adult Stem Cells: A Potential Marriage for the Treatment of Malignant Glioma? *Oncotarget* 4 (3), 378–396. doi:10.18632/oncotarget.937

Battaglia, L., Panciani, P. P., Muntoni, E., Capucchio, M. T., Biasibetti, E., De Bonis, P., et al. (2018). Lipid Nanoparticles for Intranasal Administration: Application to Nose-To-Brain Delivery. *Expert Opin. Drug Deliv.* 15 (4), 369–378. doi:10.1080/17425247.2018.1429401

Bilmin, K., Kujawska, T., and Grieb, P. (2019). Sonodynamic Therapy for Gliomas. Perspectives and Prospects of Selective Sonosensitization of Glioma Cells. *Cells* 8 (11), 1428. doi:10.3390/cells8111428

Bonferoni, M. C., Sandri, G., Rossi, S., Usai, D., Liakos, I., Garzoni, A., et al. (2017). A Novel Ionic Amphiphilic Chitosan Derivative as a Stabilizer of Nanoemulsions: Improvement of Antimicrobial Activity of Cymbopogon Citratus Essential Oil. *Colloids Surf. B Biointerfaces* 152, 385–392. doi:10.1016/j.colsurfb.2017.01.043

Boshtam, M., Asgary, S., Kouhpayeh, S., Shariati, L., and Khanahmad, H. (2017). Aptamers against Pro- and Anti-inflammatory Cytokines: A Review. *Inflammation* 40 (1), 340–349. doi:10.1007/s10753-016-0477-1

Cabello-Verrugio, C. (2018). Role of Transforming Growth Factor Family of Peptides in Health and Diseases. *Curr. Protein Pept. Sci.* 19 (12), 1136–1137. doi:10.2174/1389203719121809261252 39

Charalabidis, A., Sfouni, M., Bergström, C., and Macheras, P. (2019). The Biopharmaceutics Classification System (Bcs) and the Biopharmaceutics Drug Disposition Classification System (Bddcs): Beyond Guidelines. *Int. J. Pharm.* 566, 264–281. doi:10.1016/j.ijpharm.2019.05.041

Chen, Y., Qi, Z., Qiao, B., Lv, Z., Hao, Y., and Li, H. (2019). Oxymatrine Can Attenuate Pathological Deficits of Alzheimer's Disease Mice through Regulation of Neuroinflammation. *J. Neuroimmunol.* 334, 576978. doi:10.1016/j.jneuroim.2019.576978

Chen, Z., Wang, Z., and Gu, Z. (2019). Bioinspired and Biomimetic Nanomedicines. *Acc. Chem. Res.* 52 (5), 1255–1264. doi:10.1021/acs.accounts.9b00079

Choi, W. G., Kim, J. H., Kim, D. K., Lee, Y., Yoo, J. S., Shin, D. H., et al. (2018). Simultaneous Determination of Chlorogenic Acid Isomers and Metabolites in Rat Plasma Using Lc-Ms/Ms and its Application to a Pharmacokinetic Study Following Oral Administration of Stauntonia Hexaphylla Leaf Extract (Yra-1909) to Rats. *Pharmaceutics* 10 (3), 143. doi:10.3390/pharmaceutics10030143

Clugston, R. D., and Blaner, W. S. (2014). Vitamin a (Retinoid) Metabolism and Actions: What We Know and what We Need to Know about Amphibians. *Zoo. Biol.* 33 (6), 527–535. doi:10.1002/zoo.21140

Corriger, A., and Pickering, G. (2019). Ketamine and Depression: A Narrative Review. *Drug Des. Devel Ther.* 13, 3051–3067. doi:10.2147/DDDT.S221437

Dehaini, D., Fang, R. H., Luk, B. T., Pang, Z., Hu, C. M., Kroll, A. V., et al. (2016). Ultra-Small Lipid-Polymer Hybrid Nanoparticles for Tumor-Penetrating Drug Delivery. *Nanoscale* 8 (30), 14411–14419. doi:10.1039/c6nr04091h

Diao, X., Deng, P., Xie, C., Li, X., Zhong, D., Zhang, Y., et al. (2013). Metabolism and Pharmacokinetics of 3-N-Butylphthalide (Nbp) in Humans: The Role of Cytochrome P450s and Alcohol Dehydrogenase in Biotransformation. *Drug Metab. Dispos.* 41 (2), 430–444. doi:10.1124/dmd.112.049684

Diao, X. X., Zhong, K., Li, X. L., Zhong, D. F., and Chen, X. Y. (2015). Isomer-Selective Distribution of 3-N-Butylphthalide (Nbp) Hydroxylated Metabolites, 3-Hydroxy-Nbp and 10-Hydroxy-Nbp, across the Rat Blood-Brain Barrier. *Acta Pharmacol. Sin.* 36 (12), 1520–1527. doi:10.1038/aps.2015.64

Dibaei, M., Rouini, M. R., Sheikholeslami, B., Gholami, M., and Dinarvand, R. (2019). The Effect of Surface Treatment on the Brain Delivery of Curcumin Nanosuspension: *In Vitro* and *In Vivo* Studies. *Int. J. Nanomedicine* 14, 5477–5490. doi:10.2147/IJN.S199624

Dinis-Oliveira, R. J. (2016). Metabolomics of Δ9-tetrahydrocannabinol: Implications in Toxicity. *Drug Metab. Rev.* 48 (1), 80–87. doi:10.3109/03602532.2015.1137307

Emami, J., Yousefian, H., and Sadeghi, H. (2018). Targeted Nanostructured Lipid Carrier for Brain Delivery of Artemisinin: Design, Preparation, Characterization, Optimization and Cell Toxicity. *J. Pharm. Pharm. Sci.* 21 (1s), 225s–241s. doi:10.18433/jpps30117

Enslin, J. M. N., Rohlwink, U. K., and Figaji, A. (2020). Management of Spasticity after Traumatic Brain Injury in Children. *Front. Neurol.* 11, 126. doi:10.3389/fneur.2020.00126

Espinoza, L. C., Silva-Abreu, M., Clares, B., Rodríguez-Lagunas, M. J., Halbaut, L., Cañas, M. A., et al. (2019). Formulation Strategies to Improve Nose-To-Brain Delivery of Donepezil. *Pharmaceutics* 11 (2), 64. doi:10.3390/pharmaceutics11020064

Fan, Y., Luo, Q., Wei, J., Lin, R., Lin, L., Li, Y., et al. (2018). Mechanism of Salvianolic Acid B Neuroprotection against Ischemia/Reperfusion Induced Cerebral Injury. *Brain Res.* 1679, 125–133. doi:10.1016/j.brainres.2017.11.027

Fu, W. Y., Hung, K. W., Lau, S. F., Butt, B., Yuen, V. W., Fu, G., et al. (2021). Rhynchophylline Administration Ameliorates Amyloid-β Pathology and Inflammation in an Alzheimer's Disease Transgenic Mouse Model. *ACS Chem. Neurosci.* 12 (22), 4249–4256. doi:10.1021/acschemneuro.1c00600

Funabashi, M., Grove, T. L., Wang, M., Varma, Y., McFadden, M. E., Brown, L. C., et al. (2020). A Metabolic Pathway for Bile Acid Dehydroxylation by the Gut Microbiome. *Nature* 582 (7813), 566–570. doi:10.1038/s41586-020-2396-4

Fusar-Poli, L., Vozza, L., Gabbiadini, A., Vanella, A., Concas, I., Tinacci, S., et al. (2020). Curcumin for Depression: A Meta-Analysis. *Crit. Rev. Food Sci. Nutr.* 60 (15), 2643–2653. doi:10.1080/10408398.2019.1653260

Garofalo, S., Grimaldi, A., Chece, G., Porzia, A., Morrone, S., Mainiero, F., et al. (2017). The Glycoside Oleandrin Reduces Glioma Growth with Direct and Indirect Effects on Tumor Cells. *J. Neurosci.* 37 (14), 3926–3939. doi:10.1523/jneurosci.2296-16.2017

Giménez-Bastida, J. A., Zielinski, H., Piskula, M., Zielinska, D., and Szawara-Nowak, D. (2017). Buckwheat Bioactive Compounds, Their Derived Phenolic Metabolites and Their Health Benefits. *Mol. Nutr. Food Res.* 61 (7), 1600475. doi:10.1002/mnfr.201600475

Graf, W. D., Kekatpure, M. V., and Kosofsky, B. E. (2013). Prenatal-Onset Neurodevelopmental Disorders Secondary to Toxins, Nutritional Deficiencies, and Maternal Illness. *Handb. Clin. Neurol.* 111, 143–159. doi:10.1016/B978-0-444-52891-9.00014-2

Grossi, C., Guccione, C., Isacchi, B., Bergonzi, M. C., Luccarini, I., Casamenti, F., et al. (2017). Development of Blood-Brain Barrier Permeable Nanoparticles as Potential Carriers for Salvianolic Acid B to Cns. *Planta Med.* 83 (5), 382–391. doi:10.1055/s-0042-101945

Gu, F., Chauhan, V., and Chauhan, A. (2017). Monoamine Oxidase-A and B Activities in the Cerebellum and Frontal Cortex of Children and Young Adults with Autism. *J. Neurosci. Res.* 95 (10), 1965–1972. doi:10.1002/jnr.24027

Guo, L. T., Wang, S. Q., Su, J., Xu, L. X., Ji, Z. Y., Zhang, R. Y., et al. (2019). Baicalin Ameliorates Neuroinflammation-Induced Depressive-like Behavior through Inhibition of Toll-like Receptor 4 Expression via the Pi3k/Akt/Foxo1 Pathway. *J. Neuroinflammation* 16 (1), 95. doi:10.1186/s12974-019-1474-8

Guo, Y., Wang, L. P., Li, C., Xiong, Y. X., Yan, Y. T., Zhao, L. Q., et al. (2018). Effects of Ginsenoside Rb1 on Expressions of Phosphorylation Akt/Phosphorylation Mtor/Phosphorylation Pten in Artificial Abnormal Hippocampal Microenvironment in Rats. *Neurochem. Res.* 43 (10), 1927–1937. doi:10.1007/s11064-018-2612-x

Han, L., and Jiang, C. (2021). Evolution of Blood-Brain Barrier in Brain Diseases and Related Systemic Nanoscale Brain-Targeting Drug Delivery Strategies. *Acta Pharm. Sin. B* 11 (8), 2306–2325. doi:10.1016/j.apsb.2020.11.023

He, Q., Liu, J., Lan, J. S., Ding, J., Sun, Y., Fang, Y., et al. (2018). Coumarin-Dithiocarbamate Hybrids as Novel Multitarget Ache and Mao-B Inhibitors against Alzheimer's Disease: Design, Synthesis and Biological Evaluation. *Bioorg Chem.* 81, 512–528. doi:10.1016/j.bioorg.2018.09.010

He, Y., Ruganzu, J. B., Lin, C., Ding, B., Zheng, Q., Wu, X., et al. (2020). Tanshinone Iia Ameliorates Cognitive Deficits by Inhibiting Endoplasmic Reticulum Stress-Induced Apoptosis in App/Ps1 Transgenic Mice. *Neurochem. Int.* 133, 104610. doi:10.1016/j.neuint.2019.104610

Hou, Q., Zhu, L., Wang, L., Liu, X., Xiao, F., Xie, Y., et al. (2022). Screening On-Chip Fabricated Nanoparticles for Penetrating the Blood-Brain Barrier. *Nanoscale* 14 (8), 3234–3241. doi:10.1039/d1nr05825h

Huang, X. W., Xu, Y., Sui, X., Lin, H., Xu, J. M., Han, D., et al. (2019). Scutellarein Suppresses Aβ-Induced Memory Impairment via Inhibition of the NF-Kb Pathway *In Vivo* and *In Vitro*. *Oncol. Lett.* 17 (6), 5581–5589. doi:10.3892/ol.2019.10274

Hyman, S. E. (2005). Neurotransmitters. *Curr. Biol.* 15 (5), R154–R158. doi:10.1016/j.cub.2005.02.037

Ishak, R. A. H., Mostafa, N. M., and Kamel, A. O. (2017). Stealth Lipid Polymer Hybrid Nanoparticles Loaded with Rutin for Effective Brain Delivery - Comparative Study with the Gold Standard (Tween 80): Optimization, Characterization and Biodistribution. *Drug Deliv.* 24 (1), 1874–1890. doi:10.1080/10717544.2017.1410263

Iyanagi, T. (2007). Molecular Mechanism of Phase I and Phase Ii Drug-Metabolizing Enzymes: Implications for Detoxification. *Int. Rev. Cytol.* 260, 35–112. doi:10.1016/S0074-7696(06)60002-8

Jia, G., Han, Y., An, Y., Ding, Y., He, C., Wang, X., et al. (2018). Nrp-1 Targeted and Cargo-Loaded Exosomes Facilitate Simultaneous Imaging and Therapy of Glioma *In Vitro* and *In Vivo*. *Biomaterials* 178, 302–316. doi:10.1016/j.biomaterials.2018.06.029

Jia, M., Li, C., Zheng, Y., Ding, X., Chen, M., Ding, J., et al. (2017). Leonurine Exerts Antidepressant-like Effects in the Chronic Mild Stress-Induced Depression Model in Mice by Inhibiting Neuroinflammation. *Int. J. Neuropsychopharmacol.* 20 (11), 886–895. doi:10.1093/ijnp/pyx062

Jiang, Z., Wang, X., Zhang, Y., Zhao, P., Luo, Z., and Li, J. (2015). Effect of Capsaicin-Loading Nanoparticles on Gliomas. *J. Nanosci. Nanotechnol.* 15 (12), 9834–9839. doi:10.1166/jnn.2015.10313

Jin, J., Wang, H., Hua, X., Chen, D., Huang, C., and Chen, Z. (2019). An Outline for the Pharmacological Effect of Icariin in the Nervous System. *Eur. J. Pharmacol.* 842, 20–32. doi:10.1016/j.ejphar.2018.10.006

Johnsen, K. B., Bak, M., Kempen, P. J., Melander, F., Burkhart, A., Thomsen, M. S., et al. (2018). Antibody Affinity and Valency Impact Brain Uptake of Transferrin Receptor-Targeted Gold Nanoparticles. *Theranostics* 8 (12), 3416–3436. doi:10.7150/thno.25228

Karch, C. M., and Goate, A. M. (2015). Alzheimer's Disease Risk Genes and Mechanisms of Disease Pathogenesis. *Biol. Psychiatry* 77 (1), 43–51. doi:10.1016/j.biopsych.2014.05.006

Karve, I. P., Taylor, J. M., and Crack, P. J. (2016). The Contribution of Astrocytes and Microglia to Traumatic Brain Injury. *Br. J. Pharmacol.* 173 (4), 692–702. doi:10.1111/bph.13125

Kaur, D., Sharma, V., and Deshmukh, R. (2019). Activation of Microglia and Astrocytes: A Roadway to Neuroinflammation and Alzheimer's Disease. *Inflammopharmacology* 27 (4), 663–677. doi:10.1007/s10787-019-00580-x

Kaur, P., and Sharma, S. (2018). Recent Advances in Pathophysiology of Traumatic Brain Injury. *Curr. Neuropharmacol.* 16 (8), 1224–1238. doi:10.2174/1570159x15666170613083606

Khan, N., and Smith, M. T. (2015). Neurotrophins and Neuropathic Pain: Role in Pathobiology. *Molecules* 20 (6), 10657–10688. doi:10.3390/molecules200610657

Kim, Y. K., Na, K. S., Myint, A. M., and Leonard, B. E. (2016). The Role of Pro-inflammatory Cytokines in Neuroinflammation, Neurogenesis and the Neuroendocrine System in Major Depression. *Prog. Neuropsychopharmacol. Biol. Psychiatry* 64, 277–284. doi:10.1016/j.pnpbp.2015.06.008

Kojima, R., Bojar, D., Rizzi, G., Hamri, G. C., El-Baba, M. D., Saxena, P., et al. (2018). Designer Exosomes Produced by Implanted Cells Intracerebrally Deliver Therapeutic Cargo for Parkinson's Disease Treatment. *Nat. Commun.* 9 (1), 1305. doi:10.1038/s41467-018-03733-8

Kotta, S., Mubarak Aldawsari, H., Badr-Eldin, S. M., Alhakamy, N. A., and Md, S. (2021). Coconut Oil-Based Resveratrol Nanoemulsion: Optimization Using Response Surface Methodology, Stability Assessment and Pharmacokinetic Evaluation. *Food Chem.* 357, 129721. doi:10.1016/j.foodchem.2021.129721

Kyu, H. H., Abate, D., Abate, K. H., Abay, S. M., Abbafati, C., Abbasi, N., et al. (2018). Global, Regional, and National Disability-Adjusted Life-Years (Dalys) for 359 Diseases and Injuries and Healthy Life Expectancy (Hale) for 195 Countries and Territories, 1990–2017: A Systematic Analysis for the Global Burden of Disease Study 2017. *Lancet* 392 (10159), 1859–1922. doi:10.1016/s0140-6736(18)32335-3

Li, N., Feng, L., Tan, Y., Xiang, Y., Zhang, R., and Yang, M. (2018). Preparation, Characterization, Pharmacokinetics and Biodistribution of Baicalin-Loaded Liposome on Cerebral Ischemia-Reperfusion after I.V. Administration in Rats. *Molecules* 23 (7), 1747. doi:10.3390/molecules23071747

Liang, S., Wang, Z., Yuan, J., Zhang, J., Dai, X., Qin, F., et al. (2019). Rapid Identification of Tanshinone IIA Metabolites in an Amyloid-B1-42 Induced Alzherimer's Disease Rat Model Using UHPLC-Q-Exactive Qrbitrap Mass Spectrometry. *Molecules* 24 (14), 2584. doi:10.3390/molecules24142584

Libien, J., Kupersmith, M. J., Blaner, W., McDermott, M. P., Gao, S., Liu, Y., et al. (2017). Role of Vitamin a Metabolism in Iih: Results from the Idiopathic Intracranial Hypertension Treatment Trial. *J. Neurol. Sci.* 372, 78–84. doi:10.1016/j.jns.2016.11.014

Liebner, S., Dijkhuizen, R. M., Reiss, Y., Plate, K. H., Agalliu, D., and Constantin, G. (2018). Functional Morphology of the Blood-Brain Barrier in Health and Disease. *Acta Neuropathol.* 135 (3), 311–336. doi:10.1007/s00401-018-1815-1

Liu, H., Zhong, L., Zhang, Y., Liu, X., and Li, J. (2018). Rutin Attenuates Cerebral Ischemia-Reperfusion Injury in Ovariectomized Rats via Estrogen-Receptor-Mediated Bdnf-Trkb and Ngf-Trka Signaling. *Biochem. Cell Biol.* 96 (5), 672–681. doi:10.1139/bcb-2017-0209

Liu, X., An, C., Jin, P., Liu, X., and Wang, L. (2013). Protective Effects of Cationic Bovine Serum Albumin-Conjugated Pegylated Tanshinone Iia Nanoparticles on Cerebral Ischemia. *Biomaterials* 34 (3), 817–830. doi:10.1016/j.biomaterials.2012.10.017

Liu, Y. M., Hu, C. Y., Shen, J. D., Wu, S. H., Li, Y. C., and Yi, L. T. (2017). Elevation of Synaptic Protein Is Associated with the Antidepressant-like Effects of Ferulic Acid in a Chronic Model of Depression. *Physiol. Behav.* 169, 184–188. doi:10.1016/j.physbeh.2016.12.003

Liu W, W., Li, G., Hölscher, C., and Li, L. (2015). Neuroprotective Effects of Geniposide on Alzheimer's Disease Pathology. *Rev. Neurosci.* 26 (4), 371–383. doi:10.1515/revneuro-2015-0005

Liu, Z., Zhao, H., Shu, L., Zhang, Y., Okeke, C., Zhang, L., et al. (2015a). Preparation and Evaluation of Baicalin-Loaded Cationic Solid Lipid Nanoparticles Conjugated with Ox26 for Improved Delivery across the Bbb. *Drug Dev. Ind. Pharm.* 41 (3), 353–361. doi:10.3109/03639045.2013.861478

Liu, Z., Liu, W., Shi, J., Zhu, L., Dong, L., Luo, F., et al. (2015b). Reductive Metabolism of Oxymatrine Is Catalyzed by Microsomal Cyp3a4. *Dddt*, 5771. doi:10.2147/dddt.S92276

Lu, Y., Sun, G., Yang, F., Guan, Z., Zhang, Z., Zhao, J., et al. (2019). Baicalin Regulates Depression Behavior in Mice Exposed to Chronic Mild Stress via the Rac/Limk/Cofilin Pathway. *Biomed. Pharmacother.* 116, 109054. doi:10.1016/j.biopha.2019.109054

Ma, F., Yang, L., Sun, Z., Chen, J., Rui, X., Glass, Z., et al. (2020). Neurotransmitter-Derived Lipidoids (Nt-Lipidoids) for Enhanced Brain Delivery through Intravenous Injection. *Sci. Adv.* 6 (30), eabb4429. doi:10.1126/sciadv.abb4429

Majid, N., Siddiqi, M. K., Khan, A. N., Shabnam, S., Malik, S., Alam, A., et al. (2019). Biophysical Elucidation of Amyloid Fibrillation Inhibition and Prevention of Secondary Nucleation by Cholic Acid: An Unexplored Function of Cholic Acid. *ACS Chem. Neurosci.* 10 (11), 4704–4715. doi:10.1021/acschemneuro.9b00482

Miao, M., Cao, L., Li, R., Fang, X., and Miao, Y. (2017). Protective Effect of Chlorogenic Acid on the Focal Cerebral Ischemia Reperfusion Rat Models. *Saudi Pharm. J.* 25 (4), 556–563. doi:10.1016/j.jsps.2017.04.023

Milane, L., Singh, A., Mattheolabakis, G., Suresh, M., and Amiji, M. M. (2015). Exosome Mediated Communication within the Tumor Microenvironment. *J. Control Release* 219, 278–294. doi:10.1016/j.jconrel.2015.06.029

Mo, J., Yang, R., Li, F., Zhang, X., He, B., Zhang, Y., et al. (2018). Scutellarin Protects against Vascular Endothelial Dysfunction and Prevents Atherosclerosis via Antioxidation. *Phytomedicine* 42, 66–74. doi:10.1016/j.phymed.2018.03.021

Morad, G., Carman, C. V., Hagedorn, E. J., Perlin, J. R., Zon, L. I., Mustafaoglu, N., et al. (2019). Tumor-Derived Extracellular Vesicles Breach the Intact Blood-Brain Barrier via Transcytosis. *ACS Nano* 13 (12), 13853–13865. doi:10.1021/acsnano.9b04397

Morales, A. M., Mukai, R., Murota, K., and Terao, J. (2018). Inhibitory Effect of Catecholic Colonic Metabolites of Rutin on Fatty Acid Hydroperoxide and Hemoglobin Dependent Lipid Peroxidation in Caco-2 Cells. *J. Clin. Biochem. Nutr.* 63 (3), 175–180. doi:10.3164/jcbn.18-38

Morotti, A., Crivellaro, S., Panuzzo, C., Carrà, G., Guerrasio, A., and Saglio, G. (2017). IκB-α: At the Crossroad between Oncogenic and Tumor-Suppressive Signals. *Oncol. Lett.* 13 (2), 531–534. doi:10.3892/ol.2016.5465

Mukherjee, A., Waters, A. K., Kalyan, P., Achrol, A. S., Kesari, S., and Yenugonda, V. M. (2019). Lipid-Polymer Hybrid Nanoparticles as a Next-Generation Drug Delivery Platform: State of the Art, Emerging Technologies, and Perspectives. *Int. J. Nanomedicine* 14, 1937–1952. doi:10.2147/IJN.S198353

Najm, R., Rao, A., and Huang, Y. (2020). Too Much Tau in Interneurons Impairs Adult Hippocampal Neurogenesis in Alzheimer's Disease. *Cell Stem Cell* 26 (3), 297–299. doi:10.1016/j.stem.2020.02.004

Narad, M. E., Kennelly, M., Zhang, N., Wade, S. L., Yeates, K. O., Taylor, H. G., et al. (2018). Secondary Attention-Deficit/Hyperactivity Disorder in Children and Adolescents 5 to 10 Years after Traumatic Brain Injury. *JAMA Pediatr.* 172 (5), 437–443. doi:10.1001/jamapediatrics.2017.5746

Nho, K., Nudelman, K., Allen, M., Hodges, A., Kim, S., Risacher, S. L., et al. (2020). Genome-Wide Transcriptome Analysis Identifies Novel Dysregulated Genes Implicated in Alzheimer's Pathology. *Alzheimers Dement.* 16 (9), 1213–1223. doi:10.1002/alz.12092

Pattni, B. S., Chupin, V. V., and Torchilin, V. P. (2015). New Developments in Liposomal Drug Delivery. *Chem. Rev.* 115 (19), 10938–10966. doi:10.1021/acs.chemrev.5b00046

Qiang, W., Cai, W., Yang, Q., Yang, L., Dai, Y., Zhao, Z., et al. (2018). Artemisinin B Improves Learning and Memory Impairment in Ad Dementia Mice by Suppressing Neuroinflammation. *Neuroscience* 395, 1–12. doi:10.1016/j.neuroscience.2018.10.041

Ren, D., Fu, Y., Wang, L., Liu, J., Zhong, X., Yuan, J., et al. (2021). Tetrandrine Ameliorated Alzheimer's Disease through Suppressing Microglial Inflammatory Activation and Neurotoxicity in the 5xfad Mouse. *Phytomedicine* 90, 153627. doi:10.1016/j.phymed.2021.153627

Rollyson, W. D., Stover, C. A., Brown, K. C., Perry, H. E., Stevenson, C. D., McNees, C. A., et al. (2014). Bioavailability of Capsaicin and its Implications for Drug Delivery. *J. Control Release* 196, 96–105. doi:10.1016/j.jconrel.2014.09.027

Sasaki, K., Iwata, N., Ferdousi, F., and Isoda, H. (2019). Antidepressant-Like Effect of Ferulic Acid via Promotion of Energy Metabolism Activity. *Mol. Nutr. Food Res.* 63 (19), e1900327. doi:10.1002/mnfr.201900327

Scott, K. A., Dalgleish, A. G., and Liu, W. M. (2014). The Combination of Cannabidiol and Δ9-tetrahydrocannabinol Enhances the Anticancer Effects of Radiation in an Orthotopic Murine Glioma Model. *Mol. Cancer Ther.* 13 (12), 2955–2967. doi:10.1158/1535-7163.MCT-14-0402

Shah, V., and Kochar, P. (2018). Brain Cancer: Implication to Disease, Therapeutic Strategies and Tumor Targeted Drug Delivery Approaches. *Recent Pat. Anticancer Drug Discov.* 13 (1), 70–85. doi:10.2174/1574892812666171129142023

Shang, Z., Xin, Q., Zhao, W., Wang, Z., Li, Q., Zhang, J., et al. (2017). Rapid Profiling and Identification of Puerarin Metabolites in Rat Urine and Plasma after Oral Administration by Uhplc-Ltq-Orbitrap Mass Spectrometer. *J. Chromatogr. B Anal. Technol. Biomed. Life Sci.* 1068-1069, 180–192. doi:10.1016/j.jchromb.2017.10.038

Sharma, G., Sharma, A. R., Lee, S. S., Bhattacharya, M., Nam, J. S., and Chakraborty, C. (2019). Advances in Nanocarriers Enabled Brain Targeted Drug Delivery across Blood Brain Barrier. *Int. J. Pharm.* 559, 360–372. doi:10.1016/j.ijpharm.2019.01.056

Shi, Z. H., Li, N. G., Wang, Z. J., Tang, Y. P., Dong, Z. X., Zhang, W., et al. (2015). Synthesis and Biological Evaluation of Methylated Scutellarein Analogs Based on Metabolic Mechanism of Scutellarin *In Vivo*. *Eur. J. Med. Chem.* 106, 95–105. doi:10.1016/j.ejmech.2015.10.039

Song, F. X., Wang, L., Liu, H., Wang, Y. L., and Zou, Y. (2017). Brain Cell Apoptosis Inhibition by Butylphthalide in Alzheimer's Disease Model in Rats. *Exp. Ther. Med.* 13 (6), 2771–2774. doi:10.3892/etm.2017.4322

Syed, Y. Y. (2020). Sodium Oligomannate: First Approval. *Drugs* 80 (4), 441–444. doi:10.1007/s40265-020-01268-1

Tang, M., and Taghibiglou, C. (2017). The Mechanisms of Action of Curcumin in Alzheimer's Disease. *J. Alzheimers Dis.* 58 (4), 1003–1016. doi:10.3233/JAD-170188

Tang, Y., Huang, D., Zhang, M. H., Zhang, W. S., Tang, Y. X., Shi, Z. X., et al. (2016). Salvianolic Acid B Inhibits Aβ Generation by Modulating BACE1 Activity in SH-Sy5y-APPsw Cells. *Nutrients* 8 (6). doi:10.3390/nu8060333

Tian, T., Zhang, H. X., He, C. P., Fan, S., Zhu, Y. L., Qi, C., et al. (2018). Surface Functionalized Exosomes as Targeted Drug Delivery Vehicles for Cerebral Ischemia Therapy. *Biomaterials* 150, 137–149. doi:10.1016/j.biomaterials.2017.10.012

Tsou, Y. H., Zhang, X. Q., Zhu, H., Syed, S., and Xu, X. (2017). Drug Delivery to the Brain across the Blood-Brain Barrier Using Nanomaterials. *Small* 13 (43), 1701921. doi:10.1002/smll.201701921

Unsicker, K. (2013). Neurotrophic Molecules in the Treatment of Neurodegenerative Disease with Focus on the Retina: Status and Perspectives. *Cell Tissue Res.* 353 (2), 205–218. doi:10.1007/s00441-013-1585-y

VanItallie, T. B. (2019). Traumatic Brain Injury (Tbi) in Collision Sports: Possible Mechanisms of Transformation into Chronic Traumatic Encephalopathy (Cte). *Metabolism* 100S, 153943. doi:10.1016/j.metabol.2019.07.007

Wang, C., Yue, F., Ai, G., and Yang, J. (2018). Simultaneous Determination of Evodiamine and its Four Metabolites in Rat Plasma by Lc-Ms/Ms and its Application to a Pharmacokinetic Study. *Biomed. Chromatogr.* 32 (7), e4219. doi:10.1002/bmc.4219

Wang, J., Qi, Q., Zhou, W., Feng, Z., Huang, B., Chen, A., et al. (2018). Inhibition of Glioma Growth by Flavokawain B Is Mediated through Endoplasmic Reticulum Stress Induced Autophagy. *Autophagy* 14 (11), 2007–2022. doi:10.1080/15548627.2018.1501133

Wang, Y., Li, Y., Yang, W., Gao, S., Lin, J., Wang, T., et al. (2018). Ginsenoside Rb1 Inhibit Apoptosis in Rat Model of Alzheimer's Disease Induced by Aβ1-40. *Am. J. Transl. Res.* 10 (3), 796–805.

Wang, H., Sui, H., Zheng, Y., Jiang, Y., Shi, Y., Liang, J., et al. (2019). Curcumin-primed Exosomes Potently Ameliorate Cognitive Function in AD Mice by Inhibiting Hyperphosphorylation of the Tau Protein through the AKT/GSK-3β Pathway. *Nanoscale* 11 (15), 7481–7496. doi:10.1039/c9nr01255a

Wang, X., Sun, G., Feng, T., Zhang, J., Huang, X., Wang, T., et al. (2019). Sodium Oligomannate Therapeutically Remodels Gut Microbiota and Suppresses Gut Bacterial Amino Acids-Shaped Neuroinflammation to Inhibit Alzheimer's Disease Progression. *Cell Res.* 29 (10), 787–803. doi:10.1038/s41422-019-0216-x

Wang, L., Huang, S., Chen, B., Zang, X. Y., Su, D., Liang, J., et al. (2016). Characterization of the Anticoagulative Constituents of Angelicae Sinensis Radix and Their Metabolites in Rats by Hplc-Dad-Esi-It-Tof-Msn. *Planta Med.* 82 (4), 362–370. doi:10.1055/s-0035-1558309

Wang, T., Jiang, H., Cao, S., Chen, Q., Cui, M., Wang, Z., et al. (2017). Baicalin and its Metabolites Suppresses Gluconeogenesis through Activation of Ampk or Akt in Insulin Resistant Hepg-2 Cells. *Eur. J. Med. Chem.* 141, 92–100. doi:10.1016/j.ejmech.2017.09.049

Wang, T., Kuang, W., Chen, W., Xu, W., Zhang, L., Li, Y., et al. (2020). A Phase II Randomized Trial of Sodium Oligomannate in Alzheimer's Dementia. *Alz Res. Ther.* 12 (1), 110. doi:10.1186/s13195-020-00678-3

Wang, Z. S., Luo, P., Dai, S. H., Liu, Z. B., Zheng, X. R., and Chen, T. (2013). Salvianolic Acid B Induces Apoptosis in Human Glioma U87 Cells through

P38-Mediated Ros Generation. *Cell Mol. Neurobiol.* 33 (7), 921–928. doi:10.1007/s10571-013-9958-z

Watt, G., and Karl, T. (2017). *In Vivo* Evidence for Therapeutic Properties of Cannabidiol (Cbd) for Alzheimer's Disease. *Front. Pharmacol.* 8, 20. doi:10.3389/fphar.2017.00020

Xie, X., Li, Y., Zhao, D., Fang, C., He, D., Yang, Q., et al. (2020). Oral Administration of Natural Polyphenol-Loaded Natural Polysaccharide-Cloaked Lipidic Nanocarriers to Improve Efficacy against Small-Cell Lung Cancer. *Nanomedicine* 29, 102261. doi:10.1016/j.nano.2020.102261

Xie, Y. Z., Zhang, X. J., Zhang, C., Yang, Y., He, J. N., and Chen, Y. X. (2019). Protective Effects of Leonurine against Ischemic Stroke in Mice by Activating Nuclear Factor Erythroid 2-related Factor 2 Pathway. *CNS Neurosci. Ther.* 25 (9), 1006–1017. doi:10.1111/cns.13146

Xu, D., Qiu, C., Wang, Y., Qiao, T., and Cui, Y. L. (2021). Intranasal Co-Delivery of Berberine and Evodiamine by Self-Assembled Thermosensitive *In-Situ* Hydrogels for Improving Depressive Disorder. *Int. J. Pharm.* 603, 120667. doi:10.1016/j.ijpharm.2021.120667

Xu, R., Wang, J., Xu, J., Song, X., Huang, H., Feng, Y., et al. (2020). Rhynchophylline Loaded-Mpeg-Plga Nanoparticles Coated with Tween-80 for Preliminary Study in Alzheimer's Disease. *Int. J. Nanomedicine* 15, 1149–1160. doi:10.2147/IJN.S236922

Xu, W., Liu, J., Ma, D., Yuan, G., Lu, Y., and Yang, Y. (2017). Capsaicin Reduces Alzheimer-Associated Tau Changes in the Hippocampus of Type 2 Diabetes Rats. *Plos One* 12 (2), e0172477. doi:10.1371/journal.pone.0172477

Yan, X., Hu, G., Yan, W., Chen, T., Yang, F., Zhang, X., et al. (2017). Ginsenoside Rd Promotes Non-amyloidogenic Pathway of Amyloid Precursor Protein Processing by Regulating Phosphorylation of Estrogen Receptor Alpha. *Life Sci.* 168, 16–23. doi:10.1016/j.lfs.2016.11.002

Yang, J., Li, K., He, D., Gu, J., Xu, J., Xie, J., et al. (2020). Toward a Better Understanding of Metabolic and Pharmacokinetic Characteristics of Low-Solubility, Low-Permeability Natural Medicines. *Drug Metab. Rev.* 52 (1), 19–43. doi:10.1080/03602532.2020.1714646

Yao, Y., Chen, X., Bao, Y., and Wu, Y. (2017). Puerarin Inhibits β amyloid Peptide 142 induced Tau Hyperphosphorylation via the Wnt/β catenin Signaling Pathway. *Mol. Med. Rep.* 16 (6), 9081–9085. doi:10.3892/mmr.2017.7702

Zeng, J., Chen, L., Wang, Z., Chen, Q., Fan, Z., Jiang, H., et al. (2017). Marginal Vitamin A Deficiency Facilitates Alzheimer's Pathogenesis. *Acta Neuropathol.* 133 (6), 967–982. doi:10.1007/s00401-017-1669-y

Zeng, M., Yang, L., He, D., Li, Y., Shi, M., and Zhang, J. (2017). Metabolic Pathways and Pharmacokinetics of Natural Medicines with Low Permeability. *Drug Metab. Rev.* 49 (4), 464–476. doi:10.1080/03602532.2017.1377222

Zhang, F. X., Cui, S. S., Yuan, Y. L., Li, C., and Li, R. M. (2022). Dissection of the Potential Anti-Diabetes Mechanism of Salvianolic Acid B by Metabolite Profiling and Network Pharmacology. *Rapid Commun. Mass Spectrom.* 36 (1), e9205. doi:10.1002/rcm.9205

Zhang, J. Q., Wu, X. H., Feng, Y., Xie, X. F., Fan, Y. H., Yan, S., et al. (2016). Salvianolic Acid B Ameliorates Depressive-like Behaviors in Chronic Mild Stress-Treated Mice: Involvement of the Neuroinflammatory Pathway. *Acta Pharmacol. Sin.* 37 (9), 1141–1153. doi:10.1038/aps.2016.63

Zhang, W., Cao, Y. A., Xia, J., Tian, L., Yang, L., and Peng, C. S. (2017). Neuroprotective Effect of Tanshinone Iia Weakens Spastic Cerebral Palsy through Inflammation, P38mapk and Vegf in Neonatal Rats. *Mol. Med. Rep.* doi:10.3892/mmr.2017.8069

Zhang, X., Liu, S., Pi, Z., Liu, Z., and Song, F. (2017). Simultaneous Quantification Method for Comparative Pharmacokinetics Studies of Two Major Metabolites from Geniposide and Genipin by Online Mircrodialysis-UPLC-MS/MS. *J. Chromatogr. B Anal. Technol. Biomed. Life Sci.* 1041–1042, 11–18. doi:10.1016/j.jchromb.2016.12.010

Zhang, X., Chen, S., Duan, F., Liu, A., Li, S., Zhong, W., et al. (2021). Prebiotics Enhance the Biotransformation and Bioavailability of Ginsenosides in Rats by Modulating Gut Microbiota. *J. Ginseng Res.* 45 (2), 334–343. doi:10.1016/j.jgr.2020.08.001

Zhang, Z., Guan, J., Jiang, Z., Yang, Y., Liu, J., Hua, W., et al. (2019). Brain-Targeted Drug Delivery by Manipulating Protein Corona Functions. *Nat. Commun.* 10 (1), 3561. doi:10.1038/s41467-019-11593-z

Zhao, J., Li, Y., He, D., Hu, X., Li, K., Yang, Q., et al. (2020). Natural Oral Anticancer Medication in Small Ethanol Nanosomes Coated with a Natural Alkaline Polysaccharide. *ACS Appl. Mater Interfaces* 12 (14), 16159–16167. doi:10.1021/acsami.0c02788

Zhao J, J., Liu, S., Hu, X., Zhang, Y., Yan, S., Zhao, H., et al. (2018). Improved Delivery of Natural Alkaloids into Lung Cancer through Woody Oil-Based Emulsive Nanosystems. *Drug Deliv.* 25 (1), 1426–1437. doi:10.1080/10717544.2018.1474970

Zhao, Y., Li, H., Fang, F., Qin, T., Xiao, W., Wang, Z., et al. (2018). Geniposide Improves Repeated Restraint Stress-Induced Depression-like Behavior in Mice by Ameliorating Neuronal Apoptosis via Regulating Glp-1r/Akt Signaling Pathway. *Neurosci. Lett.* 676, 19–26. doi:10.1016/j.neulet.2018.04.010

Zhao, T., Zhang, X., Zhao, Y., Zhang, L., Bai, X., Zhang, J., et al. (2014). Pretreatment by Evodiamine Is Neuroprotective in Cerebral Ischemia: Up-Regulated pAkt, pGSK3β, Down-Regulated NF-Kb Expression, and Ameliorated BBB Permeability. *Neurochem. Res.* 39 (8), 1612–1620. doi:10.1007/s11064-014-1356-5

Zhao, X., Yang, D. H., Xu, F., Huang, S., Zhang, L., Liu, G. X., et al. (2015). The *In Vivo* Absorbed Constituents and Metabolites of Danshen Decoction in Rats Identified by Hplc with Electrospray Ionization Tandem Ion Trap and Time-Of-Flight Mass Spectrometry. *Biomed. Chromatogr.* 29 (2), 285–304. doi:10.1002/bmc.3275

Zheng, X., Cheng, Y., Chen, Y., Yue, Y., Li, Y., Xia, S., et al. (2019). Ferulic Acid Improves Depressive-like Behavior in Prenatally-Stressed Offspring Rats via Anti-inflammatory Activity and Hpa Axis. *Int. J. Mol. Sci.* 20 (3), 493. doi:10.3390/ijms20030493

Zhou, R., Wang, J., Han, X., Ma, B., Yuan, H., and Song, Y. (2019). Baicalin Regulates the Dopamine System to Control the Core Symptoms of Adhd. *Mol. Brain* 12 (1), 11. doi:10.1186/s13041-019-0428-5

Zhu, Q., Ling, X., Yang, Y., Zhang, J., Li, Q., Niu, X., et al. (2019). Embryonic Stem Cells-Derived Exosomes Endowed with Targeting Properties as Chemotherapeutics Delivery Vehicles for Glioblastoma Therapy. *Adv. Sci. (Weinh)* 6 (6), 1801899. doi:10.1002/advs.201801899

Zhu, Q., Zhang, J., Yang, P., Tan, B., Liu, X., Zheng, Y., et al. (2014). Characterization of Metabolites of Leonurine (Scm-198) in Rats after Oral Administration by Liquid Chromatography/Tandem Mass Spectrometry and Nmr Spectrometry. *Sci. World J.* 2014, 11. doi:10.1155/2014/947946

Zhu, Y., Tang, Q., Wang, G., and Han, R. (2017). Tanshinone Iia Protects Hippocampal Neuronal Cells from Reactive Oxygen Species through Changes in Autophagy and Activation of Phosphatidylinositol 3-Kinase, Protein Kinas B, and Mechanistic Target of Rapamycin Pathways. *Curr. Neurovasc Res.* 14 (2), 132–140. doi:10.2174/1567202614666170306105315

Zuchero, Y. J., Chen, X., Bien-Ly, N., Bumbaca, D., Tong, R. K., Gao, X., et al. (2016). Discovery of Novel Blood-Brain Barrier Targets to Enhance Brain Uptake of Therapeutic Antibodies. *Neuron* 89 (1), 70–82. doi:10.1016/j.neuron.2015.11.024

Conflict of Interest: The authors declare that the research was conducted in the absence of any commercial or financial relationships that could be construed as a potential conflict of interest.

Publisher's Note: All claims expressed in this article are solely those of the authors and do not necessarily represent those of their affiliated organizations, or those of the publisher, the editors and the reviewers. Any product that may be evaluated in this article, or claim that may be made by its manufacturer, is not guaranteed or endorsed by the publisher.

GLOSSARY

ACTH Adrenocorticotropic hormone
Aβ Amyloid plaques
AD Alzheimer's disease
ADM Adrenomedullin
APP Amyloid precursor protein
ATF6 Activating transcription factor 6
AUC Area under the plasma concentration-time curve
BBB Blood-brain barrier
BCS Biopharmaceutics classification system
BDNF Brain-derived neurotrophic factor
CB1 Cannabinoid receptor 1
CB2 Cannabinoid receptor 2
CHOP CCAAT/enhancer-binding protein homologous protein
Cl Clearance
C_{max} Maximum plasma
CNS Central nervous system
CNTF Ciliary neurotrophic factor
CRF Corticotropin-releasing factor
CT-1 Cardiotrophin-1
CT-2 Cardiotrophin-2
D_0 Dose number
eIF2α Eukaryotic initiation factor 2-alpha
EphA4 Erythropoietin-producing hepatocellular A4
EPO Erythropoietin
ER Endoplasmic reticulum
ERα Estrogen receptor alpha
ERβ Estrogen receptor beta
FGF Fibroblast growth factor
GFAP Glial fibrillary acidic protein
GLUT-1 Glucose transporter 1
GR Glucocorticoid receptor
GRP78 Glucose regulated protein 78GSK-3β
GSK-3β Glycogen synthase kinase 3 beta
GSTs Glutathione S-transferases
HIF-1α Hypoxia-inducible factor alpha
HMGB1 High-mobility group box 1
HPA Hypothalamic-pituitary-adrenal
IGF Insulin-like growth factor
IκB-α B-cells inhibitor alpha
IL-6 Interleukin-6
iNOS Inducible nitric oxide synthase
I/R Ischemia/reperfusion
IRE1α Inositol-requiring enzyme 1α
JNK c-Jun N-terminal kinase
LIF Leukemia inhibitory factor
Log P Oil-in-water partition coefficient
LPHNPs Lipid polymer hybrid nanoparticles
MAPKs Mitogen-activated protein kinases
MCAO Middle cerebral artery occlusion
NF-κB Nuclear factor kappa-light-chain-enhancer of activated B cells
NGF Nerve growth factor
NMCs Natural medicines that affect cerebral metabolism
NMs Natural medicines
Nrf-2 Nuclear factor erythroid 2-related factor 2
PPARα Peroxisome proliferator-activated receptor-alpha
PPARγ Peroxisome proliferator-activated receptor-gamma
sAPPα Soluble amyloid precursor protein alpha
SULTs Sulfotransferases
S100B S100 calcium-binding protein B
TBI Traumatic brain injury
TGF-β Transforming growth factor-β
TLR4 Toll-like receptor 4
TPGS D-α-tocopheryl polyethylene glycol 1000 succinate
TrkA Tropomyosin receptor kinase A
TrkB Tropomyosin receptor kinase B
UGTs UDP-glucuronosyltransferases
VEGF Vascular endothelial growth factor

frontiers | Frontiers in Pharmacology

ORIGINAL RESEARCH
published: 04 July 2022
doi: 10.3389/fphar.2022.936846

Pharmacokinetic Study of Four Major Bioactive Components of Liandan Xiaoyan Formula in Ulcerative Colitis and Control Rats Using UPLC-MS/MS

Kaihui Zhang[1†], Zenghui Lu[1†], Qian Wang[1], Fangle Liu[2], Meiqi Wang[1], Chaozhan Lin[1]* and Chenchen Zhu[1]**

[1]School of Pharmaceutical Sciences, Guangzhou University of Chinese Medicine, Guangzhou, China, [2]School of Basic Medical Sciences, Guangzhou University of Chinese Medicine, Guangzhou, China

OPEN ACCESS

Edited by:
Ling Ye,
Southern Medical University, China

Reviewed by:
Xiaobo Li,
Shanghai Jiao Tong University, China
Jin-Jian Lu,
University of Macau, China
Jun Chen,
China Pharmaceutical University, China

***Correspondence:**
Meiqi Wang
wangmeiqi@gzucm.edu.cn
Chaozhan Lin
linchaozhan@gzucm.edu.cn
Chenchen Zhu
zhucc@gzucm.edu.cn

[†]These authors have contributed equally to this work and share first authorship

Specialty section:
This article was submitted to Drug Metabolism and Transport, a section of the journal Frontiers in Pharmacology

Received: 05 May 2022
Accepted: 17 June 2022
Published: 04 July 2022

Citation:
Zhang K, Lu Z, Wang Q, Liu F, Wang M, Lin C and Zhu C (2022) Pharmacokinetic Study of Four Major Bioactive Components of Liandan Xiaoyan Formula in Ulcerative Colitis and Control Rats Using UPLC-MS/MS. Front. Pharmacol. 13:936846. doi: 10.3389/fphar.2022.936846

Liandan Xiaoyan Formula (LXF), a classic Traditional Chinese medicine (TCM) formula, is composed of two Chinese herbal medicines for treating bowel disease under the TCM theory. This study aimed to develop a rapid, stable, sensitive, and reliable method based on ultra-high performance liquid chromatography-tandem mass spectrometry (UPLC-MS/MS) to simultaneously determine four major bioactive components of LXF (andrographolide, dehydroandrographolide, 1-methoxicabony-β-carboline, 4-methoxy-5-hydroxy-canthin-6-one) in rat serum and evaluate the pharmacokinetic characteristics of LXF in ulcerative colitis (UC) and control rats. After pretreating by protein precipitation with methanol, separation was performed on a UPLC C18 column using gradient elution with a mobile phase consisting of acetonitrile and 0.1% formic acid at a flowing rate of 0.4 ml/min. Detection was performed on Triple-TOF™ 5600 mass spectrometry set at the positive ionization and multiple reaction monitoring (MRM) mode. The validated method showed good linearity ($R^2 \geq 0.9970$), the intra- and inter-day accuracy were within ±11.58%, whereas the intra- and inter-day precision were less than 13.79%. This method was validated and applied to compare the pharmacokinetic profiles of the analytes in serum of UC induced by dextran sulphate sodium (DSS) and control rats after oral administration of LXF. The results showed that four major bioactive components of LXF were quickly absorbed after oral administration in both groups, with higher exposure levels in the UC group. This relationship between the active ingredients' pharmacokinetic properties provided essential scientific information for applying LXF in clinical.

Keywords: Liandan Xiaoyan Formula, pharmacokinetic, ulcerative colitis, bioactive component, UPLC-MS/MS

Abbreviations: AUC, area under the serum concentration-time curve; CE, collision energy; C_{max}, maximum serum concentration; DSS, dextran sulphate sodium; IBD, inflammatory bowel disease; IS, internal standard; LLOQ, lower limit of quantification; LXF, Liandan Xiaoyan Formula; MRT, mean residence time; QC, quality control; RSD, relative standard deviation; RT, retention time; $T_{1/2}$, elimination half-time; TCM, Traditional Chinese medicine; T_{max}, maximum serum concentration; UC, ulcerative colitisPharmacokinetics of Liandan Xiaoyan Formula.

1 INTRODUCTION

Ulcerative colitis (UC) is an idiopathic, relapsing, chronic inflammatory bowel disease (IBD) that occurs in the colon and rectum (Feuerstein et al., 2019; Sun et al., 2021). Some studies suggested that it was related to inappropriate immune responses to enteric commensal microbes in genetically susceptible individuals exposed to environmental risk factors (Ng et al., 2013; Du and Ha, 2020). Inadequate treatment of UC might result in continuous bowel damage and subsequently increased risks of hospitalizations and colorectal cancer (Ungaro et al., 2017). Since the mid-20th century, the incidence and prevalence of UC have been rising (Molodecky et al., 2012; Mak et al., 2020). Millions of people worldwide are affected by UC and considering morbidity and mortality related to UC, societal costs are substantial (Cohen et al., 2010). Until today a specific cure for UC has not been found, and the treatments available are limited to alleviation. Conventional treatment for UC is combinations of pharmacologic agents, such as azathioprine, aminosalicylates, and corticosteroids to promote alleviation, prevention of relapses, and mucosal healing. However, using these drugs in UC is associated with numerous systemic and local individual adverse effects, such as headache, nausea, loss of appetite, vomiting, and rash (Roselli and Finamore, 2020). Therefore, developing novel and effective therapeutic agents for UC is urgently needed.

Traditional Chinese medicine (TCM) has been refined for thousands of years *via* its continued clinical application (Ma et al., 2016; Zhang et al., 2021). TCM stresses mixtures with more than one herb extract, and the synergistic effect of various components in these herbs produces high efficacies (Yang et al., 2016). Liandan Xiaoyan Formula (LXF), a classic TCM formula, is composed of two Chinese herbal medicines that are Herba andrographis [dried herb of *Andrographis paniculata* (Burm. f.) Nees, also called *Chuanxinlian*], and Ramulus et folium picrasmae [dried twigs and leaves of *Picrasma quassioides* (D. Don) Benn, also called *Kumu*], and this classic formula has been processed into many kinds of patent medicine with the efficiency of damp-heat dysentery, anti-bacterial, anti-inflammatory, and clear away heat and toxic material, and have been widely used for the treatment of various intestinal inflammation in clinic. Chemical components of the two herbal medicines in LXF have been reported to have several biological activities associated with their beneficial efficacy. Phytochemical research has exposed that diterpene lactones, such as andrographolide (**Figure 1**) and dehydroandrographolide (**Figures 1**, **2**), were the main bioactive components of *Chuanxinlian* (Sareer et al., 2014). The diterpene lactones possess anti-inflammatory (Burgos et al., 2020), hepatoprotective (Patil and Jain, 2021), cardioprotective (Mehta et al., 2022), and immunostimulant, anti-oxidant, anti-viral, anti-bacterial, gastroprotective activities (Wasman et al., 2011; Arifullah et al., 2013). *Kumu* has numerous alkaloids as the main active components, which were reported to have effects on various inflammatory and infectious diseases, such as acute tonsillitis, diarrhea.

Pneumonia, and acute upper respiratory tract infections (Wang et al., 2018; Hu et al., 2021). Our previous study

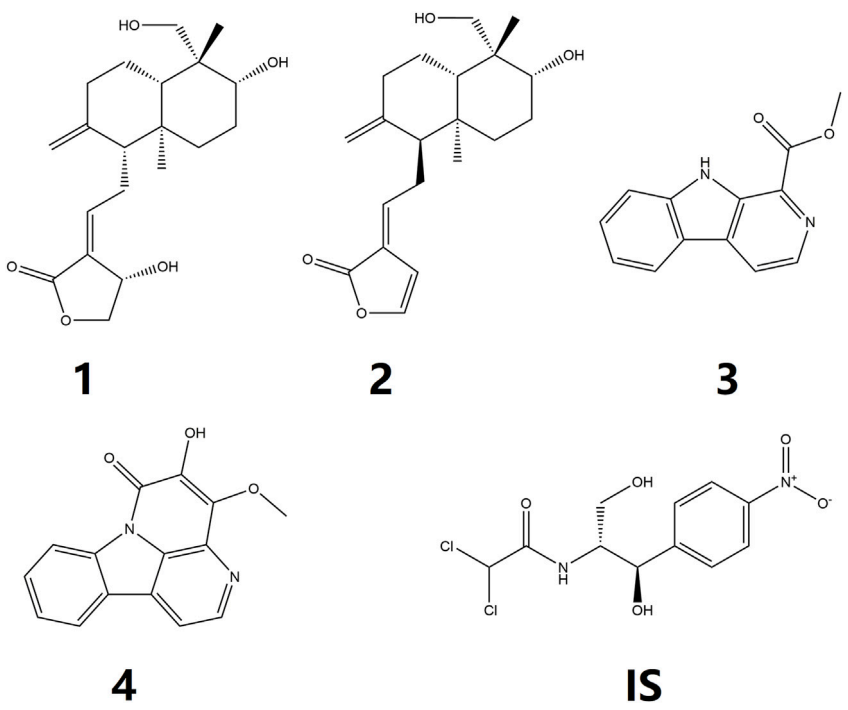

FIGURE 1 | Chemical structures of **1** andrographolide, **2** dehydroandrographolide, **3** 1-methoxicabony-β-carboline, **4** 4-methoxy-5-hydroxy-canthin-6-one, and chloramphenicol (**IS**).

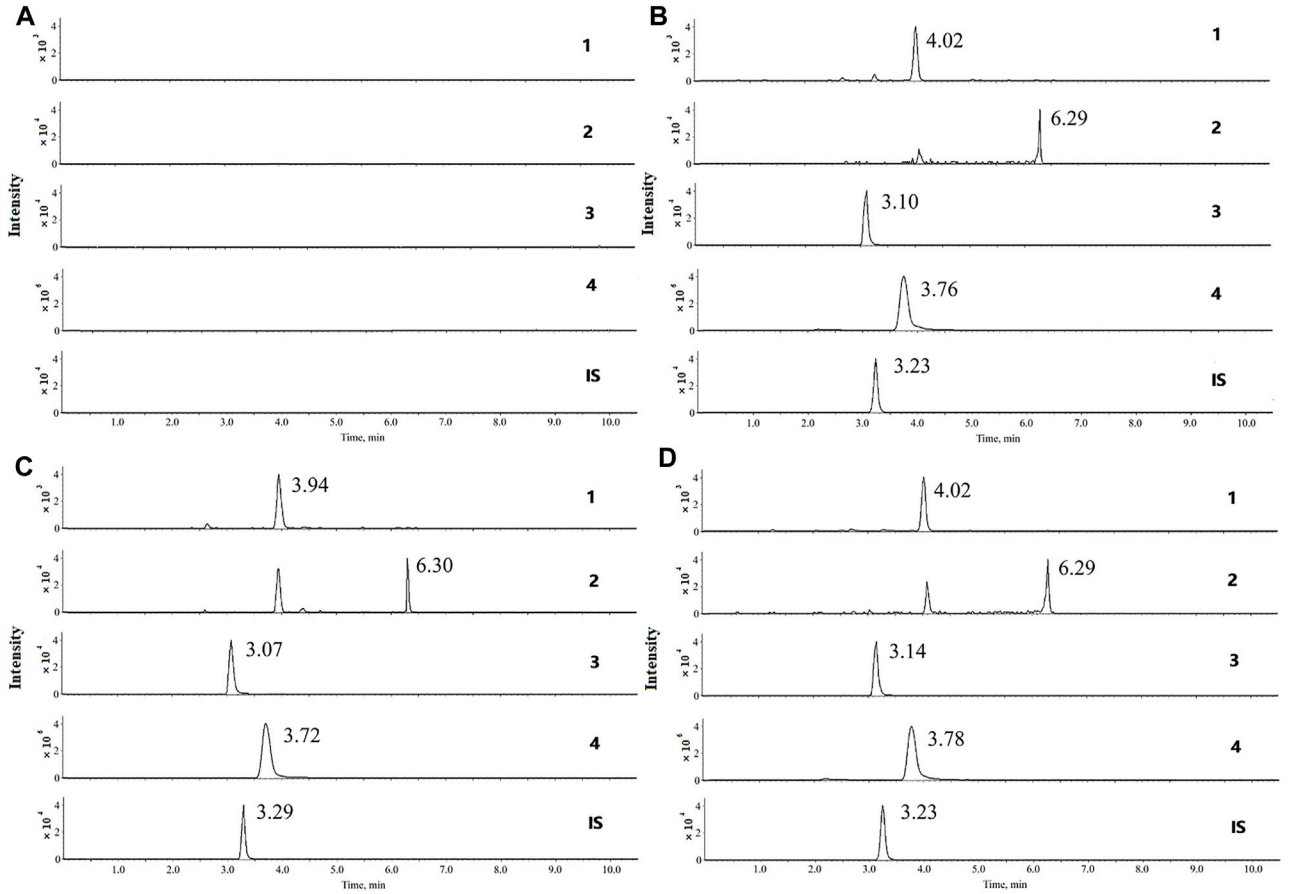

FIGURE 2 | Multiple reaction monitoring (MRM) chromatograms of the four compounds and chloramphenicol (IS) in rats. **(A)** blank serum; **(B)** blank serum with standard substance and IS; **(C)** serum of control group; **(D)** serum of UC group. **1** andrographolide, **2** dehydroandrographolide, **3** 1-methoxicabony-β-carboline, **4** 4-methoxy-5-hydroxy-canthin-6-one, and chloramphenicol (**IS**).

indicated that 1-methoxicabony-β-carboline (**Figures 1**–**3**), 4-methoxy-5-hydroxy-canthin-6-one (Figures 1–4) were the two major bioactive alkaloids in Kumu (Zhang et al., 2020). Therefore, this study focuses on these four compounds.

The pharmacokinetic characteristics of the active compounds in TCM have been used to evaluate clinical efficacy, guide the rational use of herbal medicines, and promote their development (Zhang et al., 2018; Zhu et al., 2020). These days, ultra-high performance liquid chromatography coupled with electrospray ionization tandem quadrupole/time of flight mass spectrometry (UPLC-MS/MS) has been used as a general approach for metabolic and pharmacokinetic profiling study of natural products (Yao et al., 2018; Li et al., 2019; Wu et al., 2020). Recent research has also shown that the internal environment could influence the pharmacokinetics of drugs in a pathological state, such as colitis (Liu et al., 2020). It is indicated that pharmacokinetic study of XLF in UC state is necessary to provide a basis for clinical use. Therefore, we decided to investigate the pharmacokinetic profiles of LXF *in vivo* between ulcerative colitis and normal physiological condition in this research.

In this study, we established a stable, sensitive, and reliable UPLC-MS/MS method for quantitative analysis of the concentrations of four major active compounds of LXF in rat serum. This method has been applied and validated in a comparative pharmacokinetic study after oral administration of XLF to UC and control rats.

2 MATERIALS AND METHODS

2.1 Chemicals and Reagents

Dextran sulphate sodium (DSS) (Lot number D7002900) was obtained from Yeasen Biotechnology (shanghai) Co., Ltd (Shanghai, China). Andrographolide (Lot number 110797-201609) and dehydroandrographolide (Lot number 110854-201710) were purchased from National Institutes for Food and Drug Control (Beijing, China). 1-methoxicabony-β-carboline and 4-methoxy-5-hydroxy-canthin-6-one were purified and identified using Infrared Spectroscopy (IR), UV–visible spectroscopy (UV), mass spectrometry (MS), and Nuclear Magnetic Resonance Spectroscopy (NMR) as described in our

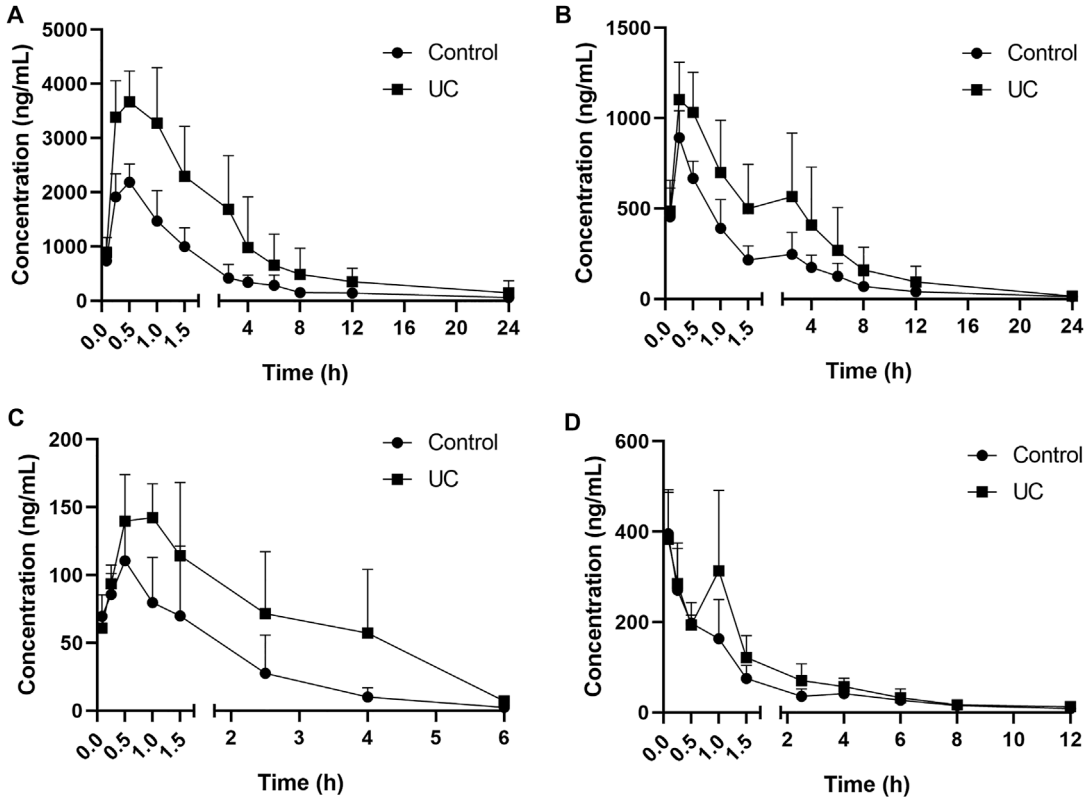

FIGURE 3 | Mean serum concentration–time curves for **(A)** andrographolide, **(B)** dehydroandrographolide, **(C)**, 1-methoxicabony-β-carboline, **(D)** 4-methoxy-5-hydroxy-canthin-6-one (n = 8).

previous studies, and the purity of them was more than 98% (Yang et al., 2016; Liu et al., 2020; Zhang et al., 2021). Chloramphenicol (Lot number Y27M6C2), internal standard (IS), was purchased from Shanghai Yuanye Bio-Technology Co., Ltd (Shanghai, China). MS-grade methanol, acetonitrile, and formic acid were obtained from Merck Co., Ltd (Darmstadt, Germany). Deionized water was purified using the Milli-Q system (Millipore, Milford, MA, United States) and used for the entire study. Furthermore, all other reagents were analytical grade from Guangzhou Chemical Reagent Co., Ltd (Guangzhou, China).

2.2 Liandan Xiaoyan Formula Extract Preparation

The preparation and intragastric dose of the LXF sample followed our previous research (Lu et al., 2021). Meanwhile, the quality of LXF was controlled according to the contents of four main components 69.78 mg/g of andrographolide, 38.17 mg/g of dehydroandrographolide, 0.79 mg/g of 1-methoxicabony-β-carboline, and 5.68 mg/g of 4-methoxy-5-hydroxy-canthin-6-one (**Supplementary Material Part A**).

2.3 Animals, Dosing, and Sampling

Sixteen male Sprague-Dawley (SD) rats (220 ± 10 g) were provided from the Liaoning Changsheng Biotechnology Co., Ltd (Benxi, China; with license No. of SCXK, 2020-0001). The rats were kept in an environment (22 ± 2°C, relative humidity 50 ± 5%) under a 12-h light-dark cycle with a free diet and water for 3 days. All experiments on animals were conducted strictly under the related ethics regulations of the Committee on Use and Care of Animals of Guangzhou University of Chinese Medicine (Guangzhou, China) (No. 712052).

All rats were assigned equally and randomly to the control and model groups. The rats of the model group were free to access 4% DSS for 7 days to induce UC, and rats of the control group were given pure water (Chen et al., 2020). Before the pharmacokinetics study, the DSS-induced UC rats (model) were established successfully (**Supplementary Material Part B**).

After fasting for 12 h, the rats were orally administered LXF at a 3.30 g/kg dose according to Prescription preparation of Chinese medicine, volume 10 (Lu et al., 2021). Serum samples (approximately 0.5 ml) were collected from the fosse orbital vein using 1.5 ml polythene tubes before the administration and at 0.083, 0.25, 0.5, 1, 1.5, 2.5, 4, 6, 8, 12, 24, 36, and 48 h after dosing and centrifuged immediately at 3,500 rpm for 15 min. Serum was transferred into clean tubes and stored at −80°C.

2.4 Sample Pretreatment

100 μl of IS solution (960 ng/ml) was added to a 100 μl serum sample and vortex-mixed for 0.5 min, and then 800 μl of

TABLE 1 | The mass spectrometry parameters of tested compounds.

No.	Compounds	RT (min)	(MRM)*m/z*	CE (eV)
1	Andrographolide	3.94	351.22→257.15	15
2	Dehydroandrographolide	6.30	333.21→257.15	15
3	1-methoxicabony-β-carboline	3.07	227.08→195.05	25
4	4-methoxy-5-hydroxy-canthin-6-one	3.72	267.08→252.05	35
IS	Chloramphenicol	3.29	323.02→275.00	20

methanol was added and vortex-mixed for 3 min. After centrifugation at 12,000 rpm for 15 min (4°C), the supernatant of the mixture was transferred to another vial and evaporated to dryness with nitrogen purging. The residue was resolved with 100 μ of methanol, vortex-mixed for 1 min, and centrifuged at 12,000 rpm for 10 min (4°C). A 2 μl aliquot of the supernatant was injected into the UPLC-MS/MS system for analysis.

2.5 Preparation of Standard and Quality Control Samples

Standard stock solutions of andrographolide (5,125 ng/ml), dehydroandrographolide (2000 ng/ml), 1-methoxicabony-β-carboline (576 ng/ml), 4-methoxy-5-hydroxy-canthin-6-one (525 ng/ml), and IS (1,000 ng/ml) were prepared in methanol. Then, the calibration standard stock solutions of gradient concentrations were gained by serial dilution. The calibration standards were prepared by spiking 100 μl of appropriate standard working solution into 100 μl of blank serum to obtain the concentrations ranging from 5,125.00 to 51.25 ng/ml for andrographolide, 2000.00–20.00 ng/ml for dehydroandrographolide, 576.00–2.30 ng/ml for 1-methoxicabony-β-carboline, 525.00–2.10 ng/ml for 4-methoxy-5-hydroxy-canthin-6-one.

Quality control (QC) samples at low, middle and high concentrations (61.50, 384.38, and 4,000.00 ng/ml for andrographolide; 24.00, 150.00, and 1,500.00 ng/ml for dehydroandrographolide; 6.91, 43.20, and 450.00 ng/ml for 1-methoxicabony-β-carboline; 6.30, 39.38, and 400.00 ng/ml for 4-methoxy-5-hydroxy-canthin-6-one) were also prepared by the same procedures.

2.6 Instrumentation and Chromatographic Conditions

Chromatographic analysis was performed using UPLC-MS/MS, utilizing a Finnigan Surveyor auto-sampler and a Finnigan Surveyor LC pump combined with a triple quadrupole TSQ Quantum mass spectrometer electrospray ionization (ESI) interface (Thermo Fisher, Palo Alto, CA). The chromatographic separation was performed on the Waters Acquity UPLC BEH C18 column (2.1 mm × 100 mm; 1.7 μm). The mobile phase consisted of acetonitrile (A) and 0.1% formic acid (B) with a gradient elution program (0-5 min, 20% A-35% A; 5-6 min, 35% A-100% A; 6–8min, 100% A; 8–8.5 min, 100% A-20% A; 8.5–10.5 min, 20% A) at a flow rate of 0.4 ml/min. The column temperature was maintained at 40°C throughout the analysis. The injection volume was 2 μl.

Quantification was performed using multiple reaction monitoring (MRM) in the positive ionization mode, and the optimized MRM parameters of the four analytes and IS are listed in **Table 1**. The MRM transition, retention time (RT), and collision energy (CE) values were based on Thermo Foundation 2.0. Curtain gas pressure at 35 psi, ion source gas 1 and gas 2 at 55 psi, ion spray voltage at 5500 V, and temperature at 500°C.

2.7 Method Validation

Specificity was assessed by analyzing blank serum samples to investigate the potential interferences of compounds and IS. The calibration curves for quantitative analysis were drawn by plotting the peak area ratio (y) of each compound to IS against the corresponding nominal concentration (x) using weighted ($1/x^2$) least-squares linear regression. Simultaneously, the lowest concentration in the calibration curve was defined as the lower limit of quantification (LLOQ) (S/N ≥ 10). The precision and accuracy were evaluated using six replicates of QC samples on three consecutive days. The intra- and inter-day accuracy and precision variations were expressed as the relative error (RE) and relative standard deviation (RSD).

The stability test of QC samples in rat serum was assessed in a different store environment, including at room temperature (25°C) for 24 h, at −80 °C for 1 month, and three freeze-thaw cycles. Recovery was determined at three QC levels and calculated by comparing the compound standard peak areas obtained from extracted samples with post-extracted samples spiked with the compound. Matrix effects were calculated by matching spiking post-extracted blank serum samples with corresponding standard clean solutions at three concentrations of QC samples.

2.8 Statistical Analyses

Non-compartment model pharmacokinetic parameters, including the time to reach the maximum serum concentration (T_{max}), the maximum serum concentration (C_{max}), the elimination half-time ($T_{1/2}$), the area under the serum concentration-time curve (AUC), and mean residence time (MRT), were calculated by DAS (version 3.2.8, Chinese Pharmacological Association, Anhui, China). The difference between the control and model groups was statistically analyzed using SPSS 26.0 (IBM Company, Chicago). All data in this study were subjected to a one-way analysis of variance

TABLE 2 | The details of the regression analysis of four compounds in rat serum.

Compounds	Calibration curves	R^2	Liner range (ng/ml)	LLOQ (ng/ml)
Andrographolide	Y = 0.0001X + 0.0056	0.9998	51.25–5,125.00	51.25
Dehydroandrographolide	Y = 0.0001X + 0.0068	0.9970	20.00–2000.00	20.00
1-methoxicabony-β-carboline	Y = 0.0445X + 0.1443	0.9981	2.30–576.00	2.30
4-methoxy-5-hydroxy-canthin-6-one	Y = 0.0682X + 0.1070	0.9989	2.10–525.00	2.10

TABLE 3 | |Precision and accuracy of four compounds in rat serum (n = 6).

Compounds	Concentration (ng/ml)	Accuracy (RE, %)		Precision (RSD, %)	
		Intra-day	Inter-day	Intra-day	Inter-day
Andrographolide	61.50	−1.46	−0.75	9.31	12.74
	384.38	11.58	3.52	6.77	9.59
	4,000.00	5.81	6.70	9.76	8.03
Dehydroandrographolide	24.00	4.76	−11.05	12.12	11.62
	150.00	7.25	4.30	4.30	9.57
	1,500.00	3.62	−1.05	3.91	8.62
1-methoxicabony-β-carboline	6.91	4.94	3.11	4.05	3.84
	43.20	3.24	1.52	4.23	4.49
	450	4.13	3.46	5.82	7.96
4-methoxy-5-hydroxy-canthin-6-one	6.30	−4.76	1.74	13.79	9.51
	39.38	2.62	7.96	2.84	4.71
	400.00	4.72	5.01	6.59	6.63

TABLE 4 | Recovery and matrix effects of the four compounds in rat serum (n = 6).

Compounds	Concentration (ng/ml)	Recovery		Matrix effect	
		Mean ± SD (%)	RSD (%)	Mean ± SD (%)	RSD (%)
Andrographolide	61.50	91.98 ± 5.07	5.51	69.98 ± 7.99	11.42
	384.38	82.03 ± 3.83	4.67	69.77 ± 2.24	3.21
	4,000.00	86.51 ± 2.09	2.42	72.36 ± 2.83	3.91
Dehydroandrographolide	24.00	65.29 ± 2.86	4.37	73.18 ± 7.43	10.15
	150.00	66.86 ± 4.03	6.03	75.50 ± 4.29	5.68
	1,500.00	66.41 ± 3.03	4.56	75.63 ± 3.55	4.69
1-methoxicabony-β-carboline	6.91	91.51 ± 0.74	0.81	109.73 ± 1.20	1.09
	43.20	91.84 ± 0.88	0.96	112.67 ± 2.41	2.14
	450.00	92.18 ± 1.21	1.31	108.91 ± 3.06	2.81
4-methoxy-5-hydroxy-canthin-6-one	6.30	80.78 ± 2.55	3.15	112.25 ± 2.10	1.87
	39.38	78.69 ± 1.48	1.88	112.36 ± 2.19	1.95
	400.00	82.74 ± 2.11	2.56	106.75 ± 2.25	2.11

(ANOVA) and then expressed by mean ± standard deviation (SD). LSD t-test was applied when the homogeneity of variance assumptions was satisfied; otherwise, Dunnett's t-test was used. A $p < 0.05$ was considered statistically significant.

3 RESULTS AND DISCUSSION

3.1 Method Validation

3.1.1 Specificity

As shown in **Figure 2**, no endogenous interference was observed in blank serum, which proves the assay specificity.

3.1.2 Calibration Curves and Lower Limit of Quantification

All calibration curves showed well linearity, and the coefficient of determination (R^2) was greater than 0.9970. **Table 2** lists regression equations, correlation coefficients, and linear ranges of the four analytes.

3.1.3 Accuracy and Precision

As shown in **Table 3**, intra- and inter-day accuracy were within ± 11.58%, whereas intra- and inter-day precision were less than 13.79%, indicating that these two parameters were all within the acceptable range for research in biological media.

TABLE 5 | The stability test of four compounds in rat serum (n = 6).

Compounds	Concentration (ng/ml)	25°C for 12 h		4°C for 24 h		–80°C for 30 days		Three freeze-thaw	
		Mean (ng/ml)	RSD (%)	Mean (ng/mL)	RSD (%)	Mean (ng/ml)	RSD (%)	Mean (ng/mL)	RSD (%)
Andrographolide	61.50	56.68 ± 4.20	7.41	58.54 ± 4.47	7.64	58.97 ± 2.93	4.97	60.13 ± 3.34	5.55
	384.38	399.59 ± 9.79	2.45	383.22 ± 9.64	2.51	370.23 ± 17.30	4.67	396.68 ± 13.05	3.29
	4,000.00	3,896.61 ± 129.89	3.33	3,915.74 ± 98.45	2.51	3,904.68 ± 126.18	3.23	3,923.07 ± 110.39	2.81
Dehydroandrographolide	24.00	23.51 ± 0.69	2.92	25.71 ± 1.69	6.59	22.46 ± 2.57	11.45	21.20 ± 2.30	10.85
	150.00	153.93 ± 10.00	6.50	156.59 ± 14.58	9.31	151.06 ± 3.31	2.19	143.60 ± 9.61	6.69
	1,500.00	1,439.13 ± 52.46	3.64	1,421.52 ± 61.75	4.34	1,419.63 ± 51.60	3.63	1,428.09 ± 67.73	4.74
1-methoxicabony-β-carboline	6.91	7.09 ± 0.16	2.19	7.71 ± 0.12	1.49	7.43 ± 0.66	8.83	6.63 ± 0.51	7.63
	43.20	42.21 ± 3.37	7.98	44.64 ± 3.27	7.32	42.66 ± 1.92	4.49	42.04 ± 2.18	5.18
	450.00	439.66 ± 16.78	3.82	442.09 ± 15.98	3.61	436.91 ± 13.57	3.11	440.84 ± 17.31	3.93
4-methoxy-5-hydroxy-canthin-6-one	6.30	5.50 ± 0.37	6.82	6.38 ± 0.41	6.38	6.39 ± 0.23	3.64	5.65 ± 0.12	2.11
	39.38	40.41 ± 3.15	7.78	39.35 ± 4.12	10.47	42.93 ± 1.44	3.35	41.43 ± 0.76	1.83
	400.00	387.02 ± 9.84	2.54	391.53 ± 10.08	2.57	381.78 ± 17.23	4.51	386.59 ± 20.07	5.19

TABLE 6 | The main pharmacokinetic parameters of the four compounds in rat serum after oral administration of XLF (n = 8).

Compounds	Group	C_{max} (ng/L)	T_{max} (h)	$T_{1/2}$ (h)	$MRT_{0\to\infty}$ (h)	$AUC_{0\to t}$ (ng/mL*h)	$AUC_{0\to\infty}$ (ng/mL*h)
andrographolide	Control	2,309.75 ± 372.63	0.53 ± 0.21	8.77 ± 2.96	8.42 ± 2.75	6,430.54 ± 1,111.78	7,120.49 ± 1,388.81
	UC	4,093.93 ± 493.79[b]	0.69 ± 0.26	7.40 ± 5.02	7.40 ± 5.02	15,854.73 ± 8,467.51[b]	18,431.87 ± 12,812.25[a]
dehydroandrographolide	Control	892.35 ± 147.60	0.28 ± 0.09	2.28 ± 1.69	5.04 ± 1.96	2,327.38 ± 512.51	2,355.73 ± 560.39
	UC	1,152.99 ± 200.01[a]	0.38 ± 0.13	2.86 ± 2.01	5.08 ± 1.53	4,694.04 ± 2,258.15[a]	4,794.15 ± 2,389.47[a]
1-methoxicabony-β-carboline	Control	128.95 ± 33.92	0.69 ± 0.37	1.02 ± 0.43	1.52 ± 0.33	214.95 ± 78.40	218.79 ± 79.21
	UC	159.58 ± 18.88[a]	1.13 ± 0.23[a]	1.20 ± 0.41	2.23 ± 0.63[a]	424.43 ± 143.29[b]	444.08 ± 153.98[b]
4-methoxy-5-hydroxy-canthin-6-one	Control	395.26 ± 97.67	0.08 ± 0.00	3.15 ± 0.96	3.59 ± 1.43	553.61 ± 74.16	594.78 ± 117.49
	UC	419.23 ± 103.53	0.43 ± 0.47	3.30 ± 1.52	3.66 ± 1.55	758.79 ± 142.16[b]	817.12 ± 177.20[a]

[a]p < *0.05 and.*
[b]p < *0.01 compared with the control group.*

3.1.4 Recovery and Matrix Effect

As shown in **Table 4**, the RSD values of extraction recovery and matrix effect were not greater than 10.15%, which indicated that recoveries were consistent and reproducible at different concentrations, and no significant matrix effects were observed for the four analytes.

3.1.5 Stability

As shown in **Table 5**, the four analytes in rat serum under different conditions were stable, and their RSD was less than 10.85%.

3.2 Pharmacokinetics

The UPLC method was applied to a comparative pharmacokinetic study of four compounds in control and UC rat serum after oral administration of LXF. The concentration-time curves of the compounds in the control and model groups are presented in **Figure 3**, and the corresponding pharmacokinetic parameters are shown in **Table 6**.

Compared with the control group, the AUC_{0-t} and $AUC_{0-\infty}$ of four compounds were significantly increased ($p < 0.05$ and $p < 0.01$) in the UC group, symbolizing higher exposure levels in the serum of the UC state. Meanwhile, longer T_{max} and $MRT_{0-\infty}$ were observed for compounds 1-methoxicabony-β-carboline in the UC group ($p < 0.05$), indicating slow absorption in the pathological state. It was also found from the serum concentration-time curves that dehydroandrographolide showed double peaks in both groups, which indicated that an enterohepatic circulation might exist. The result was inconsistent with our previous literature, which may result from the difference in the composition of Chinese herbal medicines (Zhang et al., 2021). Our previous studies evaluated the pharmacokinetic profiles of Xiaoyan Lidan Formula (XYLDF) in the normal and cholestasis states. We found that some bioactive components of XYLDF have different pharmacokinetic characteristics in two kinds of physiological states, which indicated that the state of cholestasis might led to this result. Interestingly, LXF has only one less herb (xihuancao) than XYLDF, but they are used to treat different diseases in clinical. *Xihuangcao* may affect the absorption process of dehydroandrographolide. These two research were under different instrumentation and chromatographic conditions, such as the MRM in this study was in the positive ionization mode, which might cause different results.

Andrographolide and dehydroandrographolide have highly similar chemical structures. However, the C_{max}, $AUC_{0-t,}$ and $AUC_{0-\infty}$ of andrographolide were higher than the latter. Andrographolide has one hydroxyl group than dehydroandrographolide, which may lead to greater polarity, and the content of andrographolide is higher than

dehydroandrographolide in LXF. This result is consistent with the literature (Chen et al., 2007; Xu et al., 2015). Simultaneously, 4-methoxy-5-hydroxy-canthin-6-one showed double peaks in the UC group but not showed in the control group. It is implied that the absorption and metabolism process *in vivo* might be influenced by the UC state, which is worth attention in further study.

In this study, DSS, as an inducing agent to damage gut epithelial cells and integrity of the mucosal barrier, was used to induce UC, which has been reported in the experimental animal in numerous studies (Okayasu et al., 1990; Cao et al., 2018; Dinallo et al., 2019; Li et al., 2020). UC is a debilitating and incurable disease that reduces intestinal microbes' diversity and abundance (Bucci, 2020; Lu et al., 2022). The intestinal tract of humans is the leading site of xenobiotic metabolism, and microbes inhabiting the gastrointestinal tract can affect the metabolism outcome of environmental toxicants and pharmaceuticals, then influence their pharmacokinetics (Collins and Patterson, 2020). It might reveal the difference in the serum concentration-time curves of 4-methoxy-5-hydroxy-canthin-6-one between the control and UC groups. Meanwhile, some research shows that the microbiome regulates host gene expression, such as P450 enzymes (CYP450s), multi-drug resistance proteins, and transcription factors (Nelson, 2018; Mays and Nair, 2021). CYP450s are hemoproteins' superfamily that catalyzes different oxidative reactions and metabolizes 70-80% of pharmaceuticals (Monserrat et al., 2020). The reduction in activities of some CYP450s may cause the serum concentration and AUC of the analytes in the UC group to increase. Comparing pharmacokinetic profiles in UC and normal states suggested that UC might change the absorption process of LXF *in vivo* and then affect its efficacy.

4 CONCLUSION

In summary, we first established a rapid, stable, sensitive, and reliable UPLC-MS/MS method to quantify the concentrations of four major bioactive components after oral administration of the LXF in rat serum. Moreover, this method was successfully applied in comparing the differences in pharmacokinetic profiles of LXF in states of physiological and UC. We found that four primary bioactive ingredients of LXF were quickly absorbed after oral administration in both states and higher exposure levels in the UC state. Collectively, the results of this research would offer some guidance in improving the therapeutic regimen and evaluating the clinical efficacy of LXF for the treatment of UC, promoting the development of personalized medicine.

DATA AVAILABILITY STATEMENT

The original contributions presented in the study are included in the article/**Supplementary Material**, further inquiries can be directed to the corresponding authors.

ETHICS STATEMENT

The animal study was reviewed and approved by the Care of Animals of Guangzhou University of Chinese Medicine (Guangzhou, China) (No. 712052).

AUTHOR CONTRIBUTIONS

CZ, CL, and MW provided the concept and designed the study. KZ, ZL, and QW performed the experiments and analyzed the data. KZ and ZL wrote the manuscript. MW and FL revised and proof-read the manuscript. All authors reviewed the manuscript and approved its submission.

FUNDING

This research was supported and funded by the National Natural Science Foundation of China (Grant No. 82174266, 81974520, 82104504, and 81673872) and the China Postdoctoral Science Foundation (2021M700963).

SUPPLEMENTARY MATERIAL

The Supplementary Material for this article can be found online at: https://www.frontiersin.org/articles/10.3389/fphar.2022.936846/full#supplementary-material.

REFERENCES

Arifullah, M., Namsa, N. D., Mandal, M., Chiruvella, K. K., Vikrama, P., and Gopal, G. R. (2013). Evaluation of Anti-bacterial and Anti-oxidant Potential of Andrographolide and Echiodinin Isolated from Callus Culture of Andrographis Paniculata Nees. *Asian Pac J. Trop. Biomed.* 3 (8), 604–610. doi:10.1016/S2221-1691(13)60123-9

Bucci, M. (2020). A Gut Reaction. *Nat. Chem. Biol.* 16 (4), 363. doi:10.1038/s41589-020-0514-0

Burgos, R. A., Alarcón, P., Quiroga, J., Manosalva, C., and Hancke, J. (2020). Andrographolide, an Anti-inflammatory Multitarget Drug: All Roads Lead to Cellular Metabolism. *Molecules* 26 (1). doi:10.3390/molecules26010005

Cao, H., Liu, J., Shen, P., Cai, J., Han, Y., Zhu, K., et al. (2018). Protective Effect of Naringin on DSS-Induced Ulcerative Colitis in Mice. *J. Agric. Food Chem.* 66 (50), 13133–13140. doi:10.1021/acs.jafc.8b03942

Chen, L., Yu, A., Zhuang, X., Zhang, K., Wang, X., Ding, L., et al. (2007). Determination of Andrographolide and Dehydroandrographolide in Rabbit Plasma by On-Line Solid Phase Extraction of High-Performance Liquid Chromatography. *Talanta* 74 (1), 146–152. doi:10.1016/j.talanta.2007.05.043

Chen, Y., Zhang, P., Chen, W., and Chen, G. (2020). Ferroptosis Mediated DSS-Induced Ulcerative Colitis Associated with Nrf2/HO-1 Signaling Pathway. *Immunol. Lett.* 225, 9–15. doi:10.1016/j.imlet.2020.06.005

Cohen, R. D., Yu, A. P., Wu, E. Q., Xie, J., Mulani, P. M., and Chao, J. (2010). Systematic Review: the Costs of Ulcerative Colitis in Western Countries. *Aliment. Pharmacol. Ther.* 31 (7), 693–707. doi:10.1111/j.1365-2036.2010.04234.x

Collins, S. L., and Patterson, A. D. (2020). The Gut Microbiome: an Orchestrator of Xenobiotic Metabolism. *Acta Pharm. Sin. B* 10 (1), 19–32. doi:10.1016/j.apsb.2019.12.001

Dinallo, V., Marafini, I., Di Fusco, D., Laudisi, F., Franzè, E., Di Grazia, A., et al. (2019). Neutrophil Extracellular Traps Sustain Inflammatory Signals in Ulcerative Colitis. *J. Crohns Colitis.* 13 (6), 772–784. doi:10.1093/ecco-jcc/jjy215

Du, L., and Ha, C. (2020). Epidemiology and Pathogenesis of Ulcerative Colitis. *Gastroenterol. Clin. North Am.* 49 (4), 643–654. doi:10.1016/j.gtc.2020.07.005

Feuerstein, J. D., Moss, A. C., and Farraye, F. A. (2019). Ulcerative Colitis. *Mayo Clin. Proc.* 94 (7), 1357–1373. doi:10.1016/j.mayocp.2019.01.018

Hu, H., Hu, C., Peng, J., Ghosh, A. K., Khan, A., Sun, D., et al. (2021). Bioassay-Guided Interpretation of Antimicrobial Compounds in Kumu, a TCM Preparation from Picrasma Quassioides' Stem via UHPLC-Orbitrap-Ion Trap Mass Spectrometry Combined with Fragmentation and Retention Time Calculation. *Front. Pharmacol.* 12, 761751. doi:10.3389/fphar.2021.761751

Li, H., Fan, C., Lu, H., Feng, C., He, P., Yang, X., et al. (2020). Protective Role of Berberine on Ulcerative Colitis through Modulating Enteric Glial Cells-Intestinal Epithelial Cells-Immune Cells Interactions. *Acta Pharm. Sin. B* 10 (3), 447–461. doi:10.1016/j.apsb.2019.08.006

Li, T., Ye, W., Huang, B., Lu, X., Chen, X., Lin, Y., et al. (2019). Determination and Pharmacokinetic Study of Echinatin by UPLC-MS/MS in Rat Plasma. *J. Pharm. Biomed. Anal.* 168, 133–137. doi:10.1016/j.jpba.2019.02.023

Liu, F., Zhang, Q., Lin, C., Yao, Y., Wang, M., Liu, C., et al. (2020). A Comparative Study on Pharmacokinetics and Tissue Distribution of 5-Hydroxy-4-Methoxycanthin-6-One and its Metabolite in Normal and Dextran Sodium Sulfate-Induced Colitis Rats by HPLC-MS/MS. *J. Pharm. Pharmacol.* 72 (12), 1761–1770. doi:10.1111/jphp.13285

Lu, X., Jing, Y., Zhang, N., and Cao, Y. (2022). Eurotium cristatum, a Probiotic Fungus from Fuzhuan Brick Tea, and its Polysaccharides Ameliorated DSS-Induced Ulcerative Colitis in Mice by Modulating the Gut Microbiota. *J. Agric. Food Chem.* 70 (9), 2957–2967. doi:10.1021/acs.jafc.1c08301

Lu, Z., Yuan, Y., Liu, F., Wang, M., Yao, Y., Lin, C., et al. (2021). Mechanism Study of Liandan Xiaoyan Prescription on Attenuating Ulcerative Colitis Based on the Components into the Blood Analysis. *J. Chin. Med. Mater.* (04), 863–872. doi:10.13863/j.issn1001-4454.2021.04.017

Ma, Y., Zhou, K., Fan, J., and Sun, S. (2016). Traditional Chinese Medicine: Potential Approaches from Modern Dynamical Complexity Theories. *Front. Med.* 10 (1), 28–32. doi:10.1007/s11684-016-0434-2

Mak, W. Y., Zhao, M., Ng, S. C., and Burisch, J. (2020). The Epidemiology of Inflammatory Bowel Disease: East Meets West. *J. Gastroenterol. Hepatol.* 35 (3), 380–389. doi:10.1111/jgh.14872

Mays, Z. J. S., and Nair, N. U. (2021). A Quantitative Model for Metabolic Intervention Using Gut Microbes. *Biotechnol. Prog.* 37 (5), e3125. doi:10.1002/btpr.3125

Mehta, S., Sharma, A. K., and Singh, R. K. (2022). Ethnobotany, Pharmacological Activities and Bioavailability Studies on "King of Bitters" (Kalmegh): A Review (2010-2020). *Comb. Chem. High. Throughput Screen* 25 (5), 788–807. doi:10.2174/1386207324666210310140611

Molodecky, N. A., Soon, I. S., Rabi, D. M., Ghali, W. A., Ferris, M., Chernoff, G., et al. (2012). Increasing Incidence and Prevalence of the Inflammatory Bowel Diseases with Time, Based on Systematic Review. *Gastroenterology* 142 (1), 46–e30. doi:10.1053/j.gastro.2011.10.001

Monserrat Villatoro, J., García García, I., Bueno, D., de la Cámara, R., Estébanez, M., López de la Guía, A., et al. (2020). Randomised Multicentre Clinical Trial to Evaluate Voriconazole Pre-emptive Genotyping Strategy in Patients with Risk of Aspergillosis: Vorigenipharm Study Protocol. *BMJ Open* 10 (10), e037443. doi:10.1136/bmjopen-2020-037443

Nelson, D. R. (2018). Cytochrome P450 Diversity in the Tree of Life. *Biochim. Biophys. Acta Proteins Proteom* 1866 (1), 141–154. doi:10.1016/j.bbapap.2017.05.003

Ng, S. C., Bernstein, C. N., Vatn, M. H., Lakatos, P. L., Loftus, E. V., Tysk, C., et al. (2013). Geographical Variability and Environmental Risk Factors in Inflammatory Bowel Disease. *Gut* 62 (4), 630–649. doi:10.1136/gutjnl-2012-303661

Okayasu, I., Hatakeyama, S., Yamada, M., Ohkusa, T., Inagaki, Y., and Nakaya, R. (1990). A Novel Method in the Induction of Reliable Experimental Acute and Chronic Ulcerative Colitis in Mice. *Gastroenterology* 98 (3), 694–702. doi:10.1016/0016-5085(90)90290-h

Patil, R., and Jain, V. (2021). Andrographolide: A Review of Analytical Methods. *J. Chromatogr. Sci.* 59 (2), 191–203. doi:10.1093/chromsci/bmaa091

Roselli, M., and Finamore, A. (2020). Use of Synbiotics for Ulcerative Colitis Treatment. *Curr. Clin. Pharmacol.* 15 (3), 174–182. doi:10.2174/1574884715666191226120322

Sareer, O., Ahmad, S., and Umar, S. (2014). Andrographis Paniculata: a Critical Appraisal of Extraction, Isolation and Quantification of Andrographolide and Other Active Constituents. *Nat. Prod. Res.* 28 (23), 2081–2101. doi:10.1080/14786419.2014.924004

Sun, Y., Zhang, Z., Zheng, C. Q., and Sang, L. X. (2021). Mucosal Lesions of the Upper Gastrointestinal Tract in Patients with Ulcerative Colitis: A Review. *World J. Gastroenterol.* 27 (22), 2963–2978. doi:10.3748/wjg.v27.i22.2963

Ungaro, R., Mehandru, S., Allen, P. B., Peyrin-Biroulet, L., and Colombel, J. F. (2017). Ulcerative Colitis. *Lancet* 389 (10080), 1756–1770. doi:10.1016/S0140-6736(16)32126-2

Wang, N., Li, Z. Y., Zheng, X. L., Li, Q., Yang, X., and Xu, H. (2018). Quality Assessment of Kumu Injection, a Traditional Chinese Medicine Preparation, Using HPLC Combined with Chemometric Methods and Qualitative and Quantitative Analysis of Multiple Alkaloids by Single Marker. *Molecules* 23 (4), 856. doi:10.3390/molecules23040856

Wasman, S. Q., Mahmood, A. A., Chua, L. S., Alshawsh, M. A., and Hamdan, S. (2011). Antioxidant and Gastroprotective Activities of Andrographis Paniculata (Hempedu Bumi) in Sprague Dawley Rats. *Indian J. Exp. Biol.* 49 (10), 767–772.

Wu, H., Feng, F., Jiang, X., Hu, B., Qiu, J., Wang, C., et al. (2020). Pharmacokinetic and Metabolic Profiling Studies of Sennoside B by UPLC-MS/MS and UPLC-Q-TOF-MS. *J. Pharm. Biomed. Anal.* 179, 112938. doi:10.1016/j.jpba.2019.112938

Xu, F. F., Fu, S. J., Gu, S. P., Wang, Z. M., Wang, Z. Z., He, X., et al. (2015). Simultaneous Determination of Andrographolide, Dehydroandrographolide and Neoandrographolide in Dog Plasma by LC-MS/MS and its Application to a Dog Pharmacokinetic Study of Andrographis Paniculata Tablet. *J. Chromatogr. B Anal. Technol. Biomed. Life Sci.* 990, 125–131. doi:10.1016/j.jchromb.2015.03.014

Yang, N., Xiong, A., Wang, R., Yang, L., and Wang, Z. (2016). Quality Evaluation of Traditional Chinese Medicine Compounds in Xiaoyan Lidan Tablets: Fingerprint and Quantitative Analysis Using UPLC-MS. *Molecules* 21 (2), 83. doi:10.3390/molecules21020083

Yao, Y. F., Lin, C. Z., Liu, F. L., Zhang, R. J., Zhang, Q. Y., Huang, T., et al. (2018). Identification and Pharmacokinetic Studies on Complanatuside and its Major Metabolites in Rats by UHPLC-Q-TOF-MS/MS and LC-MS/MS. *Molecules* 24 (1), 71. doi:10.3390/molecules24010071

Zhang, K., Wang, M., Yao, Y., Huang, T., Liu, F., Zhu, C., et al. (2021). Pharmacokinetic Study of Seven Bioactive Components of Xiaoyan Lidan Formula in Cholestatic and Control Rats Using UPLC-MS/MS. *Biomed. Pharmacother.* 139, 111523. doi:10.1016/j.biopha.2021.111523

Zhang, M., Lin, L., Lin, H., Qu, C., Yan, L., and Ni, J. (2018). Interpretation the Hepatotoxicity Based on Pharmacokinetics Investigated through Oral Administrated Different Extraction Parts of Polygonum Multiflorum on Rats. *Front. Pharmacol.* 9, 505. doi:10.3389/fphar.2018.00505

Zhang, Q., Lin, C., Yuan, Y., Ma, Y., and Zhu, C. (2020). Chemical Constituents of Picrasma Quassioides. *Chin. Tradit. Herb. Drugs.* 51 (19), 4884–4890. doi:10.7501/j.issn.0253-2670.2020.19.005

Zhu, L. J., Chen, L., Bai, C. F., Wu, A. G., Liang, S. C., Huang, F. H., et al. (2020). A Rapid and Sensitive UHPLC-MS/MS Method for the Determination of Ziyuglycoside I and its Application in a Preliminary Pharmacokinetic Study in Healthy and Leukopenic Rats. *Biomed. Pharmacother.* 123, 109756. doi:10.1016/j.biopha.2019.109756

Conflict of Interest: The authors declare that the research was conducted in the absence of any commercial or financial relationships that could be construed as a potential conflict of interest.

Publisher's Note: All claims expressed in this article are solely those of the authors and do not necessarily represent those of their affiliated organizations, or those of the publisher, the editors and the reviewers. Any product that may be evaluated in this article, or claim that may be made by its manufacturer, is not guaranteed or endorsed by the publisher.

frontiers | Frontiers in Pharmacology

ORIGINAL RESEARCH
published: 05 July 2022
doi: 10.3389/fphar.2022.929177

Pharmacokinetics and Main Metabolites of Anwulignan in Mice

*Cong Chen, Yanbo Feng, Han Li, Hao Lin, Shu Jing, He Li, Chunmei Wang, Jianguang Chen and Jinghui Sun**

College of Pharmacy, Beihua University, Jilin, China

Anwulignan is a representative component of Chinese traditional medicine *Schisandra sphenanthera*, with strong pharmacological activities. However, there are few reports on its pharmacokinetics and metabolites in the body. In this study, a metabolomic method based on UHPLC-Q-Orbitrap-MS was used to study the pharmacokinetics of anwulignan in the blood, organs, urine, and feces samples of mice after the intragastric administration of anwulignan (10 mg/kg). The pharmacokinetic parameters were calculated, and the distribution characteristics and main metabolites of anwulignan in the body of mice were analyzed. The results showed that the retention time of anwulignan in the body of mice was longer ($t_{1/2}$ = 7.1 h), and anwulignan was widely distributed in the body ($V_{z/F}$ = 32.81 L/kg), especially in the liver. The order of anwulignan concentration in the tissues of mice from high to low was the liver > heart > brain > kidney > lung > spleen. Anwulignan was mainly excreted through the digestive tract in the form of its prototype and metabolites, indicating that it might experience an enterohepatic circulation. A total of seven metabolites were identified, and the demethylation, hydroxylation, dehydroxylation, and demethoxylation were considered to be the main metabolic ways of anwulignan in the body of mice.

Keywords: ***Schisandra sphenanthera*, anwulignan, pharmacokinetics, metabolites, UHPLC-Q-Orbitrap-MS**

OPEN ACCESS

Edited by:
Guo Ma,
Fudan University, China

Reviewed by:
Lin-Lin Chen,
Hubei University of Chinese Medicine, China
Ling Ye,
Southern Medical University, China
Mario Juan Simirgiotis,
Austral University of Chile, Chile

****Correspondence:***
Jinghui Sun
sunjinghui2008@126.com

Specialty section:
This article was submitted to Drug Metabolism and Transport, a section of the journal Frontiers in Pharmacology

Received: *26 April 2022*
Accepted: *20 May 2022*
Published: *05 July 2022*

Citation:
Chen C, Feng Y, Li H, Lin H, Jing S, Li H, Wang C, Chen J and Sun J (2022) Pharmacokinetics and Main Metabolites of Anwulignan in Mice. Front. Pharmacol. 13:929177. doi: 10.3389/fphar.2022.929177

INTRODUCTION

Schisandra sphenanthera, the mature and dry fruit of *S. sphenanthera* Rehd. Et Wils, has been used as a representative tonic drug in China for 2,000 years (Jiang et al., 2019). The active components of *S. sphenanthera* include lignans, volatile oil, organic acids, and polysaccharides, among which lignans are the main active components, with some pharmacological effects, such as bacteriostasis, sedation and hypnosis, anti-aging, anti-oxidation, and hepatoprotection (Jiang et al., 2016; Zhang et al., 2021). Wuzhi Tablets, an alcohol-extracted preparation of *S. sphenanthera*, is used for the treatment of hepatitis and liver insufficiency caused by viruses and drugs in clinic (Chen et al., 2019). Anwulignan is a representative lignan component of *S. sphenanthera* and a characteristic component for the identification of *S. sphenanthera*, and also one of the main components in Wuzhi Tablets (Lu and Liu, 1992; Yang et al., 2014). However, there are few reports on the efficacy of anwulignan. It was found in our previous study that anwulignan, with a good antioxidant effect, could significantly alleviate the liver injury induced by intestinal ischemia reperfusion in rats (Lin et al., 2020), regulate the immune function of aging mice induced by D-galactose by activating Nrf2/ARE pathway and regulating caspase-3, BCL2, and Bax (Li et al., 2020), and alleviate the heart injury induced by oxidative stress (Liu et al.,

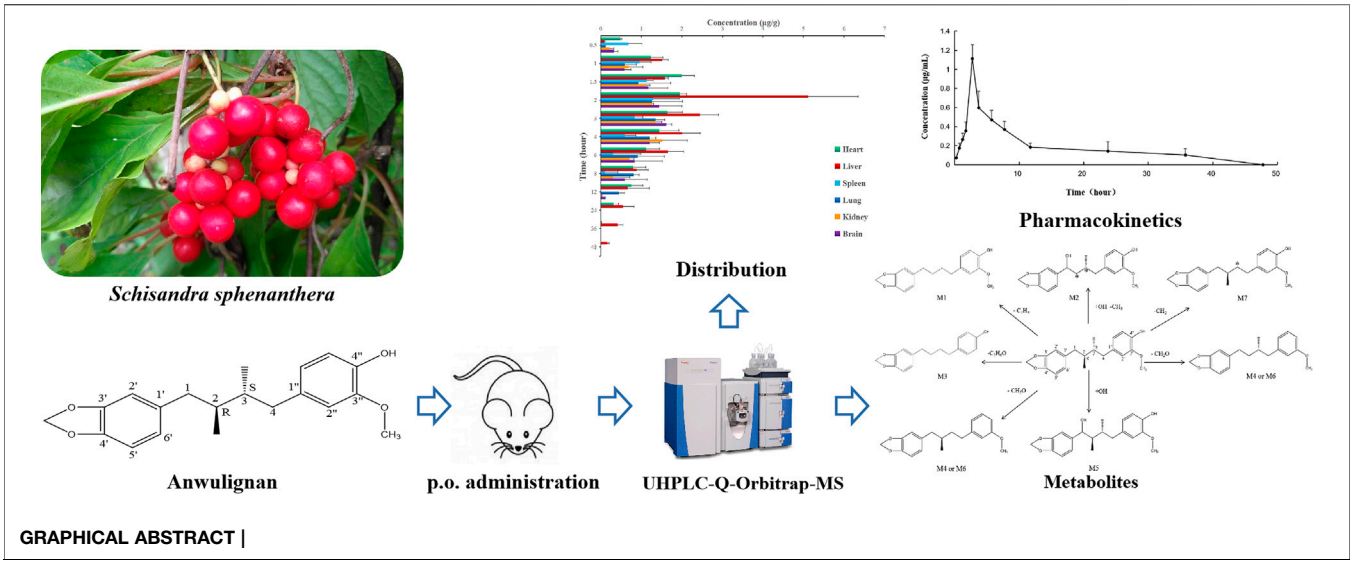

GRAPHICAL ABSTRACT |

2020a), with an anti-fatigue effect (Liu et al., 2020b; Zhang et al., 2020), demonstrating that it is worthy of further development and utilization. The pharmacokinetic study of anwulignan is particularly important to clarify the pharmacological mechanism of anwulignan *in vivo*, and not only the pharmacological effect of anwulignan on the human body can be observed but also more appropriate administration dosage and method can be found according to the absorption, distribution, and excretion law of anwulignan in various tissues and organs in the study so as to achieve the best curative effect. Therefore, it has a broad prospect for clinical research and social application to explore the action mechanism and potential targets of anwulignan based on pharmacokinetics. However, there are few studies on the pharmacokinetics of anwulignan, especially its biotransformation process *in vivo*.

The analysis of anwulignan is mainly carried out by HPLC and UV methods, and both of them are used for the study on the determination of its *in vitro* content. The main purpose of ultra-high-performance liquid chromatography–quadrupole orbitrap mass spectrometry (UHPLC-Q-Orbitrap-MS) analysis is to provide a quantitative method for candidate drugs, so as to obtain accurate and reliable conclusions in the study of pharmacokinetics. In this study, UHPLC-Q-Orbitrap-MS was used to analyze the pharmacokinetic characteristics, the distribution in tissues, and the main metabolites of anwulignan in the body of mice to seek the potentially active metabolites of anwulignan *in vivo*, which was expected to provide support in data and a reference for the pharmacodynamic material basis of anwulignan as a candidate drug.

MATERIALS AND METHODS

Chemicals and Reagents

The materials used in this study were as follows: anwulignan and schisantherin A (>98.0%, Chengdu Preferred Biotechnology Limited Company, Chengdu, Sichuan, China); methanol and ethyl acetate (HPLC–grade, TEDIA, Cincinnati, OH, United States); and de-ionized water (prepared by a Milli-Q Water purification system, Millipore, MA, United States).

Preparation of Plasma and Tissue Standards

Male ICR mice (18–22 g, Chang Chun Yisi Experimental Animal Technology Co., Ltd.) were used for experiments after the isolation and adaptation in our laboratory for 1 week. The mice were raised under the standard laboratory conditions for 1 week before experiments, with a free access to water and food. All experimental procedures were approved by Beihua University Laboratory Animal Ethics Committee (No. 20190907) and performed in accordance with the Guide for the Care and Use of Laboratory Animals.

Using methanol as the solvent, the concentration of anwulignan standard and schisandrin A (internal standard, IS) was 100 and 4 μg/ml, respectively. The different volumes of anwulignan standard stock solution and 200 μl schisandrin A were added into 200 μl of blank plasma of mice (or heart, liver, spleen, lung, kidney, and brain tissue homogenate, and a normal saline homogenate at the ratio of 1:9, w/v), which were mixed evenly. The solutions were centrifuged at 3,000 rpm for 10 min, then added with double volumes of methanol and swirled for 30 s, and centrifuged at 13,000 rpm for 10 min for obtaining the supernatants. The supernatants were blown dry until no liquid in them was found. The dried supernatant sentiments were dissolved in methanol up to a volume of 2 ml, respectively, and the solutions were swirled for 30 s and then filtered through a filter with a diameter of 0.45 μm into 1.5-ml sample bottles. Finally, the plasma (tissue) standard solutions at the final concentrations of anwulignan of 0.01, 0.02, 0.05, 0.1, 0.2, 0.5, 1, 2, and 5 μg/ml were prepared, respectively, and the concentration of schisandrin A in each sample was 4 μg/ml. A volume of 10 μl of each sample was analyzed by LC/MS to obtain the calibration curve (repeated three times). The 0.05, 0.5, and 5 μg/ml plasma (tissue) standard solutions were selected as

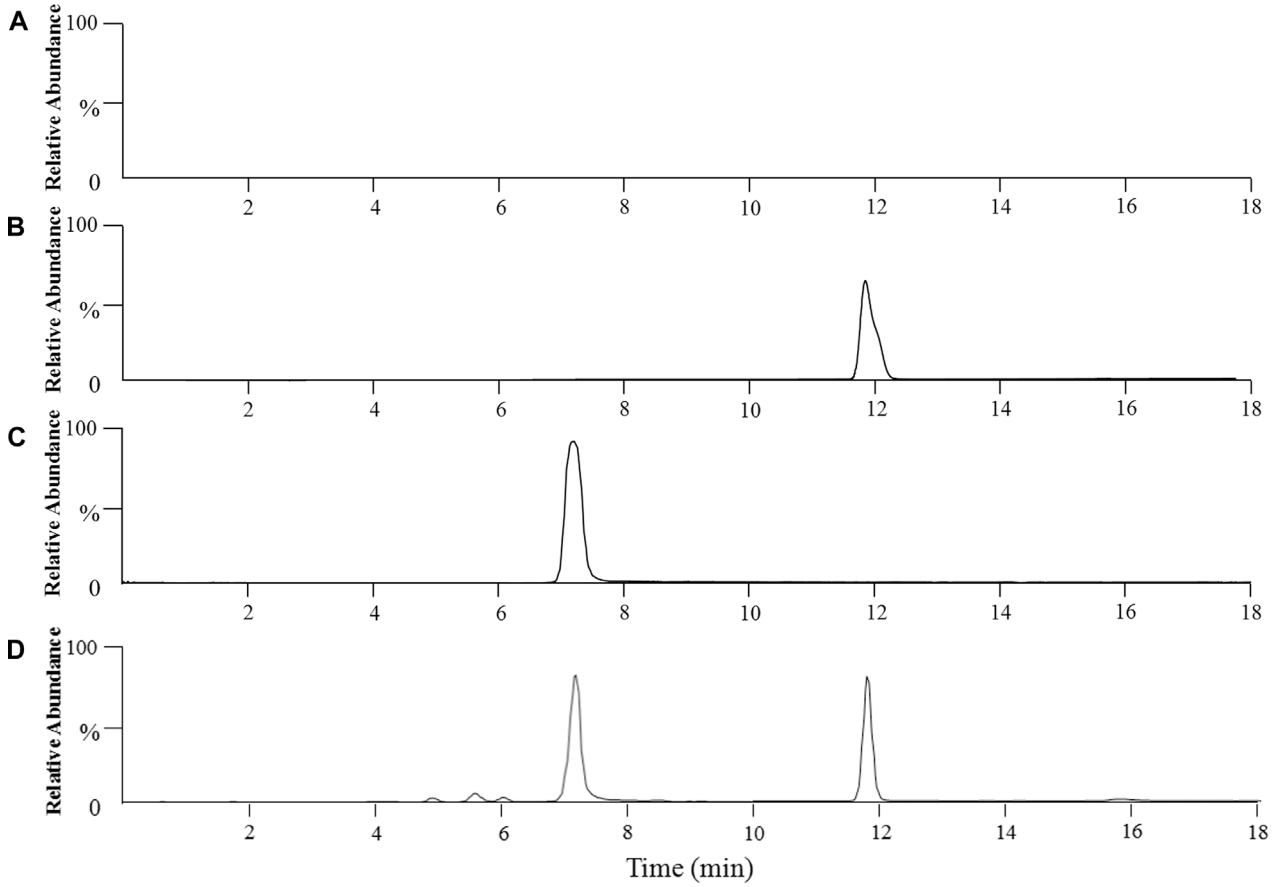

FIGURE 1 | Representative chromatograms of anwulignan and schisandrin A in the plasma of mice. Note: **(A)** blank plasma; **(B)** blank plasma spiked with anwulignan; **(C)** blank plasma spiked with schisandrin A; **(D)** a mice plasma sample collected after administration of a single dosage of anwulignan (3 h).

TABLE 1 | Regression equation of anwulignan in plasma and tissue samples.

Sample	Regression equation	R^2	Linear range (μg/ml)
Plasma	Y = 0.00005X–0.0492	0.9994	0.01–5.00
Heart	Y = 0.00006X + 0.0387	0.9991	0.02–5.00
Liver	Y = 0.00010X + 0.0154	0.9994	0.02–5.00
Lung	Y = 0.00004X + 0.0154	0.9993	0.02–5.00
Kidney	Y = 0.00004X + 0.0568	0.9992	0.02–5.00
Spleen	Y = 0.00004X–0.0372	0.9992	0.02–5.00
Brain	Y = 0.00005X + 0.0267	0.9993	0.02–5.00

the quality control (QC) samples for the method validation in this study.

Administration of Anwulignan and Collection and Preparation of Plasma and Organ Samples

Carboxymethylcellulose sodium (CMC-Na, 0.5 g) was dissolved in 1,000 ml distilled water, and 10 mg anwulignan was dissolved in 10 ml of the CMC-Na solution prepared above, at the concentration of 1 mg/ml. Sixty mice were fasted for 12 h, and then intragastrically administered with 10 mg/kg anwulignan. At 0.5, 1, 1.5, 2, 3, 4, 6, 8, 12, 24, 36, and 48 h after the administration of anwulignan, five mice were randomly selected at each time point for the preparation of homogenates. The selected mice were placed in a desiccator in which 10 ml ether was placed at the lower part. After the mice were anesthetized (about 0.5 min), the blood samples of mice were collected by removing eyeballs, and then their heart, liver, spleen, lung, kidney, and brain tissues were taken. The blood plasma and tissue homogenates were prepared according to the method in the preparation of plasma and tissue standards, and 200 μl of schisandrin A (4 μg/ml) was added into each of the plasma and tissue homogenates for the preparation of the samples to be tested.

Collection and Preparation of Urine and Feces Samples of Mice After the Intragastric Administration

Five mice were selected and intragastrically administered with anwulignan (10 mg/kg), and then the mice were placed in a mouse metabolism cage and fasted, but with a free access to water. The urine and feces were collected during 0–2 h, 2–4 h, 4–8 h, 8–12 h, 12–24 h, and 24–48 h after the administration of

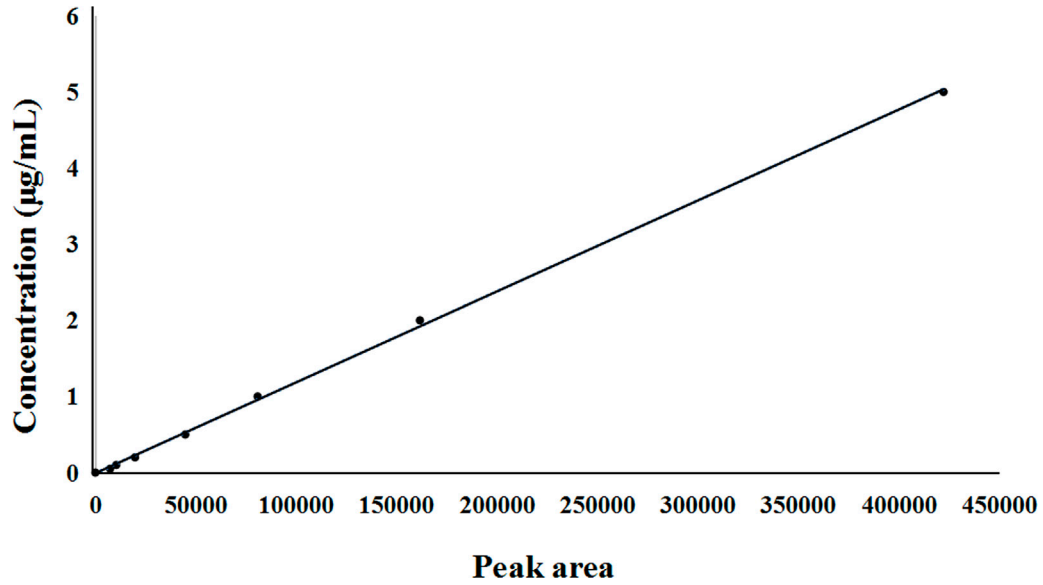

FIGURE 2 | Standard curve of anwulignan in plasma.

TABLE 2 | Matrix effect and stability of anwulignan in plasma and tissue samples.

Sample	QC (μg/ml)	Matrix effect (%)	Stability (%)		
			Short term	Long term	3 Freeze–thaw cycles
Plasma	0.05	95.7	95.6	95.4	97.7
	0.5	96.5	98.5	91.6	98.5
	5	94.7	88.5	87.6	99.4
Heart	0.05	97.6	94.5	93.5	99.2
	0.5	96.7	92.3	96.2	97.5
	5	95.9	96.7	97.4	98.8
Liver	0.05	97.2	94.5	89.5	99.2
	0.5	94.8	95.6	96.7	96.6
	5	98.2	91.5	98.2	97.5
Kidney	0.05	94.6	89.5	98.6	97.9
	0.5	97.9	96.7	89.6	97.7
	5	97.5	93.2	92.5	99.5
Spleen	0.05	98.7	94.5	93.4	99.2
	0.5	96.4	87.5	95.8	98.1
	5	96.5	95.6	92.7	98.5
Brain	0.05	98.1	94.2	95.8	97.4
	0.5	97.3	97.2	94.6	99.6
	5	97.6	93.5	93.5	97.5
Lung	0.05	95.7	87.5	92.3	98.6
	0.5	97.2	92.3	95.4	97.8
	5	96.5	88.6	93.2	97.3

anwulignan, respectively. The urine samples were blown dry, and the concentrated urine was extracted three times with an appropriate amount of ethyl acetate. The five extracts were mixed and blown dry with nitrogen, then the dried extract was added with 1 ml methanol and dissolved by vortexing. The extract-methanol solution was passed through a 0.45 μm microporous membrane and the filtrate was collected, and the volume of filtrate was adjusted to 2 ml with methanol for testing. Each of the collected feces samples was added with 5 ml of water and ground, and then added with 10 ml of ethyl acetate and extracted three times. The three extracts were mixed. The mixed extract was blown dry with nitrogen, and then the dried extract was dissolved in a small amount of methanol. The extract-methanol solution was filtered through a 0.45 μm microporous

TABLE 3 | Precision, accuracy, and recover of the method used for the determination of anwulignan.

Sample	QC (μg/ml)	Precision (%)		Accuracy (%)	Recovery (%)
		Inter-day	Intra-day		
Plasma	0.05	3.6	5.0	5.3	92.7
	0.5	–1.2	3.0	4.6	97.0
	5	2.1	4.4	1.2	95.6
Heart	0.05	3.4	–4.7	–3.2	98.4
	0.5	2.3	–2.8	–2.7	94.3
	5	1.3	3.7	2.9	95.2
Liver	0.05	–4.4	5.4	4.8	98.5
	0.5	2.6	–4.3	–3.2	98.2
	5	–3.3	–3.2	–4.5	97.3
Kidney	0.05	5.1	5.6	–4.7	96.3
	0.5	2.7	3.2	3.9	95.3
	5	–3.8	–4.2	6.4	97.2
Spleen	0.05	–2.1	4.9	1.9	98.3
	0.5	–1.6	–5.5	–3.8	98.5
	5	–2.4	4.2	5.6	97.6
Brain	0.05	4.2	5.6	3.7	94.5
	0.5	–3.3	–1.2	–5.1	96.2
	5	2.8	4.5	4.8	98.2
	0.05	2.1	3.2	5.2	93.5
Lung	0.5	3.6	5.2	–3.8	97.6
	5	4.7	1.2	–2.7	96.8

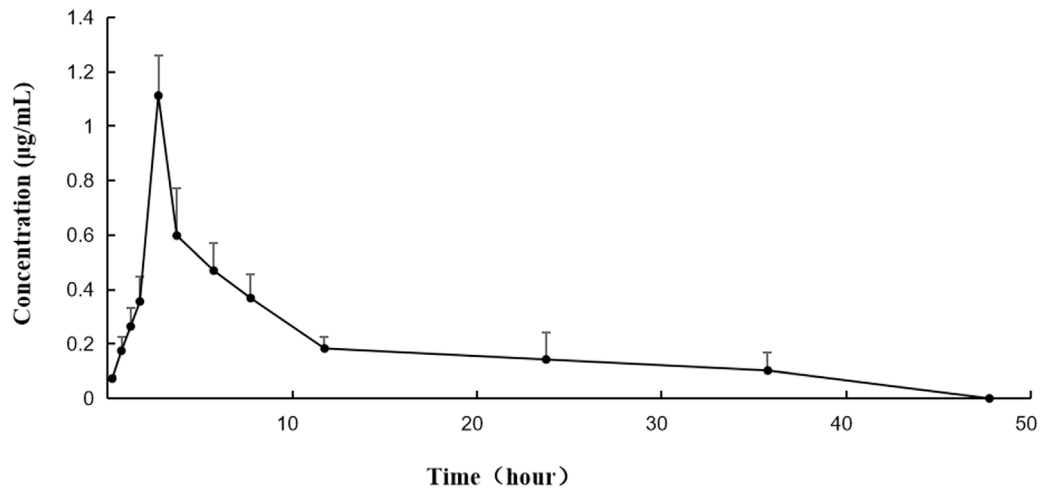

FIGURE 3 | Concentration–time curve of anwulignan in mice after the intragastric administration of anwulignan.

membrane, and the volume of the collected filtrate was adjusted to 2 ml with methanol for testing.

UHPLC-Q-Orbitrap-MS/MS Conditions

An ultimate 3,000 ultra-high-performance liquid chromatography system (Thermo, San Jose, CA, United States) was used for the separation by liquid chromatography. The separation column of HPLC was C18 column (100 mm × 30 mm, 18 μm), and the column temperature was set at 32°C and the absorbance at 230 nm. Methanol and water were used as mobile phase A and B, respectively. The gradient elution procedures were set as follows: 0–15 min (75%–90% A), 10–15 min (90%–100% A), and 15–18 min (100%–75% A). The flow rate was set at 1 ml/min and the injection volume was 10 μl. The UHPLC system was coupled to a Q-Orbitrap-MS/MS mass spectrometer.

Q-Orbitrap-MS/MS (Thermo, San Jose, CA, United States) was used for the mass spectrometry in positive-ion mode. The capillary voltage was set at +4.0 kV and the capillary temperature at 350°C. The parameters of the ion source were set as follows: the sheath gas flow was 40 Arb, the auxiliary gas flow 10 Arb, and the purge gas flow 1 Arb. A single-ion monitor (SIM) mode was used for the analysis of anwulignan and IS, and the full-scan MS data were used for the analysis of metabolites by setting the *m/z* as 150–2,000 Da, the resolution as 70,000, automatic gain control

TABLE 4 | Primary pharmacokinetic parameters of anwulignan in mice after the intragastric administration of anwulignan.

Parameter	Value
C_{max} (mg/L)	1.11 ± 0.20
T_{max} (h)	3.00 ± 0.15
$t_{1/2}$ (h)	7.10 ± 1.89
AUC_{0-t} (mg/L·h)	9.37 ± 2.36
$AUC_{0-\infty}$ (mg/L·h)	12.58 ± 3.51
MRT_{0-t} (h)	13.65 ± 4.62
$MRT_{0-\infty}$ (h)	32.90 ± 6.35
$V_{z/F}$ (L/kg)	32.81 ± 4.79
$CL_{z/F}$ (L/h/kg)	0.80 ± 0.23

(AGC), the target value as 1×10^6, and the maximum injection time (IT) as 100 ms. Full-MS/ddMS^2 mode was set to get MS/MS data, in which the resolution was 17,500, the AGC target was 1×10^5, the maximum IT was 50 ms, and the normalized collision energy (NCE) was 25–45.

Multivariate Data Analysis and Metabolite Identification

LC-MS data were extracted, filtered, and normalized using Thermo software Xcalibur (version 4.3) to obtain the molecular weight, retention time, and absorption peak area of the compounds in each sample. SIMCA 14.1 software (Umetrics, Kinnelon, NJ, United States) was used for the analysis of multivariate data, and principal component analysis (PCA) and orthogonal partial least squares discrimination analysis (OPLS-DA) were used to look for the differential compounds among the samples by analyzing the score charts and scatter plots. Xcalibur was used to compare the molecular weight, retention time, and molecular characterization of fragmented ions of the differential compounds by MS/MS mass spectrometry for their identification and structure elucidation.

Specificity

Six different batches of mouse blank plasma (tissues), and the blank plasma and tissue homogenates with anwulignan and IS were compared for the specificity investigation, in which whether the plasma could interfere with the retention time and peak area of anwulignan and IS was observed.

Standard Curve and Limit of Quantitation

The plasma (tissue) standard solution of anwulignan in each concentration gradient was selected, and the standard curve was obtained by plotting the relation curve between the peak area of anwulignan/IS and the concentration of anwulignan. The peak area of anwulignan was recorded, and the signal-to-noise ratio (SNR) 10:1 was used as the LOQ.

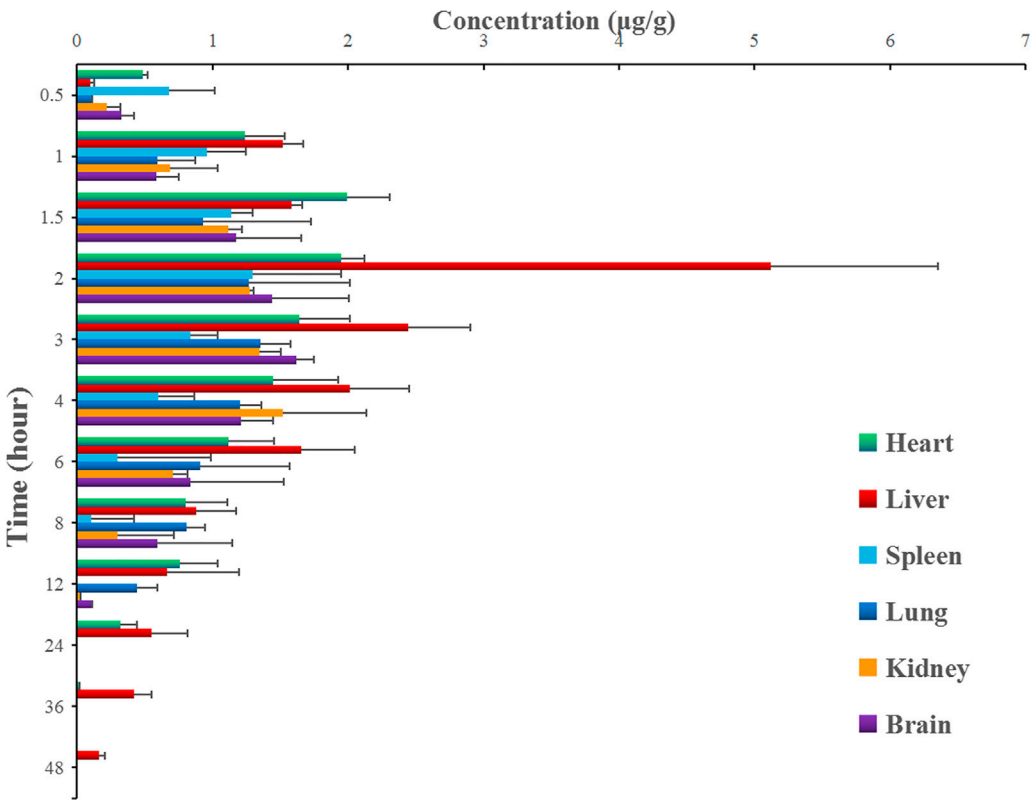

FIGURE 4 | Concentrations of anwulignan in the different tissues of mice after the intragastric administration of anwulignan.

TABLE 5 | Concentrations of anwulignan in the different tissues of mice after the intragastric administration of anwulignan.

Time	Heart	Liver	Spleen	Lung	Kidney	Brain
0.5 h	0.4865	0.0954	0.6794	0.1025	0.2214	0.3244
1 h	1.2377	1.5179	0.9607	0.5906	0.6872	0.5852
1.5 h	1.9920	1.5793	1.1341	0.9274	1.1125	1.1745
2 h	1.9513	5.1179	1.2974	1.2680	1.3420	1.4400
3 h	1.6376	2.4461	0.8331	1.3544	1.5175	1.6175
4 h	1.4442	2.0100	0.6012	1.2006	0.7064	1.2109
6 h	1.1159	1.6523	0.3012	0.9106	0.3012	0.8329
8 h	0.8021	0.8794	0.1025	0.8080	0.0160	0.5890
12 h	0.7590	0.6657	—	0.4384	—	0.1010
24 h	0.3209	0.5479	—	—	—	—
36 h	0.0140	0.4209	—	—	—	—
48 h	—	0.1602	—	—	—	—
Total	11.7612	17.0930	5.9096	7.6005	7.1787	7.8754

Note: "—" means not detected.

Precision and Accuracy

The precision and accuracy were evaluated by the intra-day analysis (three different concentrations of QC samples, six replicates for each concentration, and determined three times) and the inter-day analysis (consecutively for 3 days). The relative error (RE%) calculated based on the peak area should be less than 20%.

Matrix Effect and Stability

Three quality control samples at the different concentrations were detected by HPLC method, in which six parallel samples were set for each concentration, to obtain the peak area set 1. Thirty microliters of the above standard solution at three concentrations were added to 150 μl of the extracted blank mouse plasma and then 100 μl water was added to the standard plasma solution, well mixed by a vortex mixer, in which six parallel samples were set for each concentration, and the solution was detected to obtain the peak area set 2. The matrix effect was calculated according to the value of set 2/set 1. The stability of anwulignan was evaluated by analyzing six duplicate samples from each of the three quality control samples at the different concentrations under the different conditions, including placing at room temperature for 4 h, freezing at 80°C for 30 days, and three freeze–thaw cycles (from −20°C to room temperature), to record the relative peak area of each color spectrum peak for the calculation of its stability.

Recovery

The sample addition recovery method was used for the recovery test. Three quality control samples at the different concentrations (five samples for each concentration) were taken and anwulignan was added to the plasma (tissues), and then their chromatogram peak areas were measured under the UHPLC-Q-Orbitrap-MS/MS conditions. The measured peak areas were compared with those of the blank plasma (tissues) after the treatment with the same amount of anwulignan for the calculation of the recovery rate.

RESULTS

Method Validation

Figure 1 shows the extracted ion chromatograms (EIC) of anwulignan (*m/z* 329) and schisantherin A (*m/z* 415). The results showed that their retention time was 11.91 and 7.42 min for them, respectively, and no endogenous interference was found within the retention time of anwulignan and IS.

As shown in **Table 1**, the linear range of anwulignan in the plasma (n = 3) was 0.01–5 μg/ml, and that of anwulignan in the heart, liver, kidney, spleen, and brain homogenates (n = 3) was 0.02–5.0 μg/ml; under the selected chromatographic conditions, the LOQ was 0.02 μg/ml. The plasma standard curve of anwulignan is shown in **Figure 2**.

The matrix effect of anwulignan sample was 94.6%–98.7%, and the results of its short-term and long-term stability investigation are shown in **Table 2**. As shown in **Table 3**, the RSD value for evaluating the precision of anwulignan in each sample was less than 5.6%, the RSD value for the accuracy was less than 6.2%, the average recovery was between 92.7% and 98.5%, and the stability was less than 3.4%, indicating that the results obtained by the method should be reliable.

Pharmacokinetics and Distribution of Anwulignan *In Vivo*

After the intragastric administration of anwulignan, the peak area of each time period detected by HPLC was substituted into the standard curve to obtain the corresponding concentrations of anwulignan. The data obtained were analyzed with pharmacokinetics software DAS (version 3.2.8), and the results are shown in **Figure 3**, the pharmacokinetic parameters are shown in **Table 4**, and the contents of anwulignan in the different tissues are shown in **Figure 4**. As shown in **Figure 3**, the plasma concentration of anwulignan was the highest at 3 h after the intragastric administration of anwulignan, and lasted for a long time. Its Tmax and $T_{1/2}$ calculated by the judgment method of non-compartment model were 3.00 and 7.10 h, respectively, indicating that the duration of anwulignan is long in the body of mice. The apparent distribution volume of anwulignan was 32.81 ± 4.79 L/kg, indicating that anwulignan has a strong lipophilicity, so it is easy for it to enter cells and be widely distributed in tissues and organs rich in fat. Its AUC_{0-t} and $AUC_{0-\infty}$ were 9.37 ± 2.36 and 12.58 ± 3.51 mg/Lh, respectively, indicating that anwulignan may enter the systemic circulation more and be absorbed more completely. Its $CL_{Z/F}$ was 0.80 ± 0.23 L/h/kg, indicating that the clearance rate of anwulignan in the body is slow. The relative bioavailability of anwulignan was 23.8%, indicating that it may be metabolized through an obvious hepatointestinal circulation. As shown in **Figure 4**, anwulignan could be detected in the heart, liver, spleen, lung, kidney, and brain tissues of mice, and the order of the total concentration of anwulignan from high to low within 48 h was liver > heart > brain > kidney > lung > spleen (**Table 5**). At 2 h, the concentration of anwulignan in the liver was the highest, and

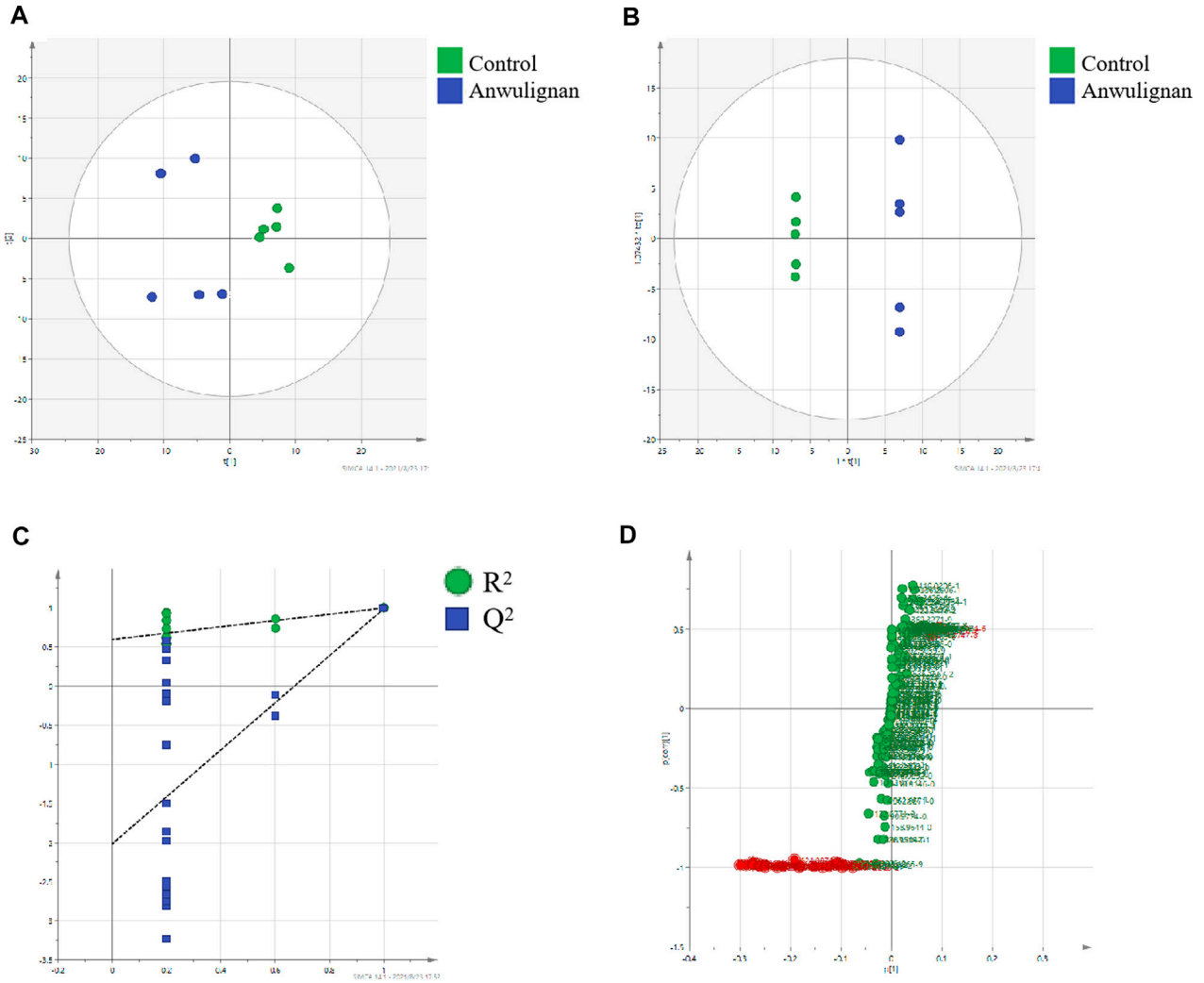

FIGURE 5 | Multivariate statistical analysis control and anwulignan group: **(A)** PCA score plot; **(B)** OPLS-DA score plot; **(C)** cross-validation plot of OPLS-DA model; and **(D)** S-plot of OPLS-DA.

the content of anwulignan in the liver is higher than that in the other tissues. The content in the liver and heart tissues was the highest within 2 h, and that in the liver, heart, and brain tissues was higher at 3 h.

In Vivo Metabolites of Anwulignan by Metabolomic Method

In order to find the metabolites of anwulignan in mice after the intragastrical administration, a metabolomic method based on UHPLC-Q-Orbitrap-MS/MS was used to analyze the samples, and the multivariate statistical analysis of anwulignan was carried out by metabonomic methods, as shown in **Figure 5**.

Taking the liver samples as an example, unsupervised PCA method was used for the matrix analysis on the data of liver samples from control mice and those treated with anwulignan at 4 h after the intragastrical administration to analyze the relationship among the data, and it could be understood from the score chart of PCA that the samples were well separated between the two groups (**Figure 5A**). Because PCA could not be used for the analysis of the unknown grouping samples, an OPLS-DA method was used to analyze the data in the two groups to obtain the score chart of OPLS-DA (**Figure 5B**), which indicated that there were significant differences between the control group and the anwulignan group, and the validity of the model was evaluated by the external model verification method (arrangement of the experiment). As shown in **Figure 5C**, both slopes of the two regression lines were larger; R^2 and Q^2 produced by the left-end alignment were smaller than those by the right-end alignment, and the difference between the two values at the right-most end was smaller, indicating that the model was valid. In order to determine the metabolites of anwulignan in the liver to the greatest extent, S-plot diagram was used for the analysis (**Figure 5D**). In the S-plot diagram, each

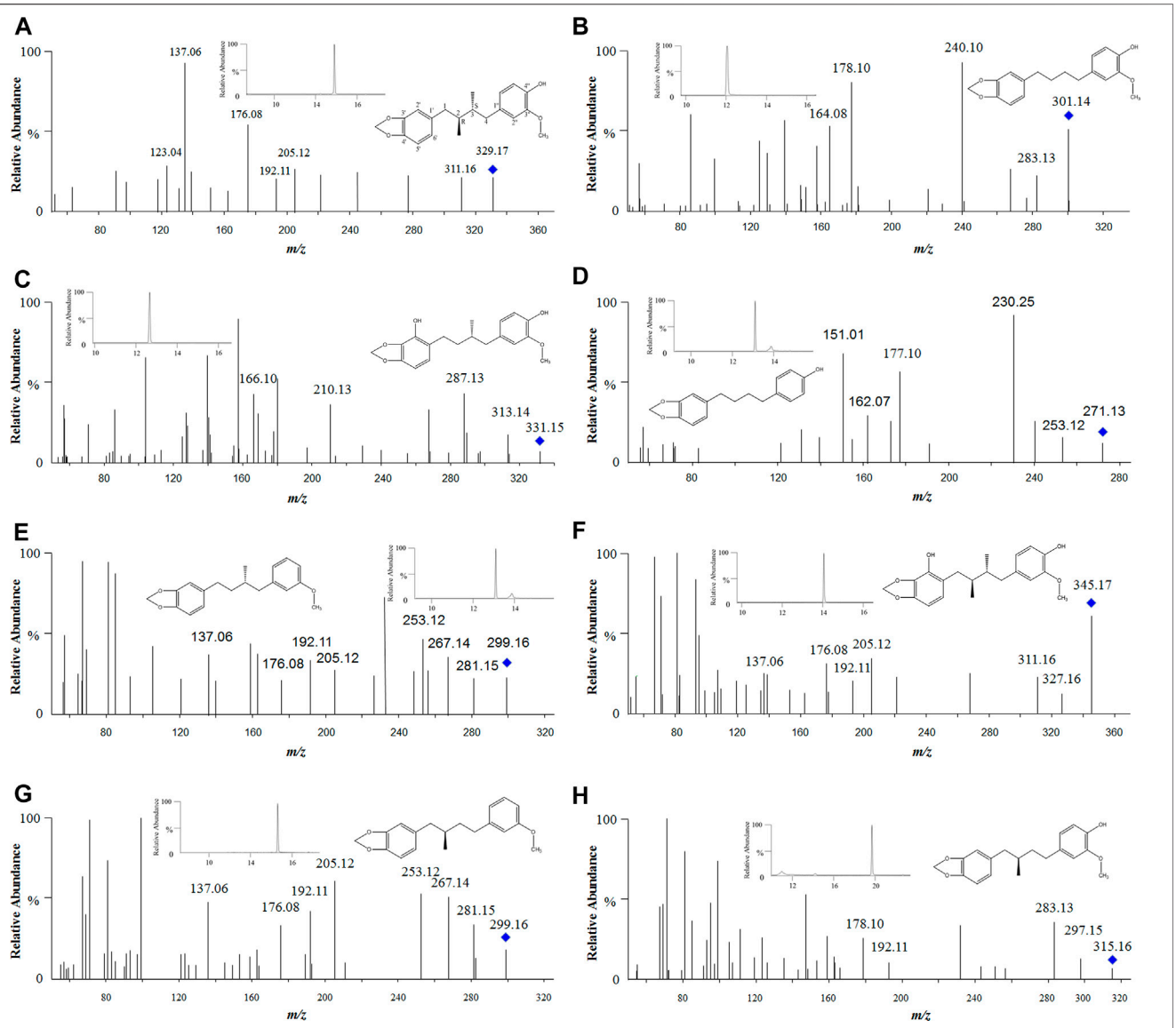

FIGURE 6 | Tandem mass spectra of anwulignan and its metabolites. Note: **(A)** anwulignan at *m/z* 329; **(B)** M1 at *m/z* 301; **(C)** M2 at *m/z* 331; **(D)** M3 at *m/z* 271; **(E)** M4 at *m/z* 299; **(F)** M5 at *m/z* 345; **(G)** M6 at *m/z* 299; and **(H)** M7 at *m/z* 315.

point represents an ion, and the farther away from the zero point, the greater the contribution of ions to the fractionation. The ions existing in the liver of mice after the intragastric administration of anwuzhisu, not in the liver of mice in the blank group, were taken as the potential metabolites, and the information on their precise molecular weight and MS/MS fragmentation ions was analyzed.

As shown in **Figure 6A**, anwulignan presented as $[M + H]^+$ in positive-ion mode and its mass to charge ratio (*m/z*) was 329, and fragment *m/z* 311 might be generated from *m/z* 329 losing H_2O (18 Da) at C-4″ position, *m/z* 205 from *m/z* 329 losing $C_7H_8O_2$ (124 Da) at C-4, *m/z* 176 from *m/z* 205 losing C_2H_5 (29 Da) at C-2 and C-3, *m/z* 135 from *m/z* 176 losing C_3H_5 (41 Da) at C-1, *m/z* 192 from *m/z* 329 losing $C_8H_9O_2$ (137 Da) at C-2, *m/z* 137 from *m/z* 192 losing C_4H_7 (55 Da) at C-4, and *m/z* 123 from *m/z* 137 losing CH_2 (14 Da) at C-1″. The fragmentation mechanism of anwulignan is simulated and shown in **Figure 7**.

A total of seven metabolites of anwulignan were detected in the blood and liver samples, and the relevant information on these metabolites is shown in **Table 6**.

The elution time of M1 (*m/z* 301) was 12.09 min (**Figure 6B**), suggesting that M1 should be a metabolite of anwulignan of losing two methyl groups, and fragment ion at *m/z* 283 might be generated from that at *m/z* 301 of losing H_2O (18 Da) at C-4″, *m/z* 178 from *m/z* 283 of losing C_7H_5O (105 Da) at C-4, and *m/z* 164 from *m/z* 178 of losing a methyl group (14 Da).

The elution time of M2 (*m/z* 331) was 12.69 min (**Figure 6C**), suggesting that M2 should be a demethylation metabolite of anwulignan after hydroxylation, and fragment ion at *m/z* 313 might be generated from that at *m/z* 331 of

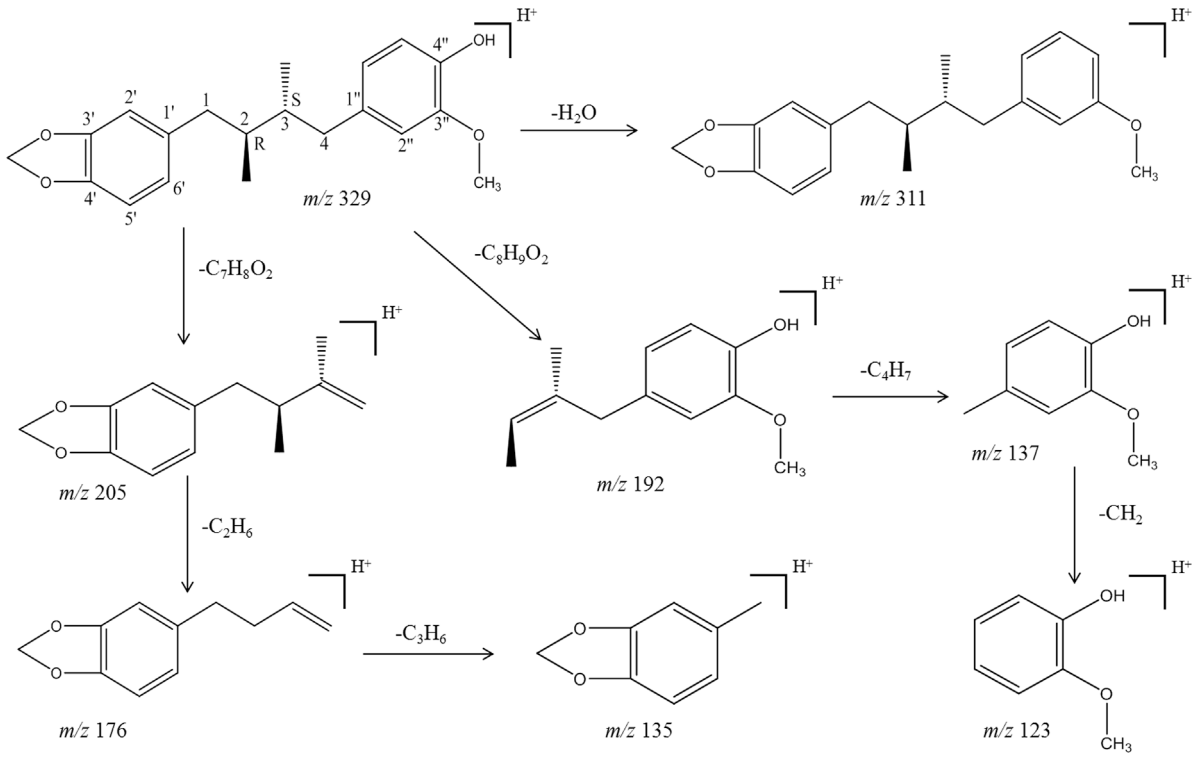

FIGURE 7 | Proposed mainly MS/MS fragmentation pathways for anwulignan.

TABLE 6 | Characterization of anwulignan and identified metabolites by UHPLC-Q-Orbitrap-MS.

Lignans	Rt (min)	Formula	*m/z* [M + H]$^+$	Error (ppm)	Detection time
Anwulignan	11.91	$C_{20}H_{24}O_4$	329.17	3.6	0.5–48 h (plasma, liver, and feces)
M1	12.09	$C_{18}H_{20}O_4$	301.14	2.1	2 h (liver)
M2	12.69	$C_{19}H_{22}O_5$	331.15	−1.5	1 h (plasma, liver)
M3	12.96	$C_{17}H_{18}O_3$	271.13	3.4	4 h (liver), 4–8 h (feces)
M4	13.07	$C_{19}H_{22}O_3$	299.16	−2.8	4 h (liver)
M5	14.09	$C_{20}H_{24}O_5$	345.17	0.9	4 h (liver)
M6	15.25	$C_{19}H_{22}O_3$	299.16	1.6	4 h (liver), 4–8 h (feces)
M7	19.11	$C_{19}H_{22}O_4$	315.16	−2.2	4 h (liver)

losing H_2O (18 Da) at C-4″, *m/z* 287 from *m/z* 331 of losing CH_2 and OCH_2 (44 Da), and *m/z* 210 from *m/z* 331 of losing $C_7H_5O_2$ (121 Da) at C-1.

The elution time of M3 (*m/z* 271) was 12.96 min (**Figure 6D**), suggesting that M3 should be the metabolite of anwulignan of losing a methoxyl group at C-3″, and a methyl group at C-2 and C-3, respectively, and fragment ion at *m/z* 253 might be generated from that at *m/z* 271 of losing a H_2O (18 Da) at C-4″, *m/z* 177 from *m/z* 253 of losing C_6H_4 (76 Da) at C-4, and *m/z* 162 from *m/z* 253 of losing C_7H_7 (91 Da) at C-3.

The elution time of M4 (*m/z* 299) was 13.07 min (**Figure 6E**), suggesting that M4 should be a dehydroxylation and demethylation metabolite of anwulignan, and fragment ion at *m/z* 281 might be generated from that at *m/z* 299 of losing H_2O (18 Da) at C-4″, fragment ions at *m/z* 267 and 253 might be generated from those at *m/z* 281 of losing one and two methyl groups, respectively, and the fragmentation characteristics of fragment ions at *m/z* 205, 192, 176, and 137 might be basically consistent with those of anwulignan. The elution time of M6 (*m/z* 299) was 15.25 min (**Figure 6G**), and the fragmentation characteristics of fragment ions at *m/z* 281, 267, 253, 205, 192, 176, and 137 were consistent with those of M4, but the retention time was different from that of M4, so M6 might be the isomer of M4.

The elution time of M5 (*m/z* 345) was 14.09 min (**Figure 6F**), indicating that M5 should be a hydroxylation metabolite of anwulignan, fragment ion at *m/z* 327 might be generated from that at *m/z* 345 of losing H_2O (18 Da) at C-4″, and the fragmentation characteristics of the other fragment ions at *m/z*

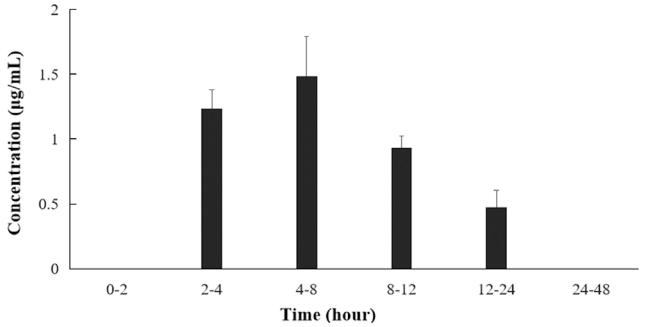

FIGURE 8 | Anwulignan concentrations in the feces of mice after the intragastric administration.

311, 205, 192, 176, and 137 were consistent with those of anwulignan.

The elution time of M7 (*m/z* 315) was 19.11 min (**Figure 6H**), indicating that M7 should be a metabolite of anwulignan of losing a methyl group, and fragment ion at *m/z* 297 might be generated from that at *m/z* 315 of losing H_2O (18 Da) at C-4″, *m/z* 283 from *m/z* 297 of losing a methyl group (14 Da), *m/z* 192 from *m/z* 315 (123 Da) of losing $C_7H_7O_2$ at C-4, and *m/z* 178 from *m/z* 192 of losing a methyl group (14 Da).

The excreta of mice within 48 h after the intragastric administration of anwulignan were taken for analysis by HPLC. The results showed that anwulignan prototype and its metabolites were not found in the urine of mice within 48 h, and anwulignan prototypes, M3 and M6, were found in the feces, as shown in **Figure 8**.

DISCUSSION

The results on the pharmacokinetics of anwulignan in mice indicated that UHPLC-Q-Orbitrap-MS/MS could be well suited for this study. Non-compartment model was used to study the pharmacokinetic characteristics of anwulignan in mice, and it was found that anwulignan was absorbed slowly in mice (T_{max} = 3 h), its duration was long ($t_{1/2}$ = 7.1 h), and the prototype of anwulignan could still be detected in the blood until 24 h, indicating that the elimination rate of anwulignan should be relatively slow and there may be an enterohepatic circulation involved in it. Based on the fact that the content of anwulignan in the liver was higher than that in the other tissues, and its residence time was longer, it could be speculated that there may be a hepatointestinal circulation in the metabolism of anwulignan in the body of mice, so it has a long half-life. Its AUC_{0-t} and $AUC_{0-\infty}$ were 9.37 ± 2.36 and 12. 58 ± 3.51 mg/Lh, respectively, suggesting that more anwulignan can enter the systemic circulation. Apparent distribution volume (V_d) can be used to infer the extent of drug distribution in the body, and the V_d value is close to 0.8–1.0 L/kg if a drug is evenly distributed in the body and the concentration of a drug in tissues is higher than that in blood when the V_d value is greater than 1.0 L/kg, which may indicate that the drug is widely distributed in the body or the tissue protein is highly bound to the drug (Weiss et al., 2021). In this study, the V_d of anwulignan was 32.81 ± 4.79 L/kg, indicating that anwulignan has strong lipophilicity, so it is easy for it to enter cells and be widely distributed in tissues through blood circulation. The relative bioavailability of anwulignan was 23.8%, which may be due to the incomplete absorption in the gastrointestinal tract or the obvious first-pass effect on the liver.

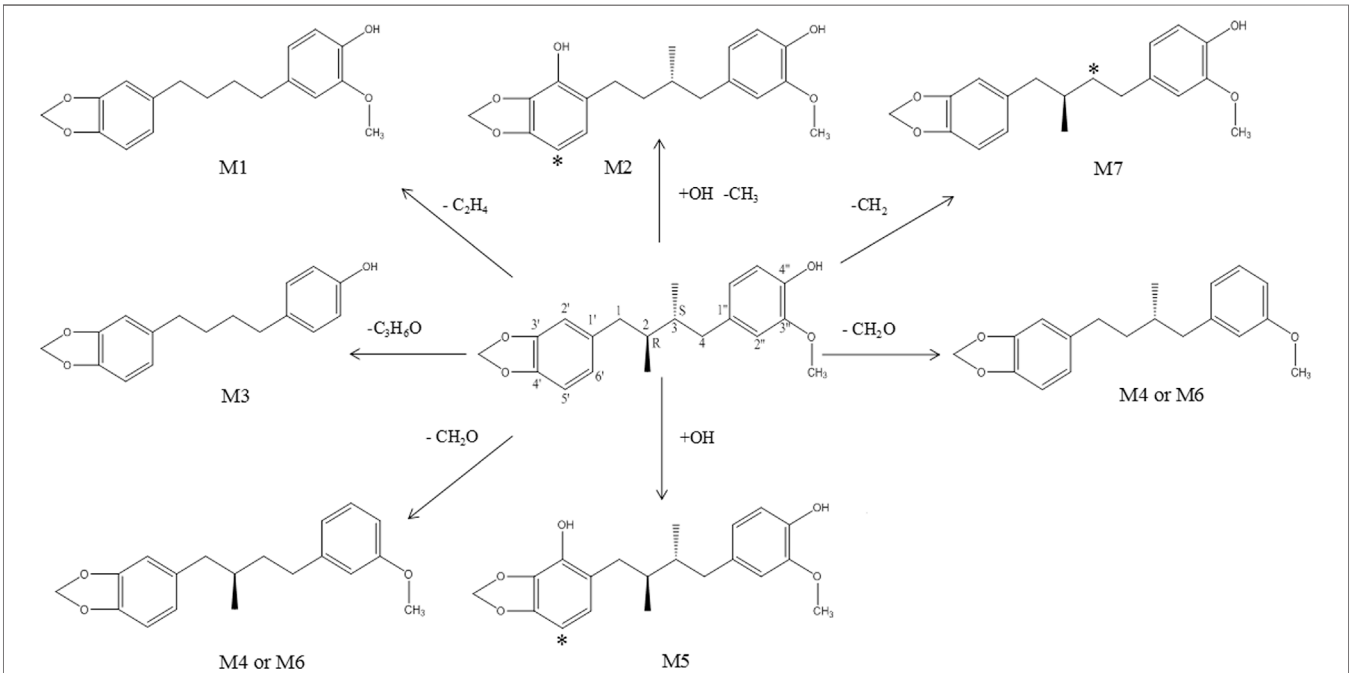

FIGURE 9 | Proposed metabolic pathway of anwulignan in mice. Note: * the potential metabolic site.

This result is also reflected by the distribution data of anwulignan in the main organs, which is consistent with that reported by Song et al. (2020).

After the intragastric administration of anwulignan, the prototype of anwulignan could be detected in all major organs of mice, indicating that anwulignan is widely distributed. The distribution of a drug in tissues is related to the blood circulation, vascular permeability, and drug protein binding (Tang and Cao, 2021), and the differential distribution of compounds in various organs mainly depends on the blood flow rate and the concentration of compounds in the organs and the affinity of compounds to the organs. Liver, kidney, and brain are organs with a rapid blood circulation, so anwulignan could be detected quickly in these tissues after the intragastric administration. The order of the concentration of anwulignan in the organs from high to low was liver > heart > brain > kidney > lung > spleen, and the concentration in liver was the highest, indicating that anwulignan may experience a slow elimination in the liver. This result may explain the reason why anwulignan has a therapeutic effect on liver injuries. The liver may be an accumulation site of anwulignan, so taking a large dosage of anwulignan may induce some adverse reactions related to liver metabolism. The content of anwulignan in the spleen was lower, indicating that the tissue distribution of anwulignan after the intragastric administration is targeted. It is worth noting that the concentration of anwulignan in the brain tissue is higher than that of other *Schisandra* lignans in the brain tissue (Lu et al., 2013; Liu et al., 2019; Liang et al., 2021), suggesting that anwulignan has a strong ability to penetrate the blood–brain barrier to play a pharmacological role in the central nervous system, which may provide a reference for the future study on the efficacy of anwulignan.

The study on the excreta of mice showed that anwulignan could be not detected in the urine of mice, but could be detected in the feces, which may be the result of the poor water solubility of anwulignan. It was found in this study that the concentration of anwulignan was highest in feces samples during 4–8 h after the intragastric administration, and anwulignan could still be detected during 12–24 h, further confirming that anwulignan may undergo an obvious enterohepatic circulation, combined with the previous results of this study. The total amount of anwulignan excreted from the body in the form of prototype drug was far less than the dosage, indicating that its excretion from the body is mainly through a metabolic elimination.

Seven metabolites of anwulignan were found in this study, of which only M2 was detected in the blood of mice and the other metabolites were found in the liver, suggesting that the main component of anwulignan to play a pharmacological role should be its prototype or M2 (except the liver), and the effect of the other metabolites should mainly act on the liver or act on the intestinal flora through the way of enterohepatic circulation, so as to indirectly exert its effect on other tissues and organs. Combined with the results of *in vivo* distribution experiment, anwulignan was primarily distributed in the liver after entering the body, and its metabolites were also primarily distributed in the liver, indicating that the liver may be the main organ in which anwulignan can play a role. Some studies have found that anwulignan has an obvious inhibitory effect on carboxylesterases 2 in the liver, and the inhibitory effect is the strongest among many *Schisandra* lignans (Fu et al., 2019). Anwulignan is mainly metabolized in the way of demethylation, hydroxylation, dehydroxylation, and demethoxylation, and studies on other *Schisandra* lignans have also shown that demethylation and hydroxylation are the main metabolic ways of lignans (Liu et al., 2014; Su et al., 2016; Liu et al., 2019; Wang et al., 2020). It was the first time that the metabolites of anwulignan in the body of animals were studied, and the main metabolic pathways are shown in **Figure 9**.

CONCLUSION

UHPLC-Q-Orbitrap-MS/MS was employed to investigate the pharmacokinetics and tissue distribution of anwulignan in mice. It was found that anwulignan was slowly absorbed in mice and widely distributed in various tissues and organs, especially in the liver. The main metabolites of anwulignan *in vivo* were analyzed for the first time, and seven metabolites were found. The results indicate that demethylation, hydroxylation, dehydroxylation, and demethoxylation may be the main metabolic ways of anwulignan, and the majority of its prototypes and metabolites may be excreted through feces.

DATA AVAILABILITY STATEMENT

The original contributions presented in the study are included in the article/Supplementary Material; further inquiries can be directed to the corresponding author.

ETHICS STATEMENT

The animal study was reviewed and approved by the Experimental Animal Ethics Committee of Beihua University.

AUTHOR CONTRIBUTIONS

Conceptualization, JS and JC; methodology, CC; software, YF; validation, HNL and HOL; investigation, CC and JS; writing—original draft preparation, YF and JS; writing—review and editing, CW and HEL; and funding acquisition, SJ and JS. All authors have read and agreed to the published version of the manuscript.

FUNDING

This research was funded by the Natural Science Foundation of Jilin Province, grant number 20200201521JC; Traditional Chinese Medicine Science and Technology project of Jilin Province, grant number 2020119; and Science and Technology Project of Jilin Provincial Education Department grant number JJKH20210065KJ.

REFERENCES

Chen, Z., Liu, F., Zheng, N., Guo, M., Bao, L., Zhan, Y., et al. (2019). Wuzhi Capsule (Schisandra Sphenanthera Extract) Attenuates Liver Steatosis and Inflammation during Non-alcoholic Fatty Liver Disease Development. *Biomed. Pharmacother.* 110, 285–293. doi:10.1016/j.biopha.2018.11.069

Fu, Q., Yang, K., Hu, R. X., Du, Z., Hu, C. M., and Zhang, X. (2019). Evaluation of the Inhibition of Human Carboxylesterases (CESs) by the Active Ingredients from Schisandra Chinensis. *Xenobiotica* 49, 1260–1268. doi:10.1080/00498254.2018.1548718

Jiang, P., Lu, Y., and Chen, D. (2016). Authentication of Schisandra Chinensis and Schisandra Sphenanthera in Chinese Patent Medicines. *J. Pharm. Biomed. Anal.* 131, 263–271. doi:10.1016/j.jpba.2016.08.040

Jiang, W., Ren, L., Guo, M., Mantri, N., Zhao, S., and Pang, X. (2019). Detecting Schisandrae Chinensis Fructus and its Chinese Patent Medicines with a Nucleotide Signature. *Genes. (Basel)* 10, 397. doi:10.3390/genes10050397

Li, X., Gao, J., Yu, Z., Jiang, W., Sun, W., Yu, C., et al. (2020). Regulatory Effect of Anwulignan on the Immune Function through its Antioxidation and Anti-apoptosis in D-Galactose-Induced Aging Mice. *Clin. Interv. Aging* 15, 97–110. doi:10.2147/CIA.S237601

Liang, D., Wu, Z., Liu, Y., Li, C., Li, X., Yang, B., et al. (2021). HPLC-MS/MS-Mediated Analysis of the Pharmacokinetics, Bioavailability, and Tissue Distribution of Schisandrol B in Rats. *Int. J. Anal. Chem.* 2021, 8862291. doi:10.1155/2021/8862291

Lin, H. J., Zhang, X., Liu, J., Yuan, L., Liu, J., Wang, C., et al. (2020). Protective Effect of Anwulignan on Liver Injury Caused by Intestinal Ischemia-Reperfusion in Rats. *Sci. Technol. Food Industry* 42, 330–336. doi:10.13386/j.issn1002-0306.2020050348

Liu, C. N., Wang, Y., Zhang, Y., Yuan, R., Zhang, X., Li, X., et al. (2020a). The Protective Effect and Mechanism of Anwulignan on D-Galactose-Induced Myocardial Injury in Aging Mice. *J. Jilin Med. Univ.* 41, 11–14. doi:10.13845/j.cnki.issn1673-2995.2020.01.004

Liu, J. W., Zhang, X., Lin, H., Yuan, L., Liu, J., Wang, C., et al. (2020b). Study on the Anti-fatigue Effect of Anwulignan on Aging Mice. *Sci. Technol. Food Industry* 41, 319–323. doi:10.13386/j.issn1002-0306.2020.18.050

Liu, M., Zhao, S., Wang, Z., Wang, Y., Liu, T., Li, S., et al. (2014). Identification of Metabolites of Deoxyschizandrin in Rats by UPLC-Q-TOF-MS/MS Based on Multiple Mass Defect Filter Data Acquisition and Multiple Data Processing Techniques. *J. Chromatogr. B Anal. Technol. Biomed. Life Sci.* 949-950, 115–126. doi:10.1016/j.jchromb.2013.12.022

Liu, X., Cong, L., Wang, C., Li, H., Zhang, C., Guan, X., et al. (2019). Pharmacokinetics and Distribution of Schisandrol A and its Major Metabolites in Rats. *Xenobiotica* 49, 322–331. doi:10.1080/00498254.2017.1418543

Lu, H., and Liu, G. T. (1992). Anti-oxidant Activity of Dibenzocyclooctene Lignans Isolated from Schisandraceae. *Planta Med.* 58, 311–313. doi:10.1055/s-2006-961473

Lu, S. W., Zhang, A. H., Sun, H., Yan, G. L., Han, Y., Wu, X. H., et al. (2013). Ultra-performance Liquid-Chromatography with Tandem Mass Spectrometry for Rapid Analysis of Pharmacokinetics, Biodistribution and Excretion of Schisandrin after Oral Administration of Shengmaisan. *Biomed. Chromatogr.* 27, 1657–1663. doi:10.1002/bmc.2976

Song, Y., Zhang, Y., Duan, X. Y., Cui, D. W., Qiu, X., Bian, Y., et al. (2020). Pharmacokinetics and Tissue Distribution of Anwulignan in Rats after Intravenous and Intragastric Administration by Liquid Chromatography-Mass Spectrometry. *Molecules* 25, 39. doi:10.3390/molecules25010039

Su, L. L., Cheng, X., Ji, J. D., Wang, L. J., Ding, X. Y., Lu, T. L., et al. (2016). Analysis of Lignans and Their Metabolites Derived from Schisandra Chinensis and Vinegar Schisandra Chinensis in Rats' Plasma, Bile, Urine and Faeces Based on UHPLC-QTOF/MS. *Yao Xue Xue Bao* 51, 1600–1608. doi:10.16438/j.0513-4870.2016-0315

Tang, Y., and Cao, Y. (2021). Modeling Pharmacokinetics and Pharmacodynamics of Therapeutic Antibodies: Progress, Challenges, and Future Directions. *Pharmaceutics* 13, 422. doi:10.3390/pharmaceutics13030422

Wang, J., Jiang, B., Shan, Y., Wang, X., Lv, X., Mohamed, J., et al. (2020). Metabolic Mapping of Schisandra Chinensis Lignans and Their Metabolites in Rats Using a Metabolomic Approach Based on HPLC with Quadrupole Time-Of-Flight MS/MS Spectrometry. *J. Sep. Sci.* 43, 378–388. doi:10.1002/jssc.201900860

Weiss, H. M., Langenickel, T., Cain, M., Kulkarni, S., Shah, B., Vemula, J., et al. (2021). Clinical Investigation of Metabolic and Renal Clearance Pathways Contributing to the Elimination of Fevipiprant Using Probenecid as Perpetrator. *Drug Metab. Dispos.* 49, 389–394. doi:10.1124/dmd.120.000273

Yang, J., Duan, J. A., Li, G. L., Zhu, Z. H., Zhu, T. L., Qian, D. W., et al. (2014). Determination of Lignans in Schisandrae Sphenantherae Fructus from Different Regions. *Zhongguo Zhong Yao Za Zhi* 39, 4647–4652. doi:10.4268/cjcmm20142332

Zhang, M. X., Huang, G. Y., Bai, Y. Q., Li, H., and Yang, B. (2021). Research Advances in Chemical Constituents and Hepatoprotective Effect of Schisandrae Sphenantherae Fructus and Schisandrae Chinensis Fructus. *Zhongguo Zhong Yao Za Zhi* 46, 1017–1025. doi:10.19540/j.cnki.cjcmm.20201127.601

Zhang, X., Jing, S., Lin, H., Sun, W., Jiang, W., Yu, C., et al. (2020). Anti-fatigue Effect of Anwulignan via the NRF2 and PGC-1α Signaling Pathway in Mice. *Food Funct.* 10, 7755–7766. doi:10.1039/c9fo01182j

Conflict of Interest: The authors declare that the research was conducted in the absence of any commercial or financial relationships that could be construed as a potential conflict of interest.

frontiers | Frontiers in Pharmacology

ORIGINAL RESEARCH
published: 08 July 2022
doi: 10.3389/fphar.2022.940137

Midazolam Ameliorates Acute Liver Injury Induced by Carbon Tetrachloride *via* Enhancing Nrf2 Signaling Pathway

Yongyan Zhang[1†], Yadi Zhu[2†], Ying Li[1], Feng Ji[1], Guangbo Ge[2] and Hua Xu[1*]*

[1]Yueyang Hospital of Integrated Traditional Chinese and Western Medicine, Shanghai University of Traditional Chinese Medicine, Shanghai, China, [2]Shanghai Frontiers Science Center of TCM Chemical Biology, Institute of Interdisciplinary Integrative Medicine Research, Shanghai University of Traditional Chinese Medicine, Shanghai, China

Oxidative stress contributes greatly to initiation and progression of liver injury. Activation of nuclear-factor erythroid 2-related factor 2 (Nrf2) has been considered as an attractive strategy for preventing and treating the oxidative damage related to liver injury. This study aimed to find an efficacious agent to activate Nrf2/HO-1 signaling pathway from clinically used therapeutic agents and to characterize the usefulness for preventing and treating CCl_4-induced acute liver injury. For this purpose, a series of clinically used therapeutic agents were collected and their activation potentials on Nrf2 were assayed by using 293T-Nrf2-luc cell line. Among all tested therapeutic agents, midazolam was found with good Nrf2 activation effect and this agent could significantly ameliorate CCl_4-induced damage to HepG2 cells. *In vivo* animal tests showed that pretreatment with midazolam reduced the liver pathological tissue damage and the serum levels of ALT and AST in CCl_4-induced liver injury mice. Further investigations showed that midazolam could strongly up-regulate the expression of both Nrf2 and HO-1 in the mice liver, accompanied by increasing of the levels of antioxidant enzyme SOD and reducing the production of MDA, as well as reducing the pro-inflammatory cytokines (IL-6, TNF-α) secretion. Collectively, our results clearly demonstrate that midazolam can ameliorate CCl_4-induced acute liver injury and oxidative stress *via* activating the Nrf2 signaling pathway.

Keywords: oxidative stress, Nrf2, midazolam, acute liver injury, molecular docking simulations

OPEN ACCESS

Edited by:
Guo Ma,
Fudan University, China

Reviewed by:
Milton Prabu,
Annamalai University, India
Lan Tang,
Southern Medical University, China
Xuan Qin,
Baylor College of Medicine, United States

***Correspondence:**
Guangbo Ge
geguangbo@dicp.ac.cn
Hua Xu
pshhuaxu@163.com

†These authors have contributed equally to this work

Specialty section:
This article was submitted to Drug Metabolism and Transport, a section of the journal Frontiers in Pharmacology

Received: *10 May 2022*
Accepted: *20 June 2022*
Published: *08 July 2022*

Citation:
Zhang Y, Zhu Y, Li Y, Ji F, Ge G and Xu H (2022) Midazolam Ameliorates Acute Liver Injury Induced by Carbon Tetrachloride via Enhancing Nrf2 Signaling Pathway. Front. Pharmacol. 13:940137. doi: 10.3389/fphar.2022.940137

INTRODUCTION

Oxidative stress is a state of imbalance between oxidation and antioxidant effects in human body, which could result in the generation of a large number of reactive oxygen species (ROS) in cells. Under physiological conditions, excessive ROS will affect a series of cell transduction pathways, influence the production and secretion of oxidative stress molecules, and regulate the balance between proliferation and apoptosis of cells. Meanwhile, it can also affect the

Abbreviations: ALT, alanine transaminase; ARE, antioxidant response element; AST, aspartate aminotransferase; GST, glutathione-S-transferase; H&E, hematoxylin and eosin; HO-1, heme oxygenase-1; Keap1, Kelch-like ECH-associated protein 1; KS, kelch-like site; MDA, malondialdehyde; NAFLD, non-alcoholic fatty liver disease; NQO1, quinone oxidoreductase1; Nrf2, nuclear-factor erythroid 2-related factor 2; ROS, reactive oxygen species; SFN, sulforaphane; SOD, superoxide dismutase.

function of mitochondria, leading to cell dysfunction, and eventually damage various tissues and organs (Giustarini et al., 2009). Particularly, for perioperative and severe patients, oxidative stress can cause serious complications (e.g., inflammation, bleeding, postoperative cognitive dysfunction and organ dysfunction), whose incidence of these complications is as high as 30% (Toro-Pérez and Rodrigo, 2021).

More and more attention has been paid to the methods of reducing perioperative oxidative stress, such as endoscopic surgery (Arsalani-Zadeh et al., 2011), reducing the concentration of inhaled oxygen (Oldman et al., 2021) and giving antioxidant drugs (Ali- Hasan- Al- Saegh et al., 2016) and other methods. However, due to the limitations of surgical methods and patients' own conditions, the clinical application of the first and second method are limited. The application of antioxidants signifies a rational curative strategy to prevent and cure liver diseases involving oxidative stress. Although conclusions drawn from clinical studies remain uncertain, animal studies have revealed the promising *in vivo* therapeutic effect of antioxidants on liver diseases. Particularly, some sedative and analgesic anesthetics have been widely concerned as treatment methods to reduce oxidative stress and protect important organ functions. Studies have shown that propofol can reduce the release of ROS and malondialdehyde (MDA) from the liver after ischemia-reperfusion, and contribute to the recovery of lung function (Chan et al., 2008). In the model of hepatic ischemia/reoxygenation, sufentanil increased superoxide dismutase (SOD), decreased MDA, reduced oxidative stress, and played a protective role in liver (Lian et al., 2019).

A large number of studies indicated that oxidative stress underlies the pathophysiology of various etiologies of liver disease, including chronic hepatitis C (Koike, 2007), alcoholic liver disease and non-alcoholic fatty liver disease (NAFLD)(Cederbaum et al., 2009), and contributes to the development of hepatocarcinogenesis (Cichoż-Lach and Michalak, 2014). Nuclear-factor erythroid 2-related factor 2 (Nrf2), known as the "main regulator" of antioxidant response, regulates a series of antioxidant and cytoprotective dependent protein genes by interacting with the antioxidant response element (ARE) sequences of antioxidant and cytoprotective genes (Kaspar et al., 2009), for example, heme oxygenase-1 (HO-1), quinone oxidoreductase1 (NQO1), glutathione-S-transferase (GST) (Tang et al., 2014). The enhanced activation of Nrf2 by pharmacologic molecules or genetic engineering has been shown to protect the liver in different oxidative stress models (Feng et al., 2021; Lim et al., 2021).

This study aimed to find drugs that effectively ameliorates acute liver injury through screen Nrf2 agonist from the commonly used analgesic. The selected positive Nrf2 agonist was applied to CCl_4 liver injury model mice to determine its antioxidant and anti-inflammatory effects by detecting inflammatory factors and oxidative stress products. The results of this study can provide a new treatment strategy for perioperative and severe patients to reduce oxidative stress.

MATERIALS AND METHODS

Construction of Stable Transfection Cells

293T-Nrf2-luc cell line was developed *via* lentiviral stable transfection of pGMLV-Nrf2-luc. pGMLV-Nrf2-luc is a kind of plasmid that designed by Genomeditech (Shanghai,

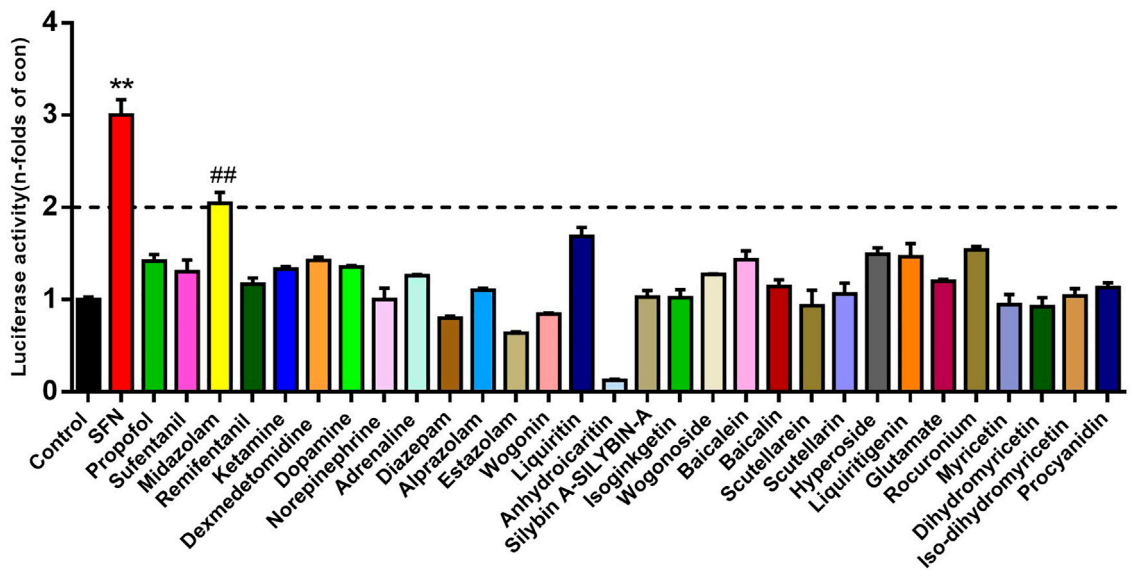

FIGURE 1 | The activation effects of different therapeutic drugs on Nrf2. Luciferase report assay analyzed the activity of Nrf2 in 293T-Nrf2-luc cells after 24 h treatment with different therapeutic agents (10 μM, final concentration). Results were presented as the mean ± S.D. of six independent experiments. SFN, sulforaphane. The results were shown as mean ± S.D. $^{**}p < 0.01$ vs. the control group; $\#\#p < 0.01$ vs. the SFN group.

China), which harbors Nrf2 promoter-luciferase reporter gene construct driven by multiple dioxin response elements. After that, 293T-Nrf2-luc cell line was obtained through antibiotic screening.

Cell Culture

Both of 293T-Nrf2-luc cell lines and HepG2 cell lines were grown in DMEM/high glucose medium (Hyclone, United States) containing 10% fetal bovine serum (Hyclone, United States) and 1% penicillin-streptomycin solution (Hyclone, United States). The culture condition was constant temperature of 37°C, a humidified atmosphere of 95% air and 5% CO_2. The fresh media were replaced every 2 days.

Nrf2 Reporter Assay

293T-Nrf2-luc cell lines were first seeded in 96-well plates at a density of 8×10^3 cells per well and grown overnight. Baicalin and iso-dihydromyricetin were prepared in our laboratory (Xiong et al., 2021; Zhao et al., 2021). Propofol (Fresenius Kabi, China), midazolam (Enhua, China), sufentanil (Humanwell, China), remifentanil (Humanwell, China), dexmedetomidine (Enhua, China), ketamine (Hengrui, China), dopamine (Fenghe, China),norepinephrine (Fenghe, China), epinephrine (Fenghe, China), diazepam (Xinyi, China), estazolam (Zhongxin, China), alprazolam (Enhua, China), rocuronium (Xianju, China), wogonin, liquiritin, anhydroicaritin, silybin A-SILYBIN-A, isoginkgetin, wogonoside, baicalein, scutellarein, scutellarin, hyperoside, liquiritigenin, glutamate, myricetin, dihydromyricetin, procyanidin (They were all purchased from Chengdu Purfield Biotechnology Co., Ltd. China), Baicalin and iso-dihydromyricetin were added at the final concentration of 10 μM, while sulforaphane (Sigma-Aldrich, United States) was used as a positive control (Russo et al., 2018). The negative control group was treated with the vehicle DMSO alone. The final concentration of DMSO in all experiments was below 1% (V/V).

Following 24 h incubation, luciferase activity was measured by the Steady-Glo® Reagent (Promega, United States) according to the manufacturer's directions. Luciferase activity was measured on Spectramax M3 (Molecular devices, United States) with luciferase production as readout. Data was shown as the percentage of fold induction of the test compound against the vehicle control group.

Cell Viability Assay

HepG2 cells were seeded in 96-well culture plates (1.0×10^4 cells/well) and grown overnight. To verify the effects of midazolam on HepG2 viability, cells were treated with midazolam at different concentrations (0, 1.25, 2.5, 5, 10, 20, 40 μM) for 24 h. The cells were incubated with CCK-8 (DOJINDO Laboratories, Japan) solution (20 μl/well) and cultured at 37°C for another 1 h. The absorbance of the dissolved solutions was detected at 450 nm on Spectramax M3.

In order to verify the protective effect of midazolam on CCl_4-induced HepG2 cells activity, different concentrations of CCl_4 (0, 0.5, 1, 2, 4, 6%) were added to culture for 24 h, and HepG2 cells activity was detected by CCK-8 to determine the IC_{50} value of CCl_4. After 24 h of intervention with different concentrations of midazolam, IC_{50} concentration of CCl_4 was added for another 24 h of intervention, and finally CCK-8 was performed to detect cell activity.

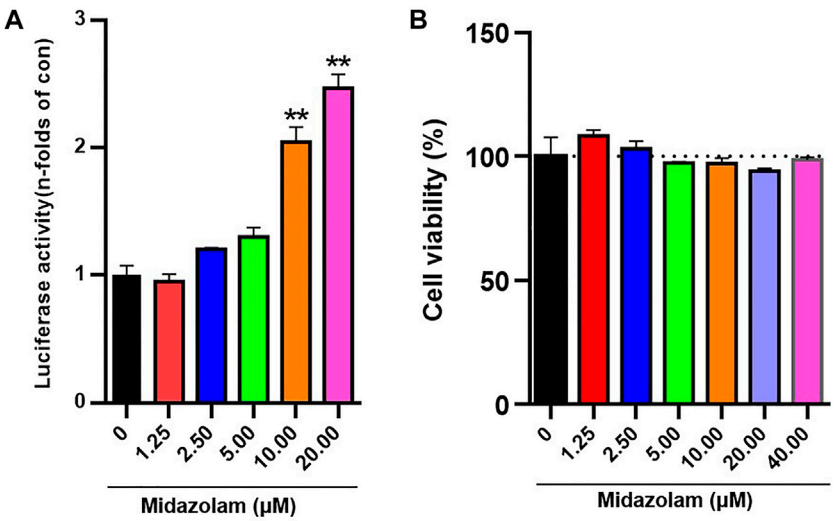

FIGURE 2 | Effects of different concentrations of midazolam on Nrf2 activation and cell viability. **(A)** Luciferase report assay analyzed the activity of 293T-Nrf2-luc cells after 24 h treatment with different concentrations of midazolam (0, 1.25, 2.5, 5, 10, 20 μM); **(B)** CCK-8 assay analyzed the effect of different concentrations of midazolam (0, 1.25, 2.5, 5, 10, 20, 40 μM) on 293T-Nrf2-luc cells viability. The results were shown as mean ± S.D. $^{**}p < 0.01$ vs. the control group.

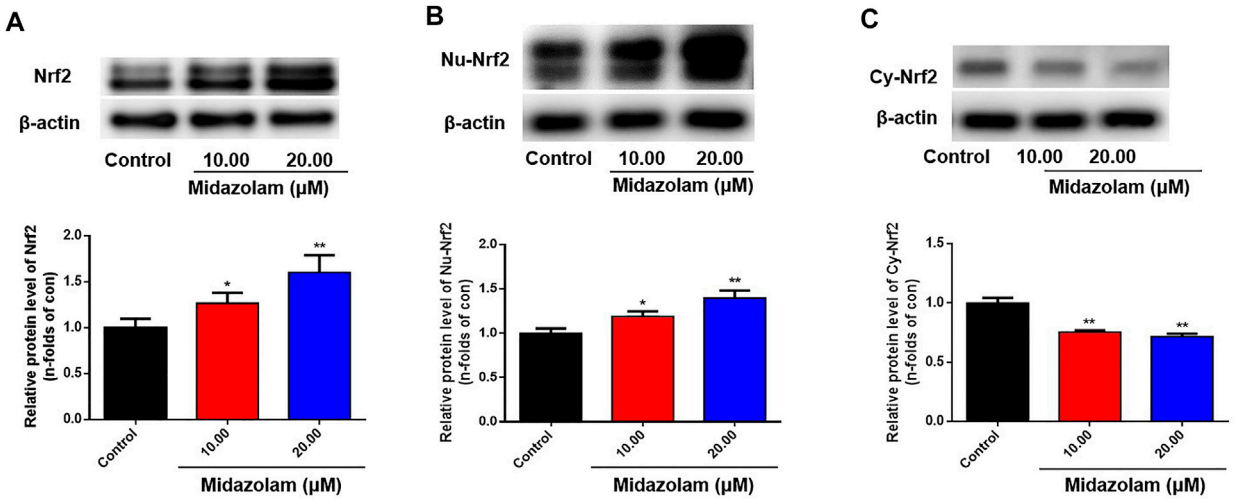

FIGURE 3 | Effects of different concentrations of midazolam on Nrf2 protein level. 293T-Nrf2-luc cells were treated with different concentrations of midazolam (0, 10, 20 μM) for 24 h, and then using western blot to measure the level of Nrf2 protein. **(A)** Total Nrf2 protein level in cells; **(B)** Nrf2 protein level in the nucleus; **(C)** Nrf2 protein level in the cytoplasm. β-actin was used as an internal control for total protein. The results were shown as mean ± S.D. $^{*}p < 0.05$ and $^{**}p < 0.01$ vs. the control group.

Animals Assay

The antioxidant effect of midazolam was tested in adult C57BL/6 mice (male, 6–8 weeks, 18–22 g) provided by Shanghai Slake Experimental Animal Co., Ltd. All mice were fed in the laboratory at a temperature of about 22°C and a relative humidity of 50%, with a light-dark cycle for 12 h. A 1-week acclimatization period was adopted before the experiment, during which the mice also had free access to food and water. All animal experiments were approved by the animal ethics committee of Yueyang Hospital of integrated traditional Chinese and Western Medicine Affiliated to Shanghai University of traditional Chinese medicine (ethics No.: YYLAC-2020-0801).

Next, 32 mice were randomly divided into the following groups (n = 8 in each group): control, CCl_4 group (CCl_4, Sinopharm Chemical Reagent, China), CCl_4 plus midazolam 4 mg/kg/day (CCl_4 + M4 group); CCl_4 plus midazolam 8 mg/kg/day (CCl_4 + M8 group). In the CCl_4 group, mice were intraperitoneally (i.p.) injected with 0.5% (v/v) CCl_4 (10 ml/kg, dissolved in corn oil). In the CCl_4 + M4 group or CCl_4 + M8 group, midazolam was respectively i. p. injected at 4 or 8 mg/kg for 3 days, and 0.5% CCl_4 was i. p. injected at 2 h after the last dose of midazolam. Mice were sacrificed 24 h after CCl4 injection, and blood and liver samples were collected. A part of the liver was immediately fixed in 10% formaldehyde for histopathological observation, while the rest was frozen in liquid nitrogen and stored at −80°C for other experiments.

In order to explore the effect of midazolam on CCl_4-induced lethality, 40 mice were used and randomly divided into the CCl_4 group and CCl_4 + midazolam group (n = 20). Midazolam was i. p. injected at 8 mg/kg for 3 days, and 50% CCl_4 (2.6 ml/kg, dissolved in corn oil) were i.p. injected at 2 h after the last dose of midazolam. The mortality of mice in each group was recorded up to 36 h after CCl_4 administration.

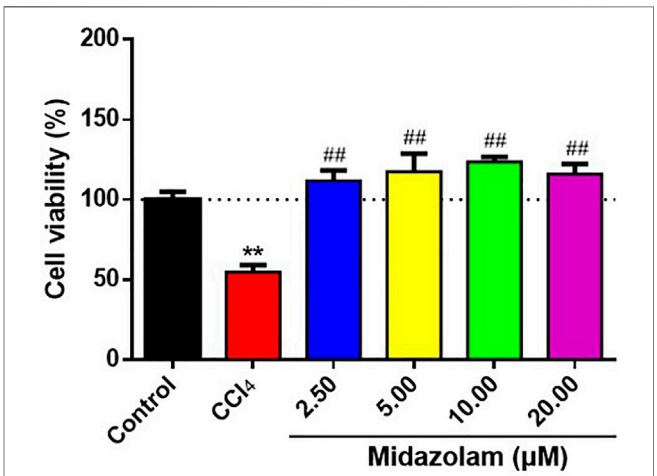

FIGURE 4 | Effects of different concentrations of midazolam on HepG2 cells activity induced by CCl_4. HepG2 cells were pretreated with different concentrations of midazolam (2.5, 5, 10, 20 Mm) for 24 h. CCl_4 (IC_{50} = 1.5%) induced HepG2 cells injury for 24 h. CCK-8 was used to analyze the effects of different concentrations of midazolam on cell viability induced by CCl_4. The results were shown as mean ± S.D. $^{**}p < 0.01$ vs. the control group; $^{\#\#}p < 0.01$ vs. the CCl_4 group.

Histological Examination of Liver Damage

The liver of each mouse (n = 8) was fixed in 10% neutral buffered formalin for 48 h and embedded in paraffin. Then 4 μm thick sections were cut and stained with hematoxylin and eosin (H&E) according to standard procedure. The

samples were observed and images were obtained using an optical microscope (Olympus, Japan).

Biochemical Analysis for Blood and Liver

Blood samples were centrifuged at 3000 × *g* for 10 min at 4°C and the serum was collected to measure the activity of aspartate aminotransferase (AST) and alanine transaminase (ALT), which were measured by kits (Nanjing Jiancheng Bioengineering Institute, China). Liver tissue homogenization was performed using tissue homogenizer (FSH-2A, XFK, China). The homogenates were centrifuged (1,000 × *g*, 15 min) at 4°C, and the obtained supernatant was used for subsequent measurement of MDA and SOD by kits (Nanjing Jiancheng Bioengineering Institute, China). The levels of TNF-α and IL-6 in the liver tissues were measured using ELISA kits according to the manufacturer's instructions (Elabscience, China).

Western Blot Assay

Total proteins were isolated from the liver tissues and cells using protein extraction kit (Beyotime Biotechnology, China). The cell nucleus proteins were extracted using Nuclear and Cytoplasmic Protein Extraction Kit (Beyotime Biotechnology, China). Protein concentrations were measured using BCA protein assay kit (Beyotime Biotechnology, China). Equal amounts of protein from each sample were subjected to 10% sodium dodecyl sulfate-polyacrylamide gel electrophoresis (SDS-PAGE), and the separated proteins were transferred to PVDF membranes. Then, the membranes were blocked with 1 × TBST containing 5%

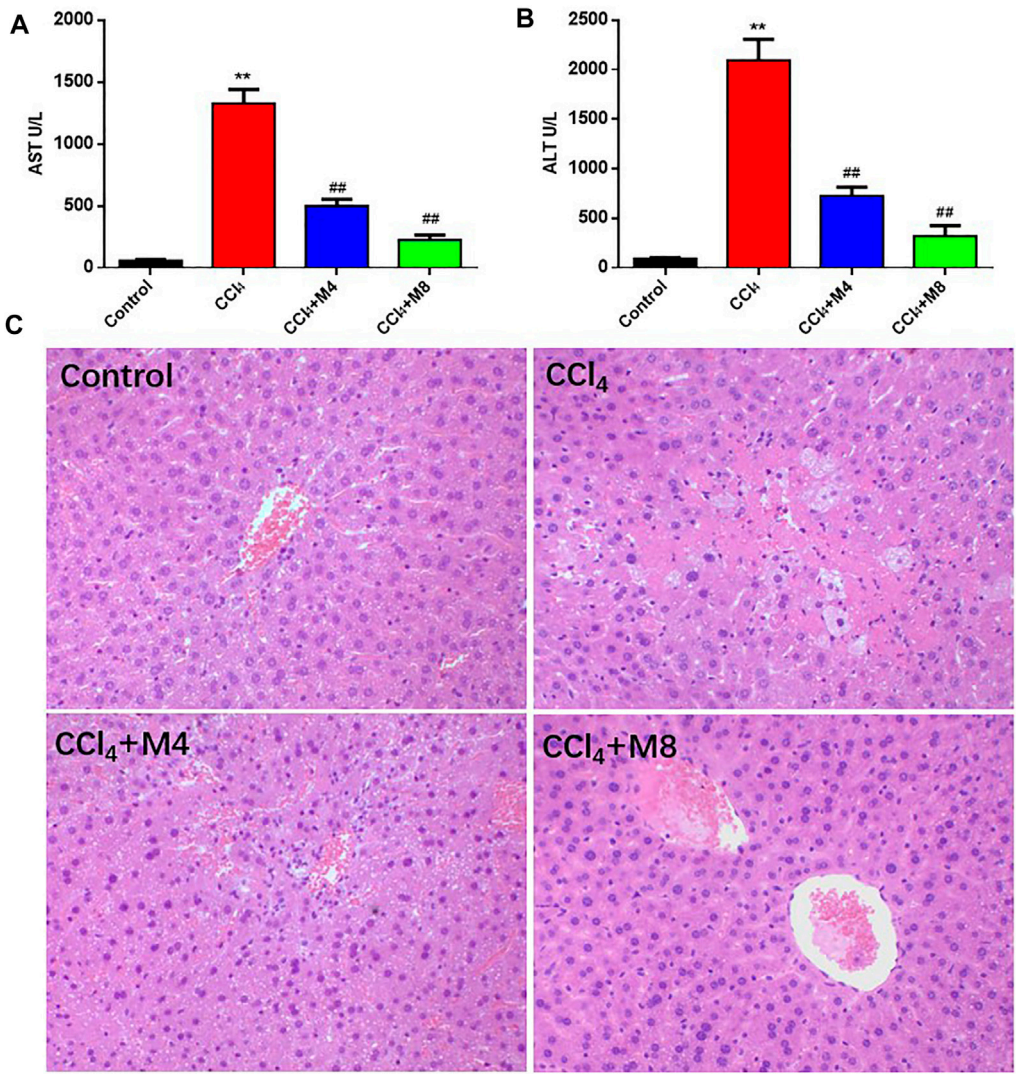

FIGURE 5 | Protective effects of midazolam on CCl_4-induced hepatic injury in mice. **(A,B)** The levels of AST and ALT in serum were detected at 24 h after CCl_4 exposure. **(C)** Pathological images of H&E stained sections of liver in control, CCl_4 and CCl_4 plus midazolam treated mice (magnification, ×200). The results were shown as mean ± S.D. $^{**}p < 0.01$ vs. the control group; $^{\#\#}p < 0.01$ vs. the CCl_4 group.

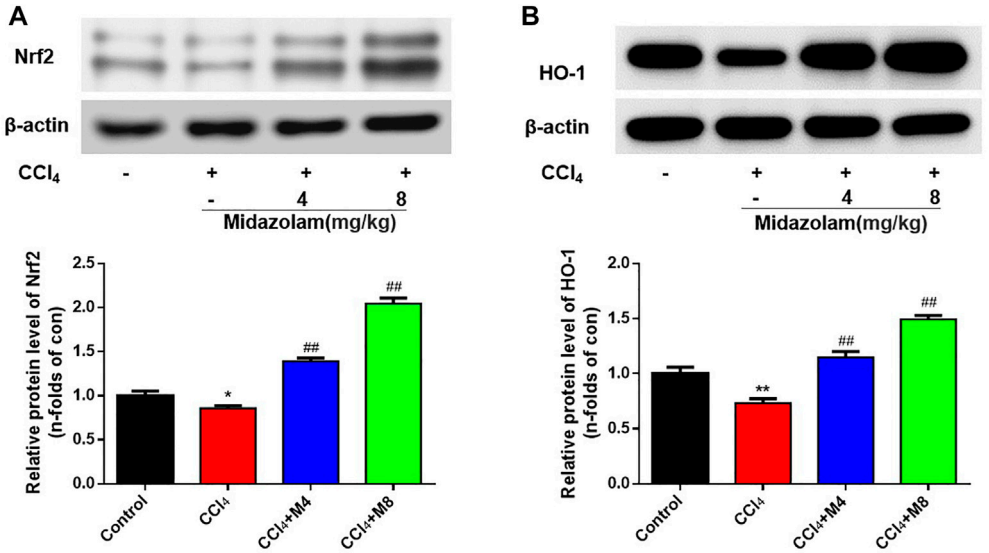

FIGURE 6 | Effect of midazolam on the expression of Nrf2 and HO-1 in mice liver. The protein levels of Nrf2 **(A)** and HO-1 **(B)** were examined at 24 h after CCl_4 exposure. (n = 8 in each group). $^{**}p < 0.01$ vs. the control group; $\#\#p < 0.01$ vs. the CCl_4 group.

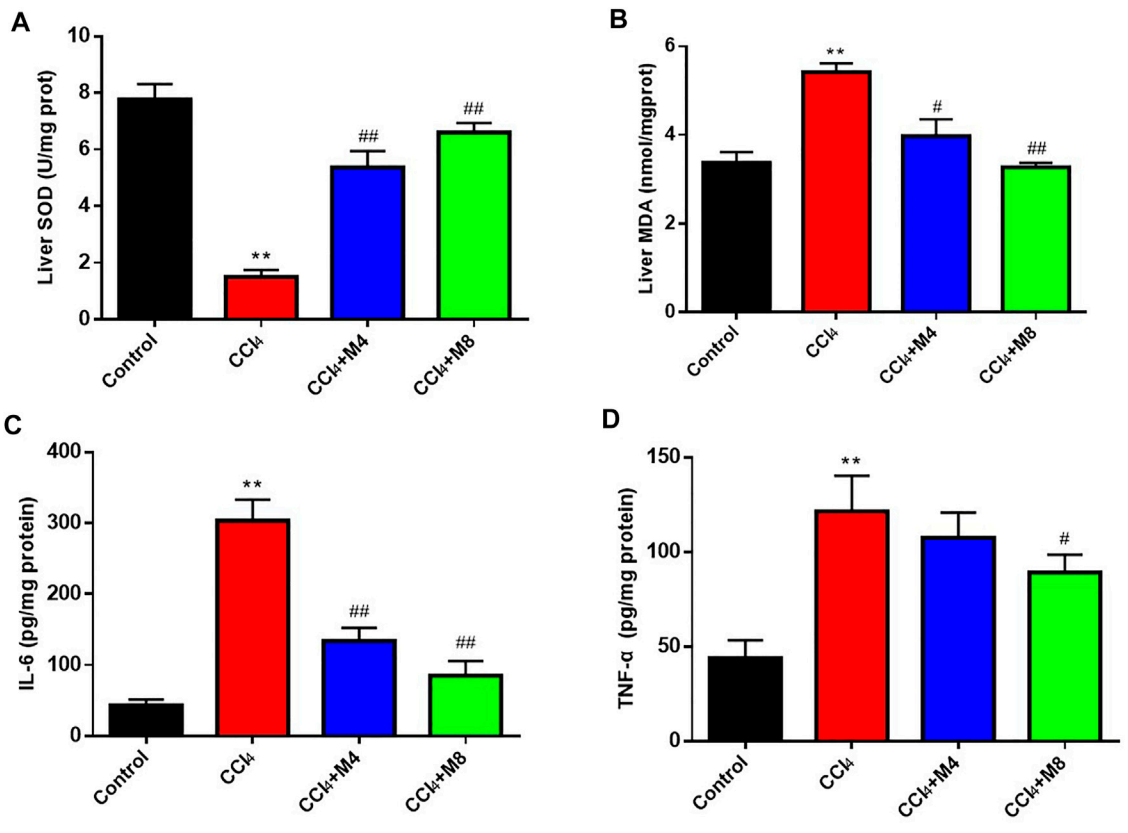

FIGURE 7 | The effects of midazolam on the levels of SOD **(A)**, MDA **(B)**, IL-6 **(C)** and TNF-α **(D)** in mice liver. (n = 8 in each group). $^{**}p < 0.01$ vs. the control group; $\#p < 0.05$ and $\#\#p < 0.01$ vs. CCl_4 group.

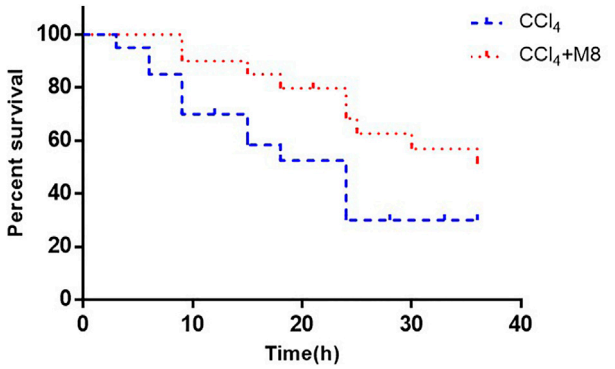

FIGURE 8 | The effect of midazolam pretreatment on the survival rate of mice in which liver injury was induced by CCl_4. Midazolam was i. p. injected at 8 mg/kg for 3 days 50% CCl_4 (2.6 ml/kg) were i. p. injected at 2 h after the last dose of midazolam ($n = 20$). The results were analyzed using the log-rank test and expressed as Kaplan-Meier survival curves.

nonfat milk for 2 h at room temperature and continued to incubate with primary antibodies against mice Nrf2 (1:1000, Abcam, United Kingdom), HO-1 (1:1000, Abcam, United Kingdom), β-actin (1:1000, Beyotime Biotechnology, China) overnight at 4°C. Subsequently, the membranes were washed three times with TBST and incubated with secondary antibody at room temperature for 2 h. Blots were visualized using a hypersensitive chemiluminescence kit (Biotechnology, China). The results were quantified by densitometry using ImageJ software.

Molecular Docking Simulations

The 3D structure of Kelch-like ECH-associated protein 1(Keap1) was downloaded from the Protein Data Bank (PDB Code:1ZGK) (Beamer et al., 2005). AutoDockTools 1.5.6 was applied to pre-process of coordinate files of the Keap1 and ligand by adding polar hydrogens, calculating Kollman charges and assigning AD4 atomic type. Docking site of Keap1 was situated at the kelch-like site (KS) as well as the functional site of Keap1 described by Beamer et al. (Beamer et al., 2005). The grid box was placed at KS, and the docking simulations was conducted by AutoDock Vina (1.1.2). Further analyses of the docking result was conducted by Discovery Studio Visualizer (BIOVIA Discovery Studio 2019; Dassault Systèmes, San Diego, United States).

Statistical Analysis

The data were analyzed with GraphPad Prism 7.0 (San Diego, CA, United States) and presented as the means ± standard deviation (S.D.). One-way ANOVA analysis was used for differences between groups. The survival rate was analyzed

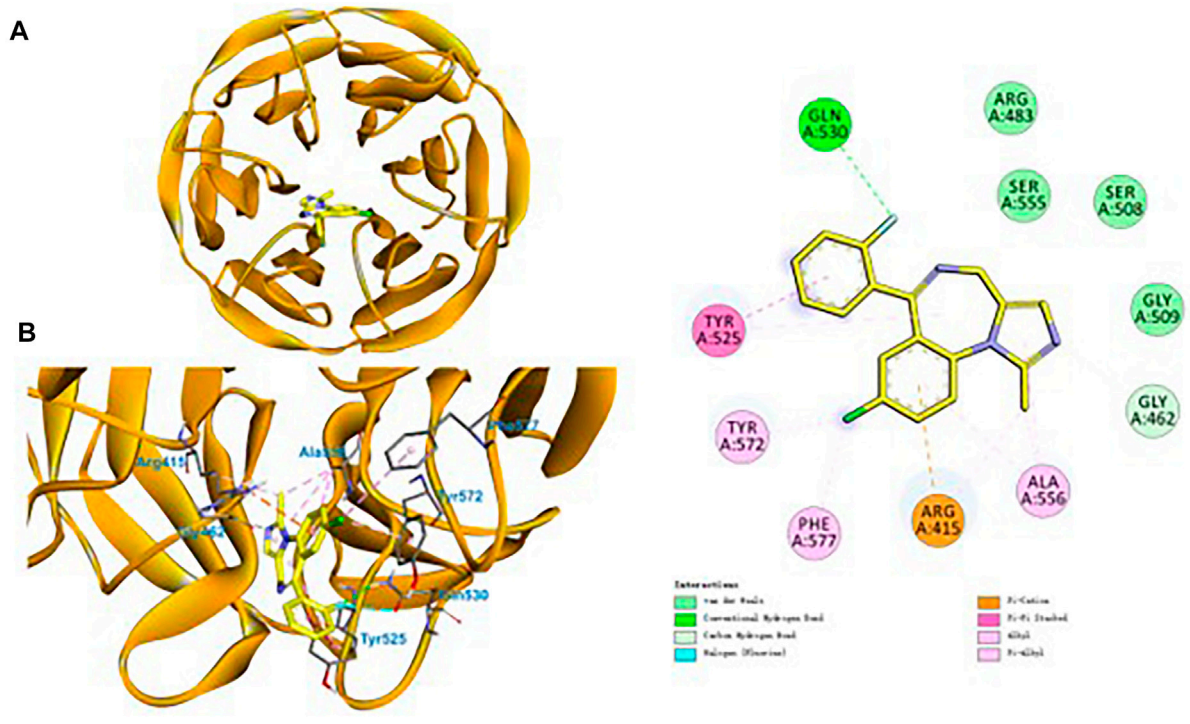

FIGURE 9 | Ligand docking of midazolam in the kelch domain of human Keap1 protein.

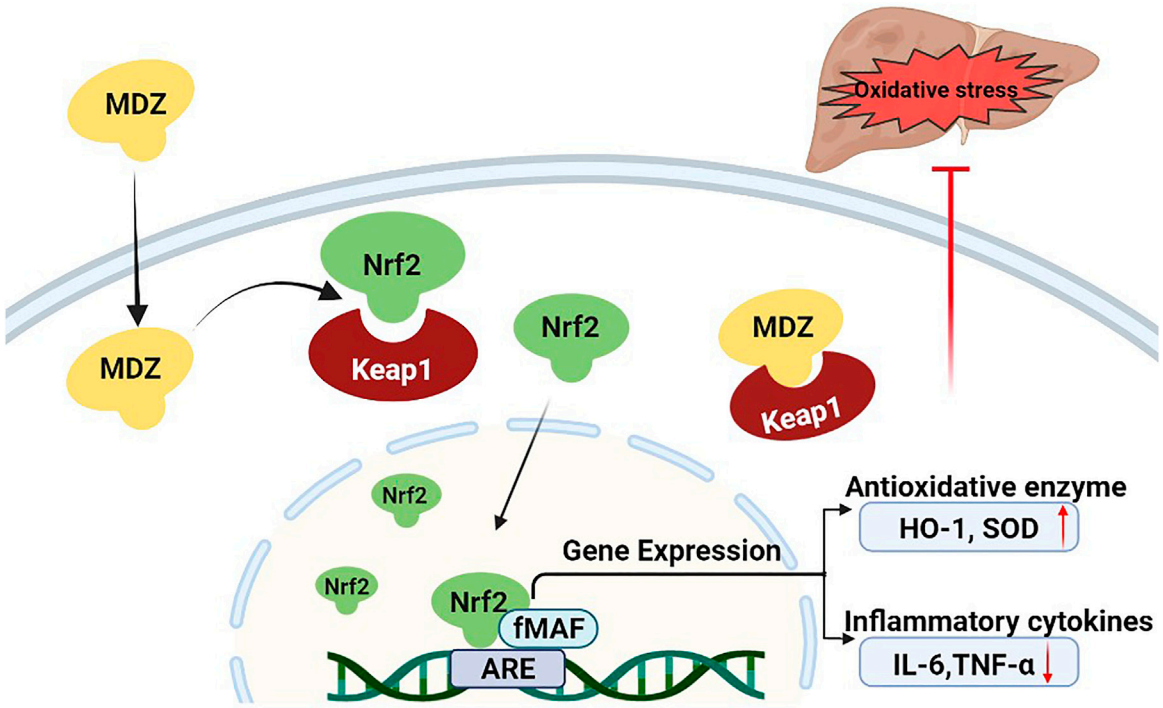

FIGURE 10 | Proposed mechanism of midazolam for ameliorating acute liver injury and related oxidative stress induced by CCL_4. Under normal physiological conditions, the Nrf2 protein level is tightly controlled by Keap1. Upon oxidative stress treatment, midazolam can bind to Keap1 stably, and hinder the coalition between Keap1 and Nrf2. Nrf2 is released and translocation to the nucleus to bind to AREs and initiate the anti-oxidative response by upregulating the expression of downstream target genes including HO-1 and SOD, which then decreases intracellular ROS production and alleviates oxidative stress-induced cytotoxicity. Midazolam ameliorates acute liver injury induced by carbon tetrachloride *via* enhancing Nrf2 signaling pathway.

by the log-rank test *p*-values less than 0.05 were considered statistically significant.

RESULTS

Screening of Therapeutic Drugs on Nrf2 Activation

Using the Nrf2 luciferease reporter construct, the active effect of Nrf2 by 30 kinds of therapeutic agents (10 μM, final concentration) were evaluated. The results showed that midazolam up-regulated the activity of Nrf2 more than 2-fold compared with the negative control group *($p < 0.01$)* (**Figure 1**).

Midazolam Dose-Dependently Enhances Nrf2 Expression

The expression of Nrf2 activity in 293T-Nrf2-luc cells increased with increasing midazolam concentration, and was dose-dependent *($p < 0.01$)* (**Figure 2A**). To determine the effect of midazolam on cell viability, cells were treated with different concentrations of midazolam for 24 h. Cell viability was measured by CCK-8 assay. As shown in **Figure 2B**, even if treatment with high-dose midazolam (40 μM), there was no significant difference compared with the control group.

To further verify the inductive effect of midazolam on Nrf2, the protein levels of Nrf2 in 293T-Nrf2-luc cells with or without midazolam treatment were determined. As shown in **Figure 3A**, Western blotting analysis showed that the protein expression of Nrf2 was elevated with the increasing concentrations of midazolam. It is well-known that Nrf2 is a transcriptional factor that needs to migrate to the nucleus to exert its function (Dinkova-Kostova et al., 2002). Under basal conditions Nrf2 is largely bound in the cytoplasm to Keap1, which is anchored to the actin cytoskeleton. When inducers disrupt the Keap1–Nrf2 complex, Nrf2 migrates to the nucleus where, in heterodimeric combinations with other transcription factors, it binds to antioxidant response element (ARE) regions of phase two genes and accelerates their transcription (Dinkova-Kostova et al., 2002). After the proteins in the nucleus and cytoplasm were extracted respectively, western blot analysis showed that with the increase of midazolam concentration, the Nrf2 protein level in the nucleus increased (**Figure 3B**) and the Nrf2 protein level in the cytoplasm decreased (**Figure 3C**). Midazolam promoted the translocation of Nrf2 to the nucleus.

Midazolam Reduces the Damage of Hepatocytes Induced by CCl_4

Next, the protective effects of midazolam on hepatocytes were investigated by using CCl_4-induced HepG2 cells were used as model cells. After pretreatment of HepG2 cells with different

concentrations of midazolam for 24 h, CCl_4 (IC_{50} = 1.5%, **Supplementary Figure S1**) was added to induce cell damage. As shown in **Figure 4**, CCl_4 significantly decreased HepG2 cells activity by more than 50% compared with the control group *($p < 0.01$)*. By contrast, midazolam could significantly improve HepG2 cells activity compared with the CCl_4 group ($p < 0.01$) even at low concentration (2.50 μM), as depicted in **Figure 4**. These findings clearly demonstrated that midazolam had good protective effects on CCl_4-induced hepatocytes.

Midazolam Attenuates CCl_4-Induced Acute Liver Injury in Mice

Next, we evaluated the protective effects of midazolam (4 and 8 mg/kg/day, lasting for 3 days, i. p. injection) on CCl_4 induced acute liver injury in mice. As shown in **Figure 5**, compared with the normal mice group, the activity levels of ALT and AST in serum of the CCl_4 group were significantly increased ($p < 0.01$). In sharp contrast, the activity levels of ALT and AST in serum collected from midazolam pretreatment group were significantly decreased ($p < 0.01$), when compared with that from the CCl_4 group (**Figures 5A,B**). Furthermore, H&E staining also suggested that the hepatocytes of the CCl_4 group were swollen, while the liver cells were necrosis and a large number of inflammatory cells infiltrated. By contrast, following Midazolam pretreatment, the hepatocyte necrosis and the inflammatory cell infiltration were significantly reduced (**Figure 5C**). The histopathological scores showed a significant lower in both 4 and 8 mg/kg midazolam pretreatment compared to the CCl_4 group ($p < 0.01$, **Figure 2S**). These findings clearly demonstrated that midazolam could attenuate CCl_4 induced acute liver injury in mice.

Midazolam Up-Regulates the Expression of Nrf2 and HO-1 in Mice Liver

As shown in **Figure 6**, Western blot analysis showed that the expression levels of Nrf2 and HO-1 in the CCl_4 group were down-regulated evidently when compared to that in the control group. However, following administration of midazolam, the protein levels of both Nrf2 and HO-1 were significantly enhanced. These findings clearly suggested that Nrf2-related signaling pathway in mice liver could be enhanced following administration of midazolam.

Midazolam Ameliorates CCl_4-Induced Oxidative Stress and Inflammation in Liver Tissue

It is well-known that SOD and MDA are typical biomarkers of antioxidation and oxidative stress, respectively. As shown in **Figure 7**, compared with the control group, MDA levels in liver were increased *($p < 0.05$)*, while SOD activity levels were decreased at 24 h after CCl_4 treatment *($p < 0.05$)*. Compared with CCl_4 group, midazolam pretreatment group reduced MDA levels *($p < 0.05$)* and increased SOD activity levels *($p < 0.05$)* (**Figures 7A,B**). Meanwhile, it was also found that CCl_4 treatment significantly increased TNF-α and IL-6 expression levels compared with the control group ($p < 0.01$). As expected, midazolam dose-dependently reduced IL-6 expression levels ($p < 0.01$) when compared with that in the CCl_4 group, while the serum levels of TNF-α were also significantly reduced following administration with high dose midazolam (8 mg/kg) ($p < 0.05$) (**Figures 7C,D**).

Midazolam Increases the Survival Rate of Mice Treated With Lethal Dose of CCl_4

To further verify the hepatoprotective effect of midazolam, we investigated the ability of midazolam to affect the survival rate of mice treated with lethal dose of CCl_4. For this purpose, a lethal dose of CCl_4 for mice (2.6 ml/kg, 50%, i. p.) was used, while midazolam (8 mg/kg) was administrated for three consecutive days (once per day). As shown in **Figure 8**, midazolam significantly improved the survival rate of mice when compared with the CCl_4 group ($p < 0.05$).

Molecular Docking Simulations

Finally, to decipher the binding modes and the molecular mechanism of midazolam in enhancing of Nrf2 signaling pathway, molecular docking simulations of midazolam into Keap1 were performed. Under homeostatic conditions, Nrf2 is kept inactive being bound to its endogenous inhibitor Keap1 (Bellezza et al., 2018). As shown in **Figure 9**, midazolam could be well-docked into the kelch-like site (KS) of Keap1, forming strong hydrophobic interactions, electrostatic and hydrogen bonding interactions with several key residuals in the inner wall of KS. Remarkably, the unsaturated and aromatic functional groups of midazolam interacted with Ala556 and Tyr525 *via* strong hydrophobic interactions including Alkyl, Pi-Alkyl and Pi-Pi stacked interactions (**Figure 9**). It was particular that three phenyl containing lipophilic residues (Phe577, Tyr572 and Tyr525) stretched the side chains orienting the sheer center direction of KS, resulting a regional hydrophobic surface of KS inner wall (**Figure 9**). In addition, the group of chlorobenzene and fluorobenzene were vital for the binding of midazolam. The group of chlorobenzene interacted with Arg415 *via* Pi-Cation interactions, while the fluorobenzene could interact with Gln530 *via* hydrogen bonding. These observations clearly suggest that midazolam could stably and tightly bind to Keap1, which in turn, blocking the coalition between Keap1 and Nrf2.

DISCUSSION

Nrf2 is a key member of cap-n-collar basic leucine zipper transcription factor family, and is also a key regulator of mammalian genes involved in cell protection and detoxification by preventing oxidative stress (Martin et al., 1998). Under physiological conditions, Nrf2 mainly binds to Keap1 in cytoplasm (Yamamoto et al., 2018). After exposure to oxidative stress, Nrf2 and Keap1 are isolated and transferred to the nucleus. By interacting with the antioxidant response element (ARE) sequence of antioxidant and cytoprotective genes, Nrf2 induces the expression of a variety of antioxidant enzymes and phase II drug metabolism enzymes, including HO-1 and NQO1, and inhibits oxidative stress (Yamamoto et al., 2018)(Bellezza et al., 2018). Therefore, looking for Nrf2 activators has become a research hotspot in the prevention and treatment of oxidative stress-related

diseases. Studies have shown that sedative and analgesic anesthetics commonly used in clinic can reduce the perioperative oxidative stress level. For example, in the acetaminophen induced liver injury animal model (Kostopanagiotou et al., 2009) and ischemia-reperfusion liver injury animal model (Chan et al., 2008), propofol can significantly reduce MDA, an index of oxidative stress in the liver. Another study has shown that ketamine can rapidly reduce the production of ROS and reduce protein damage, and play an antidepressant role in the hippocampus of ketamine treated mice through metabonomics and proteomics analysis (Weckmann et al., 2017). However, there is no comparative study on the effects of various common anesthetics on antioxidant stress. In our study, based on Nrf2 target, 30 kinds of therapeutic agents were screened by 293T-Nrf2-luc cell line to evaluate the inductive effect on Nrf2. The results showed that the inductive effect of midazolam on Nrf2 was more than 2 times, and the high dose of midazolam (20 μM) did not affect cell activity. This finding leads us to speculate that midazolam exerts stronger antioxidative stress ability than other anesthetics through Nrf2.

As the first step of metabolism, the liver is often exposed to high concentrations of exogenous and endogenous metabolites, especially vulnerable to oxidative damage caused by intermediate active substances. Nrf2/ARE, as one of the important mechanisms to protect the liver from oxidative stress, can play a protective role in liver inflammation, ischemia/reperfusion, fibrosis and regeneration by inducing target genes (Cuadrado et al., 2019; G; Bardallo et al., 2021). The activators of Nrf2, such as glycyrrhizic acid (Chen et al., 2013), sulforaphane (Wu et al., 2014), and curcumin (Peng et al., 2018), can induce the expression of antioxidant enzymes and reduce oxidative stress and liver injury. CCl_4 is a strong hepatoxic and prooxidant agent widely used to induce hepatotoxicity, and its animal model has been widely used to screen the anti-hepatotoxicity and/or hepatoprotective activity of drugs (Yang et al., 2015; Cong et al., 2017; Zou et al., 2017). CCl_4 causes a decrease in liver cells, in the activities of antioxidant enzymes and increases the protein carbonyl content, which is a protein oxidation product, at the oxidative stress biomarker MDA level (Sun et al., 2018). The purpose of this study was to evaluate the antioxidant capacity of midazolam *in vivo*, different doses of midazolam pretreatment were given to mice with acute liver injury induced by CCl_4. Our results indicated that Midazolam pretreatment could significantly reduce the level of MDA which were markers of oxidative stress in liver tissue, and increased the activities of SOD antioxidant enzymes. Liver ALT, AST and pathological sections showed the protective effect of midazolam on liver. And we found that the higher the dose of midazolam, the greater the effect of reducing liver damage. Therefore, we chose a higher dose of midazolam to test the survival rate of mice given a lethal dose of CCl_4. Midazolam significantly improved the survival rate of mice.

Midazolam is a benzodiazepine sedative, which is commonly used in clinical anesthesia and intensive care unit (ICU) (Lazzaroni and Bianchi Porro, 2003; Garcia et al., 2021). Clinical research shows that the sedation of critical patients with midazolam 48 h continuous infusion can significantly reduce the level of IL-1β, IL-6 and TNF- α in blood (Helmy and Al-Attiyah, 2001). In LPS and galactosamine induced acute liver injury model mice, midazolam can reduce serum ALT and liver TNF-α levels, reduce liver injury and protect liver function (Li J. et al., 2018). Consistently, our results suggested that midazolam could also reduce the hepatic TNF-α and IL-6 induced by CCl_4. Previous studies on the antioxidant stress of midazolam have mainly focused on the nervous system. Midazolam can inhibit oxidative stress, reduce the level of ROS, reduce the death of neurons, and play a neuroprotective role (Liu et al., 2017; Li GZ. et al., 2018). To conclude from the observation from molecular docking simulations, midazolam could bind to Keap1 stably, and hinder the coalition between Keap1 and Nrf2. This may be an important mechanism for midazolam to exert its anti-oxidative stress (**Figure 10**).

In summary, this study found that midazolam acted as an efficacious agent to activate Nrf2/HO-1 signaling pathway, which could enhance the levels of several key antioxidant proteins both *in vitro* and *in vivo*. Cell assays demonstrated that midazolam dose-dependently enhanced Nrf2 expression and showed good protective effects on CCl_4-induced HepG2 cells. Animal tests showed that midazolam could significantly reduce the liver pathological tissue damage and the serum levels of both ALT and AST in CCl_4-induced liver injury, accompanied by increasing of the levels of antioxidant enzyme SOD and reducing the production of MDA, as well as reducing the pro-inflammatory cytokines (IL-6, TNF-α) secretion. Molecular docking simulations suggested that midazolam could stably bind to Keap1 and hinder the binding of Keap1 to Nrf2. Collectively, our findings suggested that midazolam may be a good protector for alleviating CCl_4-induced acute liver injury *via* enhancing Nrf2 signaling pathway, which offered a new pharmacotherapy for preventing and treating toxin-induced organ injury.

DATA AVAILABILITY STATEMENT

The original contributions presented in the study are included in the article/**Supplementary Material**, further inquiries can be directed to the corresponding authors.

ETHICS STATEMENT

The animal study was reviewed and approved by Yueyang Hospital of integrated traditional Chinese and Western Medicine Affiliated to Shanghai University of traditional Chinese medicine (ethics No.: YYLAC-2020-0801).

AUTHOR CONTRIBUTIONS

YoZ and YaZ contributed this work equally.

FUNDING

This study was supported by grants from The National Natural Science Funds (82074228, 81922070 and 81973286).

SUPPLEMENTARY MATERIAL

The Supplementary Material for this article can be found online at: https://www.frontiersin.org/articles/10.3389/fphar.2022.940137/full#supplementary-material

REFERENCES

Ali- Hasan- Al- Saegh, S., Mirhosseini, S. J., Tahernejad, M., Mahdavi, P., Shahidzadeh, A., Karimi-Bondarabadi, A. A., et al. (2016). Impact of Antioxidant Supplementations on Cardio-Renal Protection in Cardiac Surgery: an Updated and Comprehensive Meta-Analysis and Systematic Review. *Cardiovasc Ther.* 34, 360–370. doi:10.1111/1755-5922.12207

Arsalani-Zadeh, R., Ullah, S., Khan, S., and MacFie, J. (2011). Oxidative Stress in Laparoscopic versus Open Abdominal Surgery: a Systematic Review. *J. Surg. Res.* 169, e59–68. doi:10.1016/j.jss.2011.01.038

Bardallo, R. G., Panisello-Roselló, A., Sanchez-Nuno, S., Alva, N., Roselló-Catafau, J., and Carbonell, T. (2021). Nrf2 and Oxidative Stress in Liver Ischemia/reperfusion Injury. *FEBS J.* doi:10.1111/febs.16336

Beamer, L. J., Li, X., Bottoms, C. A., and Hannink, M. (2005). Conserved Solvent and Side-Chain Interactions in the 1.35 Angstrom Structure of the Kelch Domain of Keap1. *Acta Crystallogr. D. Biol. Crystallogr.* 61, 1335–1342. doi:10.1107/S0907444905022626

Bellezza, I., Giambanco, I., Minelli, A., and Donato, R. (2018). Nrf2-Keap1 Signaling in Oxidative and Reductive Stress. *Biochim Biophys Acta Mol Cell ResMolecular Cell Res.* 1865, 721–733. doi:10.1016/j.bbamcr.2018.02.010

Cederbaum, A. I., Lu, Y., and Wu, D. (2009). Role of Oxidative Stress in Alcohol-Induced Liver Injury. *Arch. Toxicol.* 83, 519–548. doi:10.1007/s00204-009-0432-0

Chan, K. C., Lin, C. J., Lee, P. H., Chen, C. F., Lai, Y. L., Sun, W. Z., et al. (2008). Propofol Attenuates the Decrease of Dynamic Compliance and Water Content in the Lung by Decreasing Oxidative Radicals Released from the Reperfused Liver. *Anesth. Analg.* 107, 1284–1289. doi:10.1213/ane.0b013e318181f4e6

Chen, S., Zou, L., Li, L., and Wu, T. (2013). The Protective Effect of Glycyrrhetinic Acid on Carbon Tetrachloride-Induced Chronic Liver Fibrosis in Mice via Upregulation of Nrf2. *PloS one* 8, e53662. doi:10.1371/journal.pone.0053662

Cichoż-Lach, H., and Michalak, A. (2014). Oxidative Stress as a Crucial Factor in Liver Diseases. *World J. Gastroenterol.* 20, 8082–8091. doi:10.3748/wjg.v20.i25.8082

Cong, M., Zhao, W., Liu, T., Wang, P., Fan, X., Zhai, Q., et al. (2017). Protective Effect of Human Serum Amyloid P on CCl4-Induced Acute Liver Injury in Mice. *Int. J. Mol. Med.* 40, 454–464. doi:10.3892/ijmm.2017.3028

Cuadrado, A., Rojo, A. I., Wells, G., Hayes, J. D., Cousin, S. P., Rumsey, W. L., et al. (2019). Therapeutic Targeting of the NRF2 and KEAP1 Partnership in Chronic Diseases. *Nat. Rev. Drug Discov.* 18, 295–317. doi:10.1038/s41573-018-0008-x

Dinkova-Kostova, A. T., Holtzclaw, W. D., Cole, R. N., Itoh, K., Wakabayashi, N., Katoh, Y., et al. (2002). Direct Evidence that Sulfhydryl Groups of Keap1 Are the Sensors Regulating Induction of Phase 2 Enzymes that Protect against Carcinogens and Oxidants. *Proc. Natl. Acad. Sci. U. S. A.* 99, 11908–11913. doi:10.1073/pnas.172398899

Feng, X.-H., Xu, H.-Y., Wang, J.-Y., Duan, S., Wang, Y.-C., and Ma, C.-M. (2021). In Vivo hepatoprotective Activity and the Underlying Mechanism of Chebulinic Acid from Terminalia Chebula Fruit. *Phytomedicine* 83, 153479. doi:10.1016/j.phymed.2021.153479

Garcia, R., Salluh, J. I. F., Andrade, T. R., Farah, D., da Silva, P. S. L., Bastos, D. F., et al. (2021). A Systematic Review and Meta-Analysis of Propofol versus Midazolam Sedation in Adult Intensive Care (ICU) Patients. *J. Crit. Care* 64, 91–99. doi:10.1016/j.jcrc.2021.04.001

Giustarini, D., Dalle-Donne, I., Tsikas, D., and Rossi, R. (2009). Oxidative Stress and Human Diseases: Origin, Link, Measurement, Mechanisms, and Biomarkers. *Crit. Rev. Clin. Lab. Sci.* 46, 241–281. doi:10.3109/10408360903142326

Helmy, S. A., and Al-Attiyah, R. J. (2001). The Immunomodulatory Effects of Prolonged Intravenous Infusion of Propofol versus Midazolam in Critically Ill Surgical Patients. *Anaesthesia* 56, 4–8. doi:10.1046/j.1365-2044.2001.01713.x

Kaspar, J. W., Niture, S. K., and Jaiswal, A. K. (2009). Nrf2:INrf2 (Keap1) Signaling in Oxidative Stress. *Free Radic. Biol. Med.* 47, 1304–1309. doi:10.1016/j.freeradbiomed.2009.07.035

Koike, K. (2007). Pathogenesis of HCV-Associated HCC: Dual-Pass Carcinogenesis through Activation of Oxidative Stress and Intracellular Signaling. *Hepatol. Res.* 37 Suppl 2 (Suppl. 2), S115–S120. doi:10.1111/j.1872-034X.2007.00173.x

Kostopanagiotou, G. G., Grypioti, A. D., Matsota, P., Mykoniatis, M. G., Demopoulos, C. A., Papadopoulou-Daifoti, Z., et al. (2009). Acetaminophen-induced Liver Injury and Oxidative Stress: Protective Effect of Propofol. *Eur. J. Anaesthesiol.* 26, 548–553. doi:10.1097/EJA.0b013e32831c8a01

Lazzaroni, M., and Bianchi Porro, G. (2003). Preparation, Premedication and Surveillance. *Endoscopy* 35, 103–111. doi:10.1055/s-2003-37012

Li, G. Z., Tao, H. L., Zhou, C., Wang, D. D., and Peng, C. B. (2018a). Midazolam Prevents Motor Neuronal Death from Oxidative Stress Attack Mediated by JNK-ERK Pathway. *Hum. Cell* 31, 64–71. doi:10.1007/s13577-017-0184-8

Li, J., Tan, H., Zhou, X., Zhang, C., Jin, H., Tian, Y., et al. (2018b). The Protection of Midazolam against Immune Mediated Liver Injury Induced by Lipopolysaccharide and Galactosamine in Mice. *Front. Pharmacol.* 9, 1528. doi:10.3389/fphar.2018.01528

Lian, Y. H., Fang, J., Zhou, H. D., Jiang, H. F., and Xie, K. J. (2019). Sufentanil Preconditioning Protects against Hepatic Ischemia-Reperfusion Injury by Suppressing Inflammation. *Med. Sci. Monit.* 25, 2265–2273. doi:10.12659/MSM.913145

Lim, J.-Y., Lee, J.-H., Yun, D.-H., Lee, Y.-M., and Kim, D.-K. (2021). Inhibitory Effects of Nodakenin on Inflammation and Cell Death in Lipopolysaccharide-Induced Liver Injury Mice. *Phytomedicine* 81, 153411. doi:10.1016/j.phymed.2020.153411

Liu, J. Y., Guo, F., Wu, H. L., Wang, Y., and Liu, J. S. (2017). Midazolam Anesthesia Protects Neuronal Cells from Oxidative Stress-Induced Death via Activation of the JNK-ERK Pathway. *Mol. Med. Rep.* 15, 169–179. doi:10.3892/mmr.2016.6031

Martin, F., van Deursen, J. M., Shivdasani, R. A., Jackson, C. W., Troutman, A. G., and Ney, P. A. (1998). Erythroid Maturation and Globin Gene Expression in Mice with Combined Deficiency of NF-E2 and Nrf-2. *Blood* 91, 3459–3466. doi:10.1182/blood.V91.9.3459

Oldman, A. H., Martin, D. S., Feelisch, M., Grocott, M. P. W., and Cumpstey, A. F. (2021). Effects of Perioperative Oxygen Concentration on Oxidative Stress in Adult Surgical Patients: a Systematic Review. *Br. J. Anaesth.* 126, 622–632. doi:10.1016/j.bja.2020.09.050

Peng, X., Dai, C., Liu, Q., Li, J., and Qiu, J. (2018). Curcumin Attenuates on Carbon Tetrachloride-Induced Acute Liver Injury in Mice via Modulation of the Nrf2/HO-1 and TGF-β1/Smad3 Pathway. *Molecules* 23, 215. doi:10.3390/molecules23010215

Russo, M., Spagnuolo, C., Russo, G. L., Skalicka-Woźniak, K., Daglia, M., Sobarzo-Sánchez, E., et al. (2018). Nrf2 Targeting by Sulforaphane: A Potential Therapy for Cancer Treatment. *Crit. Rev. Food Sci. Nutr.* 58, 1391–1405. doi:10.1080/10408398.2016.1259983

Sun, J., Wu, Y., Long, C., He, P., Gu, J., Yang, L., et al. (2018). Anthocyanins Isolated from Blueberry Ameliorates CCl(4) Induced Liver Fibrosis by Modulation of Oxidative Stress, Inflammation and Stellate Cell Activation in Mice. *Food Chem. Toxicol.* 120, 491–499. doi:10.1016/j.fct.2018.07.048

Tang, W., Jiang, Y. F., Ponnusamy, M., and Diallo, M. (2014). Role of Nrf2 in Chronic Liver Disease. *World J. Gastroenterol.* 20, 13079–13087. doi:10.3748/wjg.v20.i36.13079

Toro-Pérez, J., and Rodrigo, R. (2021). Contribution of Oxidative Stress in the Mechanisms of Postoperative Complications and Multiple Organ Dysfunction Syndrome. *Redox Rep.* 26, 35–44. doi:10.1080/13510002.2021.1891808

Weckmann, K., Deery, M. J., Howard, J. A., Feret, R., Asara, J. M., Dethloff, F., et al. (2017). Ketamine's Antidepressant Effect Is Mediated by Energy Metabolism and Antioxidant Defense System. *Sci. Rep.* 7, 15788. doi:10.1038/s41598-017-16183-x

Wu, Q., Zhang, D., Tao, N., Zhu, Q. N., Jin, T., Shi, J. S., et al. (2014). Induction of Nrf2 and Metallothionein as a Common Mechanism of Hepatoprotective Medicinal Herbs. *Am. J. Chin. Med.* 42, 207–221. doi:10.1142/S0192415X14500141

Xiong, Y., Zhu, G. H., Zhang, Y. N., Hu, Q., Wang, H. N., Yu, H. N., et al. (2021). Flavonoids in Ampelopsis Grossedentata as Covalent Inhibitors of SARS-CoV-2 3CL(pro): Inhibition Potentials, Covalent Binding Sites and

Inhibitory Mechanisms. *Int. J. Biol. Macromol.* 187, 976–987. doi:10.1016/j.ijbiomac.2021.07.167

Yamamoto, M., Kensler, T. W., and Motohashi, H. (2018). The KEAP1-NRF2 System: a Thiol-Based Sensor-Effector Apparatus for Maintaining Redox Homeostasis. *Physiol. Rev.* 98, 1169–1203. doi:10.1152/physrev.00023.2017

Yang, B. Y., Zhang, X. Y., Guan, S. W., and Hua, Z. C. (2015). Protective Effect of Procyanidin B2 against CCl4-Induced Acute Liver Injury in Mice. *Molecules* 20, 12250–12265. doi:10.3390/molecules200712250

Zhao, D. F., Fan, Y. F., Wang, F. Y., Hou, F. B., Gonzalez, F. J., Li, S. Y., et al. (2021). Discovery and Characterization of Naturally Occurring Potent Inhibitors of Catechol-O-Methyltransferase from Herbal Medicines. *RSC Adv.* 11, 10385–10392. doi:10.1039/d0ra10425f

Zou, Y., Xiong, J. B., Ma, K., Wang, A. Z., and Qian, K. J. (2017). Rac2 Deficiency Attenuates CCl(4)-Induced Liver Injury through Suppressing Inflammation and Oxidative Stress. *Biomed. Pharmacother.* 94, 140–149. doi:10.1016/j.biopha.2017.07.074

Conflict of Interest: The authors declare that the research was conducted in the absence of any commercial or financial relationships that could be construed as a potential conflict of interest.

Publisher's Note: All claims expressed in this article are solely those of the authors and do not necessarily represent those of their affiliated organizations, or those of the publisher, the editors and the reviewers. Any product that may be evaluated in this article, or claim that may be made by its manufacturer, is not guaranteed or endorsed by the publisher.

frontiers | Frontiers in Pharmacology

ORIGINAL RESEARCH
published: 12 July 2022
doi: 10.3389/fphar.2022.944949

Comparative Pharmacokinetics of Three Bioactive Diterpenoids of *Rabdosia serra* Extract in Normal and Con A-Induced Liver Injury Rats Using UPLC-MS/MS

Fangle Liu[1,2], Yun Zeng[1], Pengyu Dai[1], Kaiwen Huang[1], Kaihui Zhang[1], Tao Tao[3], Meiqi Wang[1], Chenchen Zhu[1] and Chaozhan Lin[1]**

[1]School of Pharmaceutical Sciences, Guangzhou University of Chinese Medicine, Guangzhou, China, [2]School of Basic Medical Sciences, Guangzhou University of Chinese Medicine, Guangzhou, China, [3]Guangzhou Chest Hospital, Guangzhou, China

Rabdosia serra (Maxim.) Hara (*R. serra*), one of the source plants of "Xihuangcao", has been widely used as a Chinese folk herb with the concomitant function of both medicine and foodstuff for the prevention and treatment of liver disease. Diterpenoids were considered as the major bioactive components in *R. serra*, responsible for their effect on hepatoprotection in previous phytochemical and pharmacological studies, while few comparative pharmacokinetic studies have been conducted under the physiological and pathological conditions. To reveal the difference in the pharmacokinetics process of *R. serra* extract (RSE) in normal and Con A-induced liver injury rats, a rapid ultra-high-pressure liquid chromatography–tandem mass spectrometry method (total running time: 5 min) was established to simultaneously determine three bioactive diterpenoids (enmein, epinodosin, and isodocarpin) in rat plasma. The results showed significant differences in the pharmacokinetic properties of three analytes between the physiological and pathological states. Compared with normal rats, the AUC of the three analytes was remarkably higher in liver injury rats, while the T_{max}, $T_{1/2}$, and MRT were shortened. It indicated that RSE has higher exposure and quicker elimination in liver injury rats than that in normal rats. Our results suggested that the pharmacokinetics of hepatoprotective medications was affected by liver injury, which prospected to provide essential information for guiding the healthcare and clinical application of *R. serra* in pathological states.

Keywords: ***Rabdosia serra*, pharmacokinetic differences, diterpenoids, Con A, liver injury, UPLC-MS/MS**

OPEN ACCESS

Edited by:
Ling Ye,
Southern Medical University, China

Reviewed by:
Haiyu Zhao,
China Academy of Chinese Medical Sciences, China
Bin Quan Han,
Hong Kong Baptist University, Hong Kong SAR, China

****Correspondence:***
Chenchen Zhu
zhucc@gzucm.edu.cn
Chaozhan Lin
linchaozhan@gzucm.edu.cn

Specialty section:
This article was submitted to Drug Metabolism and Transport, a section of the journal Frontiers in Pharmacology

Received: *16 May 2022*
Accepted: *07 June 2022*
Published: *12 July 2022*

Citation:
Liu F, Zeng Y, Dai P, Huang K, Zhang K, Tao T, Wang M, Zhu C and Lin C (2022) Comparative Pharmacokinetics of Three Bioactive Diterpenoids of Rabdosia serra Extract in Normal and Con A-Induced Liver Injury Rats Using UPLC-MS/MS. Front. Pharmacol. 13:944949. doi: 10.3389/fphar.2022.944949

1 INTRODUCTION

Liver injury is a common pathological symptom of liver diseases induced by various factors like virals, drugs, and autoimmunity, and its development is often accompanied by inflammation (Qian et al. (2021). Immune liver injury, the main kind of liver injury, is a chronic inflammatory disease that is related to the abnormal immune response of liver cells, which may exist in acute hepatitis that can finally result in liver cancer, liver cirrhosis, and even death (Shojaie et al., 2021). Due to its serious impact on people's quality of life and the fact that it is difficult for treatment, developing effective medicines for immune liver injury remains a challenge.

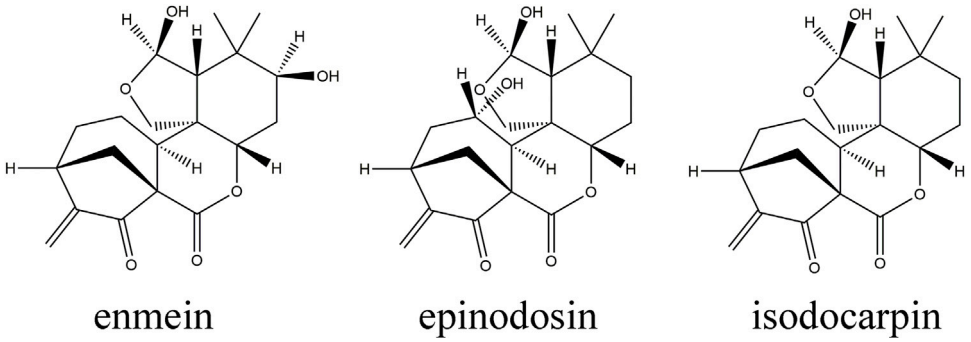

FIGURE 1 | Chemical structures of enmein, epinodosin, and isodocarpin.

Traditional Chinese medicine (TCM) has unique advantages in the clinical treatment of liver injury due to its characteristics of multitarget and multiapproach (Fu et al., 2021). The pharmacokinetic study of TCM is helpful to elucidate the *in vivo* process characteristics of the active ingredients of TCM and clarify the pharmacodynamic material basis of them (Fu et al., 2022). The liver is the crucial detoxifying organ, responsible for the body's metabolism of foreign substances, including drugs. Therefore, the metabolic process of drugs *in vivo* will be changed, which is affected by the pathological state of liver injury (Alkharfy et al., 2020). The interpretation of integrated intracorporal processes of liver-protective agents in pathological states may be a profound impact on the safety and efficacy of relevant medications in clinical applications.

Rabdosia serra, the dried aerial parts of *Rabdosia serra* (Maxim.) Hara, is one of the sources of "Xihuangcao" and has been commonly used as a medicinal and edible herb for the prevention and treatment of hepatobiliary diseases with the efficiency of heat-clearing, detoxicating, dampness, and moisture reduction for a long time in China (Liu et al., 2020). In clinics, *R. serra* showed a definite curative effect in treating hepatitis, liver injury, intrahepatic cholestasis, and so on (Yang et al., 2021). Modern research studies have also proved that *R. serra* has various pharmacological properties including hepatoprotection, anti-inflammation, antivirus, and immune regulation (Xing et al., 2020; Feng et al., 2021). Among them, liver protection and anti-inflammatory effects of *R. serra* are the most prominent (Sun et al., 2020). Our previous study also showed that *R.* serra extract (RSE) could significantly reduce the levels of AST and ALT and attenuate liver injury induced by concanavalin A (Con A) (He et al., 2016) and alpha-naphthylisothiocyanate (ANIT) (Zhang et al., 2021). However, there is a limited understanding of the comparative pharmacokinetic performance of RSE in physiological and pathological states. Phytochemical studies have presented that terpenoids, phenolic acids, and flavonoids were the predominant composition of *R. serra* (Liu et al., 2020). Diterpenoids, the active and the most characteristic constituents of *R. serra*, have been reported to possess biological effects of hepatoprotective, anti-inflammatory, and antitumor activities, which have attracted great attention from researchers (Wang and Xuan, 2016). Moreover, diterpenoids, such as enmein, isodocarpin, nodosin, epinodosin, and so on, had shown their effects on increasing the cell viability and reducing transaminase content in H_2O_2-induced BRL cells, and their strength of efficacy was closely related to their structure according to the 3D-QSAR analysis in our previous research (Liu et al., 2019). Three diterpenoids among them, enmein, epinodosin, and isodocarpin, have a similar structure with the 6,7-seco-ent-kaurene skeleton, and the difference in their structure was in the presence or absence of hydroxyl groups at C-3 and C-11 positions (shown in **Figure 1**). Thus, the three potential active diterpenoids, enmein, epinodosin, and isodocarpin, were selected as representative components to process the pharmacokinetic study of RSE.

In the present study, we aimed to establish a sensitive and rapid ultra-high-pressure liquid chromatography–tandem mass spectrometry (UPLC-MS/MS) method for the simultaneous determination of three active diterpenoids from RSE in plasma and apply this method for their pharmacokinetic study. According to the comparative pharmacokinetic study of the three bioactive diterpenoids of RSE in normal and Con A-induced liver injury rats, it would be hoped to provide significant information for the application of *R. serra*.

2 MATERIALS AND METHODS

2.1 Chemicals and Reagents

The reference standards enmein, epinodosin, and isodocarpin were isolated from *R. serra* and identified by UV, NMR, IR, and MS in our previous research (Lin et al., 2016). The purity of these (>99%) was determined by normalization of their peak areas detected by HPLC. Standard stock solutions of enmein, epinodosin, and isodocarpin at a concentration of 1 mg/ml were diluted with methanol to obtain a reference solution (1 μg/ml) and stored under −20°C until gradient dilution for analysis. Sulfamethoxazole (internal standard, IS) was purchased from Sigma-Aldrich (St. Louis, MO, United States). Concanavalin A (Con A), a reagent for the induction of liver injury in animals, was obtained from Sigma-Aldrich (St. Louis, MO, United States). The dried aerial parts of *R. serra* (voucher specimens NO. IS 20130827) were collected from Guangdong Province and were

identified by Professor Chenchen Zhu, a specialist in Pharmacognosy, who worked at Guangzhou University of Chinese Medicine.

MS-grade formic acid, methanol, and acetonitrile were obtained from Merck Co., Ltd. (Darmstadt, Germany). The other chemical reagents (analytical grade) were purchased from Tianjin Zhiyuan Chemical Reagent Co., Ltd. (Tianjin, China). The ultrapure water was prepared using a Milli-Q water purification system (Bedford, MA, United States).

2.2 Preparation of *Rabdosia serra* Extract

R. serra extract (RSE) was prepared and quality-controlled on the basis of our previous study (Huang et al., 2019). In brief, the herbal samples were crushed and extracted by refluxing with methanol for 2 h. The filtrate was combined and evaporated in vacuum. The concentrated filtrate was partitioned in different solvents; then the crude ethyl acetate (EtOAc) fraction was determined using a Sephadex LH-20 and silica gel column chromatography. The fractions containing diterpenoid components were gathered and collected as RSE used in this study. The contents of enmein, epinodosin, and isodocarpin in RSE extract were analyzed by HPLC at the concentrations of 23.95 , 29.94 , and 112.61 mg/g, respectively (shown in **Supplementary Figure S1**). The dose of RSE was determined based on the dosage conversion coefficient of rats according to our previous study (Zhang et al., 2021), and a dose of 300 mg/kg was applied in this study.

2.3 Animals

Sixteen male Sprague–Dawley (SD) rats (220 ± 20 g) were purchased from the Experimental Animal Center in Guangzhou University of Chinese Medicine [Guangdong, China; license: SYXK (Yue) 2018-0034] and housed in a stable environment (a temperature of 20–24°C, a relative humidity of 50–60%) with a 12 h light–dark cycle. Animal experiments were approved by the Animal Ethics Committee of Guangzhou University of Chinese Medicine (No. 20200201003).

2.4 Pretreatment of Plasma

The plasma sample (100 μl) was mixed with 10 μl of IS (300 ng/ml) and 1 ml of ethyl acetate and then vortexed for 3 min. After centrifugation at 12,000 r/min (4°C) for 15 min, the supernatant was dried under the gentle steam of N_2, and then the residue was dissolved with 100 μl of methanol. Two milliliters of the supernatant were injected into UPLC-MS/MS for analysis.

2.5 Instrumentation and Analytical Conditions

An Agilent 6460 triple quadrupole mass spectrometer (Agilent Technologies, Inc., United States) coupled with an electrospray ionization (ESI) source and an Agilent 1260 Infinity UHPLC system (Agilent Technologies, Inc., United States) was used for sample analysis. A Poroshell 120 EC-C_{18} column (3.0 mm × 50 mm, 2.7 μm) was used for sample separation. The mobile phase consisted of acetonitrile (A) and 0.1% formic acid (B) with the gradient elution program as 20% A–60% A (0–5 min) at a flow rate of 0.4 ml/min. The injection volume was 2 μl, and the column temperature was maintained at 25°C.

The positive ionization mode (ESI+) with multiple reaction monitoring (MRM) of the mass spectrometry detector was used, and the parameters were set as follows: drying gas (N_2) flow rate, 5.1 L/min; drying gas temperature, 300°C; nebulizer pressure, 45.0 psi; capillary voltage, 3370 V; sheath gas temperature, 300°C; sheath gas flow rate, 11.0 ml/min; and nozzle voltage, 0 V.

2.6 Quantitative Method Validation

The quantitative method validation, including specificity, linearity, sensitivity, precision, accuracy, recovery, matrix effect, and stability, was performed according to the Food and Drug Administration of the United States (USFDA) guidelines for the validation of a bioanalytical method. Comparison of the chromatograms of standard-spiked samples (three analytes and IS) with and without blank plasma from six different rats was performed to evaluate the specificity. The calibration curves for enmein, epinodosin, and isodocarpin were established by plotting the ratio of the peak area of each compound to IS (Y-axis) versus the concentrations of the compound (eight concentration levels) in the blank plasma sample (X-axis) using the least square linear regression (weighting factor $1/X^2$). The lower limit of quantification (LLOQ) was defined as the lowest concentration with a signal-to-noise ratio (S/N) of 10:1, and a coefficient of variation of no more than 20% should be acceptable. The intraday and interday precision and accuracy were calculated with six replicates of QC samples (low, middle, and high concentrations) on a single day and three consecutive days repeatedly, and the results were displayed as RSD and RE. Three concentration levels of QC samples (20, 100, and 500 ng/ml for enmein and isodocarpin; 25, 125, and 625 ng/ml for epinodosin) and LLOQ samples used in this part were prepared by spiking standard substances to the blank plasma. The recoveries of the three analytes (at three concentration levels of QC) were calculated by comparing the peak areas acquired from the pre-extraction spiked samples with those obtained from post-extraction spiked samples at the same concentration level. The matrix effect was assessed by comparing the peak areas of the three analytes (at three concentration levels of QC) from post-extraction spiked samples with standard solutions of the corresponding concentrations. Finally, the stability of the three concentration levels of QC samples was evaluated under three storage conditions, including storage at 25°C for 24 h, after three freeze-thaws from −80 to 25°C and at −80°C for 1 month.

2.7 Induction of Liver Injury Rats

The rats were grouped randomly and equally into the Con A-induced liver injury group (model group) and normal group. The rats of the model group were injected Con A (12.5 mg/kg) *via* the cauda vein, while the rats of the normal group were injected phosphate-buffered saline (PBS) instead. Before the pharmacokinetic study, the Con A-induced rats were evaluated to the established liver injury state by biochemical indicators such as the content of AST and ALT and histopathological observation of liver tissues. The concentrations of AST and ALT were measured using a

TABLE 1 | Mass spectrometry parameters of enmein, epinodosin, isodocarpin, and IS.

Analytes	RT (min)	*m/z*	CE	Tube lens
Enmein	2.1	363.0→281.0	17	124
Epinodosin	3.8	363.0→281.0	17	124
Isodocarpin	4.5	347.0→283.1	14	108
IS	2.8	254.0→156.0	27	90

commercial kit (Nanjing Jiancheng Biotechnology and Science, Inc., China) according to the manufacturer's instructions. HE staining was performed to observe the histopathological change of liver tissues used per standard procedure (Liu et al., 2021).

2.8 Pharmacokinetic Study

After injection of Con A or PBS for 8 h, all the rats were orally administrated with RSE at a concentration of 300 mg/kg. The blood samples were collected from the post-orbital venous plexus veins of each rat into centrifuge tubes containing heparin at a time of 5, 15, 30, 60, 90, 120, 150, 180, 240, 300, 480, 720, and 1440 min after a single dose of RSE and then were centrifuged at 3,800 r/min for 10 min to obtain plasma. All samples were frozen at −80°C until analysis.

2.9 Data Analysis

The pharmacokinetic parameters of enmein, epinodosin, and isodocarpin, including the time to reach the maximum drug concentration (T_{max}), the maximum plasma concentration (C_{max}), half-life ($T_{1/2}$), the area under the plasma concentration–time curve (AUC), and mean residence time (MRT), were calculated by DAS software 3.2.8 (Chinese Pharmacological Association, Anhui, China), and the noncompartmental analysis model was befitted to describe the pharmacokinetic parameters of these three analytes. Data were displayed as the mean ± standard error (SE). Statistical analyses of the data were performed by *Dunnett's t*-test using SPSS 26.0 (IBM Company, Chicago), and $p < 0.05$ was considered statistically significant.

3 RESULTS

3.1 Quantitative Method Validation

The results of method validation, including specificity, linearity, precision, accuracy, recovery, and matrix effects, showed that this method met the requirements of biological sample analysis.

3.1.1 Specificity

A UPLC-MS/MS method was established for the determination of enmein, epinodosin, and isodocarpin, for which the precursor/product ion pairs of optimized MRM were used as follows: 363.0→281.0 for enmein and epinodosin, 347.0→283.1 for isodocarpin, and 254.0→156.0 for IS (shown in **Supplementary Figure S2**). The other optimized MRM parameters are listed in **Table 1**. Representative MRM chromatograms of blank plasma, blank plasma spiked with a mixed standard substance, and plasma from the normal rats and liver injury rats after the oral administration of RSE for 2.5 h are shown in **Figure 2**, and the retention time (RT) of the three analytes (enmein, epinodosin, and isodocarpin) is 2.1, 3.8, and 4.5 min, respectively. There was no endogenous interference observed in the blank plasma, which exhibited the specificity of the method.

3.1.2 Linearity and Lower Limit of Quantification

As shown in **Table 2**, the calibration curves presented satisfactory linearity ($R^2 > 0.99$) within the concentration range of 2.45–980 ng/ml for enmein, 3.06–980 ng/ml for epinodosin, and 2.65–1060 ng/ml for isodocarpin. The lower limits of quantification (LLOQs) for enmein, epinodosin, and isodocarpin were 2.45, 3.06, and 2.65 ng/ml, respectively, which were appropriate for the quantitation of the three analytes in the pharmacokinetic study.

3.1.3 Accuracy and Precision

The results of accuracy and precision of the three analytes are displayed in **Table 3**, which exhibited that the interday and intraday accuracy and precision were less than 13.7% for the three analytes in QC levels. The accuracy and precision of the three analytes were acceptable.

3.1.4 Recovery and Matrix Effect

As shown in **Table 4**, the extraction recoveries of enmein, epinodosin, and isodocarpin ranged from 70.1% to 81.8% with RSD less than 10%, while the matrix effects of these were from 100.6% to 103.7% with RSD less than 6%. These results indicated that high extraction recoveries and no obvious matrix effects were observed under the pretreatment method of plasma samples.

3.1.5 Stability

The plasma samples containing the three analytes presented good stability (within ±15% variability limits) under different experimental conditions (**Table 5**).

3.2 Model Evaluation

Before the analysis of pharmacokinetics, the Con A-induced liver injury rats were confirmed to be established successfully through the pharmacological parameters such as AST, ALT, and histological observation of liver tissues. As shown in **Figure 3**, compared with the normal rats, the levels of AST and ALT were significantly increased in the Con A-induced rats. Meanwhile, histological observation of liver tissues indicated that injection of Con A resulted in the development of remarkable liver damage in rats, including hepatocyte necrosis, cellular edema, and inflammatory cell infiltration. These data could prove the successful replication of liver injury rats.

3.3 Pharmacokinetic Parameters

The concentrations of enmein, epinodosin, and isodocarpin were determined by using the validated UPLC-MS/MS method in the plasma samples of normal and liver injury rats after the oral administration of RSE and calculated according to the calibration curves. The drug concentration–time curves were drawn and

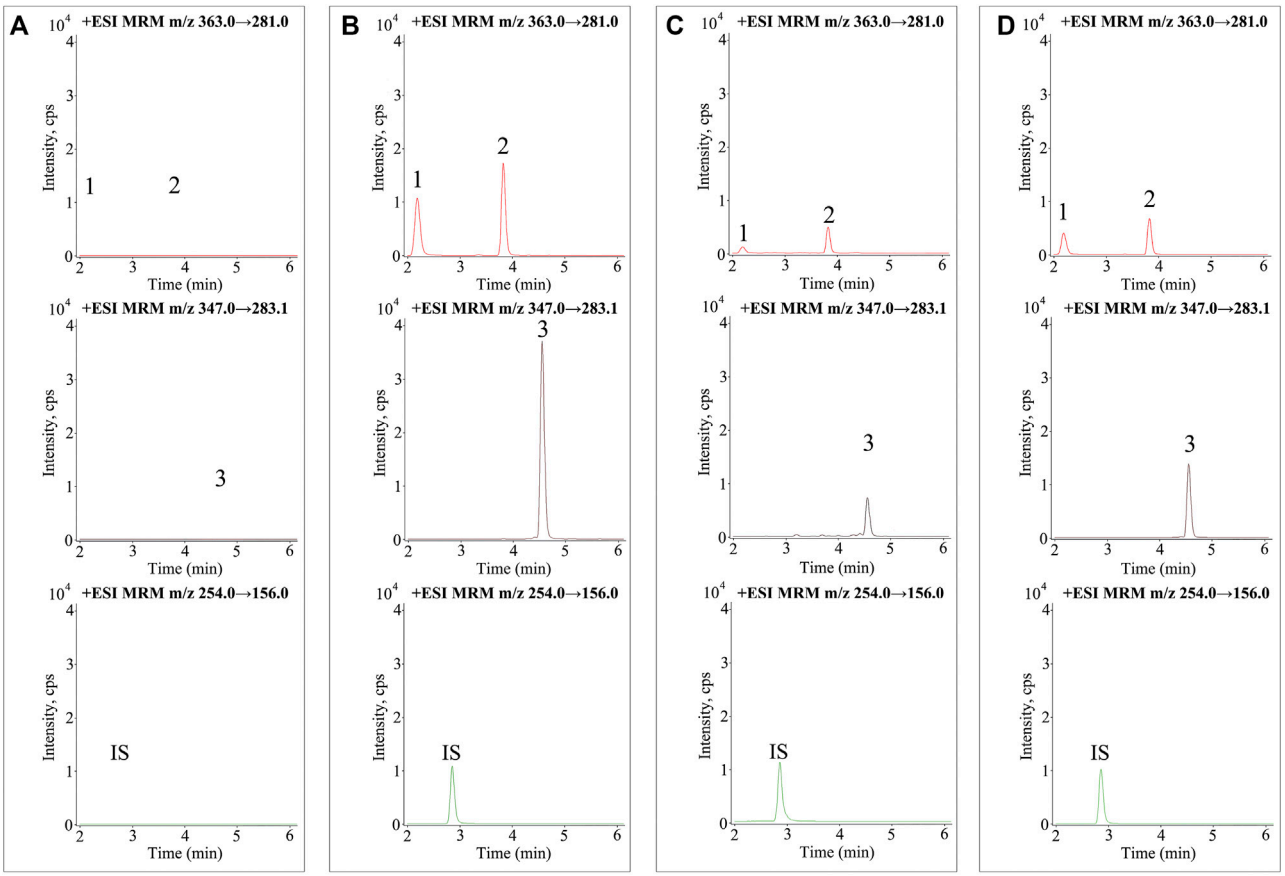

FIGURE 2 | MRM chromatograms of the three analytes and sulfamethoxazole (IS) in **(A)** blank plasma samples, **(B)** blank plasma samples spiked with mixed standards and IS, **(C)** plasma samples obtained from normal rats (2.5 h), and **(D)** plasma samples obtained from liver injury rats (2.5 h). **1**. enmein (RT 2.1 min), **2**. epinodosin (RT 3.8 min), **3**. isodocarpin (RT 4.5 min), and **IS** (RT 2.8 min).

TABLE 2 | Linear equation, correlation coefficients (R^2), linear ranges, and LLOQ of the three analytes.

Analytes	Calibration curve	R^2	Linear range (ng/ml)	LLOQ (ng/ml)
Enmein	y = 1.9259x + 0.0054	0.9996	2.45~980	2.45
Epinodosin	y = 2.045x + 0.0087	0.9998	3.06~980	3.06
Isodocarpin	y = 3.3581x + 0.037	0.9995	2.65~1060	2.65

TABLE 3 | Precision and accuracy of enmein, epinodosin, and isodocarpin in rat plasma (n = 6).

Analytes	Concentration added (ng/ml)	Intraday		Interday	
		Precision (RSD, %)	Accuracy (RE, %)	Precision (RSD, %)	Accuracy (RE, %)
Enmein	20	7.6	5.7	13.7	11.0
	100	8.3	7.2	10.2	7.6
	500	5.5	4.2	7.6	5.4
Epinodosin	25	8.3	6.0	10.9	7.6
	125	3.6	3.3	5.4	4.0
	625	3.9	2.9	5.3	3.2
Isodocarpin	20	6.4	4.9	11.6	9.3
	100	5.6	4.6	8.0	8.2
	500	4.4	3.7	8.3	6.9

TABLE 4 | Recovery and matrix effect of enmein, epinodosin, and isodocarpin in rat plasma (n = 6).

Analytes	Concentration added (ng/ml)	Recovery (%)		Matrix effect	
		Mean ± SD	RSD (%)	Mean ± SD	RSD (%)
Enmein	20	70.1 ± 3.2	5.1	101.0 ± 5.9	5.8
	100	76.3 ± 4.2	6.1	100.6 ± 3.1	3.0
	500	74.8 ± 5.7	9.1	102.2 ± 3.8	3.7
Epinodosin	25	71.3 ± 4.2	6.6	100.6 ± 4.4	4.4
	125	80.6 ± 3.5	4.9	103.4 ± 4.1	4.0
	625	81.2 ± 3.5	4.8	100.7 ± 3.6	3.6
Isodocarpin	20	75.9 ± 4.0	5.8	101.0 ± 3.7	3.6
	100	76.1 ± 4.9	7.2	103.3 ± 5.1	5.0
	500	81.8 ± 4.7	6.4	103.7 ± 4.6	4.5

TABLE 5 | Stability of enmein, epinodosin, and isodocarpin in rat plasma (n = 6).

Compounds (ng/ml)	At 25°C for 24 h		After three freeze-thaw cycles		At –80°C for 30 days	
	Measured conc. (ng/ml)	RSD (%)	Measured conc. (ng/ml)	RSD (%)	Measured conc. (ng/ml)	RSD (%)
Enmein						
20	20.1 ± 0.9	4.4	20.3 ± 1.4	6.8	21.8 ± 1.0	4.6
100	101.4 ± 3.2	3.1	101.5 ± 5.4	5.3	103.1 ± 4.8	4.7
500	503.6 ± 15.2	3.0	501.3 ± 21.4	4.2	510.1 ± 22.1	4.3
Epinodosin						
25	25.7 ± 1.6	6.2	25.3 ± 2.4	9.4	27.0 ± 2.3	8.5
125	125.8 ± 7.4	5.9	126.5 ± 5.4	4.2	128.0 ± 3.2	2.5
625	624.8 ± 23.2	3.7	626.9 ± 25.0	4.0	630.5 ± 35.5	5.6
Isodocarpin						
20	20.5 ± 0.9	4.6	20.5 ± 1.1	5.2	21.3 ± 1.4	6.8
100	102.0 ± 4.5	4.4	102.2 ± 5.1	5.0	105.4 ± 8.7	8.3
500	494.7 ± 23.3	4.7	502.8 ± 11.2	2.2	510.3 ± 30.5	6.0

used to display the concentration change profile of the pharmacokinetic process of these three analytes in normal and liver injury rats, which is shown in **Figure 4**. The pharmacokinetic parameters (**Table 6**) were calculated by DAS 3.2.8 software using a noncompartmental analysis model according to the concentration–time data.

After the oral administration of RSE, enmein, epinodosin, and isodocarpin were absorbed slowly and reached C_{max} (88.2 ± 35.2, 274.9 ± 76.8, and 267.5 ± 78.1 μg/L) in about 2.5, 2, and 3.9 h (T_{max}) in normal rats, respectively, and then were completely eliminated at approximately 24 h. Moreover, the $T_{1/2}$, $MRT_{0-\infty}$, and $AUC_{0-\infty}$ of enmein were 4.1 ± 1.1 h, 4.9 ± 0.9 h, and 437.2 ± 11.8 μg/(h·L) in normal rats, respectively; those of epinodosin were 2.3 ± 0.5 h, 4.9 ± 1.0 h, and 1656.8 ± 78.6 μg/(h·L); and those of isodocarpin were 4.3 ± 1.0 h, 6.5 ± 1.2 h, and 1796.2 ± 182.4 μg/(h·L). These results indicated that the three analytes were sufficiently exposed *in vivo* and retained stable retention rather than being rapidly metabolized and eliminated. The C_{max} of enmein, epinodosin, and isodocarpin were 166.78 ± 29.06, 182.66 ± 10.02, and 276.79 ± 34.55 μg/L, respectively, and T_{max} of them were about 0.5, 1.2, and 2.3 h, respectively, in liver injury rats after the oral administration of RSE, independently, which showed that C_{max} of enmein was significantly higher than that in normal rats, while C_{max} of epinodosin and T_{max} of the three compounds were lower than those in normal rats. In addition, the $T_{1/2}$ of these three analytes in liver injury rats were 0.87 ± 0.27 h, 1.89 ± 0.21 h, and 4.06 ± 0.33 h, and $MRT_{0-\infty}$ were 1.33 ± 0.43 h, 3.21 ± 0.48 h, and 5.01 ± 0.87 h; they were all obviously shorter than those in normal rats. The $AUC_{0-\infty}$ of enmein, epinodosin, and isodocarpin were 597.03 ± 17.28, 1781.59 ± 66.73, and 2664.86 ± 65.54 μg/(h·L), respectively, and these values were higher than those in normal rats. These results suggested that the systemic exposures (C_{max} and AUC) of the three compounds of RSE were increased, and the metabolic and elimination rate (T_{max}, $T_{1/2}$, and MRT) were significantly enhanced during the pathological state of liver injury, which might be related to the inflammation and reduction of activity of liver enzymes in liver injury rats.

4 DISCUSSION

In this study, a rapid and sensitive UPLC-MS/MS method for the quantification of enmein, epinodosin, and isodocarpin in the plasma samples has been developed and validated, and it was successfully applied to the pharmacokinetic study of these three analytes.

Three potential active diterpenoids, enmein, epinodosin, and isodocarpin, were selected as representative components

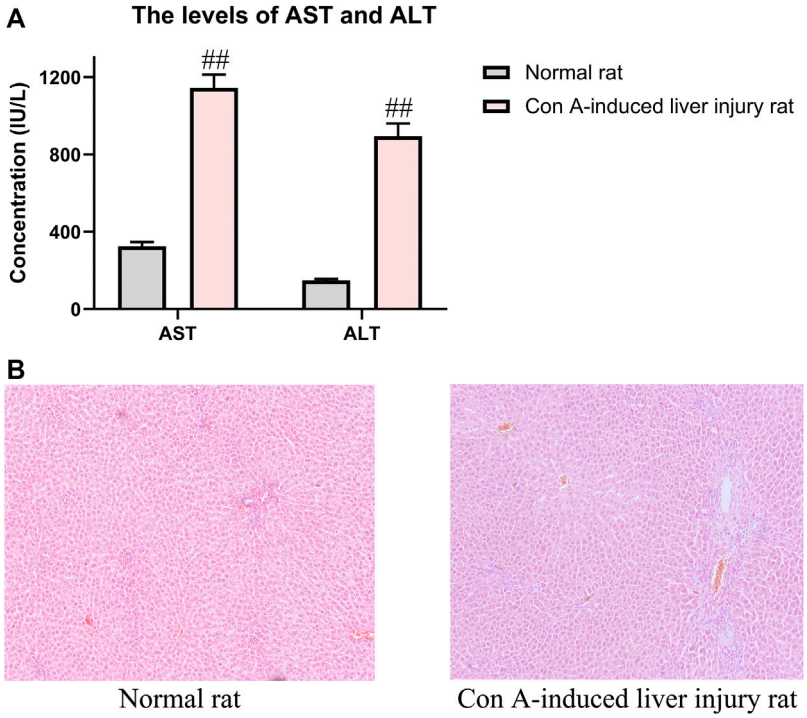

FIGURE 3 | Pharmacological indicators of evaluation of Con A-induced liver injury rats. **(A)** Contents of AST and ALT in normal and liver injury rats. **(B)** Liver histological observation in HE staining of normal and liver injury rats. The data were presented as the mean ± SE (n = 8). ##p < 0.01 compared with normal rats.

to process the pharmacokinetic study of RSE. All the three diterpenoids have the 6, 7-seco-ent-kaurene skeleton, and their structures are similar. Enmein and epinodosin are the isomers of each other, and the difference between their structure is that there is a hydroxyl group connected at different positions which are positioned at C-3 (enmein) and C-11 (epinodosin). In addition, isodocarpin lacks this hydroxyl group that causes them to form isomers (Xie et al., 2022). It would be interesting to study the correlation between their pharmacokinetics and their structural characteristics in this research. In addition, a comparative pharmacokinetic study of these three diterpenoids in the normal and liver injury rats after the oral administration of RSE would be helpful in guiding the application of *R. serra*.

According to the plasma concentration–time curves, three diterpenoids showed double or three peaks in both the normal and liver injury rats after the oral administration of RSE. Three reasons may be taken into account in the multipeak phenomenon in the pharmacokinetics of three diterpenoids (Li et al., 2018). First, drugs are absorbed and metabolized by the liver and gastrointestinal tract; they gradually reached the small intestine with gastrointestinal peristalsis, resulting in drug absorption in sequence and leading to the multipeak phenomenon. Second, it might be caused by enterohepatic circulation. Third, this performance of three diterpenoids might be caused by repeated absorption of them due to the biotransformation from other diterpenoids with the same 6, 7-seco-ent-kaurene skeleton existing in RSE after oral administration, which was considered to be the pharmacokinetic characteristic of herbal medicines.

Our previous study reported that the protective effect of diterpenoids from RSE on H_2O_2-induced liver injury cells was isodocarpin > epinodosin > enmein (Liu et al., 2019). Pharmacokinetic studies showed that the T_{max}, $T_{1/2}$, and MRT of enmein and epinodosin were similar, and those of isodocarpin were longer. Moreover, the C_{max} and AUC of epinodosin and isodocarpin were higher than that of enmein. We thought that it was due to the lipid solubility of epinodosin and isodocarpin, which are linked with or without the hydroxyl group at the C-11 position, and is better than that of enmein, which is linked with the hydroxyl group at the C-3 position, making the former two better to be absorbed into the blood circulation. These results have suggested that the activity of epinodosin and isodocarpin might be superior to that of enmein *in vivo*; it was consistent with our previous results of experiments *in vitro* and the analysis of their 3D quantitative structure–activity relationships (Liu et al., 2019).

Liver injury is a common pathological process that exists in various liver diseases, such as hepatitis, cirrhosis, hepatic fibrosis, trauma, and liver cancer, and it is mainly related to inflammatory response. It is well known that the liver, an important organ for handling the drug metabolism, plays a key role in biotransformation, metabolism, and detoxification of drugs (Marin et al., 2020). The pathological state of liver injury can influence the pharmacokinetic behaviors of drugs (Xia et al., 2021). In this study, the pharmacokinetic characteristics of the

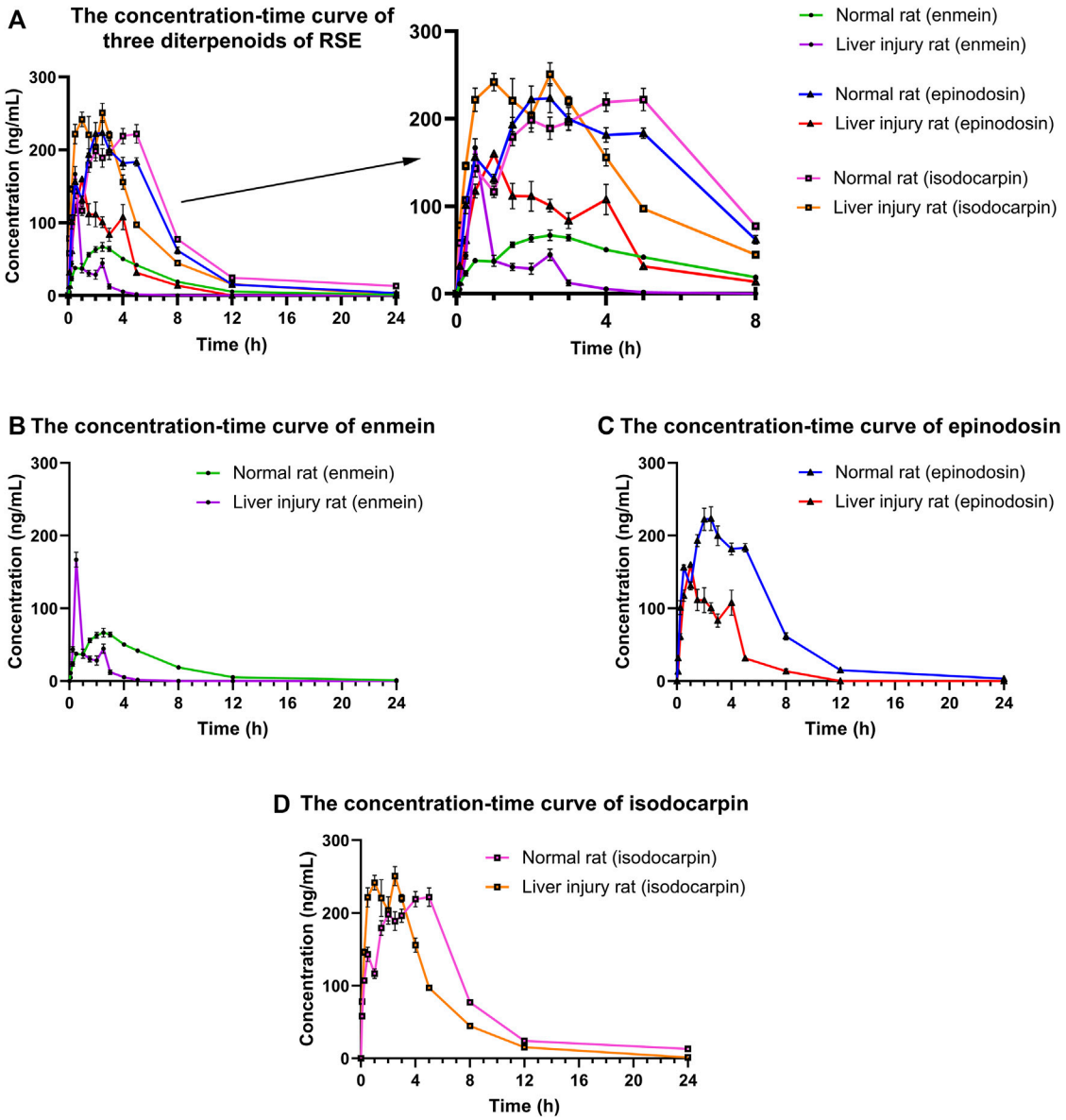

FIGURE 4 | Concentration–time curves of **(A)** three diterpenoids (enmein, epinodosin, and isodocarpin), **(B)** enmein, **(C)** epinodosin, and **(D)** isodocarpin in the plasma of normal and liver injury rats. The data were presented as the mean ± SE (n = 8). The rats were given oral administration of RSE (300 mg/kg), and the plasma samples were collected from post-orbital venous plexus veins at 5, 15, 30, 60, 90, 120, 150, 180, 240, 300, 480, 720, and 1440 min after the dose.

TABLE 6 | Pharmacokinetic parameters of enmein, epinodosin, and isodocarpin in the normal rat and liver injury rat (n = 8).

Pharmacokinetic parameters	Enmein		Epinodosin		Isodocarpin	
	Normal rat	Liver injury rat	Normal rat	Liver injury rat	Normal rat	Liver injury rat
C_{max} (μg/L)	88.2 ± 35.2	166.78 ± 29.06#	274.9 ± 76.8	182.66 ± 10.02#	267.5 ± 78.1	276.79 ± 34.55
T_{max} (h)	2.5 ± 0.4	0.50 ± 0.13#	2.0 ± 0.5	1.20 ± 0.45	3.9 ± 1.4	2.3 ± 0.45#
$T_{1/2}$ (h)	4.1 ± 1.1	0.87 ± 0.27#	2.3 ± 0.5	1.89 ± 0.21	4.3 ± 1.0	4.06 ± 0.33
$MRT_{0-\infty}$ (h)	4.9 ± 0.9	1.33 ± 0.43#	4.9 ± 1.0	3.21 ± 0.48#	6.5 ± 1.2	5.01 ± 0.87
AUC_{0-t} (μg/h/L)	432.7 ± 12.9	516.83 ± 24.11#	1635.3 ± 76.6	1781.49 ± 66.69#	1736.0 ± 125.0	2455.95 ± 52.93#
$AUC_{0-\infty}$ (μg/h/L)	437.2 ± 11.8	597.03 ± 17.28#	1656.8 ± 78.6	1781.59 ± 66.73#	1796.2 ± 182.4	2664.86 ± 65.54#

The data were expressed as mean ± SE. #p < 0.05: Compared with normal rats.

three diterpenoids were remarkably different between normal rats and liver injury rats. Based on the pharmacokinetic results, the C_{max} of enmein and isodocarpin in the liver injury rats were higher than that in normal rats after the oral administration of RS, as well as the AUC of the three analytes, which indicated that the systemic exposure of the three analytes was enhanced under the pathological state of liver injury. In addition, the T_{max}, $T_{1/2}$, and MRT of the three analytes in liver injury rats were evidently lower than those in normal rats, which suggested that the metabolic rate and elimination rate of these compounds in the model rats might be slowed down. It has been reported that liver injury might result in necrosis of liver cells, decreasing CYP450 enzymes activity (Coutant and Hall, 2018), reducing the first-pass effect (Li et al., 2018), disfunction of drug transporters (Jarvinen et al., 2021), increasing intestinal permeability (Lei et al., 2022), and so on, and then alter the fate of drugs in the body. In particular, about 70–80% of drugs are metabolized through CYP450 enzymes. The abovementioned pathological changes of liver injury might be responsible for the increased exposure of the three compounds in model rats. In addition, a lot of drug transporters and metabolic enzymes are distributed in the liver and participated in the disposition and elimination of drugs. The complex changes (upregulation or downregulation) of these transporters and metabolic enzymes in a pathological state of liver injury may affect the metabolic rate of the drug. For example, upregulation of UDP-glucuronosyltransferases (UGTs) and P-glycoprotein (P-gp) could increase the metabolic rate (Tian et al., 2019), which might be one of the reasons for shortening the parameters of T_{max}, $T_{1/2}$, and MRT of the three diterpenoids in liver injury rats. These pathological changes might synthetically result in differences in pharmacokinetic characteristics between the normal and liver injury rats after the oral administration of RSE. Nevertheless, the specific mechanisms are still needed to further investigate and validate.

The development of pharmacokinetic research is conducive to providing a scientific and rational basis for the formulation of drug regimens, and it is also conducive to making more reasonable and accurate predictions of drug toxicity. When formulating a clinical dosing plan, it is necessary to determine the size of the dose and the interval time based on the pharmacokinetics to prevent problems such as drug poisoning due to too many doses or insignificant treatment effects due to too few doses. With regard to the interval between doses, if the interval is too short, it will easily cause the problem of drug accumulation in the patient's body, and if the interval is too long, the drug will not continue to maintain an effective and reasonable blood concentration level in the patient's body and ultimately affect the treatment effect. For example, our pharmacokinetics study can provide us with many pharmacokinetic parameters in different states, such as C_{max}, AUC, MRT, and $T_{1/2}$, and these results indicated that the exposure and elimination rate of enmein, epinodosin, and isodocarpin were increased under liver-injured states. According to the changes of pharmacokinetics characteristics of RSE, including faster elimination and higher exposure in the liver-injured state than in the normal state, we have to consider whether to decrease the dosage and the dosing interval in clinical administration in order to maintain effective concentrations and avoid toxicity due to the drug's accumulation. In addition, the pharmacodynamic effect of RSE is a reflection of the extent of its intervention on liver injury, so the relationship between pharmacokinetics (PK) and pharmacodynamics (PD) should be further studied by the PK-PD model, a mathematical tool for constructing *in vivo* concentration–pharmacodynamics correlations, which could provide insight into the PK-PD relationship of RSE and thus better support to protocol design and dosing decisions when RSE or similar herbal drugs are used clinically for the treatment of liver diseases.

The comparative descriptions of pharmacokinetic characteristics of enmein, epinodosin, and isodocarpin in the normal and liver injury rats were helpful to clarify the intracorporal process of RSE and significant for guiding the clinical and healthcare application of *R. serra*.

5 CONCLUSION

To sum up, a sensitive and rapid method for the simultaneous determination of the three active diterpenoids from RSE in plasma samples was developed with method validation and was applied to their pharmacokinetic study. The distinction of pharmacokinetic behaviors of the representative active ingredients of RSE between the physiological state and pathological state was clarified. Compared with the normal rats, the higher exposure and the rapid rate of elimination of the three compounds of RSE in liver injury rats might be due to the pathologic changes. Our results provide significant information on the pharmacokinetic characteristics of RSE and are expected to be useful for the application of *R. serra*.

DATA AVAILABILITY STATEMENT

The original contributions presented in the study are included in the article/**Supplementary Material**. Further inquiries can be directed to the corresponding authors.

ETHICS STATEMENT

The animal study was reviewed and approved by the Animal Ethics Committee of Guangzhou University of Chinese Medicine.

AUTHOR CONTRIBUTIONS

FL carried out experimental work, analyzed the data, and wrote the manuscript. YZ, PD, KH, KZ, and TT participated in the investigation. CZ and CL contributed to the final preparation of this paper and submission. CZ and CL designed and supervised this research.

FUNDING

This work was supported by the Special project in key areas of ordinary universities of the Department of Education of

Guangdong Province (Grant No. 2021ZDZX2021), the National Natural Science Foundation of China (Grant No. 81673872), and the Guangzhou TCM and Integrated Traditional Chinese and Western Medicine science and technology project (Grant No. 20202A010009).

REFERENCES

Alkharfy, K. M., Ali, F. A., Alkharfy, M. A., Jan, B. L., Raish, M., Alqahtani, S., et al. (2020). Effect of Compromised Liver Function and Acute Kidney Injury on the Pharmacokinetics of Thymoquinone in a Rat Model. *Xenobiotica* 50, 858–862. doi:10.1080/00498254.2020.1745319

Coutant, D. E., and Hall, S. D. (2018). Disease-Drug Interactions in Inflammatory States via Effects on CYP-Mediated Drug Clearance. *J. Clin. Pharmacol.* 58, 849–863. doi:10.1002/jcph.1093

Feng, C.-P., Ding, H.-X., Liu, Y.-X., Di, Q.-F., Liu, Y., Liang, J., et al. (2021). Water-Soluble Total Flavonoids Isolated from Isodon Lophanthoides Var. Gerardianus (Benth.) H. Hara Promote Hepatocellular Carcinoma Sensitivity to 5-Fluorouracil. *Evid. Based Complementary Altern. Med.* 2021, 1–15. doi:10.1155/2021/6623212

Fu, K., Wang, C., Ma, C., Zhou, H., and Li, Y. (2021). The Potential Application of Chinese Medicine in Liver Diseases: A New Opportunity. *Front. Pharmacol.* 12, 771459. doi:10.3389/fphar.2021.771459

Fu, K., Zhou, H., Wang, C., Gong, L., Ma, C., Zhang, Y., et al. (2022). A Review: Pharmacology and Pharmacokinetics of Schisandrin A. *Phytotherapy Res.* 36, 2375–2393. doi:10.1002/ptr.7456

He, G., Lin, X., Wu, S., Wang, B., Xiong, T., and Zhu, C. (2016). The Study of Total Diterpenoids Extracted from Isodon Serra (Maxim.) Hara on Hepatic Mitochondria Protection and Antioxidation Based on Oxidative Stress. *Pharmacol. Clin. Chin. Mater. Med.* 6, 121–126. doi:10.13412/j.cnki.zyyl.2016.06.033

Huang, T., Wu, C., Chen, D.-J., Lin, C.-Z., and Zhu, C.-C. (2019). Simultaneous Quantitative Determination of Five Diterpenoids Contents in Rabdosia Serra by QAMS. *J. Chin. Med. Mater.* 2, 344–347. doi:10.13863/j.issn1001-4454.2019.02.023

Järvinen, E., Deng, F., Kiander, W., Sinokki, A., Kidron, H., and Sjöstedt, N. (2021). The Role of Uptake and Efflux Transporters in the Disposition of Glucuronide and Sulfate Conjugates. *Front. Pharmacol.* 12, 802539. doi:10.3389/fphar.2021.802539

Lei, W., Zhao, C., Sun, J., Jin, Y., and Duan, Z. (2022). Electroacupuncture Ameliorates Intestinal Barrier Destruction in Mice with Bile Duct Ligation-Induced Liver Injury by Activating the Cholinergic Anti-inflammatory Pathway. *Neuromodulation*. doi:10.1016/j.neurom.2022.02.001

Li, Y., Guo, S., Ren, Q., Wei, D., Zhao, M., Su, S., et al. (2018). Pharmacokinetic Comparisons of Multiple Triterpenic Acids from Jujubae Fructus Extract Following Oral Delivery in Normal and Acute Liver Injury Rats. *Int. J. Mol. Sci.* 19, 2047. doi:10.3390/ijms19072047

Lin, C. Z., Zhao, W., Feng, X. L., Liu, F. L., and Zhu, C. C. (2016). Cytotoxic Diterpenoids from Rabdosia Lophanthoides Var. Gerardianus. *Fitoterapia* 109, 14–19. doi:10.1016/j.fitote.2015.11.015

Liu, F., Chaozhan, L., and Chenchen, Z. (2019). Study on Liver-Protective Diterpenoids from Rabdosiae Herba and Their 3D Quantitative Structure-Activity Relationships. *Tradit. Chin. Drug Res. Clin. Pharmacol.* 12, 1409–1415. doi:10.19378/j.issn.1003-9783.2019.12.001

Liu, G. L., Xu, W., Liu, X. J., Yan, X. L., and Chen, J. (2020). Two New Abietane Diterpenoids from the Leaves of Rabdosia Serra. *J. Asian Nat. Prod. Res.* 22, 47–51. doi:10.1080/10286020.2018.1539081

Liu, F., Yao, Y., Lu, Z., Zhang, Q., Liu, C., Zhu, C., et al. (2021). 5-Hydroxy-4-methoxycanthin-6-one Alleviates Dextran Sodium Sulfate-Induced Colitis in Rats via Regulation of Metabolic Profiling and Suppression of NF-κB/p65 Signaling Pathway. *Phytomedicine* 82, 153438. doi:10.1016/j.phymed.2020.153438

Marin, J. J. G., Serrano, M. A., Monte, M. J., Sanchez-Martin, A., Temprano, A. G., Briz, O., et al. (2020). Role of Genetic Variations in the Hepatic Handling of Drugs. *Int. J. Mol. Sci.* 21, 2884. doi:10.3390/ijms21082884

Qian, H., Chao, X., Williams, J., Fulte, S., Li, T., Yang, L., et al. (2021). Autophagy in Liver Diseases: A Review. *Mol. Asp. Med.* 82, 100973. doi:10.1016/j.mam.2021.100973

Shojaie, L., Ali, M., Iorga, A., and Dara, L. (2021). Mechanisms of Immune Checkpoint Inhibitor-Mediated Liver Injury. *Acta Pharm. Sin. B* 11, 3727–3739. doi:10.1016/j.apsb.2021.10.003

Sun, L., Qian, F., Li, Y., and Jia, Q. (2020). Research Progress on Chemical Constituents and Pharmacological Effects of Linearstripe Rabdosia Herb from Variations Origins. *Acad. J. Shanghai Univ. Tradit. Chin. Med.* 34, 88–98. doi:10.16306/j.1008-861x.2020.06.014

Tian, X., Liu, H., Qiao, S., Yin, H., Chen, M., Hu, P., et al. (2019). Exploration of the Hepatoprotective Chemical Base of an Orally Administered Herbal Formulation (YCHT) in Normal and CCl4-Intoxicated Liver Injury Rats. Part 2: Hepatic Disposition *In Vivo* and Hepatoprotective Activity *In Vitro*. *J. Ethnopharmacol.* 236, 161–172. doi:10.1016/j.jep.2019.02.022

Wang, W. Q., and Xuan, L. J. (2016). ent-6,7-Secokaurane Diterpenoids from Rabdosia Serra and Their Cytotoxic Activities. *Phytochemistry* 122, 119–125. doi:10.1016/j.phytochem.2015.11.014

Xia, Y., Yan, M., Wang, P., Hamada, K., Yan, N., Hao, H., et al. (2021). Withaferin A in the Treatment of Liver Diseases: Progress and Pharmacokinetic Insights. *Drug Metab. Dispos.* 50, 685–693. doi:10.1124/dmd.121.000455

Xie, W., Zhang, D., Wen, X., Zhang, Y., Zhang, Z., Jin, Y., et al. (2022). A Practical Technique for Rapid Characterisation of Ent- Kaurane Diterpenoids in Isodon Serra (Maxim.) Hara by UHPLC-Q-TOF-MS/MS. *Phytochem. Anal.* 33, 517–532. doi:10.1002/pca.3106

Xing, H., An, L., Song, Z., Li, S., Wang, H., Wang, C., et al. (2020). Anti-Inflammatory Ent-Kaurane Diterpenoids from Isodon Serra. *J. Nat. Prod.* 83, 2844–2853. doi:10.1021/acs.jnatprod.9b01281

Yang, R., Du, Z., Qiu, T., Sun, J., Shen, Y., and Huang, L. (2021). Discovery and Functional Characterization of a Diverse Diterpene Synthase Family in the Medicinal Herb Isodon Lophanthoides Var. Gerardiana. *Plant Cell Physiol.* 62, 1423–1435. doi:10.1093/pcp/pcab089

Zhang, K., Yao, Y., Wang, M., Liu, F., Wang, Q., Ma, H., et al. (2021). A UPLC-MS/MS-based Metabolomics Analysis of the Pharmacological Mechanisms of Rabdosia Serra against Cholestasis. *Phytomedicine* 91, 153683. doi:10.1016/j.phymed.2021.153683

SUPPLEMENTARY MATERIAL

The Supplementary Material for this article can be found online at: https://www.frontiersin.org/articles/10.3389/fphar.2022.944949/full#supplementary-material

Conflict of Interest: The authors declare that the research was conducted in the absence of any commercial or financial relationships that could be construed as a potential conflict of interest.

Publisher's Note: All claims expressed in this article are solely those of the authors and do not necessarily represent those of their affiliated organizations or those of the publisher, the editors, and the reviewers. Any product that may be evaluated in this article or claim that may be made by its manufacturer is not guaranteed or endorsed by the publisher.

frontiers | Frontiers in Pharmacology

ORIGINAL RESEARCH
published: 19 July 2022
doi: 10.3389/fphar.2022.950525

Evaluation of Herb–Drug Interaction Between Danshen and Rivaroxaban in Rat and Human Liver Microsomes

Xu Wang[1†], Jingjing Fa[1†], Yuanjin Zhang[2†], Shengbo Huang[2], Jie Liu[2], Junqing Gao[1], Lina Xing[1,3], Zongjun Liu[1,3] and Xin Wang[2]**

[1]Department of Cardiology, Putuo Hospital, Shanghai University of Traditional Chinese Medicine, Shanghai, China, [2]Shanghai Key Laboratory of Regulatory Biology, Institute of Biomedical Sciences, School of Life Sciences, East China Normal University, Shanghai, China, [3]Putuo Clinical Medical School, Anhui Medical University, Shanghai, China

OPEN ACCESS

Edited by:
Guo Ma,
Fudan University, China

Reviewed by:
Jiangeng Huang,
Huazhong University of Science and Technology, China
Lan Tang,
Southern Medical University, China

***Correspondence:**
Zongjun Liu
lzj72@126.com
Xin Wang
xwang@bio.ecnu.edu.cn

†These authors have contributed equally to this work

Specialty section:
This article was submitted to Drug Metabolism and Transport, a section of the journal Frontiers in Pharmacology

Received: 23 May 2022
Accepted: 16 June 2022
Published: 19 July 2022

Citation:
Wang X, Fa J, Zhang Y, Huang S, Liu J, Gao J, Xing L, Liu Z and Wang X (2022) Evaluation of Herb–Drug Interaction Between Danshen and Rivaroxaban in Rat and Human Liver Microsomes. Front. Pharmacol. 13:950525. doi: 10.3389/fphar.2022.950525

The combination of *Salvia miltiorrhiza* (Danshen) and rivaroxaban is a promising treatment option in clinical practice in China, but the herb–drug interaction between Danshen and rivaroxaban remains unclear. Therefore, this study aims to reveal the interaction between Danshen and rivaroxaban. We not only investigated the inhibitory properties of Danshen tablet on rivaroxaban metabolism in rat and human liver microsomes but also evaluated the inhibitory effects of Danshen tablet and its eight active components (dihydrotanshinone I, tanshinone I, tanshinone IIA, cryptotanshinone, danshensu, salvianolic acid A, salvianolic acid B, and salvianolic acid C) on cytochrome P450 (CYP) enzymes. The results showed that Danshen tablet potently inhibited the metabolism of rivaroxaban in rat and human liver microsomes. In the CYP inhibition study, we found that dihydrotanshinone I, the active component of Danshen tablet, potently inhibited the activities of rat CYP3A and CYP2J, with IC_{50} values at 13.85 and 6.39 μM, respectively. In further inhibition kinetic study, we found that Danshen tablet is a mixed inhibitor in rivaroxaban metabolism in rat and human liver microsomes, with the K_i value at 0.72 and 0.25 mg/ml, respectively. In conclusion, there is a potential interaction between Danshen tablet and rivaroxaban. Danshen tablet inhibits the metabolism of rivaroxaban, which may be because its lipid-soluble components such as dihydrotanshinone I strongly inhibit the activities of CYP enzymes, especially CYP3A and CYP2J. Therefore, when Danshen tablet and rivaroxaban are used simultaneously in the clinic, it is necessary to strengthen the drug monitoring of rivaroxaban and adjust the dosage.

Keywords: Danshen, rivaroxaban, herb-drug interaction, metabolism, cytochrome P450 (CYP)

Abbreviations: HDI, herb–drug interaction; CYP, cytochrome P450; DOAC, direct oral anticoagulant; ACS, acute coronary syndrome; NVAF, non-valvular atrial fibrillation; HLM, human liver microsomes; RLM, rat liver microsomes; IC_{50}, half-maximal inhibitory concentration; Ki, inhibition constant.

INTRODUCTION

The combination of traditional Chinese and Western medicine can improve drug efficacy and increase patient tolerance. However, the risk of herb–drug interactions (HDI) increases. Inhibition/induction of the drug-metabolizing enzymes is an important reason for the HDI (Li et al., 2019). Cytochrome P450 (CYP) enzymes as the important phase I drug-metabolizing enzymes play an important role in HDI (Li et al., 2019). CYP enzymes are divided into 17 families and many subfamilies, among which CYP1, CYP2, and CYP3 account for about 70% of total CYP (Toselli et al., 2016).

Rivaroxaban, a direct oral anticoagulant (DOAC), inhibits factors Xa, thus preventing the blood clotting cascade and inhibiting thrombosis (Ajmal et al., 2021). Rivaroxaban is used in clinical practice to treat venous thromboembolism after elective hip and knee arthroplasty (Huang et al., 2018). It can also prevent stroke and systemic embolism in patients with non-valvular atrial fibrillation (NVAF) (Desai et al., 2020). In addition, the European Medicines Agency (EMA) has approved rivaroxaban for the prevention of thromboembolic events in patients with acute coronary syndrome (ACS) (Cowie et al., 2020). Rivaroxaban is metabolized by CYP3A4, CYP2J2, and non-enzymatic hydrolysis, and the proportions are about 18, 14, and 14%, respectively (Mueck et al., 2013; Cheong et al., 2017; Wang et al., 2021). It has been reported that ketoconazole significantly inhibits the metabolism of rivaroxaban and increases its exposure *in vivo*, which may be caused by liver CYP inhibition (Foerster et al., 2020).

Danshen tablet is effective for cardiovascular and cerebrovascular diseases and is widely used around the world, especially in China (Zhang et al., 2020). Danshen tablet contains a variety of aqueous soluble and lipid-soluble components. Water-soluble components, such as danshensu and salvianolic acid A and B, have many pharmacological activities, including antioxidant and cytoprotective effects (Wang and Yeung, 2011). Lipid-soluble components, such as tanshinone I, tanshinone IIA, dihydrotanshinone, and cryptotanshinone, possess pharmacological properties such as promoting blood circulation and antibacterial and anti-inflammatory (Wang and Yeung, 2012; Guo et al., 2020). Danshen tablet is characterized by complex composition and complicated mechanism. Its active components can affect the expression level and activity of CYP (Wang et al., 2016; Meng et al., 2021). For example, our previous studies reported that dihydrotanshinone is a non-competitive inhibitor of CYP3A4 (Wang et al., 2010).

As we all know, Danshen and rivaroxaban are always simultaneously used to treat heart disease. However, the interaction between Danshen and rivaroxaban remains unknown. From the perspective of patient safety, we should pay close attention to HDI to formulate a reasonable treatment plan and avoid adverse reactions. In this study, we explored the interaction and mechanism between Danshen tablet and rivaroxaban in rat and human liver microsomes. Clinical practitioners are expected to benefit from these findings.

MATERIALS AND METHODS

Chemicals and Reagents

Dihydrotanshinone I (purity > 97%), tanshinone I (purity > 98%), tanshinone IIA (purity > 98%), cryptotanshinone (purity > 98%), danshensu (purity > 99%), salvianolic acid A (purity > 99%), salvianolic acid B (purity > 99%), salvianolic acid C (purity > 98%), and rivaroxaban (purity > 99%) were purchased from TaoSu Biochemical Technology Co. Ltd. (Shanghai, China). Tris (hydroxymethyl) aminomethane hydrochloride (Tris-HCl), β-nicotinamide adenine dinucleotide phosphate (NADP), glucose 6-phosphate dehydrogenase (G6PDH), glucose 6-phosphate (G6P), phenacetin, bupropion, tolbutamide, dextromethorphan, chlorzoxazone, astemizole, and midazolam were purchased from Sigma Chemical Co. (St. Louis, MO, United States). Mebendazole (internal standard) was obtained from Aladdin Industrial Co. (California, United States). Danshen tablet was purchased from Shanghai Lei Yun Shang Pharmacy Co., Ltd. (Shanghai, China). Pooled rat liver microsomes (RLM) and human liver microsomes (HLM, $n = 25$) were obtained from the Research Institute for Liver Diseases Co., Ltd. (Shanghai, China) and stored at −80°C until use. Methanol and acetonitrile (HPLC grade) were purchased from Fisher Chemicals (Leicester, United Kingdom). Formic acid and ammonium formate (HPLC grade) were purchased from TEDIA Company, Inc. (Ohio, United States).

Equipment and Operating Conditions

In this study, an Agilent 1290 LC system consisting of a binary pump, a degasser, an autosampler, and a thermostatic column compartment was coupled with a 6470 triple-quadrupole mass spectrometer (Agilent Technologies, United States), which was equipped with an Agilent Jet Stream electrospray ionization (ESI) source and operated with Agilent Mass Hunter version 9.0.9037.0 software (Agilent Technologies, United States). Chromatography separation was performed on a Phenomenex Kinetex XB-C18 column (100 × 3.00 mm, 2.6 μM) protected by a Phenomenex C18 guard column (Torrance, CA, United States).

For rivaroxaban analysis, the LC-MS/MS method was implemented as described in the previous reports (Wang et al., 2020; de Oliveira et al., 2021). In brief, the mobile phase consisted of solvent A (1 mM ammonium formate in water) and solvent B (0.1% formic acid in methanol) using gradient elution at a flow rate of 0.3 ml/min. The following stepwise gradient elution program was used: 50% B (0–2 min), 50–70% B (2–6.5 min), and 70–50% B (6.5–8 min). The temperature of the column oven was maintained at 30°C, and the injection volume was 3 μL. The positive ion ESI mode was used to monitor ion transitions of *m/z* 436.1→144.9 for rivaroxaban under multiple reaction monitoring (MRM) analysis. The gas temperature was 250°C, and the gas flow rate was 10 L/min. Other parameters of ion source were as follows: nebulizer gas, 35 psi; sheath gas temperature, 350°C; sheath gas flow, 11 L/min.

For CYP substrate metabolite detection method, the optimal gradient mobile phase included solvent A (0.1% formic acid in water; v/v) and solvent B (0.1% formic acid in acetonitrile; v/v),

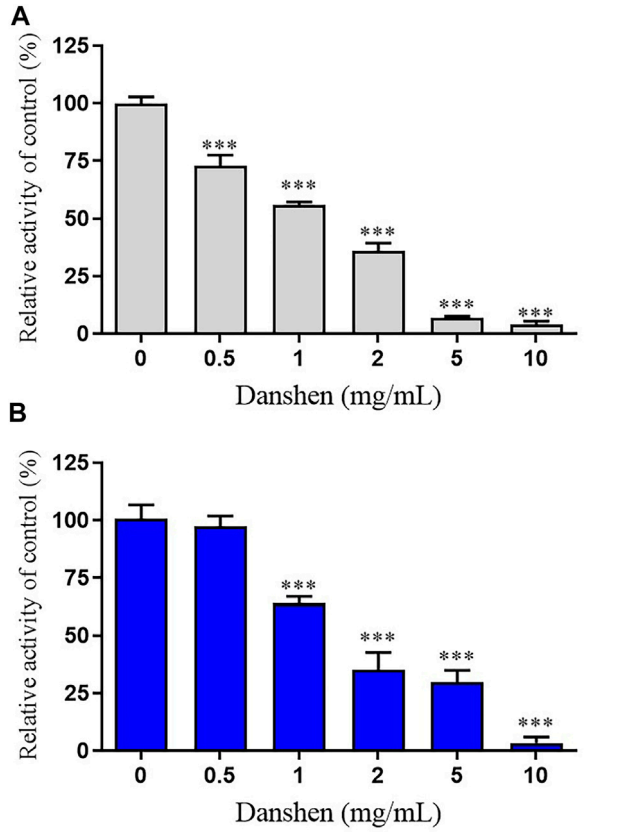

FIGURE 1 | Inhibition of rivaroxaban metabolism by Danshen tablet in rat liver microsomes (RLM) **(A)** and human liver microsomes (HLM) **(B)**. Results were mean ± SD of quadruplicate determinations. ***$p < 0.001$ compared to control (no inhibitor).

with a flow rate of 0.3 mL/min. The best elution condition was as follows: 10% B (0–2.2 min); 10–90% B (2.2–8.5 min); 90–92% B (8.5–9 min); 92% B (9–9.3 min); 92–10% B (9.3–9.6 min); 10% B (9.6–11.5 min). The temperature of the column oven was kept at 30°C. In an ESI mode, simultaneous scanning of positive and negative ions was performed by polar switching. Ions were detected under the multiple reaction monitoring (MRM) mode. The gas temperature was 250°C, and the gas flow rate was 10 L/min. Other parameters of ion source were nebulizer gas, 35 psi; sheath gas temperature, 350°C; sheath gas flow, 11 L/min. LC-MS/MS analysis for all analytes has been introduced in our previous method and validation (Chen et al., 2016; Tang et al., 2017).

Determination of Danshen–Rivaroxaban Interaction in RLM and HLM

The incubation system (200 μL) consisted of 0.05 mM Tris-HCl buffer (pH 7.4), RLM (1 mg/mL) or HLM (0.5 mg/mL), an NADPH-regenerating system including $MgCl_2$ (5 mM), G6P (10 mM), G6PDH (0.4 U/mL), and NADP (1 mM), and rivaroxaban (20 μM). To determine the half-maximal inhibitory concentration (IC_{50}), the concentration of Danshen

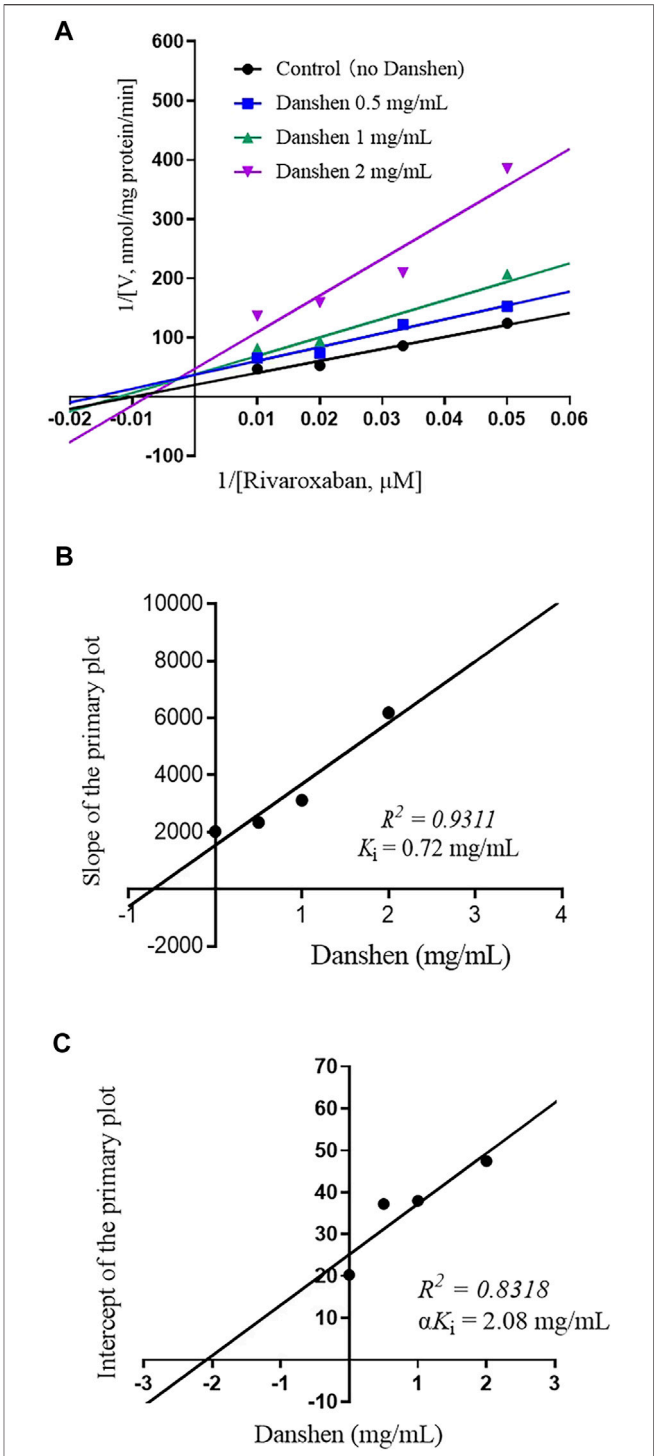

FIGURE 2 | Primary Lineweaver–Burk plot **(A)**, the secondary plot for K_i **(B)**, and the secondary plot for αK_i **(C)** for the inhibition of rivaroxaban metabolism by Danshen tablet with various concentrations (0.5, 1, and 2 mg/mL) in RLM. Rivaroxaban was used at 20, 30, 50, and 100 μM. Each data point represents the mean of quadruplicate determinations.

tablet was set at 0.5, 1, 2, 5, and 10 mg/mL. To investigate whether the inhibition effects by Danshen tablet are time- and/or concentration-independent, the IC_{50} shift experiments

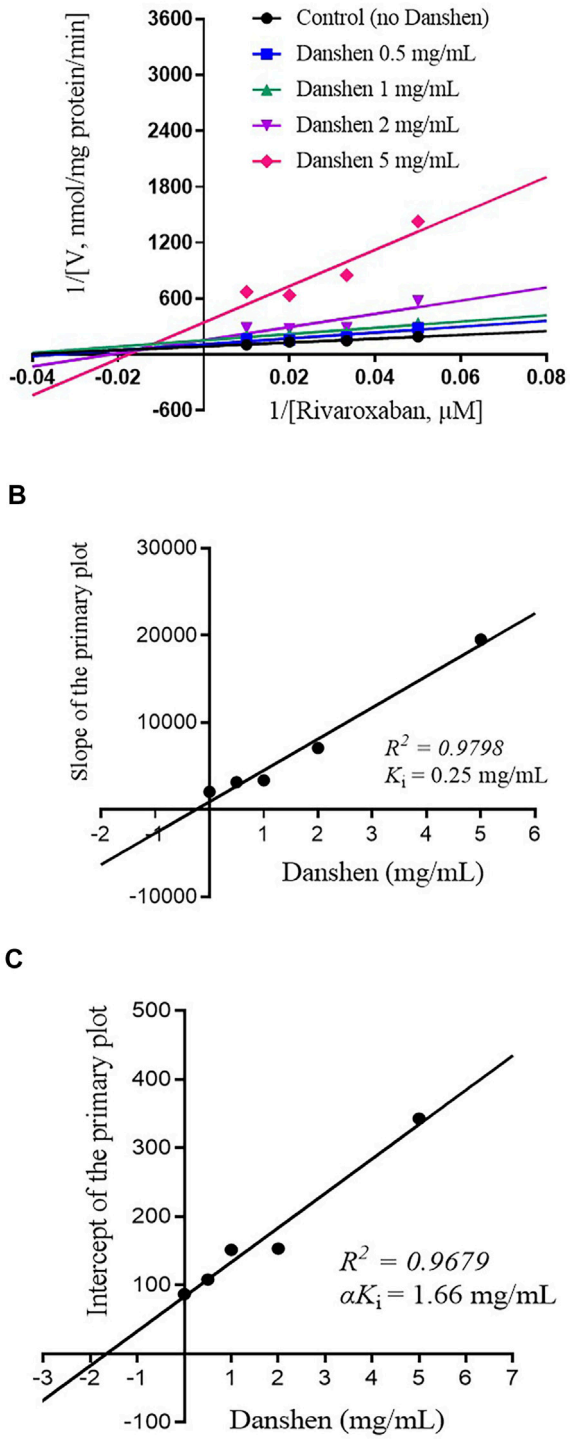

FIGURE 3 | Primary Lineweaver–Burk plot **(A)**, the secondary plot for K_i **(B)**, and the secondary plot for αK_i **(C)** for the inhibition of rivaroxaban metabolism by Danshen tablet with various concentrations (0.5, 1, 2, and 5 mg/mL) in HLM. Rivaroxaban was used at 20, 30, 50, and 100 μM. Each data point represents the mean of quadruplicate determinations.

containing RLM (1 mg/mL) or HLM (0.5 mg/mL), $MgCl_2$ (5 mM), G6P (10 mM), G6PDH (0.4 U/mL), and 0.05 M Tris/HCl buffer (pH 7.4) with Danshen (0.5–10 mg/mL) were carried out under three different conditions: 0 min pre-incubation, 20 min pre-incubation plus NADPH, and 20 min pre-incubation minus NADPH.

To determine the mechanism underlying the inhibitory effect of Danshen tablet on rivaroxaban, the concentrations of Danshen tablet were set at 0.5, 1, 2, and 5 mg/mL and the concentration of rivaroxaban was set at 20, 30, 50, and 100 μM (according to the corresponding K_m value). Then, 1 mM of NADP was added to initiate the reaction. After incubation for 60 min, the reaction was immediately terminated by adding 200 μL ice-cold acetonitrile and 20 μL mebendazole (2 μg/mL), an internal standard, to the mixture. After vortexing for 3 min and centrifugation at 16,000 *g* for 15 min, the supernatant (80 μL) was transferred into the autosampler vial, and 2 μL was used for LC-MS/MS analysis.

Inhibitory Effects of Danshen and Its Active Constituents on CYP1A2, CYP2B1, CYP2C11, CYP2D1, CYP2E1, CYP2J3, and CYP3A2 Activities in RLM

The incubation system (200 μL) consisted of 0.05 mM of Tris-HCl buffer (pH 7.4), pooled RLM (1 mg/mL), with Danshen tablet (2 mg/mL) or its main active ingredients (dihydrotanshinone I, tanshinone I, tanshinone IIA, cryptotanshinone, danshensu, salvianolic acid A, salvianolic acid B, and salvianolic acid C, 20 μM) and an NADPH-regenerating system. Substrates were added to the incubation mixture to obtain the final concentrations (10 μM phenacetin for CYP1A2, 20 μM bupropion for CYP2B1, 20 μM tolbutamide for CYP2C11, 5 μM dextromethorphan for CYP2D1, 20 μM chlorzoxazone for CYP2E1, 150 μM astemizole for CYP2J3, and 10 μM midazolam for CYP3A2). The proportion of the organic solvent was not higher than 1% (v/v) in the incubation mixture. Based on FDA guidelines, the CYP inhibition method was validated with positive inhibitors, and the results confirmed the effectiveness and reliability of the method. To determine the IC_{50} values, the concentration of Danshen tablet was set at 0.1–10 mg/mL, and the concentration of dihydrotanshinone I ranged from 0.5 to 50 μM. The mixture without NADP was pre-incubated at 37°C for 5 min. Then, 1 mM of NADP was added to initiate the reaction. After incubation for 20 min, the reaction was immediately terminated by adding 200 μL ice-cold acetonitrile and 20 μL mebendazole (2 μg/mL). The following processing steps are the same as the abovementioned experiments.

Statistical Analysis

All data were presented as mean ± SD. The IC_{50} values were determined by a nonlinear regression analysis of plotting relative

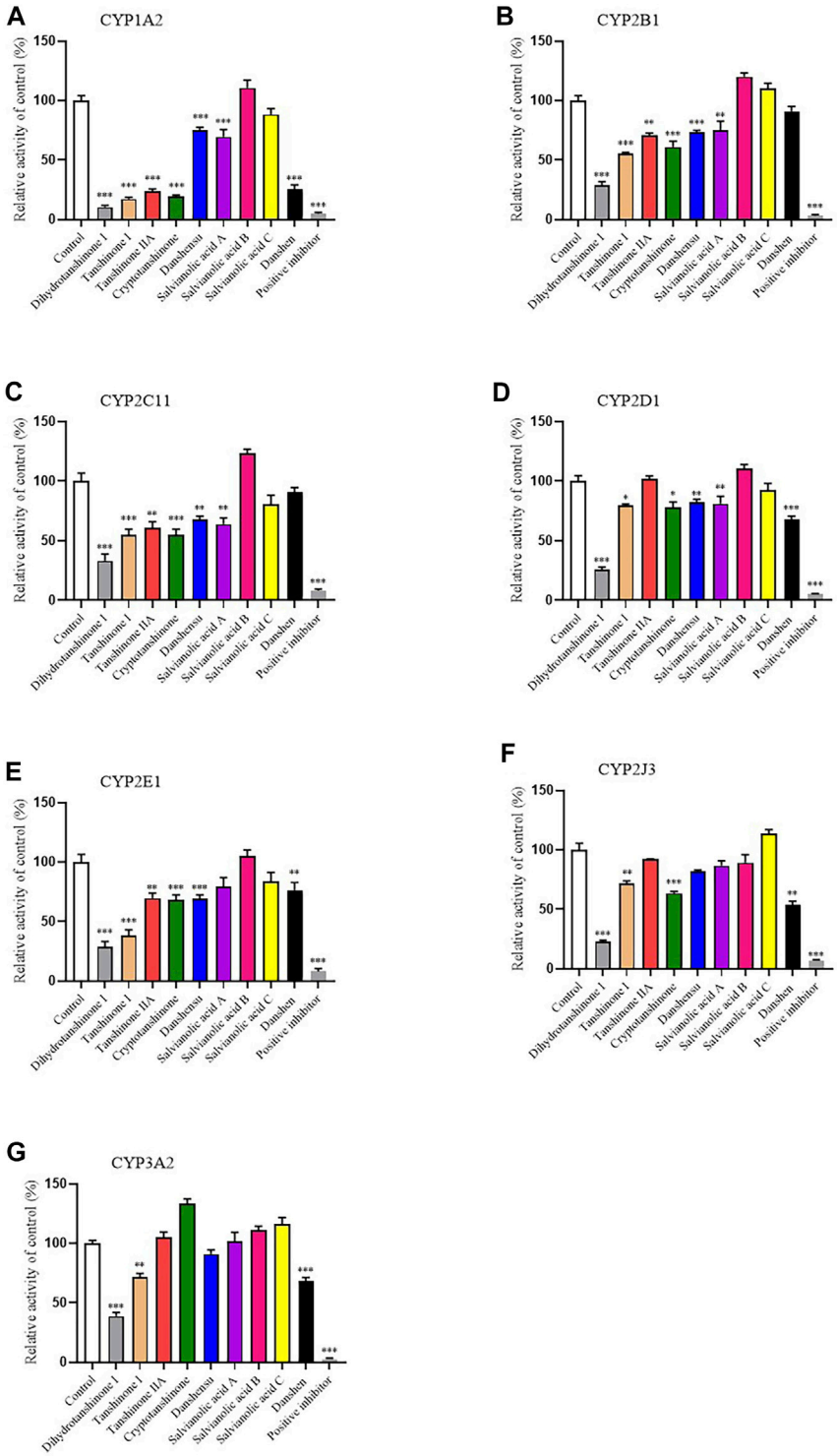

FIGURE 4 | Inhibitory effects of eight active components of Danshen (dihydrotanshinone I, tanshinone I, tanshinone IIA, cryptotanshinone, danshensu, salvianolic acid A, salvianolic acid B, and salvianolic acid C, 20 μM) and Danshen tablet (2 mg/ml) on activities of CYP1A2 **(A)**, CYP2B1 **(B)**, CYP2C11 **(C)**, CYP2D1 **(D)**, CYP2E1 **(E)**, CYP2J3 **(F)**, and CYP3A2 **(G)** in RLM. Positive inhibitors included furafylline (CYP1A2), thiotepa (CYP2B1), sulfaphenazole (CYP2C11), quinidine (CYP2D1), disulfiram (CYP2E1), flunarizine (CYP2J3), and ketoconazole (CYP3A2). Values are presented as mean ± SD (n = 4). *p < 0.05, **p < 0.01, and ***p < 0.001 compared to control (no inhibitor).

activities over the logarithm of inhibitor concentrations. Enzyme kinetics data were fitted with nonlinear regression analysis using GraphPad Prism 8.0 (GraphPad Software Inc., CA, United States). The data were fitted to the Michaelis–Menten model and further analyzed by using the Lineweaver–Burk plot (the reciprocal of reaction velocities versus the reciprocal of substrates concentrations). The Lineweaver–Burk plot was used to determine the quality of fit to a specific inhibition model. The inhibition constant (K_i) was obtained by a secondary plot using the slopes of the primary Lineweaver–Burk plot (K_m/V_{max} versus inhibitor concentration). The αK_i was obtained from a secondary plot using the y-intercepts of the Lineweaver–Burk plot ($1/V_{max}$ versus inhibitor concentration). All results were analyzed in quadruplicate. One-way analysis of variance was used to estimate the significance of differences. Statistical significance was set at $p < 0.05$.

RESULTS

Inhibitory Effect and Type of Danshen Tablet on Rivaroxaban Metabolism in RLM and HLM

Danshen tablet inhibited the rivaroxaban metabolism in a concentration-dependent manner (**Figure 1**). The IC_{50} value was further calculated, which showed that it was 1.16 and 1.85 mg/mL in RLM and HLM, respectively. To characterize the reversible or irreversible inhibition by Danshen tablet, the time- and concentration-independent experiments were used to determine whether it was both time-dependent and concentration-dependent. In the IC_{50} shift profiles, no significant changes in IC_{50} values were observed, thus suggesting Danshen tablet was a reversible inhibitor in RLM and HLM.

To further investigate the inhibitory mode of Danshen tablet, enzyme inhibition kinetic experiments were carried out with different concentrations of rivaroxaban (**Figures 2A**, **3A**). The K_i values were determined by using the secondary Lineweaver–Burk plot and then calculated at 0.72 and 0.25 mg/mL in RLM (**Figure 2B**) and HLM (**Figure 3B**), respectively. From the secondary plot of Lineweaver–Burk plot for αK_i, αK_i values were 2.08 and 1.66 mg/mL in RLM (**Figure 2C**) and HLM (**Figure 3C**), respectively. Since α values (2.89 in RLM and 6.64 in HLM) were not equal to 1, the type of inhibition for Danshen tablet was mixed inhibition.

Inhibitory Effects of Danshen Tablet and Its Active Components on CYP Activities in RLM

In order to study the effects of Danshen tablet and its main components on the activities of important CYP subtypes, we chose medium-concentration of Danshen tablets (2 mg/mL) and its main active ingredients (20 μM) to carry out the screening assay. The data showed that Danshen tablet had inhibitory effects on CYP1A2, CYP2D1, CYP2E1, CYP2J3, and CYP3A2 (**Figure 4**). Lipid-soluble components, such as tanshinone I, tanshinone IIA, dihydrotanshinone I, and cryptotanshinone, generally have stronger inhibitory effects on CYP enzymes than aqueous soluble components, such as danshensu and salvianolic acid A, B, and C. Among all components, dihydrotanshinone I showed the strongest inhibition on all CYP subtypes (**Figure 4**), indicating that it is the main component inhibiting CYP enzyme activity in Danshen tablet.

Since CYP3A4 and CYP2J2 are the main CYP enzymes mediating rivaroxaban metabolism in humans (Cheong et al., 2017; Wang et al., 2021), we further detected the value of IC_{50} values of Danshen tablet and dihydrotanshinone I on CYP3A2 and CYP2J3 in RLM. The results indicated that Danshen tablet inhibited CYP3A2 and CYP2J3 activities in a concentration-dependent manner, with IC_{50} values of 2.37 and 1.95 mg/mL, respectively (**Figure 5**). In addition, dihydrotanshinone I had a strong inhibitory effect on

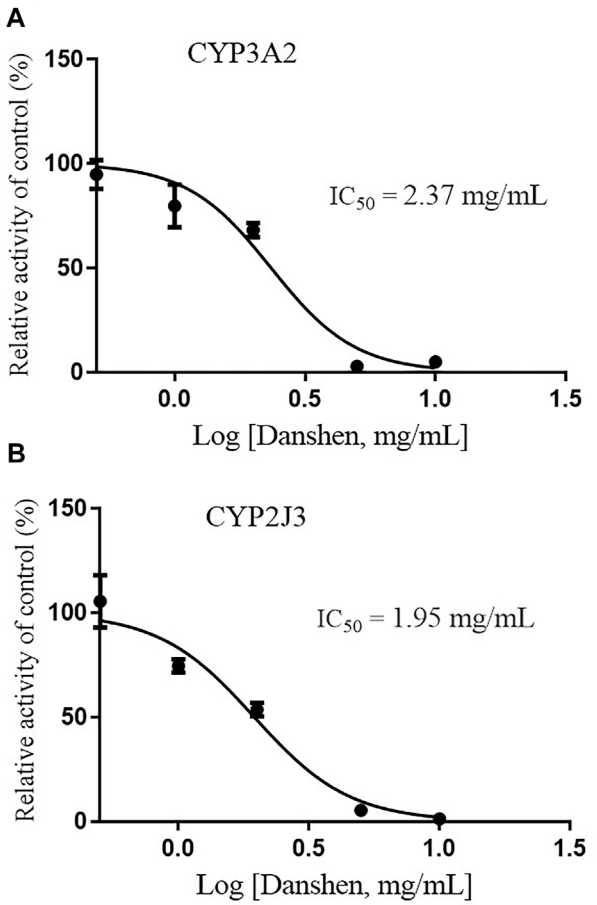

FIGURE 5 | Inhibition of CYP3A2 **(A)** and CYP2J3 **(B)** activities by Danshen tablet (0.5–10 mg/mL) in RLM. Values are expressed as mean ± SD of quadruplicate assays. The data were fit to log (Danshen concentration) and normalized response equations using GraphPad Prism 8.0.

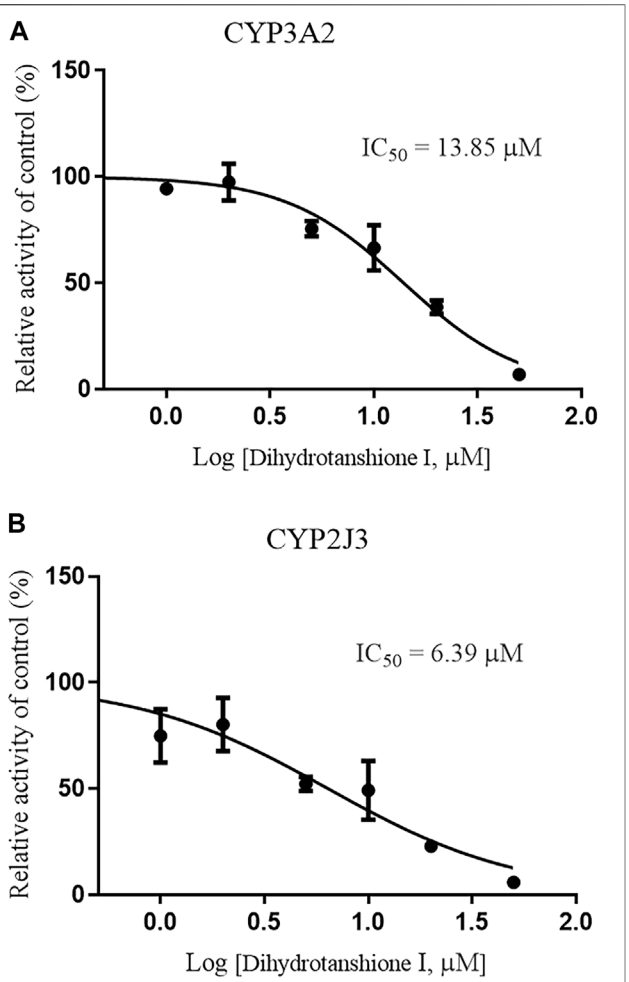

FIGURE 6 | Inhibition of CYP3A2 **(A)** and CYP2J3 **(B)** activities by dihydrotanshione I (1–50 μM) in RLM. Values are expressed as mean ± SD of quadruplicate assays. The data were fit to log (dihydrotanshione I concentration) and normalized response equations using GraphPad Prism 8.0.

CYP3A2 and CYP2J3 activities, with IC_{50} values of 13.85 and 6.39 μM, respectively (**Figure 6**).

DISCUSSION

Cardiovascular disease (CVD) is the leading cause of morbidity and mortality around the world (Zeng et al., 2022). Cardiac arrhythmias are the abnormalities of heartbeat. Atrial fibrillation (AF) is the most common cardiac rhythm disorder in hospitals, accounting for one-third of arrhythmia-related hospitalizations (Chen et al., 2019). Non-valvular AF (NVAF) is the most common form of AF with severe complications (Chen et al., 2019). Oral anticoagulants (OAC) reduce the risk of stroke and death caused by NVAF (Chen et al., 2019). OAC includes vitamin K antagonists (VKA) and non-VKA oral anticoagulants (NOAC), which inhibit activating factor Xa or thrombin (Chen et al., 2019; Purrucker et al., 2020). Factor Xa plays an important role in both intrinsic and extrinsic coagulation pathways as it leads to thrombin activation (Chen et al., 2019). The current guidelines of the European Heart Rhythm Association (EHRA) suggest that NOAC is not recommended in combination with drugs that are strong inhibitors of CYP3A4. Inhibition of CYP3A4 may affect the excretion and metabolism of NOAC, resulting in an increased risk of massive bleeding admission (Steffel et al., 2018).

Rivaroxaban, as a small-molecule inhibitor of factor Xa, can reduce the risk of recurrence of cardiovascular events. It contributes to the treatment of cardiovascular diseases, especially ACS and AF (Chen et al., 2019). Rivaroxaban combined with verapamil (inhibitor of CYP3A4 and P-gp) may be unsafe and lead to CRNM bleeding (Sychev et al., 2020). Traditional Chinese medicine (TCM) is used to prevent and treat CVD, and Danshen is a golden herbal medicine in the treatment of CVD (Wang L. et al., 2017; Li et al., 2018). Clinical studies have found that more than one-third of patients with cardiovascular disease have taken both drugs and herbs in the past 12 months (Yeh et al., 2006). Due to the diversity and complexity of herbal components and the lack of understanding of the pharmacokinetics of pathogenic components, the mechanism of interaction between herbal medicine and drugs is still unknown to a large extent. Therefore, it is necessary to further evaluate the HDI between herbs and anticoagulants in NVAF patients, especially drug-metabolizing enzymes involved. Based on the interaction mediated by CYP enzymes, this study investigated the potential interaction between Danshen tablet and rivaroxaban, which may be related to the side effects of rivaroxaban. Our results showed that Danshen tablet had a strong inhibitory effect on rivaroxaban metabolism in human and rat liver microsomes. Further inhibition kinetic study showed that the Danshen tablet was a mixed inhibitor with K_i values at 0.72 and 0.25 mg/mL in rat and human liver microsome, respectively. These data directly show that there is an interaction between Danshen tablet and rivaroxaban, and Danshen tablet inhibits rivaroxaban metabolism.

As the most important phase I drug metabolism enzyme, CYP is involved in catalyzing the metabolism of most clinical drugs (Li et al., 2019). In humans, the main CYP subtypes include CYP1A2, CYP2B6, CYP2C9, CYP2D6, CYP2E1, CYP2J2, and CYP3A4 (Tang et al., 2017). These subtypes participate in the metabolism of more than 90% of prescription drugs and play an important role in clinical practice (Ouyang et al., 2019). Inhibition or induction of CYP enzyme activity is the main cause of drug–drug or herb–drug interactions (Chen et al., 2016). Therefore, we carried out the CYP activity screening experiments on Danshen tablet and its eight main pharmacological active components. The results showed that Danshen tablet and its lipid-soluble components, such as tanshinone I, tanshinone IIA, and dihydrotanshinone I had potently inhibitory effects on CYP1A2, CYP2B1, CYP2C11, CYP2E1, CYP2J3, and CYP3A2. Our results are consistent with the data reported in previous studies. For example, tanshinone I, and tanshinone IIA are competitive inhibitors of CYP1A2, CYP2C9, and CYP2E1, but the inhibition of CYP3A4 is weak

(Wang et al., 2010). Dihydrotanshinone potently inhibits CYP1A2, CYP2C9, and CYP3A4 in human liver (Wang et al., 2010).

CYP3A4 is the most important human drug-metabolizing enzyme involved in drug metabolism (Sun et al., 2015; Li et al., 2019). At the same time, CYP3A4 is also an enzyme that maintains the homeostasis of endogenous substances (Qin and Wang, 2019). For example, CYP3A regulates bile acid (BA) homeostasis in rats and prevents hepatotoxicity caused by BA overload (Qin et al., 2021). CYP2J2 is a major cardiac CYP enzyme, which mainly metabolizes polyunsaturated fatty acids (Das et al., 2020). CYP2J2 plays an important role in CVD (Azevedo et al., 2016). For example, CYP2J2 transgenic mice have a reduced rate of arrhythmia induction (Westphal et al., 2013). Our previous study also found that knockout of CYP2J3/10 in rats led to heart disease (Lu et al., 2020). In addition, CYP2J2*7 allele has been reported to be associated with stroke and CVD (Wang SY. et al., 2017). It is worth noting that human CYP3A4 and CYP2J2 are the main enzymes involved in rivaroxaban metabolism (Cheong et al., 2017; Wang et al., 2021). Our results show that Danshen tablet and tanshinones, especially dihydrotanshinone I, can effectively inhibit the activities of CYP3A and CYP2J enzymes. Therefore, the interaction between Danshen and rivaroxaban probably occurs because Danshen and its tanshinones inhibit CYP3A and CYP2J activities and then inhibit the metabolism of rivaroxaban. Further *in vivo* experiments such as pharmacodynamics and pharmacokinetics (PD-PK) of Danshen and rivaroxaban are needed to study the interactions between Danshen and rivaroxaban and substantiate their internal mechanism.

In conclusion, the combination of Danshen tablet and rivaroxaban may have potential risks. Danshen and tanshinones may inhibit the metabolism of rivaroxaban by inhibiting CYP3A and CYP2J activities. In the follow-up study, the pharmacokinetics and pharmacodynamics of Danshen and rivaroxaban need to be tested *in vivo*, and more rigorous clinical trials in humans should be considered to verify this finding.

DATA AVAILABILITY STATEMENT

The original contributions presented in the study are included in the article/Supplementary Material; further inquiries can be directed to the corresponding authors.

AUTHOR CONTRIBUTIONS

ZL and XIW designed and supervised the experiments. XUW performed the experiments and collected data. JF and YZ analyzed the data. SH, JL, and JG provided technical support and constructive suggestions. XUW and JF drafted the manuscript. LX, ZL, and XIW reviewed and revised the manuscript.

FUNDING

This work was supported by the Shanghai Key Medical Specialties Construction Project (ZK 2019A11) and the Clinical Advantage Discipline of Health System of Putuo District in Shanghai (2019YSXK01).

REFERENCES

Ajmal, M., Friedman, J., Sipra, Q. U. A. R., and Lassar, T. (2021). Rivaroxaban: Expanded Role in Cardiovascular Disease Management-A Literature Review. *Cardiovas Ther.* 2021, 8886210. doi:10.1155/2021/8886210

Azevedo, P. S., Polegato, B. F., Minicucci, M. F., Paiva, S. A., and Zornoff, L. A. (2016). Cardiac Remodeling: Concepts, Clinical Impact, Pathophysiological Mechanisms and Pharmacologic Treatment. *Arq. Bras. Cardiol.* 106 (1), 62–69. doi:10.5935/abc.20160005

Chen, A., Zhou, X., Tang, S., Liu, M., and Wang, X. (2016). Evaluation of the Inhibition Potential of Plumbagin against Cytochrome P450 Using LC-MS/MS and Cocktail Approach. *Sci. Rep.* 6, 28482. doi:10.1038/srep28482

Chen, Y. L., Lin, Y. S., Wang, H. T., Liu, W. H., Chen, H. C., and Chen, M. C. (2019). Clinical Outcomes of Solitary Atrial Flutter Patients Using Anticoagulation Therapy: a National Cohort Study. *Europace* 21 (2), 313–321. doi:10.1093/europace/euy181

Cheong, E. J., Goh, J. J., Hong, Y., Venkatesan, G., Liu, Y., Chiu, G. N., et al. (2017). Application of Static Modeling --in the Prediction of *In Vivo* Drug-Drug Interactions between Rivaroxaban and Antiarrhythmic Agents Based on *In Vitro* Inhibition Studies. *Drug Metab. Dispos.* 45 (3), 260–268. doi:10.1124/dmd.116.073890

Cowie, M. R., Lamy, A., Levy, P., Mealing, S., Millier, A., Mernagh, P., et al. (2020). Health Economic Evaluation of Rivaroxaban in the Treatment of Patients with Chronic Coronary Artery Disease or Peripheral Artery Disease. *Cardiovasc Res.* 116 (11), 1918–1924. doi:10.1093/cvr/cvz278

Das, A., Weigle, A. T., Arnold, W. R., Kim, J. S., Carnevale, L. N., and Huff, H. C. (2020). CYP2J2 Molecular Recognition: a New axis for Therapeutic Design. *Pharmacol. Ther.* 215, 107601. doi:10.1016/j.pharmthera.2020.107601

de Oliveira, A. C., Davanço, M. G., de Campos, D. R., Sanches, P. H. G., Cirino, J. P. G., Carvalho, P. O., et al. (2021). Sensitive LC-MS/MS Method for Quantification of Rivaroxaban in Plasma: Application to Pharmacokinetic Studies. *Biomed. Chromatogr.* 35 (9), e5147. doi:10.1002/bmc.5147

Desai, R., Koipallil, G. K., Thomas, N., Mhaskar, R., Visweshwar, N., Laber, D., et al. (2020). Efficacy and Safety of Direct Oral Anticoagulants for Secondary Prevention of Cancer Associated Thrombosis: a Meta-Analysis of Randomized Controlled Trials. *Sci. Rep.* 10 (1), 18945. doi:10.1038/s41598-020-75863-3

Foerster, K. I., Hermann, S., Mikus, G., and Haefeli, W. E. (2020). Drug-Drug Interactions with Direct Oral Anticoagulants. *Clin. Pharmacokinet.* 59 (8), 967–980. doi:10.1007/s40262-020-00879-x

Guo, R., Li, L., Su, J., Li, S., Duncan, S. E., Liu, Z., et al. (2020). Pharmacological Activity and Mechanism of Tanshinone IIA in Related Diseases. *Drug Des. Devel Ther.* 14, 4735–4748. doi:10.2147/DDDT.S266911

Huang, H. Y., Lin, S. Y., Cheng, S. H., and Wang, C. C. (2018). Effectiveness and Safety of Different Rivaroxaban Dosage Regimens in Patients with Non-valvular Atrial Fibrillation: a Nationwide, Population-Based Cohort Study. *Sci. Rep.* 8 (1), 1–9. doi:10.1038/s41598-018-21884-y

Li, Y., Meng, Q., Yang, M., Liu, D., Hou, X., Tang, L., et al. (2019). Current Trends in Drug Metabolism and Pharmacokinetics. *Acta Pharm. Sin. B* 9 (6), 1113–1144. doi:10.1016/j.apsb.2019.10.001

Li, Z. M., Xu, S. W., and Liu, P. Q. (2018). Salvia miltiorrhizaBurge (Danshen): a Golden Herbal Medicine in Cardiovascular Therapeutics. *Acta Pharmacol. Sin.* 39 (5), 802–824. doi:10.1038/aps.2017.193

Lu, J., Chen, A., Ma, X., Shang, X., Zhang, Y., Guo, Y., et al. (2020). Generation and Characterization of Cytochrome P450 2J3/10 CRISPR/Cas9 Knockout Rat Model. *Drug Metab. Dispos.* 48 (11), 1129–1136. doi:10.1124/dmd.120.000114

Meng, L., Li, Y., Xue, C., Ding, C., Wang, X., Fu, R., et al. (2021). Compound Danshen Dripping Pills Affect the Pharmacokinetics of Azisartan by Regulating the Expression of Cytochrome P450 2B1, 2C6, and 2C11 in Rats. *J. Pharm. Biomed. Anal.* 195, 113887. doi:10.1016/j.jpba.2020.113887

Mueck, W., Kubitza, D., and Becka, M. (2013). Co-administration of Rivaroxaban with Drugs that Share its Elimination Pathways: Pharmacokinetic Effects in Healthy Subjects. *Br. J. Clin. Pharmacol.* 76 (3), 455–466. doi:10.1111/bcp.12075

Ouyang, H., Shen, J., Huang, X., Ma, W., Jia, Q., Yao, G., et al. (2019). Effect of Naoxintong Capsules on the Activities of CYP450 and Metabolism of Metoprolol Tartrate in Rats Evaluated by Probe Cocktail and Pharmacokinetic Methods. *Evid. Based Complement. Altern. Med.* 2019, 5242605. doi:10.1155/2019/5242605

Purrucker, J. C., Hölscher, K., Kollmer, J., and Ringleb, P. A. (2020). Etiology of Ischemic Strokes of Patients with Atrial Fibrillation and Therapy with Anticoagulants. *J. Clin. Med.* 9 (9), 2938. doi:10.3390/jcm9092938

Qin, X., and Wang, X. (2019). Role of Vitamin D Receptor in the Regulation of CYP3A Gene Expression. *Acta Pharm. Sin. B* 9 (6), 1087–1098. doi:10.1016/j.apsb.2019.03.005

Qin, X., Zhang, Y., Lu, J., Huang, S., Liu, Z., and Wang, X. (2021). CYP3A Deficiency Alters Bile Acid Homeostasis and Leads to Changes in Hepatic Susceptibility in Rats. *Toxicol. Appl. Pharmacol.* 429, 115703. doi:10.1016/j.taap.2021.115703

Steffel, J., Verhamme, P., Potpara, T. S., Albaladejo, P., Antz, M., Desteghe, L., et al. (2018). The 2018 European Heart Rhythm Association Practical Guide on the Use of Non-vitamin K Antagonist Oral Anticoagulants in Patients with Atrial Fibrillation. *Eur. Heart J.* 39 (16), 1330–1393. doi:10.1093/eurheartj/ehy136

Sun, M., Tang, Y., Ding, T., Liu, M., and Wang, X. (2015). Investigation of Cytochrome P450 Inhibitory Properties of Maslinic Acid, a Bioactive Compound from Olea Europaea L., and its Structure-Activity Relationship. *Phytomedicine* 22 (1), 56–65. doi:10.1016/j.phymed.2014.10.003

Sychev, D., Mirzaev, K., Cherniaeva, M., Kulikova, M., Bochkov, P., Shevchenko, R., et al. (2020). Drug-drug Interaction of Rivaroxaban and Calcium Channel Blockers in Patients Aged 80 Years and Older with Nonvalvular Atrial Fibrillation. *Drug Metab. Pers. Ther.* 35 (3). doi:10.1515/dmpt-2020-0127

Tang, S., Chen, A., Zhou, X., Zeng, L., Liu, M., and Wang, X. (2017). Assessment of the Inhibition Risk of Shikonin on Cytochrome P450 via Cocktail Inhibition Assay. *Toxicol. Lett.* 281, 74–83. doi:10.1016/j.toxlet.2017.09.014

Toselli, F., Dodd, P. R., and Gillam, E. M. (2016). Emerging Roles for Brain Drug-Metabolizing Cytochrome P450 Enzymes in Neuropsychiatric Conditions and Responses to Drugs. *Drug Metab. Rev.* 48 (3), 379–404. doi:10.1080/03602532.2016.1221960

Wang, L., Gai, S., Zhang, X., Xu, X., Gou, N., Wang, X., et al. (2020). Simultaneous Determination of Rivaroxaban and TAK-438 in Rat Plasma by LC-MS/MS: Application to Pharmacokinetic Interaction Study. *Bioanalysis* 12 (1), 11–22. doi:10.4155/bio-2019-0130

Wang, L., Ma, R., Liu, C., Liu, H., Zhu, R., Guo, S., et al. (2017a). Salvia Miltiorrhiza: A Potential Red Light to the Development of Cardiovascular Diseases. *Curr. Pharm. Des.* 23 (7), 1077–1097. doi:10.2174/1381612822666161010105242

Wang, R., Zhang, H., Wang, Y., Yu, X., and Yuan, Y. (2016). Effects of Salvianolic Acid B and Tanshinone IIA on the Pharmacokinetics of Losartan in Rats by Regulating the Activities and Expression of CYP3A4 and CYP2C9. *J. Ethnopharmacol.* 180, 87–96. doi:10.1016/j.jep.2016.01.021

Wang, S. Y., Xing, P. F., Zhang, C. Y., and Deng, B. Q. (2017b). Association of CYP2J2 Gene Polymorphisms with Ischemic Stroke and Stroke Subtypes in Chinese Population. *Med. Baltim.* 96 (10), e6266. doi:10.1097/MD.0000000000006266

Wang, X., Cheung, C. M., Lee, W. Y., Or, P. M., and Yeung, J. H. (2010). Major Tanshinones of Danshen (Salvia Miltiorrhiza) Exhibit Different Modes of Inhibition on Human CYP1A2, CYP2C9, CYP2E1 and CYP3A4 Activities *In Vitro*. *Phytomedicine* 17 (11), 868–875. doi:10.1016/j.phymed.2010.05.003

Wang, X., and Yeung, J. H. (2011). Effects of Salvia Miltiorrhiza Extract on the Liver CYP3A Activity in Humans and Rats. *Phytother. Res.* 25 (11), 1653–1659. doi:10.1002/ptr.3472

Wang, X., and Yeung, J. H. (2012). Investigation of Cytochrome P450 1A2 and 3A Inhibitory Properties of Danshen Tincture. *Phytomedicine* 19 (3-4), 348–354. doi:10.1016/j.phymed.2011.09.075

Wang, Y., Chen, M., Chen, H., and Wang, F. (2021). Influence of ABCB1 Gene Polymorphism on Rivaroxaban Blood Concentration and Hemorrhagic Events in Patients with Atrial Fibrillation. *Front. Pharmacol.* 12, 555. doi:10.3389/fphar.2021.639854

Westphal, C., Spallek, B., Konkel, A., Marko, L., Qadri, F., DeGraff, L. M., et al. (2013). CYP2J2 Overexpression Protects against Arrhythmia Susceptibility in Cardiac Hypertrophy. *PLoS One* 8 (8), e73490. doi:10.1371/journal.pone.0073490

Yeh, G. Y., Davis, R. B., and Phillips, R. S. (2006). Use of Complementary Therapies in Patients with Cardiovascular Disease. *Am. J. Cardiol.* 98 (5), 673–680. doi:10.1016/j.amjcard.2006.03.051

Zeng, Y., Xiong, Y., Yang, T., Wang, Y., Zeng, J., Zhou, S., et al. (2022). Icariin and its Metabolites as Potential Protective Phytochemicals against Cardiovascular Disease: From Effects to Molecular Mechanisms. *Biomed. Pharmacother.* 147, 112642. doi:10.1016/j.biopha.2022.112642

Zhang, W. J., Wang, S., Kang, C. Z., Lv, C. G., Zhou, L., Huang, L. Q., et al. (2020). Pharmacodynamic Material Basis of Traditional Chinese Medicine Based on Biomacromolecules: a Review. *Plant Methods* 16, 26. doi:10.1186/s13007-020-00571-y

Conflict of Interest: The authors declare that the research was conducted in the absence of any commercial or financial relationships that could be construed as a potential conflict of interest.

Publisher's Note: All claims expressed in this article are solely those of the authors and do not necessarily represent those of their affiliated organizations, or those of the publisher, the editors, and the reviewers. Any product that may be evaluated in this article, or claim that may be made by its manufacturer, is not guaranteed or endorsed by the publisher.

frontiers | Frontiers in Pharmacology

ORIGINAL RESEARCH
published: 19 July 2022
doi: 10.3389/fphar.2022.932686

Population Pharmacokinetics and Pharmacodynamics of Isoniazid and its Metabolite Acetylisoniazid in Chinese Population

Bing Chen[1†], Hao-Qiang Shi[1†], Meihua Rose Feng[2], Xi-Han Wang[1], Xiao-Mei Cao[3] and Wei-Min Cai[4]*

[1]Department of Pharmacy, Ruijin Hospital, School of Medicine, Shanghai Jiaotong University, Shanghai, China, [2]Department of Pharmaceutical Sciences, University of Michigan, Ann Arbor, MI, United States, [3]Department of Clinical Pharmacology, Nanjin Jinling Hospital, Nanjing, China, [4]Department of Clinical Pharmacy and Pharmaceutical Management, School of Pharmacy, Fudan University, Shanghai, China

OPEN ACCESS

Edited by:
Zipeng Gong,
Guizhou Medical University, China

Reviewed by:
Yuanying Jiang,
Tongji University, China
Gao Shen,
Changhai Hospital, China

***Correspondence:**
Bing Chen
chchenbing@163.com

[†]These authors have contributed equally to this work

Specialty section:
This article was submitted to Drug Metabolism and Transport, a section of the journal Frontiers in Pharmacology

Received: 30 April 2022
Accepted: 07 June 2022
Published: 19 July 2022

Citation:
Chen B, Shi H-Q, Feng MR, Wang X-H, Cao X-M and Cai W-M (2022) Population Pharmacokinetics and Pharmacodynamics of Isoniazid and its Metabolite Acetylisoniazid in Chinese Population. Front. Pharmacol. 13:932686. doi: 10.3389/fphar.2022.932686

Objective: We aimed to establish a population pharmacokinetic (PPK) model for isoniazid (INH) and its major metabolite Acetylisoniazid (AcINH) in healthy Chinese participants and tuberculosis patients and assess the role of the *NAT2* genotype on the transformation of INH to AcINH. We also sought to estimate the INH exposure that would achieve a 90% effective concentration (EC_{90}) efficiency for patients with various *NAT2* genotypes.

Method: A total of 45 healthy participants and 157 tuberculosis patients were recruited. For healthy subjects, blood samples were collected 0–14 h after administration of 300 mg or 320 mg of the oral dose of INH; for tuberculosis patients who received at least seven days therapy with INH, blood samples were collected two and/or six hours after administration. The plasma concentration of INH and AcINH was determined by the reverse-phase HPLC method. *NAT2* genotypes were determined by allele-specific amplification. The integrated PPK model of INH and AcINH was established through nonlinear mixed-effect modeling (NONMEM). The effect of *NAT2* genotype and other covariates on INH and AcINH disposition was evaluated. Monte Carlo simulation was performed for estimating EC90 of INH in patients with various *NAT2* genotypes.

Results: The estimated absorption rate constant (K_a), oral clearance (CL/F), and apparent volume of distribution (V_2/F) for INH were 3.94 ± 0.44 h^{-1}, 18.2 ± 2.45 L·h^{-1}, and 56.8 ± 5.53 L, respectively. The constant of clearance (K_{30}) and the volume of distribution (V_3/F) of AcINH were 0.33 ± 0.11 h^{-1} and 25.7 ± 1.30 L, respectively. The fraction of AcINH formation (F_M) was 0.81 ± 0.076. *NAT2* genotypes had different effects on the CL/F and F_M. In subjects with only one copy of NAT2 *5, *6, and *7 alleles, the CL/F values were approximately 46.3%, 54.9%, and 74.8% of *4/*4 subjects, respectively. The F_M values were approximately 48.7%, 63.8%, and 86.9% of *4/*4 subjects, respectively. The probability of target attainment of INH EC_{90} in patients with various NAT2 genotypes was different.

Conclusion: The integrated parent-metabolite PPK model accurately characterized the disposition of INH and AcINH in the Chinese population sampled, which may be useful in the individualized therapy of INH.

Keywords: isoniazid, acetylisoniazid, population pharmacokinetics, N-acetyltransferase 2, genetic polymorphism, pharmacodynamics

INTRODUCTION

Tuberculosis remains a serious public health concern in many countries (Ferguson and Rhoads, 2009; Sandhu, 2011). Although the incidence of tuberculosis has been decreasing recently, approximately 10 million cases, along with approximately 1.2 million deaths associated with the disease have been reported (Chakaya et al., 2021). China accounted for 8.4% of total global tuberculosis cases in 2019 (Chakaya et al., 2021). Isoniazid (INH), inhibits the synthesis of long-chain mycolic acids, which are indispensable components of mycobacterial cell walls. As such, it is an essential component of standard first-line prophylactic treatment/measures of tuberculosis (Winder and Collins, 1970; Takayama et al., 1972). INH is also effective in preventing resistance to co-administered anti-tuberculosis drugs (Mitchison, 1979). A fixed-dose combination (FDC) anti-tuberculosis medication is thought to be more effective and convenient, with less drug resistence occurring (Blomberg et al., 2001). The use of FDCs from different manufacturers may cause high pharmacokinetic (PK) variability, along with inter-individual differences in efficacy and toxicity of INH (Shishoo et al., 2001; McIlleron et al., 2006; Hao et al., 2014).

Therapeutic drug monitoring (TDM) of anti-tuberculosis drugs, including INH, can be used to ensure adequate treatment effect, as well as reduce toxic effects (Peloquin, 2002; Weiner et al., 2003; Zuur et al., 2016). A peak INH concentration (C_{max}) of $<3\ \mu g\ ml^{-1}$ after a daily administration, or $<9\ \mu g\ ml^{-1}$ after biweekly administration is considered ineffective (Peloquin, 2002). Some other studies suggested that a minimum area of $10.52\ \mu g{\cdot}h{\cdot}ml^{-1}$ under the concentration-time curve (AUC_{0-24}) is a suitable marker of clinical efficacy (Donald et al., 2007; Kiser et al., 2012).

The majority of INH is acetylated by *N*-acetyltransferase (NAT2) to form acetylisoniazid (AcINH), acetylhydrazine, and other metabolites, and only approximately 7–30% of INH is excreted intact as the parent drug. Although there is no evidence on the toxicity of AcINH, it may be converted to other toxic metabolites. The ratio of AcINH and INH levels in plasma at the peak time is considered to be an index of INH toxicity (Timbrell et al., 1980). NAT2 activity exhibits remarkable polymorphism, primarily due to *NAT2* genotypes. A total of seven single nucleotide polymorphisms (SNPs) have been determined in the human *NAT2* gene, consisting of more than 27 different *NAT2* alleles (Lauterburg et al., 1985a; Bell et al., 1993; Loktionov et al., 2002; Walker et al., 2009). Two of these SNPs are silent, and the other five lead to amino acid substitutions. Hein et al. found that the C341→T (rs1801280) of *5, G590→A (rs1799930) of *6, and G857→A (rs1799931) of *7 led to substitutions of Ile114→Thr, Arg197→Gln, Gly286→Glu in the NAT2 enzyme, respectively, leading to a remarkable decrease in NAT2 activity (Hein et al., 1994). *NAT2* alleles *5, *6, and *7 comprise the most important factor of slow acetylators in Whites and Asisans. The frequencies of these alleles are different among various populations (Lin et al., 1993; Agundez et al., 1996; Chen et al., 2006). Polymorphism of *NAT2* has been considered as the primary reason for inter-individual differences in PK and pharmacodynamics (PD), which may further influence the INH dosing regimen (Horai et al., 1982; Deguchi et al., 1990; Parkin et al., 1997; Denti et al., 2015).

Population PK (PPK) is suitable for characterizing the disposition of the drug in a large group of participants with limited observations for each. PPK has the ability to provide quantitative estimates of the inter- and intra-patient variability, and also to determine the influence of demographic, clinical, and genetic factors on the PKs. PPK is also used in the simulation of PKs of parent drugs and their metabolites simultaneously (Seng et al., 2015; Sundell et al., 2020). However, to our knowledge, no study has been published on the integrated PPK model of INH and AcINH in Chinese patients. Based on the PPK parameters of INH, and the distribution of minimum inhibitory concentration (MIC) in clinical isolates, the PK/PD model can be established to identify an optimal dosing regimen of INH, which is helpful in the appropriate treatment of tuberculosis (Pasipanodya and Gumbo, 2011).

The purpose of this study is to establish a PPK model for INH and its major metabolite AcINH in tuberculosis patients and healthy Chinese participants,and assess the influence of *NAT2* polymorphism on the PK/PD of INH.

MATERIALS AND METHODS

Subjects

All healthy participants were enrolled in two different PK studies of INH. In the first study, 24 healthy male subjects with different *NAT2* genotypes were recruited from 215 participants with known *NAT2* genotypes (Chen et al., 2009). In the second study, 21 healthy subjects were enrolled from a group that participated in a bioequivalence study. All subjects were Han nationals. Each subject was physically healthy and had no history of significant medical illness or hypersensitivity to any drugs. A physical examination was performed before the study. This included a complete blood chemistry, urinalysis, and an electrocardiogram. All subjects were drug-free for two weeks before, and during the study. The study protocol was approved by the Jinling Hospital Ethics Committee and all subjects gave written consent to participate.

A total of 157 tuberculosis patients were also recruited. The subjects consisted of 89 males and 68 females (age: 42.2 ± 11.5 y, weight: 56.5 ± 9.71 kg) patients. Sixty-seven patients had taken three anti-tuberculosis drugs simultaneously, 48 had consumed four drugs simultaneously, while consumed two drugs simultaneously. The drugs used in combination with INH were rifampicin, rifapentine, pyrazinamide, and ethambutol. Demographic and clinical data were recorded.

Study Protocol

For the first PK study, 24 healthy volunteers were enrolled in the study center at 8:00 p.m. on the day before the study began. After fasting overnight, three tablets of INH (100 mg/tablet, Qianjin Pharmaceutical Company, Hunan, China) were taken with 200 ml of water at 8:00 a.m. Food was provided four hours after the INH intake. Three ml of blood was drawn into a sterile anticoagulation tube just before the administration of INH, and 0.25, 0.5, 1, 1.5, 2, 3, 4, 6, 8, 10 and 14 h after.

In the second PK study, Rifater, containing INH 80 mg/tablet (Gruppo Lepetit SPA, Italy) was used as the reference formulation, and INH 80 mg/tablet or 80 mg/capsule (LanBen, Nanjing, China) was used as the test formulation. Twenty-one subjects received a single dose of 320 mg test or reference tablets or capsules after an overnight fast. Both formulations were administered with 200 ml water at 8:00 a.m. Standard meals were provided four and ten hours after drug administration. No other food or drinks containing Xanthine (e.g., tea, coffee, cola) were allowed for subjects during their time in the study center. A total of three ml of blood was collected via veins, and then transferred into sterile EDTA anticoagulation tube before dosing, and 0.25, 0.5, 1, 1.5, 1, 2, 4, 6, 9, 12 h after.

All patients received anti-tuberculosis therapy for 7–14 consecutive days before sample collection. For all patients, 3 ml of blood was drawn 2 and/or 6 h after INH administration. Blood samples were centrifuged at 1610 × *g* for 10 min. Since AcINH is not stable in plasma samples, plasma was immediately separated and stored at −70°C while awaiting further analysis.

Genotyping

NAT2 C341→T, G590→A, and G857→A represent *5, *6, and *7 alleles, respectively. These SNPs are sufficient for the reflection of the important *NAT2* genotypes have impaction on NAT2 activity. We developed allele-specific PCR (ASA-PCR) to determine the three aforementioned SNPs (Chen et al., 2004). The method was designed based on the principles of amplification refractory mutation systems. Briefly stated, allele-specific primers for different *NAT2* alleles were designed. ASA-PCR was performed using two tubes for the detection of the wild and mutant genotype of each allele. The primers were mixed with Taq DNA enzyme, dNTPs, Mg^{2+}, buffer, and genomic DNA. Upon 30 amplification cycles, the *NAT2* genotypes were analyzed after electrophoresis.

Quantification of INH and AcINH

A previously established reverse phase HPLC was used to determine plasma concentrations of INH and AcINH simultaneously (Cao et al., 2005). Perchloric acid was added to the plasma for precipitation of protein. The supernatant was separated after centrifugation and eluted with 2 mmol·L^{-1} sodium heptane sulfonate-acetonitrile (98:2) on a Lichrospher C18 column and detected at a wavelength of 266 nm. The calibration curve was linear in the range of 0.12–15.89 mg·L^{-1} (0.88–115.9 μmol·L^{-1}) for INH and in the range of 0.13–17.08 mg·L^{-1} (0.72–95.4 μmol·L^{-1}) for AcINH ($r^2 > 0.99$).

Non-Compartmental Analysis

The PK parameters of INH and AcINH in healthy subjects were determined with the WinNonlin 5.01 (Pharsight Corp., Mountain View, CA, United States). C_{max} and T_{max} were obtained from observation. The K_e was calculated using least-square regression analysis performed using the terminal phase of the concentration–time curve. The AUC was calculated by using the trapezoidal method.

Compartmental Pharmacokinetic Analysis

Data Splitting

For the 202 subjects in the present study, 122 were assigned to the model-building set (index group) and 80 to the test set (validation group), respectively. The index group included 15 subjects with one full PK profile, 12 subjects with three full PK profiles, and 95 patients with sparse sampling data. The validation group includednine subjects with one full PK profile, nine with three full PK profiles, and 62 with sparse sampling data.

Model Development

PPK modeling of INH and AcINH was constructed based on the of modeling group data. The final PPK model was constructed by using data from both the modeling group and validation group. One- and two-compartment models for INH or AcINH were evaluated during model construction. The first absorption, with or without lag time, was also tested. NONMEM (Version 6, GloboMax, Hanover, MD) was used for the model construction. The first-order conditional estimation method (FOCE) was applied. Model selection was based on objective function value (OFV), parameter estimates, and standard error. OFV is proportional to −2 log likelihood of the relevant model. The distribution of empirical Bayes estimates and ability of the model to determine reasonable INH and AcINH concentration-time profiles were also important for model assessment.

Interindividual and Residual Error Model

The inter-individual variability of the parameters was assessed using an exponential function (**Eq. 1**)

$$P_i = \theta_{TV} \cdot e^{\eta i} \quad (1)$$

P_i denotes the PK parameter value, θ_{TV} denotes the population value for the parameter described, and η_i denotes the random deviation of P_i from θ_{TV}. The values of η_i were assumed to be independently normally distributed with a mean of 0 and a variance of ω^2.

A proportional model was used for residual error analysis of INH and AcINH as (**Eq. 2**)

$$C_{obs} = C_{pred} \times (1 + \varepsilon) \quad (2)$$

C_{obs} is the observed concentration, C_{pred} is the predicted concentration, and ε is a residual error with a mean of 0 and a variance of σ^2.

Covariates

The characteristics of the subjects, including body weight, age, clearance of creatinine (CLcr), aspartate aminotransferase (ASP), alanine aminotransferase (AST), and *NAT2* genotype, were tested as covariates in the population analysis. The model of continuous covariates on the P_i was as follows (**Eqs 3–6**)

$$TV(P_i) = \theta_P \times (\text{covariate}) \quad (3)$$

$$TV(P_i) = \theta_P + \theta_C \times (\text{covariate}) \quad (4)$$

$$TV(P_i) = \theta_P \times e^{(\text{covariate} \times \theta_c)} \quad (5)$$

$$TV(P_i) = \theta_P \times (\text{covariate}/\text{means of covariate})^{\theta c} \quad (6)$$

For categorical covariate of the *NAT2* genotype, three methods representing *NAT2* genotyping were tested:

1) Subjects were placed into extensive metabolizer (EM) and poor metabolizer (PM) groups according to the NAT2 genotype, where scores of "1" and "0" were assigned to the EM and PM subjects, respectively.
2) Subjects were characterized as homogenous wild type (wt/wt), heterozygous mutant (m/wt), and homogenous mutant (m/m) based on their genotypes. Scores of "0," "1," and "2" were assigned to the three groups, respectively. P_i was modeled according to the following equation (**Eq. 7**)

$$P_i = TV(P_i) \times e^{(NAT2 \times \theta)} \quad (7)$$

3) For each allele of *5, *6 and *7, scores of 0, 1 and 2 were assigned to the w/w, m/w, and m/m genotype. Hence, subjects with *4/*4, *4/*6, *4/*7, *6/*6, *6/*7, *7/*7, and *5/*7 genotype were assigned the scores of 0/0/0, 0/1/0, 0/0/1, 0/2/0, 0/1/1, 0/0/2, and 1/0/1, respectively. P_i was modeled according to the following equation (**Eq. 8**)

$$P_i = TV(P_i) \times e^{(*5 \times \theta)} \times e^{(*6 \times \theta)} \times e^{(*7 \times \theta)} \quad (8)$$

Various covariates were included in a stepwise manner, followed by a stepwise elimination for the final regression model. Changes in the OFV were used to approximate the χ^2 distribution, with degrees of freedom (df) equal to the number of covariates introduced. When the OFV was reduced by 6.64 or higher ($p < 0.01$, df = 1), the covariate included was considered statistically significant. After all covariates significantly decreasing OFV were included, each covariate was fixed as zero in turn. This procedure was repeated until the value of the objective function failed to increase by more than 10.9 ($p < 0.001$, df = 1).

Data Analysis and Model Evaluation

The final model was tested by using a visual predictive check. A total of 1,000 new datasets for patients with different *NAT2* genotypes were simulated based on estimation of the parameters with their inter- and intra-individual variety, and *NAT2* genotypes of healthy subjects and tuberculosis patients. A 90% prediction interval was obtained by extracting the 5% and 95% quantiles of their simulated distributions. The quality of the evaluation was assessed by graphical presentation of the observed concentration *vs.* predictions. The stability and performance of the final model were also assessed through a nonparametric bootstrap, with resampling and replacement. In this study, 1,000 bootstrap samples were generated, and the PPK parameters were estimated for each sample using the final model.

Bayesian Estimation of AUC of INH

Based on the Bayesian approach, the POSTHOC subroutine of NONMEM without an estimation step (MAXEVAL = 0) was used to estimate the individual PK parameters of each patient in the validation group. The PPK parameters, inter-individual variation (IIV), and residual variability were set as the data obtained from the index group. Models of INH C_2, C_2-C_4, and C_2-C_6 plasma concentration-time points following INH administration were selected as the Bayesian estimators for estimation of the AUC of the validation group. $AUC_{0\text{-}24}$ was estimated through the equation: $AUC_{0\text{-}24}$ = dose/(CL/F). $AUC_{0\text{-}24}$ obtained from the Bayesian estimators was compared with observed values. The predictive performance was evaluated as bias and precision, which are expressed as MPE (%) and RMSE (%), respectively.

Monte Carlo Simulations

In line with previous studies, AUC_{0-24}/MIC indicated a better PK/PD index compared with C_{max}/MIC and T_{MIC}. The 90% maximal kill *Mycobacterium tuberculosis* (90% effective concentration, EC_{90}) is considered the therapeutic target of INH. AUC_{0-24}/MIC that mediates EC_{90} was 567 (Gumbo et al., 2007). The MIC of INH was obtained from previous studies on *Mycobacterium tuberculosis* strains (MIC values were 0.01, 0.02, 0.05, 0.10, and 0.25 μg/ml) (Zhao and Lu, 2019). The INH dosing regimen included 300, 600, and 900 mg daily. AUC_{0-24} of INH was estimated based on the integrated PPK model with estimated uncertainty (standard error). The simulation was performed with the data of 10,000 subjects with various *NAT2* genotypes using the Monte Carlo method (Gumbo. 2010). The probability of target attainment (PTA) of patients with various *NAT2* genotypes was summarized based on the estimated proportions of isolates.

RESULTS

INH and AcINH in Relation to *NAT2* Genotypes

The demographic and laboratory test data of all subjects obtained are shown in **Table 1**. In the first PK study performed with 24 healthy subjects, five different *NAT2* genotypes were observed: *4/*4 (8), *4/*6 (6), *4/*7 (2), *5/*7 (1), and *6/*6 (7). A total of eight subjects were characterized with a wt/wt genotype (*4/*4); eight with m/wt genotype (*4/*6 and *4/*7); 8 subjects with m/m genotype (*5/*7 and *6/*6). There was a significant difference in

TABLE 1 | Demographic data of pharmacokinetic study on healthy subjects and tuberculosis patients.

Characters	Mean ± SD		
	PK study	Bioequivalence study	Patients
Gender	Male: 21; Famale: 0	Male: 24; Famale: 0	Male: 89; Famale: 68
Age (year)	24.1 ± 2.61 (21–29)	24.4 ± 2.12 (22–28)	42.2 ± 11.5 (19–64)
weight (kg)	63.0 ± 5.82 (55–72)	64.6 ± 5.82 (55–71)	56.5 ± 9.7 (39–78) kg
Cretinine (mmol×L^{-1})	98.7 ± 11.7 (80–124)	69.1 ± 15.2 (52–97)	103.7 ± 25.6 (60–189)
BUN (mmol×L^{-1})	4.40 ± 1.12 (2.9–7.0)	5.21 ± 1.13 (2.8–6.7)	6.8 ± 2.9 (4.1–10.7)
TBIL (mmol×L^{-1})	18.0 ± 7.12 (9.5–32.1)	16.8 ± 3.77 (12.6, 23.3)	11.1 ± 2.11 (6.6–25.5)
ALT (U×L^{-1})	16.3 ± 4.81 (13–28)	14.9 ± 3.63 (11–27)	18.2 ± 8.61 (7–44)
AST (U×L^{-1})	16.8 ± 3.12 (14–28)	18.7 ± 2.31 (17–24)	22.4 ± 7.63 (12–43)

BUN, blood urea nitrogen; TBIL, total bilirubin; ALT, alanine aminotransferase; AST, glutamic-oxaloacetic transaminase.

TABLE 2 | Pharmacokinetic parameters of INH and AcINH in Chinese healthy subjects with different NAT2 genotypes.

	wt/wt	m/wt	m/m	Total
INH				
$t_{1/2}$ (h)	1.15 ± 0.18	1.76 ± 0.17‡	3.23 ± 0.28‡#	2.05 ± 0.91
C_{max} (μmol · L^{-1})	36.0 ± 13.5	41.7 ± 14.2	60.4 ± 17.5‡*	46.0 ± 18.0
AUC (μmol ·h·L^{-1})	75.5 ± 15.5	119.2 ± 22.2†	308.1 ± 62.1‡#	162.1 ± 102.3
Cl (L·h^{-1})	30.05 ± 6.02	19.17 ± 5.04	7.79 ± 1.62‡#	19.00 ± 10.28
AcINH				
$t_{1/2}$ (h)	3.84 ± 0.46	3.59 ± 0.40	6.04 ± 1.20‡#	4.57 ± 1.35
C_{max} (μmol · L^{-1})	32.5 ± 8.03	23.2 ± 2.91†	8.03 ± 1.40 ‡#	21.2 ± 11.3
AUC (μmol ·h·L^{-1})	245.4 ± 51.2	221.4 ± 31.0	115.1 ± 21.6‡#	192.7 ± 69.0

†p < *0.05*, ‡p < *0.001 compared with wt/wt genotype.* *p < *0.05*, #p < *0.001 compared with m/wt genotype.*

INH PK parameters among various groups. The C_{max} of INH in the wt/wt, m/wt, and m/m groups were 36.0 ± 13.5, 41.7 ± 14.2, and 60.4 ± 17.5 μmol·L^{-1}, and AUC_{0-14h} of INH in different groups were 71.5 ± 16.8, 115.6 ± 21.9, and 274.9 ± 55.5 μmol·h·L^{-1} ($p < 0.001$), respectively (**Table 2**). A significant difference was observed among various *NAT2* genotypes.

For the bioequivalence study performed with 21 healthy subjects who received 320 mg of INH, five different *NAT2* genotypes were observed, namely, *4/*4 (11), *4/*6 (6), *4/*7 (2), *4/*5 (1), and *6/*6 (1). A total of 11, 9, and 1 subjects were included in the *NAT2* wt/wt, m/wt, and m/m groups, respectively. The INH C_{max} in the wt/wt, m/wt, and m/m groups were 32.4 ± 13.7, 42.6 ± 11.0, and 71.6 μmol·L^{-1}, and AUC_{0-24h} of INH in different groups were 55.2 ± 10.1, 97.7 ± 16.7, and 319.9 μmol·h·L^{-1} ($p < 0.001$), respectively.

For 157 tuberculosis patients, seven different *NAT2* genotypes including *4/*4 ($n = 72$), *4/*5 ($n = 6$), *4/*6 ($n = 31$), *4/*7 ($n = 25$), *6/*6 ($n = 12$) and *7/*7 ($n = 4$), *5/*7 ($n = 2$), and *6/*7 ($n = 5$) were observed. A total of 72 (45.8%) patients with *4/*4 (wt/wt) genotype and 23 patients (14.6%) with *5/*7, *6/*7, *6/*6 or *7/*7 genotypes were classified in the m/m group. The other 62 patients (39.5%) were classified in the m/wt group. The concentrations of INH 2 h ($n = 109$) after the administration in the wt/wt, m/wt, and m/m groups were 22.8 ± 17.3, 28.2 ± 23.2, and 46.8 ± 28.8 μmol·L^{-1} ($p < 0.001$), and the concentrations of AcINH in the three groups were 35.0 ± 18.8, 21.5 ± 15.8, and 11.9 ± 8.64 μmol·L^{-1} ($p < 0.001$), respectively. The concentrations of INH 6 h ($n = 52$) after administration in the wt/wt, m/wt, and m/m groups were 3.96 ± 1.74, 6.69 ± 3.56, and 24.2 ± 9.95 μmol·L^{-1} ($p < 0.001$), and the concentrations of AcINH in the three groups were 21.3 ± 13.5, 18.1 ± 15.2, and 9.87 ± 3.35 μmol·L^{-1} ($p = 0.034$), respectively.

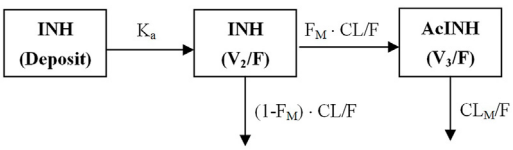

FIGURE 1 | Schematic figure of the integrated PPK model of isoniazid (INH) and acetylisoniazid (AcINH). K_a: The absorption rate constant of INH. F: The oral bioavailability of INH. CL/F: clearance of INH. F_M: The fraction of INH converted to AcINH. CL_M/F: clearance of AcINH. V_2 and V_3: volume of distribution of INH and AcINH.

Integrated Model of INH and AcINH

An integrated model describing INH and AcINH simultaneously was developed. The graphical representation of the model is provided in **Figure 1**. The structural model consisted of a one-compartment model obtained by first-order elimination process for both INH and AcINH. The PPK parameters of INH and AcINH are presented in **Table 3**. For the basic model, the K_a of INH was estimated to be 3.94 ± 0.44 h^{-1}. The clearance of INH (CL/F) was estimated to be 18.2 ± 2.45 L·h^{-1}, K_{30} (constant of clearance of AcINH) was 0.33 ± 0.11 h^{-1}, V_d/F values of INH (V_2)

TABLE 3 | Parameters of integrated PPK model of INH and AcINH in Chinese healthy subjects and tuberculosis patients.

		Basic Model		Final Model (1)		Final Model (2)		Bootstrap	
		Base	SE	Final	SE	Final	SE	mean	SE
K_a (1/h)	θ_1	3.94	0.44	3.91	0.44	3.99	0.42	3.96	0.45
CL/F (L/h)	θ_2	18.2	2.45	28.7	3.22	30.2	3.04	32.2	3.55
K_{30} (1/h)	θ_3	0.33	0.11	0.41	0.051	0.30	0.024	0.29	0.033
V_2/F (L)	θ_4	56.8	5.53	54.1	12.5	51.4	3.28	56.9	5.14
V_3/F (L)	θ_5	25.7	1.30	17.2	3.21	12.4	0.41	13.0	3.13
F_M	θ_6	0.73	0.076	0.88	0.21	0.86	0.34	0.86	0.31
M341 (CL)	θ_7			–0.55	0.11	–0.77	0.119	–0.77	0.22
M590 (CL)	θ_8					–0.60	0.066	–0.61	0.067
M870 (CL)	θ_9					–0.29	0.095	–0.27	0.011
M341 (F_M)	θ_{10}			–0.47	0.17	–0.72	0.040	–0.70	0.042
M590 (F_M)	θ_{11}					–0.45	0.046	–0.47	0.049
M870 (F_M)	θ_{12}					–0.14	0.069	–0.14	0.074
IIV									
ωK_a (%)	η_1	51.4	14.3	55.2	43.7	53.5	13.1	47.8	11.4
ωCL/F (%)	η_2	56.6	21.8	30.7	12.9	28.1	11.1	25.9	10.2
ωK_{30} (%)	η_3	20.4	9.85	21.4	12.0	22.1	8.15	16.3	8.57
ωV_2/F (%)	η_4	21.3	7.32	19.4	4.85	19.8	8.55	20.2	7.72
ωF_M (%)	η_5	35.3	15.1	10.7	5.52	9.82	4.74	6.35	4.73
Residual variance	σ_{INH}	33.9	11.0	33.3	13.4	33.9	11.4	31.9	12.4
	σ_{AcINH}	29.5	11.9	30.2	11.3	29.5	13.7	27.5	11.8

Final Model (1): NAT2 covariate: NAT2 was classified as wt/wt, m/wt, m/m; CL/F = 28.7×$e^{(-0.55\times Genotype)}$; F_M = 0.88×$e^{(-0.55\times Genotype)}$

Final Model (2): NAT2 covariate: NAT2 was classified according to various NAT2 alleles. CL/F = 30.2×$e^{(-0.77\times M341-0.60\times M590-0.29\times M803)}$; F_M = 0.86×$e^{(-0.72\times M341-0.45\times M590-0.14\times M803)}$

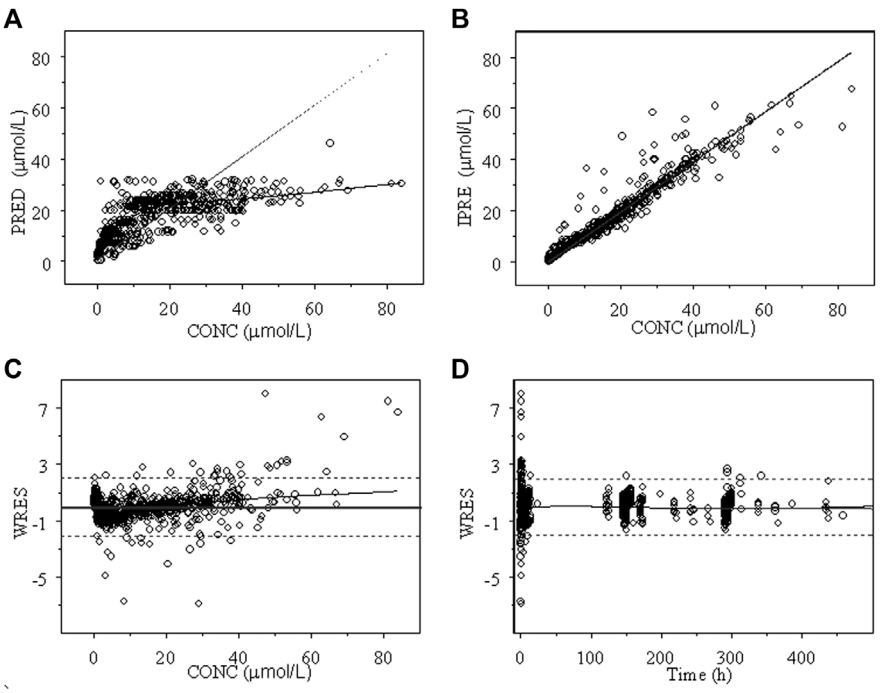

FIGURE 2 | Goodness of fit of INH from the final integrated PPK model in Chinese healthy subjects and tuberculosis patients. **(A)** Population predicted concentration (PRED) vs. observed concentration (CONC); **(B)** individual predicted concentration (IPRE) vs. DV; **(C)** weighted residual error (WRES) vs. CONC; **(D)** WRES vs. time.

and AcINH (V_3) were 56.8 ± 5.53 L and 25.7 ± 1.30 L, respectively, and the F_M was 0.81 ± 0.076.

After the forward inclusion and backward elimination step, only the effect of *NAT2* genotypes remained in the model. When the subjects were characterized with the genotypes of wt/wt, m/wt, or m/m or as EM and PM, the ΔOFV values were -275.3 and -261.4, respectively. When *5, *6 and *7 alleles were used as covariates separately, the OFV value demonstrated the most

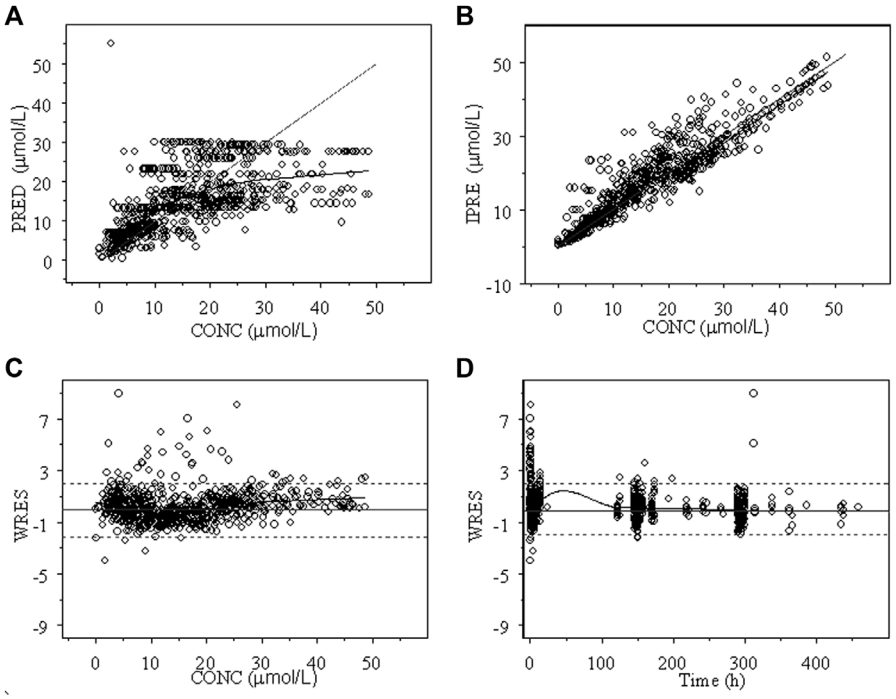

FIGURE 3 | Goodness of fit of AcINH from the final integrated PPK model in Chinese healthy subjects and tuberculosis patients. **(A)** Population predicted concentration (PRED) vs. observed concentration (CONC); **(B)** individual predicted concentration (IPRE) vs. DV; **(C)** weighted residual error (WRES) vs. CONC; **(D)** WRES vs. time.

significant reduction (ΔOFV was −315.5). In subjects with only one copy of *NAT2* *5, *6, and *7 alleles, the CL/F values were approximately 46.3%, 54.9%, and 74.8% of *4/*4 subjects, and F_M values were approximately 48.7%, 63.8%, and 86.9% of *4/*4 subjects. After inclusion of the *NAT2* genotype as a covariate, IIV of CL/F and F_M values were reduced from 56.6% to 28.1%, and 35.3% to 9.82%, respectively.

The goodness of fit plots of the population predicted (PRED) and individual predicted (IPRE) *vs.* observed concentrations (CONC) of the integrated model and the individual weighted residuals (WRES) *vs.* PRED and WRES *vs.* time for INH and AcINH are presented in **Figures 2**, **3**, respectively. The higher bias of INH is distributed in the first two hours. Hence, it seems that the absorption phase was not effectively estimated. The residual errors for INH and AcINH were 33.9% and 29.5%, respectively.

VPC from the data set simulated using the final modelisshown in **Figure 4**. The predicted medians and 5th and 95th data percentiles were similar to the observed medians and 90th percentiles for INH and AcINH. Bootstrap runs were performed successfully 89.7 percent (897 of 1000) of the time similar to the 95% CI calculated by NONMEM.

Bayesian Estimator

Using Bayesian estimation, the individually predicted INH and AcINH concentrations of the validation group (80 patients, 302 points) by correlated well with observed data. The MPE (95% CI) and MRSE % (95% CI) values were −1.16% (−4.35%, 6.68%) and 27.7% (22.2%, 33.2%) for INH and 2.46% (−0.39%, 5.31%) and 28.6% (23.0%, 34.3%) for AcINH, respectively.

Based on Bayesian method, CL/F of INH obtained from the index group was used to predict AUC_{0-24} in the validation group. The sampling strategies consisted of observation of plasma levels at 2 h (C_2), 2 and 4 h (C_2-C_4), 2 and 6 h (C_2-C_6) after INH administration (**Table 4**). The AUC_{0-24} values of various strategies were 143.4 ± 85.6 μmol·h/L (19.7 ± 11.7 μg·h/ml) and 122.0 ± 88.1 μmol·h/L (16.7 ± 12.1 μg·h/ml).

Monte Carlo Simulation for Patients With Various *NAT2* Genotypes

Using the Monte Carlo simulation method, PTAs for patients with various *NAT2* genotypes were estimated with various INH regimens. It seemed that with a daily regimen including 300 mg of INH, the PTA target could be obtained in patients with wt/wt and m/wt genotypes, with the MIC lower than 0.01 μg/ml. With a daily regimen involving administration of 600 mg INH, target PTA can be obtained with MIC values lower than 0.02 μg/ml in wt/wt and m/wt patients. For m/m patients, target PTA was obtained with MIC values of 0.02, 0.05, and 0.1 μg/ml with 300 mg INH dosing regimen. When patients were characterized with *4/*4, *4/*5, *4/*6, *4/*7, *7/*7, *5/*7, *6/*7, and *6/*6 genotype, differences in PTA among various m/m genotypes were also observed (**Figure 5**).

DISCUSSION

In this study, we established for the first time an integrated model for INH and AcINH, using the data derived from healthy Chinese

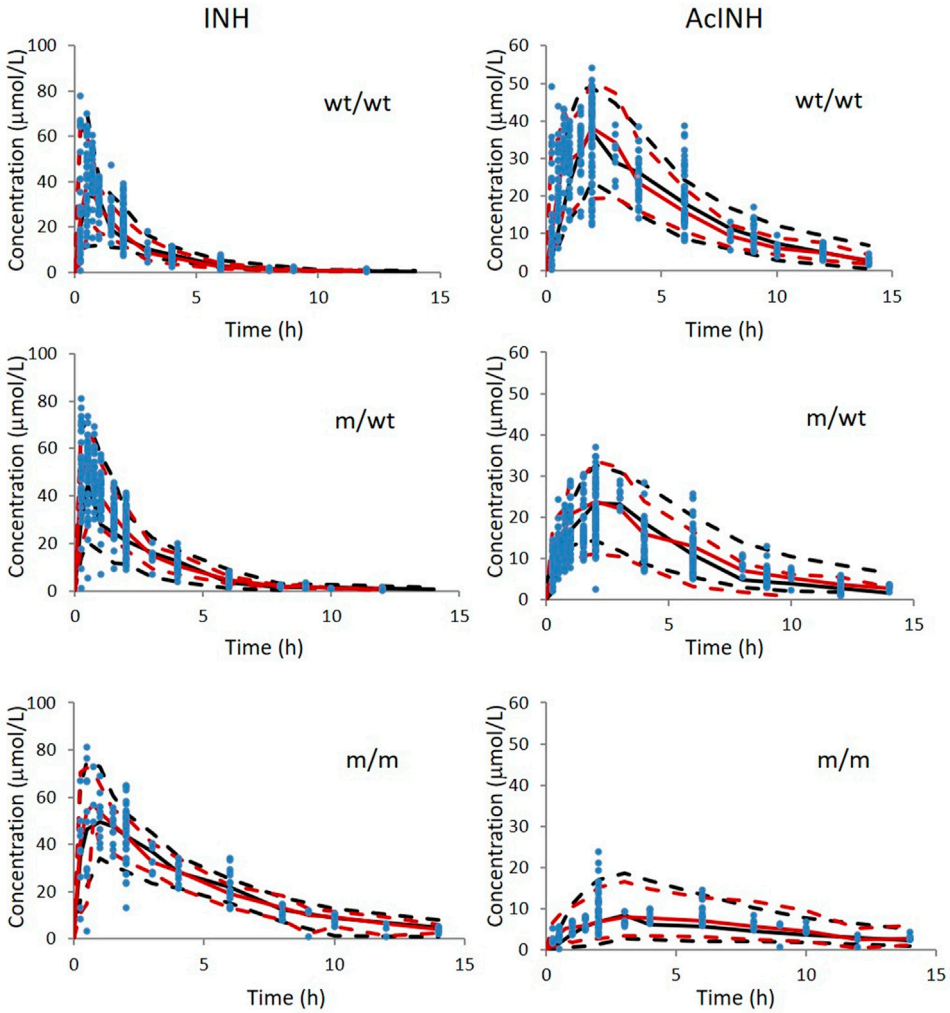

FIGURE 4 | Visual predictive check of INH and AcINH based on the integrated PPK model in Chinese healthy subjects and tuberculosis patients with therapy of INH. The red and black sold lines represent 50th of observed data and simulated data; The upper and lower red dashed lines represent 95th and 5th of observed data; The upper and lower black dashed lines represent 95th and 5th of the simulated data. The blue solid cycles represent observed data wt/wt: NAT2 homogenous wild type; m/wt: NAT2 heterozygous mutant genotype; m/m: homogenous mutant genotype.

TABLE 4 | Prediction performance of the selected limited sampling strategy of INH AUC_{0-24h}.

	Time Points	r^2	AUC(μg·h/mL)	PE (%)		MRSE (%)	
			Mean ± SD	Mean ± SD	95% CI	Mean ± SD	95% CI
1	2 h	0.825	19.8 ± 9.30	−10.4 ± 18.6	−15.9– −4.90	18.5 ± 24.8	13.9–28.5
2	2–4 h	0.835	21.6 ± 9.89	−2.46 ± 18.6	−7.96–3.04	11.7 ± 28.2	10.26–26.9
3	2–6 h	0.840	21.0 ± 9.93	−5.46 ± 18.2	−10.8– −0.080	12.4 ± 27.2	10.8–26.8

subjects and Chinese tuberculosis patients. We found that various *NAT2* alleles had different impact on INH and AcINH PKs. A Monte Carlo method was used to simulate INH dosing regimen for Chinese patients with different *NAT2* genotypes.

Efficacy and adverse effects of INH and its metabolites in the anti-tuberculosis therapy has been demonstrated. The most important metabolite of INH is AcINH, which is converted to isonicotinic acid (INA) and acetylhydrazine (AcHz) (Boxenbaum and Riegelman, 1976; Lauterburg et al., 1985a). AcHz can be converted either to relatively non-toxic diacetylhydrazine, or a reactive intermediate metabolite through CYP2E1, which may cause toxic hepatitis. INH may also be hydrolyzed to hydrazine (Hz) and INA directly. Oxidation of Hz may also lead to transformation to

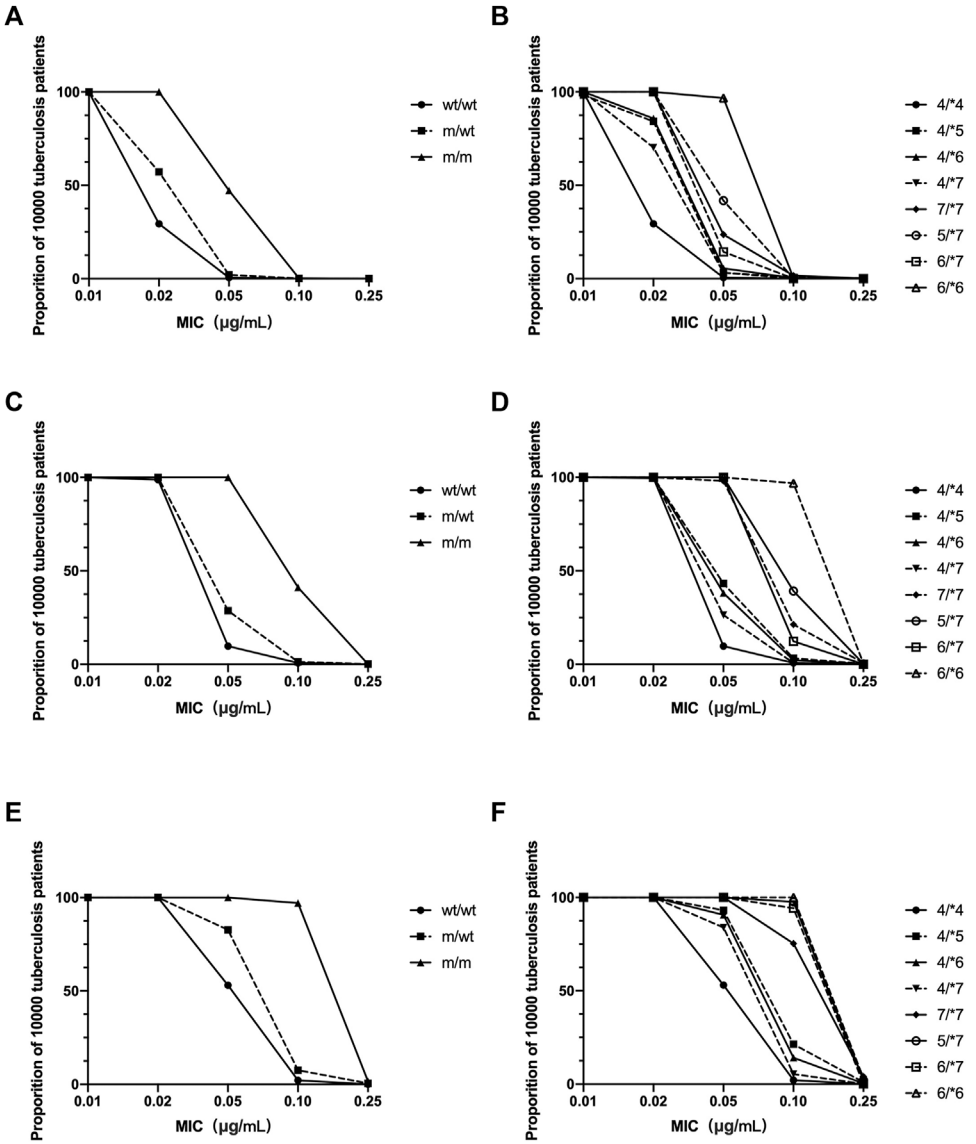

FIGURE 5 | The estimated probabilities of target attainment in patients with various NAT2 genotype and various doing regimens by a Monte Carlo simulation method. INH dosing regimen: 300 mg daily **(A,B)**; 600 mg daily **(C,D)**; 900 mg daily **(E,F)**. **(A,C,E)** NAT2 genotype was characterized as homogenous wild type (wt/wt), heterozygous mutant (m/wt), and homogenous mutant (m/m). **(B,D,F)** NAT2 genotype was characterized according to various *NAT2* alleles.

hepatoxic metabolites; however, this pathway is considered a minor part of the metabolism process, especially in subjects with EM of NAT2 (Boxenbaum and Riegelman, 1976; Lauterburg et al., 1985b). For EM subjects, 7–9%, 39–43%, 0.4–1.6%, and 23% of INH and for PM subjects, 21–32%, 18–27%, 1.1–3.1%, and 3.1–5.1% of INH is excreted as INH, AcINH, AcHz, and diacetylhydrazine, respectively, 24 h after the administration of INH. In contrast, only 0.1–0.4% and 0.5–1.0% of INH is excreted as Hz in EM and PM subjects, respectively (Peretti et al., 1987). INH, AcINH, and its further metabolites account for the major amount of INH recovered from urine. Hence, PKs of INH and AcINH reflected the disposition of INH after administration in a Chinese population sample.

PPK models of INH in different populations have been developed. Both two-compartment (Zvada et al., 2014; Seng et al., 2015; Rodriguez et al., 2019; Jing et al., 2020; Sundell et al., 2020) and one-compartment models have been applied (Cojutti et al., 2017; Aruldhas et al., 2019). The K_a was 2.47–6.69 1/h, CL/F of various populations was 5.41–23.7 L/h, and Vd/F was 29.6–72.3 L. Models integrating INH and its metabolite are limited. Seng et al. (2015) established an integrated model for INH, AcINH and INA. A two-compartment model with the best description of the first-order absorption of INH PKs; A two- and one-compartment model was suitable for the description for AcINH and INA data, respectively. They found that NAT2 was a significant covariate for INH clearance, and

creatinine clearance was a significant covariate for AcINH clearance. However, only healthy subjects were included in their study. In the present study, for the first time, an integrated model of INH and AcINH was established in both healthy Chinese subjects and tuberculosis patients . Most Chinese subjects could be classified as EM subjects. INH concentration cannot be obtained 12 h after INH administration in these subjects. We found that a one-compartment model was sufficient for most subjects, and the two-compartment model was suggested to be over parameterized. The final integrated model consisted of three compartments, including one deposit compartment and one compartment each for INH and AcINH (**Figure 1**).

The typical value of CL/F obtained from the integrated model was 18.2 ± 2.45 $L{\cdot}h^{-1}$, which was comparable with previous studies. CL/F of INH included two parts: INH converted to AcINH and direct elimination through urine (**Figure 1**). F_M was used to reflect the part of INH converted to AcINH. It was a key parameter in the integrated model. Since in the present study, INH was administered orally and the part of INH excreted as the parent drug was not determined, F_M could not be determined directly. It should be noted that the exact value of clearance (CL_M/F) and Vd/F of AcINH is difficult to obtain. Using the present integrated model, CL_M/F could be estimated by multiplying K_{30} with V_3/F. The CL_{AcINH}/F in the present study was estimated as 11.3 $L{\cdot}h^{-1}$, which was similar to that of previous studies.

Polymorphisms in NAT2 activity are responsible for the inter-individual differences in INH PKs (Donald et al., 2007; Seng et al., 2015; Sundell et al., 2020) (14, 29, 30). Most early studies on NAT2 phenotypes classified the subjects as EMs and PMs. Smith et al. found that the activity of NAT2 showed a trimodal distribution (Smith et al., 1997). Kita et al. found that the urinary recovery of INH was lower in healthy volunteers and tuberculosis patients with a higher number of active *NAT2* alleles Kita et al. (2001). Kinzig-Schippers reported that the NAT2 genotypes accounted for 88% variation of INH clearance, which can be presented as: CL/F = 10 + 9 × (number of NAT2*4 alleles) (Kinzig-Schippers et al., 2005). Various *NAT2* SNPs are related to decreased expression and enzyme instability. Hein et al. suggested that catalytic activity of recombinant *NAT2* with 341C/C, 590A/A, and 857A/A genotypes were 10%, 19–42%, and 39–70% of that NAT2 wild type, respectively (Hein et al.,1994; Hein et al., 1995). It can be inferred that although both are classified as PM, the metabolic activity of NAT2 *7/*7 might be 3–6 times higher than that of *5/*5. In our previous study, the influence of various NAT2 SNPs on MR and INH PKs was analyzed using multiple regression. We found that *5(T341→C) allele had a more significant effect than *6(G590→A) and *7(G857→A) on MR_{SM2} and MR_{INH} (Chen et al., 2009). The results showed that various *NAT2* alleles had different impacts on NAT2 activity. In the present study, different *NAT2* genotypes were tested as covariates of CL/F and F_M. The results showed that OFV decreased, and the model simulation greatly improved. We found significant improvement upon classifying the *NAT2* genotype as wt/wt, m/wt, or m/m, or classification according to various *NAT2* alleles. In the final model, IIV of CL/F and F_M was significantly decreased from the basic model (from 56.6% to 28.1%, and 35.3%–9.82%, respectively). CL/F values of *4/*7, *4/*6, *5/*7, and *6/*6 subjects were approximately 74.8%, 54.9%, 34.6%, and 30.1% of *4/*4 subjects. F_M was 0.86 in *4/*4 subjects, which was 1.57 fold higher than that of the *4/*6 (0.55) subjects and more than two times higher than that of the *5/*7 (0.36) and *6/*6 (0.35) subjects. It can be deduced that more INH was converted to AcINH in subjects with more active *NAT2* genes. In addition, various NAT2 mutant alleles have different influences on the PKs of INH and AcINH.

A combination of different anti-tuberculosis drugs is usually used for the treatment of tuberculosis; Hence, drug-drug interaction should be considered. According to previous research, rifamycins may induce several metabolic pathways, including CYP3A4, uridine diphosphate glucuronosyltransferases (UGTs), and many transporters. However, there is no evidence of the impact of rifamycin on NAT2 activity and INH PK. On the other hand, pyrazinamide and ethambutol appear to have few significant drug interactions on INH. In our study, 21 healthy subjects were administered a compound preparation including isoniazid, rifampin and pyrazinamide. There was no significant difference in INH PK parameters of these subjects compared with 24 subjects given only INH.

TDM in INH could be helpful in achieving the desired therapeutic target. INH is a concentration-dependent antibiotic; AUC_{0-24} or C_{max} of INH is suggested as the TDM index. Limited sampling strategy models, based on multiple linear regression (MLR) or maximum a posteriori (MAP) analysis, were established for the estimation of AUC in patients who were administered INH. Alshaikheid et al. (2020)established an LSS model, based on 25 patients using the MLR analysis. They found that C_3, C_2-C_6, C_0- C_1-C_6 are suitable for estimation of INH AUC_{0-24h}. Cojutti et al. (2017)established a PPK model based on 185 adult tuberculosis patients. LSS models were estimated by the Bayesian method, and C_1-C_2-C_5 and C_1-C_2-C_9 were found to be most suitable. In the present study, concentration-time points were selected based on previous studies using the MAP method. For developed models including C_2 and C_2-C_6, the MPE % were −10.4% and −5.46%, respectively, and MRSE % ranged from 18.5% to 12.4%, indicating that the sampling strategies including C_2 and C_2-C_6 were clinically acceptable. The AUC_{0-24} values were 8.31 ± 4.12, 12.2 ± 5.16, and 27.0 ± 11.4 μg·h/ml for patients with wt/wt, m/wt, and m/m genotypes.

AUC_{0-24}/MIC is considered as the most important PK/PD index for INH. Dose-scheduling studies demonstrated that antimicrobial capacity of the INH was linked to the AUC_{0-24}/MIC (r^2 = 0.83) (Donald et al., 1997; Jayaram et al., 2004). In the present study, the AUC_{0-24} of INH in Chinese patients with various *NAT2* genotypes was estimated by the Bayesian method. A Monte Carlo method was used to simulate the effect of the standard dose of 300 mg, 600 mg, or 900 mg INH in tuberculosis patients. We found that, for each *NAT2* genotype, the probability of achieving the therapeutic goal was different (**Figure 5**). Ninety percent of patients with various *NAT2* genotypes achieved the target ratio only when the MIC of INH fell below 0.01 μg/ml. For *Mycobacterium tuberculosis* with an MIC of 0.02 μg/ml,

EC90 could be achieved for m/m patients who were administered 300 mg of the drug, m/wt patients who were administered 600 mg of the drug, and wt/wt patients who were administered 900 mg of INH. We also found a difference in PTA among patients with NAT2 m/m genotype. The results showed that different INH dosage regimens could be designed for patients with different *NAT2* genotypes. As there are many more patients with a *NAT2* wt/wt genotypes in the Chinese population, the INH dose should be higher for Chinese subjects. Due to differences in tissue penetration and immunity, INH levels in the site of action, including epithelial cells and macrophages in pulmonary compartments, may exceed those found in plasma. The optimal values for the AUC_{0-24}/MIC ratios may be different in the pulmonary compartment and more patients could achieve PTA (Honeybourne et al., 2001). When determining the optimal dose of INH, the efficacy and safety profiles of the drug should also be taken into account in the context of the contributions from other anti-tuberculosis drugs co-administered.

The present study does have a few limitations. First, only INH and AcINH concentration data were obtained. Although AcINH is the most important metabolite, if other metabolites, such as AcHZ and isonicortic acid were included, the established model might have provided more information. Second, there is still high bias of INH or AcINH prediction, especially in the first two hours. Because there were limited samples in the absorption phase, more elaborate absorption models were not applied, causing the PPK model to be inaccurate in predicting K_a and C_{max}. In addition, factors other than NAT2 genotype were not introduced as covariates in the final model. The influence of those missing factors may partly explain interindividual variation and residual error. Third, the correlation between INH or AcINH and adverse effects may be more valuable. However, we did not obtain that data from patients. Finally, although the determination of the MIC of patients is more valuable for dosing regimen design, we did not do this; hence, only reference data can be used.

CONCLUSION

The integrate parent-metabolite population PK model accurately characterized the PKs of INH and AcINH in a Chinese population sample. In a study with a larger number of patients, personalized medicine regimens can be designed, which may be used to increase efficiency and diminish the side effects of INH therapy in Chinese turboculosis patients.

DATA AVAILABILITY STATEMENT

The original contributions presented in the study are included in the article/Supplementary Materials, further inquiries can be directed to the corresponding author.

ETHICS STATEMENT

The studies involving human participants were reviewed and approved by Jinling Hospital Ethics Committee. The patients/participants provided their written informed consent to participate in this study.

AUTHOR CONTRIBUTIONS

BC and H-QS contributed to conception and design of the study and PK study. MF performed the statistical analysis. X-HW organized the database. X-MC determined isoniazid and NAT2 genotying. W-MC contributed to manuscript.

FUNDING

This study was supported by the National Natural Science Foundation of China (grant number: 81973387).

REFERENCES

Agúndez, J. A., Olivera, M., Martínez, C., Ladero, J. M., and Benítez, J. (1996). Identification and Prevalence Study of 17 Allelic Variants of the Human *NAT2* Gene in a White Population. *Pharmacogenetics* 6, 423–428.

Alshaikheid, M., Chaabane, A., Ben Fredj, N., Ben Brahim, H., Ben Fadhel, N., Chadli, Z., et al. (2020). Limited Sampling Strategy for Predicting Isoniazid Exposure in Patients with Extrapulmonary Tuberculosis. *J. Clin. Pharm. Ther.* 45, 503–512. doi:10.1111/jcpt.13098

Aruldhas, B. W., Hoglund, R. M., Ranjalkar, J., Tarning, J., Mathew, S. K., Verghese, V. P., et al. (2019). Optimization of Dosing Regimens of Isoniazid and Rifampicin in Children with Tuberculosis in India. *Br. J. Clin. Pharmacol.* 85, 644–654. doi:10.1111/bcp.13846

Bell, D. A., Taylor, J. A., Butler, M. A., Stephens, E. A., Wiest, J., Brubaker, L. H., et al. (1993). Genotype/phenotype Discordance for Human Arylamine N-Acetyltransferase (NAT2) Reveals a New Slow-Acetylator Allele Common in African-Americans. *Carcinogenesis* 14, 1689–1692. doi:10.1093/carcin/14.8.1689

Blomberg, B., Spinaci, S., Fourie, B., and Laing, R. (2001). The Rationale for Recommending Fixed-Dose Combination Tablets for Treatment of Tuberculosis. *Bull. World. Health. Organ.* 79, 61–68. doi:10.1590/S0042-96862001000100012

Boxenbaum, H. G., and Riegelman, S. (1976). Pharmacokinetics of Isoniazid and Some Metabolites in Man. *J. Pharmacokinet. Biopharm.* 4, 287–325. doi:10.1007/BF01063121

Cao, X. M., Chen, B., Leng, W. W., and Li, J. H. (2005). Simultaneous Determination of Isoniazid and Acetylisoniazid in Plasma with HPLC. *J. Med. Postgr.* 18, 397–398. doi:10.3969/j.issn.1008-8199.2005.05.005

Chakaya, J., Khan, M., Ntoumi, F., Aklillu, E., Fatima, R., Mwaba, P., et al. (2021). Global Tuberculosis Report 2020 - Reflections on the Global TB Burden, Treatment and Prevention Efforts. *Int. J. Infect. Dis.* 113, S7–S12. doi:10.1016/j.ijid.2021.02.107

Chen, B., Cai, W., Li, J., and Cao, X. (2009). Estimating N-Acetyltransferase Metabolic Activity and Pharmacokinetic Parameters of Isoniazid from Genotypes in Chinese Subjects. *Clin. Chim. Acta* 405, 23–29. doi:10.1016/j.cca.2009.03.045

Chen, B., Zhang, W. X., and Cai, W. M. (2006). The Influence of Various Genotypes on the Metabolic Activity of NAT2 in a Chinese Population. *Eur. J. Clin. Pharmacol.* 62, 355–359. doi:10.1007/s00228-006-0110-6

Chen, B., Li, J. H., Huang, J., and Cao, X. M. (2004). A One-step Allele Specific Amplificaton for Genotyping of *NAT2* in Chinese Subjects. *Chin. J. Clin. Pharmacol.* 20, 49–52. doi:10.3969/j.issn.1001-6821.2004.01.012

Cojutti, P., Giangreco, M., Isola, M., and Pea, F. (2017). Limited Sampling Strategies for Determining the Area Under the Plasma Concentration-Time

Curve for Isoniazid Might Be a Valuable Approach for Optimizing Treatment in Adult Patients With Tuberculosis. *Int. J. Antimicrob. Agents.* 50, 23–28. doi:10.1016/j.ijantimicag.2017.01.036

Deguchi, T., Mashimo, M., and Suzuki, T. (1990). Correlation between Acetylator Phenotypes and Genotypes of Polymorphic Arylamine N-Acetyltransferase in Human Liver. *J. Biol. Chem.* 265, 12757–12760. doi:10.1016/s0021-9258(19)38219-5

Denti, P., Jeremiah, K., Chigutsa, E., Faurholt-Jepsen, D., PrayGod, G., Range, N., et al. (2015). Pharmacokinetics of Isoniazid, Pyrazinamide, and Ethambutol in Newly Diagnosed Pulmonary TB Patients in Tanzania. *PLoS. One.* 10, e0141002. doi:10.1371/journal.pone.0141002

Donald, P. R., Parkin, D. P., Seifart, H. I., Schaaf, H. S., van Helden, P. D., Werely, C. J., et al. (2007). The Influence of Dose and N-Acetyltransferase-2 (NAT2) Genotype and Phenotype on the Pharmacokinetics and Pharmacodynamics of Isoniazid. *Eur. J. Clin. Pharmacol.* 63, 633–639. doi:10.1007/s00228-007-0305-5

Donald, P. R., Sirgel, F. A., Botha, F. J., Seifart, H. I., Parkin, D. P., Vandenplas, M. L., et al. (1997). The Early Bactericidal Activity of Isoniazid Related to its Dose Size in Pulmonary Tuberculosis. *Am. J. Respir. Crit. Care. Med.* 156, 895–900. doi:10.1164/ajrccm.156.3.9609132

Ferguson, L. A., and Rhoads, J. (2009). Multidrug-resistant and Extensively Drug-Resistant Tuberculosis: The New Face of an Old Disease. *J. Am. Acad. Nurse. Pract.* 21, 603–609. doi:10.1111/j.1745-7599.2009.00458.x

Gumbo, T., Louie, A., Liu, W., Brown, D., Ambrose, P. G., Bhavnani, S. M., et al. (2007). Isoniazid Bactericidal Activity and Resistance Emergence: Integrating Pharmacodynamics and Pharmacogenomics to Predict Efficacy in Different Ethnic Populations. *Antimicrob. Agents. Chemother.* 51, 2329–2336. doi:10.1128/AAC.00185-07

Gumbo, T. (2010). New Susceptibility Breakpoints for First-Line Antituberculosis Drugs Based on Antimicrobial Pharmacokinetic/Pharmacodynamic Science and Population Pharmacokinetic Variability. *Antimicrob. Agents. Chemother.* 54, 1484–1491. doi:10.1128/AAC.01474-09

Hao, L. H., Guo, S. C., Liu, C. C., Zhu, H., Wang, B., Fu, L., et al. (2014). Comparative Bioavailability of Rifampicin and Isoniazid in Fixed-Dose Combinations and Single-Drug Formulations. *Int. J. Tuberc. Lung. Dis.* 18, 1505–1512. doi:10.5588/ijtld.13.0647

Hein, D. W., Doll, M. A., Rustan, T. D., and Ferguson, R. J. (1995). Metabolic Activation of N-Hydroxyarylamines and N-Hydroxyarylamides by 16 Recombinant Human NAT2 Allozymes: Effects of 7 Specific *NAT2* Nucleic Acid Substitutions. *Cancer. Res.* 55, 3531–3536.

Hein, D. W., Ferguson, R. J., Doll, M. A., Rustan, T. D., and Gray, K. (1994). Molecular Genetics of Human Polymorphic N-Acetyltransferase: Enzymatic Analysis of 15 Recombinant Wild-type, Mutant, and Chimeric NAT2 Allozymes. *Hum. Mol. Genet.* 3, 729–734. doi:10.1093/hmg/3.5.729

Honeybourne, D., Banerjee, D., Andrews, J., and Wise, R. (2001). Concentrations of Gatifloxacin in Plasma and Pulmonary Compartments Following a Single 400 Mg Oral Dose in Patients Undergoing Fibre-Optic Bronchoscopy. *J. Antimicrob. Chemother.* 48, 63–66. doi:10.1093/jac/48.1.63

Horai, Y., Ishizaki, T., Sasaki, T., Koya, G., Matsuyama, K., and Iguchi, S. (1982). Isoniazid Disposition, Comparison of Isoniazid Phenotyping Methods in and Acetylator Distribution of Japanese Patients with Idiopathic Systemic Lupus Erythematosus and Control Subjects. *Br. J. Clin. Pharmacol.* 13, 361–374. doi:10.1111/j.1365-2125.1982.tb01387.x

Jayaram, R., Shandil, R. K., Gaonkar, S., Kaur, P., Suresh, B. L., Mahesh, B. N., et al. (2004). Isoniazid Pharmacokinetics-Pharmacodynamics in an Aerosol Infection Model of Tuberculosis. *Antimicrob. Agents. Chemother.* 48, 2951–2957. doi:10.1128/AAC.48.8.2951-2957.2004

Jing, W., Zong, Z., Tang, B., Wang, J., Zhang, T., Wen, S., et al. (2020). Population Pharmacokinetic Analysis of Isoniazid Among Pulmonary Tuberculosis Patients from China. *Antimicrob. Agents. Chemother.* 64, e01736–19. doi:10.1128/AAC.01736-19

Kinzig-Schippers, M., Tomalik-Scharte, D., Jetter, A., Scheidel, B., Jakob, V., Rodamer, M., et al. (2005). Should We Use N-Acetyltransferase Type 2 Genotyping to Personalize Isoniazid Doses? *Antimicrob. Agents. Chemother.* 49, 1733–1738. doi:10.1128/AAC.49.5.1733-1738.2005

Kiser, J. J., Zhu, R., D'Argenio, D. Z., Cotton, M. F., Bobat, R., McSherry, G. D., et al. (2012). Isoniazid Pharmacokinetics, Pharmacodynamics, and Dosing in South African Infants. *Ther. Drug. Monit.* 34, 446–451. doi:10.1097/FTD.0b013e31825c4bc3

Kita, T., Tanigawara, Y., Chikazawa, S., Hatanaka, H., Sakaeda, T., Komada, F., et al. (2001). N-Acetyltransferase2 Genotype Correlated with Isoniazid Acetylation in Japanese Tuberculous Patients. *Biol. Pharm. Bull.* 24, 544–549. doi:10.1248/bpb.24.544

Lauterburg, B. H., Smith, C. V., Todd, E. L., and Mitchell, J. R. (1985b). Oxidation of Hydrazine Metabolites Formed from Isoniazid. *Clin. Pharmacol. Ther.* 38, 566–571. doi:10.1038/clpt.1985.225

Lauterburg, B. H., Smith, C. V., Todd, E. L., and Mitchell, J. R. (1985a). Pharmacokinetics of the Toxic Hydrazino Metabolites Formed from Isoniazid in Humans. *J. Pharmacol. Exp. Ther.* 235, 566–570.

Lin, H. J., Han, C. Y., Lin, B. K., and Hardy, S. (1993). Slow Acetylator Mutations in the Human Polymorphic N-Acetyltransferase Gene in 786 Asians, Blacks, Hispanics, and Whites: Application to Metabolic Epidemiology. *Am. J. Hum. Genet.* 52, 827–834.

Loktionov, A., Moore, W., Spencer, S. P., Vorster, H., Nell, T., O'Neill, I. K., et al. (2002). Differences in *N*-Acetylation Genotypes between Caucasians and Black South Africans: Implications for Cancer Prevention. *Cancer. detect. Prev.* 26, 15–22. doi:10.1016/s0361-090x(02)00010-7

McIlleron, H., Wash, P., Burger, A., Norman, J., Folb, P. I., and Smith, P. (2006). Determinants of Rifampin, Isoniazid, Pyrazinamide, and Ethambutol Pharmacokinetics in a Cohort of Tuberculosis Patients. *Antimicrob. Agents. Chemother.* 50, 1170–1177. doi:10.1128/AAC.50.4.1170-1177.2006

Mitchison, D. A. (1979). Basic Mechanisms of Chemotherapy. *Chest* 76 (Suppl. l), 771–781. doi:10.1378/chest.76.6_supplement.771

Parkin, D. P., Vandenplas, S., Botha, F. J., Vandenplas, M. L., Seifart, H. I., van Helden, P. D., et al. (1997). Trimodality of Isoniazid Elimination: Phenotype and Genotype in Patients with Tuberculosis. *Am. J. Respir. Crit. Care. Med.* 155, 1717–1722. doi:10.1164/ajrccm.155.5.9154882

Pasipanodya, J., and Gumbo, T. (2011). An Oracle: Antituberculosis Pharmacokinetics-Pharmacodynamics, Clinical Correlation, and Clinical Trial Simulations to Predict the Future. *Antimicrob. Agents. Chemother.* 55, 24–34. doi:10.1128/AAC.00749-10

Peloquin, C. A. (2002). Therapeutic Drug Monitoring in the Treatment of Tuberculosis. *Drugs* 62, 2169–2183. doi:10.2165/00003495-200262150-00001

Peretti, E., Karlaganis, G., and Lauterburg, B. H. (1987). Increased Urinary Excretion of Toxic Hydrazino Metabolites of Isoniazid by Slow Acetylators. Effect of a Slow-Release Preparation of Isoniazid. *Eur. J. Clin. Pharmacol.* 33, 283–286. doi:10.1007/BF00637563

Rodriguez, C. A., Zuluaga, A. F., Neely, M. N., Sierra, Y., Morales-Gutierrez, J., Zapata, J., et al. (2019). Nonparametric Population Pharmacokinetic Modeling of Isoniazid in Colombian Patients With Tuberculosis. *Ther. Drug. Monit.* 41, 719–725. doi:10.1097/FTD.0000000000000661

Sandhu, G. K. (2011). Tuberculosis: Current Situation, Challenges and Overview of its Control Programs in India. *J. Glob. Infect. Dis.* 3, 143–150. doi:10.4103/0974-777X.81691

Seng, K. Y., Hee, K. H., Soon, G. H., Chew, N., Khoo, S. H., and Lee, L. S. (2015). Population Pharmacokinetic Analysis of Isoniazid, Acetylisoniazid, and Isonicotinic Acid in Healthy Volunteers. *Antimicrob. Agents. Chemother.* 59, 6791–6799. doi:10.1128/AAC.01244-15

Shishoo, C. J., Shah, S. A., Rathod, I. S., Savale, S. S., and Vora, M. J. (2001). Impaired Bioavailability of Rifampicin in Presence of Isoniazid from Fixed Dose Combination (FDC) Formulation. *Int. J. Pharm.* 228, 53–67. doi:10.1016/s0378-5173(01)00831-6

Smith, C. A., Wadelius, M., Gough, A. C., Harrison, D. J., Wolf, C. R., and Rane, A. (1997). A Simplified Assay for the Arylamine N-Acetyltransferase 2 Polymorphism Validated by Phenotyping with Isoniazid. *J. Med. Genet.* 34, 758–760. doi:10.1136/jmg.34.9.758

Sundell, J., Bienvenu, E., Janzén, D., Birgersson, S., Äbelö, A., and Ashton, M. (2020). Model-Based Assessment of Variability in Isoniazid Pharmacokinetics and Metabolism in Patients Co-Infected With Tuberculosis and HIV: Implications for a Novel Dosing Strategy. *Clin. Pharmacol. Ther.* 108, 73–80. doi:10.1002/cpt.1806

Takayama, K., Wang, L., and David, H. L. (1972). Effect of Isoniazid on the *In Vivo* Mycolic Acid Synthesis, Cell Growth, and Viability of *Mycobacterium tuberculosis*. *Antimicrob. Agents Chemother.* 2, 29–35. doi:10.1128/AAC.2.1.29

Timbrell, J. A., Mitchell, J. R., Snodgrass, W. R., and Nelson, S. D. (1980). Isoniazid Hepatoxicity: the Relationship between Covalent Binding and Metabolism *In Vivo*. *J. Pharmacol. Exp. Ther.* 213, 364–369.

Walker, K., Ginsberg, G., Hattis, D., Johns, D. O., Guyton, K. Z., and Sonawane, B. (2009). Genetic Polymorphism in N-Acetyltransferase (NAT): Population Distribution of NAT1 and NAT2 Activity. *J. Toxicol. Environ. Health. B. Crit. Rev.* 12, 440–472. doi:10.1080/10937400903158383

Weiner, M., Burman, W., Vernon, A., Benator, D., Peloquin, C. A., Khan, A., et al. (2003). Low Isoniazid Concentrations and Outcome of Tuberculosis Treatment with Once-Weekly Isoniazid and Rifapentine. *Am. J. Respir. Crit. Care. Med.* 167, 1341–1347. doi:10.1164/rccm.200208-951OC

Winder, F. G., and Collins, P. B. (1970). Inhibition by Isoniazid of Synthesis of Mycolic Acids in *Mycobacterium tuberculosis*. *J. Gen. Microbiol.* 63, 41–48. doi:10.1099/00221287-63-1-41

Zhao, J. J., and Lu, Y. (2019). Research and Progress of PK/PD for Anti-tuberculosis Drugs. *Chin. J. Antituberc.* 41, 700–704. doi:10.3969/j.issn.1000-6621.2019.06.020

Zuur, M. A., Bolhuis, M. S., Anthony, R., den Hertog, A., van der Laan, T., Wilffert, B., et al. (2016). Current Status and Opportunities for Therapeutic Drug Monitoring in the Treatment of Tuberculosis. *Expert. Opin. Drug. Metab. Toxicol.* 12, 509–521. doi:10.1517/17425255.2016.1162785

Zvada, S. P., Denti, P., Donald, P. R., Schaaf, H. S., Thee, S., Seddon, J. A., et al. (2014). Population Pharmacokinetics of Rifampicin, Pyrazinamide and Isoniazid in Children With Tuberculosis: In Silico Evaluation of Currently Recommended Doses. *J. Antimicrob. Chemother.* 69, 1339–1349. doi:10.1093/jac/dkt524

Conflict of Interest: The authors declare that the research was conducted in the absence of any commercial or financial relationships that could be construed as a potential conflict of interest.

Publisher's Note: All claims expressed in this article are solely those of the authors and do not necessarily represent those of their affiliated organizations, or those of the publisher, the editors and the reviewers. Any product that may be evaluated in this article, or claim that may be made by its manufacturer, is not guaranteed or endorsed by the publisher.

frontiers | Frontiers in Pharmacology

TYPE Original Research
PUBLISHED 22 July 2022
DOI 10.3389/fphar.2022.969408

OPEN ACCESS

EDITED BY
Zipeng Gong,
Guizhou Medical University, China

REVIEWED BY
Weifeng Yao,
Nanjing University of Chinese Medicine, China
Chenchen Zhu,
Guangzhou University of Chinese Medicine, China

*CORRESPONDENCE
Yan Wang,
awangyan@aliyun.com
Hong Wu,
wuhongprof@aliyun.com

SPECIALTY SECTION
This article was submitted to Drug Metabolism and Transport, a section of the journal Frontiers in Pharmacology

RECEIVED 15 June 2022
ACCEPTED 04 July 2022
PUBLISHED 22 July 2022

CITATION
Ke J-T, Zhang H, Bu Y-H, Gan P-R, Chen F-Y, Dong X-T, Wang Y and Wu H (2022), Metabonomic analysis of abnormal sphingolipid metabolism in rheumatoid arthritis synovial fibroblasts in hypoxia microenvironment and intervention of geniposide.
Front. Pharmacol. 13:969408.
doi: 10.3389/fphar.2022.969408

Metabonomic analysis of abnormal sphingolipid metabolism in rheumatoid arthritis synovial fibroblasts in hypoxia microenvironment and intervention of geniposide

Jiang-Tao Ke[1,2,3,4], Heng Zhang[1,2,3,4], Yan-Hong Bu[1,2,3,4], Pei-Rong Gan[1,2,3,4], Fang-Yuan Chen[1,2,3,4], Xin-Tong Dong[1,2,3,4], Yan Wang[1,2,3,4]* and Hong Wu[1,2,3,4]*

[1]Key Laboratory of Xin'an Medicine, Ministry of Education, Hefei, China, [2]College of Pharmacy, Anhui University of Chinese Medicine, Hefei, China, [3]Anhui Province Key Laboratory of Research & Development of Chinese Medicine, Hefei, China, [4]Anhui Province Key Laboratory of Chinese Medicinal Formula, Hefei, China

Rheumatoid arthritis (RA) is a chronic inflammatory disease characterized by a joint hypoxia microenvironment. Our previous untargeted metabolomics study found that sphingolipid (SPL) metabolism was abnormal in the joint synovial fluid samples from adjuvant arthritis (AA) rats. Geniposide (GE), an iridoid glycoside component of the dried fruit of *Gardenia jasminoides* Ellis, is commonly used for RA treatment in many Asian countries. At present, the mechanism of GE in the treatment of RA, especially in the joint hypoxia microenvironment, is not entirely clear from the perspective of SPL metabolism. The purpose of this research was to explore the potential mechanism of abnormal SPL metabolism in RA joint hypoxia microenvironment and the intervention effect of GE, through the untargeted metabolic analysis based on the ultra-performance liquid chromatography-quadrupole time-of-flight mass spectrometry (UPLC-Q-TOF/MS). Arthritis index, foot swelling and histopathology were used to assess whether the AA rat model was successfully established. The SPLs extracts collected from AA rats' synovial tissue, serum and rheumatoid arthritis synovial fibroblasts (RASFs, MH7A cells, hypoxia/normoxia culture) were analyzed by metabolomics and lipdomics approach based on UPLC-Q-TOF/MS, to identify potential biomarkers associated with disorders of GE regulated RA sphingolipid

Abbreviations: AA, adjuvant arthritis; Cer, ceramide; DSA, D-sphinganine; GE, geniposide; HIF1α, hypoxia-inducible factor-1α; IL-1β, interleukin-1β; IFN-γ, interferon-γ; MTX, methotrexate; OPLS-DA, orthogonal partial least-squares discriminant analysis; PCA, principal component analysis; PEA, palmitoyl ethanolamine; QC, quality control; RA, rheumatoid arthritis; RASFs, rheumatoid arthritis synovial fibroblasts; RSD, relative standard deviation; SM, sphingomyelin; SMase, sphingomyelinase; S1P, sphingosine 1-phosphate; SPL, sphingolipid; TCM, traditional Chinese medicines; TNF-α, tumor necrosis factor-α; UPLC-Q-TOF/MS, ultra-performance liquid chromatography-quadrupole time-of-flight mass spectrometry.

metabolism. As a result, 11 sphingolipid metabolites related to RA were screened and identified. Except for galactosylceramide (d18:1/20:0), GE could recover the change levels of the above 10 sphingolipid biomarkers in varying degrees. Western blotting results showed that the changes in ceramide (Cer) level regulated by GE were related to the down-regulation of acid-sphingomyelinase (A-SMase) expression in synovial tissue of AA rats. To sum up, this research examined the mechanism of GE in the treatment of RA from the perspective of SPL metabolism and provided a new strategy for the screening of biomarkers for clinical diagnosis of RA.

KEYWORDS

rheumatoid arthritis, sphingolipid, metabolomics, geniposide, UPLC-Q-TOF/MS

Introduction

Rheumatoid arthritis (RA) is a common autoimmune disease whose main pathological features are abnormal hyperplasia of synovial tissue, persistent synovial inflammation, angiogenesis and pannus formation (Scott et al., 2010). The inflammatory response is the most common stress response when tissue is damaged, which plays an important role in the occurrence and development of RA (Wang L. et al., 2021). A large number of inflammatory factors such as hypoxia-inducible factor-1α (HIF-1α), tumor necrosis factor-α (TNF-α) and interleukin-1β (IL-1β) filled with synovitis microenvironment, they directly broke the balance of normal synovial metabolism (Qu et al., 2021; Tsuchiya et al., 2021). Rheumatoid arthritis synovial fibroblasts (RASFs) are the main effector cells of RA. Under the pathological state, they show the phenomenon of excessive proliferation and insufficient apoptosis, which makes the synovial tissue proliferate and hypertrophy, increases the oxygen consumption and produces an "anoxic microenvironment", resulting in the formation of a large number of synovial microvessels with abnormal structure and function, and aggravates synovial inflammation (Chen et al., 2021). In recent years, an increasing number of studies have shown that hypoxia-mediated metabolic disorders play an important role in the pathogenesis of RA. The finding of drugs that regulate metabolic disorders may help improve the disease process in RA patients.

Geniposide (GE), a kind of iridoid compound, is one of the main active components in *Gardenia jasminoides* Ellis, with anti-inflammatory, anti-allergic and immunosuppressive and other pharmacological effects (Deng et al., 2021). In Our previous studies, untargeted metabolomic analysis based on hydrophilic interaction liquid chromatography coupled to high-resolution mass spectrometry (HILIC-HRMS) was performed using the joint synovial fluid samples from adjuvant arthritis (AA) rats. It was found that 20 metabolites differed significantly between AA rats and normal rats, which were mainly involved in glycerophospholipid metabolism, sphingolipid metabolism and purine metabolism. GE could reverse the levels of 13 metabolites in AA rats, including palmitoyl ethanolamine (PEA), ceramide (Cer) and phenylacetic acid, and showed the ability to regulate unbalanced sphingolipid metabolism (Zhan et al., 2020). In addition, GE alleviated inflammation in AA rats by modulating the sphingolipid metabolic pathway and reducing the levels of sphingomyelin (SM) in jugular vein micro-dialysates and Cer and D-sphingomyelin (DSA) in knee micro-dialysates (Wang R. H. et al., 2020; Wang M. et al., 2021). In conclusion, the above studies showed that GE can regulate the biological level of Sphingolipids (SPLs) in AA rats.

Hypoxia is one of the key features of the intra-articular microenvironment in RA (Deng et al., 2022). In addition, SPLs are of interest as important cellular mediators of inflammatory hypoxia, and hypoxia is capable of disrupting sphingolipid metabolism in different organisms (e.g., increased SIP levels and decreased Cer levels in vascular smooth muscle cells under hypoxia conditions) to accelerate disease progression (Yun and Kester, 2002; Ottolenghi et al., 2020). SPLs are the most abundant class of bioactive lipids in living organisms, which are essential regulators of physiological and pathological processes including cell cycle, angiogenesis and inflammatory responses (Hannun and Obeid, 2018). There are two main production modes: sphingomyelin metabolism and *de novo* synthesis of serine and palmitoyl acyl-CoA (Mortimer and Scheller, 2020). Sphingolipid metabolites, especially Cer, sphingosine and sphingosine 1-phosphate (S1P), are important signal molecules in cell signal transduction, cell proliferation and apoptosis. These cellular processes are highly crucial in immune-inflammatory diseases (Maceyka and Spiegel, 2014; Skácel et al., 2021). Recently, people have a new understanding of the molecular mechanism of sphingolipid metabolites and their regulation of chronic inflammation, which will be more conducive to the development of new treatments for inflammatory diseases.

Metabolomics, the research of small-molecule metabolites (relative molecular mass less than 1000) in complex biological systems, is a plausible approach to elucidate the full range of metabolic changes induced by pathophysiological stimuli to biological systems (Jang et al., 2018). In particular, with the advantages of high resolution, high sensitivity, high reproducibility and less sample requirements, UPLC-Q-TOF/

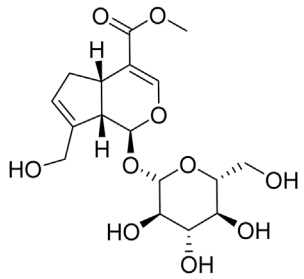

FIGURE 1
Chemical structure of geniposide.

MS has become the tool of choice for studying disease-related changes in metabolic pathways and for the discovery of endogenous metabolites (Rinschen et al., 2019; Wang et al., 2019; Yin et al., 2022). The investigation of functional endogenous metabolites in biological systems using HRMS combined with multivariate statistical analysis to identify potential biomarkers associated with the disease can provide valuable information about the pathological mechanisms and pharmacological interventions in complex diseases (Zhao et al., 2018). Lipidomics, as a separate discipline from metabolomics, specializes in the study of lipid changes in living organisms under physiological pathology and provides comprehensive lipid information in biological samples (Wang R. et al., 2020). Currently, metabolomics and lipidomics have been widely used in the study of the mechanism of active molecules in traditional Chinese medicine (TCM) (Wu et al., 2020). Numerous metabolomics studies have shown that the abnormal metabolism of RA is related to sphingolipid metabolism. Therefore, the integration of metabolomics and lipidomics can reveal the sphingolipid biomarkers of RA treatment in a more comprehensive and integrated manner.

In this study, we established a rat's model of adjuvant arthritis (AA) and a hypoxia model of MH7A cells using a hypoxia incubator to simulate the hypoxia microenvironment in the joint cavity of RA patients. Subsequently, a UPLC-Q-TOF/MS based metabolomics and lipidomics platform was employed to investigate the potential sphingolipid markers in AA rat synovial tissue, serum, and hypoxia cultured MH7A cells to reveal the mechanism of GE treatment for RA from the perspective of abnormal metabolism of SPLs.

Materials and methods

Materials and reagents

GE ($C_{17}H_{24}O_{10}$, molecular weight: 388, Purity >98%, batch number: S25627, structure shown in Figure 1) and Urethane (batch number: 20200710) were purchased from the National Institute for the Control of Pharmaceutical and Biological Products (Beijing, China). Methotrexate (MTX) (batch number: B25455) was provided by Yuanye Biotechnology Co., Ltd. (Shanghai, China). Formic acid (batch number: 100264) was obtained from Merck Chemical Technology Co., Ltd. (Shanghai, China). Freund's Complete Adjuvant (FCA) (batch number: F5881) was obtained from Sigma-Aldrich (St. Louis, MO, United States). LC-MS grade acetonitrile (batch number: A104443), methyl tert-butyl ether (MTBE, batch number: B108120), Methanol (batch number: M116126), and Isopropanol (batch number: I112020) were provided by Aladdin Bio-Chem Technology Co., Ltd. (Shanghai, China). Ultrapure water was produced by a Milli-Q Gradient A10 Ultrapure Water System (MILLIPORE Co., Ltd., United States). Dulbecco's modified Eagle's medium (DMEM) for MH7A cells culture was purchased from Hy Clone (Logan, UT, United States). Fetal bovine serum (FBS) was provided by Biological Industries Co., Ltd. (Kibbutz BH, Israel).

Establishment and evaluation of adjuvant arthritis rat model

Male Sprague-Dawley rats (180–220 g, Grade Ⅱ) were provided by the Experimental Animal Center of Anhui University of Traditional Chinese Medicine (Hefei, China). The rats were housed under the conditions of temperature at 25 ± 1°C and 45–55% relative humidity for 12 h light/12 h darkness cycles. All rats were kept under this condition for at least one week before the experiment. The experimental protocol was approved by the Animal Ethics Committee of Anhui University of Traditional Chinese Medicine (No. AHTCM-rats-2021049) and all experimental methods were carried out by following the animal experiment operation guidelines. The rat's left hind toe received a subcutaneous injection of 100 μL of FCA on day 0, and the control group rats were injected with 100 μL of physiological saline at the same time (Deng et al., 2018). On the 16th day, the rats were randomly divided into four groups (n = 24): normal control group, model group, GE (60 mg/kg/day, 14 days, intragastrically (ig)) group and MTX (positive medicine) group (0.5 mg/kg, three times a week, 14 days, ig), on day 7, day 14, day 17, day 20, day 23, day 26, day 29, the arthritis index and secondary paw swelling of the four groups of rats were evaluated. The arthritis index and secondary paw swelling of all rats were measured by two groups of relatively independent experimenters. The secondary paw swelling of the right-hand paw was calculated as (ΔmL = paw volume after modeling − paw volume before modeling). The scoring standard of the arthritis index was determined based on our past research (Li et al., 2018). On the 29th day, 2 h after the end of intragastric administration, all rats were anesthetized with 20% urethane, blood was taken from

the abdominal aorta, synovial tissues were taken, and sacrificed by cervical dislocation.

Culture of MH7A cells

RASFs (MH7A cells) were purchased from Bena Chuang Lian Biotechnology Company. The cells were cultured in DMEM medium containing 5% FBS (Biological Industries, ISR) and 1% penicillin-streptomycin (Beyotime Biotechnology) solution. MH7A cells with good growth status were divided into the normoxia/hypoxia group and normoxia/hypoxia administration group (GE, 50 μM), and the oxygen concentration was 21 and 2% in the normoxia and hypoxia groups, respectively. After each group of cells had grown to the bottom of the dish, the medium was aspirated and rinsed 3 times with cold PBS (9 ml). MH7A cells were immediately quenched with liquid nitrogen to inhibit enzymatic activity. Subsequently, cells were scraped off in 1 ml of cold methanol/H_2O (2:1, v/v). The cells were then crushed using an ultrasonic crusher (instrument parameters: operation 5 s, operation times: 4, interval 4 s). Subsequently, 1.5 ml of methanol was added and vortexed in an ice water bath for 30 s (repeated 6 times). MTBE/H_2O (4:1, v/v) was used as a solvent to extract the SPL metabolites from MH7A cells. Each EP tube was vortexed for 30 s in an ice bath and allowed to stand at room temperature for 10 min. After sample centrifugation (4°C, 15,000 rpm, 10 min), the supernatant was transferred to a 1.5 ml EP tube and allowed to stand at −80°C for 24 h. After layering, the supernatant was dried using a vacuum centrifuge dryer and re-dissolved in 200 μL methanol, then centrifuged (4°C, 15,000 rpm, 10 min) and the supernatant was transferred into sample vial.

Sample preparation

The rats were anesthetized after the last administration, blood was taken from the abdominal aorta and the synovial tissue of the left hind limb was taken out. The blood sample was allowed to stand for 1 h, then centrifuged (4°C, 3,000 rpm, 10 min) and the supernatant was aspirated for later use. After the synovial tissue was taken out, it was quenched with liquid nitrogen immediately, and then thoroughly ground with methanol and transferred into an EP tube. The samples were stored at −80°C. Before analysis, the sample was dried with a vacuum centrifugal dryer, the residue was re-dissolved in methanol, vortexed, and then centrifuged (4°C, 15,000 rpm, 10 min). 100 μL of all samples were taken and placed into different numbered injection vials for subsequent UPLC-Q-TOF/MS analysis. In order to monitor the stability of the instrument during the experiment, 10 μL of each group of samples of serum and synovium were mixed and transferred to a sample vial as a quality control (QC) sample. The QC sample was injected five times before the formal injection and once every four samples in the analysis sequence. The coefficient of variation of each characteristic metabolite in the QC sample should be calculated to be less than 30%.

UPLC-Q-TOF/MS analysis

All samples were analyzed by using the Acquity UPLC system (WATERS, Milford, United States) connected to Xevo G2-XS Q/TOF mass spectrometer (ACQUITY, WATERS, United States). A Phenomenex column (C18, 100 × 2.1 mm, 1.6 μm) was used for sample separation. The mobile phase consisted of solvent A (50% acetonitrile and water containing 0.1% formic acid) and solvent B (95% isopropanol and 5% acetonitrile). The flow rate was 0.1 ml/min. The injection volume of each sample was 1 μL and the column temperature was set to 35°C. Sequence analysis was conducted for each sample with interactive insertion. The mobile phase gradient was set as follows: 10% B at 0–3 min, 10%–30% B at 3–5 min, 30%–60% B at 5–6 min, 60%–80% B at 6–12 min, 80%–90% B at 12–18 min, 90%–100% B at 18–20 min, 100%–20% B at 20–24 min, 10% B at 24–30 min. The mass detection was performed in the positive (ESI^+) and negative (ESI^-) ion modes and the parameters were set as follows: source temperature, 120°C (ESI^+)/110°C (ESI^-); dry gas temperature, 350°C; capillary voltage, 2.5 kV (ESI^+)/2.0 kV (ESI^-); gas flow, 600 L/h; Impact energy voltage, 6 V (low)/20–30 V (high); quality scan range 50–1200 m/*z*. The correction method was used in all analyses to ensure the accuracy and repeatability of quality. Leucine enkephalin (200 ng/ml) was used to establish mass spectrometer calibration and reference mass.

Metabolomics data processing and analysis

The raw data collected by UPLC-Q-TOF/MS (ESI^+ and ESI^- modes) into the Progenesis QI V2.0 software (Waters Corp., Milford, United States) using baseline filtering, peak identification and correction functions to obtain a data matrix of retention time (t_R), mass-to-charge ratio and peak intensity. Multivariate statistical analysis was performed by EZinfo 3.0 software. First, unsupervised principal component analysis (PCA) was used to observe the overall distribution between groups of samples and the stability of the entire analysis process, and then supervised orthogonal partial least squares-discriminant analysis (OPLS-DA) was used to distinguish the overall differences in metabolic profiles between groups and to look for metabolites that differed between groups. The statistically significant differential metabolites ($p < 0.05$, fold changes ≥1.5, CV < 30%, VIP-value>1) and their ion fragments at high and low collision energy were matched with Human

Metabolomics Database (HMDB) (https://hmdb.ca/) and self-built database to confirm the differential sphingolipid metabolites. Potential biomarkers associated with GE processing were analyzed by MetaboAnalyst 4.0 (http://www.metaboanalyst.ca) and Kyoto Encyclopedia of Genes and Genomes (KEGG) database (http://www.kegg.jp) and a metabolic network was constructed according to the relationships among the identified potential biomarkers.

Western blotting

To further explore the mechanisms underlying the effects of GE on sphingolipid metabolism, rat synovial tissues were used to perform Western blotting to validate target proteins of interest. Synovial tissues were dissolved with RAPI buffer (containing 1% PMSF) and incubated in ice bath for 30 min to extract total proteins. Total protein concentration was next determined by BCA protein assay kit (Beyotime Biotechnology Corporation Co., Ltd., Shanghai, China). Equal amounts of protein samples were separated by 10% sodium dodecyl-sulfate-polyacrylamide gel electrophoresis (SDS-PAGE) and transferred to Bio Trace nitrocellulose (NC) by electrophoresis membranes. Membranes were blocked with 5% nonfat milk for 2 h at 37°C and subsequently incubated with specific antibodies recognizing acid-sphingomyelinase (A-SMase) overnight at 4°C, followed by horseradish peroxidase-conjugated secondary antibodies. Bands of interest were detected by enhanced chemiluminescence and analyzed with ImageJ software. The values of each target protein were normalized to *ß*-actin.

Date analysis

All values in the text and figure are represented by mean ± standard deviation (SD). SPSS 23.0 was used to analyze experimental data and compare the differences between the two groups, using student's *t*-test and One-way ANOVA test. $p < 0.05$ was considered statistically significant.

Results

The therapeutic effect of GE on adjuvant arthritis rats

Studies have shown that the arthritis index and secondary foot swelling of AA rats were significantly higher than those of the normal group, and reached their peak on the 23rd day (Figure 2A,B). The histopathological results of synovial tissue showed that the arrangement of synovial cells in AA rats was disordered, accompanied by inflammatory cell infiltration and the formation of pannus (Figure 2C). These results indicated that we successfully established the AA rat model. Compared with the model group, GE and MTX treatment can inhibited the increase of arthritis index in AA rats, ameliorated secondary foot swelling, reduced the degree of inflammatory cell infiltration, and modified the histopathological changes of the synovium of AA rats. On the 29th day, the GE group had a good therapeutic effect on the reduction of arthritis index and the treatment of secondary foot swelling compared with the MTX group. In summary, these results indicated that GE has a good effect on AA rats.

Validation of metabolomics methods

The results of the metabolomics experiment depend on whether high-quality experimental data can be obtained. In this study, the stability of the analytical system and samples was tested by periodic injection of QC samples. As shown in Figure 3, the score chart of PCA showed that the clustering of QC samples was obvious in ESI^+ and ESI^- modes. At the same time, we selected a characteristic peak from the chromatogram of each QC sample to obtain the t_R and peak area. The relative standard deviation (RSD) of the t_R and peak area of these characteristic peaks in the QC samples were 0.50–1.00% and 1.71–5.21% respectively. Therefore, it showed that the established metabonomic analysis method has good stability and reproducibility.

Effects of synovial inflammation on sphingolipid metabolism in serum, synovium and MH7A cells

The MS data of serum, synovium and MH7A cells sphingolipid extract were imported into SIMCA-*p* 14.1 software and used PCA to establish a multivariate statistical model for each group of samples. As shown in Figure 3, it was found that there are obvious clusters between the control group and model group in serum and synovium samples, and between the control group and administration group in MH7A samples, and the variability of samples between groups was large. To further reveal the metabolic changes of biological samples in each group and find the related metabolites of RA, the samples were analyzed by OPLS-DA with supervised technology. Generally speaking, the larger the value of R^2Y and Q^2 and the closer the ratio is to one, indicates that the established OPLS-DA model is stable and reliable and has a certain prediction ability. The range of R^2Y value was 0.82–0.99, Q^2 value was 0.78–0.96, and R^2Y/Q^2 value was 0.93–1.09 (Figure 4). In the OPLS-DA model, VIP value >1, $p < 0.05$, fold changes ≥1.5 and CV < 30% were met. By combining Human Metabolome Database, self-built SPLs database and secondary MS fragment analysis, 2, 6 and 7 differential SPLs potential biomarkers were found in serum,

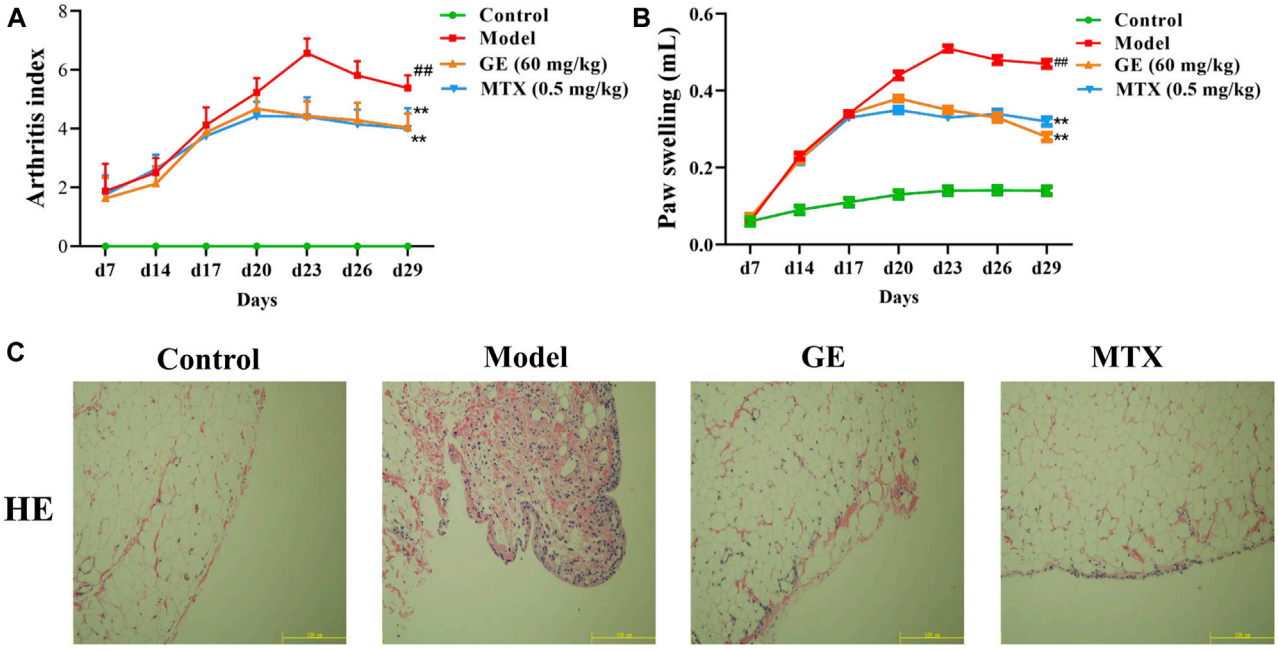

FIGURE 2
Establishment and evaluation of AA model rats and the therapeutic effect of GE. AA model rats were treated with GE for 14 days. **(A)** The arthritis index of rats in each group was measured, including control group, model group, GE administration group and MTX positive medicine group. **(B)** The degree of secondary paw swelling was measured. **(C)** Histopathological examination of synovial in AA rats. The data represent the means ± SD deviation of six samples in an independent experiment. $^{\#\#}p < 0.01$, compared with control group; $^{**}p < 0.01$, compared with model group; $n = 6$.

synovium and MH7A cells respectively. The provision of precise *m/z* data and MS/MS fragmentation data by time-of-flight mass spectrometry, which are helpful identifying differential metabolites induced by AA. Online metabolite databases and self-built databases were applied to identify interesting screening metabolites by accurate *m/z* data and MS/MS spectra. Taking an interesting variable (t_R-*m/z* 15.78_835.6648) as an example, the quasi-molecular ion *m/z* 835.6648 (ESI^+) was extracted at 15.78 min in AA rat metabolite profiling. The molecular formula of the metabolite was presumed to be $C_{47}H_{93}N_2O_6P$ by elemental composition analysis using Masslynx 4.1. A search of the 835.6648 m/*z* generated 4 candidate compounds with a mass tolerance of 5 ppm based on the Human Metabolome Database. The characteristic fragmentation ions of *m/z* 835.6648 ($[M + Na]^+$) were identified as 813.6822 m/*z* ($[M + H]^+$), 776.5899 m/*z* ($[M + Na\text{-}C_3H_9N]^+$), 652.6001 m/*z* ($[M + Na\text{-}C_5H_{14}NO_4P]^+$), 390.3715 m/*z* ($[M + Na\text{-}C_{21}H_{45}NNaO_5P]^+$), 264.2676 m/*z* ($[M + Na\text{-}C_{29}H_{60}NNaO_6P]^+$) and 86.0969 m/*z* ($[C_2H_3N(CH_3)]^+$) (Figure 5). Among these fragments, those at *m/z* 776.5899, 652.6001, 390.3715, 264.2676 and 86.0969 of SM(d18:1/24:1 (15Z)) were similar to the fragments of SM(d18:1/24:1 (15Z)) in the Human Metabolome Database. Combining the above information, including quasi-molecular ions as well as major fragment ions and the Human Metabolome Database, this AA-induced differential metabolite was annotated as SM (d18:1/24:1 (15Z)). In total, 11 potential sphingolipid biomarkers responsible for the therapeutic effect of GE on RA were screened and identified. Specific information on these potential biomarkers was summarized in Table 1.

Intervention mechanism of GE on sphingolipid metabolism in adjuvant arthritis rats and MH7A cells

Following the same data processing strategy, we compared the metabolic spectra of synovium and serum of AA rats and MH7A cells in normoxia group and hypoxia group with those obtained by GE administration group, respectively. As shown in the PCA score diagram (Figure 3), it was found in the synovium and serum sample spectra that the data matrix of GE group was more similar to that of the control group than that of the model group. It showed that GE could correct the metabolic disorder of SPLs involved in AA to a certain extent. In each sample group of MH7A cells, it was found that the hypoxia environment can change the metabolic level of SPLs in MH7A cells, while the data matrix of the hypoxia GE group had a slight regression trend compared with the hypoxia group, indicating that GE could

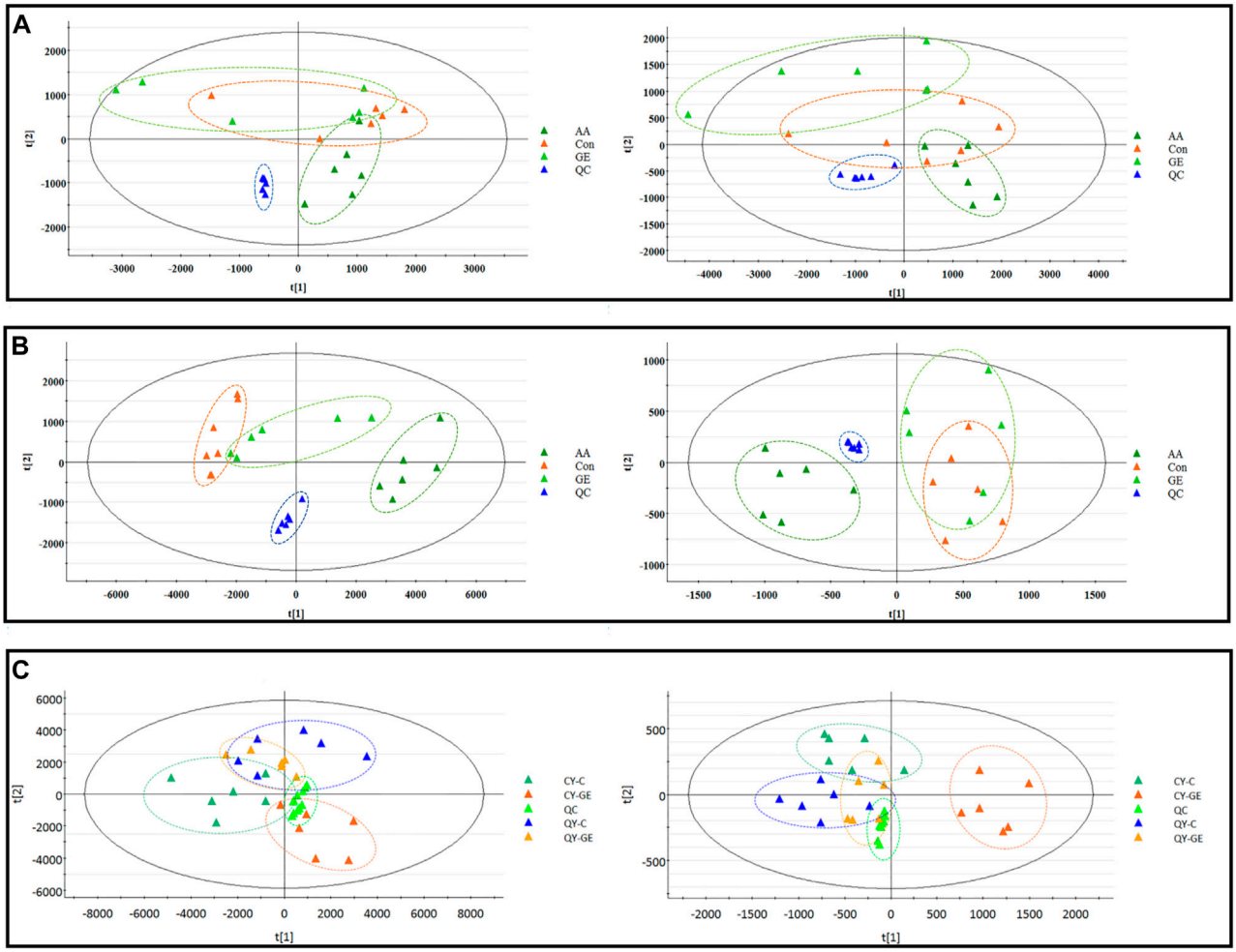

FIGURE 3
| PCA score plots of synovial, serum and MH7A cells extracts in ESI$^+$ (left) and ESI$^-$ (right) modes. **(A)** PCA score plots of synovial sample; **(B)** PCA score plots of serums sample; AA = model group; C = control group; GE = Geniposide treatment group; QC = quality group; **(C)** PCA score plots of MH7A cells extracts sample; CY-C = normoxia group; CY-GE = normoxia GE treatment group; QY-C = hypoxia group; QY-GE = hypoxia GE treatment group.

callback the metabolite level of endogenous SPLs disturbed by hypoxia to a certain extent. To explore the intervention effect of GE on sphingolipid metabolism of AA rats and normoxia/hypoxia MH7A cells, we performed OPLS-DA statistical analysis on synovial and serum of AA rats model group, administration group and sphingolipid extract of normoxia/hypoxia MH7A cells. Comparing the data from the administration group and model group, there were significant statistical differences between these sphingolipid metabolites (Figure 6). In general, GE significantly recalled 2 (including LysoSM (d18:0) and CerP (d18:1/22:0)) and 6 (including LysoSM (d18:0), SM (d18:1/18:0), Araliacerebroside, SM (d18:1/23:0), SM (d18:1/22:0) and SM (d18:1/24:1 (15Z))) sphingolipid metabolites in synovium and serum samples of AA rats, respectively. In MH7A cells sphingolipid extract, GE could significantly restore the disturbance of 6 (including LysoSM (d18:0), Palmitoyl sphingomyelin, Araliacerebroside, SM (d18:1/18:0), Cer (d18:0/14:0) and Cer (d18:0/16:0)) SPLs differential metabolites in MH7A cells (Figure 7). Their characteristic information was summarized in Table 1. The most notable finding was that the level of Cer decreased significantly after treatment with GE compared with the model group. Therefore, exploring the potential mechanism of the change of Cer level among different groups may promote the therapeutic intervention of RA and better understand the potential therapeutic mechanism of GE.

As shown in Figure 8, The sphingolipid metabolic network was mapped by KEGG to describe the interrelationship between nine biomarkers associated with the interventional effects of GE on AA rats and MH7A cells. Cer, a central component of

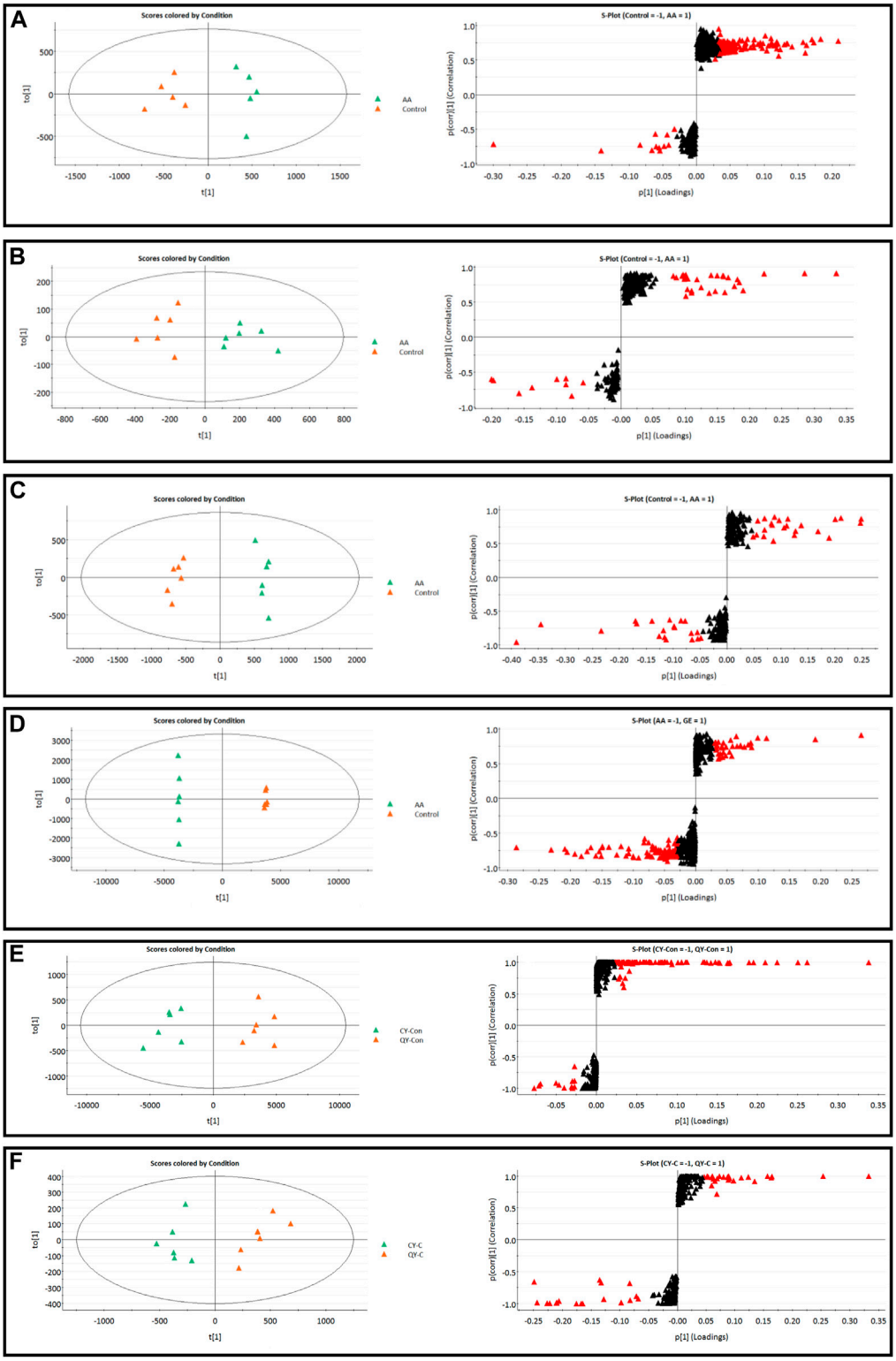

FIGURE 4
| OPLS-DA score plots and S-plots of synovial, serum and MH7A cells samples. **(A)** OPLS-DA model in ESI$^+$ mode corresponding to synovial sample (AA vs. C: $R^2Y = 0.93$, $Q^2 = 0.85$); **(B)** OPLS-DA model in ESI$^-$ mode corresponding to synovial sample (AA vs. C: $R^2Y = 0.82$, $Q^2 = 0.78$); **(C)** OPLS-DA model in ESI$^+$ mode corresponding to serum samples (AA vs. C: $R^2Y = 0.99$, $Q^2 = 0.96$); **(D)** OPLS-DA model in ESI$^-$ mode corresponding to serum samples (AA vs. C: $R^2Y = 0.98$, $Q^2 = 0.94$); **(E)** Corresponding to OPLS-DA model in ESI$^+$ mode of MH7A sample (CY-C vs. QY-C: $R^2Y = 0.85$, $Q^2 = 0.91$); **(F)** Corresponding to OPLS-DA model in ESI$^-$ mode of MH7A sample (CY-C vs. QY-C: $R^2Y = 0.84$, $Q^2 = 0.88$); the variable with VIP >1.0 was highlighted with a red frame in the S-plots of each comparison.

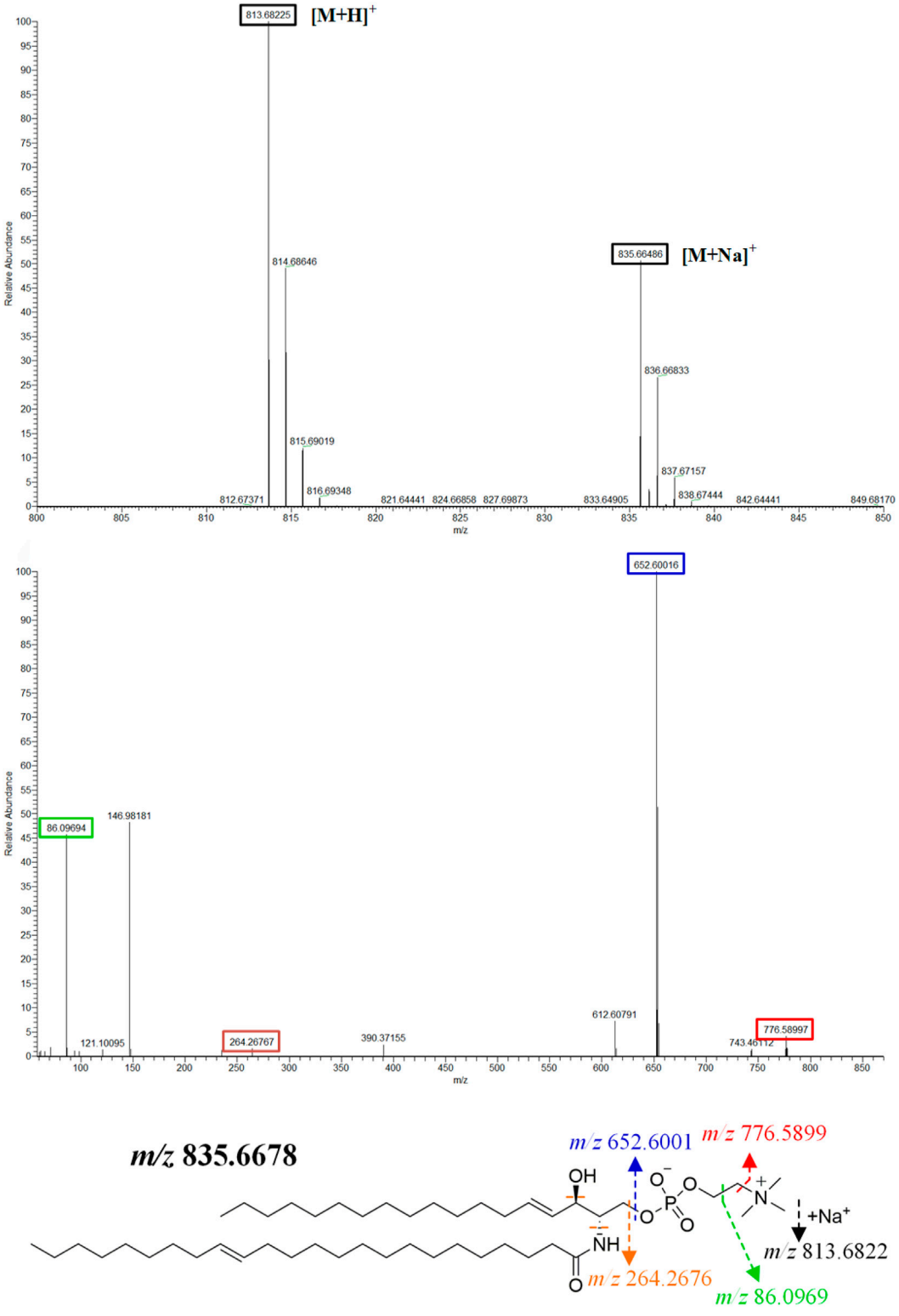

FIGURE 5
| SM (d18:1/24:1 (15Z)) primary and secondary mass spectrometry fragment attribution and cleavage pathways based on UPLC-Q-TOF/MS.

TABLE 1 | Differential sphingolipid metabolites identified in synovial, serum and MH7A cells and GE intervention.

Source	Metabolite	Formula	Retention time (min)	Measured m/z	VIP		Ion Form	HMDB	Trend	
					M/C	GE/M			M/C	GE/M
Synovial	CerP (d18:1/22:0)	$C_{40}H_{80}NO_6P$	15.55	702.5745	1.12	2.33	$[M + H]^+$	HMDB0010703	↑	↓
	LysoSM(d18:0)	$C_{23}H_{51}N_2O_5P$	16.60	933.7177	1.62	1.50	$[2\ M + H]^+$	HMDB0012082	↑	↓
Serum	Araliacerebroside	$C_{40}H_{77}NO_{10}$	13.78	732.5556	1.15	1.06	$[M + H]^+$	HMDB0033621	↑	↓
	SM(d18:1/18:0)	$C_{41}H_{83}N_2O_6P$	14.30	731.6073	1.47	1.65	$[M + H]^+$	HMDB0062559	↑	↓
	SM(d18:1/24:1 (15Z))	$C_{47}H_{93}N_2O_6P$	15.78	813.6822	3.74	2.15	$[M + H]^+$	HMDB0012107	↓	↑
	SM(d18:1/22:0)	$C_{45}H_{91}N_2O_6P$	15.87	787.6710	2.37	2.31	$[M + H]^+$	HMDB0012103	↓	↑
	SM(d18:1/23:0)	$C_{46}H_{93}N_2O_6P$	16.28	801.6855	1.97	1.85	$[M + H]^+$	HMDB0012105	↓	↑
	LysoSM(d18:0)	$C_{23}H_{51}N_2O_5P$	16.60	933.7177	1.34	1.62	$[2\ M + H]^+$	HMDB0012082	↑	↓
MH7A	Cer(d18:0/14:0)	$C_{32}H_{65}NO_3$	11.04	512.5046	1.13	2.39	$[M + H]^+$	HMDB0011759	↑	↓
	Cer(d18:0/16:0)	$C_{34}H_{69}NO_3$	11.73	540.5362	1.26	2.67	$[M + H]^+$	HMDB0011760	↑	↓
	Palmitoyl sphingomyelin	$C_{39}H_{79}N_2O_6P$	13.58	703.5761	1.41	4.16	$[M + H]^+$	HMDB0061712	↑	↓
	Araliacerebroside	$C_{40}H_{77}NO_{10}$	13.78	732.5556	5.56	3.56	$[M + H]^+$	HMDB0033621	↑	↓
	SM(d18:1/18:0)	$C_{41}H_{83}N_2O_6P$	14.36	731.6075	1.64	1.64	$[M + H]^+$	HMDB0012089	↑	↓
	Galactosylceramide (d18:1/20:0)	$C_{44}H_{85}NO_8$	15.75	756.6320	1.37	-	$[M + H]^+$	HMDB0010710	↓	-
	LysoSM(d18:0)	$C_{23}H_{51}N_2O_5P$	16.67	933.7177	1.35	9.75	$[2\ M + H]^+$	HMDB0012082	↑	↓

sphingolipid metabolism, is produced in the inflammatory hypoxia microenvironment mainly by hydrolysis of SM by A-SMase, followed by sphingosine (Sph) production catalyzed by ceramidase (El Kaffas et al., 2018). Sph is further generated by the action of sphingosine kinase 1 (SphK 1) to produce the pro-inflammatory factor SIP (Sun et al., 2020). In our study, Cer levels were restored after GE treatment, which indicated that the mechanism of action of GE intervention in Cer levels required further consideration.

Effects of GE on sphingolipids metabolizing enzyme Acid-SMase in adjuvant arthritis rats

Ceramides are the central molecules of sphingolipid metabolism (Gomez-Muñoz et al., 2016; Jeffries and Krupenko, 2018). It is now well established that ceramides are produced mainly through *de novo* synthesis initiated by condensation of serine and palmitoyl acyl-CoA or by hydrolysis of membrane sphingolipids catalyzed by acid-sphingomyelinase (A-SMase), and in particular, ceramides produced by A-SMase hydrolysis is involved in more inflammatory processes triggered by pro-inflammatory agonists (Cinque et al., 2003, Kihara, 2016). Previous studies have shown increased expression of A-SMase in the synovium and serum of AA rats, as well as in patients with RA (Miltenberger-Miltenyi et al., 2020). In addition, pharmacological blockade of A-SMase expression reduces ceramides levels and exerts effective anti-inflammatory effects *in vitro* and *in vivo* (Zhao et al., 2021). Thus, we investigated the expression of A-SMase in joint synovial tissues of AA rats in response to GE intervention. As shown in Figure 9, The expression of A-SMase in the model group was significantly higher than that in the control group. Compared with the model group, GE group significantly inhibited the expression of A-SMase in a dose-dependent manner. To sum up, the above results showed the difference in ceramides levels between AA rats and normal rats and the corrective activity of GE, which was associated with the regulation of A-SMase expression.

Discussion

The FCA-induced AA rat model is a classic model for the treatment of RA, which is characterized by persistent inflammatory hyperplasia of synovial tissue, destruction of cartilage, and progressive swelling of contralateral joints. However, the pathogenesis of RA is extremely complex, involving fibroblast-like synovial cells (FLSs), macrophages, osteoclasts and other cells (Lin et al., 2019). Studies have shown that FLSs are the main cell type of synovial intima, and the change of their biological function plays an important role in the occurrence and development of RA. Dysplastic synovial cells can secrete a large number of inflammatory factors, leading to inflammatory cell infiltration, hypoxia and destruction of the balance of synovial microenvironment,

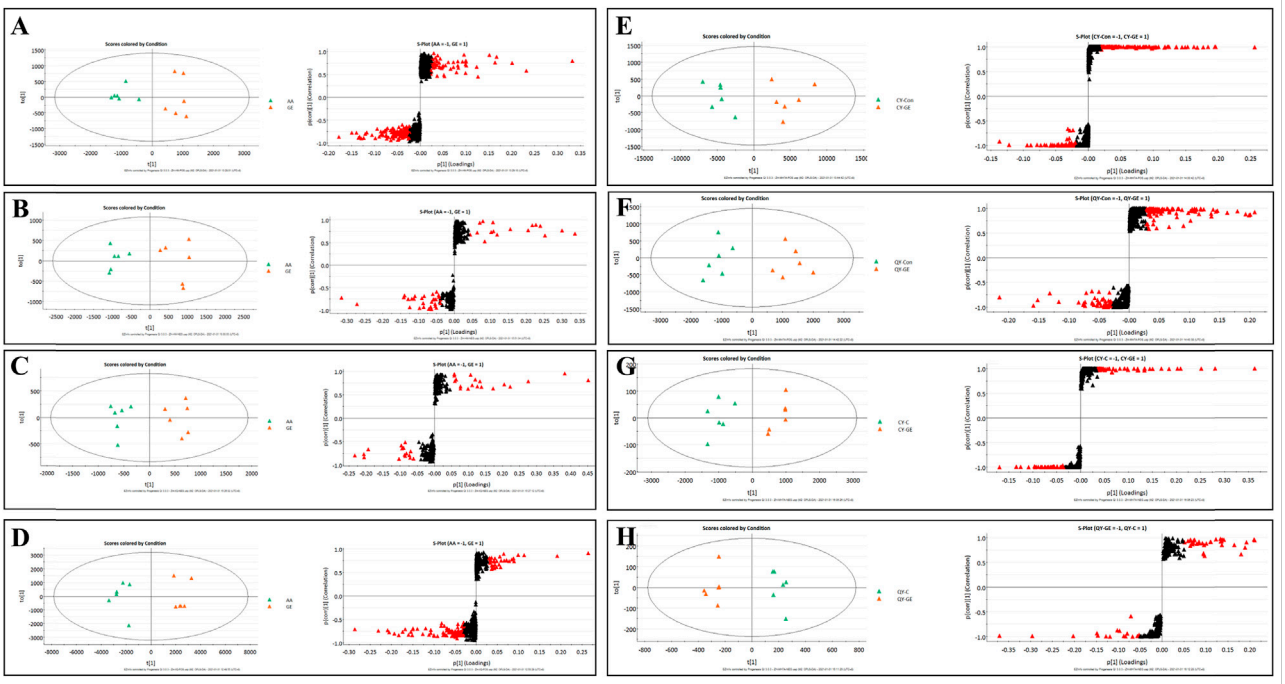

FIGURE 6
OPLS-DA score plots and S-plots of synovial, serum and MH7A cells samples after GE intervention. **(A)** OPLS-DA model in ESI^+ mode corresponding to synovial sample (GE vs. AA: $R^2Y = 0.92$, $Q^2 = 0.85$); **(B)** OPLS-DA model in ESI^- mode corresponding to synovial sample (GE vs. AA: $R^2Y = 0.84$, $Q^2 = 0.79$); **(C)** OPLS-DA model in ESI^+ mode corresponding to serum samples (GE vs. AA: $R^2Y = 0.95$, $Q^2 = 0.81$); **(D)** OPLS-DA model in ESI^- mode corresponding to serum samples (GE vs. AA: $R^2Y = 0.93$, $Q^2 = 0.86$); **(E)** and **(F)** Corresponding to OPLS-DA model in ESI^+ mode of MH7A cells sample (CY-GE vs. CY-C: $R^2Y = 0.85$, $Q^2 = 0.77$; QY-GE vs. QY-C: $R^2Y = 0.80$, $Q^2 = 0.82$); **(G)** and **(H)** Corresponding to OPLS-DA model in ESI^- mode of MH7A cells sample (CY-GE vs. CY-C: $R^2Y = 0.75$, $Q^2 = 0.82$; QY-GE vs. QY-C: $R^2Y = 0.88$, $Q^2 = 0.91$); the variable with VIP >1.0 was highlighted with a red frame in the S-plots of each comparison.

resulting in the aggravation of RA (Du et al., 2019). Therefore, RASFs (MH7A cells) and rats' synovial tissue were used for metabolic analysis. Previous studies have shown that SPLs are closely associated with the occurrence and development of RA. Among them, the expressions of Cer and S1P were up-regulated, while the expression of SM was down-regulated. During inflammation, the SPLs metabolizing enzyme SMase promotes the hydrolysis of SM into Cer, accelerates the accumulation of Cer, and then induces the release of inflammatory factors such as COX-2 and PGE2, thereby triggering various inflammatory diseases (Qu et al., 2018). To explore whether the positive effects of GE on AA rats and its mechanism are related to the callback of SPLs metabolic disorders, we collected blood and synovial tissues in AA rats for sphingolipid metabolism analysis. The results showed that there are two sphingolipid metabolites LysoSM (d18:0) and CerP (d18:1/22:0) in the synovial samples of AA rats, which are up-regulated to varying degrees compared with the normal group. In serum samples, LysoSM (d18:0), Aralia cerebroside and SM (d18:1/18:0) were up-regulated, SM (d18:1/23:0), SM (d18:1/22:0) and SM (d18:1/24:1 (15Z)) were down-regulated. In the synovial tissues and serum samples of the GE (60 mg/kg) administration group, the contents of the seven sphingolipid metabolites with metabolic disorders were significantly recovered to the normal group's metabolic level. These results provide the basis for the following view: GE, as the active ingredient of *Gardenia jasminoides Ellis*, has a positive effect on the sphingolipid metabolism disorder in AA rats.

Hypoxia is an important feature of RA. Due to the proliferation of synovial lining and the increase of immune cell infiltration, the demand for oxygen in the synovial is increased. The whole process also involves inflammation, angiogenesis, apoptosis, cartilage degradation and energy metabolism reprogramming (Veale et al., 2017). As the main effector cells of RA, RASFs were cultured in hypoxia to simulate the hypoxia environment in the articular cavity of RA patients. SPLs are important substances that mediate inflammation and other cellular processes. The dynamic balance of their metabolite levels directly affects the course of the disease (Hannun and Obeid, 2018). Sphingomyelinase is one of the key enzymes that control Cer levels in cells. The changes in glycolytic metabolism in RA patients with hypoxia in the articular cavity led to the accumulation of lactate and

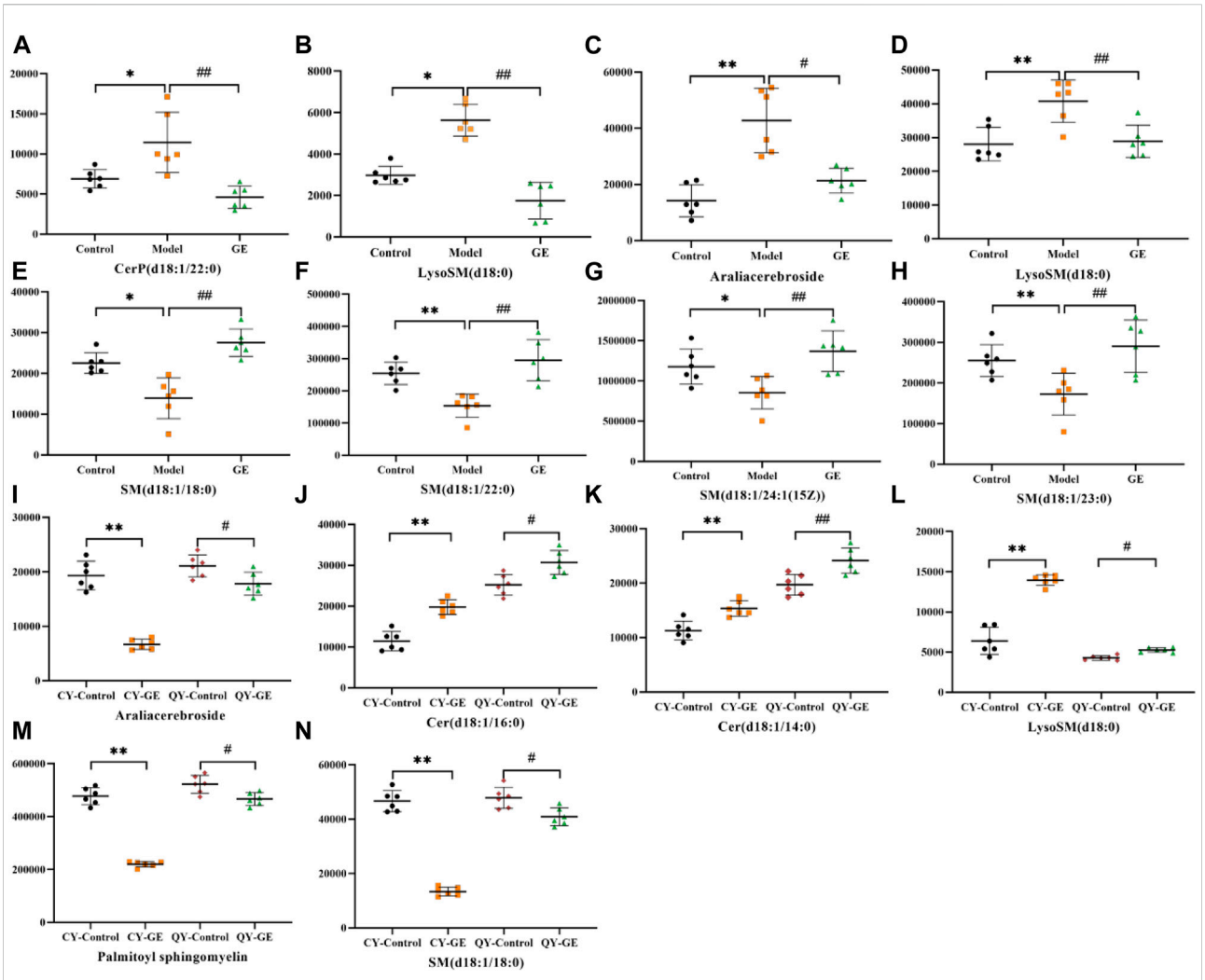

FIGURE 7
Effects of GE on the standardized abundance of 14 differential metabolites in synovial tissue **(A,B)**, serum **(C ~ H)** and MH7A cells **(I ~ N)**. Dates are represented as mean ± SD (n = 6). (In A ~ H, $^{*}p < 0.05$, $^{**}p < 0.01$ compared to the control group; $^{\#}p < 0.05$, $^{\#\#}p < 0.01$ compared to the model group; In I ~ N, $^{*}p < 0.05$, $^{**}p < 0.01$ compared to the CY-control group; $^{\#}p < 0.05$, $^{\#\#}p < 0.01$ compared to the QY-control group).

the appearance of an acidic microenvironment. However, the acidic microenvironment increases A-SMase activity and accelerates SM hydrolysis into Cer, which further promotes the occurrence and development of inflammatory response (Floudas et al., 2020; Insausti-Urkia et al., 2020). To explore the regulatory effect of GE on sphingolipid metabolism disorder of MH7A cells. We extracted SPLs metabolites of MH7A cells under hypoxia (2% oxygen) and normoxia (21% oxygen). The analysis results showed that the levels of Arabia cerebroside, palmitoyl sphingomyelin, lysosm (d18:0), SM (d18:1/18:0), Cer (d18:0/14:0) and Cer(d18:0/16:0) were up-regulated in the hypoxia control group. The level of galactosylceramide (d18:1/20:0) showed a downward trend. After GE (50 μM) intervened in MH7A cells, the levels of the above six up-regulated SPLs metabolites all returned to normal levels and had no significant effect on the level of Galactosyl ceramide (d18:1/20:0). Interestingly, the levels of all three metabolites (Aralia cerebroside, lysoSM (d18:0) and SM (d18:1/18:0)) were up-regulated *in vivo* and *in vitro*. After the intervention of GE administration, they all have recovered to normal levels, so we have reason to infer that GE has a certain regulatory effect on the abnormal metabolism of SPLs in RA.

In living organisms, the hydrophobic skeleton of all complex sphingolipids (SM, cerebroside, ganglioside) is composed of Cer (Castro et al., 2014). Cer is a bioactive metabolite of SPLs family, which is composed of sphingosine bases, but sphingosine bases are mainly composed of 18 carboaminoalcohols covalently bound to a fatty acyl side chain with variable chain length. The number of

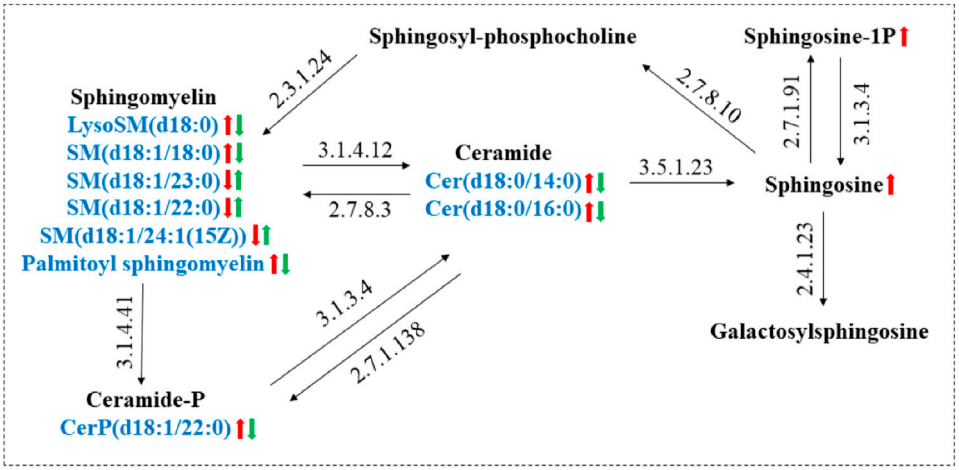

FIGURE 8
Metabolic networks of major sphingolipid metabolism markers associated with RA and the role of GE intervention. (Red arrows: trends in RA-induced changes in sphingolipid metabolites; Green arrows: trends in sphingolipid metabolites associated with GE treatment).

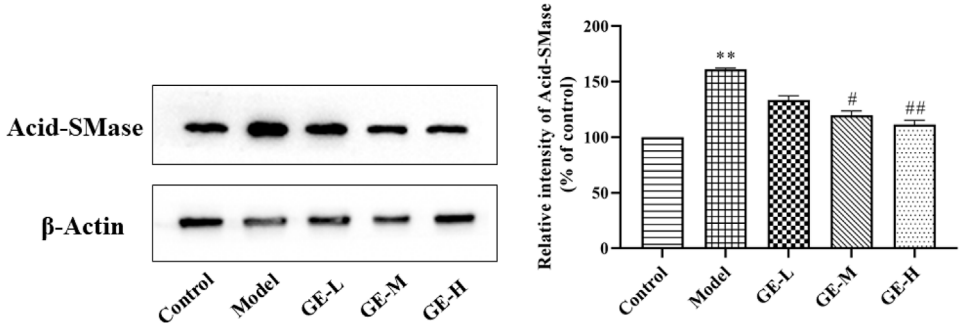

FIGURE 9
Effect of GE on the expression of Acid-SMase in the synovial tissue of AA rats. The dates are represented as mean ± SD ($n = 3$) *$p < 0.05$, **$p < 0.01$ compared to the control group; #$p < 0.05$, ##$p < 0.01$# compared to the model group, GE-L = GE (30 mg/kg/day, ig), GE-M = GE (60 mg/kg/day, ig), GE-H = GE (120 mg/kg/day, ig).

sphingosine base carbon atoms, the length of fatty acyl side chains and the double bonds at different positions jointly determine the diversity of ceramide structure and function (Clarke, 2018). In eukaryotic cells, Cer is mainly synthesized through two pathways. The first pathway is the *de novo* synthesis pathway that occurs in the endoplasmic reticulum. First, the condensation of serine and palmitoyl Co-A proceeds via catalysis by serine palmitoyl transferase (SPT) and then by ceramide synthase (Cers), which catalyzes the production of Cer. (Gomez-Muñoz et al., 2016). Interestingly, the levels of some enzymes involved in *de novo* ceramide synthesis are up-regulated in inflammatory diseases (Bikman and Summers, 2011). The second pathway is the catabolic pathway of sphingomyelinase, which generates phosphorylcholine and ceramide by hydrolyzing SM present in the plasma membrane or lysosome (Xiang et al., 2021). The most abundant sphingomyelin in mammals is SM, which has great potential to form ceramide. In fact, ceramide produced by sphingomyelinase catalyzed catabolism is involved in a variety of inflammatory processes induced by proinflammatory factors. In particular, proinflammatory factors including HIF-1α, TNF-α, IL-1β, Interferion- γ (IFN- γ) and other cytokines are important stimulators of SMase activity and have been confirmed to be involved in the inflammatory response in different cells (Jenkins et al., 2010). SMase activation is the main metabolic pathway that regulates

Cer production during inflammation. The changes in SMase activity caused by hypoxia in different cells and tissues are consistent with the changes in ceramide levels (Cogolludo et al., 2009). In this study, we found that compared with the normoxia group, the levels of sphingolipid metabolites Cer (d18:0/14:0) and Cer (d18:0/16:0) were significantly increased in the hypoxia control group. And after the intervention of GE administration, it showed a downward trend, revealing that GE may achieve the purpose of treating RA by inhibiting the accumulation of Cer in MH7A cells.

Conclusion

In summary, this study established a lipidomics analysis method based on UPLC-Q-TOF/MS, preliminarily explored the intervention effect of GE on SPLs metabolism in AA rats and the effect of GE on sphingolipid metabolism of MH7A cells in hypoxia microenvironment, and looked for potential biomarkers related to GE treatment. The results showed that except galactosylceramide (d18:1/20:0), GE could recover the change levels of the above 10 sphingolipid biomarkers in varying degrees. According to these different metabolites, GE has a certain regulatory effect on the disorder of sphingolipid metabolism of AA rats and MH7A cells cultured in hypoxia. Western blotting results confirmed that GE-regulated Cer levels were associated with its inhibition of A-SMase expression in synovial tissues of AA rats, which is crucial to reveal the potential anti-inflammatory mechanism of GE in the treatment of RA.

This study used combined metabolomics and lipidomics to explore the mechanism of GE in the treatment of RA for the first time, which may be to restore the disorder of sphingolipid metabolism, provided an experimental basis for the screening of biomarkers for clinical diagnosis of RA, and also offered a strategy for the treatment of RA with TCM.

Data availability statement

The raw data supporting the conclusions of this article will be made available by the authors, without undue reservation.

Ethics statement

The animal study was reviewed and approved by the Animal Ethics Committee of Anhui University of Traditional Chinese Medicine.

Author contributions

JK, HZ, YW, and HW conceived and designed the overall experiment. JK and HZ performed UPLC-Q-TOF/MS analysis and further metabolomic data processing. YB, FC, XD, and PG carried out experimental animal breeding, cell culture and metabolite extraction. This manuscript was written by JK. HZ, YW, and HW polished and revised the manuscript for publication. All authors were informed of the final manuscript.

Funding

This work was supported by grants from the National Natural Science Foundation of China (Nos. 81073122, 81473400, and 81874360), and Major Projects of Natural Science Research in Anhui Universities (No. KJ2021ZD0060).

Conflict of Interest

The authors declare that the research was conducted in the absence of any commercial or financial relationships that could be construed as a potential conflict of interest.

Publisher's note

All claims expressed in this article are solely those of the authors and do not necessarily represent those of their affiliated organizations, or those of the publisher, the editors and the reviewers. Any product that may be evaluated in this article, or claim that may be made by its manufacturer, is not guaranteed or endorsed by the publisher.

References

Bikman, B. T., and Summers, S. A. (2011). Ceramides as modulators of cellular and whole-body metabolism. *J. Clin. Invest.* 121 (11), 4222–4230. doi:10.1172/JCI57144

Castro, B. M., Prieto, M., and Silva, L. C. (2014). Ceramide: a simple sphingolipid with unique biophysical properties. *Prog. Lipid Res.* 54, 53–67. doi:10.1016/j.plipres.2014.01.004

Chen, J., Cheng, W., Li, J., Wang, Y., Chen, J., Shen, X., et al. (2021). Notch-1 and notch-3 mediate hypoxia-induced activation of synovial fibroblasts in rheumatoid arthritis. *Arthritis Rheumatol.* 73 (10), 1810–1819. doi:10.1002/art.41748

Cinque, B., Di Marzio, L., Centi, C., Di Rocco, C., Riccardi, C., Grazia Cifone, M., et al. (2003). Sphingolipids and the immune system. *Pharmacol. Res.* 47 (5), 421–437. doi:10.1016/s1043-6618(03)00051-3

Clarke, C. J. (2018). Neutral sphingomyelinases in cancer: friend or foe? *Adv. Cancer Res.* 140, 97–119. doi:10.1016/bs.acr.2018.04.010

Cogolludo, A., Moreno, L., Frazziano, G., Moral-Sanz, J., Menendez, C., Castañeda, J., et al. (2009). Activation of neutral sphingomyelinase is involved in acute hypoxic pulmonary vasoconstriction. *Cardiovasc. Res.* 82 (2), 296–302. doi:10.1093/cvr/cvn349

Deng, R., Li, F., Wu, H., Wang, W. Y., Dai, L., Zhang, Z. R., et al. (2018). Anti-inflammatory mechanism of geniposide: inhibiting the hyperpermeability of fibroblast-like synoviocytes via the RhoA/p38MAPK/NF-κB/F-actin signal pathway. *Front. Pharmacol.* 9, 105. doi:10.3389/fphar.2018.00105

Deng, R., Wang, Y., Bu, Y., and Wu, H. (2022). BNIP3 mediates the different adaptive responses of fibroblast-like synovial cells to hypoxia in patients with osteoarthritis and rheumatoid arthritis. *Mol. Med.* 28 (1), 64. doi:10.1186/s10020-022-00490-9

Deng, R., Wu, H., Wang, Y., and Wang, M. D. (2021). Properties and molecular mechanisms underlying geniposide-mediated therapeutic effects in chronic inflammatory diseases. *J. Ethnopharmacol.* 273, 113958. doi:10.1016/j.jep.2021.113958

Du, H., Zhang, X., Zeng, Y., Huang, X., Chen, H., Wang, S., et al. (2019). A novel phytochemical, DIM, inhibits proliferation, migration, invasion and TNF-α induced inflammatory cytokine production of synovial fibroblasts from rheumatoid arthritis patients by targeting MAPK and AKT/mTOR signal pathway. *Front. Immunol.* 10, 1620. doi:10.3389/fimmu.2019.01620

El Kaffas, A., Al-Mahrouki, A., Hashim, A., Law, N., Giles, A., Czarnota, G. J., et al. (2018). Role of acid sphingomyelinase and ceramide in mechano-acoustic enhancement of tumor radiation responses. *J. Natl. Cancer Inst.* 110 (9), 1009–1018. doi:10.1093/jnci/djy011

Floudas, A., Neto, N., Marzaioli, V., Murray, K., Moran, B., Monaghan, M. G., et al. (2020). Pathogenic, glycolytic PD-1+ B cells accumulate in the hypoxic RA joint. *JCI insight* 5 (21), e139032. doi:10.1172/jci.insight.139032

Gomez-Muñoz, A., Presa, N., Gomez-Larrauri, A., Rivera, I. G., Trueba, M., Ordoñez, M., et al. (2016). Control of inflammatory responses by ceramide, sphingosine 1-phosphate and ceramide 1-phosphate. *Prog. Lipid Res.* 61, 51–62. doi:10.1016/j.plipres.2015.09.002

Hannun, Y. A., and Obeid, L. M. (2018). Sphingolipids and their metabolism in physiology and disease. nature reviews. *Nat. Rev. Mol. Cell Biol.* 19 (3), 175–191. doi:10.1038/nrm.2017.107

Insausti-Urkia, N., Solsona-Vilarrasa, E., Garcia-Ruiz, C., and Fernandez-Checa, J. C. (2020). Sphingomyelinases and liver diseases. *Biomolecules* 10 (11), 1497. doi:10.3390/biom10111497

Jang, C., Chen, L., and Rabinowitz, J. D. (2018). Metabolomics and isotope tracing. *Cell* 173 (4), 822–837. doi:10.1016/j.cell.2018.03.055

Jeffries, K. A., and Krupenko, N. I. (2018). Ceramide signaling and p53 pathways. *Adv. Cancer Res.* 140, 191–215. doi:10.1016/bs.acr.2018.04.011

Jenkins, R. W., Canals, D., Idkowiak-Baldys, J., Simbari, F., Roddy, P., Perry, D. M., et al. (2010). Regulated secretion of acid sphingomyelinase: implications for selectivity of ceramide formation. *J. Biol. Chem.* 285 (46), 35706–35718. doi:10.1074/jbc.M110.125609

Kihara, A. (2016). Synthesis and degradation pathways, functions, and pathology of ceramides and epidermal acylceramides. *Prog. Lipid Res.* 63, 50–69. doi:10.1016/j.plipres.2016.04.001

Li, F., Dai, M., Wu, H., Deng, R., Fu, J., Zhang, Z., et al. (2018). Immunosuppressive effect of geniposide on mitogen-activated protein kinase signalling pathway and their cross-talk in fibroblast-like synoviocytes of adjuvant arthritis rats. *Mol. (Basel, Switz.* 23 (1), 91. doi:10.3390/molecules23010091

Lin, J., Yu, Y., Wang, X., Ke, Y., Sun, C., Yue, L., et al. (2019). Iguratimod inhibits the aggressiveness of rheumatoid fibroblast-like synoviocytes. *J. Immunol. Res.* 2019, 6929286. doi:10.1155/2019/6929286

Maceyka, M., and Spiegel, S. (2014). Sphingolipid metabolites in inflammatory disease. *Nature* 510 (7503), 58–67. doi:10.1038/nature13475

Miltenberger-Miltenyi, G., Cruz-Machado, A. R., Saville, J., Conceição, V. A., Calado, Â., Lopes, I., et al. (2020). Increased monohexosylceramide levels in the serum of established rheumatoid arthritis patients. *Rheumatol. Oxf. Engl.* 59 (8), 2085–2089. doi:10.1093/rheumatology/kez545

Mortimer, J. C., and Scheller, H. V. (2020). Synthesis and function of complex sphingolipid glycosylation. *Trends Plant Sci.* 25 (6), 522–524. doi:10.1016/j.tplants.2020.03.007

Ottolenghi, S., Zulueta, A., and Caretti, A. (2020). Iron and sphingolipids as common players of (Mal)Adaptation to hypoxia in pulmonary diseases. *Int. J. Mol. Sci.* 21 (1), 307. doi:10.3390/ijms21010307

Qu, F., Zhang, H., Zhang, M., and Hu, P. (2018). Sphingolipidomic profiling of rat serum by UPLC-Q-TOF-MS: application to rheumatoid arthritis study. *Mol. (Basel, Switz.)* 23 (6), 1324. doi:10.3390/molecules23061324

Qu, W., Jiang, L., and Hou, G. (2021). Circ-AFF2/miR-650/CNP axis promotes proliferation, inflammatory response, migration, and invasion of rheumatoid arthritis synovial fibroblasts. *J. Orthop. Surg. Res.* 16 (1), 165. doi:10.1186/s13018-021-02306-8

Rinschen, M. M., Ivanisevic, J., Giera, M., and Siuzdak, G. (2019). Identification of bioactive metabolites using activity metabolomics. *Nat. Rev. Mol. Cell Biol.* 20 (6), 353–367. doi:10.1038/s41580-019-0108-4

Scott, D. L., Wolfe, F., and Huizinga, T. W. (2010). Rheumatoid arthritis. *Lancet (London, Engl.* 376 (9746), 1094–1108. doi:10.1016/S0140-6736(10)60826-4

Skácel, J., Slusher, B. S., and Tsukamoto, T. (2021). Small molecule inhibitors targeting biosynthesis of ceramide, the central hub of the sphingolipid network. *J. Med. Chem.* 64 (1), 279–297. doi:10.1021/acs.jmedchem.0c01664

Sun, M., Deng, R., Wang, Y., Wu, H., Zhang, Z., Bu, Y., et al. (2020). Sphingosine kinase 1/sphingosine 1-phosphate/sphingosine 1-phosphate receptor 1 pathway: a novel target of geniposide to inhibit angiogenesis. *Life Sci.* 256, 117988. doi:10.1016/j.lfs.2020.117988

Tsuchiya, H., Ota, M., and Fujio, K. (2021). Multiomics landscape of synovial fibroblasts in rheumatoid arthritis. *Inflamm. Regen.* 41 (1), 7. doi:10.1186/s41232-021-00157-8

Veale, D. J., Orr, C., and Fearon, U. (2017). Cellular and molecular perspectives in rheumatoid arthritis. *Semin. Immunopathol.* 39 (4), 343–354. doi:10.1007/s00281-017-0633-1

Wang, L., Zhao, Q., Wang, N., Ding, Y., Kong, L., Wang, J., et al. (2021). Circ_0000396 inhibits rheumatoid arthritis synovial fibroblast growth and inflammatory response via miR-203/HBP1 axis. *J. Biol. Res.* 28 (1), 1. doi:10.1186/s40709-020-00131-4

Wang, M., Yang, L., Chen, Z., Dai, L., Xi, C., Wu, X., et al. (2021). Geniposide ameliorates chronic unpredictable mild stress induced depression-like behavior through inhibition of ceramide-PP2A signaling via the PI3K/Akt/GSK3β axis. *Psychopharmacology* 238 (10), 2789–2800. doi:10.1007/s00213-021-05895-8

Wang, R. H., Dai, X. J., Wu, H., Wang, M. D., Deng, R., Wang, Y., et al. (2020). Anti-inflammatory effect of geniposide on regulating the functions of rheumatoid arthritis synovial fibroblasts via inhibiting sphingosine-1-phosphate receptors1/3 coupling gαi/gαs conversion. *Front. Pharmacol.* 11, 584176. doi:10.3389/fphar.2020.584176

Wang, R., Li, B., Lam, S. M., and Shui, G. (2020). Integration of lipidomics and metabolomics for in-depth understanding of cellular mechanism and disease progression. *Genet. Genomics* 47 (2), 69–83. doi:10.1016/j.jgg.2019.11.009

Wang, R., Yin, Y., and Zhu, Z. J. (2019). Advancing untargeted metabolomics using data-independent acquisition mass spectrometry technology. *Anal. Bioanal. Chem.* 411 (19), 4349–4357. doi:10.1007/s00216-019-01709-1

Wu, H., Wang, L., Zhan, X., Wang, B., Wu, J., Zhou, A., et al. (2020). A UPLC-Q-TOF/MS-based plasma metabolomics approach reveals the mechanism of Compound Kushen Injection-based intervention against non-small cell lung cancer in Lewistumor-bearing mice. *Phytomedicine* 76, 153259. doi:10.1016/j.phymed.2020.153259

Xiang, H., Jin, S., Tan, F., Xu, Y., Lu, Y., Wu, T., et al. (2021). Physiological functions and therapeutic applications of neutral sphingomyelinase and acid sphingomyelinase. *Biomed. Pharmacother.* 139, 111610. doi:10.1016/j.biopha.2021.111610

Yin, F., Nian, M., Wang, N., Wu, H., Wu, H., Zhao, W., et al. (2022). Protective mechanism of gandou decoction in a copper-laden hepatolenticular degeneration model: *In vitro* Pharmacology and cell metabolomics. *Front. Pharmacol.* 13, 848897. doi:10.3389/fphar.2022.848897

Yun, J. K., and Kester, M. (2002). Regulatory role of sphingomyelin metabolites in hypoxia-induced vascular smooth muscle cell proliferation. *Arch. Biochem. Biophys.* 408 (1), 78–86. doi:10.1016/s0003-9861(02)00526-x

Zhan, X., Wu, H., and Wu, H. (2020). Joint synovial fluid metabolomics method to decipher the metabolic mechanisms of adjuvant arthritis and geniposide intervention. *J. Proteome Res.* 19 (9), 3769–3778. doi:10.1021/acs.jproteome.0c00300

Zhao, H., Liu, Y., Li, Z., Song, Y., Cai, X., Liu, Y., et al. (2018). Identification of essential hypertension biomarkers in human urine by non-targeted metabolomics based on UPLC-Q-TOF/MS. *Clin. Chim. Acta.* 486, 192–198. doi:10.1016/j.cca.2018.08.006

Zhao, M., Yang, M., Li, X., Hou, L., Liu, X., Xiao, W., et al. (2021). Acid sphingomyelinase and acid β-glucosidase 1 exert opposite effects on interleukin-1β-induced interleukin 6 production in rheumatoid arthritis fibroblast-like synoviocytes. *Inflammation* 44 (4), 1592–1606. doi:10.1007/s10753-021-01444-9

frontiers | Frontiers in Pharmacology

TYPE Review
PUBLISHED 10 October 2022
DOI 10.3389/fphar.2022.956264

OPEN ACCESS

EDITED BY
Yan-Fang Xian,
The Chinese University of Hong Kong, China

REVIEWED BY
Hui Cui,
Guangzhou University of Chinese Medicine, China
Weihong Cong,
Xiyuan Hospital (CAS), China

*CORRESPONDENCE
Delin Xu,
xudelin2000@163.com
Junhua Shi,
sjhzmu@126.com

‡These authors have contributed equally to this work

SPECIALTY SECTION
This article was submitted to Drug Metabolism and Transport, a section of the journal Frontiers in Pharmacology

RECEIVED 30 May 2022
ACCEPTED 21 September 2022
PUBLISHED 10 October 2022

CITATION
Li Q, Luo F, Jiang P, Feng C, He F, Dong L, Xu D and Shi J (2022), Application of traditional Chinese medicine in film drug delivery system. *Front. Pharmacol.* 13:956264. doi: 10.3389/fphar.2022.956264

Application of traditional Chinese medicine in film drug delivery system

Qianhang Li[1,2‡], Feng Luo[2‡], Pingnan Jiang[2‡], Chenxi Feng[2], Feifei He[2‡], Lina Dong[2‡], Delin Xu[2*] and Junhua Shi[1*]

[1]Department of Radiology, Affiliated Hospital of Zunyi Medical University, Zunyi, China, [2]Department of Cell Biology, Zunyi Medical University, Zunyi, Guizhou, China

Film drug delivery systems have the advantages of precise administration, simple process and easy portability, compared with other traditional drug delivery systems such as tablets, capsules, syrups, ointments, etc. The traditional Chinese medicine (TCM) are normally developed in four categories of film agent like patch film, coating, spray film and gel film, which are applied to the treatment of oral ulcers, chronic diseases of lower limbs, burns, scalds, gynecological disease and body care. So the TCM film has great research value and prominent market prospect. In this review, we summarized the research progress of the material composition, pharmaceutical production, clinical application and pharmacology mechanism of various TCM film agents. It may provide a comprehensive reference for further development and utilization of TCM film agents.

KEYWORDS

traditional Chinese medicine (TCM), film agent, preparation processes, clinical application, drug delivery systems

1 Introduction

Ethnic Chinese medicinal materials have thousands of years of history in clinical application, while how to achieve accurate drug delivery and precision pharmaceutical care has becoming an urgent scientific problem to be solved. Films are preparations made by mixing drugs and film-forming materials evenly, which films can be pasted and fixed in one place, which can produce local or systemic therapeutic effects. Based on the former published paper, film agent has being used in clinically related diseases of stomatology, otolaryngology, ophthalmology, gynecology, dermatology and other departments. The TCM film agent has the advantages of simple and scientific preparation processes, high curative effect, small dose and small volume, lightweight and so on.

At present, with the maturity of nanomaterial research and development technology, various high-tech technologies such as 3D printing and liquid crystal technology are based on nanomaterials and are applied to the development of film formulations (Tong et al., 2018; Hao et al., 2019). It is hoped that more precise targeted therapy can be achieved and the process of intelligent drug research and development can be promoted. At the same time, in order to more accurately evaluate the overall quality of the film, the continuous

TABLE 1 The number of Chinese medicine film preparations in the article and their main uses.

Type	Name of film agent	Indications	R and D enterprise
Film coating agent	Acne film coating	Clear heat and dry dampness, cool blood and detoxify, remove blood stasis and disperse knots. For the adjuvant treatment of acne vulgaris with accumulation of damp-heat and blood-heat stasis	Beijing Huashen Pharmaceutical Co., Ltd.
Film coating agent	Shutongan coating agent	Relaxing tendons and promoting blood circulation, reducing swelling and relieving pain	Hebei Jinzhong Pharmaceutical Co., Ltd.
Film coating agent	Snow Mountain Golden Luohan Pain Relief Film	Promote blood circulation, reduce swelling, relieve pain. For acute and chronic sprains, rheumatoid arthritis, rheumatoid arthritis, gout, frozen shoulder, pain and swelling of limbs and joints caused by bone hyperplasia, and neuropathic headaches	Tibet Nuodikang Pharmaceutical Co., Ltd.
Film coating agent	Danxiong scar film	Promote blood circulation, soften firmness, relieve itching	Weihai Life Pharmaceutical Co., Ltd.
Film coating agent	Sodium fluoride anti-caries coating agent	For the prevention of caries	Shenzhen Zhongke Jingcheng Medical Technology Co., Ltd.
Patch film agent	Sophora film	Clear heat and dry dampness, cool blood and detoxify, remove blood stasis and disperse knots. For the adjuvant treatment of acne vulgaris with accumulation of damp-heat and blood-heat stasis	Guizhou Dexuantang Hukang Pharmaceutical Co., Ltd.
Patch film agent	Boxingkang medicine film	Clearing away heat and detoxifying, drying dampness and killing insects, dispelling wind and relieving itching. For vaginal diseases (Trichomonas vaginitis, fungal vaginitis, acute and chronic cervicitis)	Guizhou Shengjitang Pharmaceutical Co., Ltd.
Patch film agent	Propolis oral film	Clearing heat and relieving pain. For recurrent aphthous ulcers.	China Resources Zizhu Pharmaceutical Co., Ltd.
Patch film agent	Erxiekang film	Warm in the middle to dispel cold and stop diarrhea. For non-infectious diarrhea in children	Shanxi Jinxin Shuanghe Pharmaceutical Co., Ltd.
Patch film agent	Chuanhua Pain Relief Film	Promote blood circulation to remove blood stasis, dispel cold and relieve pain. For rheumatism pain, bruise pain, bone hyperplasia, cervical spondylosis, frozen shoulder, lumbar muscle strain and other pain.	Jilin Province Huinan Changlong Biochemical Pharmaceutical Co., Ltd.
Gel film agent	Chitosan film former	Apply to cervical ulcer to promote ulcer healing	Heilongjiang Yunjia Medical Technology Co., Ltd.
Gel film agent	Tsubaki Gel	Clear heat and dry dampness, remove blood stasis and promote muscle	Zhuzhou Qianjin Pharmaceutical Co., Ltd.
Gel film agent	Sore Gel	For reducing swelling and analgesia, promoting blood circulation and removing blood stasis, relaxing tendons and collaterals, dissolving sputum and dissipating knots, bruises, rheumatism and joint pain, frozen shoulder, gout, and hyperplasia of breast lobules	Yunnan Baiyao Group Co., Ltd.
Gel film agent	Kangfu Gel	Expelling wind and dampness, relieving itching and killing insects, antiseptic and muscle regeneration. Used for vulvar or vaginal congestion, swelling, burning, pain, increased secretions or local ulcers, erosions, itching, etc. caused by vulvitis, vulvar ulcers, vaginitis, etc	Guizhou Jianxing Pharmaceutical Co., Ltd.
Gel film agent	Baofukang Gel	For vaginal discharge caused by damp-heat stasis, see vaginal pruritus, fungal vaginitis, senile vaginitis, cervical erosion when the amount of vaginal discharge is multi-colored and yellow	Sinopharm Group Zhonglian Pharmaceutical Co., Ltd.
Spray film agent	Biological wound spray	This product is suitable for the cleaning and care of superficial wounds in the superficial dermis and above, and has the functions of hemostasis, antibacterial and wound protection	Changsha Ruitai Medical Technology Co., Ltd.

introduction of new test methods can fully reflect the effect of each link in the preparation process on the final film, thereby helping the R&D personnel to further improve the process. In addition, the latest research direction of TCM film concentrates on the elucidation of the effective mechanism of TCM for disease treatment, which mainly starts from the regulation of related genes, the expression of related proteins, enzymes and factors, and the impact of related signaling pathways (Huang and Wang., 2022).

We learned from the China National Drug Administration and Monitoring Bureau that there are many traditional Chinese medicine films on the market. The common ones are patch film, film coating, and spray film, and there are fewer spray film agents. According to statistics, there are few TCM films listed abroad, and most of them are developed and produced in China. We have listed some typical listed TCM films and their indications (Table 1).

This paper summarizes the pharmaceutical process and clinical application of TCM films in recent years, and puts forward ideas and prospects. It may provide a clue for the following development and utilization of TCM film and the expansion and upgrading of clinical applications (Figure 1).

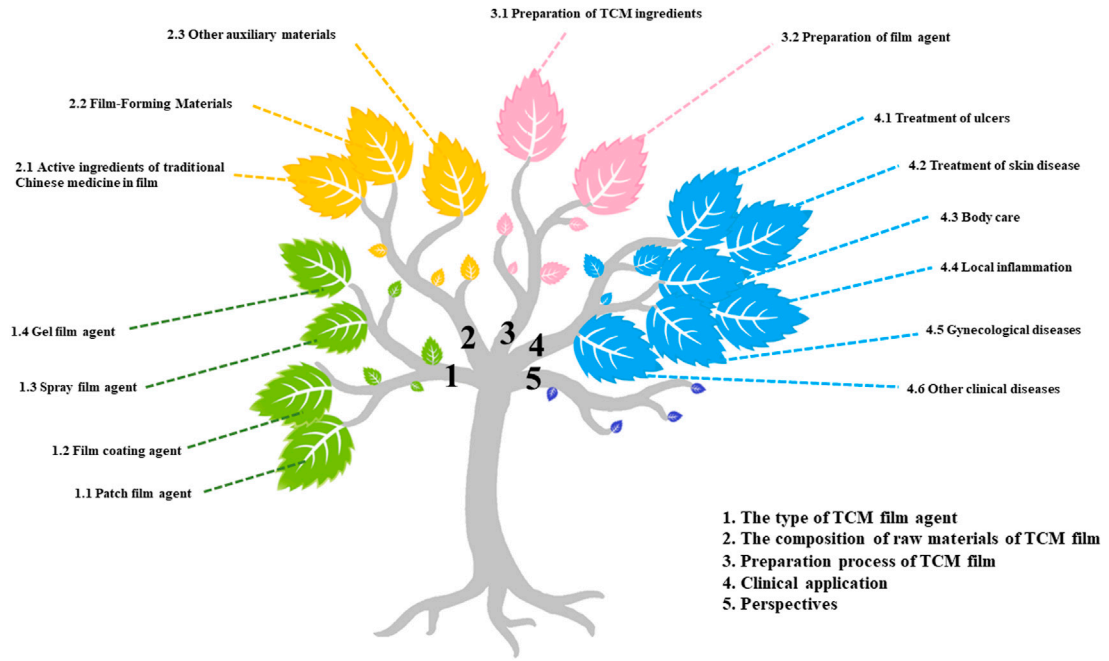

FIGURE 1
Mind map of the article.

2 The type of TCM film agent

There are many kinds of TCM film agents and their classification methods are also different. In the light of the structure, they can be classified into monolayer film, double-layer film and sandwich film. According to different application sites can be roughly categorized into oral film, eye film, nasal film, vaginal film, skin or mucosal external film, periodontal film and implant film. Film preparations are roughly divided into three categories: liquid preparations, semi-solid preparations, and solid preparations according to their physical form, and their use methods are different. Liquid preparations include spray film, and the method of use is spray film formation. Semi-solid preparations include film coating agent and gel film agent, and the method of use is smearing to form a film. Solid preparations are applied directly to the affected area. Due to the different use methods can be roughly divided into patch film, coating film, spray film and gel film (Kathe and Kathpalia., 2017). This paper summarizes the classification and application of the following four common film agents.

2.1 Patch film agent

Patch film agent refers to some TCM mixed with film-forming materials made of convenient and portable lamellar film. Because of its sustainable adhesion in the specific surface of a wound, it can be used for the treatment of the diseases in the oral cavity, eyes, nasal cavity or vagina, through the skin and mucous membrane percutaneous treatment of specific parts of the disease (Figure 2). The self-made Kouyanqing sustained-release film made of Kouyanqing granules and polyvinyl alcohol by Li et al. has a good clinical effect on oral ulcers and can relieve the pain symptoms of patients (Li et al., 2013). Yuan et al. showed that the film made of compound broad-leaf valerian, safflower, camphor wood, impatiens and carbomer had strong analgesic and anti-inflammatory activities (Yuan et al., 2013). Studies have shown that the patch film can also be used to treat lumbar muscle strain. Li et al. used modern technology to make seven kinds of traditional Chinese medicines such as angelica, safflower, and angelica into dry powder paste, and added the volatile oil and borneol extracted by distillation into ethanol solution to make a diluent, and combined the two to make a patch. When applied to the waist, the drug can quickly reach the diseased part, making the local meridians unobstructed, promoting blood circulation and removing blood stasis, dispelling wind and dispelling cold, and disappearing symptoms such as low back pain (Li et al., 2005). In addition, some studies have shown that the traditional Chinese medicine film can also be used to treat angina pectoris. Among the 35 cases in the traditional Chinese medicine film treatment group, 24 cases were cured, and the recovery rate accounted for 68.57%. The role of myocardial ischemia is a safe and effective traditional Chinese medicine preparation that can be used for the treatment of coronary heart disease and angina

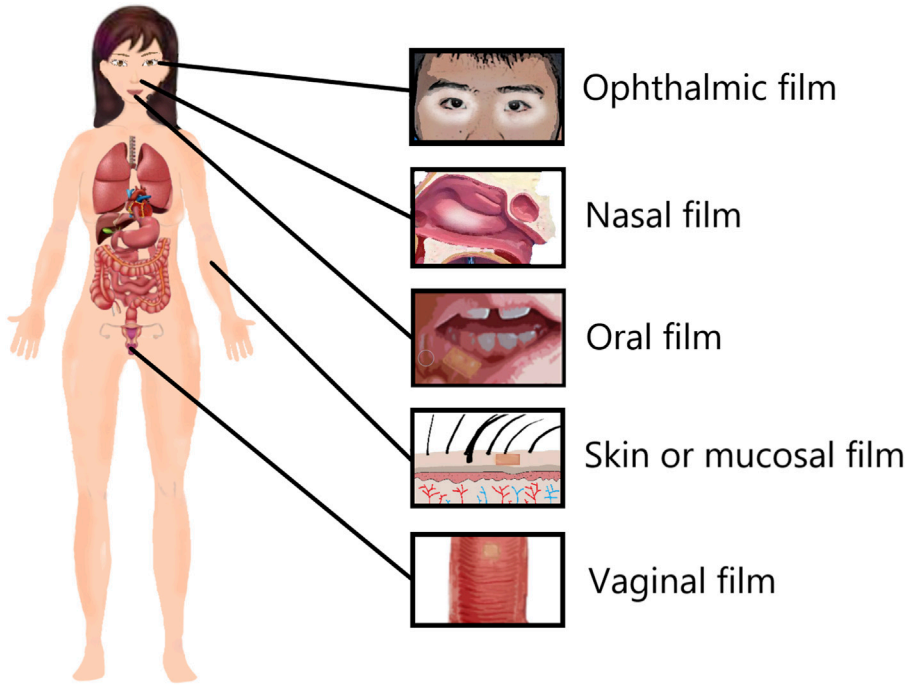

FIGURE 2
Classification of patch film agent.

pectoris (Niu et al., 2007). All in all, the patch film has the advantages of being convenient to carry, simple to use, and simple to prepare. It is widely used in several clinical fields and is one of the most popular film formulations.

2.2 Film coating agent

Film coating agent refers to a liquid preparation in which some Chinese medicines are dissolved or dispersed in the solvent containing film-forming materials, and the solvent volatilizes after applying the affected area to form a film. It can be used for the treatment of skin burns, wound infection, acne, rash, eczema, surface anesthesia, soft tissue injury, etc. The compound membrane (CPCF) made by curcumin, PVA and collagen can effectively promote the healing of skin wounds. The experiment showed that the film had obvious inhibition zone to *Staphylococcus aureus* and *Escherichia coli,* and the wound healing rate of rats 15 days after operation was 98.03 ± 0.79%, which were higher than those of the control group (Leng et al., 2020). Wang et al. made the film coating agent with nine TCMs, which is stable in administration and has a good therapeutic effect on skin scars. The total cure rate was 88.69%, which was significantly higher than that of the control group (6.48%), and the inhibition rate of the drug on the proliferation and growth of fibroblasts detected by the MTT method was 83.27 ± 7.33% (Wang et al., 2018). It is also shown that the coating agent can also be applied to the field of frostbite prevention. Nanogel coating agent prepared from *Ganoderma lucidum* (GLT) containing triterpenoids has an obvious therapeutic effect on frostbite in rats. Among them, the combination of GLT nanogel and TUS has a beneficial effect on the healing process of frostbite by increasing the survival area and improving the pathological tissue in frostbite rats (Shen et al., 2016). In addition, clinical application shows that film coating agent can also nourish and whiten the skin. The surface coating agent is made of white *Poria cocos*, Trichosanthin, *Bletilla striata* and other TCMs, which can clear away heat, remove dampness and detoxify the skin with the help of the active ingredients of the medicine, and has a significant therapeutic effect on chloasma (Chen et al., 2018). In short, the coating agent is widely used in the clinical field because of its simple preparation, convenient use and significant curative effect.

2.3 Spray film agent

Spray film agent refers to some TCMs and suitable auxiliary materials filled in containers, released in mist when used. It could be directly sprayed to the skin and mucous membranes to form a film for treating the skin and mucous membrane and other parts of the disease. Former researchers found that the spray film made

of *Rhizoma bolbostemmae*, PVP and carbomer has antiviral and antibacterial effects, which could be used to treat infectious skin diseases, and has a significant clinical effect in the treatment of condyloma acuminatum (Ye et al., 2013). In addition, clinical applications have shown that spray film can treat limb swelling, bruises, etc. For example, 36 cases of traumatic limb swelling were successfully treated with *Xiaoding* spray film (Xin, 2012). Some studies have also shown that the spray film of removing blood stasis and swelling made of peach seed, Chuanxiong rhizome, *Angelica* root, PVP-k30 and PVA 1788. This film has the effects of promoting blood circulation, removing blood stasis, swelling and relieving pain, mainly used for soft tissue swelling, ecchymosis, stasis and heat in the early stage of injury (Zhu et al., 2015). In general, spray film agents can not only protect the wound surface but also release drugs to play a local or systemic therapeutic effect, which is expected to provide a direction for the clinical treatment of skin mucosal injury and percutaneous treatment.

2.4 Gel film agent

Gel film is a thick liquid or semi-solid preparation with gel properties, being made by certain drugs and excipients that can form a gel or a thin film on the affected area. In most clinical applications, the use of dressings that maintain a moist environment promotes proper wound healing, such as hydrogels have good fluid absorption capacity, water retention capacity, water vapor transmission rate and integrity value. The hydrogel has an immediate response to gel formation when in contact with wound exudate, and high fluid absorption occurs through strongly hydrophilic gel formation, with potential use in biomedical applications (Jantrawut et al., 2019). Summarizing dressings for superficial and partial thickness burns, Wasiak et al. found that hydrogels have a greater ability to absorb fluids and therefore can cope with higher levels of wound exudate, and their fluid-donating properties may also help wounds debridement and helps maintain a moist wound environment. In addition, burn wounds covered with hydrogel dressings healed faster than those treated with various conventional care regimens (Wasiak et al., 2013). Lu et al. reviewed four commonly used methods for preparing soluble chemical cross-linked hydrogels, environmentally sensitive physical cross-linked hydrogels and supramolecular self-assembled hydrogels, providing ideas for designing traditional Chinese medicine gel film agents for clinical use (Lu et al., 2018). Studies have shown that sodium alginate (SA) and pectin (PC) as film-forming materials, crosslinking Ca^{2+} leads to the formation of a strong hydrogel, which can absorb a large amount of water, but is insoluble in aqueous solution and has enhanced mechanical properties and fluid absorption capacity, which is expected to be applied in the field of TCM and guide the direction of new dosage forms (Rezvanian et al., 2017).

At present, the hydrogels used in film formulations include chitosan, sodium alginate, polyvinyl alcohol, polyurethane (PU), etc (Tavakoli and Klar., 2020). The polyelectrolyte composite membrane made of *Bletilla striata* polysaccharide combined with chitosan by Wang et al. has sustained-release properties, which can increase the drug concentration at the lesion, which is helpful for the treatment of oral ulcers (Wang et al., 2020). Guo et al. used Ca^{2+} as a cross-linking agent and glycerol as a moisturizing agent to make the asiaticoside sodium alginate repair patch, which has the effect of inhibiting the high expression of pro-inflammatory factors and promoting the formation of collagen fibers in the wound tissue. At the same time, it can reduce the local inflammation of the wound, thereby promoting the repair of the wound and shortening the healing time of the wound skin (Guo et al., 2020).

In general, the gel film has good biocompatibility and tissue adhesion, is easy to use due to its elasticity and flexibility, allows proper oxygen and water exchange during wound healing. And it is able to absorb the serous secretions of lesions, reducing the interference with the wound healing process, which is of great help in wound healing.

The four types listed above are common types of TCM films. In addition, there are acupoint application. The difference between TCM film preparations and chemical transdermal preparations is that the former not only exerts curative effects locally on the skin or enters the body through the skin, but also exerts curative effects through meridian points (Li et al., 2022). For some special TCM film, it is under the guidance of TCM theory, the medicine is pasted on certain acupoints of the human body. Through the percutaneous absorption of the drug, it not only stimulates the local meridian points, but also stimulates the whole-body meridian to prevent and treat diseases (Xue et al., 2022). Zhao et al. used the oral traditional Chinese medicine decoction prepared by red peony, Chuanxiong rhizome, etc., combined with acupoint sticking prepared by *Evodia*, *cassia* twig, etc. to treat tubal infertility. They found that taking traditional Chinese medicine decoction can achieve the effects of removing blood stasis and clearing the meridians, promoting blood circulation and relieving pain, warming the meridians and dispelling cold. The acupoint application uses the point of view of acupuncture and moxibustion of traditional Chinese medicine, and selects the four acupoints of Zhongji, Zhongwan, Qihai and Tianshu for drug application, which can promote the absorption and introduction of drugs, achieve the effect of reconciling the meridians and collaterals, nourishing blood and consolidating the root. It can be seen that the traditional Chinese medicine decoction combined with acupoint sticking combined with tubal drainage has better efficacy in the treatment of tubal infertility (Zhao et al., 2021). The film prepared by Liu et al. using TCMs such as *Scutellaria baicalensis* and *Ephedra* has the effect of relieving cough and relieving asthma. Through acupoint percutaneous administration, it was found that the skin resistivity rate decreased, the Na^+-K^+-ATPase activity

increased, and the transdermal absorption increased after administration, which was significantly different from that of non-acupoint administration (Liu et al., 2000). In a word, the traditional Chinese medicine film administered through acupoints can make the medicine reach the lesions directly, and can also enhance the regulating effect of the body through the stimulation of acupoints, and obviously enhance the therapeutic effect. At the same time, it has the advantages of less toxic and side effects and long drug release time, which can reduce the shortage of oral administration.

3 The composition of raw materials of TCM film

TCM films are generally composed of active ingredients of TCM and film-forming materials, and some films also contain film-forming auxiliary materials such as penetration enhancers and pressure-sensitive agents.

3.1 Active ingredients of traditional Chinese medicine in film

TCM refers to the drugs collected, processed and prepared under the guidance of TCM theory to explain the mechanism of action and guide clinical application. It is the main component of TCM films. TCM film refers to the film dosage form made of the active ingredients or their extracts obtained from a single or compound TCM through a reasonable process and suitable excipients or substrates under the guidance of the theory of TCM. TCM compound is an organic combination of multiple TCMs for specific diseases, which is a major feature of TCM treatment. For the TCM compound itself: the TCM compound has many flavors, complex components, most of the pharmacodynamic chemicals basis is not clear, and the amount of most active ingredients in the medicinal components is relatively low, which also brings great difficulties to the determination of active ingredients. In addition, the active ingredients of medicinal materials may vary greatly due to factors such as origin, climate, processing technology, etc., so this brings greater challenges to the quality control of compound recipes composed of different medicinal flavors (Li et al., 2005). In the research of TCM film preparation, reasonable methods and processes should be selected as far as possible according to the composition and compatibility of the original prescription. It is necessary to pay attention not only to in-depth chemical, pharmacy and clinical research on the original formula, including pharmacokinetic research, but also to combine the requirements for approval of new drugs, and try to avoid the use of drug bases containing heavy metals (Yuan et al., 2003). In TCM treatment, after the film is administered through the skin and cavity, it not only avoids the first-pass effect of the liver, but also reduces the irritation and adverse reactions of the drug to the gastrointestinal tract, and improves the bioavailability (Wang et al., 2017).

TCM mainly comes from natural medicine and its processed products, including botanical medicine, animal medicine, mineral medicine and some chemical and biological products. The ingredients of TCM are complex and diverse, mild and non-irritating, and have few side effects. In recent years, the research on TCM films has found that TCM can not only function as their active ingredients, but also serve as film-forming materials, penetration enhancers, colorants, and flavoring agents (sweeteners, aromatics, Acidic agents, effervescent agents and bitterness inhibitors, etc.) are involved in the preparation of film formulations to achieve “medicine and supplementary integration”. For example, in the article of Zhu et al., it is correctly pointed out that the composition of the dosage form that *Bletilla Striata* Gum participates in, as the main drug, it can be used for the preparation of film coating agents, etc., as a pharmaceutical excipient, it can be used as a gel matrix, and the film-forming material is further prepared Gels and films (Zhu et al., 2019). Chen et al. stated that the volatile oil of TCM has good transdermal absorption characteristics, such as *Asarum*, cinnamon, etc., and can be used as a penetration enhancer to participate in the preparation of film preparations (Chen et al., 2016). As a natural pigment, TCM not only has a wide range of sources, but also has low harm. While it could be safe and reliable as medicine uses for multiple purposes with special dosage and preparation (Zhang et al., 2007). The konjac glucomannan-based gardenia yellow pigment film prepared by (Liu and Cui. 2019) has good performance and stable colour. This study shows that TCM can be used as a colorant to participate in the preparation of the film (Liu et al., 2021). In addition, TCM can also be used as a flavoring agent to participate in the preparation of various dosage forms, such as honey, mint, fennel, musk, etc (Xiao et al., 2021). The above content shows that Chinese herbal medicines are not limited to exerting a single effect, but have multiple effects.

The therapeutic effect of the film is empowered by the composition of TCM, most of which are plants and cannot be directly used as medicine. It needs to be used as medicine by decocting or concocting to extract the active ingredients in TCM. The active ingredient of TCM is the key factors for the film to exert its curative effect. It is mainly composed of active ingredients of TCM decoction or powder medicine that are not suitable for decoction. We selected some representative TCM films and listed their active ingredients, indications and pharmacological effects of the main TCM (Table 2).

3.2 Film-forming materials

The film-forming material is the carrier of TCM ingredients, and its physical and chemical properties are stable and do not react with TCM ingredients. It has the characteristics of non-

TABLE 2 Traditional Chinese medicine components and pharmacological action of film agent.

Name of film agent	Active ingredients of films	Indications	Pharmacological effects of main Chinese medicines
Bletilla Oral Ulcer Film (Zhang, Sun et al., 2014)	*Bletilla*	Oral Ulcer	Traumatic bleeding due to the efficacy of arresting bleeding with astringent action (He et al., 2017)
Indigo Naturalis Film (Fan et al., 2008)	Indigo naturalis, Borneol	Oral Ulcer	Indigo Naturalis has the effect of clearing heat and detoxifying, cooling blood and eliminating spots, reducing fire, and calming shock (Fan et al., 2008)
Oral Ulcer Double-layer Membranes (Cheng et al., 2017)	Cortex Phellodendri	Oral Ulcer	Cortex Phellodendri has antibacterial and anti-inflammatory effects, as well as obvious antifungal and immunomodulatory effects (Kitt et al., 2015).
Lavender Essential Oil Film (Wu, 2021)	Lavender	Burns	Lavender essential oil has the functions of drying dampness, relieving pain, purging fire and detoxifyingm (Wu, 2021)
"Ophthalmic Washing Solution No.1" Chinese traditional medicine liniment (Zhang et al., 2016)	*Rheum officinale, Coptis Chinensis, Scutellaria baicalensis, Phellodendron*	External eye disorder caused by heat toxin	Rheum Officinale, Coptis Chinensis, Scutellaria baicalensis, Phellodendron have heat-clearing and detoxifying effects (Zhang et al., 2016)
Qumin Tongbi Nasal Spraying Agent (Chen et al., 2011)	*Astragalus membranaceus*, Flower bud of lily magnolia, Smoked plum, *Lithospermum*, *Asarum*, *Eclipta alba*	Perennial allergic rhinitis	Several drugs cooperate with each other, tonifying lung and kidney, dispelling cold (Chen et al., 2011)
Erhuangsan Bletillae Rhizoma Gelatin Sustained Release Double-layer Membrane (Wang et al., 2019)	*Bletilla*, *Acacia catechu*, *Coptis chinensis*, Alum	Treatment of cervical precancerous lesions	Bletilla has the effects of antibacterial and anti-inflammatory, removing saprophytic muscle, reducing drug toxicity and anti-tumorm (Chen et al., 2011)
Whitening and Moisturizing Facial Mask (Zhou et al., 2019)	*Angelica*, *Poria*	Whitening and moisturizing	Angelica and Poria have the ability to eliminate excessive pigment accumulation in tissues Ability to promote skin cell metabolism (Zhou et al., 2019)
New Compound Chinese Medicine Coating Agent (Wang et al., 2018)	*Creeping oxalis*, *Poria, Achyranthes bidentata*, *Forsythia suspensa*, *Menthol*, *etc*	Skin scar	Creeping oxalis has an antioxidant effect and can inhibit the inflammation of scars. *Achyranthes* bidentata and Forsythia suspensa have anti-inflammatory and detumescent effects (Zhou et al., 2019)

toxicity, no side effects, good film-forming and film-releasing, and low cost. It can be divided into natural polymer film-forming materials and synthetic polymer film-forming materials.

In general, most of the common traditional Chinese medicine films are mainly used in the above two categories of film-forming materials. With the deepening of research on nanomaterials, many nanomaterials have been used in drug delivery systems, such as liposomes, transfersomes, alcohol liposomes, nanoparticles and copolymer carriers (Wang et al., 2016). Due to the small particle size of nano-drugs and their good effects in drug retention and specific targeting, new types of nano-material-based membrane agents are gradually being used in the treatment of clinical diseases. Nunes et al. provided an efficient method for the development of wound dressing materials with enhanced properties based on biocompatible chitosan and poly (vinyl alcohol) hydrogels with embedded silver nanoparticles as a potent antimicrobial agent (Nunes et al., 2011). However, few nanomaterials have been used in traditional Chinese medicine films in the current. It is believed that with continuous research, more nanomaterials will be used in traditional Chinese medicine film drug delivery systems, so that the film drug system can play a more powerful effect.

3.2.1 Natural polymer film-forming material

The commonly used natural polymer film-forming materials are starch, dextrin, cellulose, chitosan, agar, gum arabic, sodium alginate, etc. Cellulose is the main component of plant cell walls, which is non-toxic, biodegradable, hydrophilic, and biocompatible. The cellulose extracted from plants shows excellent properties, making it suitable for the pharmaceutical industry (Naomi et al., 2020).

Chitosan and chitin have similar chemical structures with cellulose. Chitosan is the product of N-deacetylation of chitin and completely non-toxic, so it could be safely used in oral. Besides, it has several advantages in biomedical applications, such as biocompatibility and controlled biodegradability, which can produce degradation products that are non-toxic and do not generate inflammatory responses. In addition, chitosan can control drug delivery for use as wound dressings due to its unique polycationic, nontoxic, antibacterial, and bioabsorbable properties (Muxika et al., 2017). It also has good film-forming properties after being dissolved, and has good biocompatibility with the human body. Therefore, the chitosan is currently recognized as a natural polymer film-forming material with great potential for development.

Sodium alginate is a by-product of extracting iodine and mannitol from the brown algae kelp or *Sargasso*. It contains a

large amount of acetate, which can show polyanionic behavior in aqueous solution and has certain adhesion. This chemical is popular be used as a drug carrier for the treatment of mucosal tissues (Moebus et al., 2012). It can enhance the viscosity of liquid medicine without toxicity, and the film-forming conditions are relatively stable, so it is a good film-forming material.

3.2.2 Synthetic polymer film-forming materials

At present, synthetic polymer film-forming materials can be classified with three categories according to their molecular structure: polyvinyl alcohol compounds, acrylic copolymers and cellulose derivatives.

3.2.2.1 Polyvinyl alcohol compounds

Polyvinyl alcohol (PVA) is one of the widely studied synthetic polymers for biomedical applications, especially the fabrication of wound dressings based on nanofiber membranes, which are biocompatible, biodegradable, electrostatically spin-dry, hydrophilic properties, bioadhesives, non-toxicity and chemical resistance (Kamoun, et al., 2021). Therefore, PVA is a good film-forming material and is widely used in film formulations. At present, medical polyvinyl alcohol has specifications such as PVA05-88, PVA17-8 and PVA-124 (Zhang et al., 2004).

3.2.2.2 Acrylic copolymers

Among acrylic copolymers, polyacrylate and carbomer have good film-forming properties. Polyacrylate can form a film agent with good gloss and strong water resistance, which has good adhesion, good flexibility, elasticity, and good weather resistance, but poor pull resistance. Carbopol is a polymer of acrylic acid-bonded allyl sucrose or pentaerythritol allyl ether. It is a white loose powder, soluble in water and organic matters of glycerol and ethanol, and has excellent film-forming properties and adhesion. Liu et al. made Shuanghuang gel with carbomer-940, which has good transdermal absorption ability, no greasy feeling, even smear, easy cleaning, good coupling with the skin, and high bioavailability (Liu et al., 2019).

3.2.2.2 Cellulose derivatives

Cellulose derivatives of carboxymethyl cellulose (CMC), hydroxypropyl methylcellulose (HPMC) and methylcellulose (MC) are common food additives. They are attached to the main chain of anhydrous glucose to make their corresponding cellulose derivatives show hydrophilicity and water solubility for enhancing properties of film-forming and releasing (He et al., 2021). Hydroxypropyl methylcellulose (HPMC) and sodium carboxymethyl cellulose (CMC-NA) are film-forming materials of cellulose derivatives commonly used in TCM. As a water-soluble polymer material, HPMC has good water solubility, dispersion, thickening, water retention and film-forming properties. The formed coating film is colorless, odorless, tough and transparent, and is widely used as drug coating and rate-controlling polymer materials for sustained release formulations (Wang, 2018). Sodium Carboxymethyl Cellulose (CMC-Na) is normally a kind of powder, granular or fibrous substance with white to light yellow colour. Due to its strong hygroscopicity, soluble in water, and certain thickening and adhesive properties, it is easy to form a film. CMC-Na was used as a film-forming material in the preparation of oral patches and the obtained patch is smooth without bubbles, flexible and uniform, and has excellent adhesion properties (Chen et al., 2020).

3.3 Other auxiliary materials

In order to improve the performance of the film and facilitate storage, some film formulations also add auxiliary materials such as penetration aids, pressure sensitive agents, preservatives, plasticizers, etc.

3.3.1 Penetration enhancer

Penetration enhancers are substances that increase or accelerate the penetration of a drug through the skin. The ideal penetration enhancer has no irritation or damage to the skin and mucous membranes, and is physically and chemically stable. In addition, it can also promote faster transdermal delivery of Chinese herbal ingredients without reacting with them. Penetration enhancers can be classified into alcohols and polyols, lactams and their analogs, esters and ethers, surfactants, fatty acids, terpenes, steroids, and miscellaneous items according to the molecular structure (Vasyuchenko et al., 2021). The commonly used penetration enhancers in TCM films are azone, linoleic acid, propylene glycol, borneol, menthol and wormwood, etc. Chen et al. focused on the effects of propylene glycol, azone, menthol and oleic acid on the transdermal absorption of evodiol base in the preparation of the Evodiamine Hydrogel Patches, among which propylene glycol has the better effect of promoting penetration (Chen et al., 2021).

3.3.2 Pressure-sensitive agent

Pressure sensitive agent is an important auxiliary material of TCM film, which belongs to viscose material. It enables the film to have strong adhesion under a slight pressing force but also easy to peel off. According to its composition, pressure-sensitive adhesives can be divided into the following categories: polyisobutylene pressure-sensitive adhesives, polyacrylate pressure-sensitive adhesives, cinnamon rubber pressure-sensitive adhesives, cinnamone pressure-sensitive adhesives, hot-melt pressure-sensitive adhesives, etc (Ke et al., 2018).

3.3.3 Plasticizer

The plasticizer is a kind of material that can reduce the rigidity and brittleness of polymer. Plasticizers in the film-

forming system can increase the flexibility and ductility of dry film and prevent the rupture of dry film, and some plasticizers can also promote permeability (Asghar, 2020). Plasticizers commonly used in TCM films include glycerol, dibutyl sebacate, sorbitol, and so on. Wang et al. added an appropriate amount of glycerol in the preparation of Spray Film with Clematis Root, and the obtained film spray had good film-forming properties, and had good hygroscopicity, moisture retention and air permeability (Wang et al., 2019).

3.3.4 Preservatives

The preservative is a kind of food additive that can inhibit the activity of microorganisms and prevent the spoilage of food. Preservatives added to the film agent can effectively prevent the film agent from spoilage. A large number of studies have pointed out that the main preservative of the coating agent is paraben ester series, which could increase the stability of the liquid preparation and extend the shelf life (Jin et al., 2012). Paraben is a white crystalline powder or colorless crystal, easily soluble in alcohol, ether and acetone, very slightly soluble in water, and can be used as a bactericidal preservative in TCM films. Sorbic acid, benzyl alcohol, paraben, etc. are commonly used preservatives in TCM. Cai et al. added an appropriate amount of ethyl paraben as a preservative in the preparation of the compound sore film, so that the film can be stored for a long time (Cai et al., 2012).

In short, the above list is the composition of common traditional Chinese medicine film preparations. Interestingly, some Chinese medicinal active ingredients have their special film-forming properties. For example, konjac glucomannan (KGM), white jelly polysaccharide, etc. have superior self-film-forming properties. Using it in the film has the effect of killing two birds with one stone (Dong et al., 2019; Liu et al., 2021). In addition, polymers such as S-nitrosoglutathione (GSNO), dialdehyde starch, titanium dioxide and whey protein isolate, zein, iodine, etc. can be seen in some chemical films different from traditional Chinese medicine films. Unique membrane components like copper (CuI) nanoparticle dispersions, liposomes, etc. It has been reported that by using chitosan and GSNO to make a film-type dressing that can release NO, it has better sterilization and wound healing effects (Kim et al., 2015). Alizadeh San et al. used dialdehyde starch as a cross-linking agent to optimize the properties of films made from a mixture of collagen, hyaluronic acid, and chitosan, making them smoother, more elastic, and resistant to breakage (Sionkowska et al., 2020). Furthermore, nanocomposite films are widely used due to their controlled release of antimicrobial compounds and their biodegradability. For example, whey protein isolate, cellulose nanofibers, TiO2 nanoparticles, and rosemary essential oil nanocomposite films have significant broad-spectrum bioinhibitory effects and can be used as safe and good biological preservatives (Alizadeh Sani et al., 2017). Studies have shown that the addition of zein to a single-layer film coating for colon-targeted drug delivery can protect the active agent from degradation and early release in the stomach and small intestine, improving the drug-targeted transport capacity in colonic delivery systems (Nguyen et al., 2019). Applying CuI nanoparticle dispersions to films and fabrics can be used as anti-SARS-CoV-2 materials by virtue of their ability to release copper ions with high virucidal ability (Takeda et al., 2021). Studies have shown that liposomes, as a biocompatible and biodegradable drug delivery system, can encapsulate lipophilic drugs and release drugs slowly and continuously at the lesion site. And it has less cytotoxic effect on normal tissue, and is a good carrier of tumor chemotherapy drugs (Wang et al., 2019). The above film components show their unique advantages and effects in chemical medicine films. It is expected that the advantages of such materials can be fully absorbed in the future development of traditional Chinese medicine films, so as to make the best use of them and complement each other.

4 Preparation process of TCM film

There are many kinds of TCM film agents, but the preparation process is roughly similar, which can be divided into the preparation of TCM components and film agents. The film preparation can be divided into two parts: the dissolution of the film-forming material and the mixing of the TCM and the film-forming material (Figure 3).

4.1 Preparation of TCM ingredients

The traditional methods for extracting ingredients from TCM include decoction, immersion, percolation, reflux extraction, steam distillation, etc. The hydroalcoholic method is commonly used for purification. With the continuous introduction of new technologies, several new approaches like enzymatic extraction, ultrasonic extraction, supercritical fluid extraction and soon are applied (Figure 4), to reduce the impurities (Hou and Li., 2011).

4.2 Preparation of film agent

When preparing a film agent, usually the film-forming material should be fully dissolved with water or ethanol first, and then the preparation method will be different depending on the type of film agent. After the film preparation is completed, strict performance tests are also carried out for screening and perfecting the formula.

Film coating agent, spray film agent and gel film agent are prepared by mixing film-forming materials with TCM ingredients. For example, when preparing Chushi Tongluo film coating agent, take appropriate amounts of CMC-Na and PVA-124, respectively add distilled water to swell, heat to swell

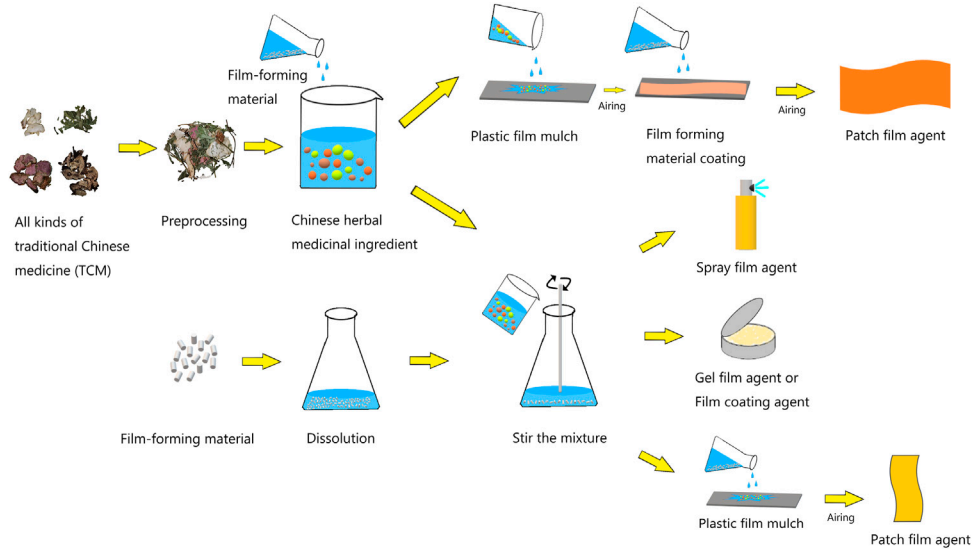

FIGURE 3
Preparation process of TCM film agent.

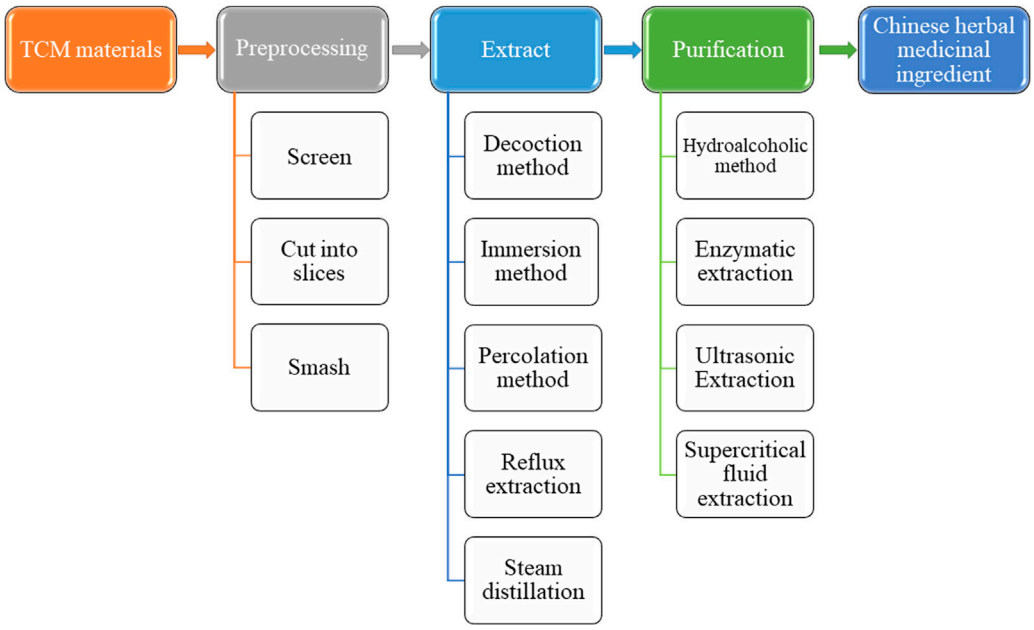

FIGURE 4
Preparation of TCM ingredients.

into a gel, mix and stir evenly, and serve as a matrix for use. Then take the medicinal extract of the formula amount and add it to the base with slow stirring (Wu et al., 2019). The patch film is first mixed with the TCM ingredients and some auxiliary film-forming materials, and then spread on a glass plate or petri dish to dry. Then the film-forming materials are spread on the dried TCM ingredients, and finally the preparation is completed by drying.

Among them, Scarpa et al. summarized the thin film casting of solutions, suspensions or melts, usually by solvent casting,

semi-solid casting, rolling, coating, and hot-melt sheet extrusion (Scarpa et al., 2017). At the same time, different preparation methods are used when preparing some chemical membranes. Wang et al. use electrostatic spinning legal preparation of dexamethasone palmitate-loaded electrospun nanofiber membrane for ocular application. It has the advantages of equipment and experimental costs, high fiber production rate, and effectively increase the absorption of drugs (Wang et al., 2020). In addition, Varan et al. cervical films prepared using inkjet printing technology show that printing technology may be suitable for the development of biological viscosity membrane combinations of antiviral and anticancer drug loads. The amount of drugs can also be controlled and modified in a specific way of patients. In addition, the diaphragm made by inkjet printing can obtain extended drug release time (Varan et al., 2017).

The formulation detailed of oral patch film by Jacob et al. is a worthy reference of the film preparation. Its commonly used film casting method is the solvent casting method, which begins with precise dispensing of the drug, adding the solvents in the proper sequence to a thermostatically controlled mixer. Then mix with an appropriate high or low shear mixer to ensure homogeneity (Jacob et al., 2021). However, the dose usually prepared in the laboratory is small, and there is no large-scale machine, but the coating method, casting method, and glue injection method are commonly used.

Pre-clinical film product development includes rigorous physical and chemical testing to assess product functionality and consistency. Standard tests for film formulations include drug content, drug content uniformity, contact angle, water content, solubility, disintegration, as well as tensile strength, puncture strength, elongation, young's modulus, folding endurance, etc (Bala et al., 2013). Among them, dosage form disintegration and dissolution are two of the most critical parameters for determining the effective level of a drug at the desired site. Grab et al. developed a quantitative texture analyser method that reduces user bias and standardizes testing, which is accurate and predictable. The disintegration time of the vaginal membrane is measured repeatedly and can also be modified to apply to other membrane types (Grab and Rohan., 2018).

The film formulation will finally complete the delivery of the active ingredients of the drug to the clinic through preparation design, absorption and release, and clinical application composed of raw materials and matrix (Ma et al., 2022). During the period, the evaluation of the efficacy of each link can reflect the overall quality of the film. It can be roughly divided into *in vivo* and *in vitro* consistency evaluation. *In vitro* includes formulation properties, *in vitro* release properties and *in vitro* transdermal properties (Zhu et al., 2020). Among them, the *in vitro* release test (IVRT) can characterize the drug solubility, particle size, etc., distinguish the difference in release ability between film agents, or evaluate the influence of small differences in the preparation process on the performance of the preparation. The most classic and convenient method is the diffusion cell method (Shao et al., 2021). In addition, emerging research methods of pharmaceutical rheology can reflect the dynamic properties of various films including flow behavior, viscoelasticity and deformation behavior. This reflects the external characteristics of the film itself, such as the viscosity of the film itself, the degree of adhesion to the medicinal site and the storage stability, and the volume and shape changes in response to external forces (Liu et al., 2022). The *in vivo* consistency evaluation pays more attention to the clinical safety and efficacy of film preparations, including studies on the equivalence of clinical endpoints, the equivalence of pharmacodynamic endpoints, the equivalence of pharmacokinetic endpoints, and skin pharmacokinetics (Zhu et al., 2020).

5 Clinical application

With the continuous development of research, the clinical contribution of TCM is becoming more and more prominent. The philosophy of TCM presents a holistic and systematic view of the treatment of various diseases. Its characteristic is to reach multiple targets and affect various pathways through synergistic therapeutic effects. Normalizes functions and maintains the balance of "yin" and "yang" in the body. In addition, TCM also has a two-way regulating effect. Common forms include regulating "yin" and "yang," cold and heat, internal and external, inhibition and stimulation, blood circulation and blood disorders. Thus, exerting a more powerful therapeutic effect than a single ingredient (Peng et al., 2022). The application of these films is gradually discovered and confirmed for treating various ulcers, skin diseases, skin repair, local inflammation and gynecological disease. In recent years, more scholars have found that TCM film agent can be further applied to other clinical diseases, which reflects that film agent has great clinical application value. At present, the research on TCM film is focusing on elucidating the effective mechanism of its efficacy, in order to provide a theoretical basis for the application of this medicine.

5.1 Treatment of ulcers

5.1.1 Oral ulcer

Oral ulcer is a common mucosal disease in the clinic and its pathogenesis is still unclear. It has the characteristics of limitation, self-healing effect, recurrence, severe wound pain. Thus, oral ulcer has a significant impact on the quality of life of patients. At present, more and more TCM films are used in the treatment of oral ulcer, greatly relieve the pain of patients. Because it can not only form a moist and airtight space on the ulcer surface to isolate the complex environment in the oral cavity, but also make the medicinal ingredients infiltrate the

TABLE 3 Commonly used oral ulcer patch formula and pharmacological mechanism.

Name of film agent	Major Chinese medicines	Pharmic function
Okra Flavonoids Oral Ulcer Film(Zhang and Chen, 2018)	Okra Flavonoids (Li et al., 2021)	Okra flavonoids have antipyretic, detoxifying, anti-inflammatory, and bacteriostatic and analgesic properties
Yang Yin Sheng Ji Pulvis (Hu et al., 2019)	Indigo naturalis, Cortex Phellodendri, Catechu, Mentha, Gentian, Bezoar, Glycyrrhiza	Bezoar detoxification, cool and refreshing, with oral pharynx sore swelling poison, pain, and decay effect
		Gentian purifies fire and dampness of the liver
		Licorice has a healing ulcer, detoxification anti-inflammatory effect
Xiaobo Muti Oral Ulcer Film (Wang et al., 2017)	*Berberis amurensis*	Barberry has the effect of clearing heat and dampness, anti-inflammatory and analgesic, reduce
		The crude extract from the fruiting body of the fungus of lamella planta had anti-inflammatory and analgesic effects
Oral Ulcer Double-layer Membrane (Cheng et al., 2017)	Cortex Phellodendri	Phellodendron has the effect of clearing heat and detoxifying, detoxifying, and treating sores
Periplaneta americana Oral Film (Li et al., 2018)	Abstract of *Periplaneta americana* L.	Periplaneta Americana can enhance immunity, promote wound healing, tissue repair and improve microcirculation
Double-layer Drug Films Of Compound Resin Draconis (Zhang et al., 2017)	Dragon's blood, *Coptis chinensis*	Dragon blood exhaust, coptis have the effect of activating blood and relieving pain

wound stably and continuously to improve the curative effect (Table 3). At present, a large number of studies have shown that traditional Chinese medicine may treat oral ulcers by affecting the NF-κB inflammatory pathway and the PTEN/AKT/GSK3β pathway (Gao et al., 2021; Zheng et al., 2021).

5.1.2 Chronic skin ulcer

Chronic skin ulcer (CSU) are skin defects caused by various causes and commonly seen in patients with leprosy and diabetes. Besides, CSU has a tendency of cancerization if it is not cured on time and it has a possibility of recurrence after curing. At present, some studies have confirmed that some TCM compound films have a certain curative effect on CSU. For example, the Shixiang plaster can promote ulcer healing by inducing angiogenesis in wound granulation tissue in diabetic foot ulcers (Fei et al., 2019). Moreover, chitosan, tea polyphenol and vitamin B_{12} were used to prepare the compound chitosan film. And researchers proved that the therapeutic effect of the film group was much higher than the control group by establishing an animal model with rabbit, providing a strong basis for clinical application of the film (Guo et al., 2007). TCM may repair the mucosa by regulating the NLRP3/Caspase-1 signaling pathway and the TGF-β1/p38MAPK signaling pathway, thereby treating skin ulcers (Huang and Wang., 2022; Xu et al., 2022).

5.2 Treatment of skin disease

As the first defense against bacteria and viruses of body, the skin is directly exposing to the outside world. Therefore, when subjected to various strong stimuli, the skin barrier is easy to be broken-down. On the other hand, the scars left by improper treatment of damaged skin tissue can seriously affect the appearance of the skin. These have both physical and psychological effects on the patient.

In recent years, more and more TCM patches have been widely used in clinical treatment of skin diseases such as warts and acne, and the effect is very remarkable. For example, through analysis on treatment of facial condyloma latum in 110 cases by Chinese herbal mask, Guo and colleagues found that feature an efficacy method. And the results showed that the effective rate was 92.63%, which has clinical promotion value (Guo and Lu., 2006). And in 2018, a statistical comparison conducted for exploring the therapeutic effect of TCM mask on acne found that TCM film has a good anti-inflammatory effect and can effectively cure acne (Ma et al., 2018). Furthermore, the application of TCM film in the treatment of skin burns and scar repair is gradually accepted. For example, Bo et al., made a burn type II spray film with a variety of TCMs such as *Radix Scutellaria*, safflower and *Cortex phellodendron*, and then a disinfectant spray film appeared in 2020, both of which can prove that the TCM film can indeed be used to treat burns and scalds (Dang et al., 2019; Ju et al., 2020). And referring to the comparative study of Wang et al., it was observed that the new compound TCM coating agent can effectively treat skin scars, and it was found that TCM can effectively inhibit the proliferation of fibroblasts (Wang et al., 2018). All indicated that TCM has a good therapeutic effect in the treatment of skin tissue damage. Studies have shown that the treatment of such skin diseases by TCM is achieved by regulating the TLR-2/NF-κB pathway, the TGF-β1/Smads signaling pathway, and the targeting of miR-21 to regulate the mTOR pathway (Ai et al., 2021; Tang et al., 2021; Xue et al., 2021).

5.3 Body care

TCM mask is a common coating formulation of TCM cosmetics. For people pursuing green, safe and high-effective beauty products, it is more inclined to develop a compound TCM mask based on doctor's prescription and penetrate directly to the skin. To improve wrinkles, chloasma, dry skin, dark yellow after long acne, facial pigmentation after burns and other common skin problems (Lei et al., 2010). For instance, the chitosan TCM mask made of *Angelica dahurica*, *Scutellaria baicalensis*, *Cape jasmine*, *Honeysuckle* and dandelion in a certain proportion. Then let 30 patients with dry skin, dark color and severe pigmentation use it for 1 month to observe the effect. The results showed that the mask has good antibacterial, whitening and moisturizing functions. And it is a new type of TCM mask with natural materials and no side effects (Xu et al., 2011). Studies have shown that the whitening effect of TCM may be managed through signaling pathways of cyclic adenosine monophosphate (cAMP)/protein kinase A (PKA)/response element binding protein (CREB), mitogen-activated protein kinase (MAPK), stem cell Factor (SCF)/c-Kit receptor, secreted glycoprotein (Wnt) etc. (Yang et al., 2021).

5.4 Local inflammation

Inflammation refers to the defensive response of living tissue with vascular system to the stimulation of various damage factors. But under certain circumstances, the body's excessive inflammatory response can cause serious damage to itself. Common local inflammatory diseases include arthritis, endophthalmitis, periodontitis, and psoriasis. The anti-inflammatory effects of herbal extracts and their related films have been extensively studied. A variety of inflammation models have confirmed that both the external treatment of TCM films and the combination of Chinese and Western medicine have a positive effect on this kind of inflammation (Li et al., 2007; Liu et al., 2019; Qiu et al., 2021).

In Wang's report, 60 patients were applied for evaluating the clinical effect of Xueshan Jinluohan analgesic film combined with diclofenac sodium sustained-release tablets in the treatment of acute gouty arthritis. It was found that the total clinical effective rate of the treatment group using the combination therapy was 86.67%, while that of the control group was only 70.00%. Thus, it refers that the use of this film to intervene in acute gouty arthritis can reduce inflammatory damage, relieve joint pain and swelling, and promote the recovery of joint function (Wang and Liu, 2018).

In the report on the treatment of endophthalmitis, the experiments by constructing a rabbit model of bacterial endophthalmitis showed that implantation of chitosan film into the suprachoroidal space could allow the drug to be absorbed from the abundant blood vessels in the choroid. Not only reduce the toxic and side effects of drugs on the retina, but also avoid the blocking effect of iris on the absorption of medicinal components. Provide experimental basis for clinical application (Li et al., 2007). Studies have confirmed that traditional Chinese medicine may play an anti-inflammatory role by acting on the COX-2/NF-κB pathway and Wnt/β-catenin and other signaling pathways (Zhang et al., 2021; Xiao et al., 2022).

5.5 Gynecological diseases

By application of TCM preparations in gynecological diseases such as cervical erosion, cervical cancer, primary dysmenorrhea, it found that the administration of films through the vaginal mucosa can increase the area of drug action, improve the utilization rate of drugs, which opened a new way on therapy gynecological diseases (Yu et al., 2018). For instance, in order to prolong the drug retention time and reduce the number of dressing changes, Wang et al., improved Erhuang Powder into a film, which has a satisfactory effect on the treatment of cervical intraepithelial neoplasia (CIN). And the film provides a feasible modern Chinese medicine preparation for treating cervical cancer (Wang et al., 2019). Studies have shown that TCM can intervene in diseases by regulating the NF-κBTGF-β1Smad pathway and endometrial receptivity-related signaling pathways such as Wnt, MAPK and STAT3 (Hu et al., 2020; Zhao et al., 2021).

5.6 Other clinical diseases

In addition to the clinical application of TCM film agents in the above studies, it is also involved in other aspects, but there are few reports on relevant studies at present (Table 4).

The above is an overview of the current stage of the clinical application of common TCM films. However, in recent years, studies have also shown that the combination of TCM film preparations with physical transdermal technology including iontophoresis and ultrasound introduction can expand the scope of transdermal drug delivery (Li et al., 2022). For example, TCM acupoint iontophoresis therapy is a new and improved treatment method, which mainly uses direct current to introduce TCM ions into the diseased part through acupoints for treatment. Xie et al. found that acupoint sticking and iontophoresis combined with oral administration of TCM are significantly more effective than oral traditional Chinese medicines alone (Xie et al., 2021). In the same way, ultrasound introduction promotes drug absorption through ultrasound technology. Fan et al. reported that the effect of ultrasonic introduction of compound *Panax notoginseng* pain-relieving ointment in the treatment of rabbit knee osteoarthritis was significantly better than the control group (Fan et al., 2017).

TABLE 4 Other clinical application and pharmacological mechanism of Chinese medicine film agent.

Name of film agent	Major Chinese medicines	Application	Pharmic function
Dragon's Blood Gel (Shi et al., 2019)	Dragon's blood, *Bletilla*	Bedsore infection	Dragon's blood is used externally to nourish muscle and collect sores, remove stasis and detumescence
Chushi Tongluo Linimen (Wu et al., 2019)	radix *Aconiti Kusnezoffii*, *Cinnamomum cassia*, *Lycopodium clavatum*, Olibanum	Eliminating dampness and dredging channels	Dispelling wind and dehumidification, activating blood and removing stasis, clearing collaterals, and relieving pain
Compound Huoxue Huayu Spraying-film (Lao et al., 2018)	*Angelica*, *Carthamus tinctorius* L.	Promoting blood circulation to remove blood stasis	Angelica indications invigorate blood, fall and fall injury. Safflower has the effect of promoting blood circulation, dispersing blood stasis, and relieving pain
Ganoderma Triterpene Nanogel (Ye et al., 2013)	*Ganodorma lucidum*	Resistance to frostbite	Triterpenoids extracted from Ganoderma lucidum have an anti-frostbite effect
Compound Liquorice Microemulsion Gel (Wang, et al., 2020)	*Glycyrrhiza*, Sophora alopecuroide	Treatment of eczema	Clear heat and detoxify, dehumidify and relieve itching
Germinal Coating Agent (Zhao et al., 2021)	*Polygonum multiflorum, Rehmannia glutinosa, Angelica*	Treatment of loose hair, sparse or total shedding, alopecia areata, alopecia totalis, and alopecia universalis	*Polygonum multiflorum* and *Rehmannia glutinosa* can nourish liver and kidney, nourish blood and grow hair

In addition to TCM films, some newly discovered medicinal film composition materials and film-forming technologies have more unique advantages and stronger therapeutic effects in clinical applications. For example, in clinical medicine, the culture of human stem cells and tumor cells plays a crucial role. The traditional cell culture method is monolayer cell culture, but it has great limitations. The hyaluronic acid-modified chitosan, graphene and other materials were used to make biofilms by means of photolithography and stamping, then construct a spheroid cell culture system. It effectively enhances the stemness and proliferation ability of some cells *in vitro*, and ensures the quality and quantity of cell culture (Ryu et al., 2019). Furthermore, the COVID-19 vaccine is the most effective means of preventing COVID-19. The newly developed vaccine-loaded nano or microparticle films can be administered orally or sublingually. The film induces protective immunity at mucosal sites, including mucosal immunity and systemic immunity. And under a large-scale epidemic, it has higher acceptability and safety. Compared with vaccine intramuscular injection, it has greater advantages (Shah et al., 2021). Moreover, conductive biomaterials based on conductive polymers, carbon nanomaterials, or conductive inorganic nanomaterials demonstrate great potential in wound healing and skin tissue engineering, owing to the similar conductivity to human skin, good antioxidant and electrically controlled drug delivery, and photothermal effect. So, infiltrating it into dressings such as films and hydrogels supplemented by electrotherapy to generate electrical stimulation can effectively promote the healing process of acute and chronic wounds at all stages (Yu et al., 2021). Besides, many 2D nanomaterials such as graphene, layered double hydroxides, etc., have been used for synaptic modulation, neuroinflammation reduction, stem cell fate modulation, and damaged nerve cell/tissue repair. Break through the difficult problems of nervous system diseases that are difficult to solve by conventional TCM films (He et al., 2022). It is expected that the above new progress in the clinical application of medicinal films can provide new inspiration and direction for the development of TCM films in the future, so that the TCM films will show greater clinical value and charm.

6 Perspectives

Film preparation is a leap from traditional drug delivery systems (tablets, powders, capsules) to new preparations of TCM preparations. Its development is rapid and related reports are increasing. With the in-depth research, the film gradually reflects the characteristics of high precision, simple process, exact curative effect, convenient portability, comfortable use and low cost. In addition, as a new type of controlled drug delivery system, film formulations have the advantages of stable administration, maintenance of local mucosal and plasma drug concentrations, greatly improved drug utilization, less side effects, direct contact with wounds for protection and isolation. Therefore, it has an irreplaceable role in clinical treatment, and it also conforms to the trend of modernization and reform of TCM preparations, and has a lot of room for development.

At the same time, the development of film agents also faces many challenges. In the early stage of preparation, the extraction process of Chinese herbal medicines is rough, the quality of the extracted active ingredients of Chinese herbal medicines is

difficult to control, and there is no standardized, easy to quantify and visualized standards for reference. In the process of preparation, factors such as operating equipment, preparation method, sample adding sequence, dose difference, and film-forming environment will affect the character and texture of film agent to a certain extent. After the preparation is completed, the application and evaluation of the finished product also needs to be updated, including the drug content, drug content uniformity, thickness, disintegration and dissolution rate of the film formulations, etc. So It is necessary to improve or invent faster, better and more economical testing methods. In addition, the pharmacological mechanism of some TCM films to exert their efficacy is still unclear. It is still necessary to continuously study and explore its pharmacological mechanism to provide a scientific basis for the cure of certain diseases and a more assured guarantee for the use of patients.

The above-mentioned problems restrict the further development of film formulations. Therefore, this paper aims to summarize the application status of Chinese medicinal materials in the film drug delivery system, in order to provide help for the research of Chinese medicinal film for the majority of scholars. In addition, in the development direction of future drug delivery systems, some scholars have continuously proposed the use of advanced nanoscale materials as drug targeted delivery carriers. The advantage of using nanomaterials is that the drug carrier is shifted from macroscopic research to microscopic, forming intelligent targeted delivery, and accurately predicting the drug delivery rate. But whether its safety and cost-effectiveness can generalize its application remains to be further investigated. It is believed that with the continuous deepening of research, more effective and more mature TCM film production technology will be launched in the future. And the TCM film with better performance and curative effect can be produced, which can be used in clinical practice to solve more medical problems.

Author contributions

DX and JS conceived, supervised, writing-reviewed the manuscript, cofounded and co-administrated the project. All other authors took a part in originally draft writing and reviewing. Authors approved the final version.

Funding

This research was supported financially by the National Natural Science Foundation of China (31560079, 32260089), the Science and Technology Department Foundation of Guizhou Province of China No. 20175733-050, 2019-027, 20195657, 20204Y018), the Special Joint Bidding Project of Zunyi Sci & Tech Bureau and Zunyi Medical University (ZSKHHZ-2020-91).

Conflict of interest

The authors declare that the research was conducted in the absence of any commercial or financial relationships that could be construed as a potential conflict of interest.

Publisher's note

All claims expressed in this article are solely those of the authors and do not necessarily represent those of their affiliated organizations, or those of the publisher, the editors and the reviewers. Any product that may be evaluated in this article, or claim that may be made by its manufacturer, is not guaranteed or endorsed by the publisher.

References

Ai, J., Yu, Y., Fei, M. H., Chen, Z. Y., and Ma, S. L. (2021). Experimental study on the effect of echinacoside on human hypertrophic scar fibroblasts and TGF-β1/Smads signaling pathway. *Chin. J. Aesthetic Plastic Surg.* 32 (3), 187–189. doi:10.3969/j.issn.1673-7040.2021.03.016

Alizadeh Sani, M., Ehsani, A., and Hashemi, M. (2017). Whey protein isolate/cellulose nanofibre/TiO2 nanoparticle rosemary essential oil nanocomposite film: Its effect on microbial and sensory quality of lamb meat and growth of common foodborne pathogenic bacteria during refrigeration. *Int. J. Food Microbiol.* 251, 8–14. doi:10.1016/j.ijfoodmicro.2017.03.018

Asghar, B. (2020). An overview on the recent developments in reactive plasticizers in polymers. *Polym. Adv. Technol.* 31 (3), 355–367. doi:10.1002/pat.4790

Bala, R., Pawar, P., Khanna, S., and Arora, S. (2013). Orally dissolving strips: A new approach to oral drug delivery system. *Int. J. Pharm. Investig.* 3 (2), 67–76. doi:10.4103/2230-973X.114897

Cai, J. L., G N, X., C, L. Y., and J, S. G. (2012). Optimization of preparation technology for compound abscess plaster. *Chin. J. Exp. Traditional Med. Formulae* 18 (2), 29–32. doi:10.3969/j.issn.1005-9903.2012.02.009

Chen, H. X., Zhang, H. Y., Liu, T. F., Li, Y., Yao, F. X., and Zhang, Q. E. (2018). Clinical effect of nanocrystalline microneedle combined with traditional Chinese medicine facial mask in treatment of female chloasma: A clinical study. *J. Anhui Univ. Chin. Med.* 37 (6), 32–34. doi:10.3969/j.issn.2095-7246.2018.06.010

Chen, J., Liu, P., and Jiang, Q. D. (2016). Idea and method of regularity knowledge of Chinese materia medica on essential oils as potential penetration enhancers based on drug property characteristics. *Chin. Traditional Herb. Drugs* 47 (24), 4305–4312. doi:10.7501/j.issn.0253-2670.2016.24.001

Chen, M., K, X. Y., Li, L. X., and Gao, Y. (2020). Formulation optimization and adhesion performance test of oral film. *J. Arrhythm.* 47 (7), 82–83. doi:10.1002/joa3.12260

Chen, X. X., Fu, J. X., and Huang, J. (2011). Clinical study of curing patients with perennial allergic rhinitis by qumin tongbi nasal spraying agent. *Chin. J. Integr. Traditional West. Med.* 31 (5), 643–646. doi:10.1007/s10008-010-1224-4

Chen, Y. S., Y, J. X., and W, Z. (2021). Preparation and quality evaluation of evodiamine hydrogel patches. *China Pharm.* 24 (3), 571–574. doi:10.3969/j.issn.1008-049X.2021.03.034

Cheng, H. D., Xing, Z. F., Jiang, S. M., and Wang, Q. L. (2017). Preparation technology and release rate of oral ulcer double-layer membranes. *Strait Pharm. J.* 29 (2), 15–17. doi:10.3969/j.issn.1006-3765.2017.02.005

Dang, X., Song, Y., Liu, M., Chen, T., Wu, D., Fan, M., et al. (2019). Study on preparation technology and quality evaluation of burn II spray film. *China Pharm.* 22 (5), 827–830. doi:10.3969/j.issn.1008-049X.2019.05.008

Dong, Y. C., Wang, Q. B., Gao, L., Zheng, T., Zhang, C. N., and Chen, L. (2019). Research progress in the external preparations containing Bletilla striata. *China Pharm.* 22 (1), 133–136. doi:10.3969/j.issn.1008-049X.2019.01.036

Fan, L. C., Shi, L. H., and Liu, S. C. (2008). Preparation of indigo naturalis film and the determination of its content. *China Med. Her.* 5 (7), 24–25. doi:10.3969/j.issn.1673-7210.2008.07.014

Fan, S. Q., Li, S., Liang, J., Lin, R. H., and Luo, Q. L. (2017). Influences of sonophoresis of Fufang Sanqi Xiaotong (Compound Notoginseng Pain-relieving) Ointment on synovial morphology and expressions of chondrocyte caspase-9 and XIAP in rabbits with knee osteoarthritis. *J. Beijing Univ. Traditional Chin. Med.* 40 (9), 750–757. doi:10.3969/j.issn.1006-2157.2017.09.008

Fei, J., Ling, Y. M., Zeng, M. J., and Zhang, K. W. (2019). Shixiang plaster, a traditional Chinese medicine, promotes healing in a rat model of diabetic ulcer through the receptor for advanced glycation end products (RAGE)/Nuclear factor kappa B (NF-κB) and vascular endothelial growth factor (VEGF)/Vascular cell adhesion molecule-1 (VCAM-1)/Endothelial nitric oxide synthase (eNOS) signaling pathways. *Med. Sci. Monit.* 25, 9446–9457. doi:10.12659/MSM.918268

Gao, J. Y., Li, Q. L., and Geng, Q. S. (2021). Lizhong decoction on the repair of the mucosa with recurrent oral ulcer in rats and the effect on NF-κB inflammation pathway. *J. Pract. Stomatology* 37 (5), 610–615. doi:10.3969/j.issn.101-3733.2021.05.005

Grab, S., and Rohan, L. C. (2018). A quantitative disintegration method for polymeric films. *J. Pharm. Innov.* 13 (4), 321–329. doi:10.1007/s12247-018-9325-1

Guo, J. Q., Guo, M. H., Kong, S. Z., Lu, S. T., and Quan, W. Y. (2020). Preparation of asiaticoside sodium alginate repair patch and its wound healing effect. *Chin. Traditional Herb. Drugs* 51 (19), 4934–4942. doi:10.7501/j.issn.0253-2670.2020.19.012

Guo, M., Yang, T., and Li, C. X. (2007). Experimental study of the compound chitosan pellicle enhancing healing of skin ulcer in rabbit. *J. Liaoning Univ. Traditional Chin. Med.* 9 (2), 137–139. doi:10.3969/j.issn.1673-842X.2007.02.097

Guo, W. L., and Lu, J. (2006). Analysis on treatment of facial condyloma latum in 110 cases by transfer factor combined with Chinese herbal mask. *J. Henan Univ. Sci. Technol. Med. Sci.* 24 (3), 227–228. doi:10.3969/j.issn.1672-688X.2006.03.040

Hao, W. Y., Li, R. T., Du, L. N., and Jin, Y. G. (2019). 3D printing technology in drug delivery system. *J. Int. Pharm. Res.* 46 (10), 725–737. doi:10.13220/j.cnki.jipr.2019.10.001

He, X. R., Wang, X. X., Fang, J. C., Zhao, Z. F., Huang, L., Guo, H., et al. (2017). Bletilla striata: Medicinal uses, phytochemistry and pharmacological activities. *J. Ethnopharmacol.* 195, 20–38. doi:10.1016/j.jep.2016.11.026

He, X. X., Lu, W., Sun, C. X., Khalesi, H., Mata, A., Andaleeb, R., et al. (2021). Cellulose and cellulose derivatives: Different colloidal states and food-related applications. *Carbohydr. Polym.* 255, 117334. doi:10.1016/j.carbpol.2020.117334

He, X., Zhu, Y., Ma, B., Xu, X., Huang, R., Cheng, L., et al. (2022). Bioactive 2D nanomaterials for neural repair and regeneration. *Adv. Drug Deliv. Rev.* 187, 114379. doi:10.1016/j.addr.2022.114379

Hou, F. Y., and Li, J. (2011). Chinese traditional medicine extraction modern new technology is reviewed. *Guid. J. Traditional Chin. Med. Pharm.* 17 (1), 101–103. doi:10.3969/j.issn.1672-951X.2011.01.052

Hu, Y. S., Li, X. X., and Liu, J. G. (2019). A systematic review of Yang Yin Sheng Ji pulvis (membranae) for the treatment of recurrent oral ulcer. *J. Pract. Stomatology* 35 (1), 66–70. doi:10.3969/j.issn.1001-3733.2019.01.015

Hu, Y., Zhong, X. L., Zhou, Z. Q., and Du, X. L. (2020). Research progress on the influence of traditional Chinese medicine on signal pathways related to endometrial peceptivity. *J. Liaoning Univ. Traditional Chin. Med.* 22 (6), 201–205. doi:10.13194/j.issn.1673-842x.2020.06.053

Huang, W. D., and Wang, Z. H. (2022). MicroRNA-based approach for quantification of the drug efficacy of traditional Chinese medicine. *Chin. J. Med. Guide* 24 (2), 116–121. doi:10.3969/j.issn.1009-0959.2022.02.002

Jacob, S., Nair, A. B., Boddu, S. H. S., Gorain, B., Sreeharsha, N., and Shah, J. (2021). An updated overview of the emerging role of patch and film-based buccal delivery systems. *Pharmaceutics* 13 (8), 1206. doi:10.3390/PHARMACEUTICS13081206

Jantrawut, P., Bunrueangtha, J., Suerthong, J., and Kantrong, N. (2019). Fabrication and characterization of low methoxyl pectin/gelatin/carboxymethyl cellulose absorbent hydrogel film for wound dressing applications. *Mater. (Basel)* 12 (10), 1628. doi:10.3390/ma12101628

Jin, L., Wang, J. Y., Tong, Y., Dong, M. H., Ma, Z. S., and Wang, L. (2012). Review of researches on plastics. *Chin. J. Exp. Traditional Med. Formulae* 18 (8), 277–280. doi:10.3969/j.issn.1005-9903.2012.08.082

Ju, B., Tang, H., Tang, Q., Zhang, X., Lan, Z. P., and Tan, L. H. (2020). Preparation process of a disinfection spray film. *China Pharm.* 29 (19), 36–39. doi:10.3969/j.issn.1006-4931.2020.19.010

Kamoun, E. A., Loutfy, S. A., Hussein, Y., and Kenawy, E. S. (2021). Recent advances in PVA-polysaccharide based hydrogels and electrospun nanofibers in biomedical applications: A review. *Int. J. Biol. Macromol.* 187, 755–768. doi:10.1016/J.IJBIOMAC.2021.08.002

Kathe, K., and Kathpalia, H. (2017). Film forming systems for topical and transdermal drug delivery. *Asian J. Pharm. Sci.* 12 (6), 487–497. doi:10.1016/j.ajps.2017.07.004

Ke, Y. S., Zhang, C., Pei, L., Wang, L., Liu, W., and Cui, J. (2018). Research review on new TCM external preparations. *Acta Chin. Med.* 33 (5), 835–839. doi:10.16368/j.issn.1674-8999.2018.05.199

Kim, J. O., Noh, J. K., Thapa, R. K., Hasan, N., Choi, M., Kim, J. H., et al. (2015). Nitric oxide-releasing chitosan film for enhanced antibacterial and *in vivo* wound-healing efficacy. *Int. J. Biol. Macromol.* 79, 217–225. doi:10.1016/j.ijbiomac.2015.04.073

Kitt, E., Friderici, J., Kleppel, R., and Canarie, M. (2015). Procedural sedation for MRI in children with ADHD. *Paediatr. Anaesth.* 25 (10), 1026–1032. doi:10.1111/pan.12721

Lao, R., Zhao, F., Jin, X., Lu, J., and Liu, R. (2018). Preparation of Compound Huoxue Huayu spraying-film (CHH-SF) preparation based on central composite design and artificial neural network modeling. *Tianjin J. Traditional Chin. Med.* 35 (12), 951–955. doi:10.11656/j.issn.1672-1519.2018.12.21

Lei, F., Tang, Y. L., Xie, W. G., Zhang, Y., Zhang, W. D., and Huang, W. W. (2010). Treatment of facial pigmentation after burns with traditional Chinese medicine mask and skin care. *Chin. J. Burns* 26 (6), 420–424. doi:10.3760/cma.j.issn.1009-2587.2010.06.005

Leng, Q., Li, Y., Pang, X., Wang, B., Wu, Z., Lu, Y., et al. (2020). Curcumin nanoparticles incorporated in PVA/collagen composite films promote wound healing. *Drug Deliv.* 27 (1), 1676–1685. doi:10.1080/10717544.2020.1853280

Li, C. X., Wang, X. C., Yu, Y. X., Chen, K. X., Li, X. M., and Miao, M. S. (2022). Research progress of new external preparations of traditional Chinese medicine. *China Pharm.* 33 (3), 372–377. doi:10.6039/j.issn.1001-0408.2022.03.19

Li, J., Chen, Z. J., Shi, J. F., Xiao, Q., Wang, M., Jiang, H. J., et al. (2018). Preparation of *Periplaneta americana* oral film and investigation of its antioral ulcer action. *Chin. J. Exp. Traditional Med. Formulae* 24 (23), 29–36. doi:10.13422/j.cnki.syfjx.20182007

Li, J., Wang, D. M., Xu, Y. H., and Tang, Z. (2005). Survey on transdermal drug delivery preparation of Chinese materia medica compound prescription. *Chin. Traditional Herb. Drugs* 36 (8), 1254–1257. doi:10.3321/j.issn:0253-2670.2005.08.056

Li, L. J., Jin, Z. Q., Zhou, H. Z., Zhou, X., Yan, Y. H., and Gao, Y. X. (2007). Chitosan drug membrane administrated into perichoroidal space against bacterial endophthalmitis in rabbits. *Recent Adv. Ophthalmol.* 27 (12), 904–907. doi:10.13389/j.cnki.rao.2007.12.013

Li, P., Li, L., Zhuang, Y., Guo, H. Q., Chen, Q., and An, B. C. (2005). The creation of Laosun Yutie plaster and safety experiment. *China J. Chin. Materia Medica* 30 (9), 697–699. doi:10.3321/j.issn:1001-5302.2005.09.016

Li, Q., Wu, Y., Zheng, J., and Lu, H. Q. (2013). Efficacy of self-made sustained release film of kouyanqing on recurrent aphthous UlcerA clinical observation of 58 cases. *Guiding J. Traditional Chin. Med. Pharmacol.* 6, 19–21. doi:10.3969/j.issn.1672-951X.2013.06.007

Li, Y., Ma, Z. H., Yang, X., Gao, Y. P., Ren, Y., Li, Q. M., et al. (2021). Investigation into the physical properties, antioxidant and antibacterial activity of Bletilla striata polysaccharide/chitosan membranes. *Int. J. Biol. Macromol.* 182 (35), 311–320. doi:10.1016/J.IJBIOMAC.2021.04.037

Liu, A. T., Zhang, H. C., Luo, Y. P., Huang, W. L., and Liao, H. W. (2019). Preparation and application of Shuanghuang gel. *China Contin. Med. Educ.* 11 (28), 144–146. doi:10.3969/j.issn.1674-9308.2019.28.061

Liu, J. P., Li, Y. M., Zhang, L. X., and Sun, Y. (2000). Studies on the antitussive and antiasthmatic film. *J. China Pharm. Univ.* 31 (6), 426–428. doi:10.13684/j.cnki.spkj.2021.10.035

Liu, L. H., Xu, G. J., Cheng, R., Chen, K., and Zhao, A. X. (2021). Preparation and characterization of konjac glucomannan based gardenia yellow pigment film. *Food Sci. Technol.* 46 (10), 221–226. doi:10.13684/j.cnki.spkj.2021.10.035

Liu, Y. L., and Cui, G. C. (2019). Effect of metronidazole membrane combined with minocycline hydrochloride ointment on the level of inflammatory factors and

periodontal index in patients with chronic periodontitis. *J. Community Med.* 17 (21), 1352–1355. doi:10.19790/j.cnki.JCM.2019.21.11

Liu, Z. H., Heng, W. L., Qian, S., Wei, Y. F., Zhang, J. J., and Gao, Y. (2022). Advances in rheological study of topical preparations for skin. *J. China Pharm. Univ.* 53 (1), 105–112. doi:10.11665/j.issn.1000-5048.20220116

Lu, H., Yuan, L., Yu, X. Z., Wu, C. Z., He, D. F., and Deng, J. (2018). Recent advances of on-demand dissolution of hydrogel dressings. *Burns Trauma* 6 (4), 35–254. doi:10.1186/s41038-018-0138-8

Ma, J. H., Zhong, X., Qin, Z. Y., Lin, H. J., and Xu, H. D. (2018). The study of the therapeutic effect of traditional Chinese medicine mask on the acne animal models. *Chin. J. Aesthetic Med.* 27 (7), 72–75. doi:10.15909/j.cnki.cn61-1347/r.002489

Ma, L. X., Qi, Y. L., Zhuang, X. Y., Zhang, J., and Yu, Y. X. (2022). Research progress on quality transfer process and evaluation methods of TCM external preparations. *J. Nanjing Univ. Traditional Chin. Med.* 38 (1), 9–17. doi:10.14148/j.issn.1672-0482.2022.0009

Moebus, K., Siepmann, J., and Bodmeier, R. (2012). Novel preparation techniques for alginate-poloxamer microparticles controlling protein release on mucosal surfaces. *Eur. J. Pharm. Sci.* 45 (3), 358–366. doi:10.1016/j.ejps.2011.12.004

Muxika, A., Etxabide, A., Uranga, J., Guerrero, P., and de la Caba, K. (2017). Chitosan as a bioactive polymer: Processing, properties and applications. *Int. J. Biol. Macromol.* 105 (2), 1358–1368. doi:10.1016/j.ijbiomac.2017.07.087

Naomi, R., Bt Hj Idrus, R., and Fauzi, M. B. (2020). Plant- vs. Bacterial-derived cellulose for wound healing: A review. *Int. J. Environ. Res. Public Health* 17 (18), 6803. doi:10.3390/ijerph17186803

Nguyen, M. N. U., Tran, P. H. L., and Tran, T. T. D. (2019). A single-layer film coating for colon-targeted oral delivery. *Int. J. Pharm.* 559, 402–409. doi:10.1016/j.ijpharm.2019.01.066

Niu, W. H., Gao, C. X., Luo, Q. J., Zhou, Y. F., Ji, Y. R., and Tan, L. (2007). The clinical research of sticking membrane for coronary heart disease to treating coronary heart disease and angina. *China J. Chin. Med.* 22 (5), 34. doi:10.3969/j.issn.1674-8999.2007.05.017

Nunes, P. S., Albuquerque-Junior, R. L., Cavalcante, D. R., Dantas, M. D., Cardoso, J. C., Bezerra, M. S., et al. (2011). Collagen-based films containing liposome-loaded usnic acid as dressing for dermal burn healing. *J. Biomed. Biotechnol.* 2011, 761593. doi:10.1155/2011/761593

Peng, X., Tang, F., Yang, Y., Li, T., Hu, X., Li, S., et al. (2022). Bidirectional effects and mechanisms of traditional Chinese medicine. *J. Ethnopharmacol.* 30, 115578. doi:10.1016/j.jep.2022.115578

Qiu, F., Xi, L., Chen, S., Zhao, Y., Wang, Z., and Zheng, Y. (2021). Celastrol niosome hydrogel has anti-inflammatory effect on skin keratinocytes and circulation without systemic drug exposure in psoriasis mice. *Int. J. Nanomedicine* 16, 6171–6182. doi:10.2147/IJN.S323208

Rezvanian, M., Ahmad, N., Mohd Amin, M. C., and Ng, S. F. (2017). Optimization, characterization, and *in vitro* assessment of alginate-pectin ionic cross-linked hydrogel film for wound dressing applications. *Int. J. Biol. Macromol.* 97, 131–140. doi:10.1016/j.ijbiomac.2016.12.079

Ryu, N. E., Lee, S. H., and Park, H. (2019). Spheroid culture system methods and applications for mesenchymal stem cells. *Cells* 8 (12), 1620. doi:10.3390/cells8121620

Scarpa, M., Stegemann, S., Hsiao, W. K., Pichler, H., Gaisford, S., Bresciani, M., et al. (2017). Orodispersible films: Towards drug delivery in special populations. *Int. J. Pharm.* 523 (1), 327–335. doi:10.1016/j.ijpharm.2017.03.018

Shah, S. M., Alsaab, H. O., Rawas-Qalaji, M. M., and Uddin, M. N. (2021). A review on current COVID-19 vaccines and evaluation of particulate vaccine delivery systems. *Vaccines (Basel)* 9 (10), 1086. doi:10.3390/vaccines9101086

Shao, P., Zheng, J. Q., Pan, F. F., Liang, W. Q., Gao, J. Q., and Hong, L. Y. (2021). *In vitro* release tests and equivalence evaluation for topical semisolid dosage forms. *Chin. J. Mod. Appl. Pharm.* 38 (20), 2481–2487. doi:10.13748/j.cnki.issn1007-7693.2021.20.001

Shen, C. Y., Shen, B. D., Shen, G., Li, J., Zhang, F. C., Xu, P. H., et al. (2016). Therapeutic effects of nanogel containing triterpenoids isolated from Ganoderma lucidum (GLT) using therapeutic ultrasound (TUS) for frostbite in rats. *Drug Deliv.* 23 (7/8), 2643–2650. doi:10.3109/10717544.2015.1044051

Shi, C., Wang, K. D., Zhang, R. P., and Geng, Z. H. (2019). The preparation and clinical application of Dragon′s blood gel. *J. Hebei Med. Univ.* 40 (2), 208–212. doi:10.3969/j.issn.1007-3205.2019.02.021

Sionkowska, A., Michalska-Sionkowska, M., and Walczak, M. (2020). Preparation and characterization of collagen/hyaluronic acid/chitosan film crosslinked with dialdehyde starch. *Int. J. Biol. Macromol.* 15 (149), 290–295. doi:10.1016/j.ijbiomac.2020.01.262

Takeda, Y., Jamsransuren, D., Nagao, T., Fukui, Y., Matsuda, S., and Ogawa, H. (2021). Application of copper iodide nanoparticle-doped film and fabric to inactivate SARS-CoV-2 via the virucidal activity of cuprous ions (Cu+). *Appl. Environ. Microbiol.* 87 (24), e0182421. doi:10.1128/AEM.01824-21

Tang, Z. M., Ding, J. C., and Zhai, X. X. (2021). Effect of galla chinensis ointment extracting solution on the proliferation and apoptosis of keloid fibroblasts by miR-21 regulating mTOR signaling pathway. *J. Pract. Dermatology* 14 (3), 129–135. doi:10.11786/sypfbxzz.1674-1293.20210301

Tavakoli, S., and Klar, A. S. (2020). Advanced hydrogels as wound dressings. *Biomolecules* 10 (8), 1169. doi:10.3390/biom10081169

Tong, X. L., Bian, Q., Zhang, J. Y., and Luo, H. F. (2018). Liquid crystal technology and its application in topical preparation. *Chin. J. Pharm.* 49 (3), 284–291. doi:10.16522/j.cnki.cjph.2018.03.002

Varan, C., Wickström, H., Sandler, N., Aktaş, Y., and Bilensoy, E. (2017). Inkjet printing of antiviral PCL nanoparticles and anticancer cyclodextrin inclusion complexes on bioadhesive film for cervical administration. *Int. J. Pharm.* 531 (2), 701–713. doi:10.1016/j.ijpharm.2017.04.036

Vasyuchenko, E. P., Orekhov, P. S., Armeev, G. A., and Bozdaganyan, M. E. (2021). CPE-DB: An open database of chemical penetration enhancers. *Pharmaceutics* 13 (1), 66. doi:10.3390/PHARMACEUTICS13010066

Wang, H. C., and Liu, J. (2018). Clinical study on xueshan jinluohan analgesic coating agent combined with diclofenac sodium sustained release tablets in treatment of acute gouty arthritis. *Drugs & Clin.* 33 (10), 2642–2646. doi:10.7501/j.issn.1674-5515.2018.10.038

Wang, H., Qu, R. J., Liu, Y., and Zhao, X. X. (2018). Study of the efficacy and mechanism of new compound Chinese medicine coating agent on skin scars. *Chin. J. Aesthetic Plastic Surg.* 29 (2), 89–92. doi:10.3969/j.issn.1673-7040.2018.02.007

Wang, H. Y. (2018). Study on the application performance of hydroxylpropyl methyl cellulose as a kind of membrane-forming agent. *Tianjin Agric. Sci.* 24 (6), 60–62. doi:10.3969/j.issn.1006-6500.2018.06.015

Wang, J., Huang, Z. G., Chen, H. L., and Liu, C. C. (2017). Study on the processing technology of transdermal preparation of Chinese herbal compound preparation based on rapid release transdermal delivery system. *J. Chin. Med. Mater.* 40 (12), 2913–2916. doi:10.13863/j.issn1001-4454.2017.12.038

Wang, J. Y., Ma, S. W., Zhao, X. Y., Chen, J. J., Liu, Y. J., Deng, L. L., et al. (2020). Preparation of compound liquorice microemulsion gel and its pharmacodynamics evaluation. *China J. Chin. materia medica* 45 (21), 5193–5199. doi:10.19540/j.cnki.cjcmm.20200819.302

Wang, M., Chen, L., Huang, W., Jin, M., Wang, Q., Gao, Z., et al. (2019). Improving the anti-keloid outcomes through liposomes loading paclitaxel-cholesterol complexes. *Int. J. Nanomedicine* 14, 1385–1400. doi:10.2147/IJN.S195375

Wang, Q., Li, Y. R., Li, Q., Hu, X. Y., Liu, S., Wei, H., et al. (2019). Preparation and evaluation of the spray film with Clematis root. *J. Qingdao Univ. Sci. Technol. Nat. Sci. Ed.* 40 (5), 37–43. doi:10.16351/j.1672-6987.2019.05.005

Wang, X., Sun, X. Y., and Cao, J. (2020). Preparation and evaluation of dexamethasone palmitate-loaded electrospun nanofiber membrane for ocular application. *Med. J. Wuhan Univ.* 41 (5), 832–835. doi:10.14188/j.1671-8852.2018.1041

Wang, X., Zhang, L. Y., and Chen, Y. (2016). Nanocarrier-based topical drug delivery system for the treatment of skin diseases. *J. Pract. Dermatology* 9 (1), 41–44. doi:10.11786/sypfbxzz.1674-1293.20160113

Wang, Y. H., Yang, L., Wang, C., Guan, F., Han, F. J., and Pharmacy, S. O. (2019). Optimization of formulation of erhuangsan bletillae rhizoma gelatin sustained release double-layer membrane by central composite design-response surface methodology. *Chin. J. Exp. Traditional Med. Formulae* 25 (4), 146–152. doi:10.13422/j.cnki.syfjx.20182406

Wang, Y. L., Guo, P. J., Wang, T. H., Ding, J. L., Li, D. Y., and Bao, H. Y. (2017). Preparation and pharmacodynamic analysis of xiaobo muti oral ulcer film. *Chin. J. Exp. Traditional Med. Formulae* 23 (20), 20–24. doi:10.13422/j.cnki.syfjx.2017200020

Wang, Y. R., Feng, B., Ju, J., Cheng, L. F., Wang, J., Gu, Y., et al. (2020). Carboxymethyl *Bletilla striata* polysaccharide-chitosan@curcumin polyelectrolyte complex films: Preparation and characterization. *Chin. Traditional Herb. Drugs* 51 (4), 978–985. doi:10.7501/j.issn.0253-2670.2020.04.023

Wasiak, J., Cleland, H., Campbell, F., and Spinks, A. (2013). Dressings for superficial and partial thickness burns. *Cochrane Database Syst. Rev.* 2013 (3), Cd002106. doi:10.1002/14651858.CD002106.pub4

Wu, X. L., Sun, J. S., Bai, Z. X., and Guo, D. L. (2019). Preparation and *in vitro* transdermal behavior of Chushi Tongluo liniment. *J. Chin. Med. Mater.* 42 (1), 156–160. doi:10.13863/j.issn1001-4454.2019.01.033

Wu, Z. (2021). Analysis on the curative effect of lavender essential oil film in the treatment of second-degree scalds on hands. *Chin. J. Burns Wounds Surf. Ulcers* 33 (2), 115–117. doi:10.3969/j.issn.1001-0726.2021.02.010

Xiao, Q., Guo, Z. L., and Yang, X. H. (2022). Study of the mechanism of ligustrazine in delaying cartilage degeneration in knee osteoarthritis based on

wnt/β-catenin signaling pathway. *Guid. J. Traditional Chin. Med. Pharmacol.* 28 (2), 3752–3842. doi:10.13862/j.cnki.cn43-1446/r.2022.02.041

Xiao, Z., Li, Z., Sun, Y. Y., Lin, R. Q., and Mo, X. M. (2021). Review of taste masking techniques in Chinese patent medicine. *Chin. Med. J.* 2, 333–339. doi:10.19540/j.cnki.cjcmm.20200827.602

Xie, Z. H., Luo, C., Xu, H. T., and Zhang, T. T. (2021). Clinical observation on treatment of sequelae of pelvic inflammatory disease by acupoint application and iontophoresis combined with traditional Chinese medicine. *World Clin. Drugs* 42 (4), 274–278. doi:10.13683/j.wph.2021.04.008

Xin, Z. B. (2012). Analysis on curative efficacy of XiaoDing PenMoJi in treating 36 cases of traumatic limb swelling. *West. J. Traditional Chin. Med.* 25 (9), 49–50. doi:10.3969/j.issn.1004-6852.2012.09.022

Xu, J., Guan, C. M., and Wang, T. (2011). Research on the Mask of Chitosan mixed with Chinese traditional medicine. *Chin. J. Aesthetic Med.* 20 (4), 664–666. doi:10.3969/j.issn.1008-6455.2011.04.053

Xu, X. Y., Yang, X., Liang, G. Q., Zhu, H. P., Huang, X., Wang, A. M., et al. (2022). Effect of quyu humo paste on the repair of esophageal mucosa in rats with reflux esophagitis by regulating NLRP3/caspase-1 signaling pathway. *J. Nanjing Univ. Traditional Chin. Med.* 38 (4), 315–322. doi:10.14148/j.issn.1672-0482.2022.0315

Xue, B., Zhao, Y. P., Cheng, X. M., Xue, S. S., Ren, W. W., Yang, C. R., et al. (2021). Improving function of qing Xiao method on local inflammatory response of acne in rats by regulating TLR-2/NF-κB pathway. *Chin. J. Basic Med. Traditional Chin. Med.* 27 (8), 12751331–12761278. doi:10.19945/j.cnki.issn.1006-3250.2021.08.021

Xue, Q., Cong, Z. F., Xiao, Z. D., Yu, X. J., He, M. Y., Gao, P., et al. (2022). Review on research of acupoint Application preparation of traditional Chinese medicine in recent ten years. *Chin. J. Basic Med. Traditional Chin. Med.* 28 (5), 785–791. doi:10.19945/j.cnki.issn.1006-3250.2022.05.024

Yang, X., Lu, Y. H., Mao, Y. X., Niu, S. R., Dong, Z. B., Qin, K. M., et al. (2021). Evaluation of bioequivalence between generic and brand-name clozapine in Chinese schizophrenic patients: A randomized, two-period, crossover study. *Int. J. Clin. Pharmacol. Ther.* 23 (6), 578–584. doi:10.5414/CP203864

Ye, Y. J., Shu, X., Liu, M., and Gong, W. J. (2013). Optimization of the formulation of Beima spraying-film preparation by the central composite design-response surface methodology. *Chin. J. Hosp. Pharm.* 33 (11), 878–880. doi:10.13286/j.cnki.chinhosppharmacyj.2013.11.004

Yu, R., Zhang, H., and Guo, B. (2021). Conductive biomaterials as bioactive wound dressing for wound healing and skin tissue engineering. *Nanomicro. Lett.* 14 (1), 1. doi:10.1007/s40820-021-00751-y

Yu, S., Wen, Y., Xia, W., Yang, M., Lv, Z., Li, X., et al. (2018). Acupoint herbal plaster for patients with primary dysmenorrhea: Study protocol for a randomized controlled trial. *Trials* 19 (1), 348. doi:10.1186/s13063-018-2682-8

Yuan, J. R., Wang, A. W., Jing, S. H., and Yuan, H. (2003). Research progression of transcutaneous administration in Chinese medicine and percutaneous absorption of Chinese herbs and drugs. *China J. Traditional Chin. Med. Pharm.* 18 (4), 243–246. doi:10.3969/j.issn.1673-1727.2003.04.019

Yuan, Y., Shen, H. P., Zhao, F. L., Wang, Q., and Li, Q. P. (2013). Experimental study of anti-inflammatory and analgesic effect of Fufangyatong film. *J. Luzhou Med. Coll.* 5, 451–454. doi:10.3969/j.issn.1000-2669.2013.05.008

Zhang, C. Z., and Chen, J. (2018). Preparation and evaluation of okra flavonoids oral ulcer film. *Strait Pharm. J.* 8, 6–9. doi:10.3969/j.issn.1006-3765.2018.08.002

Zhang, N., Hou, X., Zhang, W., and Shi, B. H. (2021). Glycyrrhizin plays a role in the treatment of periodontitis by regulating the COX-2/NF-κB signaling pathway. *J. Mol. Diagnosis Ther.* 13 (9), 1469–1472. doi:10.3969/j.issn.1674-6929.2021.09.024

Zhang, P., Liu, M. X., Pang, Y. J., Chen, H. Y., Zhu, Y. Z., and Chen, X. (2016). Research on the preparation of "Ophthalmic Washing Solution No.1" Chinese traditional medicine liniment. *Tianjin J. Traditional Chin. Med.* 33 (7), 437–439. doi:10.11656/j.issn.1672-1519.2016.07.14

Zhang, Q. L., Zhang, Z. L., and Lei, G. L. (2007). Survey of studies on traditional chinese medicine pigment. *Tradit. Chin. Med.* 26 (6), 1270–1272. doi:10.3969/j.issn.1673-7717.2007.06.084

Zhang, S. X., Yu, X. L., and Zou, Y. L. (2017). Development of double-layer drug films of compound resina draconis against recurrent oral ulcer. *Chin. J. Hosp. Pharm.* 37 (4), 322–324. doi:10.13286/j.cnki.chinhosppharmacyj.2017.04.02

Zhang, S. Y., Sun, D. F., and Zhu, C. L. (2014). Studies on Bletilla oral ulcer film. *Chin. Wild Plant Resour.* 33 (4), 68–71. doi:10.3969/j.issn.1006-9690.2014.04.019

Zhang, Y. H., Li, N., Xu, J. C., and Li, X. (2004). Applications of polyvinyl alcohol in modern preparations of TCM. *China J. Chin. Materia Medica* 29 (2), 101–103. doi:10.3321/j.issn:1001-5302.2004.02.003

Zhao, F. F., Chi, B., Li, D. H., and Feng, J. T. (2021). AThe mechanism of Taohong Siwu decoction regulating NF-κB/TGF-β1/Smad pathway to inhibit intrauterine adhesion. *Med. J. West China* 33 (12), 1732–1736. doi:10.3969/j.issn.1672-3511.2021.12.004

Zhao, J., Li, H. H., and Wang, X. (2021). Effect of oral decoction of traditional Chinese medicine combined with acupoint application for assisted treating women with tubal infertility after hydrotubation. *Chin. J. Fam. Plan.* 29 (8), 1660–1663. doi:10.3969/j.issn.1004-8189.2021.08.025

Zheng, L., Li, G. F., Yang, P. P., and Shan, Z. M. (2021). Effect of yiqi yangyinshengji prescription on the healing of oral ulcer in rats and its mechanism in PTEN/AKT/GSK3β pathway. *Pharmacol. Clin. Chin. Materia Medica* 37 (3), 023. doi:10.13412/j.cnki.zyyl.2021.03.023

Zhou, T. T., Cai, Z. Y., Pan, Y., Wang, C. Y., and Qian, Y. Y. (2019). Preparation and performance evaluation of traditional Chinese medicine whitening and moisturizing facial mask. *Deterg. Cosmet.* 42 (9), 30–33. doi:10.3969/j.issn.1006-7264.2019.09.008

Zhu, S. M., Chen, H. Y., and Fan, Z. D. (2019). Research progress on dosage forms of Bletilla striata gum. *Chin. J. Mod. Appl. Pharm.* 36 (24), 3130–3135. doi:10.13748/j.cnki.issn1007-7693.2019.24.028

Zhu, Y. F., Zhang, Z. Q., and Xu, C. (2020). R&D requirements and consistency evaluation of topical skin preparations in *in vitro* and *in vivo* tests. *Chin. J. Pharm.* 51 (4), 524–531. doi:10.16522/j.cnki.cjph.2020.04.017

Zhu, Y. L., Huang, H., Ding, X. L., and Ren, Y. Z. (2015). Preparation technology of huayu xiaozhong spray films. *J. Chin. Med. Mater.* 38 (11), 2399–2403. doi:10.13863/j.issn1001-4454.2015.11.039

Frontiers in Pharmacology

Explores the interactions between chemicals and living beings

The most cited journal in its field, which advances access to pharmacological discoveries to prevent and treat human disease.

Discover the latest Research Topics

See more →

Frontiers

Avenue du Tribunal-Fédéral 34
1005 Lausanne, Switzerland
frontiersin.org

Contact us

+41 (0)21 510 17 00
frontiersin.org/about/contact